

4-22-2015 12:00 AM

Stellar Spectroscopy: New Methods and Insights

Sanaz S. Golriz, *The University of Western Ontario*

Supervisor: Professor John Landstreet, *The University of Western Ontario*

Joint Supervisor: Professor Jan Cami, *The University of Western Ontario*

A thesis submitted in partial fulfillment of the requirements for the Doctor of Philosophy degree
in Astronomy

© Sanaz S. Golriz 2015

Follow this and additional works at: <https://ir.lib.uwo.ca/etd>



Part of the [Atomic, Molecular and Optical Physics Commons](#), [Other Astrophysics and Astronomy Commons](#), [Other Physics Commons](#), [Physical Processes Commons](#), and the [Stars, Interstellar Medium and the Galaxy Commons](#)

Recommended Citation

Golriz, Sanaz S., "Stellar Spectroscopy: New Methods and Insights" (2015). *Electronic Thesis and Dissertation Repository*. 2758.

<https://ir.lib.uwo.ca/etd/2758>

This Dissertation/Thesis is brought to you for free and open access by Scholarship@Western. It has been accepted for inclusion in Electronic Thesis and Dissertation Repository by an authorized administrator of Scholarship@Western. For more information, please contact wlsadmin@uwo.ca.

STELLAR SPECTROSCOPY: NEW METHODS AND INSIGHTS
(Thesis format: Integrated Article)

by

Sanaz Golriz

Graduate Program in Physics and Astronomy

A thesis submitted in partial fulfillment
of the requirements for the degree of
Doctor of Philosophy

The School of Graduate and Postdoctoral Studies
The University of Western Ontario
London, Ontario, Canada

© Sanaz Sadat Golriz 2015

Abstract

The study of the chemical evolution of stars is of crucial importance since they play a major role in the enrichment of the chemistry of the universe. Throughout their lifetime, stars undergo several processes that can alter their chemistry. Gradually, the nucleosynthesis products from the interior of the star are radiatively and convectively levitated and mixed with the upper layers of the atmosphere. In the later stages of their evolution, low to intermediate mass stars ($0.8-8.0 M_{\odot}$) eject a significant fraction of these nucleosynthesis products, resulting in a circumstellar envelope of gas and dust around the central star with a very different and intriguing chemical composition. Through radiation pressure, this material will sail into the interstellar medium.

We offer the first extensive study concerning the atmospheric abundance determination using ultraviolet spectra, for two slow rotating non-magnetic early A-type (HD72660) and B-type (iota Herculis) stars. We carry out spectrum synthesis of the available UV spectra using the program ZEEMAN followed by a detailed abundance analysis. We find lines of several previously unstudied elements in the atmospheres of the two stars under study, implying the activity of phenomena such as radiative levitation against gravity. In addition to finding new elements, we demonstrate that spectrum synthesis using ZEEMAN in the ultraviolet is indeed a reliable source for abundance determination.

This study is followed by a very careful and detailed infrared spectroscopy of a sample of evolved AGB stars in the final stages of their evolution. The sample is unique in a sense that properties such as distance, metallicity, initial mass of the parent star are comparable while the only variable is the age on the AGB phase. Throughout this study we shed light on the significance of interstellar extinction and its previously under-acknowledged influence on the infrared spectra. We introduce tools and methods that will allow us to separately model the spectrum of the photosphere and the molecular layers alone. We extract the dust spectra and present a qualitative analysis of the intriguing peculiarities.

Keywords: Stellar Spectroscopy, Stellar Evolution, Synthesis, Infrared, UV

Co-Authorship Statement

This thesis consists of three articles and each of them are based on the work in collaboration with the several co-authors.

Chapters 2 and 3: These two chapters respectively, present an extensive study of elemental abundance determination using ultraviolet spectrum synthesis for the two early type stars; Iota Herculis and HD72660. The main project was the original idea of Dr. J. D. Landstreet and was accomplished by myself under his supervision.

Chapter 4: In this chapter, we present a thorough study of the infrared spectra using a unique sample of AGB stars in the Galactic bulge. The principal investigator for this project is Dr. J.A.D.L. Blommaert. The majority of the work involved with the project was carried out by myself under supervision of Dr. J. Cami. This article is published in MNRAS in collaboration with; E. Vanhollebeke, M.A.T. Groenewegen, H.J. Habing, F. Kemper, M. Schultheis, A.G.G.M. Tielens, L.B.F.M. Waters, P.R. Wood.

Acknowledgements

First and foremost I offer my sincerest gratitude to my supervisor, Dr. John Landstreet, who has supported me throughout my project with his patience and knowledge whilst allowing me the room to work in my own way. I attribute the level of my PhD degree to his encouragement and effort and without him this work, too, would not have been accomplished.

I would like to show my gratitude to my advisory committee, Dr. Shantanu Basu and Dr. Sarah Gallagher who provided me with numerous constructive advices which guided me in my way to accomplish this work. It is a pleasure to thank the Department of Physics and Astronomy for providing the support I have needed to pursue and complete my projects. I would like to thank Dr. Jan Cami for his support on the last chapter of this thesis.

To my friends, Hamidreza Kaviani, Dr. Maysam Mirahmadi, Gabe Keenleyside, and Dimuthu Hemachandra. I thank you for all your support throughout these years and for the friendships that will last a lifetime.

Last but not least, I thank my family with special thanks to Vida Golriz, Sheila Eghbali, Golnaz Golriz, Sarah Andalibi, and Samad Nikpour for their kindness and support through the most difficult times. I specially thank my mother, Fatemeh Andalibi, for the unconditional love and support she offered me throughout all my endeavours, granting me the opportunity to fulfill my dreams. I thank you for your never ending encouragement and for your confidence in me. I am truly blessed to have you by my side on my journey through life. I dedicate this thesis to my father, Dr. Parviz Golriz, who is no longer among us (R.I.P.) and I thank him for the legacy he left behind with me that is the never ending thirst for knowledge.

Contents

Abstract	ii
Co-Authorship Statement	iii
Acknowledgments	iv
List of Figures	x
List of Tables	xxxiv
List of Appendices	xxxvi
1 Introduction	1
1.1 Stellar Evolution of Low and Intermediate Mass Stars	2
1.1.1 Main Sequence Evolution	2
Evolution on Main Sequence	4
1.1.2 Post Main Sequence Evolution: To AGB & Beyond	5
1.2 Stellar Spectroscopy: History & Development	7
1.3 Spectral Lines: Formation & Analysis	8
1.3.1 Atomic Spectroscopy	10
Electron Scattering	11
Bound-Free Transition	11
Free-Free Transition	12
Bound-Bound Transition	13
H ⁻ Opacity	13
1.3.2 Molecular Spectroscopy	14
1.3.3 Equation of Radiative Transfer	16
1.3.4 Spectral Line Formation: The Milne-Eddington Model	18
1.4 Spectral Analysis: Tools and Methods	19
1.4.1 Spectrum Synthesis in Ultraviolet: Abundance Analysis	20
1.4.2 Infrared Spectroscopy: Dust & Molecules	20
List of Abbreviations, Symbols, and Nomenclature	1
2 Ultraviolet Spectral Synthesis of Iota Herculis	28
2.1 Introduction	28
2.2 Observation and Data Reduction	29

2.3	Methods	30
2.3.1	Line Broadening Mechanisms and Considerations	30
	Microturbulence	30
	Macroturbulence	31
	Rotational Velocity	31
2.3.2	Abundance Determination Method	31
2.3.3	Sources of Uncertainty	33
2.4	Summary of Individual Elements	35
2.4.1	Boron, Z=5	35
2.4.2	Carbon, Z=6	36
2.4.3	Nitrogen, Z=7	38
2.4.4	Oxygen, Z=8	38
2.4.5	Magnesium, Z=12	38
2.4.6	Aluminum, Z=13	39
2.4.7	Silicon, Z=14	40
2.4.8	Phosphorus, Z=15	41
2.4.9	Sulfur, Z=16	42
2.4.10	Chlorine, Z=17	44
2.4.11	Argon, Z=18	46
2.4.12	Calcium, Z=20	47
2.4.13	Titanium, Z=22	47
2.4.14	Vanadium, Z=23	48
2.4.15	Chromium, Z=24	48
2.4.16	Manganese, Z=25	49
2.4.17	Iron, Z=26	50
2.4.18	Cobalt, Z=27	52
2.4.19	Nickel, Z=28	53
2.4.20	Copper, Z=29	55
2.4.21	Zinc, Z=30	56
2.4.22	Germanium, Z=32	56
2.4.23	Platinum, Z=78	57
2.4.24	Mercury, Z=80	58
2.4.25	The Missing Lines	59
2.5	Discussion and Conclusions	60
2.5.1	Comparison with Literature	60
2.5.2	Further Considerations and future work	61
2.6	Acknowledgments	62
3	Ultraviolet Spectral Synthesis of HD72660	69
3.1	Introduction	69
3.2	Observation and Data Reduction	69
3.3	Methods	70
3.3.1	Line Broadening Mechanisms and Considerations	70
	Microturbulence	70
	Macroturbulence	71

	Rotational Velocity	71
3.3.2	Abundance Determination Method	71
3.3.3	Sources of Uncertainty	73
3.4	Summary of Individual Elements	74
3.4.1	Carbon, $Z=6$	74
3.4.2	Nitrogen, $Z=7$	75
3.4.3	Oxygen, $Z=8$	75
3.4.4	Magnesium, $Z=12$	76
3.4.5	Aluminum, $Z=13$	77
3.4.6	Silicon, $Z=14$	77
3.4.7	Phosphorus, $Z=15$	78
3.4.8	Sulfur, $Z=16$	80
3.4.9	Calcium, $Z=20$	81
3.4.10	Scandium, $Z=21$	83
3.4.11	Titanium, $Z=22$	84
3.4.12	Vanadium, $Z=23$	84
3.4.13	Chromium, $Z=24$	85
3.4.14	Manganese, $Z=25$	87
3.4.15	Iron, $Z=26$	88
3.4.16	Cobalt, $Z=27$	89
3.4.17	Nickel, $Z=28$	91
3.4.18	Copper, $Z=29$	91
3.4.19	Zinc, $Z=30$	91
3.4.20	Yttrium, $Z=39$	92
3.4.21	Zirconium, $Z=40$	93
3.4.22	Molybdenum, $Z=42$	96
3.4.23	Ruthenium, $Z=44$	96
3.4.24	Rhodium, $Z=45$	97
3.4.25	Tin, $Z=50$	97
3.4.26	Barium, $Z=56$	97
3.4.27	Ytterbium, $Z=70$	97
3.4.28	Osmium, $Z=76$	99
3.4.29	Platinum, $Z=78$	99
3.4.30	Gold, $Z=79$	100
3.4.31	Mercury, $Z=80$	100
3.4.32	Lead, $Z=82$	100
3.4.33	The Missing Lines	101
3.5	Discussion & Conclusion	102
3.5.1	Comparison with Literature	102
3.5.2	Further considerations and future work	103
3.6	Acknowledgement	104
4	IR Spectroscopy of AGB Stars in the Galactic Bulge	110
4.1	Introduction	110
4.2	The sample selection	114

4.3	Observations and data reduction	115
4.4	Interstellar emission towards the galactic bulge	116
4.5	Stellar and molecular contributions	117
4.5.1	Molecular bands: Inventory	118
4.5.2	Molecular bands: Models	120
4.5.3	Modelling the naked stars	121
4.5.4	Modelling results	124
4.6	Interstellar Extinction	125
4.6.1	The IR extinction curve	126
4.6.2	Literature A_K values	127
4.6.3	A_K values from the slab models	127
4.6.4	A model-independent approach	128
4.7	The Full Spitzer-IRS spectra	130
4.8	The Dust Spectra	134
4.8.1	Extracting the dust spectra	134
4.8.2	A spectral inventory	136
	The 10- μm region	136
	The 13- μm feature – the first condensate?	140
	The band at 19.5- μm	141
	The band at 28.5- μm	141
4.8.3	Variations in the dust composition	141
4.8.4	The SE classification of our targets	143
4.9	Summary & Conclusions	146
5	Summary & Open Questions	152
A		160
A.1	Stellar Evolution: A Comprehensive Description	160
A.1.1	Main Sequence Evolution	160
A.1.2	Post-AGB Evolution	173
	Mass loss & AGB circumstellar environments	173
A.1.3	Principles of the Mass Loss Process	173
A.1.4	Circumstellar Envelopes of AGB Stars	175
A.1.5	Observational studies & Mass Loss	177
A.2	Dust Formation in O-Rich CSEs	181
B	Iota Herculis Models	184
C	HD72660 Models	195
D	Background Removal	222
E	A_K Values	224
E.0.1	c32	224
E.0.2	c35	224
E.0.3	Ogle	227

E.0.4	NGC 6522	228
F		231
G		238
Curriculum Vitae		293

List of Figures

1.1	<i>Left:</i> The reactions involved in the CNO cycle. <i>Right:</i> The reactions involved in <i>pp</i> -chain [66].	3
1.2	This plot illustrates the contribution of the CNO cycle and <i>pp</i> -chain in energy production as a function of temperature. The CNO cycle dominates the <i>pp</i> chain at higher temperatures [66].	4
1.3	The theoretical Hertzsprung-Russel diagram including the zero-age main sequence (solid line) for various initial masses and their corresponding evolutionary tracks (Figure taken from Schaller et al. [107]).	6
1.4	<i>Left:</i> The bound-free absorption coefficient of the H^- ion per cm^2 per ion per electron pressure. <i>Right:</i> The free-free absorption coefficient of the H^- ion per cm^2 per ion [Figures taken from 31].	14
1.5	This figure shows the energy level diagram for three different transitions; electronic, vibrational and rotational [Figure taken from 72].	16
2.1	This figure shows the observation (in black), calculated model with $\log(n_B/n_H) = -10.1$ (in blue) and without boron (in red).	36
2.2	The figure shows the observation (in black), calculated model with $\log(n_C/n_H) = -3.55 \pm 0.30$ (in blue) and without carbon (in red). <i>Top left:</i> The unblended multiplet (11) triplet of C II at 1324 Å. <i>Top right:</i> The single line of multiplet (9) of C III at 1247 Å. <i>Bottom:</i> The C III lines of multiplet (4) around 1174 Å, with prominent wings extending to several Å from the deepest part of the feature.	37
2.3	The figure shows the observation (in black), the best-fitting model calculated with $\log(n_N/n_H) = -4.65 \pm 0.80$ (in blue) and without nitrogen (in red). <i>Top left:</i> N I UV multiplet (5) at 1243 Å, <i>Top right:</i> N II multiplet (1) at 1085 Å, <i>Bottom left:</i> N II multiplet at 1275–1276 Å, <i>Bottom right:</i> N I multiplet (1) at 1199–1200 Å	39
2.4	The figure shows the observed line (in black), the best-fitting model calculated with $\log(n_O/n_H) = -3.5 \pm 0.3$ (in blue) and without oxygen (in red). The lines are blended with iron. <i>Top left:</i> O II triplet at 1132 Å. <i>Top right:</i> O I doublet at 1041 Å, <i>Bottom left:</i> Strong O I at 1302 Å, <i>Bottom Right:</i> O I doublet at 1305–1306 Å.	40
2.5	This figure shows the observation (in black), the calculated model with $\log(n_{Mg}/n_H) = -3.9 \pm 0.19$ (in blue) and without magnesium (in red). <i>left:</i> Mg II doublet at 1367 Å, <i>right:</i> strong line at Mg II 1240 Å	41

- 2.6 This figure shows the observation (in black), the calculated model with $\log(n_{\text{Al}}/n_{\text{H}}) = -5.90 \pm 0.58$ (in blue) and without aluminum (in red). *Top left:* Al III line at 1379 Å. *Top right:* Al III triplet at 1352 Å, *Bottom left:* Al II triplet at 1189 Å, *Bottom right:* Al II triplet at 1191 Å. 42
- 2.7 This figure shows the observation (in black), the best-fitting model spectrum with $\log(n_{\text{Si}}/n_{\text{H}}) = -4.65 \pm 0.26$ (in blue) and without silicon (in red). *Top:* Strong Si III lines of multiplet (4) between 1294–1310 Å, we only show 1298.892 Å (*left*) and 1301.149 Å (*right*), *Middle:* A multiplet (5) of Si II between 1260–64 Å at 1260.422 Å (*left*) and 1264.737 Å (*right*), *Bottom left:* An Si II multiplet (4) between 1190–93 Å at 1190.415 Å, *Bottom right:* A strong Si,IV line at 1128.340 Å. 43
- 2.8 This figure shows the observation (in black), the calculated model with $\log(n_{\text{P}}/n_{\text{H}}) = -6.7 \pm 0.7$ (in blue), and without phosphorus (in red). *Top left:* P III doublet at 1344.326, 1344.850 Å, *Top right:* P II line at 1249.829 Å, *Bottom left:* P III at 1003.600 Å *Bottom right:* A resonance P III line at 1334.813 Å 44
- 2.9 This figure shows the observation (in black), the calculated model with $\log(n_{\text{S}}/n_{\text{H}}) = -5.20 \pm 0.10$ (in blue), and without sulfur (in red). *Top left:* The strong S III triplet at 1200.956, 1201.722, 1202.120 Å, *Top right:* The S IV doublet at 1072.996, 1073.528 Å, *Middle:* strong S II resonance doublet line at 1250.584, 1253.811 Å, *Bottom left:* A strong resonance S II line at 1259.519 Å, *Bottom right:* A strong S II line at 1072.996 Å 45
- 2.10 This figure shows the observation (in black), the calculated model with $\log(n_{\text{Cl}}/n_{\text{H}}) = -7.150 \pm 0.100$ (in blue), and without chlorine (in red). *Left:* Cl II line at 1071.036 Å, *Right:* Cl II line at 1075.229 Å. 46
- 2.11 This figure shows the observation (in black), the calculated model with $\log(n_{\text{Ar}}/n_{\text{H}}) = -4.900 \pm 0.100$ (in blue), and without argon (in red). *Left:* Ar I line at 1048.220 Å *Right:* Ar I line at 1066.660 Å. 47
- 2.12 This figure shows the observation (in black), the calculated model using $\log(n_{\text{Ca}}/n_{\text{H}}) = -5.30 \pm 0.10$ (in blue), and without calcium (in red). *Left:* Ca II line at 1432.502 Å, *Right:* Ca II line at 1369.559 Å. 48
- 2.13 This figure shows the observation (in black), the calculated model with $\log(n_{\text{Ti}}/n_{\text{H}}) = -6.90 \pm 0.17$ (in blue), and without titanium (in red). All the plots belong to the same ionization state Ti III; *Top left:* A resonance line at 1286.232, a part of a UV multiplet at 1286.368 Å, *Top right:* at 1282.483 Å, *Bottom left:* at 1295.883 Å, *Bottom right:* at 1298.697 Å 49
- 2.14 This figure shows the observation (in black), the calculated model with $\log(n_{\text{V}}/n_{\text{H}}) = -8.15 \pm 0.18$ (in blue), and without vanadium (in red). All of the plots belong to the same state of ionization; V III at; *Top left:* 1160.761 Å, *Top right:* 1154.225 Å, *Bottom left:* 1252.104 Å, *Bottom right:* 1332.002 Å 50
- 2.15 This figure shows the observation (in black), the calculated model with $\log(n_{\text{Cr}}/n_{\text{H}}) = -6.10 \pm 0.65$, and without chromium (in red). The plots belong to the same ionization state; Cr III doublet at 1098.609, 1098.736 Å (*Top left*), Cr III doublet at 1064.317, 1064.409 Å (*Top right*), Cr III resonance at 1040.059 with contribution from a part of a multiplet at 1040.168 Å (*Bottom left*), strong Cr III line at 1051.897 Å (*Bottom right*) 51

- 2.16 This figure shows the observation (in black), the calculated model with $\log(n_{\text{Mn}}/n_{\text{H}}) = -6.78 \pm 0.45$, and without manganese (in red). These plots belong to the same ionization state of Mn III; doublet lines at 1088.705, 1088.735 Å (*Top left*), doublet line at 1046.180, 1046.479 Å (*Top right*), doublet line 1239.239, 1239.255 Å (*Bottom left*), doublet line at 1111.103, 1111.212 Å (*Bottom right*). 52
- 2.17 This figure shows the observation (in black), the calculated model with $\log(n_{\text{Fe}}/n_{\text{H}}) = -4.9 \pm 0.4$ (in blue), and without iron (in red). *Top left*: The Fe III lines at 1130.396, 1130.410 Å, blended with Fe II lines at 1130.175, 1130.443, 1130.342 Å, *Top right*: A set of Fe II doublets at 1135.548, 1135.577 Å, and 1135.302, 1135.184 Å, *Bottom left*: Fe III doublet at 1154.573, 1154.615 Å, *Bottom right*: The strong Fe III line at 1142.95 blended with Fe II lines at 1142.757, 1143.225, 1143.325 Å. 53
- 2.18 This figure shows the observation (in black), the calculated model with $\log(n_{\text{Co}}/n_{\text{H}}) = -7.55 \pm 0.49$ (in blue), and without cobalt (in red). *Top left*: Co III line at 1043.242 Å, *Top right*: Co III line at 1046.756 Å, *Bottom left*: Co III line at 1088.508 Å, *Bottom right*: Co II line at 1466.211 Å. 54
- 2.19 This figure shows the observation (in black), the calculated model with $\log(n_{\text{Ni}}/n_{\text{H}}) = -5.70 \pm 0.35$ (in blue), and without nickel (in red). *Top left*: Ni III triplet at 1322.254, 1321.324, 1321.799 Å, *Top right*: a resonance Ni II lines at 1370.132 Å, *Bottom left*: a resonance Ni II line at 1345.878 Å, *Bottom right*: a resonance Ni II line at 1308.865 Å. 55
- 2.20 This figure shows the observation (in black), the calculated model with $\log(n_{\text{Cu}}/n_{\text{H}}) = -9.00$ (in blue), and without copper (in red). This is a resonance Cu II line at 1358.773 Å. 56
- 2.21 This figure shows the observation (in black), the calculated model with $\log(n_{\text{Zn}}/n_{\text{H}}) = -6.85 \pm 0.20$ (in blue), and without zinc (in red). *Top*: Zn III doublet at 1456.709, 1464.180 Å. *Bottom*: Zn III doublet at 1359.601, 1359.799 Å. 57
- 2.22 This figure shows the observation (in black), the calculated model with $\log(n_{\text{Ge}}/n_{\text{H}}) = -8.50$ (in blue), and without germanium (in red). *left*: A strong line at 1237.072 Å, *right*: A part of a doublet at 1261.913 Å. 58
- 2.23 This figure shows the observation (in black), the calculated model with $\log(n_{\text{Pt}}/n_{\text{H}}) = -8.825$ (in blue), and without platinum (in red). This is the Pt III line at 999.665 Å. 58
- 2.24 This figure shows the observation (in black), the calculated model with $\log(n_{\text{Hg}}/n_{\text{H}}) = -8.95 \pm 0.13$ (in blue), and without mercury (in red). *Left*: Hg III at 1377.830 Å, *Right*: Hg III at 1330.770 Å 59
- 2.25 This figure shows a comparison between the solar abundances of 24 elements and the abundances derived from this work and the literature. Note that the literature values are the mean taken from Table 2.1. 60
- 3.1 This figure shows the observation (in black), calculated model with $\log(n_{\text{C}}/n_{\text{H}}) = -4.10 \pm 0.10$ (in blue) and without carbon (in red). *Left*: a cluster of C I lines; Strong resonance line at 1656.928 Å, a doublet at 1657.379, 1657.907 Å, a doublet at 1657.008, 1658.121 Å. *Right*: A strong UV multiplet (62) at 1751.823 Å. 75

- 3.2 This figure shows the observation (in black), calculated model with $\log(n_{\text{N}}/n_{\text{H}}) = -4.7 \pm 0.3$ (in blue) and without nitrogen (in red). *Left*: Strong N I UV multiplet (9) at 1745.252, 1745.260 Å, *Right*: strong N I UV multiplet (9) at 1742.729, 1742.719 Å, This panel clearly shows that this value is an upper limit. 76
- 3.3 This figure shows the observation (in black), calculated model with $\log(n_{\text{O}}/n_{\text{H}}) = -2.5 \pm 0.3$ (in blue) and without Oxygen (in red). *Left*: Relatively weak and blended O I line at 1641.305 Å *Right*: Weak O I line at 1868.655 Å 77
- 3.4 This figure shows the observation (in black), calculated model with $\log(n_{\text{Mg}}/n_{\text{H}}) = -4.20 \pm 0.22$ (in blue) and without magnesium (in red). *Top left*: Clean and unblended Mg I resonance line at 1827.935 Å, *Top right*: strong resonance UV multiplet (1) of Mg I at 2852.126 Å, *Bottom*: A strong resonance UV multiplet (1) of Mg II at 2802.705 Å (*left*) and 2795.528 Å (*right*) 78
- 3.5 This figure shows the observation (in black), calculated model with $\log(n_{\text{Al}}/n_{\text{H}}) = -4.9 \pm 0.31$ (in blue) and without aluminum (in red). *Top left*: clean and strong Al II UV multiplet (6) at 1719.442, 1721.244, 1721.271 Å, *Top right*: An unblended strong Al I doublet at 1766.381, 1769.133 Å, which is only partly shown due to the large gap in wavelengths. *Bottom*: The strong resonance Al II line at 1670.787 Å. 79
- 3.6 This figure shows the observation (in black), the calculated model with $\log(n_{\text{Si}}/n_{\text{H}}) = -4.20 \pm 0.18$ (in blue), and without silicon (in red). *Top*: An unblended UV multiplet (1) of Si II at 1808.012 Å (*Left*), and 1816.928, 1817.451 Å (*Right*) but we have shown this multiplet in two plots, due to the long wavelength gap. *Bottom*: A strong UV multiplet (75) at 1770.629 Å (*Left*) and 1853.152 Å (*Right*), Note that we only chose two out of several lines in this multiplet for illustration. . . . 80
- 3.7 This figure shows the observation (in black), the calculated model with $\log(n_{\text{P}}/n_{\text{H}}) = -7.10 \pm 0.11$ (in blue), and without phosphorus (in red). *Top*: A strong unblended P I UV multiplet (1) at 1774.949 (*Left*), 1782.829, and 1787.647 Å (*Right*), but we have only shown the first and last here. *Bottom left*: A strong P I UV multiplet (5) at 1858.871, 1859.401 Å, *Bottom right*: A strong P I UV multiplet (4) at 2135.469, 2136.182, 2149.142 Å. 81
- 3.8 This figure shows the observation (in black), the calculated model with $\log(n_{\text{S}}/n_{\text{H}}) = -4.50 \pm 0.98$ (in blue), and without sulfur (in red). *Top*: S I UV multiplet (2) at 1807.311, 1820.341 (*Left*), and 1826.244 Å (*Right*), *Bottom left*: UV multiplet (1) at 1900.286 Å, *Bottom right*: A relatively strong S II line at 1824.024 Å. . . 82
- 3.9 This figure shows the observation (in black), the calculated model with $\log(n_{\text{Ca}}/n_{\text{H}}) = -5.40 \pm 0.26$ (in blue), and without calcium (in red). *Top Left*: Ca II UV multiplet (11) at 1807.337 to 1814.647 Å, *Top Right*: A UV multiplet (4) at 1838.008 to 1840.060 Å, *Bottom left*: A UV multiplet (3) at 2128.750 to 2132.304 Å, *Bottom right*: A UV multiplet (9) at 2197.786 to 2208.610 Å. 83
- 3.10 This figure shows the observation (in black), the calculated model with $\log(n_{\text{Sc}}/n_{\text{H}}) = -9.50 \pm 0.30$ (in blue), and without scandium (in red). UV multiplet (1) at 2552.354 Å (*Left*) and 2563.189 Å (*Right*). 84

- 3.11 This figure shows the observation (in black), the calculated model with $\log(n_{\text{Ti}}/n_{\text{H}}) = -6.60 \pm 0.18$ (in blue), and without titanium (in red). *Top*: Ti II UV multiplet (16) at 2862.319 Å (*left*), and 2851.101 Å (*Right*), *Bottom left*: A UV multiplet (14) at 2877.434 Å, *Bottom right*: triplet of Ti II at 1642.630, 1650.623, 1830.463 Å. 85
- 3.12 This figure shows the observation (in black), calculated model with $\log(n_{\text{V}}/n_{\text{H}}) = -7.2 \pm 0.26$ (in blue) and without vanadium (in red). *Top left*: V II UV multiplet (12) at 2880.016, 2882.494 Å, *Top right*: UV multiplet (18) at 1636.023 Å, *Bottom*: UV multiplet (18) at 1637.562 Å (*Left*), 1643.059 Å (*Right*). 86
- 3.13 This figure shows the observation (in black), calculated model with $\log(n_{\text{Cr}}/n_{\text{H}}) = -5.65 \pm 0.31$ (in blue) and without chromium (in red). *Top left*: A part of a Cr II multiplet at 1718.475 Å, *Top right*: A small part of a Cr II UV multiplet at 2860.933, 2862.570, 2858.908 Å, *Bottom left*: Cr II UV multiplet at 1898.980 Å, together with a rather weak but unblended Cr II line at 1899.642 Å, *Bottom right*: A part of another UV multiplet at 1732.073 Å. 87
- 3.14 This figure shows the observation (in black), calculated model with $\log(n_{\text{Mn}}/n_{\text{H}}) = -5.90 \pm 0.22$ (in blue) and without manganese (in red). *Top left*: A part of an Mn II UV multiplet at 1868.585 Å, *Top right*: A strong Mn II resonance line at 2576.103 Å, *Bottom left*: A small window of an Mn II UV multiplet at 1714.385 Å, *Bottom right*: A resonance strong Mn I at 2798.266 Å. 88
- 3.15 This figure shows the observation (in black), calculated model with $\log(n_{\text{Fe}}/n_{\text{H}}) = -3.75 \pm 0.24$ (in blue) and without iron (in red). *Top left*: A small window of a Fe II UV multiplet at 1685.954 Å, *Top right*: One window of an Fe II UV multiplet at 2828.626 Å, *Bottom left*: A part of an Fe III multiplet at 1895.473 Å, *Bottom right*: A strong resonance Fe I lines at 1883.778 Å. 89
- 3.16 This figure shows the observation (in black), calculated model with $\log(n_{\text{Co}}/n_{\text{H}}) = -6.50 \pm 0.12$ (in blue) and without cobalt (in red). *Top left*: A small window of a Co II UV multiplet at 2694.683 Å, *Top right*: A small part of a Co II UV multiplet at 1687.847 Å, *Bottom left*: A small part of a Co II UV multiplet at 1706.899 Å, *Bottom right*: A small part of a Co II UV multiplet at 1845.927 Å . 90
- 3.17 This figure shows the observation (in black), calculated model with $\log(n_{\text{Ni}}/n_{\text{H}}) = -5.05 \pm 0.36$ (in blue) and without nickel (in red). *Top left*: a strong resonance Ni II line at 1703.410 Å, *Top right*: A resonance Ni I line at 2320.034 Å and a strong Ni I line at 2321.383 Å, *Bottom left*: A small window of an Ni II multiplet at 2312.917 Å together with a strong Ni II line at 2312.315 Å, *Bottom right*: A very strong Ni II line at 1900.929 Å. 92
- 3.18 This figure shows the observation (in black), calculated model with $\log(n_{\text{Cu}}/n_{\text{H}}) = -7.00 \pm 0.21$ (in blue) and without copper (in red). *Top left*: A strong unblended Cu II line at 2148.983 Å, *Top right*: A strong unblended Cu II line at 2189.629 Å, *Bottom left*: An unblended Cu I line at 2165.095 Å, *Bottom right*: a relatively weak and blended Cu I line at 2230.085 Å. 93

- 3.19 This figure shows the observation (in black), calculated model with $\log(n_{\text{Zn}}/n_{\text{H}}) = -6.70 \pm 0.30$ (in blue) and without zinc (in red). *Left:* This shows a Zn II line at 2557.948 Å which illustrates that this value is also an upper limit upon increase of which the model will no longer fit the observation properly. *Right:* Zn I line at 2138.573 Å, in which if we add any more abundance to zinc, it will appear as an excess absorption on top of what already looks like a relatively good fit. 94
- 3.20 This figure shows the observation (in black), calculated model with $\log(n_{\text{Y}}/n_{\text{H}}) = -7.90 \pm 0.30$ (in blue) and without yttrium (in red). Both line are relatively clean Y III lines at *Left:* 2367.228 Å, and *Right:* 2414.643 Å. 94
- 3.21 This figure shows the observation (in black), calculated model with $\log(n_{\text{Zr}}/n_{\text{H}}) = -8.30 \pm 0.29$ (in blue) and without zirconium (in red). *Top left:* A strong unblended Zr III at 1798.047 Å, *Top right:* A moderately strong Zr III line at 1790.113 Å, *Bottom left:* A blended Zr II line at 2571.391, 2571.457 Å, *Bottom right:* A resonance blended Zr II line at 2567.637 Å. 95
- 3.22 This figure shows the Mo II lines at 2683.234, 2684.140 Å (in black), calculated model with $\log(n_{\text{Mo}}/n_{\text{H}}) = -9.00 \pm 0.30$ (in blue) and without molybdenum (in red). 96
- 3.23 This figure shows the Sn II line at 1757.905 Å (in black), calculated model with $\log(n_{\text{Sn}}/n_{\text{H}}) = -8.8 \pm 0.4$ (in blue) and without tin (in red). 98
- 3.24 This figure shows the observation (in black), calculated model with $\log(n_{\text{Ba}}/n_{\text{H}}) = -9.65 \pm 0.30$ (in blue) and without barium (in red). Both lines are Ba II, *left:* one at 2304.249 Å, and *right:* the other at 2335.270 Å. 98
- 3.25 This figure shows the Yb III at 1873.879 Å (in black), calculated model with $\log(n_{\text{Yb}}/n_{\text{H}}) = -9.00 \pm 0.30$ (in blue) and without ytterbium (in red). 99
- 3.26 This figure shows the observation (in black), calculated model with $\log(n_{\text{Pt}}/n_{\text{H}}) = -9.50 \pm 0.30$ (in blue) and without platinum (in red). Both lines belong to Pt II at *left:* 1777.086 Å and *right:* 1883.058 Å. 100
- 3.27 This figure shows the line at 1649.937 Å (in black), calculated model with $\log(n_{\text{Hg}}/n_{\text{H}}) = -9.20 \pm 0.30$ (in blue) and without mercury (in red). 101
- 3.28 This figure shows a comparison between the solar abundances of 29 elements and the abundances obtained from this work and the literature. Note that the literature values are the mean taken from Table 3.1. The arrows represent upper limits. 102

- 4.1 [15]/K_{s,o}-[15] colour-magnitude diagrams for all sources detected in our selected ISOGAL fields (left panel) showing a linear sequence of increasingly redder colours (and thus mass-loss rates) for brighter 15- μ m. The right panel shows the representative sample that we have selected. For comparison, we show three tracks corresponding to AGB stars with luminosities of 2000, 4000, and 10,000 L_⊙ (bottom, middle and top curve respectively) and with mass loss rates increasing from 10⁻⁹ to 3×10⁻⁶ M_⊙yr⁻¹ (squares on the 4000 L_⊙ track indicate mass-loss rates of 10⁻⁹, 10⁻⁸, 5×10⁻⁸, 10⁻⁷, 5×10⁻⁷, 10⁻⁶ and 3×10⁻⁶ M_⊙yr⁻¹). The tracks were obtained using a mixture of amorphous silicate and aluminium-oxide dust [see 24, 25, for the radiative transfer models]. The vertical dot-dashed line represents a track of increasing luminosity without mass loss. Note that the six OH/IR stars in our sample that were selected from IRAS have no corresponding 2MASS and ISOGAL fluxes and are therefore not shown in this CMD (Figures Taken From [6], with permission) 112
- 4.2 The location of our targets in galactic coordinates. Note that targets in c32 and c35 are at roughly the same angular distance (about one degree) to the galactic centre. 114
- 4.3 The (average) interstellar emission spectra for each of the fields. Note how the spectra reveal significant changes in the excitation conditions for the interstellar gas and dust for the different fields as one moves away from the galactic centre. Note that depending on telescope pointing accuracy, there can be mismatch between SL2/SL1, SL1/LL2, or LL2/LL1. 117
- 4.4 All our target spectra in the wavelength range 5–9- μ m, showing the main molecular bands. The spectra are normalized to the flux at 6- μ m, and are shown in order of increasing flux ratio at 10- μ m to 6- μ m (see § 4.6, This ratio is taken from the fully corrected spectra and is the same as Fig. 4.15). Stars that we have classified as naked stars are shown in blue. For comparison, the top panel shows a few model spectra for the three most common molecular species (H₂O, SiO and SO₂). 119
- 4.5 This figure illustrates how plane-parallel slab models can be used as an approximation to a spherical geometry when analyzing the molecular bands around AGB stars. The leftmost slab (yellow) represents the stellar photosphere; the other two slabs are molecular layers characterized by their own temperature and column densities of contributing species. Radiative transfer is calculated along the three indicated rays. Changing the size of the layers changes the relative importance of emission to absorption. Figure taken from Cami [8] (with permission). 120

4.6	The infrared model spectra of three different slab models that only differ in their effective temperature and in the amounts of water. All models include a ($T = 1000$ K) layer of only water vapor. The green model represents pure absorption (I_1 in Fig. 4.5) with only moderate amounts of water. This is the only model where the overall shape of the spectrum is similar to a blackbody at the object's effective temperature (in this case 2500 K, green dashed line). When only increasing the amount of water, we obtain the blue model. In this case, the shape of the spectrum looks more like a 1000 K blackbody (dashed purple line) – the temperature of the water layer. In the red model, we have changed the effective temperature but it looks almost identical to the blue model: the water layer hides the stellar photosphere. Note that the spectra are normalized to their own maximum.	123
4.7	The raw <i>Spitzer-IRS</i> spectrum of c35-2 (grey), and the extinction-corrected spectrum (black) adopting a galactic centre extinction law with $A_K = 0.49$. The best-fitting model is shown in purple. Note the clear signature of interstellar extinction at $9.7\text{-}\mu\text{m}$ (silicate absorption) in the original spectrum.	125
4.8	The nine naked star spectra and their best-fitting models. The original, uncorrected spectrum is shown in gray and the best-fitting extinction-corrected spectrum in black. The best-fitting stellar and molecular model spectrum is shown in purple.	126
4.9	(Left) The <i>Spitzer-IRS</i> spectrum of the reddened naked star c35-4 (blue) compared to the least reddened naked star NGC 6522-15 (black). (Right) The result of dividing the spectrum of c35-4 by NGC 6522-15 (black). The green curve is the GC extinction curve by Chiar & Tielens [13].	128
4.10	Extinction values (A_K) for our naked stars from different sources and methods. .	129
4.11	The full extinction-corrected <i>Spitzer-IRS</i> spectra of OH/IR stars (<i>top</i>), dusty targets(<i>middle</i>) and naked stars (<i>bottom</i>). The spectra at longer wavelengths are trimmed in cases where data seemed too noisy thus unreliable. The spectra are colour coded for better illustration. The spectra are normalized to their flux at $6\text{-}\mu\text{m}$ and are sorted as a function of increasing $10/6\text{-}\mu\text{m}$ flux ratio except for the dusty targets (<i>middle</i>) where the spectra are sorted as a function of increasing mass loss rates (listed in table 4.4). Shortward of $9.7\text{-}\mu\text{m}$, the molecular features are present with no clear trend however this figure represents a sequence of increasing dust optical depth (See text for more details). Note: Due to lack of space in this plot, we exceptionally used NGC as a short form of NGC 6522.	131

- 4.12 F_{mol} as a function of $F_{\text{dust}}/F_{\text{mol}}$ for all objects in our sample. The black vertical dashed line on the left represents the locus for dust-free AGB stars for various luminosities at the distance of the galactic bulge. The solid blue lines represent models for such AGB stars (at 2000, 6000 and 10,000 L_{\odot}) surrounded by optically thin dust shells (of pure silicates) with increasing mass-loss rates; the blue dashed lines are lines of constant mass loss rate (assuming a dust-to-gas ratio of 0.005). The solid black lines on top represent pure blackbody emitters at $L = 2000L_{\odot}$ (lower) and $10,000L_{\odot}$ (upper) as an approximation of extremely optically thick dust shells. At the bottom, we have indicated the expected $F_{\text{dust}}/F_{\text{mol}}$ values for respectively an Engelke function and for pure blackbodies with varying effective temperatures. The grey dash-dotted line is a least absolute deviation fit to the data points (excluding the OH/IR stars). See text for details. 132
- 4.13 A comparison of different model spectra for the naked stars: models obtained from fitting the 6–14- μm range (blue), and from fitting only the 6–8.5- μm range (magenta). The two models are virtually indistinguishable between 6 and 8.5- μm , and in almost all cases, correspond to roughly the same stellar parameters. The black curve shows the residual difference between the two models. Note that the residuals are scaled ($\times 5$) for clarity. 137
- 4.14 This figure shows the dust spectrum of target NGC 6522-5 which seems to have a particularly rich variety of dust features; some of those are indicated with arrows. For comparison, we also show the dust scattering efficiencies for some minerals that have been proposed as carriers for these dust features: silicates (the olivine MgFeSiO_4 is shown in red [17]), gehlenite ($\text{Ca}_2\text{Al}_2\text{SiO}_7$; magenta [59]), Alumina (Al_2O_3 [2]), iron oxide (FeO , purple [32]) and magnesiowüstite (MgFeO , blue [32]). 138
- 4.15 This figure shows the final dust spectra sorted based on increasing mass loss rate. Mass loss rates are estimated using equation 4.3. Overall as we go from bottom to top, different features show noticeable variations in terms of strength, shape and peak wavelength (see text for more details). 139
- 4.16 The SE classification for our sample after applying an extinction correction (*top*) and without applying an extinction correction (*bottom*). Flux ratios for our targets are indicated with the black diamonds; the green symbols indicate ratios obtained when using a similar stellar template as Sloan & Price [77]. The solid curve indicates the power law through the classes derived by Sloan & Price [77] and the SE classes themselves are separated by grey lines (dashed and dotted for better illustration). 145
- A.1 This figure illustrates the fraction of ^4He produced via *ppI*, *ppII* or *ppIII* Branch, as function of temperature in which $T_6 = T/(10^6 \text{ K})$ [20]. In lower temperatures, the abundance of ^3He is highest therefore *ppI* Branch dominates. At slightly higher temperature where the abundance of ^4He increases the probability of *ppII* Branch increases and in very high temperatures where the abundance of ^7Be grows, the *ppIII* Branch becomes more dominant. 162

A.2	<i>Left:</i> The reactions involved in the CNO cycle. <i>Right:</i> The reactions involved in <i>pp</i> -chain [66].	163
A.3	This plot illustrates the contribution of the CNO cycle and <i>pp</i> -chain in energy production as a function of temperature. The CNO cycle dominates the <i>pp</i> chain at higher temperatures [66].	164
A.4	The evolutionary track of a $5M_{\odot}$ star in the Hertzsprung-Russel diagram (Figure from Habing & Olofsson [47]).	166
A.5	This figure shows the evolution of interior structure of stars as it ages. The cloudy areas represent the convective regions, the hatched areas are regions where nuclear energy generation occurs. Dotted regions have variable chemical composition. <i>Left:</i> For a $1 M_{\odot}$ star [120]. <i>Right:</i> For a $5 M_{\odot}$ star [65].	167
A.6	This plot shows the change in central temperature versus central density during the helium flash. As long as the matter is degenerate (below the border dashed line), the temperature rises in constant density. As a result the star enters the non-degenerate regime followed by core expansion and density decreases. This will stabilize the helium fusion process [66].	169
A.7	The structure of a $1 M_{\odot}$ and $5M_{\odot}$ E-AGB Stars [see Chapter 2 47]. In general terms, AGB stars are cool ($T=3000$ K) giants (typical $R=3 \times 10^{13}$ cm) with an inert, degenerate CO core, two burning shells (one He, one H) and large inactive convective envelopes.	170
A.8	This figure shows the movement of mass shells as a function of time. The pulses originating around periods 100,102 and 104 trigger dust formation. The radiation will push these newly formed material away from the star therefore the density is not high enough for shocks around periods 101 and 103 to trigger dust formation.	174
A.9	Schematic diagram of the AGB stellar structure and the surrounding circum-stellar envelope. It illustrates the chemical evolution of the stellar ejecta as it moves further away. The shocks occur in dynamical atmosphere and result in the formation of different molecules. Different dust species condense out and get accelerated by radiation pressure in the acceleration zone. The interstellar radiation will give rise to photo-chemistry in the CSE [see chapter one 47]. . .	176
A.10	This figure shows the difference between the spectral features in oxygen-rich and carbon-rich stars. The top spectrum belongs to UX Cyg and the lower one is R Scl, representing oxygen-rich and carbon-rich stars, respectively. CO is a common species between the two stars [134].	177
A.11	This figure shows the formation sequence of Aluminum bearing condensates. [18]	183

D.1	This figure illustrates the strong background emission in our observations, and how this emission can vary significantly at small spatial scales (within the slit). <i>(Left)</i> : The CCD image of the IRS observation corresponding to target c35-5 (LL, Order 2, Nod 2). Wavelength decreases from bottom to top. The dashed lines indicate three different spatial positions within the slit; the target trace can be seen between the green and the blue dashed lines. <i>(Right)</i> : The background spectra corresponding to the spatial positions indicated on the image. All three show clear PAH emission between 16 and 18- μm as well as a strong [S III] line at 18.7- μm . Note how the intensity of the [S III] line increases from the left to the right, while the PAH emission weakens.	223
E.1	The GLIMPSE II [15] 8- μm IRAC image containing our targets in c32. The position of our targets is indicated, and the number corresponds to the ID in Table 4.1. Note that there is only one naked star in this field – object c32-8. . .	225
E.2	The 8- μm IRAC image [83] of our five targets in c35. The position of our targets is indicated, and the number corresponds to the ID in Table 4.1. Objects c35-2 and c35-4 are naked stars.	225
E.3	The best-fitting model for target c35-2 using A_K values of 0.54 (model-independent, shown in brown) and 0.86 (Gonzalez et al. [28], shown in black). The green shows the raw spectrum without extinction correction and the Galactic centre extinction curve is also overplotted in grey. The best-fitting models are overplotted in blue (for $A_K=0.87$) and magenta (for $A_K=0.54$).	226
E.4	This figure shows the raw spectrum of target c35-4 (in black) corrected for $A_K=0.55$ from Schultheis et al. [73] (in brown) and its corresponding best fit model (in magenta) and corrected spectrum using $A_K=0.92$ from model independent method (in blue). The Galactic centre extinction curve is also overplotted in grey.	227
E.5	The GLIMPSE II 8- μm IRAC image [15] of our seven targets in the Ogle field. The position of our targets is indicated, with the number corresponding to the ID in table 4.1. The objects Ogle-4 and Ogle-6 are naked stars.	228
E.6	This figure shows the best-fitting models for Ogle-4(left) and Ogle-6(right) when no extinction correction is applied at all (i.e. $A_K = 0$).	228
E.7	The 8- μm IRAC image [83] of our targets in NGC 6522. The position of our targets is indicated, with the number corresponding to the ID in table 4.1. . . .	229
F.1	Different dust extraction methods for naked stars c32-1, c32-3, c32-4, c32-5, c32-6 and c32-7. See text for more details.	232
F.2	Different dust extraction methods for naked stars c32-9, c32-10, c32-11, c32-12, c32-13 and c32-14. See text for more details.	233
F.3	Different dust extraction methods for naked stars c32-15, c32-16, c35-1, c35-3, c35-5 and Ogle-1. See text for more details.	234
F.4	Different dust extraction methods for naked stars Ogle-2, Ogle-3, Ogle-5, NGC6522-1, NGC6522-2, and NGC6522-3. See text for more details.	235

F.5	Different dust extraction methods for naked stars NGC6522-5, NGC6522-8, NGC6522-9, NGC6522-10, NGC6522-11, and NGC6522-12. See text for more details.	236
F.6	Different dust extraction methods for naked stars NGC6522-13, NGC6522-14, NGC6522-16, NGC6522-17, NGC6522-18, and NGC6522-19. See text for more details.	237
G.1	(c32-1) Both nods of the short low modules (SL1 & SL2) of this target contain only one target in the slit whereas in the long low module (LL1 & LL2) a second source appears very close to c32-1 (see Fig. G.2). The position of the extracted sources are shown in the Figure G.2. The spectrum shows residuals from insufficient bad pixel removal around $20.5\text{-}\mu\text{m}$ which was properly masked. The background of this source is strong and variable with prominent PAH features. However, it can be properly modeled and corrected using the IDL program discussed in the text. In the obtained spectrum, there is a slight mismatch between long low and short low modules. We treated this mismatch by scaling the long low modules with respect to the short low modules. The scaling factors used are listed below.	240
G.2	SL and LL modules spatial profiles after subtraction of the background	240
G.3	(c32-2) The number of extracted sources in each nod and module is shown in Fig. G.4 along with their position. In the extracted spectrum, there was a mismatch between the two nods of the SL1 module. Specifically, close to the edges of the module this mismatch was more noticeable. In order to correct for that we have modified the point spread function in SMART by specifying new parameters for the central position and full-width-half-maximum(FWHM)of the PSF. The background of this target was strong and variable and quite similar to c32-1 since they are both in the field c32. The background for the long low modules was properly modeled by the program explained in the text but for the SL2 module we have subtracted the background assuming a first order polynomial within optimal extraction of SMART. Finally, The mismatch between the modules was corrected by scaling the short low modules with respect to long low modules, with the following scale factors.	241
G.4	SL and LL modules spatial profiles after subtraction of the background	241
G.5	(c32-3) As indicated in Figure G.6, the number of sources that have been extracted in each nod and module. There was a significant mismatch between the two nods of SL1 module which was corrected by modifying the point spread function(central position and FWHM). After extraction the residual features were masked properly (e.g. $19.5\text{-}\mu\text{m}$). This target is located in field c32 but the background is properly corrected through modeling except SL1 module. For this module, we have assumed a constant offset for the background (polynomial order zero) and performed the subtraction using optimal extraction within SMART. Finally, we scaled long low modules with respect to the short low modules using the following scale factors, in order to eliminate the mismatch between modules and obtain the continuum shown here.	242
G.6	SL and LL modules spatial profiles after subtraction of the background	242

G.7	(c32-4) All nods of both modules (SL and LL) of this target contain only one source in the slit except first nod of SL2 module which contains a very faint second source (see Fig. G.8). The position of the extracted targets are shown in the figure G.8. The residuals we represent after extraction which were properly masked (e.g. 18.5- μm) The background for this source is strong and variable but properly modeled and corrected. Finally, we applied the following scale factors on the corresponding module to eliminate the mismatch between modules and obtain the final continuum shown here.	243
G.8	SL and LL modules spatial profiles after subtraction of the background	243
G.9	(c32-5) This is the final spectrum of c32-5. Figure G.10 indicates the number of sources that have been extracted in each nod of each module. After extraction there was no obvious residuals left for us to remove manually. As shown in Figure G.10 the observation for the second nod of SL1 module did not contain any useful information to extract, therefore for this module, we only took into account the data in the first nod. The background for this source is strong and variable but properly modeled and corrected. Finally, we scaled the long low modules with respect to the short low in order to eliminate the mismatch between modules and obtain the continuum shown here.	244
G.10	SL and LL modules spatial profiles after subtraction of the background	244
G.11	(c32-6) This is the final spectrum of c32-6. Figure G.12 indicates the number of sources that have been extracted in each nod of each module. The mismatch between the nods of SL1 module was removed by modifying the point spread function (central position and FWHM). After extraction the residual features were masked (e.g. 19.5- μm). In all modules, the background could be corrected by means of modeling except the LL1 module, in which case we have subtracted the background assuming an order one polynomial (linear gradient) in manual optimal extraction within Smart. Finally, we scaled the long low modules with respect to the short low modules in order to eliminate the mismatch between modules and obtain the continuum shown here.	245
G.12	SL and LL modules spatial profiles after subtraction of the background	245
G.13	(c32-7) This is the final spectrum of c32-7. Figure G.14 indicates the number of sources that have been extracted in each nod and module. There was a slight mismatch between the two nods of SL1 module which was removed by modifying the point spread function (central position and FWHM). After extraction the sharp and unrealistic residual features were masked (e.g. 19.5- μm). The background for this source is properly corrected through modeling. Finally, we applied the following scale factors on the corresponding module to eliminate the mismatch between modules and obtain the final continuum shown here.	246
G.14	SL and LL modules spatial profiles after subtraction of the background	246

G.15 (c32-8) This is the final spectrum of c32-8. Figure G.16 indicates the number of sources that have been extracted in each nod and module. There was a slight mismatch between the two nods of SL1 module which was removed by modifying the point spread function (central position and FWHM). After extraction there were no significant residuals to mask. The background is properly corrected through modeling. Finally, we scaled the long low modules with respect to the short low modules using the following scale factors, in order to eliminate the mismatch between them and obtain the continuum shown here.	247
G.16 SL and LL modules spatial profiles after subtraction of the background	247
G.17 (c32-9) This is the final spectrum of c32-9. Figure G.18 indicates the number of sources that have been extracted in each nod and module. There was a slight mismatch between the two nods of SL1 module which was removed by modifying the point spread function (central position and FWHM). After extraction the sharp and unrealistic residual features were masked (e.g. 19.5- μ m). The background is properly modelled and corrected. Finally, we scaled the long low modules with respect to the short low modules using the following scale factors, in order to eliminate the mismatch between modules and obtain the continuum shown here.	248
G.18 SL and LL modules spatial profiles after subtraction of the background	248
G.19 (c32-10) This is the final spectrum of c32-10. Figure G.20 indicates the number of sources that have been extracted in each nod and module. There was a slight mismatch between the two nods of SL1 module which was removed by modifying the point spread function (central position and FWHM). After extraction the sharp and unrealistic residual features were masked (e.g. 19.5- μ m). The background for this source is properly corrected through modeling. Finally, we scaled all modules with respect to the SL1 module using the following scale factors, in order to eliminate the mismatch between modules and obtain the continuum shown here.	249
G.20 SL and LL modules spatial profiles after subtraction of the background	249
G.21 (c32-11) This is the final spectrum of c32-11. Figure G.22 indicates the number of sources that have been extracted in each nod and module. There was a significant mismatch between the two nods of SL1 module which was corrected by modifying the point spread function (central position and FWHM). After extraction there were no significant residuals to mask. The background for all modules is properly corrected through modeling except SL1 module. For this module, we have assumed a constant offset for the background (polynomial order zero) and performed the subtraction using optimal extraction within SMART. Finally, we scaled all modules with respect to the SL1 module using the following scale factors, in order to eliminate the mismatch between modules and obtain the continuum shown here.	250
G.22 SL and LL modules spatial profiles after subtraction of the background	250

G.23 (c32-12)	This is the final spectrum of c32-12. Figure G.24 indicates the number of sources that have been extracted in each nod and module. There was a significant mismatch between the two nods of SL1 module which was removed by modifying the point spread function (central position and FWHM). After extraction there were no significant residuals to mask. The background is properly corrected through modeling. Finally, we scaled all modules with respect to the SL1 module using the following scale factors, in order to eliminate the mismatch between modules and obtain the continuum shown here.	251
G.24	SL and LL modules spatial profiles after subtraction of the background	251
G.25 (c32-13)	This is final spectrum of c32-13. Figure G.26 indicates the number of sources that have been extracted in each nod and module. There was an extreme mismatch between the two nods of SL1 module which was corrected by modifying the point spread function (central position and FWHM). After extraction the residual features were masked properly (e.g. 19- μ m). The background for all modules was properly corrected through modeling except LL2 module. For this module, we have assumed a constant offset for the background (polynomial order zero) and performed the subtraction using optimal extraction within SMART. Finally, we scaled all modules with respect to the SL1 module using the following scale factors, in order to eliminate the mismatch between modules and obtain the continuum shown here.	252
G.26	SL and LL modules spatial profiles after subtraction of the background	252
G.27 (c32-14)	This is the final spectrum of c32-14. Figure G.28 indicates the number of sources that have been extracted in each nod and module. There was an extreme mismatch between the two nods of SL1 module which was removed by modifying the point spread function (central position and FWHM). After extraction a few residual features were masked (e.g. 19.5- μ m).The background for this source was properly corrected through modeling. Finally, we scaled long low modules with respect to the short low modules using the following scale factors, in order to eliminate the mismatch between modules and obtain the continuum shown here.	253
G.28	SL and LL modules spatial profiles after subtraction of the background	253
G.29 (c32-15)	This is the final spectrum of c32-15. Figure G.30 indicates the number of sources that have been extracted in each nod and module. There was a significant mismatch between the two nods of SL1 module which was removed by modifying the point spread function (central position and FWHM). After extraction the sharp and unrealistic residual features were masked (e.g. 19.5- μ m). The background for this source was properly corrected through modeling. Finally, we scaled long low modules with respect to the short low modules using the following scale factors, in order to eliminate the mismatch between modules and obtain the continuum shown here.	254
G.30	SL and LL modules spatial profiles after subtraction of the background	254

G.31 (c32-16)	This is the final spectrum of c32-16. Figure G.32 indicates the number of sources that have been extracted in each nod and module. There was a slight mismatch between the two nods of SL1 and SL2 modules which were removed by modifying the point spread function (central position and FWHM). After extraction there was no significant residual left to mask. The background for this source is properly corrected through modeling. Finally, we scaled all modules with respect to the SL1 module using the following scale factors, in order to eliminate the mismatch between modules and obtain the continuum shown here.	255
G.32	SL and LL modules spatial profiles after subtraction of the background	255
G.33 (c35-1)	This is the final spectrum of c35-1. Figure G.34 indicates the number of sources that have been extracted in each nod and module. After extraction the sharp and unrealistic residual features were masked (e.g. 19.5- μm). The strong and variable background with prominent PAH feature was properly modeled and corrected. Finally, we scaled long low modules with respect to the short low modules using the following scale factors, in order to eliminate the mismatch between them and obtain the continuum shown here.	256
G.34	SL and LL modules spatial profiles after subtraction of the background	256
G.35 (c35-2)	This is the final spectrum of c35-2. Figure G.36 indicates the number of sources that have been extracted in each nod and module. After extraction the sharp and unrealistic residual features were masked (e.g. 19.5- μm). The strong and variable background with prominent PAH feature was properly modeled and corrected. Finally, we scaled long low modules with respect to the short low modules using the following scale factors, in order to eliminate the mismatch between them and obtain the continuum shown here.	257
G.36	SL and LL modules spatial profiles after subtraction of the background	257
G.37 (c35-3)	This is the final spectrum of c35-3. Figure G.38 indicates the number of sources that have been extracted in each nod and module. After extraction the residual features were masked (e.g. 19.5- μm). The strong and variable background with prominent PAH feature was properly modeled and corrected. Finally, we scaled long low modules with respect to the short low modules using the following scale factors, in order to eliminate the mismatch between modules and obtain the continuum shown here.	258
G.38	SL and LL modules spatial profiles after subtraction of the background	258
G.39 (c35-4)	This is the final spectrum of c35-4. Figure G.40 indicates the number of sources that have been extracted in each nod and module. There was a slight mismatch between the two nods of LL2 module which was removed by modifying the point spread function (central position and FWHM). After extraction the residual features were masked (e.g. 19.5- μm). The strong and variable background with prominent PAH feature was properly modeled and corrected. Finally, we scaled long low modules with respect to the short low modules using the following scale factors, in order to eliminate the mismatch between modules and obtain the continuum shown here.	259
G.40	SL and LL modules spatial profiles after subtraction of the background	259

G.41 (c35-5) This is the final spectrum of c35-5. Figure G.42 indicates the number of sources that have been extracted in each nod and module. After extraction, sharp residual features were masked (e.g. 19.5- μm). The strong and variable background with prominent PAH feature was properly modeled and corrected. Finally, we scaled long low modules with respect to the short low modules using the following scale factors, in order to eliminate the mismatch between modules and obtain the continuum shown here.	260
G.42 SL and LL modules spatial profiles after subtraction of the background	260
G.43 (Ogle-1) This is the final spectrum of Ogle-1. Figure G.44 indicates the number of sources that have been extracted in each nod and module. After extraction the sharp and unrealistic residual features were masked (e.g. 19.5- μm). The strong and variable background for this source was properly corrected through modeling. Finally, we scaled long low modules with respect to the short low modules using the following scale factors, in order to eliminate the mismatch between modules and obtain the continuum shown here.	261
G.44 SL and LL modules spatial profiles after subtraction of the background	261
G.45 (Ogle-2) This is the final spectrum of Ogle-2. Figure G.46 indicates the number of sources that have been extracted in each nod and module. After extraction the residual features were masked (e.g. 19.5- μm). The strong and variable background for this source was properly corrected through modeling. Finally, we scaled long low modules with respect to the short low modules using the following scale factors, in order to eliminate the mismatch between modules and obtain the continuum shown here.	262
G.46 SL and LL modules spatial profiles after subtraction of the background	262
G.47 (Ogle-3) This is the final spectrum of Ogle-3. Figure G.48 indicates the number of sources that have been extracted in each nod and module. After extraction the residual features were masked (e.g. 16.5- μm). The strong and variable background for this source was properly corrected through modeling. The only exception was the first nod of LL1 module which indicated strong background residuals, therefore we have also subtracted a constant offset (polynomial order zero) from the background after it has already been corrected through modeling. In this particular case, there was no mismatch between the modules therefore the continuum shown here was obtained without any further scaling. .	263
G.48 SL and LL modules spatial profiles after subtraction of the background	263
G.49 (Ogle-4) This is the final spectrum of Ogle-4. Figure G.50 indicates the number of sources that have been extracted in each nod and module. After extraction, residual features were masked (e.g. 19.5- μm). The strong and variable background for this source was properly corrected through modeling. Finally, we scaled long low modules with respect to the short low modules using the following scale factors, in order to eliminate the mismatch between modules and obtain the continuum shown here.	264
G.50 SL and LL modules spatial profiles after subtraction of the background	264

G.51 (Ogle-5) This is final spectrum of Ogle-5. Figure G.52 indicates the number of sources that have been extracted in each nod and module. After extraction the sharp and unrealistic residual features were masked (e.g. 18- μ m). The strong and variable background for this source was properly corrected through modeling. In this particular case, there was no mismatch between the modules therefore the continuum shown here was obtained without any further scaling.	265
G.52 SL and LL modules spatial profiles after subtraction of the background	265
G.53 (Ogle-6) This is the final spectrum of Ogle-6. Figure G.54 indicates the number of sources that have been extracted in each nod and module. After extraction the sharp and unrealistic residual features were masked (e.g. 19.5- μ m). The background for this source is similar to other sources in field Ogle which was properly corrected through modeling. Finally, we scaled long low modules with respect to the short low module using the following scale factors, in order to eliminate the mismatch between modules and obtain the continuum shown here.	266
G.54 SL and LL modules spatial profiles after subtraction of the background	266
G.55 (Ogle-7) This is the final spectrum of Ogle-7. Figure G.56 indicates the number of sources that have been extracted in each nod and module. After extraction, residual features were masked (e.g. 16.5- μ m). The strong and variable background for this source was properly corrected through modeling. Finally, we scaled all modules with respect to the SL1 module using the following scale factors, in order to eliminate the mismatch between modules and obtain the continuum shown here.	267
G.56 SL and LL modules spatial profiles after subtraction of the background	267
G.57 (NGC 6522-1) This is the final spectrum of NGC 6522-1. Figure G.58 indicates the number of sources that have been extracted in each nod and module. After extraction the sharp and unrealistic residual features were masked (e.g. 19.5- μ m). The background for this source is strong but it shows slightly less variation over the observed wavelength range, compared to other fields. This background was properly corrected through modeling. Finally, we scaled long low modules with respect to the short low modules using the following scale factors, in order to eliminate the mismatch between them and obtain the continuum shown here.	268
G.58 SL and LL modules spatial profiles after subtraction of the background	268
G.59 (NGC 6522-2) This is the final spectrum of NGC 6522-2. Figure G.60 indicates the number of sources that have been extracted in each nod and module. There was a slight mismatch between the two nods of SL1 module which was removed by modifying the point spread function (central position and FWHM). After extraction the sharp and unrealistic residual features were masked (e.g. 19.5- μ m). This source is located in the field covering NGC6522 and its background is similar to that of NGC 6522-1 therefore it was similarly corrected through modeling. Finally, we scaled long low modules with respect to the short low modules using the following scale factors, in order to eliminate the mismatch between them and obtain the continuum shown here.	269
G.60 SL and LL modules spatial profiles after subtraction of the background	269

G.61 (NGC 6522-3) This is the final spectrum of NGC 6522-3. Figure G.62 indicates the number of sources that have been extracted in each nod and module. After extraction the sharp and unrealistic residual features were masked (e.g. 20.5- μ m). This source is located in the field covering NGC6522 and its background is similar to that of the rest of the field thus similarly it was corrected through modeling. Finally, we scaled long low modules with respect to the short low modules using the following scale factors, in order to eliminate the mismatch between them and obtain the continuum shown here.	270
G.62 SL and LL modules spatial profiles after subtraction of the background	270
G.63 (NGC 6522-4) This is the final spectrum of NGC 6522-4. Figure G.64 indicates the number of sources that have been extracted in each nod and module. There was a slight mismatch between the two nods of SL1 module which was removed by modifying the point spread function (central position and FWHM). After extraction, residual features were masked (e.g. 19.5- μ m). This source is located in the field covering NGC6522 and its background is similar to that of the rest of the field thus similarly it was corrected through modeling. Finally, we scaled all modules with respect to the SL1 module using the following scale factors, in order to eliminate the mismatch between them and obtain the continuum shown here.	271
G.64 SL and LL modules spatial profiles after subtraction of the background	271
G.65 (NGC 6522-5) This is the final spectrum of NGC 6522-5. Figure G.66 indicates the number of sources that have been extracted in each nod and module. After extraction the sharp and unrealistic residual features were masked (e.g. 19.5- μ m). This source is located in the field covering NGC6522 and its background is similar to that of the rest of the field thus similarly it was corrected through modeling. Finally, we scaled long low modules with respect to the short low modules using the following scale factors, in order to eliminate the mismatch between them and obtain the continuum shown here.	272
G.66 SL and LL modules spatial profiles after subtraction of the background	272
G.67 (NGC 6522-6) This is the final spectrum of NGC 6522-6. Figure G.68 indicates the number of sources that have been extracted in each nod and module. After extraction, residual features were masked (e.g. 19.5- μ m). This source is located in the field covering NGC6522 and its background is similar to that of the rest of the field thus similarly it was corrected through modeling. Finally, we scaled long low modules with respect to the short low modules using the following scale factors, in order to eliminate the mismatch between them and obtain the continuum shown here.	273
G.68 SL and LL modules spatial profiles after subtraction of the background	273

G.69 (NGC 6522-7)	This is the final spectrum of NGC 6522-7. Figure G.70 indicates the number of sources that have been extracted in each nod and module. There was a slight mismatch between the two nods of SL1 module which was removed by modifying the point spread function (central position and FWHM). After extraction, residual features were masked (e.g. 19.5- μ m). This source is located in the field covering NGC6522 and its background is similar to that of the rest of the field thus similarly it was corrected through modeling. Finally, we scaled long low modules with respect to the short low modules using the following scale factors, in order to eliminate the mismatch between them and obtain the continuum shown here.	274
G.70	SL and LL modules spatial profiles after subtraction of the background	274
G.71 (NGC 6522-8)	This is the final spectrum of NGC 6522-8. Figure G.72 indicates the number of sources that have been extracted in each nod and module. There was a slight mismatch between the two nods of SL1 module which was removed by modifying the point spread function (central position and FWHM). After extraction the sharp and unrealistic residual features were masked (e.g. 19.5- μ m). This source is located in the field covering NGC6522 and its background is similar to that of the rest of the field thus similarly it was corrected through modeling. Finally, we scaled long low modules with respect to the short low modules using the following scale factors, in order to eliminate the mismatch between them and obtain the continuum shown here.	275
G.72	SL and LL modules spatial profiles after subtraction of the background	275
G.73 (NGC 6522-9)	This is the final spectrum of NGC 6522-9. Figure G.74 indicates the number of sources that have been extracted in each nod and module. After extraction the sharp and unrealistic residual features were masked (e.g. 19.5- μ m). This source is located in the field covering NGC6522 and its background is similar to that of the rest of the field thus similarly it was corrected through modeling. Finally, we scaled long low modules with respect to the short low modules using the following scale factors, in order to eliminate the mismatch between them and obtain the continuum shown here.	276
G.74	SL and LL modules spatial profiles after subtraction of the background	276
G.75 (NGC 6522-10)	This is the final spectrum of NGC 6522-10. Figure G.76 indicates the number of sources that have been extracted in each nod and module. After extraction the sharp and unrealistic residual features were masked (e.g. 19.5- μ m). This source is located in the field covering NGC6522 and its background is similar to that of the rest of the field thus similarly it was corrected through modeling. Finally, we scaled long low modules with respect to the short low modules using the following scale factors, in order to eliminate the mismatch between them and obtain the continuum shown here.	277
G.76	SL and LL modules spatial profiles after subtraction of the background	277

G.77 (NGC 6522-11) This is the final spectrum of NGC 6522-11. Figure G.78 indicates the number of sources that have been extracted in each nod and module. There was a slight mismatch between the two nods of SL1 module which was removed by modifying the point spread function (central position and FWHM). After extraction the sharp and unrealistic residual features were masked (e.g. 19.5- μ m). This source is located in the field covering NGC6522 and its background is similar to that of the rest of the field thus similarly it was corrected through modeling. Finally, we scaled long low modules with respect to the short low modules using the following scale factors, in order to eliminate the mismatch between them and obtain the continuum shown here.	278
G.78 SL and LL modules spatial profiles after subtraction of the background	278
G.79 (NGC 6522-12) This is the final spectrum of NGC 6522-12. Figure G.80 indicates the number of sources that have been extracted in each nod and module. There was a slight mismatch between the two nods of SL1 module which was removed by modifying the point spread function (central position and FWHM). After extraction the sharp and unrealistic residual features were masked (e.g. 19.5- μ m). This source is located in the field covering NGC6522 and its background is similar to that of the rest of the field thus similarly it was corrected through modeling. Finally, we scaled long low modules with respect to the short low modules using the following scale factors, in order to eliminate the mismatch between them and obtain the continuum shown here.	279
G.80 SL and LL modules spatial profiles after subtraction of the background	279
G.81 (NGC 6522-13) This is the final spectrum of NGC 6522-13. Figure G.82 indicates the number of sources that have been extracted in each nod and module. After extraction the sharp and unrealistic residual features were masked (e.g. 19.5- μ m). This source is located in the field covering NGC6522 and its background is similar to that of the rest of the field thus similarly it was corrected through modeling. Finally, we scaled long low modules with respect to the short low modules using the following scale factors, in order to eliminate the mismatch between them and obtain the continuum shown here.	280
G.82 SL and LL modules spatial profiles after subtraction of the background	280
G.83 (NGC 6522-14) This is the final spectrum of NGC 6522-14. Figure G.84 indicates the number of sources that have been extracted in each nod and module. After extraction the sharp and unrealistic residual features were masked (e.g. 19.5- μ m). This source is located in the field covering NGC6522 and its background is similar to that of the rest of the field thus similarly it was corrected through modeling. Finally, we scaled long low modules with respect to the short low modules using the following scale factors, in order to eliminate the mismatch between them and obtain the continuum shown here.	281
G.84 SL and LL modules spatial profiles after subtraction of the background	281

G.85 (NGC 6522-15)	This is the final spectrum of NGC 6522-15. Figure G.86 indicates the number of sources that have been extracted in each nod and module. There was a slight mismatch between the two nods of SL1 module which was removed by modifying the point spread function (central position and FWHM). After extraction, residual features were masked (e.g. 19.5- μ m). This source is located in the field covering NGC6522 and its background is similar to that of the rest of the field thus similarly it was corrected through modeling. Finally, we scaled long low modules with respect to the short low modules using the following scale factors, in order to eliminate the mismatch between them and obtain the continuum shown here.	282
G.86	SL and LL modules spatial profiles after subtraction of the background	282
G.87 (NGC 6522-16)	This is the final spectrum of NGC 6522-16. Figure G.88 indicates the number of sources that have been extracted in each nod and module. There was a slight mismatch between the two nods of SL1 module which was removed by modifying the point spread function (central position and FWHM). After extraction the sharp and unrealistic residual features were masked (e.g. 19.5- μ m). This source is located in the field covering NGC6522 and its background is similar to that of the rest of the field thus similarly it was corrected through modeling. Finally, we scaled long low modules with respect to the short low modules using the following scale factors, in order to eliminate the mismatch between them and obtain the continuum shown here.	283
G.88	SL and LL modules spatial profiles after subtraction of the background	283
G.89 (NGC 6522-17)	This is the final spectrum of NGC 6522-17. Figure G.90 indicates the number of sources that have been extracted in each nod and module. After extraction the sharp and unrealistic residual features were masked (e.g. 19.5- μ m). This source is located in the field covering NGC6522 and its background is similar to that of the rest of the field thus similarly it was corrected through modeling. Finally, we scaled long low modules with respect to the short low modules using the following scale factors, in order to eliminate the mismatch between them and obtain the continuum shown here.	284
G.90	SL and LL modules spatial profiles after subtraction of the background	284
G.91 (NGC 6522-18)	This is the final spectrum of NGC 6522-18. Figure G.92 indicates the number of sources that have been extracted in each nod and module. After extraction, residual features were masked (e.g. 19.5- μ m). This source is located in the field covering NGC6522 and its background is similar to that of the rest of the field thus similarly it was corrected through modeling. Finally, we scaled long low modules with respect to the short low modules using the following scale factors, in order to eliminate the mismatch between them and obtain the continuum shown here.	285
G.92	SL and LL modules spatial profiles after subtraction of the background	285

G.93 (NGC 6522-19) This is the final spectrum of NGC 6522-19. Figure G.94 indicates the number of sources that have been extracted in each nod and module. After extraction the sharp and unrealistic residual features were masked (e.g. 19.5- μ m). This source is located in the field covering NGC6522 and its background is similar to that of the rest of the field thus similarly it was corrected through modeling. Finally, we scaled long low modules with respect to the short low modules using the following scale factors, in order to eliminate the mismatch between them and obtain the continuum shown here.	286
G.94 SL and LL modules spatial profiles after subtraction of the background	286
G.95 (IRAS-17251-2821) This is the final spectrum of IRAS-17251-2821. Figure G.96 indicates the number of sources that have been extracted in each nod and module. After extraction, residual features were masked (e.g. 16.5- μ m). This background was corrected through modeling. Finally, we scaled all modules with respect to the SL1 modules using the following scale factors, in order to eliminate the mismatch between them and obtain the continuum shown here. . .	287
G.96 SL and LL modules spatial profiles after subtraction of the background	287
G.97 (IRAS-17276-2846) This is the final spectrum of IRAS-17276-2846. Figure G.98 indicates the number of sources that have been extracted in each nod and module. After extraction, residual features were masked (e.g. 16.5- μ m). The background was corrected through modeling except that, in the long low modules, there were residuals left from the background. We removed those residuals by further subtracting a constant offset (zeroth order polynomial). This particular case results in no mismatch between the modules therefore the continuum shown here is obtained without any further scaling.	288
G.98 SL and LL modules spatial profiles after subtraction of the background	288
G.99 (IRAS-17323-2424) This is the final spectrum of IRAS-17323-2424. Figure G.100 indicates the number of sources that have been extracted in each nod and module. After extraction, no significant residual was left to mask. The background was corrected through modeling. Finally, we scaled long low modules with respect to the short low modules using the following scale factors, in order to eliminate the mismatch between them and obtain the continuum shown here.	289
G.100 SL and LL modules spatial profiles after subtraction of the background	289
G.101 (IRAS-17347-2319) This is the final spectrum of IRAS-17347-2319. Figure G.102 indicates the number of sources that have been extracted in each nod and module. After extraction, no significant residual was left to mask. The background was corrected through modeling except that, after modeling, there was still residuals left from the background. Therefore we have corrected the residuals with further subtracting a constant offset (polynomial order zero). Finally, we scaled long low modules with respect to the short low modules using the following scale factors, in order to eliminate the mismatch between them and obtain the continuum shown here.	290
G.102 SL and LL modules spatial profiles after subtraction of the background	290

G.103	IRAS-17413-3531) This is the final spectrum of IRAS-17413-3531. Figure G.104 indicates the number of sources that have been extracted in each nod and module. After extraction, no significant residual was left to mask. The background was corrected through modeling except that, in the long low modules, there were residuals left from the background. We removed those residuals by further subtracting a constant offset (polynomial order zero). Finally, we scaled all modules with respect to the SL1 modules using the following scale factors, in order to eliminate the mismatch between them and obtain the continuum shown here.	291
G.104	SL and LL modules spatial profiles after subtraction of the background	291
G.105	IRAS-18042-2905) This is the final spectrum of IRAS-18042-2905. Figure G.106 indicates the number of sources that have been extracted in each nod and module. After extraction, no significant residual was left to mask. The background was corrected through modeling. Finally, we scaled all modules with respect to the SL1 modules using the following scale factors, in order to eliminate the mismatch between them and obtain the continuum shown here. . .	292
G.106	SL and LL modules spatial profiles after subtraction of the background	292

List of Tables

- 2.1 Iota Herculis- Summary of Literature Abundances. (1) Pintado & Adelman [35]; (2) Schmidt [50]; (3) Balona [6]; (4) Lester et al. [28]; (5) Kane et al. [17]; (6) Barnett & McKeith [7]; (7) Grigsby [12]; (8) Dufton et al. [11]; (9) Peters & Polidan [34] ; (10) Peters & Aller [33]; (11) Nieva & Przybilla [32]. Note: Solar Abundances are taken from Scott et al. [32, I & II], Grevesse et al. [9] and [1] 63
- 2.2 This table shows the abundances determined in this work for every ion and the recommended value for every element, the solar abundances from Scott et al. [32, I & II], Grevesse et al. [9] and Asplund et al. [1], and the wavelengths used to determine these values. 64
- 2.3 The percentile ionization ratios directly measured from the Saha equation. Note that n_{tot} is the total number density in every state ($n_{tot} = n_0 + n_1 + n_2 + n_3$). Note that this table shows the calculations at two different regions; *left column*: The region where the continuum and weak lines are formed ($\tau=0.2$, $T \sim 17000\text{K}$, $n_e \sim 3.84 \times 10^{14}$) and *right column*: The region where line core of strong line are formed ($\tau=7 \times 10^{-4}$, $T \sim 11800\text{K}$, $n_e \sim 5.13 \times 10^{12}$), respectively [14]. . . . 65
- 3.1 HD72660 - Summary of Literature Abundances ($\log N/N_H$). (1) Varenne [33] with $v \sin i = 6 \text{ km s}^{-1}$, $\xi = 2.5 \text{ km s}^{-1}$, (2) Landstreet et al. [21, and unpublished] with $v \sin i = 5.0 \pm 0.5$ and $\xi = 2.3 \pm 0.3$ for the published work and $v \sin i = 5.6 \text{ km s}^{-1}$, $\xi = 2.3 \text{ km s}^{-1}$ for the unpublished work in the optical, (3) Varenne & Monier [34] with $v \sin i = 10 \pm 2 \text{ km s}^{-1}$, for which superscripts u and o mean that the value is obtained from UV or Optical lines, respectively. (4) Wahlgren & Leckrone [37] with $v \sin i = 6.0 \pm 0.5$ and $\xi = 2.0$ whose results imply a typical abundance in the range of +1.0 to +1.5 dex, with respect to the solar values. . . 105
- 3.2 This table shows the abundances determined in this work for every element studied, solar abundances from Scott et al. [32, I & II], Grevesse et al. [9] and Asplund et al. [1], and the wavelengths used to determine these values. The sign \downarrow means the given value is an upper limit. 106
- 3.3 The percentile ionization ratios directly measured from the Saha equation. Note that n_{tot} is the total number density in every state ($n_{tot} = n_0 + n_1 + n_2 + n_3$). Note that this table shows the calculations at two different regions; *left column*: The region where the continuum and weak lines are formed ($\tau \sim 0.3$ near the short wavelength and ~ 1.0 near the long wavelength end of the data, $T \sim 9600\text{K}$, $n_e \sim 2.71 \times 10^{14}$). and *right column*: The region where line core of strong line are formed ($\tau = 3 \times 10^{-4}$, $T \sim 6900\text{K}$, $n_e \sim 1.35 \times 10^{12}$), respectively. [14]. 107

4.1	Basic data for our sample of galactic bulge AGB stars.	113
4.2	The resulting best-fit parameters for our naked star models, and literature values for the extinction.	122
4.3	This table provides a list of a few key features that characterize all our spectra and is sorted based on increasing mass loss rate. Note that symbols such as Δ & \bigcirc are used when the profile has a noticable triangular or round apperance. In cases where it is not easy to determine the actual shape of the profiles individually, we have used \checkmark to denote the presence of the features. Note also the actual peak wavelength of these features can be slightly variable throughout our sample (e.g. $\lambda_{peak} \in [9.7-10.3], [10.8-11.2], [12.8-13.2]\mu\text{m}$).	142
4.4	Extinction values for all our targets as well as SE classification. Note that naked stars (NS) do not belong to any SE class. The CC abbreviation refers to the method of using Correlation Coefficient.	144
G.1	Colors used for each nod and module.	238

List of Appendices

Appendix A	160
Appendix B Iota Herculis Models	184
Appendix C HD72660 Models	195
Appendix D Background Removal	222
Appendix E A_K Values	224
Appendix F	231
Appendix G	238

Chapter 1

Introduction

Astronomy, since ancient times, was the only branch of science that quenched the thirst of mankind to investigate the heavens. Beginning with the smallest of steps, the field of astronomy grew over time to become one of the most intriguing of all modern sciences. The curiosity about heavenly objects goes far back to ancient times, for example when astronomers followed the motion and behavior of celestial objects over time through observing with the naked eye. This curiosity continued on into development of basic primitive telescopes and the very first telescopic observations. Through further observations in time, it became known that these apparently fixed luminous points in sky, in fact evolve on very long timescales.

In this thesis, we investigate the spectroscopic nature of stars as they evolve from early to final stages of their evolution and are about to reach the end of their lives.

The study of these stars is of crucial importance since they play a major role in the enrichment of the chemistry of the universe. Throughout their lifetime, stars convert hydrogen into heavier elements in their interior. Through various processes (e.g. radiative levitation, convective dredge ups, etc.) these products will diffuse higher and higher in the envelope. In the late stages of their evolution, stars eject a significant fraction of these nucleosynthesis products in the form of stellar winds, resulting in a circumstellar envelope of gas and dust around the central star with a very different and intriguing chemical composition. Through radiation pressure, this material will sail into the interstellar medium.

The elemental analysis of the nucleosynthesis products in young stars is commonly carried out. In contrast, the study of circumstellar environments is often done using infrared spectroscopy since stellar radiation is absorbed by dust and re-emitted in the infrared. Every atomic or molecular species and any dust mineral has its own unique fingerprint. Thus, to this day, the study of the stellar chemistry still fascinates astronomers.

This chapter is organized as follows. In §1.1, we briefly describe the processes involved in stellar evolution intermediate mass stars, from early A- and B-type stars to the AGB stages. In §1.2 we discuss the history and development of spectroscopy. In §1.3, we describe the theory behind formation of spectral lines and in §1.4 we cover the tools and methods that can be used to analyze them.

1.1 Stellar Evolution of Low and Intermediate Mass Stars

Stellar evolution is determined primarily by a star's initial mass. The flow of this thesis begins with the study of two specific early A-, B-type stars with intermediate initial mass. Upon evolution, they eventually evolve into AGB stars and become the focus of the third project presented in this thesis. Therefore, we discuss only the evolution of those stars with low and intermediate mass stars that will evolved to AGB phase.

In this context, intermediate mass stars are those with masses between 1.8 to 8 solar masses ($1.8M_{\odot} < M < 8M_{\odot}$) [45]. The two main sequence stars studied in later chapters are near the two extremes of intermediate mass stars with masses of about $6 M_{\odot}$ (ι Her) and $2 M_{\odot}$ (HD72660).

1.1.1 Main Sequence Evolution

We start our description of stellar evolution at the point where stars start fusing hydrogen in their core. On the Hertzsprung-Russell (HR) diagram, stars that are fusing hydrogen into helium in their center are found on a locus known as the main sequence (MS, see Figure 1.3) .

Main Sequence Lifetime

Stars spend the longest period of their lifetime on the main sequence while their luminosity during this time slightly fluctuates. An estimate for MS lifetimes can be obtained from

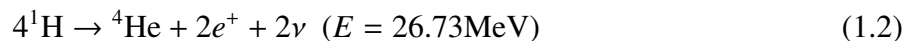
$$\tau_H = \frac{E_H}{L} \quad (1.1)$$

where E_H is the total nuclear energy released by hydrogen fusion in the core. Since nuclear fusion produces energy through converting mass to energy, the higher the mass content of hydrogen is, the more fuel is available for fusion to occur therefore the more energy can be released. This yields a direct dependency between the energy and the total mass content of hydrogen and by extension the total mass of the star ($E_H \propto M_H \rightarrow E_H \propto M$) since about 0.5% of stellar mass energy is released by $H \rightarrow He$, $E_H \lesssim 0.005Mc^2$.

Main Sources of Energy Production

Stars on the main sequence produce energy through two mechanisms: the proton-proton chain (or pp -chain) and CNO cycle. On the main sequence, the hydrogen fusion process takes place through both the pp -chain and the CNO cycle [see Chapter 2 in 47]. In what follows we briefly describe both mechanisms.

The net effect of the proton-proton chain, as shown in equation 1.2, is the conversion of four hydrogen atoms into helium accompanied by the release of 26.731 MeV of energy (corresponding to an 0.71 percent mass defect). However, neutrinos carry away 2-30% of this energy; therefore depending on the exact reactions this value can change [see e.g. 20].



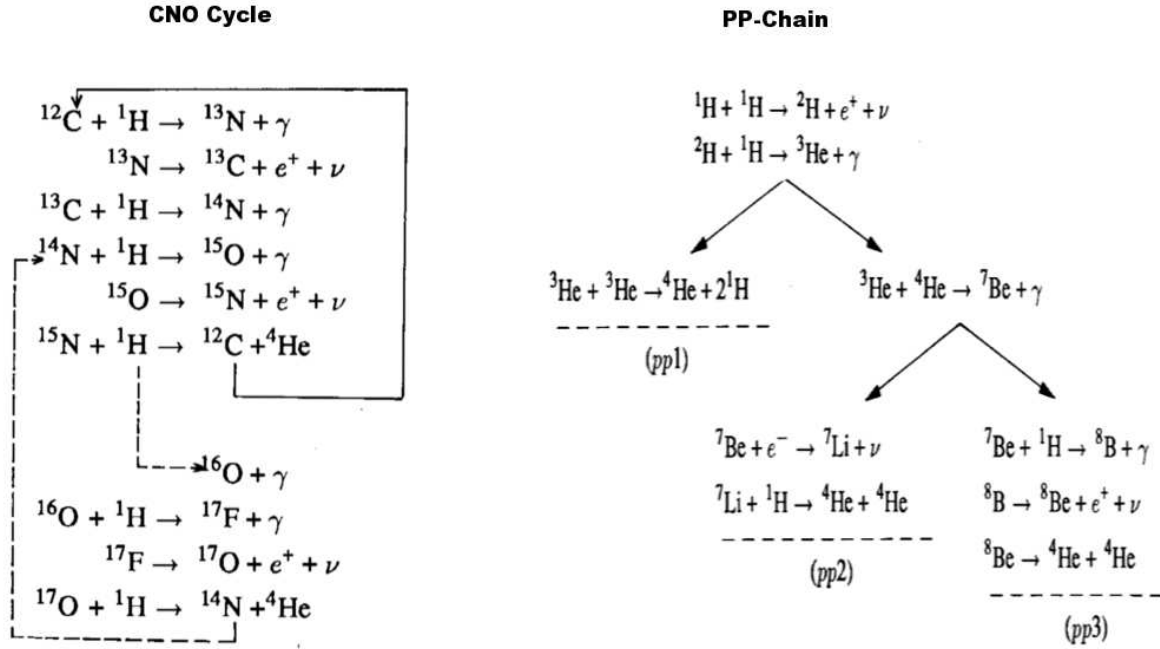
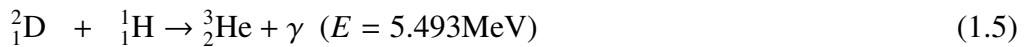
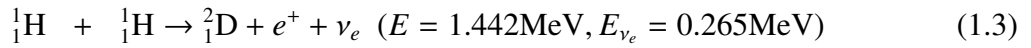


Figure 1.1: *Left:* The reactions involved in the CNO cycle. *Right:* The reactions involved in *pp*-chain [66].

The steps involved in *pp*-chain were understood by von Weizsäcker [126] and Bethe [9]; in all cases, the first few reactions are:



The *pp*-reaction chain begins with the formation of deuterium (${}^2_1\text{H}$ or ${}^2_1\text{D}$) releasing a positron and a neutrino (see Eq. 1.3). Almost immediately, the positron annihilates with an electron and produces two gamma ray photons with a total energy of 1.02MeV (Eq. 1.4). Thereafter, the combination of deuterium produced in step 1.3 with another hydrogen nucleus leads to the formation of ${}^3\text{He}$ (Eq. 1.5). From here on the ${}^4\text{He}$ can form through three possible paths (or branches). Figure 1.1 shows the steps involved in each branch. The branching of the proton-proton chain to any one of these three possibilities depends on temperature and the ratio of helium to hydrogen abundance [For more details see e.g. 20, 86, 66].

Another source of energy production is the CNO Cycle (a.k.a. Bethe-Weizsäcker Process) in which carbon, nitrogen and oxygen act as catalysts for the combination of four protons which leads to formation of helium-4 [9]. The sequence of the CNO cycle reaction is shown in Figure 1.1. The reaction ${}^{14}\text{N}(p,\gamma){}^{15}\text{O}$ is the bottleneck reaction of the CNO cycle and will cause the abundance of ${}^{14}\text{N}$ to exceed that of any other CNO nucleus [17]. When the CNO cycle reaches the reaction (${}^{15}\text{N}+{}^1\text{H}$) the cycle takes two possible paths (CNO bi-cycle). It can produce ${}^{12}\text{C}$ and repeat the main cycle (CNO-I), or (once out of every 10^4 cases) it can produce

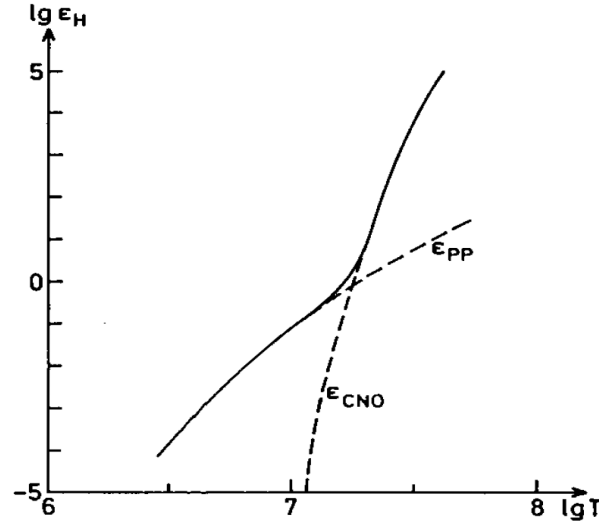


Figure 1.2: This plot illustrates the contribution of the CNO cycle and pp -chain in energy production as a function of temperature. The CNO cycle dominates the pp chain at higher temperatures [66].

^{16}O and enter a secondary cycle (CNO-II).

The CNO cycle is much more temperature dependent than the pp -chain, therefore the proton-proton chain dominates at the lower temperatures of low mass stars while the CNO cycle takes over the energy generation at higher temperatures [66]. This is because unlike pp -chain, the reactions in CNO cycle start occurring at the higher temperature of intermediate mass stars and the rate of energy production rapidly increases with increasing temperature. Figure 1.2 shows the contribution of each as a function of temperature.

Evolution on Main Sequence

As a star spends time on the main sequence, the composition of the core slowly changes from mostly hydrogen to mostly helium. As the star consumes its hydrogen on the main sequence, four hydrogen nuclei get converted to one helium nucleus, which results in a slight decrease in the pressure and therefore the star gradually contracts. This slow contraction releases gravitational potential energy, thus heating up the core, which increases the rate of fusion. Over the MS lifetime, this process slightly increases the luminosity of the star and thus pressure so that balance is restored. This creates a width for the main sequence band which distinguishes the zero-age main sequence stars from those stars that have already spend some time on the main sequence.

Main sequence stars are classified based on their temperature and spectral characteristics. The Morgan–Keenan(MK) system classifies stars following a sequence of letters; O, B, A, F, G, K, and M which represented a sequence from the highest temperature (O-type) to the lowest temperature (M-type). Furthermore, each of these classes are subdivided into 10 numeric digits with 0 being hottest and 9 being coolest. The MK system also includes a luminosity-based classification which is denoted using Roman numerals; Supergiants(I), Bright Giants (II), Giants (III), Subgiants (IV), Main Sequence Stars (V). In the next two chapters of this thesis, we

will focus our attention on two specific classes: A- and B-type stars.

A-type stars occupy about 0.63% of the main sequence stars in the solar neighborhood. They usually have surface temperatures between 7600–10,000K. In their spectra they show strong hydrogen Balmer lines, lines of ionized metals such as Fe II, Mg II, Si II, and weak CaK lines.

B-type stars occupy about 0.13% of the main sequence stars in the solar neighborhood. They usually have surface temperatures between 10,000–30,000K. In their spectra they show strong hydrogen Balmer lines, neutral helium (He I) lines, and ionized metal lines including Mg II, Si II, and Si III. Their characteristics will be discussed in greater detail in the following chapters.

1.1.2 Post Main Sequence Evolution: To AGB & Beyond

As low to intermediate mass stars exhaust hydrogen in their core, they evolve off the main sequence. From this point on the evolutionary path is slightly different for low mass stars than it is for intermediate mass stars. We present a very brief overview in this chapter. The details involved in every step of the evolution are slightly marginal to the purpose of this thesis but are included in an appendix for the interested reader (see Appendix A).

In summary, after the core gradually exhausts hydrogen, it will turn into an inactive helium core with a fusing hydrogen shell. The shell fusion will add more helium to the inactive core. This process leads to the expansion of the hydrogen shell and contraction of the helium core. Upon reaching the Hayashi limit, the star becomes fully convective. The luminosity increase at this stage will cause the star to move up the HR diagram almost vertically onto the Red Giant Branch (RGB). It is worthwhile to mention that convection can penetrate the interior layer and bring up nucleosynthesis products to the surface. This is known as the “first dredge-up” which can change the surface abundance of elements such as ^{13}C , ^{14}N , and ^{12}C [see e.g. 59, 41, 35, 19, 5, and references therein for further details]

As the star ascends the RGB branch, the inactive helium core continues to contract gravitationally which results in temperature and density increase until it reaches temperatures of about $\approx 10^8$ K when helium can ignite. In case of a low mass star the core will become electron-degenerate and the helium will burn in an explosive manner also known as the “helium flash”. In the case of an intermediate mass star, there will be no degenerate condition, so helium fusion will take place in a gentle manner. Helium fusion (in both degenerate and non-degenerate conditions) occurs through a process known as the triple-alpha (3α) process. The 3α process converts three α particles (^4He) into one carbon nucleus (^{12}C). The triple-alpha process is very sensitive to the temperature: the nuclear reaction rates scale typically with T^{40} [66]. Both low and intermediate mass stars that are fusing helium steadily in their core will settle down on the horizontal branch (HB) on the HR-diagram.

As helium gradually burns in the core, the supply of helium as well as the radiation pressure decreases; once again, this leads to a slight drop in pressure and the core slowly undergoes gravitational contraction to maintain hydrostatic equilibrium. When the core runs out of He, the gradual contraction heats up the surrounding shell and switches on the shell burning process. As before, this results in an increase in luminosity and a decrease in effective temperature through expansion. The star has then reached the asymptotic giant branch (AGB) phase [76], so called because it asymptotically touches the RGB.

The structure of an early-AGB star consists of a hot and dense electron degenerate core of carbon and oxygen, surrounded by two shells of helium and hydrogen which are mostly

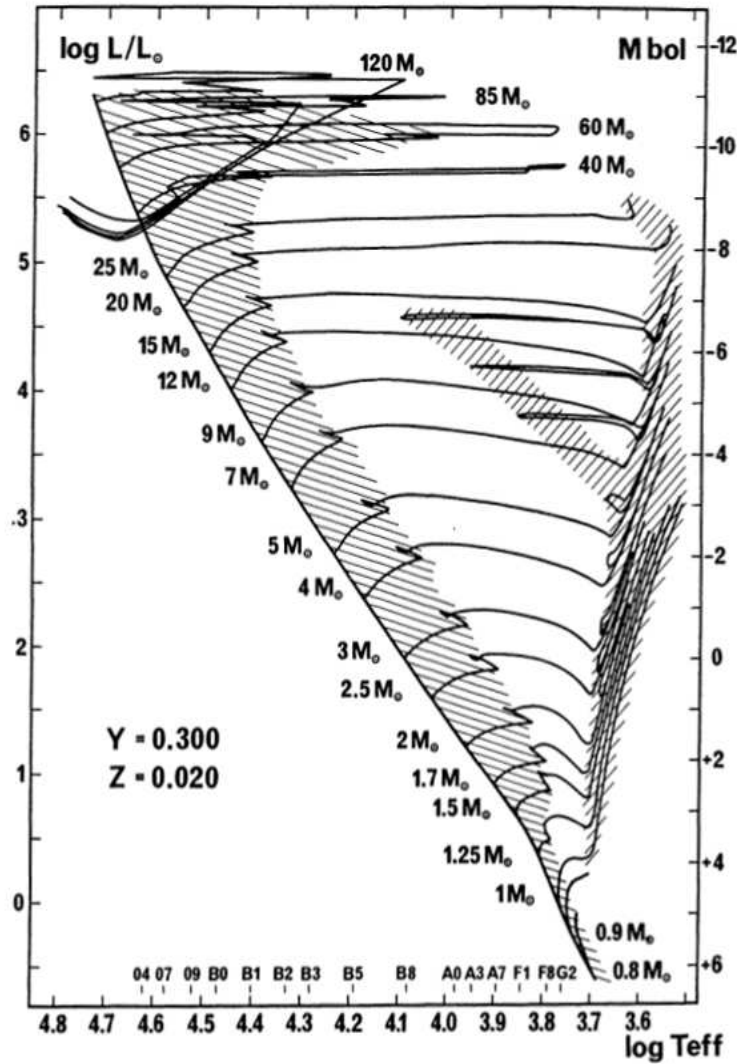


Figure 1.3: The theoretical Hertzsprung-Russell diagram including the zero-age main sequence (solid line) for various initial masses and their corresponding evolutionary tracks (Figure taken from Schaller et al. [107]).

responsible for the luminosity in this phase. These two shells are not always actively burning at the same time. However, the nuclear energy released from one shell can reignite the other shell and begin a phenomenon known as “double shell burning”. It is worthwhile to mention a phenomenon that occurs in this stage known as the “second dredge-up”. It only occurs in intermediate mass stars with masses greater than $4 M_{\odot}$ [47, 3] because the convection can penetrate the region in between the hydrogen and helium shells and it can bring up the leftover products of nucleosynthesis in that region. This can lead to changes in surface abundances of a few elements such as ^{16}O , ^{14}N , ^{18}O , ^{22}Ne [see 3, & Appendix A].

The He shell becomes thinner as more He is consumed. It eventually undergoes a certain type of thermal instability described in detail by Schwarzschild H arm [112] and give rise to

“thermal pulses” or “helium shell flash”. Thermal pulses introduce a second stage of AGB evolution known as the thermally pulsing AGB (or TP-AGB). As a result of the helium shell flash, the region between two shells becomes convective. As in the first and second dredge-up, the convective layer will bring nucleosynthesis products to the surface in a series of events collectively referred to as “third dredge-up” which changes the surface abundances of particularly ^{12}C and ^4He [43, 47].

A key ingredient in the evolution of AGB stars is that stellar winds reduce the mass of the envelope from the outside through mass loss (see Appendix A). Unlike most other phases in stellar evolution for which the amount and consumption rate of fuel determines the evolution, the AGB stellar evolution is characterized by rates at which material is removed from the outer layers of the star. At rates of 10^{-8} – $10^{-3} M_{\odot}$ per year (with mass loss rates increasing as stars climb the AGB), mass loss sets an AGB lifetime of $\approx 2 \times 10^6$ yr [54]. It is thought that near the tip of the AGB, AGB stars will experience a so-called superwind phase with mass-loss rates of up to $10^{-3} M_{\odot}/\text{yr}$, which effectively ejects the entire remaining stellar envelope in a short amount of time (~ 1000 years), and leads to the termination of AGB phase.

After that, in what is known as post-AGB phase, the deeper and hotter layers will gradually be exposed as the outer layers are expelled. The steps include the formation of a pre-planetary nebula phase (PPN) which then turns into a short phase of planetary nebula (PN) from which the remnant is a compact electron degenerate core of carbon and oxygen known as white dwarf. Upon formation, the white dwarf is quite stable and it will start its cooling journey on timescales of billions of years.

1.2 Stellar Spectroscopy: History & Development

In year 1835, a well known French philosopher, Auguste Comte, stated that humans will never comprehend the chemical composition of stars. Not too long after that, scientists proved this statement wrong. The two new fields of study, spectroscopy and photography, emerged. The father of stellar spectroscopy was Josef von Fraunhofer (1787-1826) who made the first crude spectroscope by mounting a prism in front of a telescope. He observed dark lines in the spectrum of the sun or bright stars like Sirius, but he could not ascribe a cause to these lines, therefore his contribution was confined to data acquisition. A major advance was made by Gustav Kirchhoff (1824-1887) and Robert Bunsen (1811-1899) who interpreted the dark lines as selective absorption of light by chemical elements in the atmosphere of stars. They also found that every chemical element has a one of a kind spectral signature known as its “finger print”. The discovery of helium in the sun and its later confirmation by chemist William Ramsay solidified spectroscopy as an investigative technique in astronomy.

In the 19th century, scientists like William Huggins and Angelo Secchi used photographic plates to gather as many spectra as possible and came up with the first basic classification of stars; blue/white, yellow (or solar-type stars), and red stars. In continuation of this program, by mid-19th century, Edward C. Pickering and Annie Jump Cannon gathered over a quarter of a million stellar spectra and developed the classification system which is accepted by astronomers to this day. This system was also described in §1.1.1 and contains O, B, A, F, G, K, and M which classifies stars based on their atmospheric temperature (from 40,000 down to 3000K).

After establishing spectroscopy as a promising tool for the science of astrophysics, the tools also began to evolve over the years. The early spectrographs involved optical tools such as prisms but the dispersion was insufficient, particularly in the red. The early designs were gradually replaced by alternatives like diffraction gratings which could result in higher resolution and larger dispersion. Gratings are evenly spaced grooves ruled on a surface which uses the wave nature of light to break it into a spectrum. This method was later improved by Henry A. Rowland, an American physicist, who introduced Rowland's gratings into spectroscopy. His design made line spacing of the grating much more accurate than before. He also introduced concave gratings which focused the spectra directly on a photographic plate [128].

However, the science of spectroscopy is definitely not limited to the dispersion of visible light into rainbow colors, but it also covers other regions of the electromagnetic spectrum. In year 1800, Sir Frederick William Herschel (1738-1822), discovered infrared light through measuring the temperature of a solar spectrum beyond the red portion of the visible spectrum. He realized that the temperature increased from the violet end to the red end and reached its highest beyond the red. Not too long after that, in year 1801, Johann Ritter (1776-1810) discovered ultraviolet radiation through observing the reactions of silver chloride to the violet end of the spectrum.

The birth of infrared and ultraviolet spectroscopy opened a whole new chapter in astrophysics. Astronomy is now equipped with tools that can help us learn about stellar physics, structure and evolution. In the following two sections we will provide an overview of the details involved in the analysis of the stellar spectra (§1.3) and present day implications of UV and IR spectroscopy (§1.4).

1.3 Spectral Lines: Formation & Analysis

When emitted radiation at wavelength λ flows through a medium, it can either be absorbed, reflected or transmitted. The fractions of the radiation that is absorbed, reflected or transmitted is called **ABSORPTANCE**, **REFLECTANCE** AND **TRANSMITTANCE**. The sum of these three is unity. If we have an object for which the absorptance is equal to unity at all wavelengths, we call that object a “blackbody” and if the absorptance is less than unity at all wavelengths then we have a “grey body”.

In mid-nineteenth century, Gustav Kirchhoff's (and Bunsen's) studies greatly influenced the foundations of spectroscopy. The first of Kirchhoff's principal results was that “good emitters are good absorbers”. Let's consider a cavity, at a certain temperature, that is filled with radiation E_λ . If the absorptance is $a(\lambda)$ then the energy absorbed by the walls of the cavity is $a(\lambda)E_\lambda$. Upon this absorption, the body will become warm and begins to radiate energy. If the rate at which it radiates energy is denoted by M_λ then the Kirchhoff's Law states that in thermal equilibrium $a(\lambda)E_\lambda = M_\lambda$. In case of a blackbody, the absorptance is unity, thus the “blackbody radiation” or “cavity radiation” refers to a system that absorbs all the radiation that is incident upon it and re-radiates the same amount. Therefore, for a blackbody the absorptance is unity and the emission is determined by the Planck function.

The atmosphere of a star is a layer of gas that approximates a blackbody radiator. Thus the stellar atmosphere emits into space a continuous spectrum at all wavelengths that roughly follows the Planck function. The remainder of Kirchhoff's laws are concerned with the ab-

sorption and emission spectrum. In general terms a hot diffuse gas (low density) will emit at specific wavelengths once placed against a cooler background which creates an emission line spectrum, and a cool diffuse gas will absorb light at specific wavelengths once placed in front of a hotter source of continuum spectrum, which creates an absorption spectrum.

In astronomy, we often make a simplifying assumption regarding the structure of the stellar interior. The atmosphere is for example, sometimes approximated as an isothermal homogeneous slab where temperature and density are invariant with radius, whereas in reality, the gas layer from which stellar radiation is emitted into space, has a steep pressure and mass gradient and a temperature that declines rather modestly through the atmosphere while the energy flux remains constant. The atmosphere is usually in hydrostatic equilibrium:

$$\frac{dm}{dr} = 4\pi r^2 \rho(r) \quad (1.6)$$

$$\frac{dP}{dr} = -\frac{Gm}{r^2} \rho(r) \quad (1.7)$$

Equation 1.6 is known as the mass conservation which represents the infinitesimally small element of mass in the stellar atmosphere as a function of density. The total mass of the atmosphere will be the integration of equation 1.6 from bottom to top. Equation 1.7 is known as the hydrostatic equilibrium. It describes the balance between forces of upward pressure and downward gravity at any point in the stellar interior (r) for any hypothetical element of mass of Δm with height dr and surface area of dS . It shows that the stellar atmosphere is not isobaric and that pressure varies with radius. The derivation of these equations is marginal to the purpose of this section but an interested reader may look into [66].

As mentioned above, the basic treatment of stellar atmospheres involve several assumptions. However, in addition to equations 1.6 and 1.7, we adopt the assumption of Local Thermodynamic Equilibrium (LTE) when dealing with stellar atmosphere. This rather self explanatory term means that all thermodynamic properties in a small volume have the thermodynamic equilibrium values at the local values of temperature and pressure. These thermodynamic properties can include: number density of atoms in a certain excitation or ionization level, opacity, emissivity, etc.

The assumption of LTE is particularly good, when purely collisional processes are dominant, since conditions are naturally determined on a local basis. However, if we consider a medium where the mean free path of photons is larger than that of particles, then this assumption may break down. In stellar atmospheres, this can be the case where one region of the atmosphere is not only locally influenced by the collision of particles but also influenced by the radiation field from other parts of the atmosphere. In general, when the radiation field starts playing a major role in the ionization/excitation of particles, LTE assumption is replaced by non-LTE (nLTE). However, non-LTE calculations are far more complex and time consuming. Thus for simplicity of calculations, we adopt the assumption of LTE throughout this work. Under the assumption of LTE, we can simplify the following calculations;

I. The velocity distribution of ions and electrons is Maxwellian and is given by;

$$\frac{dn(v)}{dv} = n \left(\frac{m}{2\pi k T_k} \right)^{3/2} e^{-\frac{mv^2}{2kT_k}} \quad (1.8)$$

II. In any given atomic gas, the population of each level of one excitation state of one

element, is dependent on various factors and it is formulated by Boltzman's Law,

$$\frac{n_j}{n_i} = \frac{g_j}{g_i} e^{-(E_j - E_i)/kT} \quad (1.9)$$

where n is the population of any given level, g is the statistical weight and E is the energy of that level relative to the ground state.

III. The population distribution between ionization states in an atom is also dependent on its physical conditions such as temperature, and it can be formulated by the Saha equation,

$$\frac{n_{r+1}}{n_r} P_e = \frac{u_{r+1}}{u_r} 2 \frac{(2\pi m_e)^{3/2}}{h^3} (kT)^{5/2} e^{-\chi_r/kT}$$

where χ_r is the ionization potential of state r and u is the partition function for each ionization state.

IV. Locally, the source function is equal to a Planck function at the local temperature $S_\nu = B_\nu(T)$. If an emergent photon from the hot interior, is now absorbed by an atom, higher up in the atmosphere of the star, it is going to cause an absorption line in an otherwise continuous spectrum because the temperature-dependent source function is directly related to the emergent intensity and high up in the atmosphere the temperature cools down. In the following sections 1.3 and 1.3.2, we will discuss several difference sources of opacity in a star which are also used in the following chapters of this thesis.

1.3.1 Atomic Spectroscopy

In an otherwise uniform continuum, there sometimes appears a deficiency or excess of photons over a range of wavelengths. The deficiency is referred to as “absorption lines” and the excess is referred to as “emission lines”. The spectral region for atomic and molecular lines spans from microwave to ultraviolet, depending on the specific transition. The opacity caused by interactions between photon and microscopic particles (atoms, electrons, etc.) include; bound-bound (bb), bound-free(bf), free-free (ff) transitions which includes electron scattering (es). Thus the total opacity in the stellar interior is given by;

$$K_\nu = K_{\nu,bb} + K_{\nu,bf} + K_{\nu,ff} + K_{\nu,es}$$

It is evident that lines in stellar spectra show a clear variety in terms of strength and shape. There are several factors that go into describing a line. A line in the spectrum of a star, is characterized by its **PROFILE**, which is essentially the distribution of energy as a function of frequency. Let's denote the distribution of flux in the line by F_ν , the continuum flux by F_c and the absorption depth by A_ν . The simplest form for the line profile function, considering only thermal broadening is;

$$\phi_\nu = \frac{1}{\sqrt{\pi}\Delta\nu} e^{-\left(\frac{\nu - \nu_0}{\Delta\nu}\right)^2} \quad (1.10)$$

where $\Delta\nu = \xi_0 \nu_0/c$ is the thermal width and $\xi_0 = (2kT/m)^{1/2}$ is the most probable thermal velocity. The absorption depth of a line is then,

$$A_\nu \propto 1 - \frac{F_\nu}{F_c}, \quad 0 \leq A_\nu \leq 1 \quad (1.11)$$

A_ν represents the line strength at any given wavelength, however the integrated line strength is called the equivalent width $W_\nu (= \int_0^\infty A_\nu d\nu)$. The absorbing effect of a line, however, is dependent on various other factors: The number of absorbers per unit volume capable of absorbing photons at that particular frequency (n_i), the classical total absorption cross section ($\pi e^2/m_e c$), the equivalent number of electrons or the oscillator strength ($f_{ij} \sim 0.01-0.1$), as well as the normalized line profile ϕ_ν such that $\int \phi_\nu d\nu = 1$. The absorption coefficient of a spectral line can be written as follows;

$$l_\nu = n_i \left(\frac{\pi e^2}{m_e c} \right) f_{ij} \phi_\nu$$

This expression is general and it can vary according to the specific type of transition. The continuous absorption coefficient is the sum of the absorption resulting from many physical processes which once measured in per neutral hydrogen atom it is denoted by κ_ν . This is per units of square centimeter per gram and has frequency (or wavelength $A_\lambda = A_\nu$) dependence. In what follows we briefly describe each of the processes for an atmosphere that consists of pure hydrogen. The detailed discussions are available in [66, 79].

Electron Scattering

Another form of free-free interactions is known as scattering where incident photons are scattered by a free electron. These transitions, appears as individual absorption/emission lines in the spectrum.

Let's consider a pure hydrogen gas. In case of electron scattering, the absorption coefficient is proportional to the number density of electrons in the medium (n_e/ρ), the cross-section for scattering of photons off electrons (σ_e), the total number of atoms (N_A);

$$\kappa_{es} = \frac{n_e}{\rho} \sigma_e$$

where most of the electrons are provided from hydrogen.

$$\sigma_e = \frac{8\pi}{3} \left(\frac{e^2}{m_e c^2} \right)^2 = 0.665 \times 10^{-24} \text{ cm}^2 \quad (1.12)$$

In this equation σ_e is the Thomson cross-section for electron. Therefore, in the stellar atmosphere, assuming that it is only made of hydrogen and that hydrogen is fully ionized, the electron scattering opacity is directly related to the mass fraction of hydrogen (X). Note that all the expressions for electron scattering are independent of wavelength.

Bound-Free Transition

In this transition, the electron moves between an atomic state and an unbound state. Similar to bound-bound transitions, this type of transition can also result in continuous opacity as opposed to a single spectral line. For example, a photon with the minimum energy of 13.6eV is capable of moving a bound electron in the ground state ($n=1$) of the hydrogen atom to the first unbound ionized state ($n=\infty$). Note that the bound-free transition of hydrogen can occur from any level ($n=1,2,3,4,\dots$) to the continuum ($n=\infty$). The bound-free opacity is also computed numerically.

The bound-free absorption coefficient was first derived by Kramers [62] and the later modified by Gaunt [32] which brought it into agreement with quantum mechanical results;

$$\begin{aligned} A_n(\lambda) &= \frac{A_0 g'_n \lambda^3}{n^5}, \quad \lambda < \lambda_n \\ &= 0, \quad \lambda > \lambda_n \end{aligned}$$

with $A_0 = 1.044 \times 10^{-26}$ and λ is the wavelength in angstroms, e is the electron charge with the value of 4.803×10^{-10} esu and g'_n is the Gaunt factor which is different from the g_n used for the statistical weight. Note that A_n is only effective before the wavelength limit of any given series; Lyman ($\lambda=912 \text{ \AA}$), Balmer ($\lambda=3646 \text{ \AA}$), Paschen, Brackett, etc and it drops abruptly to zero at the highest wavelength edge of each series (see Figure 8.2 in Gray [31]). The bound-free opacity is then just the sum of the numbers of absorbers in each level times the absorption coefficient A_n ;

$$\kappa_{bf,v} = \sum_{n_0}^{\infty} A_{v,n} \frac{N_n}{N} \quad \text{cm}^2 \text{ g}^{-1} \quad (1.13)$$

where, N_n/N is the number of hydrogen atoms excited to the n th level per neutral hydrogen atom. We refer the reader to the Boltzman equation presented in 1.9. This is roughly 100 times greater than the free-free opacity.

Free-Free Transition

This transition occurs when a free electron picks up an acceleration upon passing close to an ion. An accelerated charge will emit a radiation which is referred to as free-free emission or Bremsstrahlung emission. If the electron passes close enough to an ion it can absorb radiation and lead to a free-free absorption. This transition becomes important, in highly ionized plasma which occurs at extremely high temperatures or very low densities.

The free-free absorption coefficient is proportional by several factors; The number density of electrons and ions that are present in the plasma, the minimum velocity that is needed to result in an absorption of a photon of frequency ν , which considering a Maxwellian distribution is $v_{min} = (2h\nu/m_e)^{1/2}$, the temperature (T) of the medium, and in the end of course the density of the medium itself (ρ). Taking into account all of these factors, the free-free absorption coefficient can be written as;

$$A_{ff,v} \sim \frac{2}{3\sqrt{3}} \frac{h^2 e^2 R}{\pi m^3} \frac{1}{\nu^3} \left(\frac{2m}{\pi kT} \right)^{1/2} \quad (1.14)$$

where R is the Rydberg constant for hydrogen ($1.0968 \times 10^5 \text{ cm}^{-1}$). The free-free opacity can then be simplified to the following expression;

$$\kappa_{ff,v} = \frac{A_{ff,v} g_f N_i N_e}{N_0} = A_{ff,v} g_f \frac{(2\pi m kT)^{3/2}}{h^3} e^{-hcR/kT} \quad (1.15)$$

where $R = 2\pi^2 m e^4 / h^3 c$, and N_i , N_e , N_0 are number densities of ions, electrons and neutral hydrogen, g_f is the free-free Gaunt factor [32].

Bound-Bound Transition

In this transition, the electron moves up or down in between two bound states in an atom or ion. As a result there will be a photon emitted or absorbed with the energy equal to that of the difference between the two energy levels involved. This efficiency of this process is inversely related to temperature of the medium.

The main direct process that is involved with bound-bound transitions is the direct absorption of a photon with the energy of $h\nu = |E_i - E_j|$ which leads to a transition upward from a lower bound state (i) to a higher bound state (j). There are also two return possibilities associated with this process; spontaneous emission of a photon, and stimulated emission which is an emission induced by a radiation field.

The computation of bound-bound opacity is usually carried out numerically which involves the summation of millions of individual absorption lines. The spectral lines due to bound-bound transitions will influence the structure of the atmosphere by altering the temperature gradient so that the continuum flux entering the atmosphere from inside the star can still emerge from in between the blocking spectral lines. The bound-bound transitions also influence the spectral line shape itself through blending with other spectral lines. This effect will be illustrated with examples in chapters 2 and 3.

H⁻ Opacity

In the envelopes of cooler stars, such as AGB, the negative hydrogen ion (H⁻) can be a dominant source of opacity. When a free electron passes by a neutral hydrogen atom, the negative charge in the electron can introduce a dipole moment in the atom. The positive side of the dipole, can now hold on to the electron for a short time and result in hydrogen anion or negative hydrogen ion H⁻. This rather fragile bond can absorb energies in the range of 0.75-4.0 eV through either bound-free or free-free absorption;

$$\kappa_{bf} : H^- + h\nu \rightleftharpoons H + e^-(\nu) \quad (1.16)$$

$$\kappa_{ff} : H + e^-(\nu) + h\nu \rightleftharpoons H + e^-(\nu) \quad (1.17)$$

The photons would be absorbed in the visible or infrared region of the electromagnetic spectrum. The opacity associated with this process will indeed depend on a number of factors; the number density of H⁻ ions which can be calculated from Saha equation and the metallicity (Z) since the presence of metals can enhance the H⁻ opacity by their additional supply of free electrons. This source of opacity becomes less dominant in the coolest stars due to a decreased supply of free electrons.

The bound-free atomic absorption coefficient has been calculated [see 31, and references therein]. It is accepted that on a logarithmic scale, the bound-free absorption coefficient varies nearly parabolically as a function of wavelength λ with a peak around 8000 Å (see Figure 1.4). The bound-free component of the H⁻ opacity is most important in the optical.

The free-free component however, becomes dominant in the infrared. The detailed derivation of the absorption coefficient can be found in Gray [31, and references therein]. The behavior of H⁻ absorption coefficient A_{ff} as a function of wavelength λ is shown in figure 1.4. We leave the detailed derivation of absorption coefficients and opacities to the interested reader [see 66, 79, 31, and references therein].

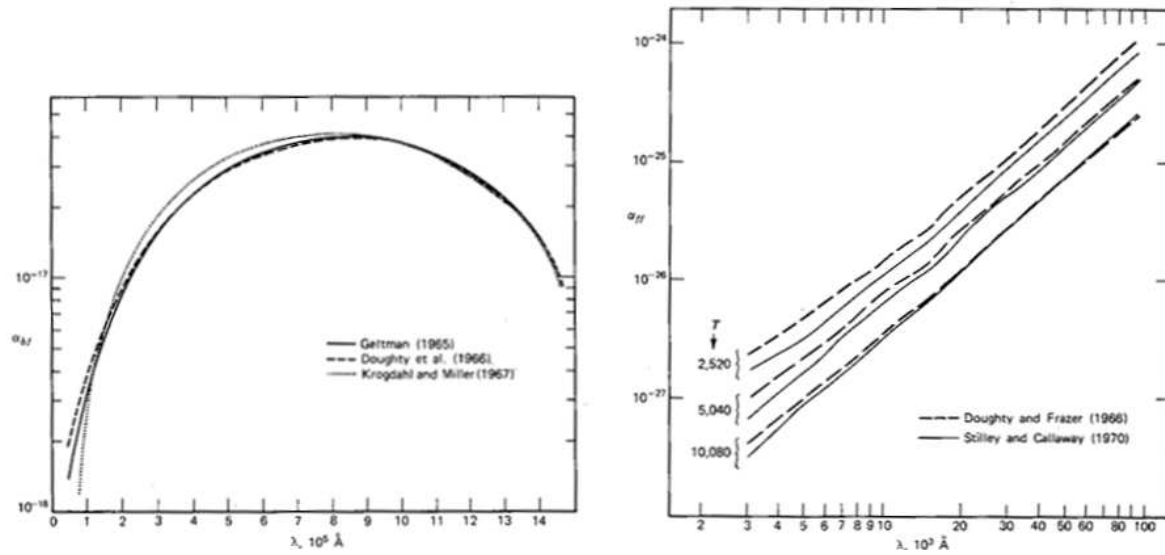


Figure 1.4: *Left*: The bound-free absorption coefficient of the H^- ion per cm^2 per ion per electron pressure. *Right*: The free-free absorption coefficient of the H^- ion per cm^2 per ion [Figures taken from 31].

1.3.2 Molecular Spectroscopy

Interactions of radiation with matter is not limited to atoms. Molecules and dust particles can interact with photons and create their own unique set of absorption and emission features. In this section we provide a very brief overview of the types of transitions that occur in molecule-photon interactions.

Molecular species can be categorized as diatomic, triatomic, and polyatomic. The theory of quantum mechanics dictates that all energy levels in atoms or molecules are discrete and are given by the solution to the Schrödinger equation;

$$\left[-\frac{\hbar^2}{2\mu}\nabla^2 + V(r)\right]\psi = E\psi \quad (1.18)$$

where $\hbar = h/2\pi$ (h = Planck's constant), ψ is the wavefunction and $\mu (= m_1 m_2 / (m_1 + m_2))$ is the reduced mass, E and $V(r)$ represent energy levels and potential energy, respectively.

Depending on the geometry of the molecule, it is possible to solve the Schrödinger equation to find a theoretical expression for the energy levels (linear, symmetric top molecules), however in some cases the solution can only be achieved numerically with help of a computer (asymmetric top molecules). Furthermore, selection rules will put further constraint on transitions as to which ones are and are not allowed. We do not include details of such calculations here, but we refer the interested reader to the book "Spectra of Atoms and Molecules" By Bernath [11] for extensive details.

The energy of a molecule can change through three main transitions; electronic, vibrational, and rotational. At times a combined transition will take place such as Rotational-vibrational or Rovibronic (Rotation-Vibration-Electronic) transitions. According to Born-Oppenheimer

approximation the energies associated with these three transitions can be treated separately ($E_{tot} = E_{el} + E_{vib} + E_{rot}$). The spectral region of all these molecular transitions also fall into the range between microwave to ultraviolet region of the electromagnetic spectrum.

Let's consider a diatomic molecule such as carbon monoxide (CO). It consists of two nuclei and an electron cloud. The molecule is in its ground electronic state if all the electrons have their lowest possible energies. If a photon has the exact energy to take an electron to another orbit at a higher energy level, then the molecule is said to be in an excited electronic state. The photons that lead to electronic excitation of molecules are typically in the ultraviolet and visible regions.

In addition to electronic excitation, molecules can also undergo vibrational motions. Consider a diatomic molecule as two atoms that are connected by a spring and are vibrating like a harmonic oscillator. Therefore, the solution to equation 1.18 using the harmonic oscillator potential $V(r) = 1/2k(r_e - r)^2$ becomes,

$$\frac{E_v}{hc} = G_v = \omega(v + \frac{1}{2}) \text{ [cm}^{-1}\text{]} \quad (1.19)$$

where ν is the frequency of vibration and v is an integer for the vibrational energy level. Thus, $\nu=0$ corresponds to the lowest, and higher ν values correspond to higher vibrational frequencies. Molecular vibration can only occur at discrete frequencies therefore has discrete energies. The vibrational energy states give a fine structure to the electronic states, thus within electronic states (typically separated by $\sim 20,000 \text{ cm}^{-1}$) there will be several vibrational states (typically separated by $\sim 2000 \text{ cm}^{-1}$). Of course, this is a very simplified approach; the solution using Morse function will result in a more accurate structure for the energy levels. We will not include the extensive calculations here [see 11, for detailed calculations].

In addition to this, molecules can also rotate at certain frequencies. Therefore, it is possible to measure the quantized energy state of molecules as they rotate. These energies can be derived theoretically under the assumption that molecules are rigid rotators. This assumption allows us to solve the Schrödinger's equation for $V(r) = 0$ and find;

$$E_J = \frac{h^2}{8\pi^2 I} J(J + 1)$$

where J is an integer, I is the moment of inertia (μr_0^2) and μ is the reduced mass. Similar to equation 1.19, for rotational energy levels we can write;

$$F_J = \frac{E_J}{hc} = \frac{h}{8\pi^2 c I} J(J + 1) = BJ(J + 1) \text{ [cm}^{-1}\text{]} \quad (1.20)$$

where J corresponds to rotational state. Thus $J=0$ corresponds to the lowest, and higher J numbers correspond to higher rotational energy states. Overall, the rotational energy states result in a fine structure in every vibrational state, therefore within vibrational states (typical separation $\sim 2000 \text{ cm}^{-1}$), there will be several rotational energy states (typical separation \sim few hundreds of cm^{-1}). A comparison between the three kinds of energy levels, electronic, vibrational, and rotational, is illustrated in an energy level diagram in figure 1.5.

Note that rotational transitions mostly result in microwave and far-infrared absorption bands, vibrational transitions appear in the mid- and near-infrared and electronic transition

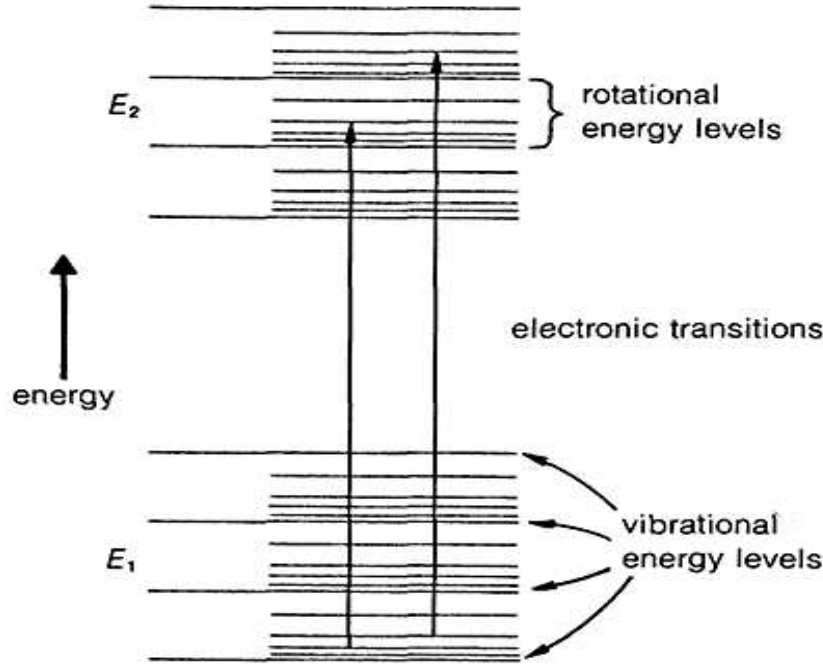


Figure 1.5: This figure shows the energy level diagram for three different transitions; electronic, vibrational and rotational [Figure taken from 72].

occur in the ultraviolet regions. This knowledge is indeed important in many ways. As an example, the mid- to near-infrared spectra of AGB stars is dominated by molecular features. In chapter 4 of this thesis, we will attempt to model these molecular features in a set of mid- to near-infrared ($\sim 5\text{--}38\mu\text{m}$) AGB spectra. Knowledge of specific spectra helped us identify the vibrational bands of several molecular species such H_2O , SiO , CO , etc. (see chapter 4 for more details).

1.3.3 Equation of Radiative Transfer

In section 1.3, we briefly covered several atom-photon interactions that can lead to transitions. Now the question that remains is how can we determine the emergent electromagnetic spectrum, taking into account all the effects of the atomic medium that the photon passed through before it had reached the observer. We consider a very simple model of radiation emerging from a stellar atmosphere.

The equation of radiative transfer describes the change that occurs in specific intensity of a light as it passes through an isothermal slab. The quantity that describes the radiation is called the *specific intensity* $I_\nu(\theta, \phi)$ which measures the energy passing per second and per unit frequency, through a normal unit area and solid angle $d(\theta, \phi) = d\Omega$ and take the units of $\text{ergs cm}^{-2} \text{ s}^{-1} \text{ Hz}^{-1} \text{ ster}^{-1}$. Here, we assume for simplicity that the incident photons only undergo absorption and emission transition and that scattering is negligible. The probability of photons of a certain frequency ν being absorbed per unit length, is called the absorption coefficient (κ_ν), and the energy radiated by the medium per unit time, frequency, solid angle and volume is called the emission coefficient (j_ν).

Therefore, what happens to the beam of radiation passing through a medium can be formulated as follows;

$$dI_\nu = (-\kappa_\nu I_\nu + j_\nu)ds \quad (1.21)$$

$$\frac{dI_\nu}{ds} = -\kappa_\nu I_\nu + j_\nu \quad (1.22)$$

This is the basic form of the radiative transfer equation. The length through which the beam of light travels ds , can be written as $ds = dz/\mu$ where $\mu = \cos \theta$. Another useful definition in this context is the optical depth τ which is a measure of how much light is allowed to pass through a given medium. The optical depth depends on the depth in the atmosphere (z) and the absorption coefficient (κ_ν) and is defined as a function of frequency as such, $\tau_\nu = -\kappa_\nu dz$. We can re-write equation 1.22 in terms of optical depth as follows:

$$\mu \frac{dI_\nu}{d\tau_\nu} = I_\nu - \frac{j_\nu}{\kappa_\nu} = I_\nu - S_\nu \quad (1.23)$$

where S_ν is the source function. The optical depth and source function are generally simpler physical quantities than emission and absorption coefficients. For this reason this form of radiative transfer equation is more commonly used.

Now let's consider a star whose atmosphere is in local thermal equilibrium. This means that according to equation 1.23, $I_\nu = S_\nu$ which in case of a stellar atmosphere it simply means that the radiation flow is solely determined by a blackbody spectrum $S_\nu(T) = B_\nu(T)$ at the local temperature T .

In order to solve equation 1.23 for more general cases, we multiply each side of the equation by $e^{-\tau_\nu/\mu}$ and get;

$$\mu \frac{dI_\nu}{d\tau_\nu} e^{-\tau_\nu/\mu} - I_\nu e^{-\tau_\nu/\mu} = \mu \frac{d}{d\tau_\nu} (I_\nu e^{-\tau_\nu/\mu}) = -S_\nu e^{-\tau_\nu/\mu} \quad (1.24)$$

If we consider a beam of radiation that flows from somewhere in the atmosphere outwards to infinity, then this equation can be solved through integration from some optical depth of τ_ν to ∞ as follows,

$$I_\nu(\tau_\nu) = e^{\tau_\nu/\mu} \int_{\tau_\nu}^{\infty} S_\nu(\tau') e^{-\tau'/\mu} d\tau' / \mu \quad (1.25)$$

This is the general solution to the equation of radiative transfer. We can divide this solution by separating it into two integrations; The intensity integrated from τ_ν within the atmosphere to the surface of the stellar atmosphere where $\tau = 0$ for all frequencies, and the intensity which is integrated from stellar atmosphere to infinity;

$$I_\nu(\tau_\nu) = I_\nu(0) e^{-\tau_\nu/\mu} + \int_0^{\tau_\nu} S_\nu(\tau') e^{-(\tau_\nu - \tau')/\mu} d\tau' / \mu \quad (1.26)$$

where $I_\nu(0)$ is the initial intensity diminished by absorption and the second term is the integrated source diminished by absorption. Let's consider a simplified case of an isothermal slab model, for which the source function is a constant. The solution to equation 1.26 then becomes,

$$I_\nu(\tau_\nu) = (I_\nu(0) - S_\nu)e^{-\tau_\nu/\mu} + S_\nu \quad (1.27)$$

When $\tau_\nu \rightarrow \infty$ then $I_\nu \rightarrow S_\nu$ and as $\tau_\nu \rightarrow 0$ then $I_\nu(0) \rightarrow S_\nu(0)$ so the physical interpretation would be that the specific intensity always approaches the source function at a given optical depth. Now let's consider a slightly more realistic case, where the atmosphere is no longer isothermal. In reality, the temperature changes as we move up in the atmosphere. For simplicity, let's assume this change occur in a linear fashion, assuming that the source function at a given frequency, can be modeled with a straight line as a function of optical depth of the continuum τ_c . The source function is truly a more complicated function of position z but we make this approximation for simplicity.

$$S(\tau_c) = S_0(1 + \beta\tau_c) \quad (1.28)$$

where S_0 is the source function at the surface. In this case, the solution to equation 1.26 takes the form of;

$$I(0) = S_0(1 + \beta\mu) = S(\tau_c = \mu) \quad (1.29)$$

The physical interpretation of this result is similar to the case of an isothermal slab. The specific intensity emerging from the atmosphere at any given angle θ (where $\cos \theta = \mu$), tends to approach the source function at the continuum optical depth $\tau_c = \mu$. Therefore, we can model the emerging specific intensity in various directions, for instance when a beam is emerging vertically $\theta = 90^\circ$, then $I = S(\tau_c=1)$ or when a ray is emerging almost horizontally then $I = S_0$. The specific intensity at different angles effectively sample the source function at different depths in the atmosphere. In what follows, we will discuss the details involved in the formation of spectral lines.

1.3.4 Spectral Line Formation: The Milne-Eddington Model

A spectral absorption (or emission) line is characterized by its frequency dependent absorption coefficient.

$$l_\nu = l_0 e^{-(\nu-\nu_0)^2/\Delta\nu^2} \quad (1.30)$$

where l_0 is the absorption coefficient at the center of the line and ν_0 is the frequency of the line center and $\Delta\nu = \xi_0\nu_0/c$ is the thermal width in which $\xi_0 = (2kT/m)^{1/2}$ is the most probably thermal velocity. Note this is the simplest form where we only take into account the thermal broadening (which could include microturbulence).

Now let's consider an atmosphere in which the ratio l_ν/κ_c is a constant η_ν . Therefore the total probability of absorption κ is the sum of the continuum and the line absorption coefficients;

$$\kappa = \kappa_c + \kappa_\nu = (1 + \eta_\nu)\kappa_c \quad (1.31)$$

η_ν is a function of frequency but we assume that it does not change with depth. From the relation between τ and κ we can write;

$$\tau_\nu = (1 + \eta_\nu)\tau_c \quad (1.32)$$

from which the continuum optical depth can be written as;

$$\tau_c = \left(\frac{1}{1 + \eta_\nu}\right)\tau_\nu \quad (1.33)$$

Instead of a linear relation as a function of continuum optical depth (τ_c)(§1.22), we can now approximate the source function in terms of a frequency dependent optical depth τ_ν as follows;

$$S(\tau_\nu) = S_0\left(1 + \frac{\beta}{1 + \eta_\nu}\tau_\nu\right) \quad (1.34)$$

Substituting this source function into equation 1.26, one can solve the radiative transfer equation for a spectral line as follows;

$$I_\nu(0) = S_0\left(1 + \frac{\beta\mu}{1 + \eta_\nu}\right) \quad (1.35)$$

where $I_\nu(0)$ is the specific intensity of the spectral line which in this case is pure absorption (we did not take into account scattering). The ratio of line to continuum absorption coefficient η_ν , varies with frequency and it reaches its maximum at the line center (ν_0). The intensity of the absorption line as shown in equation 1.35, is inversely related to η_ν . This implies that the intensity of the spectral line, as we go from one side to the other starts from a continuum level, goes down to a very small value $\sim S_0$, then goes back up to the continuum level. Note that $\mu = \cos \theta$ depends on the direction with which light beam is emerging. In case of $\mu \ll 1$ the line will be depressed less which is referred to as line weakening.

In case of a strong absorption line, the coefficient of absorption of the line is much greater than that of the continuum ($\eta_\nu \gg 1$). In this scenario, the second term in equation 1.35 become negligible which means that the depth of the line in that region does not vary with increased abundance anymore, except for the wings of the line where η_ν is of the order of one or slightly less. This is known as saturation. In case of weaker lines, where $\eta_\nu \ll 1$, the equivalent width and depth of the line increase linearly with increasing line strength (e.g. increased abundance, increased oscillator strength, etc.). This is because when $\eta_\nu \ll 1$ we can approximate the second term of equation 1.35 with $1/(1 + \eta_\nu) \sim (1 - \eta_\nu)$ which implies that the depth of line $I_c - I_\nu$ is linearly proportional to η_ν . The behavior is also referred to as the curve of growth.

1.4 Spectral Analysis: Tools and Methods

In the field of astronomy, a wide variety of spectral lines are observed, covering a wide range of wavelengths and sources. In this thesis, we will focus our attention on ultraviolet and infrared spectroscopy. The proper interpretation of a stellar spectrum requires a diagnostic tool in order to infer the state of the atmosphere and the circumstellar environments. This yields a quantitative chemical abundance analysis which helps astronomers construct a coherent picture of the structure, current state and evolution of the universe. In sections 1.3 and 1.4.2 we will briefly discuss the tools and methods used in this work.

1.4.1 Spectrum Synthesis in Ultraviolet: Abundance Analysis

The focus of the first two projects (chapters 2 and 3) in this thesis is on performing spectrum synthesis on two early main sequence stars, for the purpose of better determining their atmospheric chemical abundances. The abundance analysis is particularly important, since in later stages of evolution of these stars, the chemistry of the circumstellar envelope and the material returned into the ISM via mass loss is closely linked to these initial atmospheric abundances.

There are several tools to carry out the process of spectrum synthesis but here we use the FORTRAN program ZEEMAN [74]. The original program was designed to model the magnetic Ap stars but it works equally well for non-magnetic atmospheres. The code is designed under the assumption of Local Thermodynamic Equilibrium. The detailed description of the code is documented by Landstreet [74]. Here we only provide a brief application of the code on our specific cases of study.

The ZEEMAN.f program essentially solves the radiative transfer equation under the assumption of LTE (§1.3). The program uses a stellar atmospheric model [71] with solar composition precomputed for us by Piskunov & Kupka [101], and a set of atomic line data from the Vienna Atomic Line Database (VALD; Piskunov et al. [99], Ryabchikova et al. [104], Kupka et al. [70, 100]). As input parameters, the program requires the effective temperature (T_e), gravitational acceleration ($\log g$), rotational velocity ($v \sin i$), microturbulent parameter (ξ), and individualized abundances, in order to compute the emergent atmospheric spectrum. The program first computes a spectrum with the given parameters, then optimizes the fit to the observed spectrum through iteratively searching for best-fit abundances.

The process of spectrum synthesis has been carried out extensively in the optical region of the electromagnetic spectrum. In this work, we want to show that spectrum synthesis in the ultraviolet is as useful and accurate for the purpose of abundance determination. There are a number of elements that do not have any lines appearing in the optical region but have plenty of transition in the ultraviolet. The practice of abundance determination through UV spectral synthesis is relatively new to the literature.

In chapters 2 and 3, we will carry out an abundance analysis for two early main sequence stars; The B-type star HD160762 (ι Her) and A-type star HD72660 (HR 3383). Our assessments provided new results for this particular branch of stellar spectroscopy. The atmospheric abundances of elements provide valuable insights about the formation and evolution history of stars.

The two stars presented in this work both have intermediate initial masses and upon evolution will turn into AGB stars. The study of atmospheric chemical abundances in the early phases of stellar evolution can hold keys to explain the more complex chemistry observed in later stages of evolution, such as molecules and dust chemistry around circumstellar environments of AGB stars, the details of which are discussed in Appendix A.

1.4.2 Infrared Spectroscopy: Dust & Molecules

In chapter 4 of this thesis, we will shift our focus from ultraviolet to Infrared spectroscopy and from stellar atmospheres to circumstellar envelopes. We will present a study of a homogeneous sample of asymptotic giant branch (AGB) stars in the Galactic bulge population from the ISO-GAL survey. Our target stars cover a wide range of mass loss rates ($\sim 10^{-8}$ – $10^{-4} M_{\odot} \text{ yr}^{-1}$)

and differ primarily by their age on the AGB. This homogeneous sample is thus ideally suited for the primary purpose of our study which is to assess the correlation between dust formation process and age on the AGB phase.

The observations were carried out by the Infrared Spectrograph [IRS, 39] on board the *Spitzer* Space Telescope [127]. The raw data requires further processing in order to yield an informative spectrum. We reduced the *Spitzer-IRS* observations using the SMART package [40] and custom IDL routines. There are several procedures available within the SMART package that will assist the users with a more accurate data reduction (e.g. IRSfringe, IRSclean, Optical Extraction, etc. Higdon et al. [see e.g. 40], Lebouteiller et al. [see e.g. 73]).

Based on previous infrared spectroscopic studies, a typical infrared spectrum of an AGB star would, in addition to its continuum, include molecular absorption/emission lines as well as a dust emission depending on the stage of evolution. In our sample, we find that several stars show no signs of a detectable dust feature. We used these “naked stars” to characterize the stellar and molecular contributions to the infrared spectra of our target stars.

A reliable and relatively recent tool available for studying and modeling the molecular features is the SPECTRAFACTORY database [12]. SPECTRAFACTORY is an online database of molecular absorption/emission model spectra which is accessible to users through a web-based interface. The parameters can be adjusted based on the user’s needs. The database overall contains 250,000 model spectra for 41 molecular species covering wavelengths ranging from 350 nm–3 mm, temperatures ranging from 100–3000K and column densities ranging from 10^{16} – 10^{24} cm⁻² [see 12, for details.] This tool greatly facilitates the modeling of molecular lines in the AGB infrared spectra. As will be described in great detail in chapter 4, with help of molecular model spectra extracted from SPECTRAFACTORY, we managed to construct the spectrum of the photosphere and the molecular layers that lie under the dust features. Now one can easily obtain the dust spectrum by subtracting this model.

The resulting dust spectra contain a wealth of information concerning the formation history and evolution of the stars. In case of our targets, they show a significant variety in their spectral appearance, pointing to differing dust compositions for the targets. For instance, the silicate emission at 10 μ m is common in almost all our spectra. This fact can be used to classify the spectra based on the shape of the 10- μ m feature, following the scheme by Sloan & Price [77]. We find that the early silicate emission (SE) classes associated with oxide dust, are generally underrepresented in our sample due to extinction effects. We also find a weak 13- μ m dust feature in two of our otherwise naked star spectra, suggesting that the carrier of this feature could potentially be the first condensate in the sequence of dust condensation. This is a brief overview of the usefulness of infrared spectroscopy. The details of our study are provided in the following chapters.

Bibliography

- [1] Blommaert, J. A. D. L., Cami, J., Szczerba, R., & Barlow, M. J. 2005, *Space Sci. Rev.* , 119, 215
- [2] Becker, S. A. 1981, *ApJ*, 248, 298
- [3] Becker, S. A., & Iben, I., Jr. 1979, *ApJ*, 232, 831
- [4] Becker, S. A., & Iben, I., Jr. 1980, *ApJ*, 237, 111
- [5] Busso, M., Gallino, R., & Wasserburg, G. J. 1999, *ARA&A* , 37, 239
- [6] Bowers, P. F., & Hagen, W. 1984, *ApJ* , 285, 637
- [7] Boyer, M. L., Srinivasan, S., van Loon, J. T., et al. 2011, Why Galaxies Care about AGB Stars II: Shining Examples and Common Inhabitants, 445, 473
- [8] Benjamin, R. A., Churchwell, E., Babler, B. L., et al. 2003, *PASP* , 115, 953
- [9] Bethe, H. A. 1939, *Physical Review*, 55, 434
- [10] Blommaert, J. A. D. L., Vanhollebeke, E., Cami, J., et al. 2007, Why Galaxies Care About AGB Stars: Their Importance as Actors and Probes, 378, 164
- [11] Bernath, P. F. 1995, *Spectra of Atoms and Molecules*, Oxford University Press, Inc., ISBN 0-19-507598-6
- [12] Cami J., van Malderen R., Markwick A.J., 2010, *ApJS* 187, 409
- [13] Caputo, D. P., Speck, A. K., Barlow, M. J., et al. 2008, *Bulletin of the American Astronomical Society*, 40, 196
- [14] Cameron, A. G. W. 1955, *ApJ*, 121, 144
- [15] Chaboyer, B., & Kim, Y.-C. 1995, *ApJ* , 454, 767
- [16] Carbon, D. F., Chiar, J. E., & Goorvitch, D. 2003, *Astrophysics of Dust*, 58
- [17] Caughlan, G. R. 1965, *ApJ*, 141, 688
- [18] Cami, J. 2002, Ph.D. Thesis,

- [19] Charbonnel, C. 1994, *A&A* , 282, 811
- [20] Clayton, D. D. 1968, New York: McGraw-Hill, 1968,
- [21] Carroll, B. W., & Ostlie, D. A. 1996, Institute for Mathematics and Its Applications,
- [22] Decin, L., De Beck, E., Brünken, S., et al. 2010, *A&A*, 516, AA69
- [23] Dirks, U., Schirrmacher, V., & Sedlmayr, E. 2008, *A&A* , 491, 643
- [24] Dotter, A., Chaboyer, B., Jevremović, D., et al. 2007, *aj* , 134, 376
- [25] De Beck, E., Decin, L., de Koter, A., et al. 2010, *A&A* , 523, AA18
- [26] Schöier, F. L. 2007, Why Galaxies Care About AGB Stars: Their Importance as Actors and Probes, 378, 216
- [27] Ford, K. E. S., Neufeld, D. A., Schilke, P., & Melnick, G. J. 2004, *ApJ*, 614, 990
- [28] Fowler, W. A. 1986, Highlights of Modern Astrophysics: Concepts and Controversies, 3
- [29] Fazio, G. G., Hora, J. L., Allen, L. E., et al. 2004, *ApJS* , 154, 10
- [30] Foukal, P., Fröhlich, C., Spruit, H., & Wigley, T. M. L. 2006, *Nature* , 443, 161
- [31] Gray, D. F. 2008, The Observation and Analysis of Stellar Photospheres, by David F. Gray, Cambridge, UK: Cambridge University Press, 2008,
- [32] Gaunt, J., A. 1930, *Phil. Trans. Roy. Soc. Lond. Ser. A* , 229, 163
- [33] Gielen, C., Cami, J., Bouwman, J., Peeters, E., & Min, M. 2011, *A&A*, 536, AA54
- [34] Girardi, L., Bressan, A., Bertelli, G., & Chiosi, C. 2000, *A&As* , 141, 371
- [35] Gilroy, K. K., & Brown, J. A. 1991, *ApJ* , 371, 578
- [36] García-Lario, P., Manchado, A., & Pottasch, S. R. 1993, European Southern Observatory Conference and Workshop Proceedings, 46, 129
- [37] Gérard, E., & Le Bertre, T. 2006, *aj* , 132, 2566
- [38] Gilman, R. C. 1969, *ApJl* , 155, L185
- [39] Houck J.R., Roellig T.L., van Cleve J., et al., 2004, *ApJS* 154, 18
- [40] Higdon, S. J. U., Devost, D., Higdon, J. L., et al. 2004, *PASP* , 116, 975
- [41] Harris, M. J., Fowler, W. A., Caughlan, G. R., & Zimmerman, B. A. 1983, *ARA&A*, 21, 165
- [42] Herwig, F., Bloeker, T., & Driebe, T. 2000, *memsai* , 71, 745
- [43] Herwig, F., Bloeker, T., Schoenberner, D., & El Eid, M. 1997, *A&A* , 324, L81

- [44] Herwig, F. 2004, *ApJ* , 605, 425
- [45] Herwig, F. 2005, *ARA&A* , 43, 435
- [46] Hayashi, C. 1966, *ARA&A* , 4, 171
- [47] Habing, H. J., & Olofsson, H. 2004, *Springer-Verlag* , 1, 402
- [48] Hartmann, L., & MacGregor, K. B. 1980, *ApJ* , 242, 260
- [49] Höfner, S., Gautschi-Loidl, R., Aringer, B., & Jørgensen, U. G. 2003, *A&A* , 399, 589
- [50] Höfner, S. 2011, Why Galaxies Care about AGB Stars II: Shining Examples and Common Inhabitants, 445, 193
- [53] Höfner, S. 2007, Why Galaxies Care About AGB Stars: Their Importance as Actors and Probes, 378, 145
- [52] Habing, H. J. 1996, *A&Ar* , 7, 97
- [53] Höfner, S., & Andersen, A. C. 2007, *A&A* , 465, L39
- [54] Iben, I., Jr., & Renzini, A. 1983, *ARA&A*, 21, 271
- [55] Iben, I., Jr. 1975, *ApJ*, 196, 549
- [56] Iben, I., Jr. 1968, *ApJ* , 154, 581
- [57] Iben, I., Jr. 1965, *ApJ* , 141, 993
- [58] Imbriani, G., Costantini, H., Formicola, A., et al. 2004, *A&A* , 420, 625
- [59] Iben, I., Jr. 1967, *ARA&A* , 5, 571
- [60] Justtanont, K., Khouri, T., Maercker, M., et al. 2012, *A&A*, 537, AA144
- [61] Jones, T. W., & Merrill, K. M. 1976, *ApJ* , 209, 509
- [62] Kramers, H. A. 1923, *Phil. Mah.* 46, 836
- [63] Kholopov, P. N. 1987, General Catalogue of Variable Stars.. The fourth edition containing information on variable stars discovered and designated till 1982. Volume III: Constellations Pavo-Vulpecula. P. N. Kholopov (Editor-in-Chief). Nauka, Moscow, USSR. 368 pp. (1987). In Russian and English.,
- [64] Karakas, A. I. 2011, Asymmetric Planetary Nebulae 5 Conference, 144
- [65] Kippenhahn, R. 1965, *Mitteilungen der Astronomischen Gesellschaft Hamburg*, 19, 53
- [66] Kippenhahn, R., & Weigert, A. 1990, *Stellar Structure and Evolution*, XVI, 468 pp. 192 figs.. Springer-Verlag Berlin Heidelberg New York. Also Astronomy and Astrophysics Library,

- [67] Kučinskas, A. 1998, *Baltic Astronomy*, 7, 495
- [68] Kemper, F., Waters, L. B. F. M., de Koter, A., & Tielens, A. G. G. M. 2001, *A&A* , 369, 132
- [100] Kupka, F. G., Ryabchikova, T. A., Piskunov, N. E., Stempels, H. C., & Weiss, W. W. 2000, *Baltic Astronomy*, 9, 590
- [70] Kupka, F., Piskunov, N., Ryabchikova, T. A., Stempels, H. C., & Weiss, W. W. 1999, *A&As*, 138, 119
- [71] Kurucz, R. L. 1970, *SAO Special Report*, 309,
- [72] Roberts, J. D., Caserio, M. C., 1977, *Basic Principles of Organic Chemistry*, second edition. W. A. Benjamin, Inc. , Menlo Park, CA.
- [73] Lebouteiller V., Bernard-Salas J., Sloan G.C., Barry D.J., 2010, *PASP* 122, 231
- [74] Landstreet, J. D. 1988, *ApJ*, 326, 967
- [75] Le Bertre, T., Winters, J. M., & Sedlmayr, E. 1998, *IAU Symposium*, 191, 306P
- [76] Lattanzio, J. C. 2002, *nar* , 46, 469
- [77] Larson, R. B. 1969, *MNRAS* , 145, 271
- [78] Larson, R. B. 1969, *MNRAS* , 145, 271
- [79] Mihalas, D. M. 1982, *Stellar atmospheres..* D. M. Mihalas. Translated from the English edition. Mir, Moskva. Part I. 352 pp. Part II. 424 pp. (1982). In Russian. -,
- [80] Marengo, M., Evans, N. R., Matthews, L. D., et al. 2011, arXiv:1112.0619
- [81] Murray, N. 2011, *ApJ*, 729, 133
- [82] Minamidani, T., Tanaka, T., Mizuno, Y., et al. 2011, *aj*, 141, 73
- [83] McDonald, I., Zijlstra, A. A., Sloan, G. C., & Matsuura, M. 2011, *Why Galaxies Care about AGB Stars II: Shining Examples and Common Inhabitants*, 445, 241
- [84] McDonald, I., Sloan, G. C., Zijlstra, A. A., et al. 2010, *ApJl* , 717, L92
- [85] Meixner, M., Gordon, K. D., Indebetouw, R., et al. 2006, *aj* , 132, 2268
- [86] Mitalas, R. 1988, *ApJ* , 325, 476
- [87] Mauron, N., & Huggins, P. J. 2006, *A&A* , 452, 257
- [88] Mestel, L. 1974, *memsai* , 45, 397
- [89] Molster, F. J., Yamamura, I., Waters, L. B. F. M., et al. 1999, *Nature* , 401, 563

- [90] Neilson, H. R., Langer, N., & Cantiello, M. 2011, 9th Pacific Rim Conference on Stellar Astrophysics, 451, 327
- [91] Neufeld, D. A., González-Alfonso, E., Melnick, G., et al. 2011, *Astrophys. Lett.* , 727, LL29
- [92] Niyogi, S. G., & Speck, A. 2009, American Institute of Physics Conference Series, 1170, 155
- [93] Ojha, D. K., & Omont, A. 2003, The Proceedings of the IAU 8th Asian-Pacific Regional Meeting, Volume 1, 289, 121
- [94] Omont, A., Gilmore, G. F., Alard, C., et al. 2003, *A&A* , 403, 975
- [95] PuŁEcka, M., Schmidt, M. R., & Szczerba, R. 2005, ESA Special Publication, 577, 457
- [96] Pols, O. R., Tout, C. A., Lattanzio, J. C., & Karakas, A. I. 2001, Evolution of Binary and Multiple Star Systems, 229, 31
- [97] Persi, P., Ferrari-Toniolo, M., Grasdalen, G. L., & Spada, G. 1980, *A&A* , 92, 238
- [98] Pijpers, F. P., & Habing, H. J. 1989, *A&A* , 215, 334
- [99] Piskunov, N. E., Kupka, F., Ryabchikova, T. A., Weiss, W. W., & Jeffery, C. S. 1995, *A&As*, 112, 525
- [100] Kupka, F. G., Ryabchikova, T. A., Piskunov, N. E., Stempels, H. C., & Weiss, W. W. 2000, *Baltic Astronomy*, 9, 590
- [101] Piskunov, N., & Kupka, F. 2001, *ApJ* , 547, 1040
- [102] Posch, T., Kerschbaum, F., Mutschke, H., Dorschner, J., Jaumlger, C. 2002, *A&A* , 393, L7
- [103] Popper, D. M. 1980, *ARA&A* , 18, 115
- [104] Ryabchikova, T. A., Piskunov, N. E., Kupka, F., & Weiss, W. W. 1997, *Baltic Astronomy*, 6, 244
- [106] Renzini, A., & Fusi Pecci, F. 1988, *ARA&A* , 26, 199
- [106] Renzini, A., & Fusi Pecci, F. 1988, *ARA&A* , 26, 199
- [107] Schaller, G., Schaerer, D., Meynet, G., & Maeder, A. 1992, *A&As* , 96, 269
- [108] Schirmacher, V., Woitke, P., & Sedlmayr, E. 2003, *A&A*, 404, 267
- [109] Speil, J. 2006, Journal of the American Association of Variable Star Observers (JAAVSO), 35, 88
- [110] Sipahi, E. 2012, *na*, 17, 377

- [111] Smith, V. V., & Lambert, D. L. 1986, *ApJ*, 311, 843
- [112] Schwarzschild, M., Hárm, R. 1965, *ApJ*, 142, 855
- [113] Sedlmayr, E. 1989, *Interstellar Dust*, 135, 467
- [114] Skrutskie, M. F., Schneider, S. E., Stiening, R., et al. 1997, *The Impact of Large Scale Near-IR Sky Surveys*, 210, 25
- [115] Spitzer, L., Jr. 1968, *Nebulae and Interstellar Matter*, 1
- [116] Salpeter, E. E. 1952, *ApJ*, 115, 326
- [117] Tenenbaum, E. D., Woolf, N. J., & Ziurys, L. M. 2007, *ApJl*, 666, L29
- [118] Tenenbaum, E. D., Apponi, A. J., Ziurys, L. M., et al. 2006, *ApJl*, 649, L17
- [119] Templeton, M., Willson, L. A., & Foster, G. 2008, *Journal of the American Association of Variable Star Observers (JAAVSO)*, 36, 1
- [120] Thomas, H.-C. 1967, *zap*, 67, 420
- [121] Truong-Bach, Nguyen-Q-Rieu, Omont, A., Olofsson, H., & Johansson, L. E. B. 1987, *A&A*, 176, 285
- [122] Ueta, T., Speck, A. K., Stencel, R. E., et al. 2006, *Astrophys. Lett.*, 648, L39
- [123] van Loon, J. T., Groenewegen, M. A. T., de Koter, A., et al. 1999, *A&A*, 351, 559
- [124] Villaver, E., García-Segura, G., & Manchado, A. 2007, *Why Galaxies Care About AGB Stars: Their Importance as Actors and Probes*, 378, 345
- [125] de Vries, B. L., Klotz, D., Lombaert, R., et al. 2011, *Why Galaxies Care about AGB Stars II: Shining Examples and Common Inhabitants*, 445, 621
- [126] von Weizsäcker, C. F., 1938, *ber Elementumwandlungen in Innern der Sterne II, Physikalische Zeitschrift*, 39, 633
- [127] Werner M.W., Roellig T.L., Low F.J., et al., 2004, *ApJS* 154, 1
- [128] Waterhouse, J. 1890, *Memorie della Societa Degli Spettroscopisti Italiani*, 18, 14
- [129] Whitelock, P. A. 2012, *Ap&SS*, 341, 123
- [130] Woitke, P. 2006, *A&A*, 460, L9
- [131] Winters, J. M., Le Bertre, T., Jeong, K. S., Nyman, L.-Å., & Epchtein, N. 2003, *A&A*, 409, 715
- [132] Waters, L. B. F. M., Cami, J., de Jong, T., et al. 1998, *Nature*, 391, 868
- [133] Willson, L. A. 2000, *ARA&A*, 38, 573
- [134] Yamamura, I., & de Jong, T. 2000, *ISO Beyond the Peaks: The 2nd ISO Workshop on Analytical Spectroscopy*, 456, 155

Chapter 2

Ultraviolet Spectral Synthesis of Iota Herculis

2.1 Introduction

The star ι Herculis (HD 160762, HR 6588; B3 IV) is a slow-rotating early B-type star. Such stars are of great interest for elemental abundance analysis, since their initial chemical abundances remain fairly intact throughout their short lifetimes. Although B-type stars are usually rapid rotators ($v \sin i \gtrsim 100 \text{ km/s}$), ι Herculis is an exception. Its very low rotational velocity makes this star particularly suitable for the measurement of weak and/or blended spectral lines.

Over the past four decades, the optical spectrum of ι Herculis has been exhaustively studied; the literature now approximately agrees on the values of effective temperature, surface gravity and rotational velocity [see 13]. The literature contains numerous studies regarding the chemical composition of ι Herculis [see e.g. 33, 17, 11, 27, 6, 34, 28, 7, 12, 35, 13, 32]. Table 2.1 summarizes these abundance determinations. The measurements listed in Table 2.1 have mostly been carried out at visible wavelengths except for those of Peters & Polidan [34] who studied the abundances of ι Herculis in the ultraviolet, using the same spectrum as this project, and reported near solar abundance for all the elements they identified.

Since then, however, the literature has not yet converged into a fully consistent set of abundances, and the number of elements included in the analyses is rather limited. Therefore, a complementary study of this target may be very useful and potentially improve the situation. In this paper we model a high resolution, high signal-to-noise ratio (SNR) spectrum of ι Herculis covering the full spectral window from 999 to 1400 Å, in an attempt to improve our knowledge of the elemental abundances in this star. In spite of being publicly available data, this ultraviolet spectrum has not previously been used for modern analysis very much. We will further investigate: (1) the usefulness of full spectrum synthesis of small windows as a tool to measure abundances in crowded spectral regions; (2) the accuracy and completeness of the line-list in the UV for spectrum synthesis; (3) the accuracy of abundance measurements that can be achieved in the UV in comparison to abundances determined in the optical in the previous literature; (4) abundance values of elements that are accessible in the UV but have not been previously measured in the literature; (5) and we try to understand how well LTE

synthesis works at this temperature in the UV.

Section 2.2 describes the observation and reduction of the data in more detail. In Section 2.3.2 we discuss the modeling methods and tools used in this work. Section 2.4 provides a comprehensive element-by-element discussion of our results as well as of the "missing lines". Finally, in Section 2.5, we compare our results to the literature and summarize our new results.

2.2 Observation and Data Reduction

The results presented in this work are based on the high-spectral-resolution ultraviolet observations obtained from the *Copernicus* Spectral Atlas of ι Herculis [52]. The *Copernicus* satellite was the third Orbiting Astronomical Observatory (OAO-3), launched in August 1972; it operated until 1982.

The *Copernicus* satellite contained a Paschen-Runge scanning spectrometer including six data channels: U1-3, and V1-3. The U and V channels were movable photo-multipliers which were sensitive to two wavelength ranges between 910-1450Å, and 2000-3000Å, respectively [16]. The spectrometer used a concave reflection grating with a 3mm long and 24.2μm wide entrance slit which covered $390'' \times 0.314''$ on the sky. The light struck the concave grating and was then focused onto the Rowland circle. Photo-multipliers moving along this circle collected the data [for more details see 39, 48, 47].

An exit slit followed by an open-face photo-tube counted the number of photo-electrons for 14 seconds at a fixed wavelength. The photo-tube was next moved by 0.025Å in about 2 seconds and the same observing procedure was repeated. A second U photo-multiplier was held at a fixed position to provide ratio measurements which compensated for small guiding variations [for more details see 48]. The spectra used in this work contain two orders, covering wavelengths from 999.3-1422.2Å (U1, second order) and 1417.9-1467.7Å (U1, first order). The data have reasonably high spectral resolution of $\lambda/\Delta\lambda \sim 14,000$ in first order, and $\lambda/\Delta\lambda \sim 24,000$ in second order, and the co-added data reach $S/N > 100$ [16].

The acquired data from *Copernicus* spectrometer have been reduced with considerable care, including wavelengths calibration, spectrometer temperature correction, Doppler shift corrections, background corrections for cosmic rays and charged particles, an estimate of scattered light, and corrections for the stellar image drift on the spectrometer slit [see 52, for more details]. The *Copernicus* wavelength scale was calibrated using an optimized algorithm that could bring the wavelengths of numerous identified absorption lines of τ Sco (e.g. Lyman interstellar bands of H_2 between 1028-1116Å) into agreement with their laboratory values [see e.g. 47]. The wavelength calibration algorithm is accurate to ± 10 mÅ, and the average wavelength difference between the observed and laboratory spectral lines is less than 1mÅ. The remaining 10mÅ difference arises from other potential sources of error such as misidentification of features and errors in the laboratory wavelength measurements [see 40, for more details].

Due to the presence of background counts, the direct readings from the photo-multipliers do not represent the stellar flux. Rogerson & Upson [40] discuss the removal of the two sources of background counts: the cosmic ray counts obtained when the photo-multipliers are not exposed to stellar flux, and also the photo-multiplier's fluorescence after exposures to strong flux.

A normalized version of the spectrum is also provided in the *Copernicus* atlas, using a smooth envelope defined by maxima in the Fourier-smoothed spectra. However, this normal-

ization is not a very accurate representation of the real stellar continuum. The total uncertainty of the results of the atlas, range between 4-18% of local continuum in both orders [52].

We originally used the normalized atlas spectrum in our modeling routine, but we found a clear mismatch between models and the observations in the sense that the computed high points in the spectrum often lie above the atlas continuum (see §3.3.2 for details). We resolved this by re-normalizing the spectrum in three steps; (1) specifying continuum points using the graphics cursor over intervals of $\sim 20 \text{ \AA}$, (2) fitting the continuum as the exponential of a cubic spline, and (3) dividing the spectrum by our smooth fit. The re-normalization process was iterated until the least mismatch between the observation and model was achieved (see section §3.3.2). However, this process introduces a new source of uncertainty which will be discussed in section §3.3.3.

2.3 Methods

2.3.1 Line Broadening Mechanisms and Considerations

Over the years, there have been many studies of the sources of line broadening in massive hot stars. In order to bring the computed shapes of the lines into agreement with observations, we must take into consideration a few phenomena; microturbulence, macroturbulence, and rotational velocity. In what follows we briefly discuss each of them.

Microturbulence

The microturbulent velocity ξ is the non-thermal component of the local gas velocity in the spectral line formation region of the stellar atmosphere [7]. The validity of this concept has been the subject of debate for decades. For instance, it has been suggested that the use of non-LTE in spectral analysis should eliminate the need for microturbulence.

However, Cowley [7] argues that, similar to the solar surface observations [26], we can safely assume that the velocity fields in the atmospheric gas also exist in other stars. They have incorporated these motions in the calculations of the emergent intensity and shown that the microturbulence term is indeed present, regardless of the computational line formation algorithm, LTE or non-LTE. The same result is found by Nieva & Simón-Díaz [25], who find that consistent fitting of many spectral lines in early B stars with an advanced non-LTE code still requires the introduction of microturbulence.

It is suggested that the origin of the photospheric microturbulence in hot stars is the sub-surface convection. Convective regions in the envelope of a hot massive star are generated by the opacity peaks of ionized iron and (nearer the surface) of the He II to He III ionization zone [see 6, for more details]. (There may also be very weak convection at the He I to He II ionization zone, which is within the visible atmosphere.)

Nieva & Przybilla [32] have carefully carried out an extensive non-LTE analysis of high-resolution optical spectra for a sample of early B-type stars including ι Herculis. Through an iterative process, they have constrained the stellar parameters including the microturbulence. They find a microturbulence of $\xi \sim 1 \text{ km/s}$ for ι Herculis. We have included their result in our calculations.

Macroturbulence

In contrast to microturbulence, macroturbulence is the photospheric velocity field with scales much longer than the mean free path of the photons. This broadening component changes the overall shape of spectral lines from roughly Gaussian (when thermal and microturbulent broadening dominate) or U-shaped (when rotational velocity broadening dominates) to a more triangular form. It has been proposed that macroturbulent broadening in hot stars may be the result of many low-amplitude pulsation modes [3].

In general, to explain the observed line shapes of early B stars, we need rotational broadening and microturbulence together with macroturbulence. However, Nieva & Przybilla [32] showed that in case of ι Herculis, macroturbulence is negligible since the spectral line profiles can be reproduced with only rotational broadening and microturbulence.

Rotational Velocity

The rotational motion of the star about its axis usually introduces broadening into the spectral lines. The portion of the stellar surface that has a radial velocity component ($v \sin i$) toward the observer is blue-shifted. Similarly, the portion that is moving away from the observer is red-shifted.

It is crucial to take into account the impact of microturbulence as well as macroturbulence, when measuring the $v \sin i$ values [49]. The $v \sin i$ value of 6 km s^{-1} , determined by Nieva & Przybilla [32], satisfies this important condition. It also fits the UV data well, confirming the claimed resolving power of *Copernicus*. Therefore, we have used this result here.

2.3.2 Abundance Determination Method

In this work, we use the FORTRAN spectral synthesis program ZEEMAN.f [74, 23, 39]. This program was originally designed for magnetic stellar atmospheres, but works well (if a little slowly) for non-magnetic stellar spectra as well. Thus far, the literature does not contain any conclusive evidence for the presence of magnetic fields in the atmosphere of Iota Herculis. Recent attempts to search for weak or complex magnetic fields in this star have not detected any non-zero Zeeman signatures [40].

ZEEMAN uses stellar atmospheric models produced with the code of Kurucz [71] with solar composition, precomputed for us by Piskunov & Kupka [101], and a set of atomic line data from the Vienna Atomic Line Database (VALD; Piskunov et al. [99], Ryabchikova et al. [104], Kupka et al. [70, 100]). As input parameters, the program requires the effective temperature (T_e), gravitational acceleration ($\log g$), rotational velocity ($v \sin i$), microturbulent parameter (ξ), and individualized abundances, in order to compute the emergent atmospheric spectrum. For our synthesis we used $T_e = 17500 \text{ K}$, $\log g = 3.8$, $\xi = 1 \text{ km/s}$, and $v \sin i = 6.0 \text{ km/s}$ [see Table 5; 32]. These parameters were not varied. ZEEMAN can then adjust the abundance of any element of choice through an iterative process until a least squares best fit with (automatically selected) spectral features is achieved. This process of course works best for unblended lines for which the abundance can be adjusted without any contamination from other elements.

ZEEMAN was designed for LTE conditions; this is marginally appropriate for ι Herculis, whose effective temperature is near the boundary at which non-LTE effects start to become important. However, Przybilla et al. [28] have shown that for the main sequence stars with effective temperatures ($T \lesssim 22000\text{K}$) and carefully selected spectral lines, pure LTE modeling can yield meaningful results. They also show that despite the conceptual superiority of NLTE modeling, inadequate model atoms can potentially result in larger systematic errors than LTE modeling.

In this work, we will use LTE modeling, even though an ideal global match between synthetic and observed spectra can only be achieved when the NLTE effects of the lines are also carefully and properly taken into consideration. We used a spectral line list retrieved from VALD covering wavelengths 900.01791 to 1499.9723 Å, selected for significant depth at the effective temperature and gravity of ι Her. The elements included in the resulting line list within this spectral range, assuming solar abundance, are all listed in Table 2.2.

We extracted line data from the VALD database using the *Extract Stellar* option. The criteria we used to select our line-list were the following: starting wavelength: 900 Å, ending wavelength: 1500 Å, detection threshold: 0.01(fraction, in the range 0-1), microturbulence: 1km/s, T_e : 17500 K, and $\log g$: 4 (in cgs units). We requested the long extraction format in October, 2014. Recall that one of the purposes of this project is to investigate the completeness of the VALD list in this wavelength region for such high temperature and ionization level, in order to explore the extent to which there is a need for additional data.

One of the main challenges in using a crowded spectral region for abundance analysis is to identify spectral features that respond primarily to the abundance of a single element. ZEEMAN has a mode for determination of abundance of elements one at time, in which the program first tries to identify features that respond primarily to the abundance of the element being fit, and then iteratively modifies the abundance until a best least squares fit is achieved to the features, or parts of features, identified as sensitive primarily to that element. The identification of such features is carried out by computing two trial synthetic spectra of the observational window being fit, one with an assumed abundance of the element being fit that is slightly enhanced compared to the final value expected (or guessed), and a second computed with the element entirely absent. ZEEMAN compares these two spectra and then selects individual wavelengths in the model spectrum to use for fitting based on simple criteria (which can be adjusted by the user by modifying a couple of lines of code). An example of criteria used would be to require that any blending feature (i.e. still present in the spectrum with the fitted element removed) either (1) be no deeper than 0.95 of the continuum, and that the depth of the feature with the desired element present be deeper than 0.7 of the continuum, or (2) that the line be deeper than 0.7 of the continuum, and more than 4 times deeper than blending features.

After selecting a list of wavelength grid points in the computed spectrum based on such criteria, ZEEMAN iterates the abundance of the desired element to find a least squares best fit to the selected wavelengths, using a downhill simplex method. At the end of the process, the value of the abundance which produces the best fit and the value of χ^2/ν averaged over all points used is reported, along with a plot file of the current best fit spectrum for the window, the initial spectrum without the element being fit, and a map of wavelengths used in the fit. Graphical visual examination of these spectra enables the user to decide if the program has actually found useful spectral features or not, to decide if the fit found is based on strong enough evidence to consider that the reported value is useful, and to see whether the best fit

is consistent over the various features available in the window used or not. Many such fits to small windows, comparing the observed spectrum to both the model spectrum with a best fitting abundance, and also to a spectrum with the fitted element absent (e.g. Figure 1), will be used in this paper to illustrate our results. The examination of such comparison spectra is an extremely useful technique for studying synthetic spectral models of crowded spectral regions.

Using the techniques outlined above, we find that several elements exhibit a few apparently clean and unblended lines. After identifying those lines, we used them to adjust the abundances of those elements (see §3.4). Table 2.2, which presents the abundance values (ion by ion) that are found to best fit the observed spectrum, lists the lines that we found to be most useful.

For some elements of interest, reasonably strong lines are present in our spectrum, but most are not really free of blends. The analysis of blended lines is slightly more challenging since they can have more than one element contributing to the overall shape of the line profile. In these cases, a few more steps are required. We first iterated over the abundance of each element, assuming solar abundance for the rest in order to identify which wavelength window could best be used to adjust the abundance of that particular element. This first approximate model gives us a first estimate of the abundance even though it is not the final result. Once the first iterations are carried out, we are left with an initial set of model parameters. Having selected the most useful window(s) for each element, we then iterated the abundances of both the element of interest and also the blending element(s) until we obtained the best possible global fit to the observation.

The computed model spectrum, using the final set of abundances, results in a reasonably good fit to the observed spectrum (see Appendix B), although it is quite clear that there are lines in the observed spectrum that are missing from the VALD list. One significant source of such lines is due to absorption by the Lyman bands of interstellar H_2 .

2.3.3 Sources of Uncertainty

The stellar parameters used here (e.g. T and $\log g$), of course, are not exact but have relatively small uncertainties. The uncertainties associated with T and $\log g$ are about ± 200 K and ± 0.05 (cgs), respectively [see Table 5; 32]. We find that an increase of 0.05 in surface gravity would result in an increase of typically about 0.02 in the abundance, and the rise in temperature by 200K will cause the abundance to increase by 0.035. Therefore, the uncertainty arising from uncertain stellar parameters is roughly about 0.04.

Another, probably more important, source of error is the re-normalization of the spectrum (§3.2). In order to evaluate this uncertainty, we have used multiple spectral lines of one atom and attempted to determine abundance for each of them separately (see e.g. nickel §3.4.17).

A similar source of error is the correction for background and scattered light, which sets the zero level of the spectrum. In some parts of the spectrum, the strongest computed lines are deeper than the observed lines (for example in the cores of the C II resonance doublet of UV multiplet (1) at 1335 Å), suggesting that the background correction should be a little larger than the one used by Upson & Rogerson [52]. We have not tried to correct for this effect. The uncertainty actually introduced by this effect is small because in lines deep enough for this to be a significant source of error, we frequently have fitted the (sometimes rather broad) damping wings rather than the core depth.

In some cases, the best-fitting models of several individual lines or multiplets will not result in the same abundance value for that element. This may be produced by the effect of lines missing from our VALD line list, by inaccurate atomic data, and by non-LTE effects of under- or over-ionization of minority ionization stages.

The effects of missing blending lines can sometimes be identified by careful comparison of the observed and calculated line profiles. It is not possible to generalize about the uncertainty resulting from this problem, but in a few cases we can include an estimate of the effect in our uncertainty estimates.

The atomic data uncertainties for individual lines can be estimated in some cases from the literature, especially for resonance lines for which very accurate theoretical and/or experimental oscillator strengths are sometimes available (for example, according to the NIST database [10] the accuracy of the oscillator strengths of the C II resonance lines of multiplets (1) (at 1335 Å) and (2) (at 1036 Å) is "A", with uncertainties of about $\pm 3\%$ or 0.01 dex).

For most of the line data in VALD, very accurate oscillator strengths are not available (typical uncertainties for logarithmic oscillator strengths of a light ion such as Si II are of the order of ± 0.1 dex, while those of Fe II lines are of the order of ± 0.2 dex, for example). These uncertainties are similar to those for the optical lines often used for abundance analysis [e.g. 38], and probably set an important lower limit to uncertainty. Except when we use lines of very well determined oscillator strengths, we will assume that atomic data introduce uncertainties of this order.

Non-LTE effects can alter the relative populations of various levels of a single ionization stage, and also the relative numbers of different ionization stages. We do not have any very useful method for identifying such effects within a single ionization stage except by looking for large discrepancies between different "reliable" lines of that ionization stage, and comments in the literature about individual lines and multiplets. In contrast, we expect the non-LTE effects on relative numbers of different ionization stages to affect primarily the ionization stages with relatively small populations. In order to identify the sensitive stages, we have computed (in LTE) the relative populations of various ions of interest for temperature – electron density values appropriate to about continuum optical depth (evaluated at 5000 Å) $\tau_{\text{cont}} \sim 0.2$ and ~ 0.001 . The results are given in Table 2.3. We believe that abundances derived for ionization stages that in LTE account for at least about 10% of the total population of an element are not very sensitive to under- or over-ionization effects, but that less populated stages may be. Thus we may be able to identify a few cases of non-LTE ionization effects by finding systematic discrepancies between abundances derived from dominant ionization stages and from weakly populated stages.

In a general way, we expect that the effects discussed above will lead to uncertainties in the derived (logarithmic) abundances of the order of ± 0.3 dex or perhaps somewhat more (or less) in some cases. We shall sometimes be able to estimate the abundance uncertainties of individual atoms by looking at the dispersion of results obtained from different multiplets, and the scatter is indeed often of this amplitude.

2.4 Summary of Individual Elements

In this section, we present separately our results for every element clearly identified in the spectrum of ι Her. We have usually used several spectral lines for abundance determination, in order to reduce the bias due to the kinds of uncertainties discussed above. The final abundances determined for individual ionization stages of these elements are listed in Table 2.2. In section 3.5, we will compare our results to the literature values and we will put them in the context of the stellar evolution state of ι Herculis.

We have correspondingly omitted from our modeling a few Å on either side of Lyman α (1215.67 Å) and Lyman β (1025.72 Å). In fact the wings of these two lines extend to approximately ± 20 and ± 15 Å from line center respectively. ZEEMAN has not been enabled to compute these lines correctly, although there would be no difficulty in principle with this. The modification of the code and the proper analysis of these lines will be the focus of future work. We have modeled strong lines in the farther wings of these two lines in spite of the omission of Lyman line wing opacity, because the opacity of strong lines so completely overwhelms the opacity of the Lyman line wings (important mainly in the deeper atmosphere layers in any case) that the line strengths are largely independent of the neglect of the Lyman line wings. In fact the syntheses of the strong metallic lines in the Lyman line wings are surprisingly successful.

It is worthwhile to mention that iron provides strong line opacity over the entire wavelength range studied here. Probably most of the lines of other elements are at least slightly blended with iron. Therefore, iron was the first element for which we determined the abundance (see section §3.4.15). However, the following sections are presented in ascending order of atomic number.

2.4.1 Boron, Z=5

There are only a few boron lines in our VALD line list. According to the Saha equation (see Table 2.3), the dominant states of ionization in the atmosphere are B II and III. We have used the B II resonance line at 1362.461 Å for abundance determination. This is the only boron line expected to be detectable in our spectrum, and fortunately it is not heavily blended. The oscillator strength is very precisely known (it has quality "A" on the NIST Atomic Spectra Database scale, corresponding to an uncertainty of the transition probability of only about 3% [10], and since this is a resonance line of a dominant ionization state, our LTE treatment should introduce no important errors. We estimate the uncertainty from fitting to be about ± 0.1 . Therefore the abundance is $\log(n_B/n_H) = -10.1 \pm 0.1$ for this element. Figure 2.1 shows the fit to the observed profile.

Boron is a rare and fragile light element that is not produced through stellar nucleosynthesis (except for the very minor PP III chain), but is destroyed in the interiors of stars. There are several suggestion regarding the formation of this element, such as cosmic ray interactions with the ISM, or supernova neutrino spallation on particularly ^4He or ^{12}C [see 53, for extensive details].

In comparison with the solar abundance of $\log(n_B/n_H) = -9.30 \pm 0.03$ [1], the abundance value found here is about a factor of 6 smaller. The presence of boron may indicate that outer layers of ι Her have at most been partially mixed into the stellar interior since the period of star formation. (In contrast, for instance, in Sirius A, the absence of detectable boron is consistent

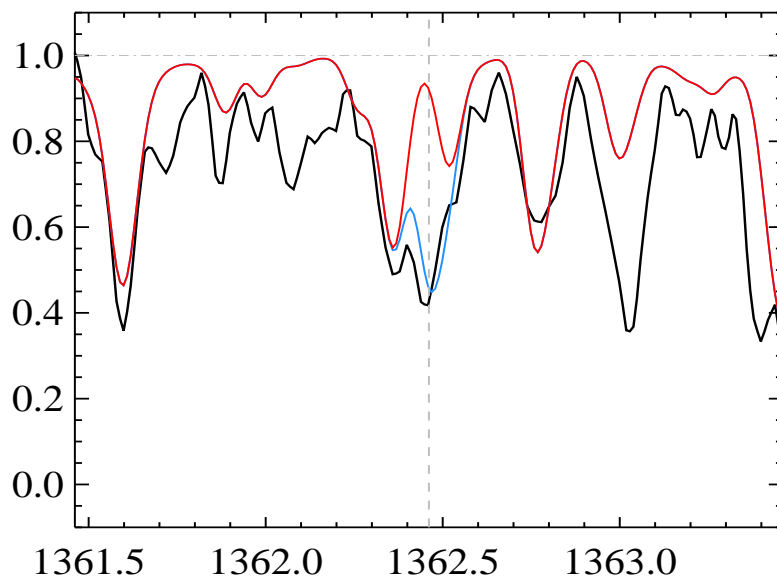


Figure 2.1: This figure shows the observation (in black), calculated model with $\log(n_B/n_H) = -10.1$ (in blue) and without boron (in red).

with the hypothesis that the outer layers were earlier inside its companion [29].)

2.4.2 Carbon, $Z=6$

Carbon is a very abundant element in the spectrum of ι Herculis. In the VALD line list used here, most of the carbon lines are in neutral form. The rest are lines of C II, C III, and C IV. The distribution of carbon over ionization states in LTE in the atmosphere of ι Her is shown in Table 2.3. Most carbon is in the form of C II and C III, and both contribute numerous lines. However, even though it is a very minor constituent, weaker C I lines are evident throughout the spectrum. No C IV lines are detected.

We determined the abundance of carbon using a simultaneous fit to lines of C I UV multiplet (4) at 1329 Å, C II UV multiplet (11) at 1324 Å and UV multiplet (1) at 1335 Å, and C III UV multiplet (4) between 1172 and 1180 Å, and UV multiplet (9) at 1247 Å. Although most of these lines have saturated line cores, several have strong wings that are reasonably sensitive to abundance. A good global fit is found for a logarithmic abundance of -3.55 , quite close to the solar value.

The 5 C III triplet lines at 1174-76 Å and the singlet line at 1247.38 Å have "A+" gf values according to NIST. The 1175 Å triplets are at 6.5 eV, the 1247 Å line is at 12.7 eV. The 4 C II lines at 1323.9 Å have "A" gf s, and are at 9.3 eV. The C II resonance lines at 1334-35 Å also have "A" quality gf s. Non-LTE effects may play a role but the gf values are very accurate, and contribute negligibly to the overall uncertainty.

It is notable that the worst fit in these windows is to the C I lines at 1329 Å. These lines are considered by Kramida et al. [10] to have accuracy "B", with uncertainties of about ± 0.04 in $\log gf$, so the atomic data make an unimportant contribution to the total error budget. The abundance derived from the best fit of these lines is about -4.65 , about one dex lower than that

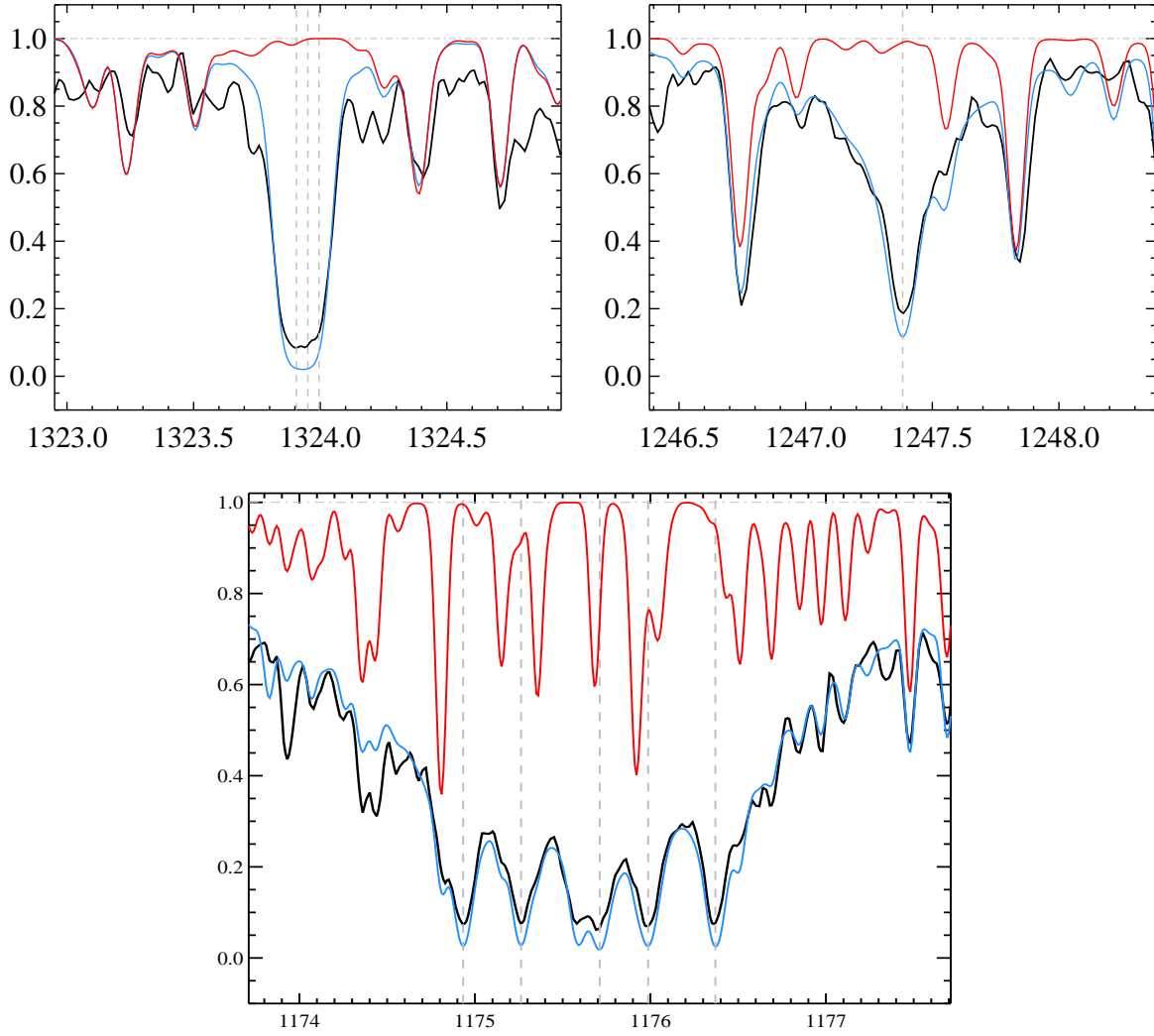


Figure 2.2: The figure shows the observation (in black), calculated model with $\log(n_{\text{C}}/n_{\text{H}}) = -3.55 \pm 0.30$ (in blue) and without carbon (in red). *Top left:* The unblended multiplet (11) triplet of C II at 1324 Å. *Top right:* The single line of multiplet (9) of C III at 1247 Å. *Bottom:* The C III lines of multiplet (4) around 1174 Å, with prominent wings extending to several Å from the deepest part of the feature.

derived from lines of C II and C III, the two dominant ionization stages. This illustrates the dangers of relying on a (very) minor ionization stage, which in this case seems to be subject to quite significant overionisation.

It is worthwhile to mention that we removed from our VALD3 linelist, six lines of C I at the following wavelengths; 1253.410, 1253.467, 1253.539, 1253.541, 1254.489, 1254.511 Å, due to apparently inaccurate values of oscillator strength and/or damping constants. There are large inconsistencies between the values reported in VALD2 and VALD3, and neither set resulted in a good fit with our observation. Figure 2.2 shows the fit to the observed profile at these wavelengths.

2.4.3 Nitrogen, $Z=7$

The selected subset of the VALD database contains overall 233 lines of nitrogen. Almost half of these lines are for the neutral form (N I), and the rest are N II and N III, together with a few N IV lines. The strongest nitrogen contribution to the UV spectrum seems to be primarily due to N II. There are only a few strong lines of N I and N III. All the N IV lines are much weaker and less prominent. This distribution is consistent with the expected ionization ratios in the atmosphere according to the Saha equation (see Table 2.3).

With a few exceptions, most nitrogen lines are rather blended in the UV spectrum of this target. Although some N I lines appear largely unblended, the tiny fraction of N in this form makes abundance determination using such lines rather unreliable. Instead we have used the weakly blended N II line of UV multiplet (1) at 1083.99 Å and lines of N II at 1275.04, 1276.20 and 1276.22 Å to estimate the abundance of nitrogen. Uncertainty in both the zero point and continuum normalization, together with the fairly weak dependence of line strength on abundance, lead to a large uncertainty on the best compromise abundance of -4.65 ± 0.8 dex.

Several observed lines as well as the model are shown in Figure 2.3.

2.4.4 Oxygen, $Z=8$

Oxygen - has a few very strong but blended lines in the spectrum of Iota Herculis. The selection of VALD lines used here contains 218 oxygen lines, of which half are in neutral form and the rest are in the form of O II and O III, together with a few O IV lines. The UV spectrum of ι Herculis shows a strong presence of O II and O III with a moderate contribution from O I and absolutely no trace of O IV, which is expected given the effective temperature of this target. This distribution is consistent with the expected ionization ratios measured from the Saha equation (see Table 2.3).

We used the strong O II triplet at 1131 Å. These lines are slightly blended with nickel and iron, for which we have reasonable abundance estimates (see §3.4.15 & §3.4.17). The best-fitting model yields $\log(n_{\text{O}}/n_{\text{H}}) = -3.5 \pm 0.3$. We have used the strong O I UV multiplet (3) at 1039–1041 Å to confirm this value; the figure 2.4 shows only the longer wavelength end of the feature due to a long gap between strong lines. We also used the strong 1302–1306 Å lines of O I of UV multiplet (2); in the figure 2.4, we have shown only the short wavelength end. These lines are blended with iron lines (see §3.4.15). The best-fitting model results in the same value of $\log(n_{\text{O}}/n_{\text{H}}) = -3.5 \pm 0.3$, thus we adopted this value for the oxygen abundance. Figure 2.4 shows the observation and the models.

2.4.5 Magnesium, $Z=12$

In our subset of VALD database, there are only a few magnesium lines. The dominant ionization stage is predicted by the Saha equation to be Mg III (see Table 2.3). However, because the lowest excited states are more than 50 eV above the ground state, no lines of Mg III are present in our window. We are therefore obliged to use lines of the weakly populated Mg II. There are numerous lines in our window that arise from low excitation levels about 4.5 eV above ground, and even a couple of resonance lines. However, all these lines have very small $\log gf$ values, around -3.

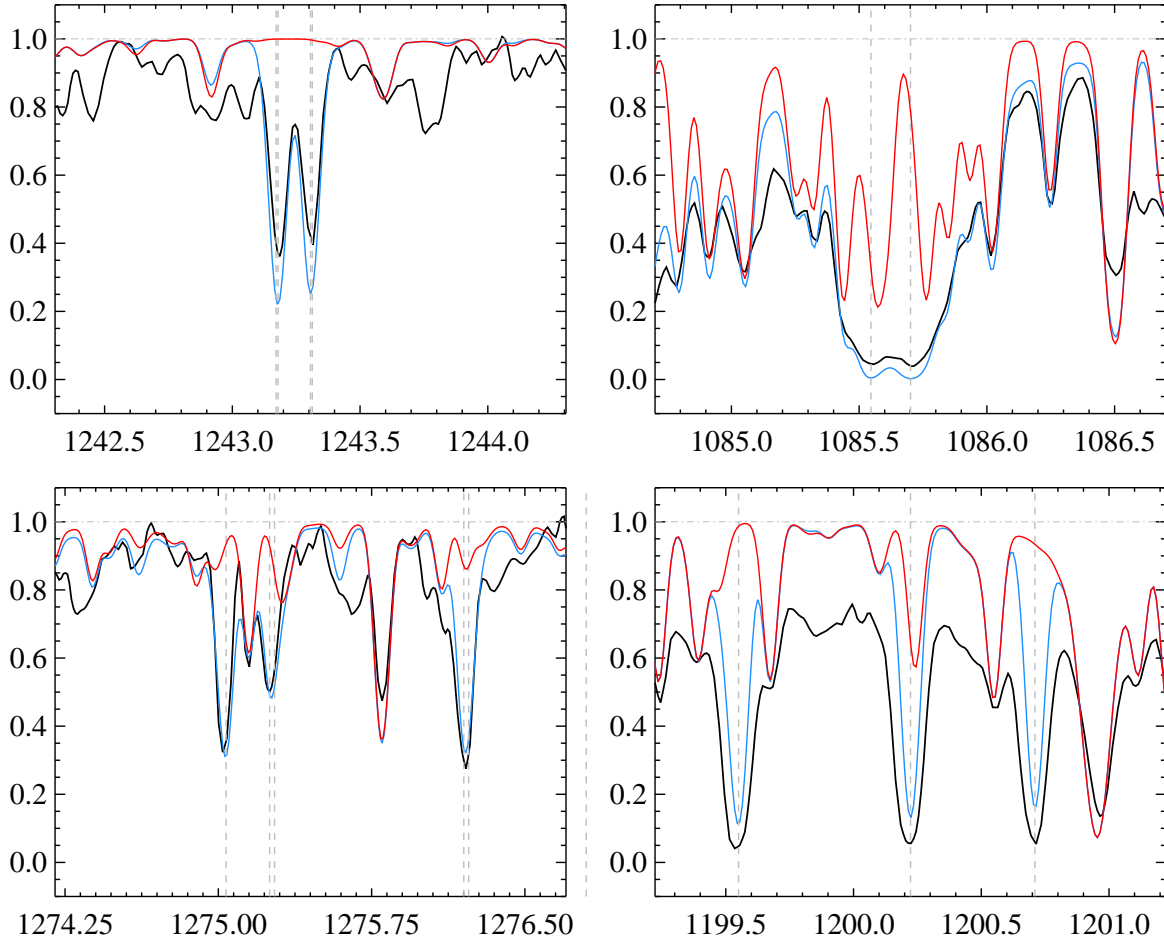


Figure 2.3: The figure shows the observation (in black), the best-fitting model calculated with $\log(n_{\text{N}}/n_{\text{H}}) = -4.65 \pm 0.80$ (in blue) and without nitrogen (in red). *Top left*: N I UV multiplet (5) at 1243 Å, *Top right*: N II multiplet (1) at 1085 Å, *Bottom left*: N II multiplet at 1275–1276 Å, *Bottom right*: N I multiplet (1) at 1199–1200 Å

We used the Mg II doublet at 1367 Å to determine the abundance of magnesium. We find $\log(n_{\text{Mg}}/n_{\text{H}}) = -3.90 \pm 0.19$. We confirmed this value using the strong line at Mg II 1240 Å. Figure 3.4 shows the fit to the observed profile at these wavelengths.

2.4.6 Aluminum, $Z=13$

Aluminum is most prominent at longer wavelengths. Our selection of the VALD lines contains 88 aluminum lines in total; more than half of them are in the form of Al II and the rest are in Al III form. At this temperature, almost all of aluminum is expected to be in Al III form with a moderate Al IV contribution (see table 2.3). In the spectrum of ι Herculis, most of the aluminum lines present are contributed by Al II, with a moderate number of Al III lines and no trace of Al IV. The lack of lines of Al IV is clearly due to the atomic energy structure, which has only no excited states below 75 eV.

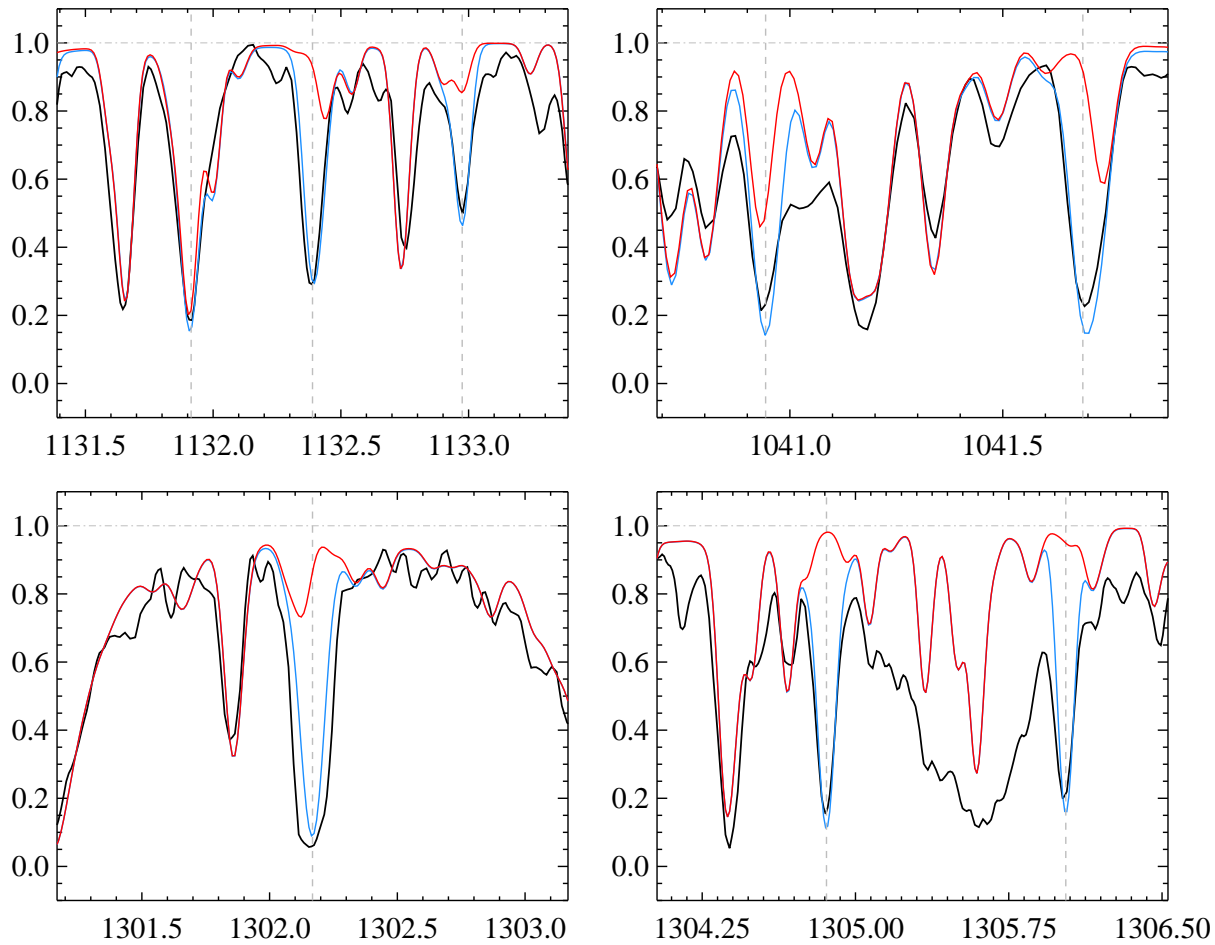


Figure 2.4: The figure shows the observed line (in black), the best-fitting model calculated with $\log(n_{\text{O}}/n_{\text{H}}) = -3.5 \pm 0.3$ (in blue) and without oxygen (in red). The lines are blended with iron. *Top left:* O II triplet at 1132 Å. *Top right:* O I doublet at 1041 Å, *Bottom left:* Strong O I at 1302 Å, *Bottom Right:* O I doublet at 1305–1306 Å.

The available lines of Al are heavily blended throughout the spectrum. We used the Al III line at 1379 Å which is only blended with iron (see §3.4.15). The best-fitting model results in the abundance of $\log(n_{\text{Al}}/n_{\text{H}}) = -5.90 \pm 0.58$ for aluminum. We confirmed this value by fitting the following lines; Al II triplet at 1189–1190 Å, a strong Al III triplet at 1352 Å, and another Al II triplet at 1191 Å. Figure 3.5 shows the observation and the model fits.

2.4.7 Silicon, Z=14

The VALD lines selected here include 361 silicon lines. The majority of these lines are in the form of Si II and Si III and a small fraction of them are in the form of Si I and Si IV. In the UV spectrum of ι Herculis, silicon is largely observed in the form of Si II and Si III with a very minor contribution from Si IV and no trace of Si I. This is generally consistent with the expectations from the Saha equation. The fact that lines of Si II, Si III and Si IV are all found in the spectrum

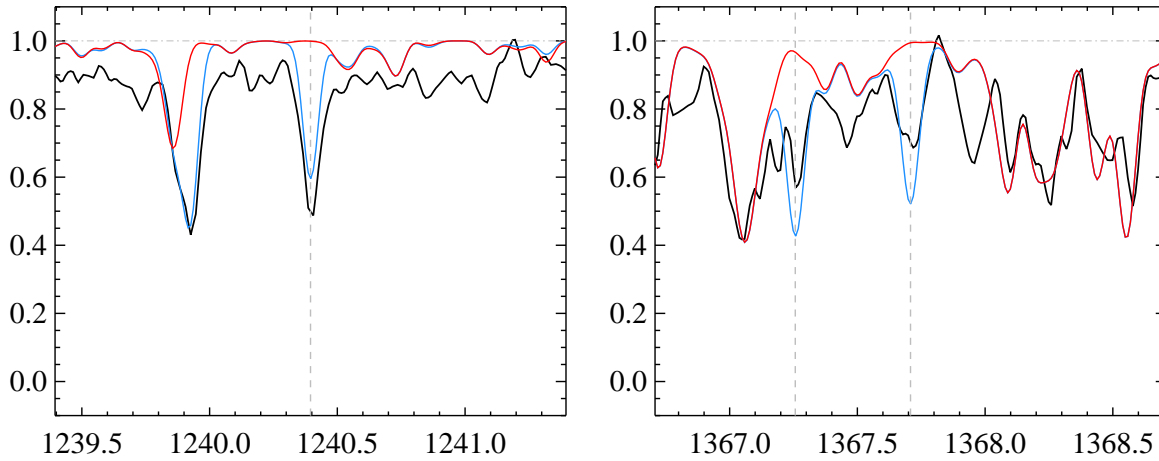


Figure 2.5: This figure shows the observation (in black), the calculated model with $\log(n_{\text{Mg}}/n_{\text{H}}) = -3.9 \pm 0.19$ (in blue) and without magnesium (in red). *left*: Mg II doublet at 1367 Å, *right*: strong line at Mg II 1240 Å

is because all these ionization stages have lines arising from the ground state or low lying level that occur in the window we are modeling.

We determined the abundance of Si using the relatively unblended and strong Si III lines of multiplet (4) between 1294–1310 Å, and the lines of multiplet (5) between 1108–1114 Å. We find the abundance of $\log(n_{\text{Si}}/n_{\text{H}}) = -4.65 \pm 0.26$ for silicon. For confirmation, we have used this abundance to model the blended multiplets (4) and (5) lines of Si II at 1190–93 Å and 1260–64 Å, and strong Si IV multiplet (3) line at 1128 Å. Figure 2.7 shows the best-fitting models and the observed spectrum.

Note that the fit to the lines of Si II in the middle panel is poor, and suggests an abundance of Si larger than we have chosen. Major discrepancies between abundances deduced with Si II and Si III are common in hot stars, and may represent important departures from LTE or possibly stratification of Si in the atmosphere [5], but in this case the discrepancies may be due to unidentified blends.

2.4.8 Phosphorus, Z=15

There are overall 133 phosphorus lines in the subset of the VALD database selected here; mostly in the form of P II, a smaller subset are in the form of P IV, P III, and there are only a few P I and P V lines. In the UV spectrum of ι Herculis, phosphorus lines are mostly observed in the form of P II and P III and there is a very minor contribution from other ionization states (e.g. P IV, P V and P I). This is consistent with the ionization ratios obtained from the Saha equation at this temperature (see Table 2.3). All the P II and P III lines in the wavelength range studied here arise from low lying energy levels (0–1.1 eV) which justifies their clear appearance in the observed spectrum.

We have used a strong P III lines of UV multiplet (1) at 1344–45 Å. These lines both arise from low initial energy level (0.07 eV) with a fairly accurate [10]) oscillator strength value of “D” $\log gf \sim -1.5$. They are slightly blended with iron for which we have a reasonable

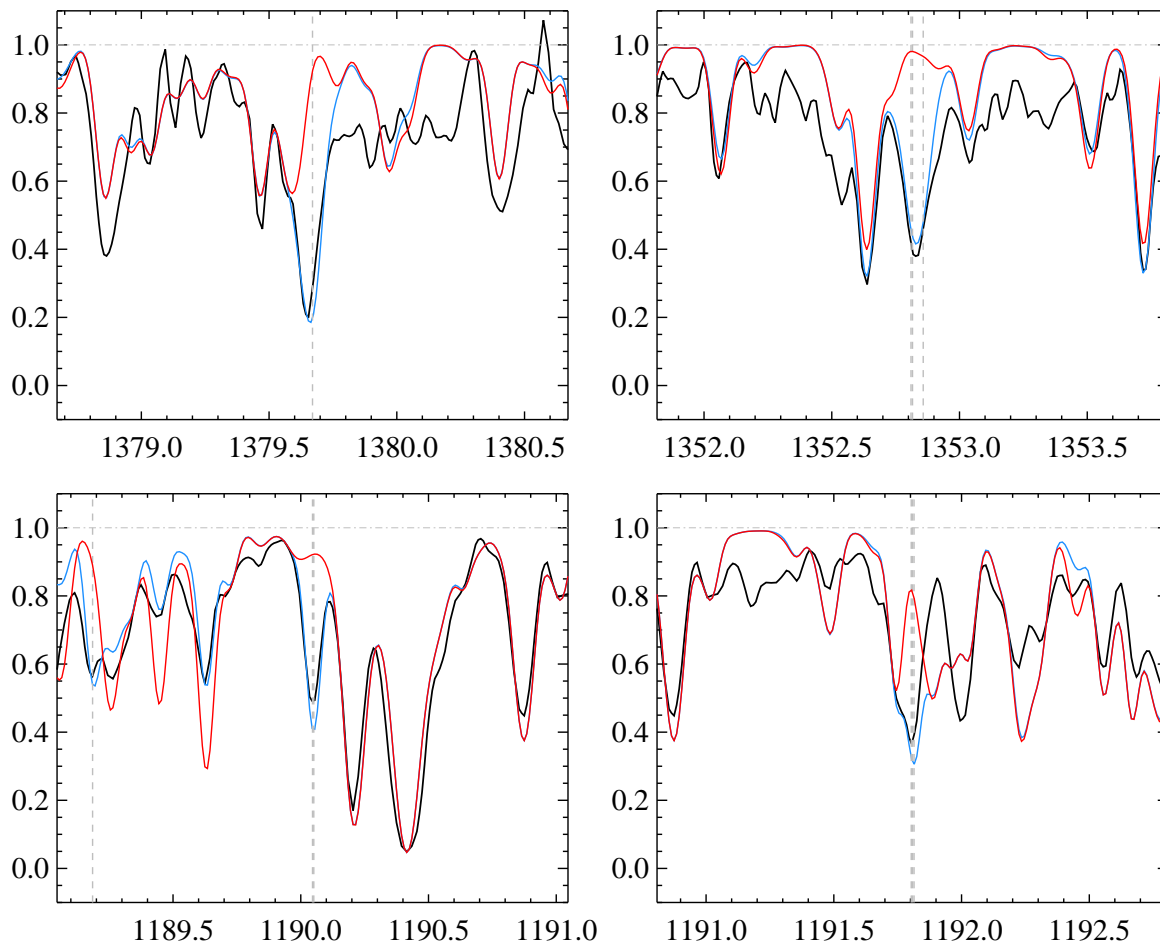


Figure 2.6: This figure shows the observation (in black), the calculated model with $\log(n_{\text{Al}}/n_{\text{H}}) = -5.90 \pm 0.58$ (in blue) and without aluminum (in red). *Top left:* Al III line at 1379 Å. *Top right:* Al III triplet at 1352 Å, *Bottom left:* Al II triplet at 1189 Å, *Bottom right:* Al II triplet at 1191 Å.

abundance determination (see §3.4.15). Modeling these lines yields $\log(n_{\text{P}}/n_{\text{H}}) = -6.7 \pm 0.7$. We confirmed this value using two strong lines of P II at 1249.8 Å and P III at 1003.6 Å with $\log gf$ values close to zero and a P III resonance line at 1334.8 Å with “D” $\log gf$ values close to -1. Figure 2.8 shows the observation and the best-fitting models.

2.4.9 Sulfur, $Z=16$

There are 474 lines in the subset of the VALD database used here. In the observed UV spectrum of ι Herculis as well as the VALD database, sulfur has a few strong lines in the form of S II, S III and S IV and a large number of weaker S I lines. This is consistent with the expected ionization ratios predicted by the Saha equation.

We have modeled the strong S III resonance lines of UV multiplet (1) at 1200 Å. The best-fitting model results in the value of $\log(n_{\text{S}}/n_{\text{H}}) = -5.20 \pm 0.10$. We confirmed this value using

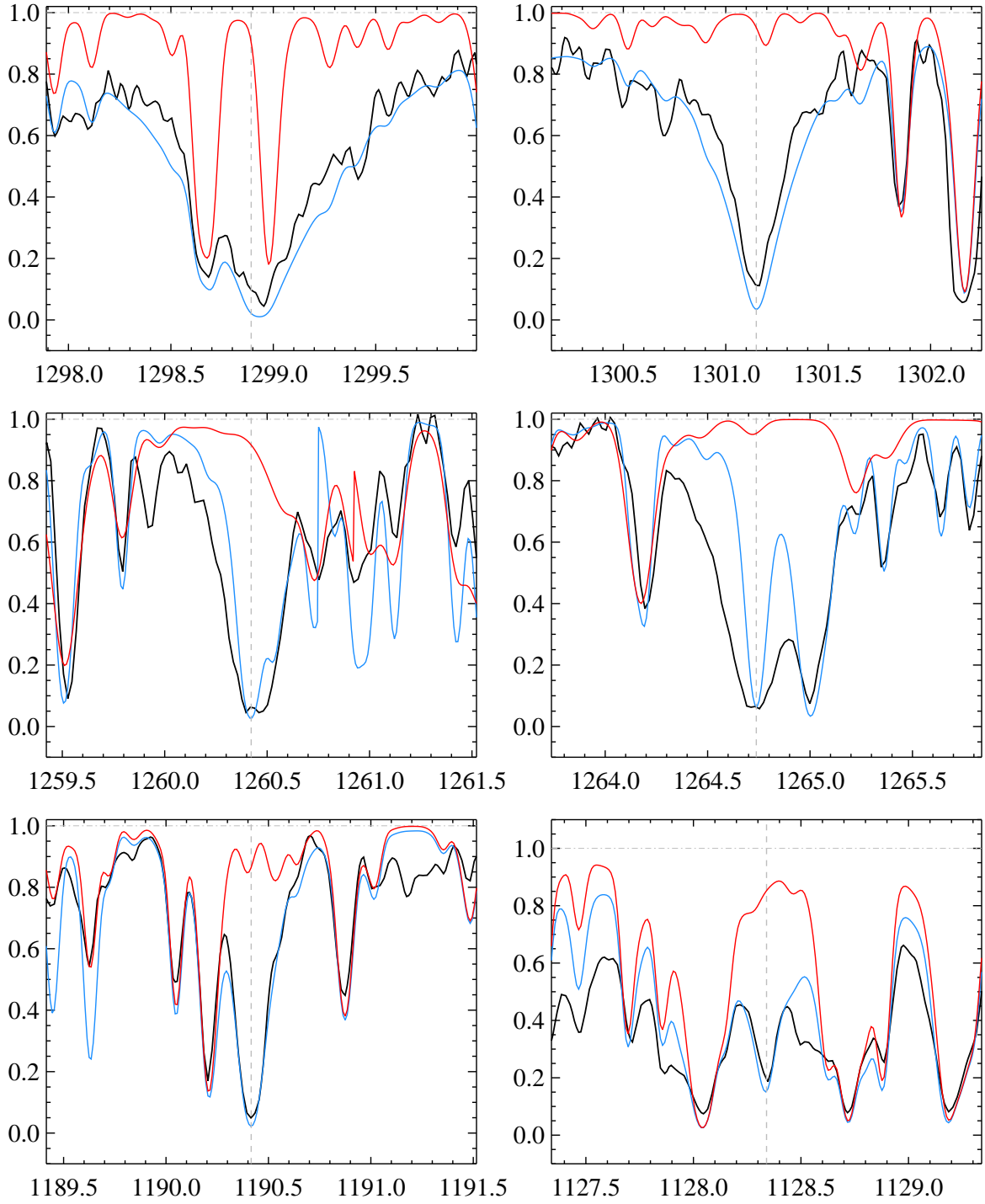


Figure 2.7: This figure shows the observation (in black), the best-fitting model spectrum with $\log(n_{\text{Si}}/n_{\text{H}}) = -4.65 \pm 0.26$ (in blue) and without silicon (in red). *Top:* Strong Si III lines of multiplet (4) between 1294–1310 Å, we only show 1298.892 Å (*left*) and 1301.149 Å (*right*), *Middle:* A multiplet (5) of Si II between 1260–64 Å at 1260.422 Å (*left*) and 1264.737 Å (*right*), *Bottom left:* An Si II multiplet (4) between 1190–93 Å at 1190.415 Å, *Bottom right:* A strong Si_{IV} line at 1128.340 Å.

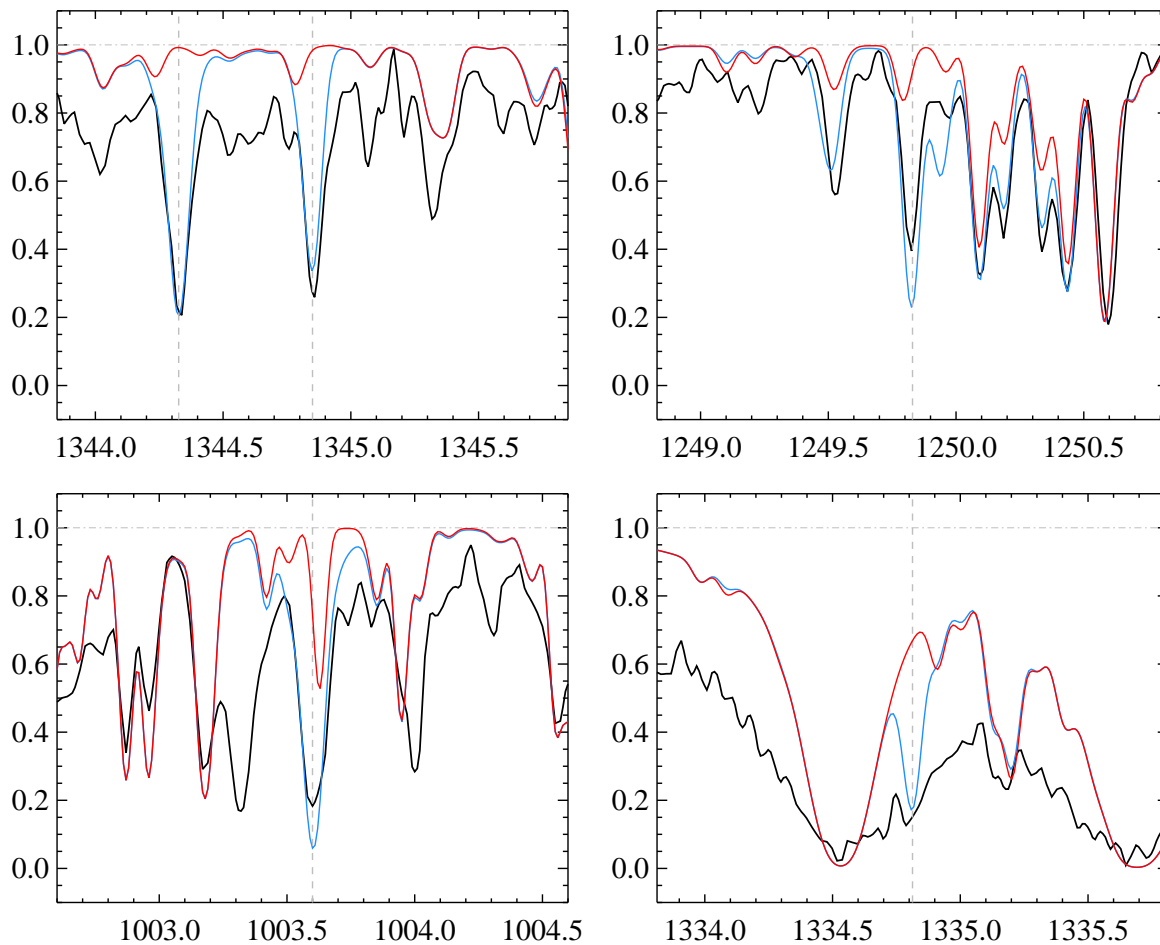


Figure 2.8: This figure shows the observation (in black), the calculated model with $\log(n_P/n_H) = -6.7 \pm 0.7$ (in blue), and without phosphorus (in red). *Top left*: P III doublet at 1344.326, 1344.850 Å, *Top right*: P II line at 1249.829 Å, *Bottom left*: P III at 1003.600 Å *Bottom right*: A resonance P III line at 1334.813 Å

the S IV multiplet (1) at 1072 Å. This line is blended with iron, nickel and manganese, but can still be used for our purposes (see §3.4.15, §3.4.17, §3.4.14). We also used S II resonance lines of multiplet (1) in the window between 1250-59 Å, and a S II resonance line at 1072 Å. The oscillator strength of all the lines used here are around -1 with a “D” accuracy [10] and they all arise from low energy levels. The observation and models are shown in Figure 2.9.

2.4.10 Chlorine, $Z=17$

Chlorine has 117 lines in our selected database majority of which are in neutral form. In our spectral window of ι Herculis, chlorine is observed mostly in shorter wavelengths. The observed spectrum is mostly dominated by Cl I lines with minor contribution from other ionization states (e.g. Cl II, Cl III, and Cl IV). As predicted by the Saha equation (see Table 2.3), the dominant ionization state at this temperature should be Cl III. However, this ionization state

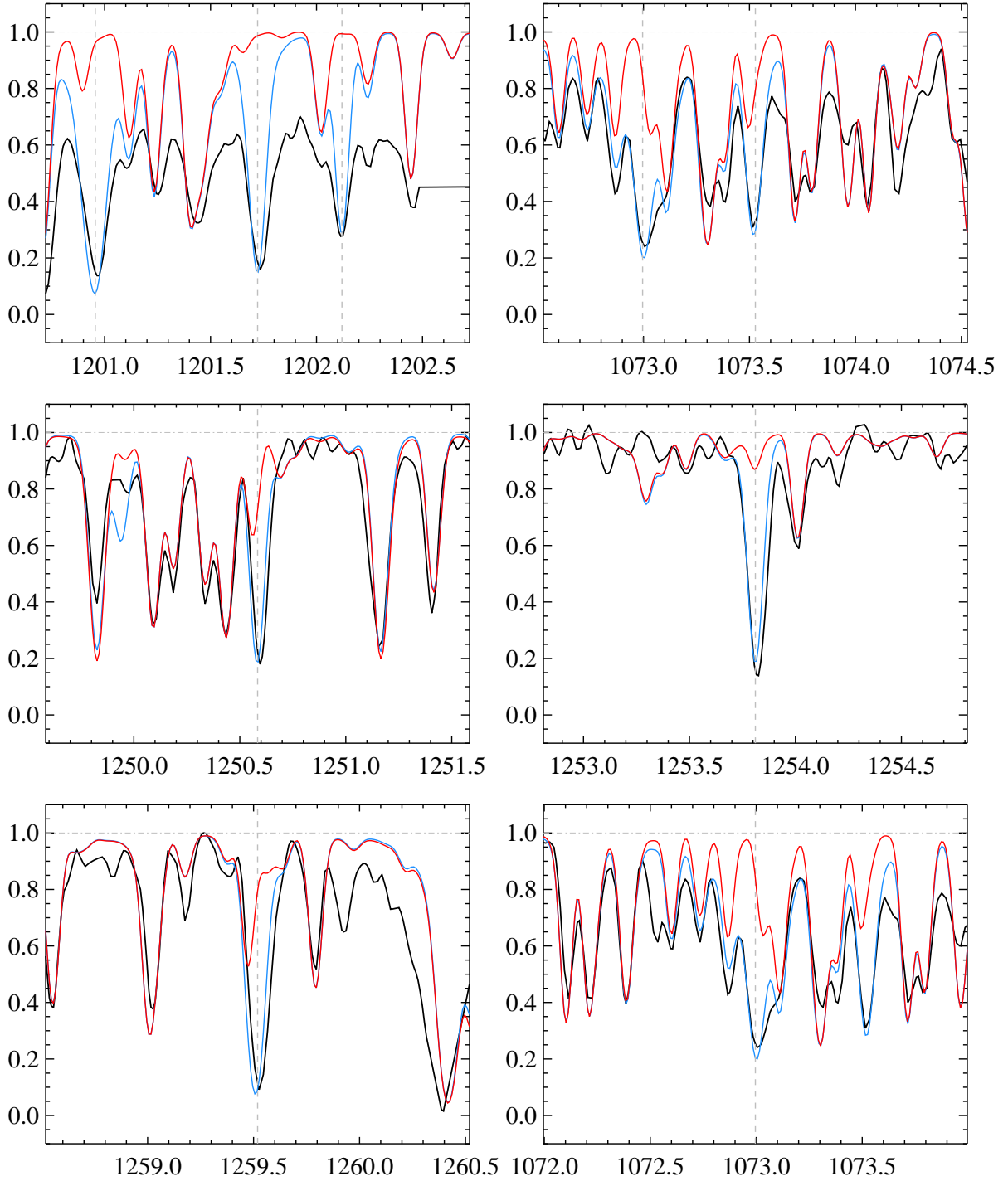


Figure 2.9: This figure shows the observation (in black), the calculated model with $\log(n_S/n_H) = -5.20 \pm 0.10$ (in blue), and without sulfur (in red). *Top left:* The strong S III triplet at 1200.956, 1201.722, 1202.120 Å, *Top right:* The S IV doublet at 1072.996, 1073.528 Å, *Middle:* strong S II resonance doublet line at 1250.584, 1253.811 Å, *Bottom left:* A strong resonance S II line at 1259.519 Å, *Bottom right:* A strong S II line at 1072.996 Å

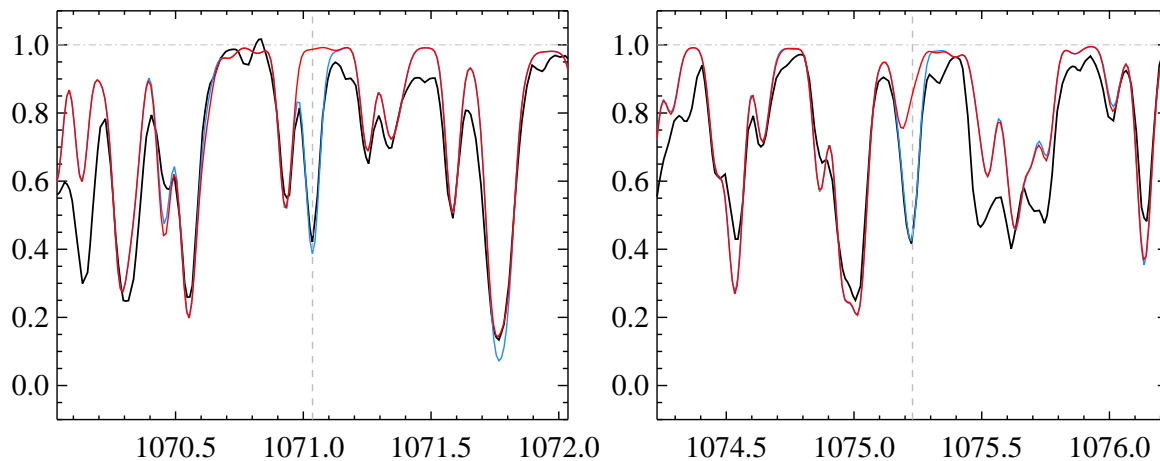


Figure 2.10: This figure shows the observation (in black), the calculated model with $\log(n_{\text{Cl}}/n_{\text{H}}) = -7.150 \pm 0.100$ (in blue), and without chlorine (in red). *Left:* Cl II line at 1071.036 Å, *Right:* Cl II line at 1075.229 Å.

contributes only very weakly. The lowest excited states of Cl III are 18 eV above the ground state [10], which explains why there are virtually no Cl III lines seen in the spectral window studied here.

We determined the abundance of chlorine using the unblended Cl II resonance line of multiplet (1) at 1071 Å shown in Figure 2.10. This line has a “C” $\log gf$ value of roughly -1 . The best-fitting model to this line results in the value of $\log(n_{\text{Cl}}/n_{\text{H}}) = -7.15 \pm 0.10$. We confirmed this value by also modeling the Cl II line at 1075 Å. This line also arises from a very low energy level of 0.1 eV and has a “C” $\log gf$ of -1.7 [10]. The observation and models are shown in Figure 2.10.

2.4.11 Argon, Z=18

Argon appears with 66 lines in the subset of VALD database selected here. In the spectrum of ι Herculis, argon is observed mostly in the form of weak Ar II lines with a minor contribution from stronger Ar I and Ar III lines. As measured from the Saha equation, the dominant ionization state at this temperature is Ar II (see Table 2.3). The reason for the under-population of Ar II lines in the observed spectrum is that in this wavelength window, almost all of the Ar II lines arise from high excitation energy levels which are at least ~ 16 eV above the ground state.

For the abundance determination, we modeled two suitable lines of Ar I; first a UV multiplet (1) line at 1048 Å as well as another UV multiplet (1) line at 1066 Å. These two lines are both resonance lines and have relatively well determined “C+” $\log gf$ values of around -0.5 and -1.0 , respectively [10], and the line at 1048 Å appears unblended. The best-fitting model yields $\log(n_{\text{Ar}}/n_{\text{H}}) = -4.90 \pm 0.10$ in both cases. Figure 2.11 shows the observation and the models.

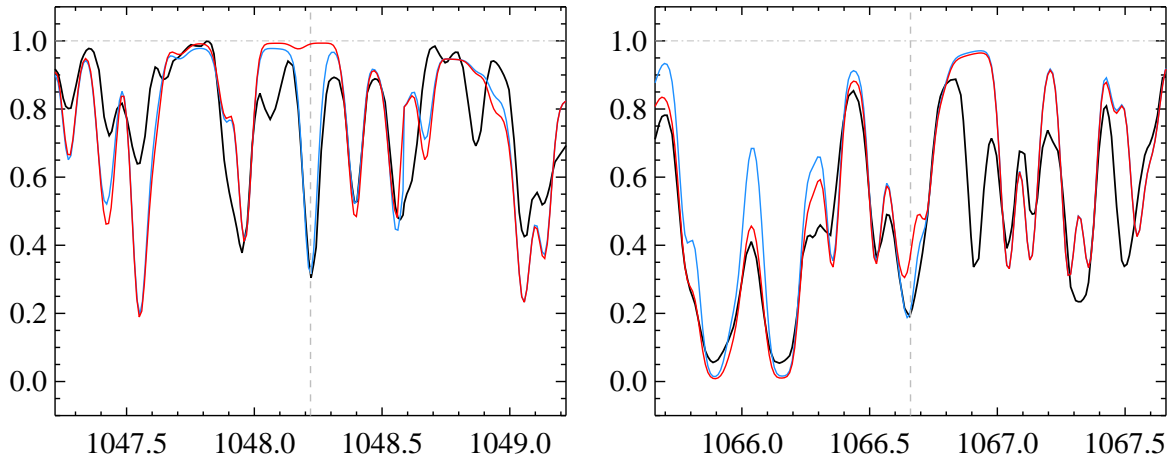


Figure 2.11: This figure shows the observation (in black), the calculated model with $\log(n_{\text{Ar}}/n_{\text{H}}) = -4.900 \pm 0.100$ (in blue), and without argon (in red). *Left:* Ar I line at 1048.220 Å. *Right:* Ar I line at 1066.660 Å.

2.4.12 Calcium, $Z=20$

In the UV spectrum of ι Herculis, calcium is not strongly observed. The subset of VALD database selected here contains overall 43 calcium lines which are almost equally distributed between Ca II and Ca III. The prediction of the Saha equation shows that Ca III must be the dominant state of ionization at this temperature (see Table 2.3). However, because the lowest excited states are more than 30 eV, there is almost no contribution from Ca III state in the observed spectrum of ι Herculis.

Despite the lack of clean and unblended lines, we could determine the abundance using blended lines. Modeling the two Ca II lines at 1369 and 1432 Å window yields $\log(n_{\text{Ca}}/n_{\text{H}}) = -5.30 \pm 0.10$. These lines are suited for our purpose since they both arise from a low energy state (~ 1.6 eV). They both have relatively well determined “C” $\log gf$ values of -0.8 [10]. Figure 2.12 shows the observations and models.

2.4.13 Titanium, $Z=22$

Titanium has 156 titanium lines in our selected database. Most of them are in Ti III form and a smaller fraction of them are in Ti II with little to contribution from Ti IV. In the UV spectrum of ι Herculis, Ti III is dominantly observed and there is a minor contribution from Ti II lines at longer wavelengths. This is consistent with the ionization ratios calculated from the Saha equation for this temperature (see Table 2.3).

We determined the abundance of titanium using lines of the two strong Ti III multiplets (1) and (2) in the 1286-93 Å window. They are suitable choices because they arise from low lying energy levels (~ 0.00 - 0.05) and have relatively well determined (“D”) $\log gf$ values of around -0.5 . Only parts of these multiplets are shown in Figure 2.13.

The best-fitting model results in the abundance of $\log(n_{\text{Ti}}/n_{\text{H}}) = -6.90 \pm 0.17$. We confirmed this abundance by modeling the Ti III UV multiplet (2) at 1282 Å at 0.02 eV and Ti III resonance

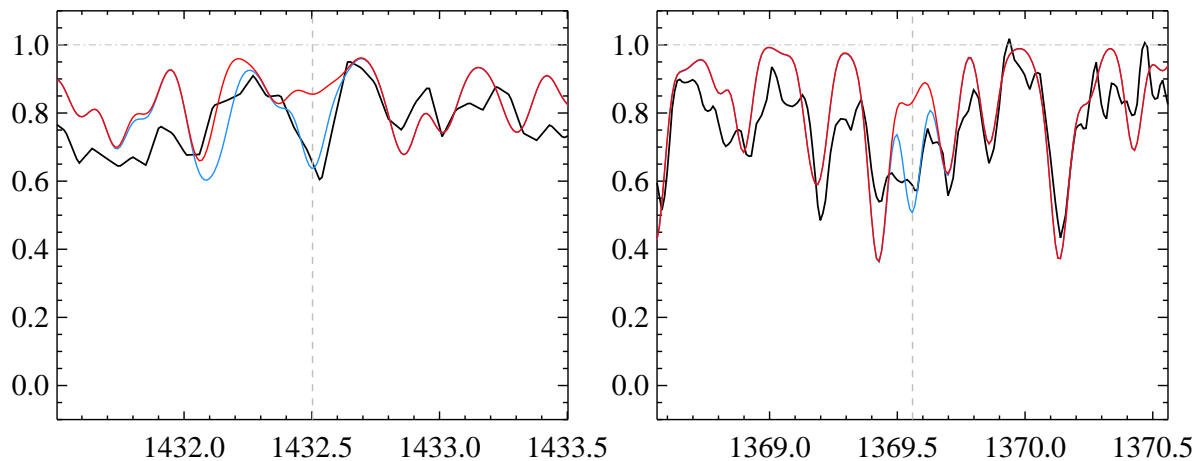


Figure 2.12: This figure shows the observation (in black), the calculated model using $\log(n_{\text{Ca}}/n_{\text{H}}) = -5.30 \pm 0.10$ (in blue), and without calcium (in red). *Left:* Ca II line at 1432.502 Å, *Right:* Ca II line at 1369.559 Å.

lines at 1295-98 Å. These lines all have a “D” $\log gf$ values of around -0.50 and despite a slight blending with nickel (see §3.4.17) they still serve our purpose. Figure 2.13 shows the observed lines as well as the calculated models.

2.4.14 Vanadium, $Z=23$

Our line database contains 234 vanadium lines where all are in the form of V III. In the spectrum of ι -Herculis vanadium is also observed only in V III form. The predictions of the Saha equation shows (see Table 2.3) that V III is the dominant state of ionization and V I, V II are severely underpopulated in this temperature and wavelength range. The lines of V IV are absent because the allowed transitions in our spectral region arise from excited states that are higher than (~ 18 eV).

We have used the four strong and fairly clean V III lines at 1154-1160, 1252, 1332 Å. They all arise from low lying energy levels (~ 1.5 eV) and $\log gf$ values around zero. Despite slight blending with Ni II line (see §3.4.17), they still serve our purpose.

The best-fitting model to these lines, resulted from a vanadium abundance of $\log(n_{\text{V}}/n_{\text{H}}) = -8.15 \pm 0.18$. Figure 2.14 shows the best-fitting model to the observation. The blending of nickel and vanadium provides a reasonable fit to the observation.

2.4.15 Chromium, $Z=24$

The selected line-list contains 1645 chromium lines. In the UV spectrum of ι -Herculis, chromium is mostly observed in Cr III form, with smaller contributions from Cr II and Cr IV. This is consistent with the ionization ratios predicted from the Saha equation (see Table 2.3).

We used the Cr III doublet in the 1098 Å window to determine the abundance. This line is unblended and it arises from a fairly low lying energy level of 2 eV and $\log gf$ of ~ -2 . The

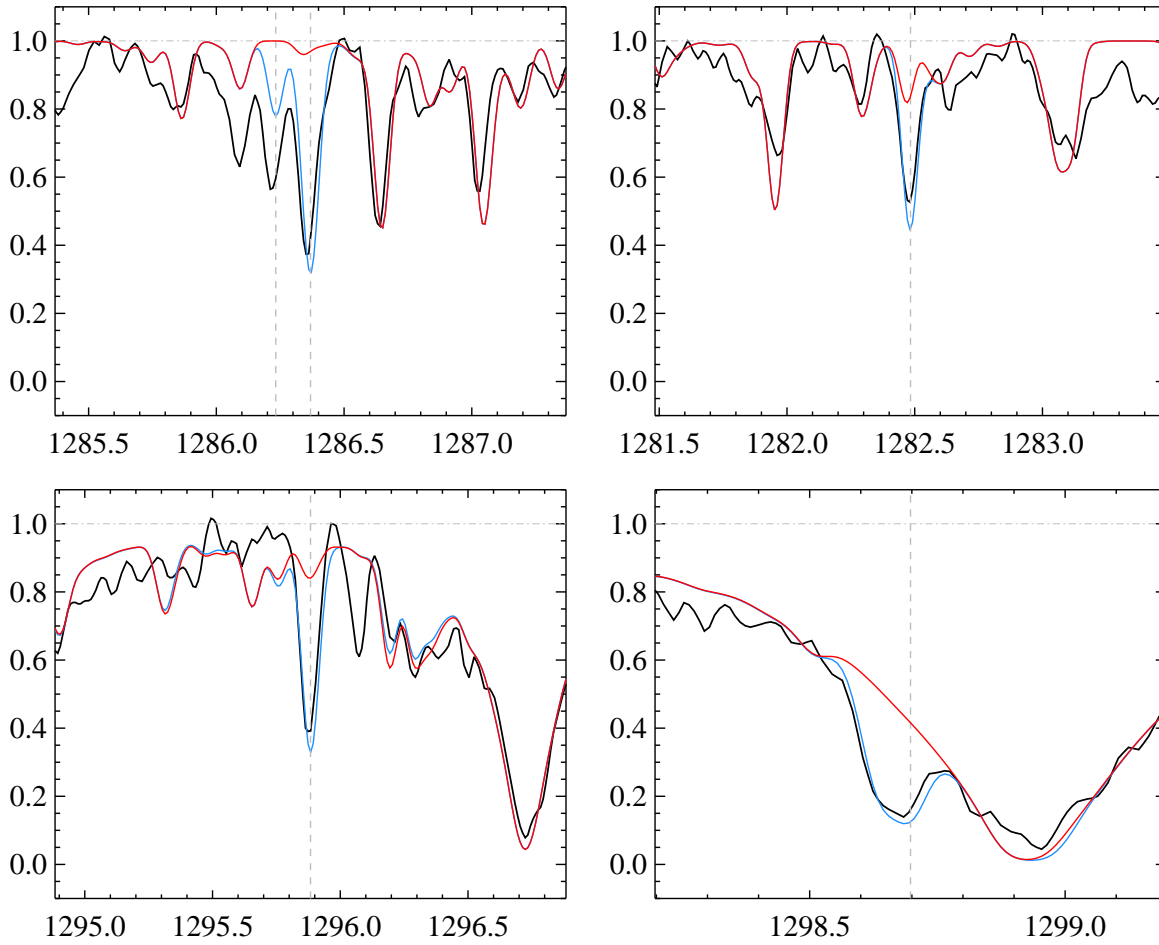


Figure 2.13: This figure shows the observation (in black), the calculated model with $\log(n_{\text{Ti}}/n_{\text{H}}) = -6.90 \pm 0.17$ (in blue), and without titanium (in red). All the plots belong to the same ionization state Ti III; *Top left*: A resonance line at 1286.232, a part of a UV multiplet at 1286.368 Å, *Top right*: at 1282.483 Å, *Bottom left*: at 1295.883 Å, *Bottom right*: at 1298.697 Å

accuracy on the oscillator strengths of chromium lines are not known very well. The best-fitting model results in $\log(n_{\text{Cr}}/n_{\text{H}}) = -6.10 \pm 0.65$.

We confirmed this value using Cr III doublets at 1040 Å and 1064 Å windows and a strong Cr III line at 1051 Å. What they all have in common is that they arise from low energy levels and have oscillator strengths that is between 0 and -1. Figure 2.15 shows the observation and the best-fitting models.

2.4.16 Manganese, Z=25

In database selected here, there are 1448 manganese lines. Almost all of them are in the form of Mn III, and the rest are in the form of Mn II with very few lines of Mn IV. In the UV spectrum of ι Herculis manganese is observed mostly in the form of Mn III lines throughout, with a few strong Mn II lines. The contribution from Mn IV is too weak to be discernible. The

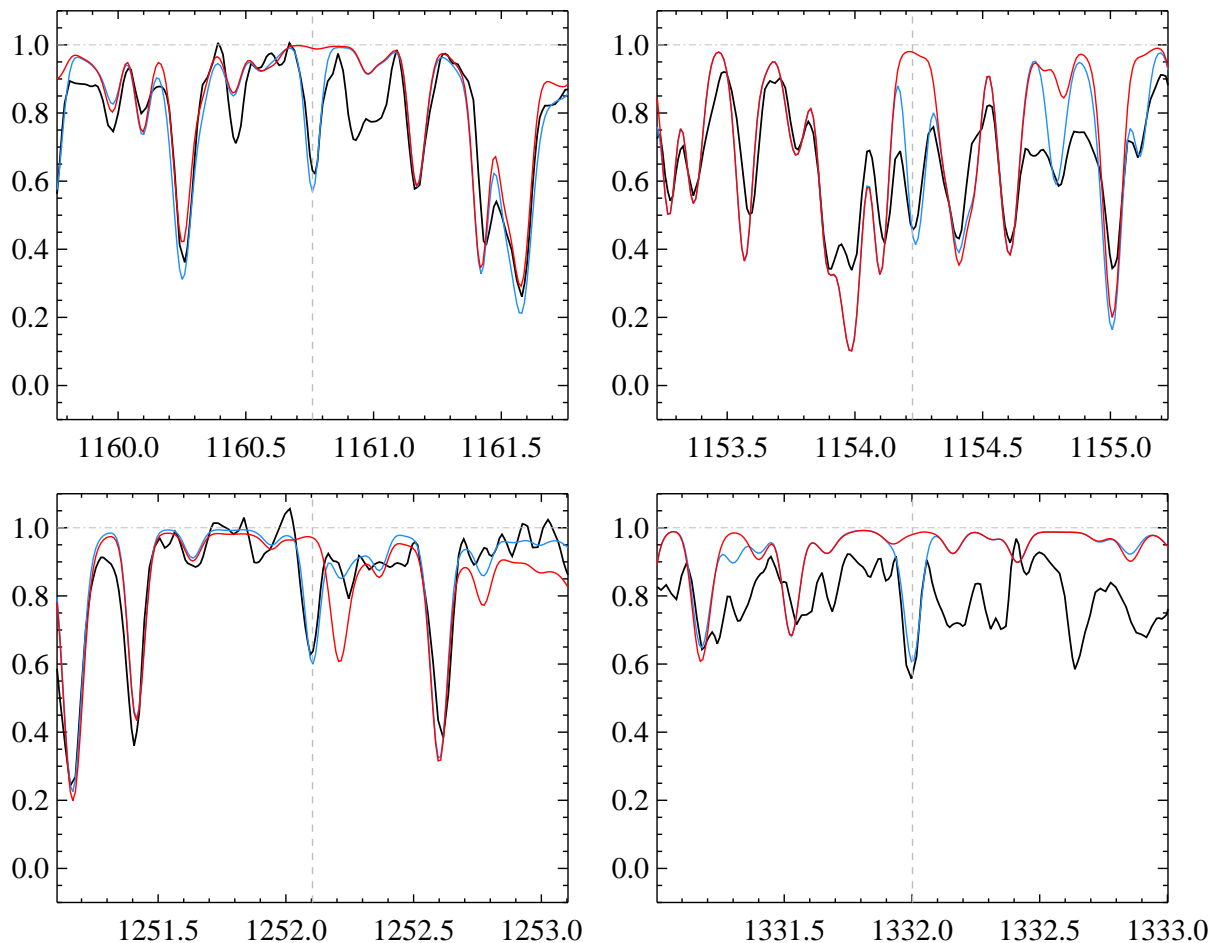


Figure 2.14: This figure shows the observation (in black), the calculated model with $\log(n_V/n_H) = -8.15 \pm 0.18$ (in blue), and without vanadium (in red). All of the plots belong to the same state of ionization; V III at; *Top left*: 1160.761 Å, *Top right*: 1154.225 Å, *Bottom left*: 1252.104 Å, *Bottom right*: 1332.002 Å

measurements from the Saha equation, indicates that Mn III is the dominant state of ionization at this temperature which is consistent with our observation.

We have used the unblended strong Mn III lines in the 1088 Å window to determine the abundance. We find $\log(n_{\text{Mn}}/n_{\text{H}}) = -6.78 \pm 0.45$ for manganese. We confirmed this value by also modeling the Mn III doublet lines in the 1046, 1239 and 1111 Å windows. All the lines chosen here have $\log gf$ values around -1 and arise from low lying energy levels (~ 4 eV). The observed spectrum and models are shown in Figure 2.16.

2.4.17 Iron, $Z=26$

Iron lines are prominent in almost every region of the UV spectrum of ι Herculis. Our selection of the VALD database contains 8165 iron lines, more than half of them are in the form of Fe II. The Fe III lines, even though fewer in number, seem to be stronger and deeper than the lines of

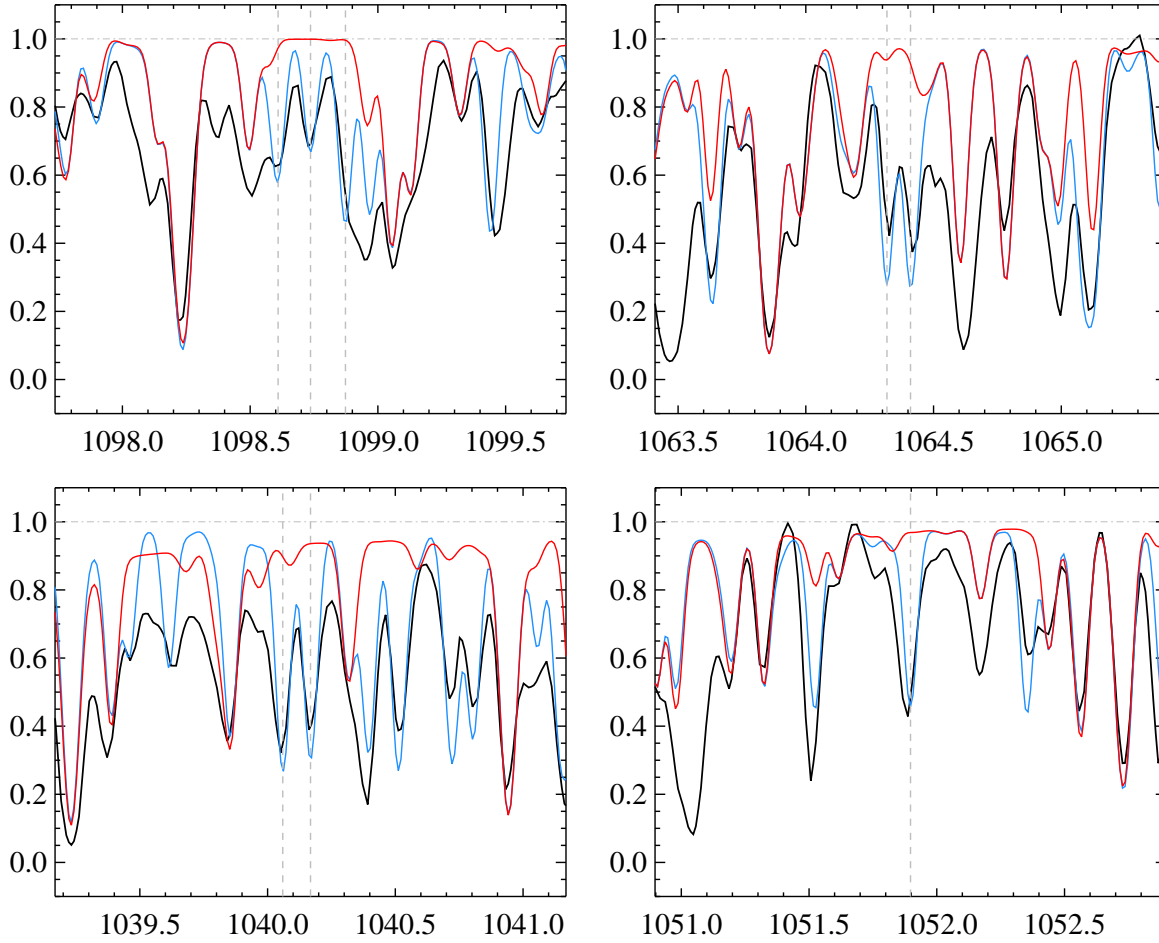


Figure 2.15: This figure shows the observation (in black), the calculated model with $\log(n_{\text{Cr}}/n_{\text{H}}) = -6.10 \pm 0.65$, and without chromium (in red). The plots belong to the same ionization state; Cr III doublet at 1098.609, 1098.736 Å (*Top left*), Cr III doublet at 1064.317, 1064.409 Å (*Top right*), Cr III resonance at 1040.059 with contribution from a part of a multiplet at 1040.168 Å (*Bottom left*), strong Cr III line at 1051.897 Å (*Bottom right*)

Fe IV which are very weak.

In the UV spectrum of ι Herculis the majority of iron lines are observed in the form of moderately strong Fe II lines and fewer Fe III lines. The lowest excited state is ~ 19 eV above the ground state, therefore Fe IV does not appear in our observed spectral window. The calculations from the Saha equation (see Table 2.3) indicate that the dominant ionization state at this temperature is Fe III. Fe III lines do not appear as much since for most such lines the lower level is on average 10 eV or more above the ground state. In contrast the lower levels of strong Fe II lines are only slightly (about 4 eV) above the ground state which makes this state more populated.

Despite the frequency of Fe II lines in the spectrum, they are heavily blended and are not ideal for abundance measurements. We instead used the strong pair of Fe III lines in the 1130 Å window with a slight overlapping blend from Fe II lines. This set of lines is suited for our

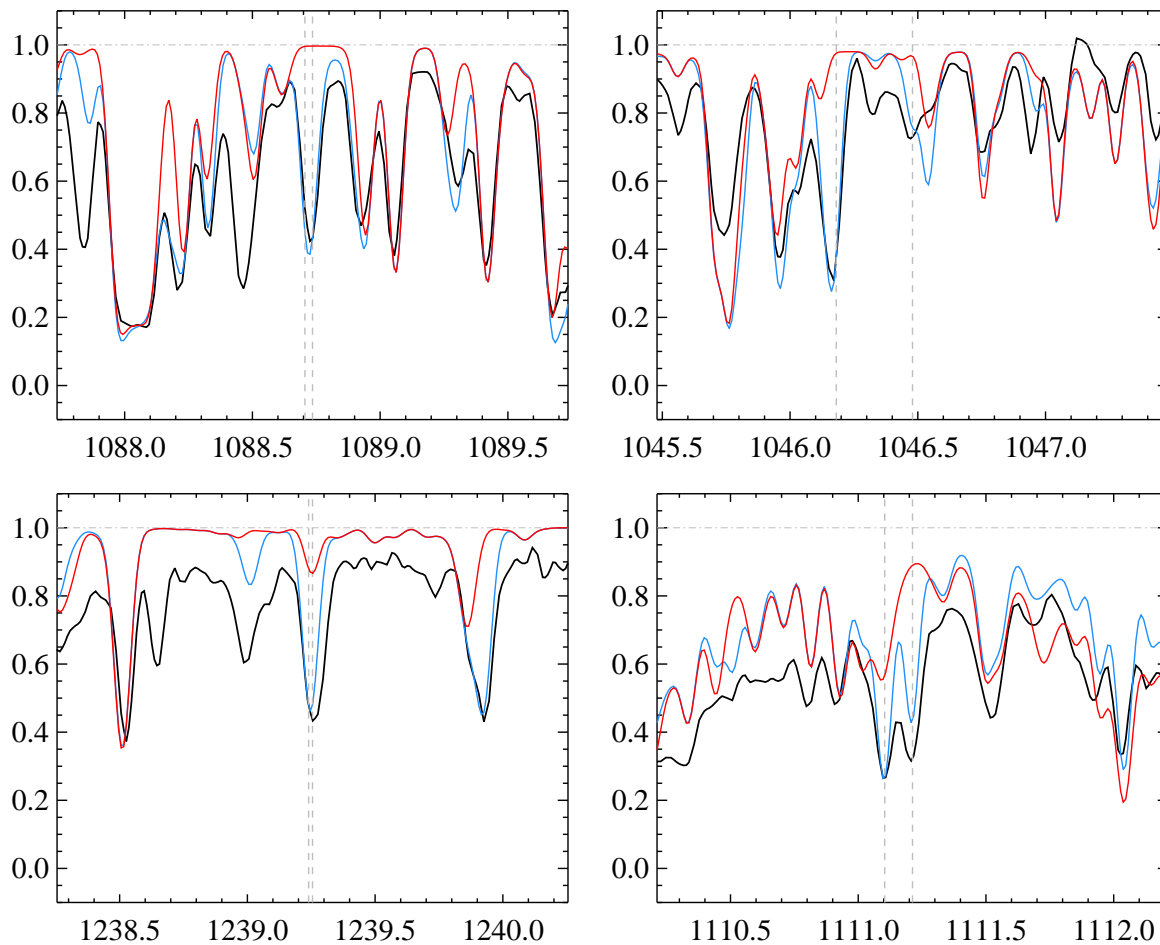


Figure 2.16: This figure shows the observation (in black), the calculated model with $\log(n_{\text{Mn}}/n_{\text{H}}) = -6.78 \pm 0.45$, and without manganese (in red). These plots belong to the same ionization state of Mn III; doublet lines at 1088.705, 1088.735 Å (*Top left*), doublet line at 1046.180, 1046.479 Å (*Top right*), doublet line 1239.239, 1239.255 Å (*Bottom left*), doublet line at 1111.103, 1111.212 Å (*Bottom right*).

purpose because they, not only are unblended, but also arise from very low lying energy state (0.1 eV) with $\log gf$ of -1 (VALD3). The best-fitting model results in $\log(n_{\text{Fe}}/n_{\text{H}}) = -4.9 \pm 0.4$.

We confirmed this value through modeling a cluster of iron lines in the 1142-43 Å window including Fe III and Fe II lines, Fe II lines around 1135-26 Å, and Fe III lines in the 1154 Å window. All these lines arise from very low lying energy levels (0-4 eV) and have $\log gf$ values around zero or -1. Figure 2.17 shows the observation and the modeled spectra.

2.4.18 Cobalt, Z=27

The selected database here contains 581 cobalt lines. In the UV spectrum of ι Herculis, cobalt is observed over the entire wavelength range. Almost all of the strong lines are in the form of Co III, with a few Co II lines and only one Co IV line. The Saha equation predictions shown in

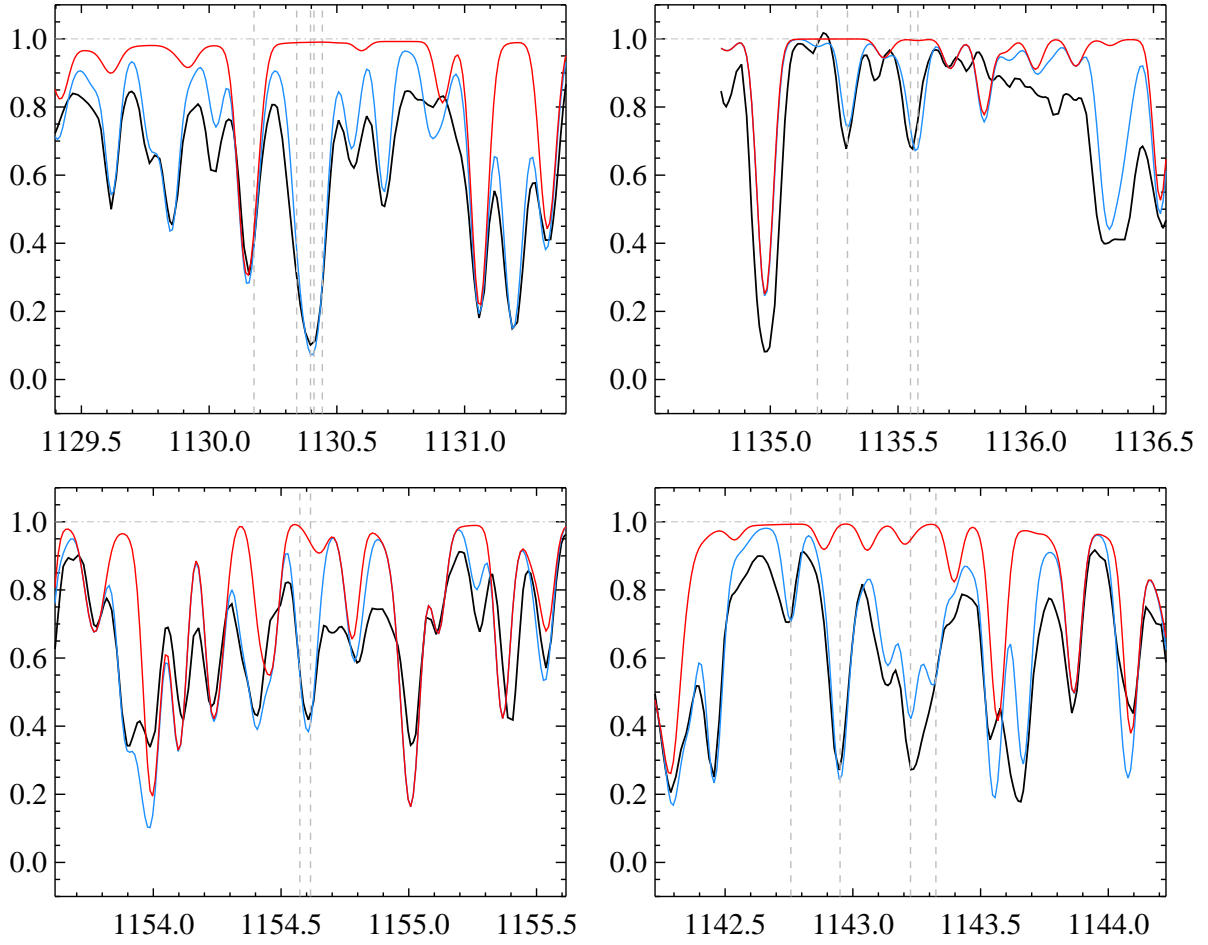


Figure 2.17: This figure shows the observation (in black), the calculated model with $\log(n_{\text{Fe}}/n_{\text{H}}) = -4.9 \pm 0.4$ (in blue), and without iron (in red). *Top left:* The Fe III lines at 1130.396, 1130.410 Å, blended with Fe II lines at 1130.175, 1130.443, 1130.342 Å, *Top right:* A set of Fe II doublets at 1135.548, 1135.577 Å, and 1135.302, 1135.184 Å, *Bottom left:* Fe III doublet at 1154.573, 1154.615 Å, *Bottom right:* The strong Fe III line at 1142.95 Å blended with Fe II lines at 1142.757, 1143.225, 1143.325 Å.

Table 2.3 are consistent with the observed ionization ratio.

We modeled a group of Co III in the window between 1043-88 and found $\log(n_{\text{Co}}/n_{\text{H}}) = -7.55 \pm 0.49$. These lines all arise from low energy states at 1.9 eV with well determined oscillator strength values around -1 (VALD3). We tested this value by also modeling the resonance Co II line at 1466 Å. Figure 2.18 shows the best-fitting model and the observation.

2.4.19 Nickel, Z=28

The line list selected for this work contains 2145 nickel lines. More than half of the lines in the list are in the form of Ni III. A smaller fraction is in the form of Ni II plus only a few lines of Ni IV. In the UV spectrum of ι Herculis nickel is observed mostly as Ni III and Ni II with very

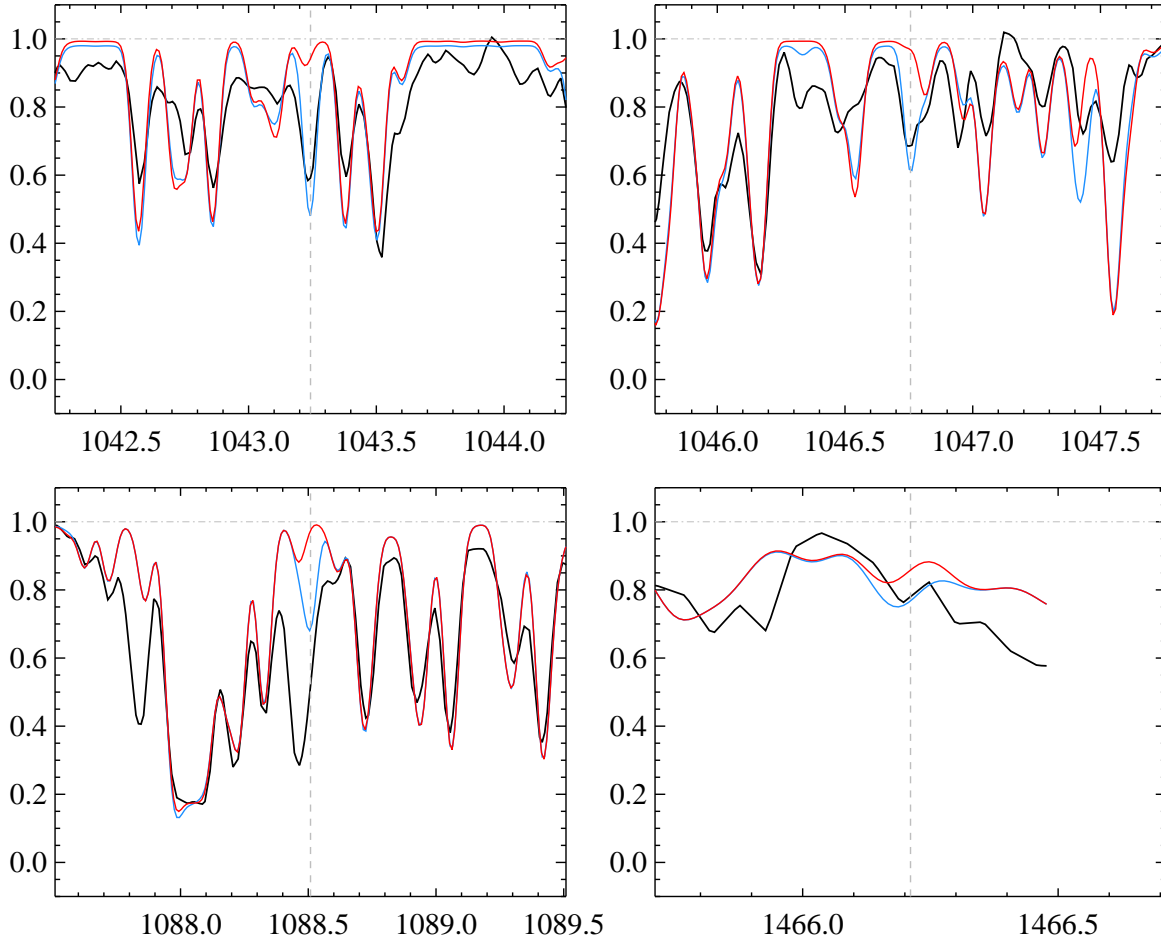


Figure 2.18: This figure shows the observation (in black), the calculated model with $\log(n_{\text{Co}}/n_{\text{H}}) = -7.55 \pm 0.49$ (in blue), and without cobalt (in red). *Top left:* Co III line at 1043.242 Å, *Top right:* Co III line at 1046.756 Å, *Bottom left:* Co III line at 1088.508 Å, *Bottom right:* Co II line at 1466.211 Å.

little contribution from Ni IV. The Ni IV lines hardly appear in the spectrum because the excited states are at least 14 eV above the ground state (VALD3). This distribution is consistent with the ratios estimated from the Saha equation (see Table 2.3).

We determined the abundance of this element using the Ni III triplet in the 1321–22 Å window and found $\log(n_{\text{Ni}}/n_{\text{H}}) = -5.70 \pm 0.35$. These lines arise from ~ 6 eV and have $\log gf$ around -2 , but they are suitable for this purpose because they are clean and unblended.

We confirmed this value by modeling three resonance Ni II lines in three wavelength windows including 1308, 1345, 1370 Å. Figure 2.19 shows the resulting model using this abundance and the fit to the observation.

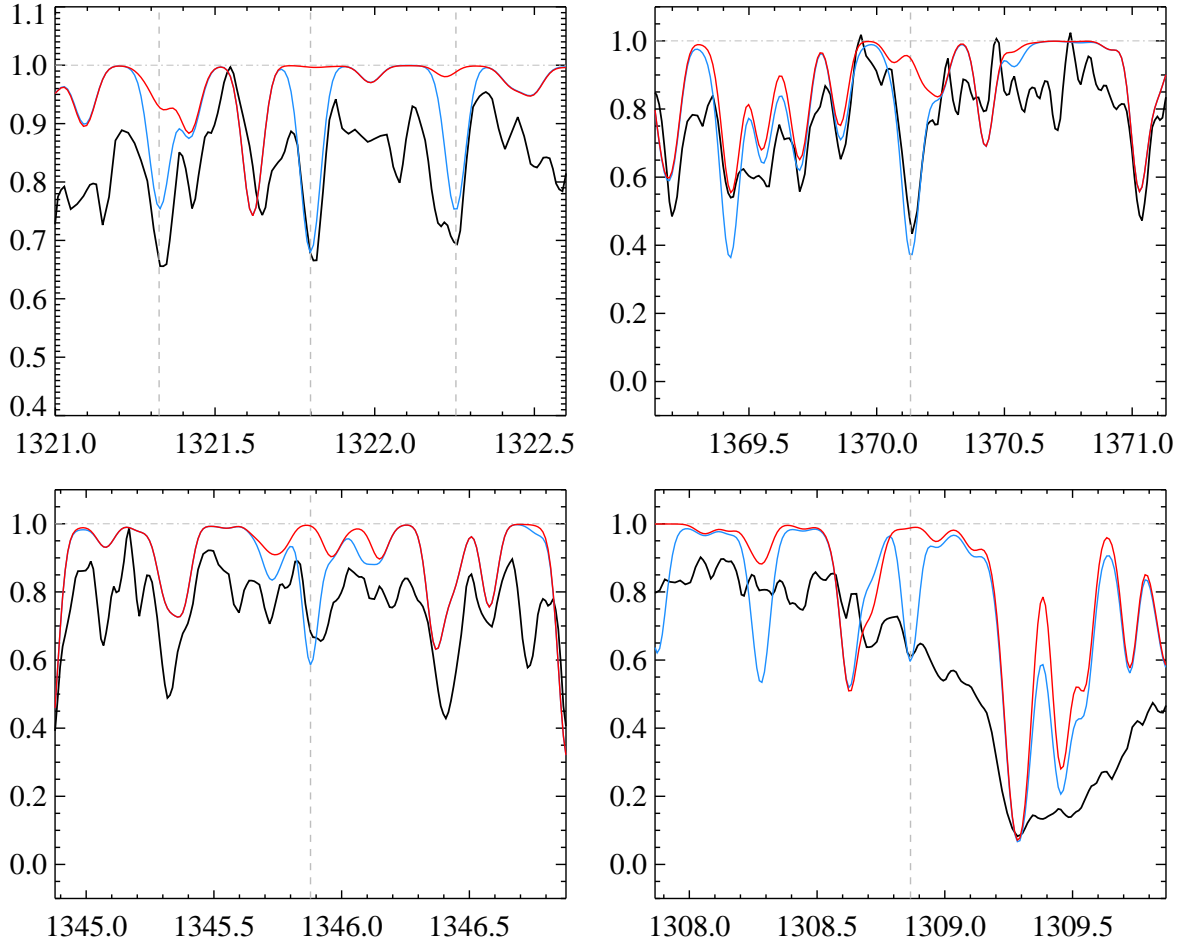


Figure 2.19: This figure shows the observation (in black), the calculated model with $\log(n_{\text{Ni}}/n_{\text{H}}) = -5.70 \pm 0.35$ (in blue), and without nickel (in red). *Top left*: Ni III triplet at 1322.254, 1321.324, 1321.799 Å, *Top right*: a resonance Ni II lines at 1370.132 Å, *Bottom left*: a resonance Ni II line at 1345.878 Å, *Bottom right*: a resonance Ni II line at 1308.865 Å.

2.4.20 Copper, $Z=29$

In the subset of VALD database used here there are 62 Cu II lines. In the UV spectrum of ι -Herculis, copper is observed in the form of Cu II throughout the entire wavelength range studied here. The results of the Saha equation indicate that copper must be dominated by Cu III at this temperature which is inconsistent with our line list. The reason seems to be a lack of atomic data about Cu III.

We modeled the strong resonance line of Cu II at 1358 Å with $\log gf$ of almost 0, and found an abundance of $\log(n_{\text{Cu}}/n_{\text{H}}) = -9.0$. This line is the only unblended line that we have available in our spectrum. We present this as an upper limit for this element due to lack of other unblended lines for comparison. The uncertainty could not be estimated on this value since there are not enough clean lines for comparison. The least uncertainty on this value is due to stellar parameter inaccuracy which is of the order of 0.04 dex (see §3.3.3). Figure 2.20 shows the observation and the model.

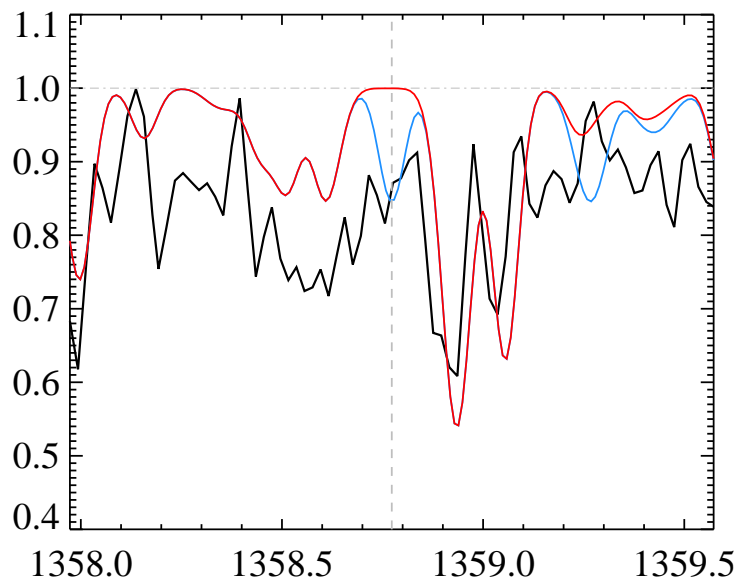


Figure 2.20: This figure shows the observation (in black), the calculated model with $\log(n_{\text{Cu}}/n_{\text{H}}) = -9.00$ (in blue), and without copper (in red). This is a resonance Cu II line at 1358.773\AA .

2.4.21 Zinc, $Z=30$

Zinc has 127 weak lines in the form of Zn III in our selected VALD line list. In the spectrum of ι Herculis, zinc is mostly observed in the longer wavelengths and it appears only in the form of Zn III. This ionization distribution is consistent with the ratios estimated from the Saha equation (see Table 2.3).

The lines are weak and heavily blended and arise from at least 9 eV above the ground state. The lowest excited energy state belongs to a Zn III doublet line in the $1456\text{--}64\text{\AA}$ window. These lines are weak but fairly unblended. We have used them for abundance determination and found $\log(n_{\text{Zn}}/n_{\text{H}}) = -6.85 \pm 0.20$. The uncertainty arises from the fact that each of these lines can best be modeled with a slightly different abundance (see Figure 2.21). The Zn III doublet line at 1359\AA window can also be used to confirm this value. The observation and models are shown in Figure 2.21.

2.4.22 Germanium, $Z=32$

In the VALD line list selected here, there are 8 Ge II lines. All of these lines arise from very low lying energy states ($0\text{--}0.2$ eV) with $\log gf$ values between 0 to -1. However, most of these lines are heavily blended which greatly complicates the task of abundance determination. We have used a relatively strong resonance Ge II line at 1237\AA to find $\log(n_{\text{Ge}}/n_{\text{H}}) = -8.50$. We do not have any other clean lines to confirm this value but a Ge II doublet in $1261\text{--}64\text{\AA}$ region shows that this value can provide an upper limit. Figure 2.22 shows the model and observation.

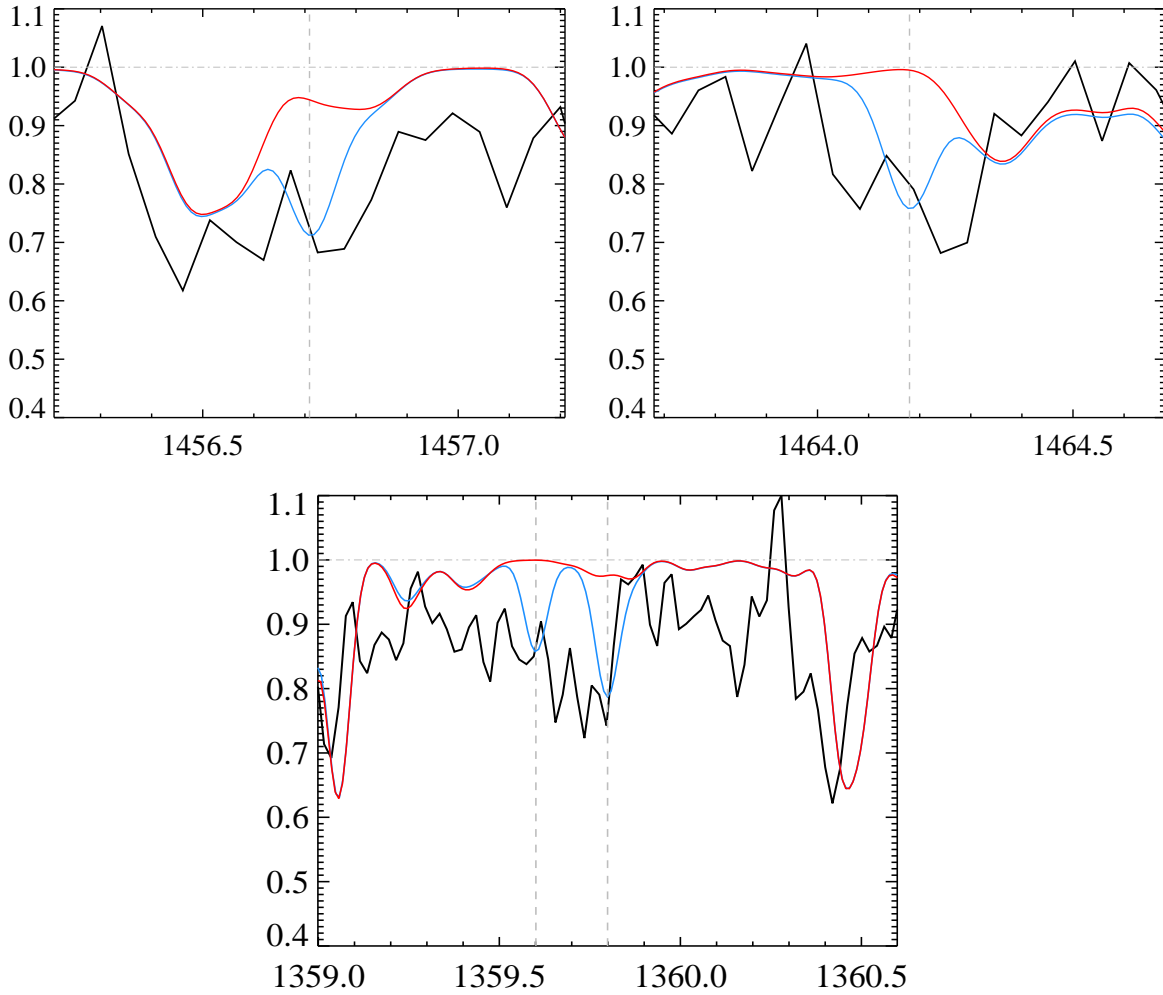


Figure 2.21: This figure shows the observation (in black), the calculated model with $\log(n_{\text{Zn}}/n_{\text{H}}) = -6.85 \pm 0.20$ (in blue), and without zinc (in red). *Top*: Zn III doublet at 1456.709, 1464.180 Å. *Bottom*: Zn III doublet at 1359.601, 1359.799 Å.

2.4.23 Platinum, $Z=78$

The selection of VALD list used here, contains 148 platinum lines. All of them are in the form of Pt III. There is only one Pt II line in the selected list. The dominant state of ionization as estimated by the Saha equation (see Table 2.3), is consistent with what is observed in the spectrum of ι -Herculis.

There are only a few weak lines throughout the spectrum with a minor concentration at shorter wavelengths. We have used a fairly clean Pt III line around 999 Å. This calculation yields $\log(n_{\text{Pt}}/n_{\text{H}}) = -8.825$. Results are shown in Figure 2.23. This value was not confirmed with any other line since there are no other clean and unblended lines available throughout our data. Therefore, we present this value as an upper limit for this element for which we can not determine an uncertainty.

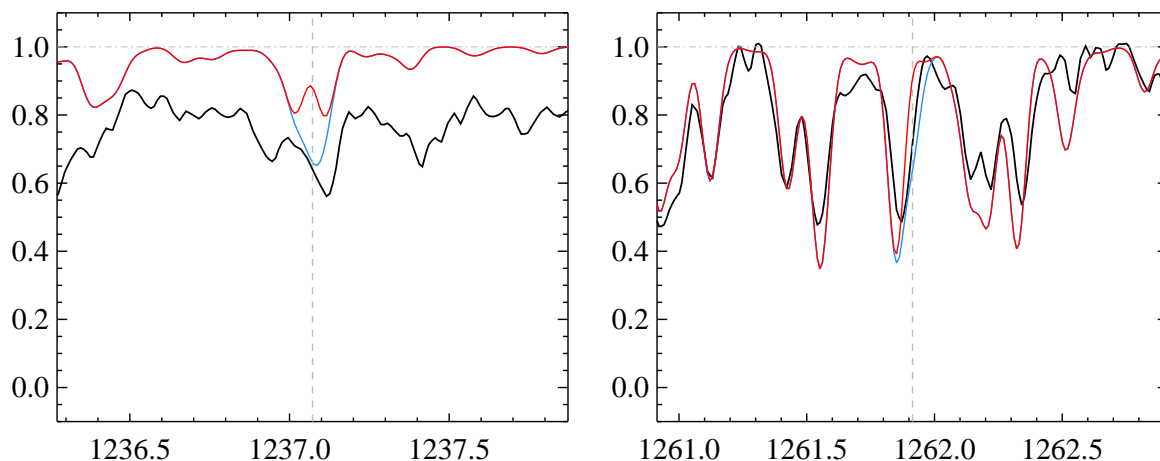


Figure 2.22: This figure shows the observation (in black), the calculated model with $\log(n_{\text{Ge}}/n_{\text{H}}) = -8.50$ (in blue), and without germanium (in red). *left*: A strong line at 1237.072\AA , *right*: A part of a doublet at 1261.913\AA .

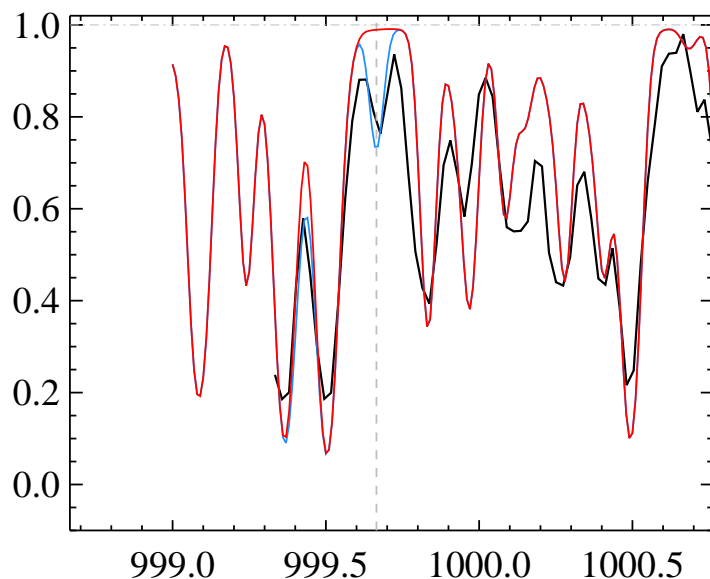


Figure 2.23: This figure shows the observation (in black), the calculated model with $\log(n_{\text{Pt}}/n_{\text{H}}) = -8.825$ (in blue), and without platinum (in red). This is the Pt III line at 999.665\AA .

2.4.24 Mercury, $Z=80$

The subset of the VALD database selected here contains 13 mercury lines. In the observed spectrum of ι Her, the majority of mercury lines are observed in Hg III form with a minor contribution from Hg II. In our wavelength range, apart from two resonance lines, the rest of Hg II lines arise from higher energy states of around ~ 7 eV. At this temperature, the Saha equation also predicts the same ionization distribution.

There are only very few mercury lines suitable for our purpose and they are mostly blended.

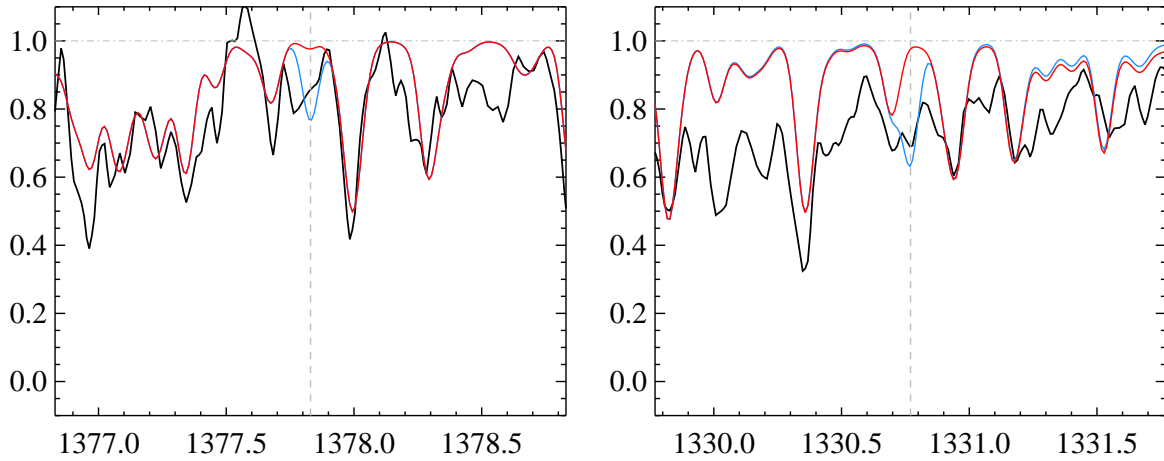


Figure 2.24: This figure shows the observation (in black), the calculated model with $\log(n_{\text{Hg}}/n_{\text{H}}) = -8.95 \pm 0.13$ (in blue), and without mercury (in red). *Left:* Hg III at 1377.830 Å, *Right:* Hg III at 1330.770 Å

We used the Hg III line at 1377 Å and 1330 Å and we find $\log(n_{\text{Hg}}/n_{\text{H}}) = -8.95 \pm 0.13$. Figure 2.24 shows the resulting model and the observation.

2.4.25 The Missing Lines

We have done the spectrum synthesis from which we have derived abundances using the atomic data provided in the VALD database. However, the spectrum of ι Her (shown in Appendix C) still contains some fairly strong lines that are partially or entirely missing from the calculated model (see e.g. 1001.85 Å, 1003.33 Å, 1051.05 Å, 1062.9 Å, 1077.72 Å, 1078.95 Å, etc. in Appendix B).

One source of lines missing from our synthesis is lines due to interstellar absorption by the Lyman bands of the H_2 molecule. The transitions that affect our data are the resonance lines of electronic transitions between the ground electronic-vibrational state (the normal state for interstellar H_2 below about 30 K) and the low vibrational states of the first electronic state. The relevant wavelengths are provided for example in Table 4 of Swamy & Tarafdar [43]. These absorption lines are all present in ι Her, in some cases clearly coinciding with strong observed lines for which our synthesis has no match whatever (1001.8 Å, 1062.9 Å, 1077.1 Å, in other cases also coinciding with strong absorption lines, but with ones for which stellar lines in our synthesis fill a part of the profile (1012.8 Å, 1092.2 Å). It is quite clear that H_2 Lyman band interstellar absorption contributes a number of significant lines to the observed spectrum of ι Her below 1108 Å.

We also investigated the possibility that a few of the missing lines might be in the VALD database with incorrect $\log gf$ values. Using the “Extract all” option, we requested all lines in the database close to some of the strongest unidentified features, and examined the resulting short lists for good wavelength coincidence. We then considered how large a change in oscillator strength would be required to fit the observations, and whether such a change would be plausible. Although we found a few good coincidences, in all cases no reasonable change

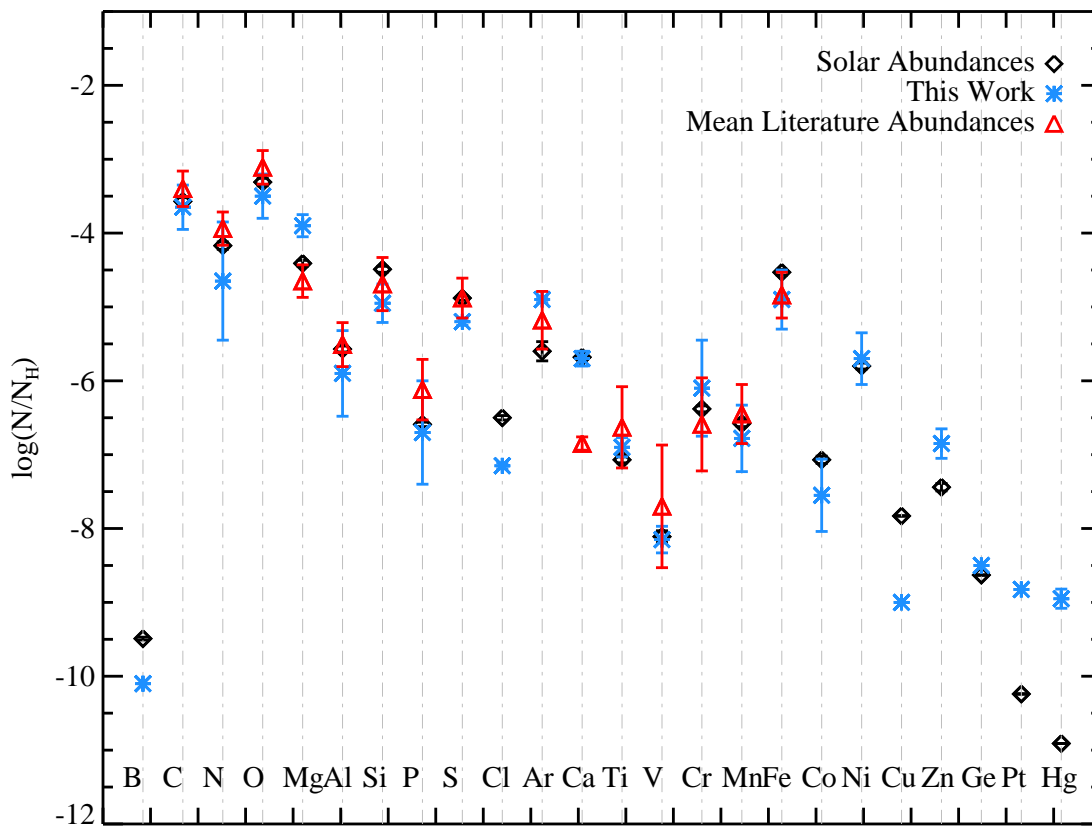


Figure 2.25: This figure shows a comparison between the solar abundances of 24 elements and the abundances derived from this work and the literature. Note that the literature values are the mean taken from Table 2.1.

in oscillator strength would lead to a good fit. This line of investigation was eventually abandoned.

We suspect that most of the remaining strong unidentified features are high-excitation lines of abundant ions, perhaps usually of iron peak elements, that simply lack oscillator strengths.

2.5 Discussion and Conclusions

2.5.1 Comparison with Literature

This work presents the first detailed UV spectral synthesis for Iota Herculis. It is important to compare the outcome of this new approach with previous work. In this project, we investigated the abundance of 27 elements starting from $Z=5$ up to $Z=80$. We could not determine the abundance of a few elements that we tried to detect, specifically neon ($Z=10$), gold ($Z=79$), tin ($Z=50$) because their spectral features were too weak and heavily blended to be useful for

abundance analysis. Among the remaining 24 elements, there are 16 that have been studied in previous works.

The results of this study are listed in Table 2.2, and shown graphically in Figure 2.25. All 16 elements, except for one, are in good agreement with previous work (see Table 2.1) within the estimated uncertainties. The UV spectrum synthesis was not commonly accepted as reasonable tool for abundance determination. However, this work indicates that it is, at least for sharp-line stars with fundamental parameters similar to ι Her.

The only exception to this generalization is magnesium. We find a higher abundance of -3.90 ± 0.19 for magnesium that even within the measured uncertainties, is still higher than previous estimates. This difference is probably due to the fact, discussed in Sec. 4.5, that the dominant ionization state for magnesium at this temperature is Mg III, but the line list contains only lines of Mg II. Thus abundance determinations for this element are likely to be affected by non-LTE effects which may well vary from line to line.

The line list used here does contain a few lines of gold ($Z=79$), tin ($Z=50$), neon ($Z=10$). These lines are found to be very weak and heavily blended. Thus, unfortunately, they do not enable us to determine the abundance of these elements. However, we have been able to estimate a value or an upper limit for the abundance of nine elements that were not previously studied, presumably because of a lack of useful lines in the optical wavelength window usually used for analysis; boron (-10.10 ± 0.10), chlorine (-7.15 ± 0.05), cobalt (-7.55 ± 0.49), nickel (-5.70 ± 0.36), copper (-9.00), zinc (-6.85 ± 0.24), germanium (-8.5), platinum (-8.825 ± 0.100), and mercury (-8.95 ± 0.17). In the atmosphere of ι Herculis the abundance of boron is sub-solar, nickel and cobalt and germanium are almost solar, and platinum and mercury are slightly more than solar.

Overall, the aims of this project, as described in §3.1, have been addressed. In addition to identifying seven previously unreported elements that could be studied in the available UV spectrum, we find – in spite of severe line blending – that abundances of previously studied elements are generally in acceptable agreement with previous work, and that the uncertainties we find are usually comparable to or only moderately larger than those from optical region studies. Because of severe line blending even at very low $v \sin i$ values, this conclusion probably only applies to quite sharp-line stars. We find that LTE modeling in the UV is a useful tool for determining elemental abundances, at least in stars with T_e not much higher than that of ι Her. Finally, in agreement with the results reported by Landstreet [29], we find that the available VALD line lists seem to be missing a significant number of moderately strong lines (quite possibly many are high-excitation lines of iron peak elements), and that the incompleteness of the line lists appears to grow with decreasing wavelength, even over the limited wavelength range of this study.

2.5.2 Further Considerations and future work

We have searched our data for possible indications of a stellar wind. Numerous studies have shown that early type stars reveal the presence of a stellar wind primarily through blue-shifted excess absorption in the wings of resonance lines [15, 16]. We have modeled resonance lines of C II at 1334-35 Å, of N II at 1083-85 Å, and Si IV at 1393-1402 Å. These appear to be the strongest such lines present in regions for which we have data and that we can model confidently (i.e. they are not in the wings of Lyman α or Lyman β). All these lines were modeled reasonably well (e.g. Figure 3), and in none of them did we find any hint of excess blue wing

absorption. Modeling with a code able to model the Lyman lines, and/or data covering a larger wavelength window, could further clarify this situation. In any case, the absence of a detectable (mixed) stellar wind in this star is consistent with the wind computations of Babel [4].

Diffusion is also another process that can occur in the stable atmosphere of slow rotating B stars. Under the action of gravity alone, heavier atoms would sink through the ambient hydrogen down into the stellar interior under the influence of gravity.

However, sometimes observation shows a large abundance of heavy elements (e.g. Mn, Sr, Pt, Hg, etc.) in the atmosphere, and an under-abundance of lighter elements (e.g. He, Ne, O, etc.). This kind of abundance peculiarity occurs when radiation pressure from the radiation flowing out of the stellar interior reverses the downward drift of low-abundance elements. This phenomenon is known as “radiative levitation”. Radiative levitation can operate particularly effectively in slowly rotating stars, and although we do not know the actual rotation rate of ι Her, its very low $v \sin i$ value suggests that it may well be a slow rotator.

In the atmosphere of ι Herculis, we find, in agreement with other studies, that most of our light elements have almost solar abundances, but heavier elements such as zinc ($Z=30$), platinum ($Z=78$) and mercury ($Z=80$), apparently have a higher abundance than the solar value. These values, even with their uncertainties, are still much higher than solar abundance. This over-abundance of heavy elements in the atmosphere of ι Herculis may potentially be explained by radiative levitation in this star. In a way, it mirrors the phenomenon observed by Hill & Landstreet [8], that even most normal but slowly rotating A0V stars seem to have overabundance of some heavy elements such as Zr, Ba and La.

Chemical abundances of stars provide probably the most powerful probes of their structure and of the complex mixing and separation processes that occur in the stellar interior and envelope and that influence evolution on the main sequence and in later stages. Obtaining accurate measurements of the relative abundances of as many elements as possible is an essential first step to interpreting the information content of stellar chemistry. This work has shown that the ultraviolet wavelength window can make a very useful contribution to this step towards a better understanding of such sharp-line mid-B stars as ι Her.

2.6 Acknowledgments

SSG acknowledges support from the Department of Physics and Astronomy of the University of Western Ontario. SSG and JDL acknowledge financial support for this work from the Natural Sciences and Engineering Council of Canada. This work is based on observations made with *Copernicus* satellite or Orbiting Astronomical Observatory 3 (OAO-3), a collaborative effort between the USA(NASA) and the UK(SERC). The UV telescope on board belonged to the Princeton University. Some of the data presented in this paper were obtained from the Mikulski Archive for Space Telescopes (MAST). STScI is operated by the Association of Universities for Research in Astronomy, Inc., under NASA contract NAS5-26555. Support for MAST for non-HST data is provided by the NASA Office of Space Science via grant NNX13AC07G and by other grants and contracts.

Table 2.1: Iota Herculis- Summary of Literature Abundances. (1) Pintado & Adelman [35]; (2) Schmidt [50]; (3) Balona [6]; (4) Lester et al. [28]; (5) Kane et al. [17]; (6) Barnett & McKeith [7]; (7) Grigsby [12]; (8) Dufton et al. [11]; (9) Peters & Polidan [34] ; (10) Peters & Aller [33]; (11) Nieva & Przybilla [32]. Note: Solar Abundances are taken from Scott et al. [32, I & II], Grevesse et al. [9] and [1]

Species	1	2	3	4	5	6	7	8	9	10	11	$\log(N/N_{\text{H}})_{\odot}$
He I	-1.07						-0.042					-1.07±0.01
C II	-3.39±0.28	-3.50	-3.47	-3.30	-3.87	-3.87	-3.48			-3.23±0.38	-3.60±0.07	-3.57±0.05
N II	-3.84±0.17				-4.10		-3.99	-4.10	-4.11±0.39	-3.72±0.22	-4.11±0.12	-4.17±0.05
O I									-3.01±0.15		-3.20±0.09	-3.31±0.05
O II	-2.91±0.23				-3.30		-3.11		-3.33±0.44			-3.31±0.05
Ne I										-3.35±0.19	-3.95±0.07	-4.07±0.10
Ne II							-3.97		-3.36±0.26			-4.07±0.10
Mg II	-4.78±0.26						-4.46		-4.66±0.09	-4.72±0.09	-4.44±0.06	-4.41±0.04
Al II	-6.03						-5.57					-5.57±0.04
Al III	-5.49±0.25								-5.58±0.24	-5.47±0.17		
Si II	-5.16±0.23						-4.49		-4.96±0.47	-4.86±0.34	-4.49±0.05	-4.49±0.03
Si III	-4.45±0.34								-4.59±0.44	-4.45±0.25		
Si IV									-4.61±0.06			
P II	-5.90								-5.63±0.55	-5.65±0.36		-6.59±0.03
P III	-6.25±0.13								-6.98±0.6			
S II	-4.91±0.20								-4.83±0.35	-4.90±0.18		-4.88±0.03
S III	-4.64±0.10								-5.05±0.36	-4.99±0.43		
Ar II	-5.18±0.25								-5.14±0.59	-5.22±0.33		-5.60±0.13
Ca II	-6.03								-5.84	-6.85±0.09		-5.68±0.03
Ti III									-6.63±0.55			-7.07±0.04
V III									-7.70±0.83			-8.11±0.08
Cr III									-6.59±0.63			-6.38±0.04
Mn III									-6.45±0.40			-6.58±0.04
Fe II	-5.14±0.24						-4.37		-5.18±0.41	-5.87±0.43	-4.49±0.08	-4.53±0.04
Fe III	-4.35±0.24								-4.50±0.31	-4.37±0.23		-4.53±0.04

Table 2.2: This table shows the abundances determined in this work for every ion and the recommended value for every element, the solar abundances from Scott et al. [32, I & II], Grevesse et al. [9] and Asplund et al. [1], and the wavelengths used to determine these values.

Element or ion	Abundance (this work)	$\log(N/N_H)$	$\log(N/N_H)_\odot$	Useful Line Wavelengths[Å]
B II	-10.100±0.100	-10.100±0.100	-9.300±0.020	1362.461
C II		-4.450±0.300		1323.905,1323.951,1323.995,1141.624, 1141.657,1141.744
C III		-3.750±0.250		1247.383, 1174.933, 1175.263, 1175.711 , 1175.987, 1176.370
C	-3.55±0.300		-3.570±0.05	
N I		-4.350±0.340		1199.550, 1200.223, 1200.710, 1243.171, 1243.179, 1243.306, 1243.313
N II		-4.860±0.340		1085.546, 1085.701, 1275.038, 1275.251, 1275.275, 1276.201, 1276.225, 1276.800
N	4.650±0.800		-4.170±0.050	
O I		-3.500±0.300		1040.943 1041.688
O II		-3.550± 0.300		1131.914,1132.389,1132.975
O	-3.500± 0.300		-3.310±0.050	
Mg II	-3.900±0.150	-3.900±0.190	-4.410±0.040	1240.395, 1367.257, 1367.708
Al III	-5.900±0.580	-5.900±0.580	-5.570±0.040	1379.670, 1352.858, 1189.185, 1190.046, 1190.051, 1191.803, 1191.808, 1191.814
Si II		-4.650±0.27		1190.415,1265.002,1264.737
Si III		-4.950±0.20		1144.309, 1144.959, 1145.669, 1301.149
Si IV		-4.750±0.15		1128.340
Si	-4.780±0.260		-4.490±0.030	
P III		-6.750±0.680		1344.326 ,1344.850
P II		-6.400±0.660		1152.818, 1249.829, 1301.874
P	-6.700± 0.700		-6.590±0.030	
S II		-5.300±0.050		1250.584,1253.811,1259.519,1072.996
S III		-5.200±0.100		1200.956, 1201.722, 1202.120
S IV		-5.200±0.100		1072.996, 1073.528
S	-5.200± 0.100		-4.880±0.030	
Cl II	-7.150±0.100	-7.150±0.041	-6.500±0.030	1071.036, 1075.229
Ar I	-4.900±0.100	-4.900±0.041	-5.600±0.13	1048.220, 1066.660
Ca II	-5.700±0.100	-5.700±0.010	-5.680±0.030	1330.912, 1368.422
Ti III	-6.900±0.170	-6.900±0.130	-7.070±0.040	1282.483,1286.232,1286.368, 1295.883, 1298.697
V III	-8.150±0.180	-8.150±0.180	-8.110±0.080	1154.225, 1160.761, 1252.104, 1332.002
Cr III	-6.100±0.650	-6.100±0.650	-6.380±0.040	1040.059, 1040.168, 1064.317, 1064.409, 1098.609, 1098.736, 1051.897
Mn III	-6.780±0.450	-6.780±0.450	-6.580±0.040	1046.180, 1046.479, 1088.705,1088.735, 1111.103, 1111.212, 1239.239, 1239.255,
Fe II		-4.950±0.390		1130.175, 1130.443, 1130.342, 1135.548
				1135.577, 1135.302, 1135.184, 1142.757, 1143.225, 1143.325
Fe III		-4.750±0.400		1130.396, 1130.410, 1142.95
Fe	-4.900±0.400		-4.530±0.040	
Co II		-7.550±0.100		1466.211
Co III		-7.450±0.490		1043.242, 1046.756, 1088.508
Co	-7.55±0.490		-7.070±0.050	
Ni II		-5.500 ±0.360		1370.132, 1345.878, 1317.217
Ni III		-5.800 ±0.300		1322.254, 1321.324, 1321.799
Ni	-5.700±0.350		-5.800±0.040	
Cu II	-9.000		-7.830	1358.772
Zn III	-6.850±0.200	-6.850±0.200	-7.440 ±0.050	1359.601,1359.799, 1456.709, 1464.180
Ge II	-8.500		-8.630	1237.072, 1261.913
Pt III	-8.825	-8.825	-10.240	999.665
Hg III	-8.950±0.130	-8.950±0.130	-10.910	1330.770, 1377.830

Table 2.3: The percentile ionization ratios directly measured from the Saha equation. Note that n_{tot} is the total number density in every state ($n_{tot} = n_0 + n_1 + n_2 + n_3$). Note that this table shows the calculations at two different regions; *left column*: The region where the continuum and weak lines are formed ($\tau=0.2$, $T \sim 17000\text{K}$, $n_e \sim 3.84 \times 10^{14}$) and *right column*: The region where line core of strong line are formed ($\tau=7 \times 10^{-4}$, $T \sim 11800\text{K}$, $n_e \sim 5.13 \times 10^{12}$), respectively [14].

Species	$\tau = 0.2$				$\tau = 7 \times 10^{-4}$			
	[I]/ n_{tot}	[II]/ n_{tot}	[III]/ n_{tot}	[IV]/ n_{tot}	[I]/ n_{tot}	[II]/ n_{tot}	[III]/ n_{tot}	[IV]/ n_{tot}
B	0.002	27.30	72.69	0.009	2.07×10^{-3}	97.52	2.50	4.25×10^{-8}
C	0.007	72.84	27.14	1.71×10^{-5}	0.01	99.53	0.46	0.00
N	0.03	95.68	4.29	3.03×10^{-7}	0.08	99.91	9.76×10^{-3}	0.00
O	0.073	99.55	0.37	0.00	0.17	99.83	1.3×10^{-4}	0.00
Ne	1.11	98.88	0.005	0.00	26.31	73.70	1.81×10^{-7}	0.00
Mg	4.98×10^{-7}	0.17	99.83	0.00	5.60×10^{-7}	0.60	99.40	0.00
Al	5.80×10^{-6}	0.49	92.73	6.77	1.34×10^{-5}	6.42	93.56	2.20×10^{-2}
Si	1.49×10^{-5}	1.19	97.84	0.97	2.93×10^{-5}	6.39	93.61	5.53×10^{-4}
P	5.02×10^{-5}	2.84	96.42	0.73	4.75×10^{-4}	33.66	66.34	9.06×10^{-4}
S	7.30×10^{-4}	8.92	90.96	0.12	5.35×10^{-3}	84.85	15.15	7.78×10^{-6}
Cl	5.70×10^{-3}	40.64	59.34	0.01	2.50×10^{-2}	97.84	2.13	3.05×10^{-8}
Ar	0.02	72.46	27.52	4.00×10^{-4}	0.11	99.74	0.16	0.00
Ca	2.13×10^{-8}	0.02	99.98	2.48×10^{-5}	0.00	2.55×10^{-2}	99.97	0.00
Ti	9.53×10^{-8}	0.04	88.28	11.68	5.68×10^{-8}	9.44×10^{-2}	99.85	5.80×10^{-2}
V	1.98×10^{-7}	0.05	94.16	5.78	1.53×10^{-7}	0.18	99.80	1.47×10^{-2}
Cr	2.01×10^{-7}	0.05	97.01	2.94	2.82×10^{-7}	0.32	99.68	4.20×10^{-3}
Mn	6.37×10^{-7}	0.14	98.06	1.79	8.30×10^{-7}	0.65	99.35	1.02×10^{-3}
Fe	1.27×10^{-6}	0.22	98.99	0.79	2.30×10^{-6}	1.15	98.85	1.21×10^{-3}
Co	2.23×10^{-6}	0.24	99.32	0.43	5.22×10^{-6}	1.72	98.28	2.60×10^{-4}
Ni	4.03×10^{-6}	0.33	99.46	0.21	1.25×10^{-5}	3.27	96.73	7.07×10^{-5}
Cu	3.57×10^{-6}	0.29	99.60	0.11	2.25×10^{-5}	5.64	94.36	2.05×10^{-5}
Zn	1.14×10^{-5}	1.19	98.73	0.07	5.50×10^{-5}	10.36	89.64	5.10×10^{-6}
Ge	9.60×10^{-6}	0.91	98.49	0.60	1.54×10^{-5}	4.32	95.67	2.72×10^{-4}
Sn	2.60×10^{-6}	0.36	92.80	6.84	2.46×10^{-6}	1.21	98.78	1.17×10^{-2}
Pt	1.07×10^{-5}	0.75	82.89	16.36	6.54×10^{-5}	9.53	90.41	6.61×10^{-2}
Au	5.20×10^{-5}	3.04	92.20	4.75	3.81×10^{-4}	42.40	57.60	5.65×10^{-3}
Hg	1.95×10^{-5}	1.01	98.68	0.30	1.72×10^{-4}	11.34	88.66	1.30×10^{-4}

Bibliography

- [1] Asplund, M., Grevesse, N., Sauval, A. J., & Scott, P. 2009, *ARAA*, 47, 481
- [3] Aerts, C., Puls, J., Godart, M., & Dupret, M.-A. 2009, *Communications in Asteroseismology*, 158, 66
- [3] Aerts, C., Puls, J., Godart, M., & Dupret, M.-A. 2009, *Communications in Asteroseismology*, 158, 66
- [4] Babel, J. 1996, *aap* , 309, 867
- [5] Bailey, J. D., & Landstreet, J. D. 2013, *A&A* , 551, AA30
- [6] Balona, L. A. 1984, *mnras*, 211, 973
- [7] Barnett, E. W., & McKeith, C. D. 1988, *MNRAS*, 234, 325
- [6] Cantiello, M., Langer, N., Brott, I., et al. 2009, *Communications in Asteroseismology*, 158, 61
- [7] Cowley, C. R. 1996, *M.A.S.S., Model Atmospheres and Spectrum Synthesis*, 108, 223
- [10] Dufton, P. L., & McKeith, C. D. 1980, *A&A*, 81, 8
- [11] Dufton, P. L., Kane, L., & McKeith, C. D. 1981, *MNRAS*, 194, 85
- [12] Grigsby, J. A. 1991, *ApJ*, 380, 606
- [13] Grigsby, J. A., Mulliss, C. L., & Baer, G. M. 1996, *PASP*, 108, 953
- [8] Hill, G. M., & Landstreet, J. D. 1993, *A&A* , 276, 142
- [10] Kramida, A., Ralchenko, Yu., Reader, J. and NIST ASD Team, 2014, NIST Atomic Spectra Database (version 5.2), [Online]. Available: <http://physics.nist.gov/asd> [Saturday, 24-Jan-2015 16:37:16 EST]. National Institute of Standards and Technology, Gaithersburg, MD
- [16] Klinglesmith, D. A., III, Sonneborn, G., Polidan, R. S., et al. 1996, *Astronomical Data Analysis Software and Systems V*, 101, 521
- [17] Kane, L., McKeith, C. D., & Dufton, P. L. 1980, *A&A*, 84, 115

- [70] Kupka, F., Piskunov, N., Ryabchikova, T. A., Stempels, H. C., & Weiss, W. W. 1999, *A&AS*, 138, 119
- [100] Kupka, F. G., Ryabchikova, T. A., Piskunov, N. E., Stempels, H. C., & Weiss, W. W. 2000, *Baltic Astronomy*, 9, 590
- [14] Kurucz, R. L. 1979, *ApJS*, 40, 1
- [71] Kurucz, R. L. 1970, *SAO Special Report*, 309,
- [20] Landsman, W. B. 1993, *Astronomical Data Analysis Software and Systems II*, 52, 246
- [15] Lamers, H. J. G. L. M. 1981, *IAU Colloq. 59: Effects of Mass Loss on Stellar Evolution*, 89, 181
- [16] Lamers, H. J. G. L. M., Gathier, R., & Snow, T. P., Jr. 1982, *ApJ*, 258, 186
- [74] Landstreet, J. D. 1988, *ApJ*, 326, 967
- [23] Landstreet, J. D., Barker, P. K., Bohlender, D. A., & Jewison, M. S. 1989, *ApJ*, 344, 876
- [27] Lennon, D. J. 1983, *MNRAS*, 205, 829
- [28] Lester, J. B., Gray, R. O., & Kurucz, R. L. 1986, *ApJS*, 61, 509
- [29] Landstreet, J. D. 2011, *A&A*, 528, A132
- [26] Nordlund, A., & Stein, R. F. 1995, *Liege International Astrophysical Colloquia*, 32, 75
- [25] Nieva, M.-F., & Simón-Díaz, S. 2011, *A&A*, 532, A2
- [32] Nieva, M.-F., & Przybilla, N. 2012, *A&A*, 539, A143
- [33] Peters, G. J., & Aller, L. H. 1970, *ApJ*, 159, 525
- [34] Peters, G. J., & Polidan, R. S. 1985, *Calibration of Fundamental Stellar Quantities*, 111, 417
- [35] Pintado, O. I., & Adelman, S. J. 1993, *MNRAS*, 264, 63
- [28] Przybilla, N., Nieva, M.-F., & Butler, K. 2011, *Journal of Physics Conference Series*, 328, 012015
- [101] Piskunov, N., & Kupka, F. 2001, *ApJ*, 547, 1040
- [38] Ryabchikova, T. A., Hill, G. M., Landstreet, J. D., Piskunov, N., & Sigut, T. A. A. 1994, *MNRAS*, 267, 697
- [39] Rogerson, J. B., Spitzer, L., Drake, J. F., et al. 1973, *ApJl*, 181, L97
- [40] Rogerson, J. B., Jr., & Upson, W. L., II 1977, *ApJS*, 35, 37

- [41] Ross, J. E., & Aller, L. H. 1976, *Science*, 191, 1223
- [104] Ryabchikova, T. A., Piskunov, N. E., Kupka, F., & Weiss, W. W. 1997, *Baltic Astronomy*, 6, 244
- [43] Swamy, K. S. K., & Tarafdar, S. P. 1972, *A&A* , 18, 415
- [9] Grevesse, N., Scott, P., Asplund, M., & Sauval, A. J. 2014, arXiv:1405.0288
- [31] Scott, P., Asplund, M., Grevesse, N., Bergemann, M., & Sauval, A. J. 2014, arXiv:1405.0287
- [32] Scott, P., Grevesse, N., Asplund, M., et al. 2014, arXiv:1405.0279
- [47] Spitzer, L., Jr., & Morton, W. A. 1976, *ApJ* , 204, 731
- [48] Spitzer, L. 1976, *QJRAS* , 17, 97
- [49] Simón-Díaz, S., & Herrero, A. 2014, *A&A*, 562, A135
- [50] Schmidt, E. G. 1979, *aj*, 84, 1739
- [99] Piskunov, N. E., Kupka, F., Ryabchikova, T. A., Weiss, W. W., & Jeffery, C. S. 1995, *A&AS*, 112, 525
- [52] Upson, W. L., II, & Rogerson, J. B., Jr. 1980, *ApJS*, 42, 175
- [53] Vangioni-Flam, E., Cassé, M., & Audouze, J. 2000, *Phys. Rev. P* , 333, 365
- [39] Wade, G. A., Bagnulo, S., Kochukhov, O., et al. 2001, *A&A*, 374, 265
- [40] Wade, G. A., Folsom, C. P., Petit, P., et al. 2014, arXiv:1407.3991

Chapter 3

Ultraviolet Spectral Synthesis of HD72660

3.1 Introduction

The star HD 72660 (HR 3383, HIP 42028; A1 V) is a slowly rotating ($v \sin i = 6 \text{ km s}^{-1}$), relatively hot early Am-type star. For decades, the elemental abundance analysis of this target has been the subject of study. Earlier studies were carried out in the visible wavelengths [33, 34]. In more recent years, the UV spectrum has also been used on occasions to derive abundances [37].

These studies have reported a high abundance for heavy post-iron group elements such as Pt, Au, and Hg. However, a more complete table of abundances, covering all accessible elements from $Z = 6$ to $Z = 82$, is a worthwhile goal for this target. In this paper we study the high resolution ultraviolet spectra of HD 72660 covering two spectral windows between 1650-1999 Å and 2650-2900 Å, in order to obtain a complete abundance table. In addition we will investigate the efficiency and completeness of the line-list in the ultraviolet; (2) the accuracy of abundance measurements in the UV in comparison to available measurements based on visible spectra; (3) elements that have not been previously measured in the literature; (4) how well LTE synthesis works at this temperature in the UV.

This paper is organized as follows; in Section 3.2 we explain the details of data acquisition and reduction. In Section 3.3 we discuss the modeling methods and tools used in this work. Section 3.4 provides a comprehensive results and discussions for each individual element and also the “missing lines”. Finally, in Section 3.5, we compare our results to the literature and discuss their implications in the context of stellar evolution for HD 72660.

3.2 Observation and Data Reduction

In this paper, we have used the high resolution ultraviolet spectra obtained by Space Telescope Imaging Spectrograph (STIS) on board Hubble Space Telescope (HST).

STIS has two types of detector systems; CCDs and MAMAs. Despite the efficiency of CCDs in the optical and near IR, they face unsolved difficulties at UV wavelengths. In order to observe in the UV, we need filters to block the visible flux. However, the combination of CCDs and filters did not yield the desired efficiency. Instead, for a higher photon-count rate and better efficiency, CCDs have been replaced by MAMA (Multinode Microchannel Array)

detector technology. This kind of detector uses either CsI or Cs₂Te photocathodes, which reject visible photons. The wavelength range between 1650-3100 Å is covered by a Cs₂Te MAMA detector [see 38, and references therein, for details on the detector's function]

The spectral data used here contains two windows; The wavelength region between 1650-1999 Å was retrieved from the MAST archive and obtained with the STIS/NUV-MAMA instrument (ID : 9146, PI: Evans, Observation ID: O6G403010). The wavelength region between 2650-2900 Å was retrieved from the MAST archive and obtained with the same instrument (ID : 9455, PI: Peterson, Observation ID: O6LM51020). The resolving power of both these spectra is $R \approx 114,000$.

We normalized the spectrum by first specifying continuum points by means of a graphics cursor over intervals of ~ 20 Å, then fitting the continuum as the exponential of a cubic spline [order 2, see norm.pro taken from IDL library 20], and finally dividing the spectrum by our smooth fit.

The re-normalization process was iterated until the least mismatch between the observation and model was achieved (see section §3.3.2). This of course can give rise to a new source of uncertainty that will be addressed in section §3.3.3.

3.3 Methods

3.3.1 Line Broadening Mechanisms and Considerations

In order for the models to match the observation, we need first to consider line broadening effects. Microturbulence, macroturbulence, and rotational velocity, are three phenomena that can introduce broadening to the observed lines. In this section we discuss all three.

Microturbulence

The non-thermal component of the local gas velocity in the spectral line formation region of the stellar atmosphere is referred to as the microturbulent velocity and denoted with the symbol ξ [7]. Microturbulence has been referred to as a “fudge” factor many times and it has been suggested that the use of non-LTE in spectral analysis would eliminate the need for this phenomena. However, there are extensive studies in the literature showing that independent of the computation algorithm (LTE or non-LTE), a microturbulence term is present in the spectra of many kinds of stars [7, 26].

It is believed that the origin of the photospheric microturbulence in stars such as HD 72660 is the atmospheric and sub-surface convection. A convective region in the outer envelope of a hot intermediate-mass star is generated by the opacity peak (near the surface) of the He II to He III ionization zone [see 6, for more details]. In and immediately below the atmosphere, convection is due to the He I to He II and the H I to H II ionization zones.

Landstreet et al. [21] have carried out an extensive spectroscopic survey of B and A-type stars including HD76220. Through comparison of observed with model spectra, they have constrained the stellar parameters including the microturbulence. They find a microturbulence of $\xi \sim 2.3 \pm 0.3 \text{ km s}^{-1}$ for HD72660. We have included this result in our calculations.

Macroturbulence

The photospheric velocity fields that occur over longer scales compared to the mean free path of the photons are called macroturbulence. In the absence of this broadening mechanism the shape of spectral lines are roughly Gaussian, however, in presence of macroturbulence they can become more U-shaped, or triangular and asymmetric. The former occurs when rotational velocity dominates and the latter occurs when microturbulent broadening takes over. It has been proposed that macroturbulent broadening in hot stars may be the result of many low-amplitude pulsation modes [3]. In this work, we do not include macroturbulence since Landstreet et al. [21] argued that this star shows no significant trace of macroturbulence.

Rotational Velocity

The rotational velocity is the angular motion of the star around its own axis, which can result in spectral line broadening. The part of the stellar atmosphere that has a radial velocity component toward the observer ($v \sin i$) is blue-shifted and the part that is moving away from the observer is red-shifted. A recent high resolution spectroscopic survey of B and A-type stars reports a low $v \sin i$ value of $5.0 \pm 0.5 \text{ km s}^{-1}$ for this star Landstreet et al. [21].

3.3.2 Abundance Determination Method

Because the ultraviolet spectra region of intermediate temperature stars has very high line density, classical abundance analysis by modeling single unblended lines is of limited value. Spectrum synthesis provides a more powerful tool, both for identifying suitable lines for abundance determination and for optimizing the model of the observed spectrum for a best-fitting abundance table.

The observed UV spectra of HD72660 has been modeled using the FORTRAN spectrum synthesis program ZEEMAN.f [version zabn4.f, see 74, 23, 39, for detailed description]. This program was originally designed to model line profiles of magnetic stars, however it can be used for non-magnetic cases as well. Spectropolarimetric studies have classified Am stars as non-magnetic [35, 4]

Kurucz [71] developed the FORTRAN program ATLAS which can compute stellar atmospheres for a very wide range of parameters. Piskunov & Kupka [101] used this ATLAS with some experimental ODFs (opacity distribution functions) to compute a grid of model atmospheres for solar abundances. The Zeeman program uses this grid, and a set of atomic line data from the Vienna Atomic Line Database (VALD; Piskunov et al. [99], Ryabchikova et al. [104], Kupka et al. [70, 100])

As input parameters, the program requires the effective temperature (T_e), gravitational acceleration ($\log g$), approximate rotational velocity ($v \sin i$ and micro-turbulent (ξ) parameters, and individualized abundances, in order to compute the emergent atmospheric spectrum. Landstreet et al. [21] find the following stellar parameters for HD72660; $T = 9650 \pm 300 \text{ K}$, $\log g_f = 4.05 \pm 0.25$, $v \sin i = 5.0 \pm 0.5 \text{ km s}^{-1}$, $\xi = 2.3 \pm 0.3 \text{ km s}^{-1}$. We use these values as fixed input parameters to our synthesis program.

A major problem in making abundance analysis in crowded spectral windows is identifying lines or features that respond primarily to the abundance of a single element. ZEEMAN deals

with this problem by synthesizing two versions of a potentially useful window, one with the abundance of the element under study enhanced somewhat from the expected value, and a second with the desired element completely absent. Comparison of these two computations allows the program to identify wavelength regions that can safely be used to determine the abundance of the studied element, and later allow the user to visually see whether the identified regions are useful for abundance analysis, and to evaluate the quality of the final fit.

The program can automatically carry out an iterative process to adjust the abundance of any chosen element, until a least squares best fit is achieved with the automatically selected spectral features. The optimum results happen when lines are clean and unblended where a particular element can be adjusted without any contamination from other elements. However, good results can be achieved even with spectral lines that are weakly or partially blended with lines of other elements.

We used a spectral line list retrieved from VALD covering two wavelength windows; between 1628 to 1903 Å (sp170) and between 2100 to 2900 Å (sp285). We extracted the line data from the VALD database using the *Extract Stellar* option. Our search criteria included; detection threshold: 0.01(fraction, in the range 0-1), microturbulence: 2.3 km s⁻¹, T_{eff} : 9650 K, and log g : 4 (in cgs units). The request was submitted for the long extraction format (required by ZEEMAN), on November, 2014.

The process of abundance determination has several steps. At first we divide our full spectra into several wavelength windows for the purpose of running the program faster. The main challenge for every element is then to find a few specific lines that are sensitive to the abundance of that particular element alone. ZEEMAN determines the abundance of elements of interest one at a time. The program first tries to identify features that respond primarily to the abundance of the element being fit, then enters an iterative process over the abundance of that element until the best least square fit of the model spectrum to the particular features selected by the program is achieved.

In order to identify the relevant features of a certain element, the program computers the spectra once in complete absence of the element and once again including the element with an initial estimate of the abundance. In the next step, ZEEMAN selects individual wavelength windows for fitting that chosen element. This process is carried out based on simple criteria that can be manually altered by the user. For example one set of criteria could be to require that any blending feature (i.e. still present in the spectrum with the fitted element removed) is no deeper than 0.95 of the continuum, and that the depth of the feature with the desired element present is strong enough have a central depth at least 0.8 (where the continuum is at 1.0), or more than four times deeper than any weak blend. At the end of the iterations, the output of the program contains the best-fitting spectrum for that window, the χ^2/ν value and best abundance for each iteration, the original input spectrum, and a map of wavelengths used in the fit.

The results show that, in most cases, different wavelength window, results in a slightly different abundance for their best-fitting model spectrum. Through graphical visual examination of these windows, the user can select the best and most useful representative lines for each element. Once a few representative lines are selected, a smaller window surrounding them will be plotted including the observation and the model spectrum computed with the best-fitting abundance and the model in the absence of that element. This illustration technique is quite useful when studying crowded spectra and an example of this is shown in Figure 3.1.

We used the techniques explained above and find that a number of elements exhibit a few

apparently clean and unblended lines even in the very crowded spectrum of HD 72660. After identifying those lines, we used them to adjust the abundances of those elements (see §3.4). Table 3.2, which presents the abundance values (ion by ion) that are found to best fit the observed spectrum, includes the wavelengths that we found to be most useful.

In the UV spectrum of HD72660, some elements shows clean and unblended lines that are ideally suited for abundance determination. On the other hand, for some elements we only have lines that are slightly blended. The abundance determination is slightly more difficult in these cases since the overall shape of the line is influenced by more than one element. In these cases, a few more steps are required. We first iterated over the abundance of each element, assuming solar abundance for the rest in order to identify which wavelength window could best be used to adjust the abundance of that particular element. This first approximate model, gives us a first estimate of the abundance even though it is not the final result. Once the first iterations are carried out, we are left with an initial set of model parameters. Having selected the most useful window(s) for each element, we then keep re-iterating the abundances of both the element of interest and also the blending element(s) until we obtained the best possible global fit with the observation.

The computed model spectrum, using the final set of abundances, results in a reasonably good fit to the observed spectrum (see Appendix C), although it is quite clear that there are lines in the observed spectrum that have incorrect atomic data or are missing entirely from the VALD list. The missing lines will be discussed in section §3.4.33.

3.3.3 Sources of Uncertainty

There is an important source of error from the fact that stellar parameters are only known with a limited precision. The effective temperature used here is accurate within $\pm 3\%$ and the surface gravity $\log g$ is known to about ± 0.25 dex [see table 1 21]. We find that these two parameters together influence the abundance determinations by roughly ± 0.1 dex. The microturbulence ξ is also only accurate within 0.3 dex. We have chosen the strong resonance C I line at 1656.92 Å, and modeled it with ξ value 2.6 and 2.0. The influence of this uncertainty on the abundance determination is of the order of 0.08 dex.

An additional uncertainty is the re-normalization process described in section §3.2. As a result of the uncertain normalization process, different ionization stages of the same element can be modeled with slightly different abundances. We have evaluated this uncertainty for each element separately and listed them in Table 3.2.

A rather small uncertainty can be introduced from the fact that we did not correct for the background and scattered light. This uncertainty is only significant for lines that are deep enough in which case we attempted to model the (sometimes rather broad) damping wings rather than the core depth.

Another source of error can be introduced from the database itself. In the NIST database [10], the accuracy of the oscillator strength on some lines are estimated. For instance, the oscillator strengths of the C I resonance line (at 1657 Å) is “A”, which corresponds to an uncertainty of about $\pm 3\%$ or 0.01 dex). If the line in use does not have a very accurate oscillator strength, we will consider an error of this order. However exceptionally, in absence of information about the uncertainty in the $\log gf$ values, we assume an uncertainty of 0.30 dex.

The collective effects of all the above-mentioned sources will lead to an uncertainty of the order of ± 0.1 dex, on the derived (logarithmic) abundances. However, this is the least uncertainty and in many cases we should be able to estimate the abundance uncertainties of individual atoms by looking at the dispersion of results obtained from different multiplets. We find that the scatter is mostly of the same order of magnitude.

3.4 Summary of Individual Elements

The abundance for every element is separately presented with relevant details. We tried to include different ionization stages for every elements in order to reduce the effects of systematic errors. The final results are listed in Table 3.2. However, for the abundance determination, we tried to select lines from those ionization states that account for at least 10% of the total population of an element. In order to do this, we used the Saha equation to compute relative populations of different ions for temperature and electron density values appropriate to continuum optical depth (evaluated at 5000 \AA) of $\tau_{\text{cont}} \sim 0.2$ and ~ 0.001 . The results are listed in Table 3.3. Those states of ionization that are less populated are usually more sensitive to non-LTE effects. This will appear as discrepancies between the abundances that would best fit different ionization states of the same element. In section 3.5, we will compare our results to the literature values and we will put them in the context of stellar evolution.

Iron provides strong line opacity over the entire wavelength range presented in this work. It is safe to assume that most of the lines of other elements are at least slightly blended with iron. Therefore, we determined the abundance of iron prior to other elements (see section §3.4.15). However, the following sections are presented in ascending order of atomic number.

3.4.1 Carbon, $Z=6$

In the subset of the VALD list selected here, there are overall 15, C I lines and 19, C II lines. However, none of C II lines and only 10 of C I lines have a depth that is equal or deeper than 0.8 of the continuum (they reach a depth at which the central intensity is no more than 0.2 in units in which the continuum is at 1.0). In the spectrum of HD 72660 such strong lines are almost always recognizable, unless they are strongly blended. In the spectrum of HD72660, carbon is mostly observed in the form of C I with a few C II lines. The measurements from the Saha equation shows that the dominant state of ionization at this temperature is C II with a small contribution from C I lines (see Table 3.3). However, the lack of strong lines of C II is mostly due to the fact that the excited states are $\sim 20 \text{ eV}$ above the ground state.

We have used a cluster of strong C I lines between $1656\text{--}58 \text{ \AA}$ to determine the abundance of this element. These lines are suitable for this purpose because of their low excitation energy ($\sim 0.005 \text{ eV}$) and “A” $\log gf$ values of ~ -0.5 . Our models result in the abundance of $\log n_{\text{C}}/n_{\text{H}} = -4.1$. We have used the following line to re-confirm this value; The C I UV multiplet (62) at 1751 \AA . The absence of strong C II lines from our list as well as lack of dispersion among the existing lines made it challenging for us to estimate the uncertainty. The oscillator strength value is accurate within 0.03 dex according to NIST which together with the inaccuracies discussed in section 3.3.3, will correspond to 0.1 dex uncertainty for this value. Figure 3.1 shows the observation and models for this element using the estimated abundance.

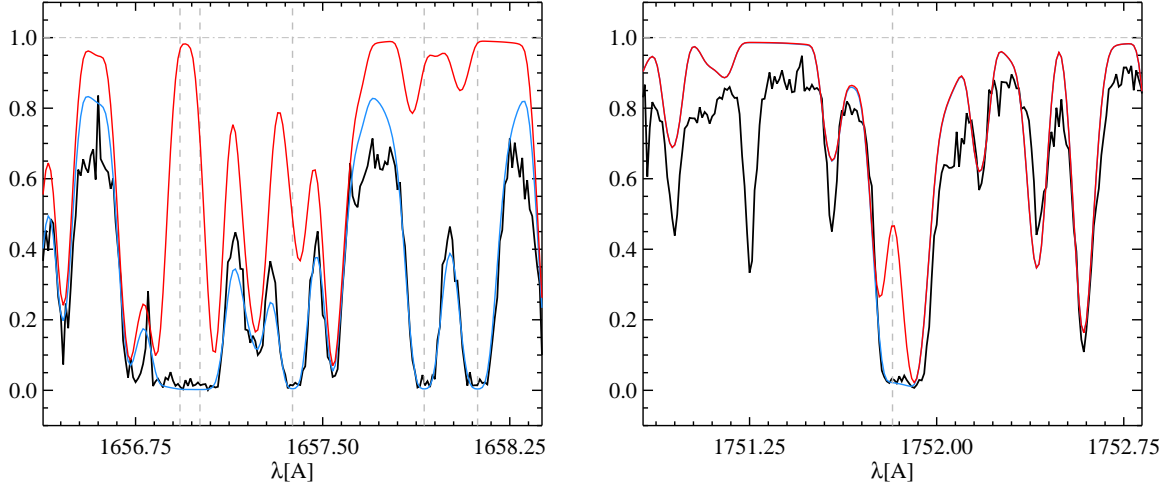


Figure 3.1: This figure shows the observation (in black), calculated model with $\log(n_{\text{C}}/n_{\text{H}}) = -4.10 \pm 0.10$ (in blue) and without carbon (in red). *Left:* a cluster of C I lines; Strong resonance line at 1656.928 Å, a doublet at 1657.379, 1657.907 Å, a doublet at 1657.008, 1658.121 Å. *Right:* A strong UV multiplet (62) at 1751.823 Å.

3.4.2 Nitrogen, $Z=7$

In our selection of VALD list, there are 4 N I lines and 6 N II lines. None of the N II lines but all 4 N I lines have a depth that is equal or deeper than 0.8 of the continuum. The Saha equation, predicts the dominant state of ionization, at this temperature to be N I with no contribution from N III lines (see Table 3.3). The fact that all of the N I lines are strong is consistent with the results of the Saha equation. The reason N II lines are scarce in this wavelength window is because they arise from high excited states of ~ 13 eV.

The strength of N II lines were too weak for us to be able to use them as tools of abundance determination. We only used a pair of strong N I UV multiplets (9) in a window between 1742-45 Å. Despite their strength, these lines are heavily blended with very strong Fe II lines between 1742-45 Å window. They arise from low lying energy levels (~ 3 eV) and they have “B” $\log gf$ values of -1 , thus they still suitable for our purpose.

Due to lack of blend-free lines, we could not determine the abundance of this element or the corresponding uncertainty. Instead, we present an upper limit of $\log(n_{\text{N}}/n_{\text{H}}) = -4.7$ for this element with an uncertainty of 0.3 dex (see §3.3.3). Figure 3.2 shows the observed lines and the best-fitting model using the given abundance. The right panel in this figure clearly shows that this value is an upper limit for nitrogen.

3.4.3 Oxygen, $Z=8$

In the wavelength windows we selected, there are only two relatively weak O I lines, which have a depth that is 0.33 and 0.03 of the continuum. The dominant ionization state is predicted by the Saha equation to be O I, at this temperature in the line forming region of the atmosphere (see Table 3.3). This is consistent with our line list however, the apparent lack of oxygen lines is mostly due to the fact that majority of oxygen lines, O I or O II lines arise from high excited

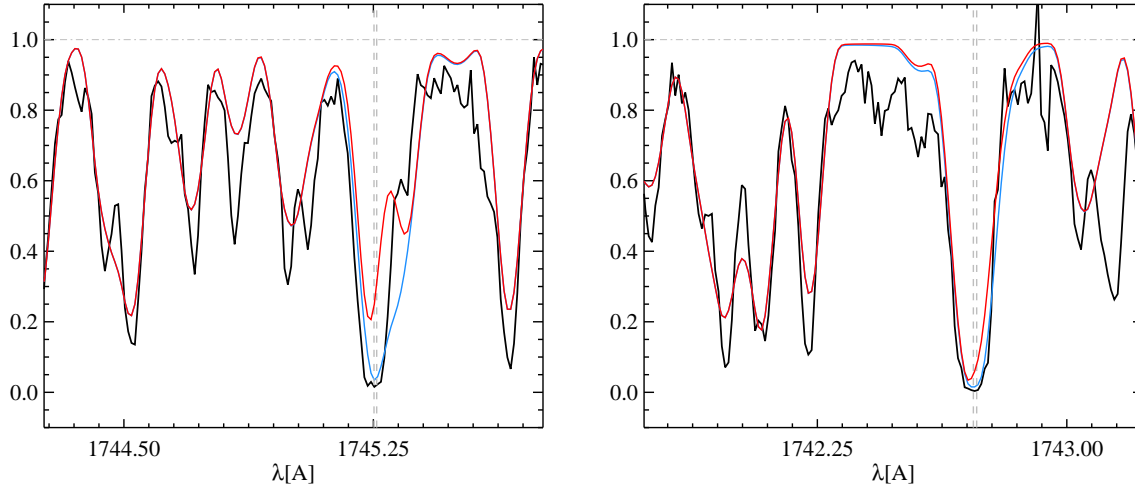


Figure 3.2: This figure shows the observation (in black), calculated model with $\log(n_{\text{N}}/n_{\text{H}}) = -4.7 \pm 0.3$ (in blue) and without nitrogen (in red). *Left:* Strong N I UV multiplet (9) at 1745.252, 1745.260 Å, *Right:* strong N I UV multiplet (9) at 1742.729, 1742.719 Å. This panel clearly shows that this value is an upper limit.

energy levels of roughly 10, and 22 eV.

The two available oxygen lines at 1641 and 1868 Å window, were not only weak but also heavily blended which made it rather challenging to model them. Due to lack of blend-free lines we could not determine an abundance for this element, however we can present an upper limit of $\log(n_{\text{O}}/n_{\text{H}}) = -2.5$. The normalization error on this value could not be measured due to lack of enough clean and unblended lines, also there is not enough information provided about the uncertainty on the oscillator strength value, thus the error on this value is 0.3 dex (see §3.3.3). Figure 3.3 show the resulting observation and models.

3.4.4 Magnesium, Z=12

In our selection of VALD list we have overall 318, Mg I lines and 28 Mg II lines. Among all of these lines, only 4 of Mg I lines and 10 of Mg II lines have a depth that is equal to or deeper than 0.8 of the continuum. The Saha equation, predicts the dominant state of ionization, at this temperature, to be Mg II with a small contribution from Mg III lines (see Table 3.3). However, in the line list used here, most of our lines are in the Mg I state and there is a shortage of lines of the two expected dominant ionization states. In the case of Mg II, most lines arise from a very high excited energy state of roughly 53 eV. There is no Mg III transition in our wavelength window because all the lines in this range arise from an excited state of at least 58 eV.

We have used the strong and unblended Mg I resonance line at 1827 Å, with a “B” $\log gf$ of -1.6 and found the abundance of $\log(n_{\text{Mg}}/n_{\text{H}}) = -4.2$. We confirmed this value by also modeling the following; A strong resonance UV multiplet (1) of Mg I around 2852 Å, and the strong resonance UV multiplet (1) of Mg II around 2795 and 2802 Å. We find the uncertainty of ± 0.22 using the Mg II lines taking into account the uncertainties discussed in section 3.3.3. Figure 3.4 shows the fit to the observed profile at these wavelengths.

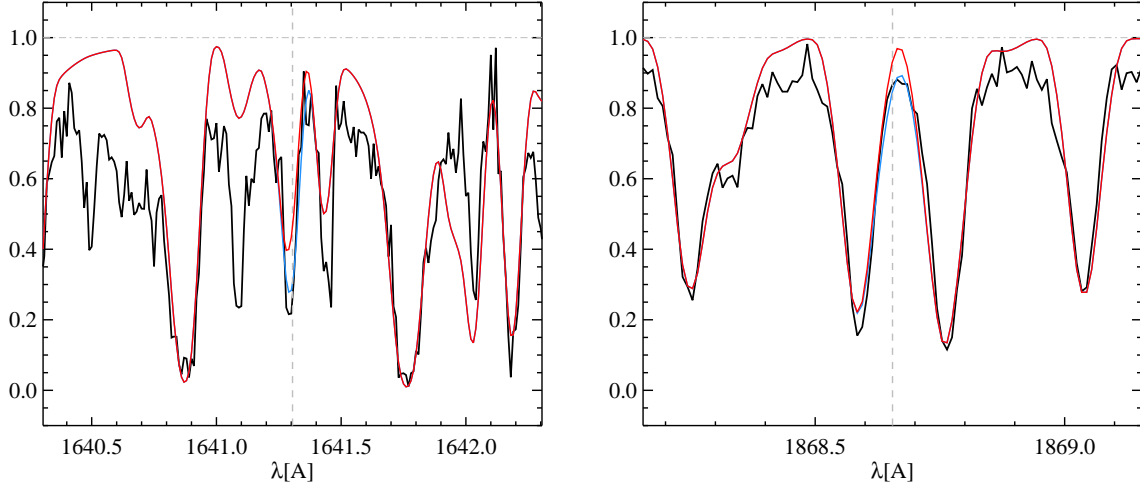


Figure 3.3: This figure shows the observation (in black), calculated model with $\log(n_{\text{O}}/n_{\text{H}}) = -2.5 \pm 0.3$ (in blue) and without Oxygen (in red). *Left:* Relatively weak and blended O I line at 1641.305 Å *Right:* Weak O I line at 1868.655 Å

3.4.5 Aluminum, $Z=13$

The subset of VALD linelist selected here contains 59 Al I lines, 63 Al II lines, and 2 Al III lines in total. However, there are only 2 Al I lines, 16 Al II lines, 2 Al III lines have a depth that is equal or greater than 0.8 of continuum. The Saha equation predicts the dominant ionization ratio to be Al II with a much smaller contribution from Al I and Al III and no contribution from Al IV (see Table 3.3). This distribution seems consistent with our current line list.

We have modeled a clean and strong Al II UV multiplet (6) at 1719.442 Å to determine the abundance and we find $\log(n_{\text{Al}}/n_{\text{H}}) = -4.9$ for aluminum. This line is at a relatively low excited state (~ 4 eV) with an “A” $\log gf$ value of -0.06 . We also confirmed this value using a very strong Al II resonance line in the 1670 Å window and also a fairly unblended strong Al I doublet at 1766-69 Å window. We can estimate the uncertainty from the dispersion in the values that best fit the available lines which in this case is of the order of 0.31 dex. Figure 3.5 show the observation and best-fitting models using this abundance.

3.4.6 Silicon, $Z=14$

In the selected line list here, there are overall 185 Si I lines, 81 Si II, and 6 Si III lines. Among these lines, there are only 93 Si I lines, 7 Si II and no Si III lines with depth equal or greater than 0.8 of the continuum. The results of Saha equation, presented in Table 3.3, predict that at this temperature, the dominant ionization stage belong to Si II. This is not reflected in our line list because most Si II lines arise from higher excitation energies (~ 6 eV).

Nevertheless, we have modeled the strong and unblended Si II UV multiplet (1) between 1808-17 Å window and determined the abundance of $\log(n_{\text{Si}}/n_{\text{H}}) = -4.20$. Note that this line is a resonance line with a “C” $\log gf$ of roughly -2 . We confirmed this abundance using a strong Si I UV multiplet (75) in the window 1770-1853 Å. Modeling lines in different ionization states while taking into account the uncertainties discussed in section 3.3.3 yields an overall

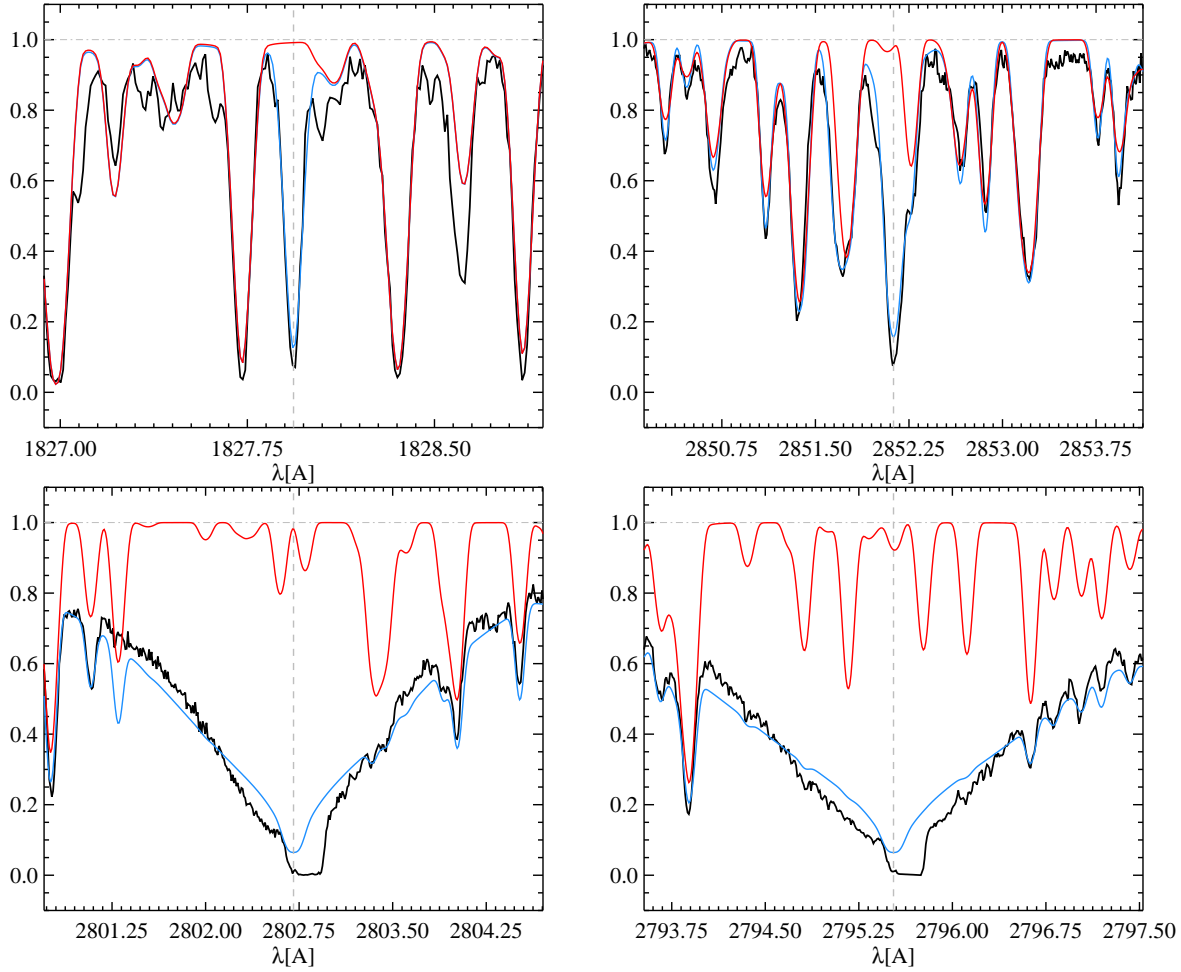


Figure 3.4: This figure shows the observation (in black), calculated model with $\log(n_{\text{Mg}}/n_{\text{H}}) = -4.20 \pm 0.22$ (in blue) and without magnesium (in red). *Top left:* Clean and unblended Mg I resonance line at 1827.935 Å, *Top right:* strong resonance UV multiplet (1) of Mg I at 2852.126 Å, *Bottom:* A strong resonance UV multiplet (1) of Mg II at 2802.705 Å (*left*) and 2795.528 Å (*right*)

uncertainty of 0.18 dex for this value. Figure 3.6 show the observation and best-fitting models.

3.4.7 Phosphorus, Z=15

In our selection of the VALD list, there are 66 P I, 6 P II lines overall. Among them, there are only 14 P I lines and no P II lines that have depth that is equal or greater than 0.8 of the continuum. The region of the stellar atmosphere where the core of strong lines are formed, with the effective temperature of HD72660, should be dominated by P II with minor contribution from P I. This results from the Saha equation (see Table 3.3). According to NIST, in the wavelength window studied here ($\sim 1600\text{--}1900$) there are no P II lines, which might be a deficiency in NIST database. Nonetheless, a few lines of P II that appear in VALD database have a very high excitation energy (~ 10 eV).

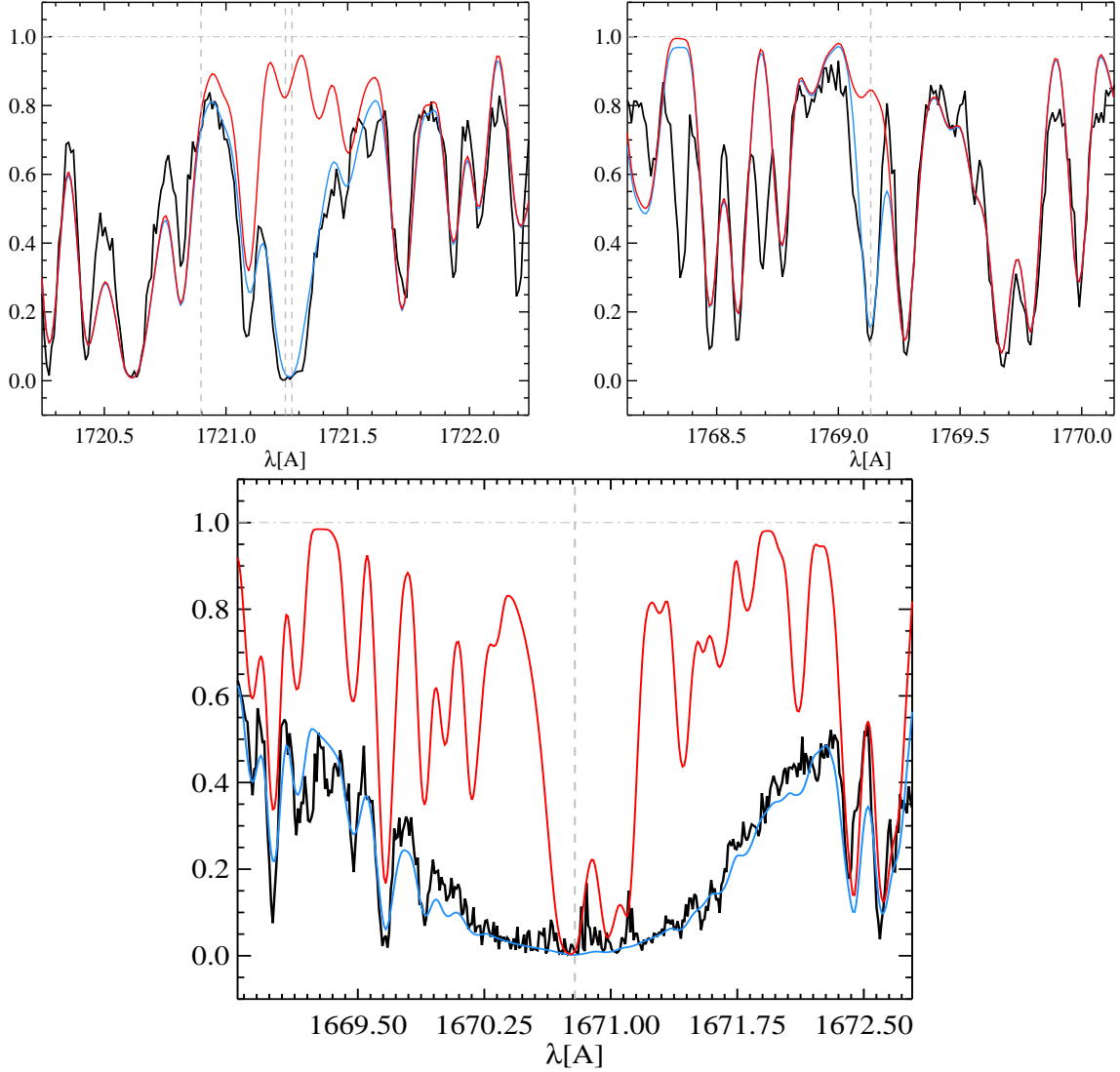


Figure 3.5: This figure shows the observation (in black), calculated model with $\log(n_{\text{Al}}/n_{\text{H}}) = -4.9 \pm 0.31$ (in blue) and without aluminum (in red). *Top left*: clean and strong Al II UV multiplet (6) at 1719.442, 1721.244, 1721.271 Å, *Top right*: An unblended strong Al I doublet at 1766.381, 1769.133 Å, which is only partly shown due to the large gap in wavelengths. *Bottom*: The strong resonance Al II line at 1670.787 Å.

We modeled the strong unblended P I UV multiplet (1) around 1774-87 Å window and we found the abundance of $\log(n_{\text{P}}/n_{\text{H}}) = -7.10$ for phosphorus. This is a suitable choice since they are resonance lines with “C” $\log gf$ of roughly -0.2 . In order to confirm this value we used the following: a strong P I UV multiplet (4) at 2135 Å, and a strong P I UV multiplet (5) at 1858 Å. From the dispersion in four values that fit the strong P I lines shown in Figure 3.7, we found an overall uncertainty of the order of 0.11 dex (see §3.3.3). Figure 3.7 shows the observation and models.

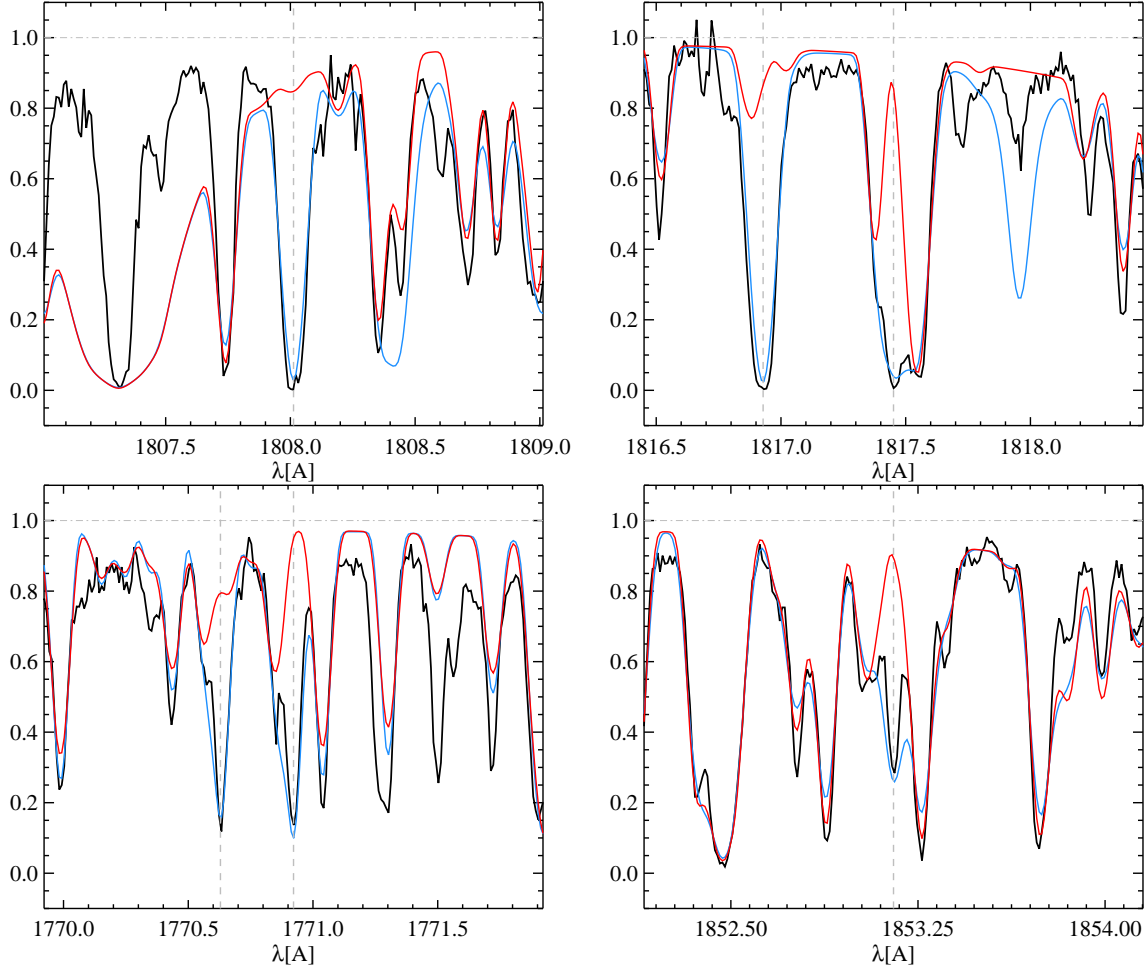


Figure 3.6: This figure shows the observation (in black), the calculated model with $\log(n_{\text{Si}}/n_{\text{H}}) = -4.20 \pm 0.18$ (in blue), and without silicon (in red). *Top* : An unblended UV multiplet (1) of Si II at 1808.012 Å (*Left*), and 1816.928, 1817.451 Å (*Right*) but we have shown this multiplet in two plots, due to the long wavelength gap. *Bottom* : A strong UV multiplet (75) at 1770.629 Å (*Left*) and 1853.152 Å (*Right*), Note that we only chose two out of several lines in this multiplet for illustration.

3.4.8 Sulfur, $Z=16$

In our selection of VALD database, there are 18 S I lines, and 4 S II lines. However, only 7 S I lines and 2 S II lines have a depth that is equal or greater than 0.8 of the continuum and can be detected easily by eye. The Saha equation predicts that, at this effective temperature, S II is the dominant state of ionization with minor contribution from S I (see Table 3.3). This is not reflected in what appears in our VALD database mostly because in the wavelength window studied here, the majority of the S II lines have excitation energies as high as at least ~ 12 eV.

We modeled the strong unblended resonance S I UV multiplet (2) around 1820 Å and found the value of $\log(n_{\text{S}}/n_{\text{H}}) = -4.5$. This resonance line has an excitation energy of ~ 0.05 eV and a “C+” $\log gf$ of -0.5 which makes it a suitable choice for our purpose. This abundance value

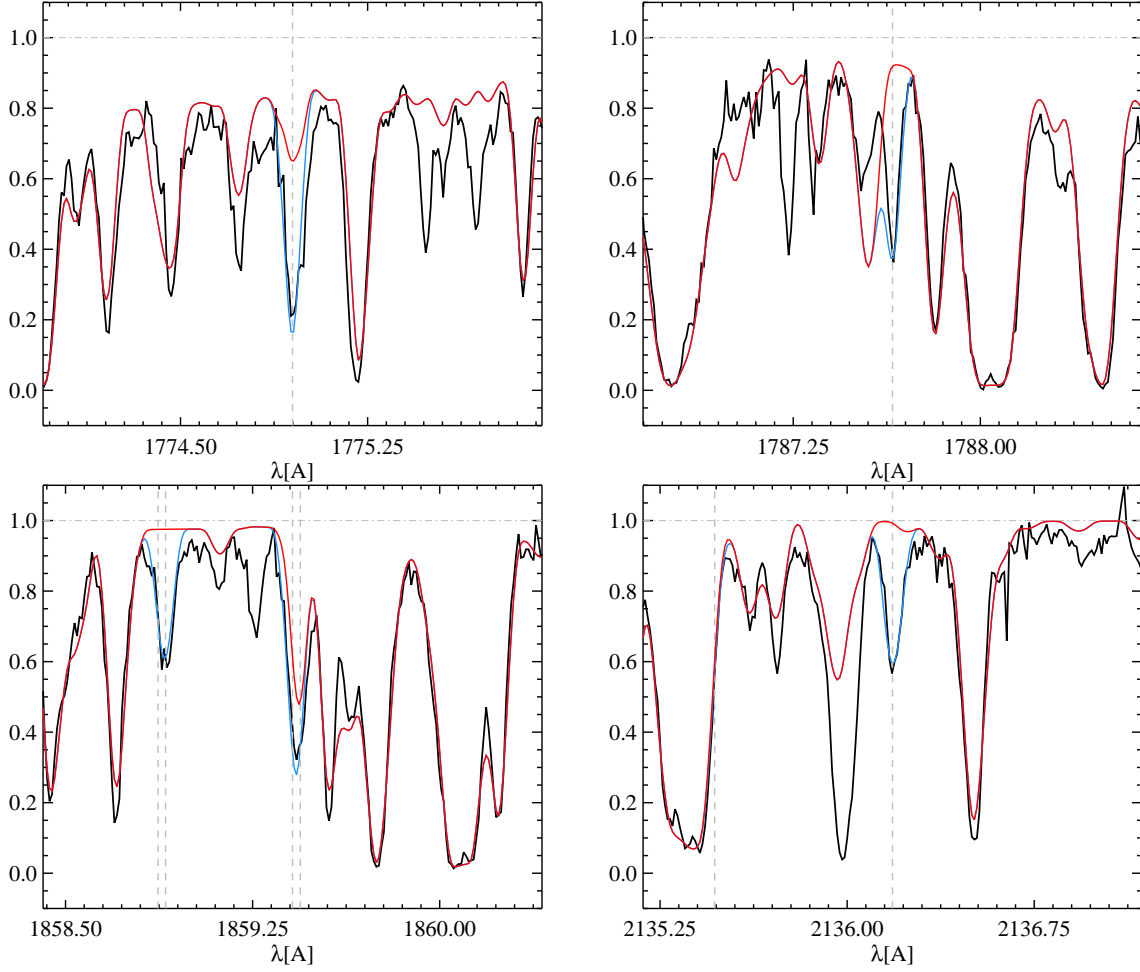


Figure 3.7: This figure shows the observation (in black), the calculated model with $\log(n_P/n_H) = -7.10 \pm 0.11$ (in blue), and without phosphorus (in red). *Top:* A strong unblended P I UV multiplet (1) at 1774.949 (*Left*), 1782.829, and 1787.647 Å (*Right*), but we have only shown the first and last here. *Bottom left:* A strong P I UV multiplet (5) at 1858.871, 1859.401 Å, *Bottom right:* A strong P I UV multiplet (4) at 2135.469, 2136.182, 2149.142 Å.

results in a very good fit for other unblended S I lines such as UV multiplet (1) at 1900 Å. However, none of the S II lines in the current linelist produced a good fit with this abundance. We have shown the S II line at 1824.024 Å as an example of this clear dispersion. This may be due to inaccurate determination of the oscillator strength of these lines but revisiting the database is beyond the scope of this work. The overall uncertainty is very high and of the order of 0.98 dex. Figure 3.8 shows the models and the observation.

3.4.9 Calcium, Z=20

In the selected linelist here, there are 6 Ca I lines and 28 Ca II lines. There are 21 Ca II and no Ca I lines that have a depth equal or greater than 0.8 of the continuum. There are no Ca III lines

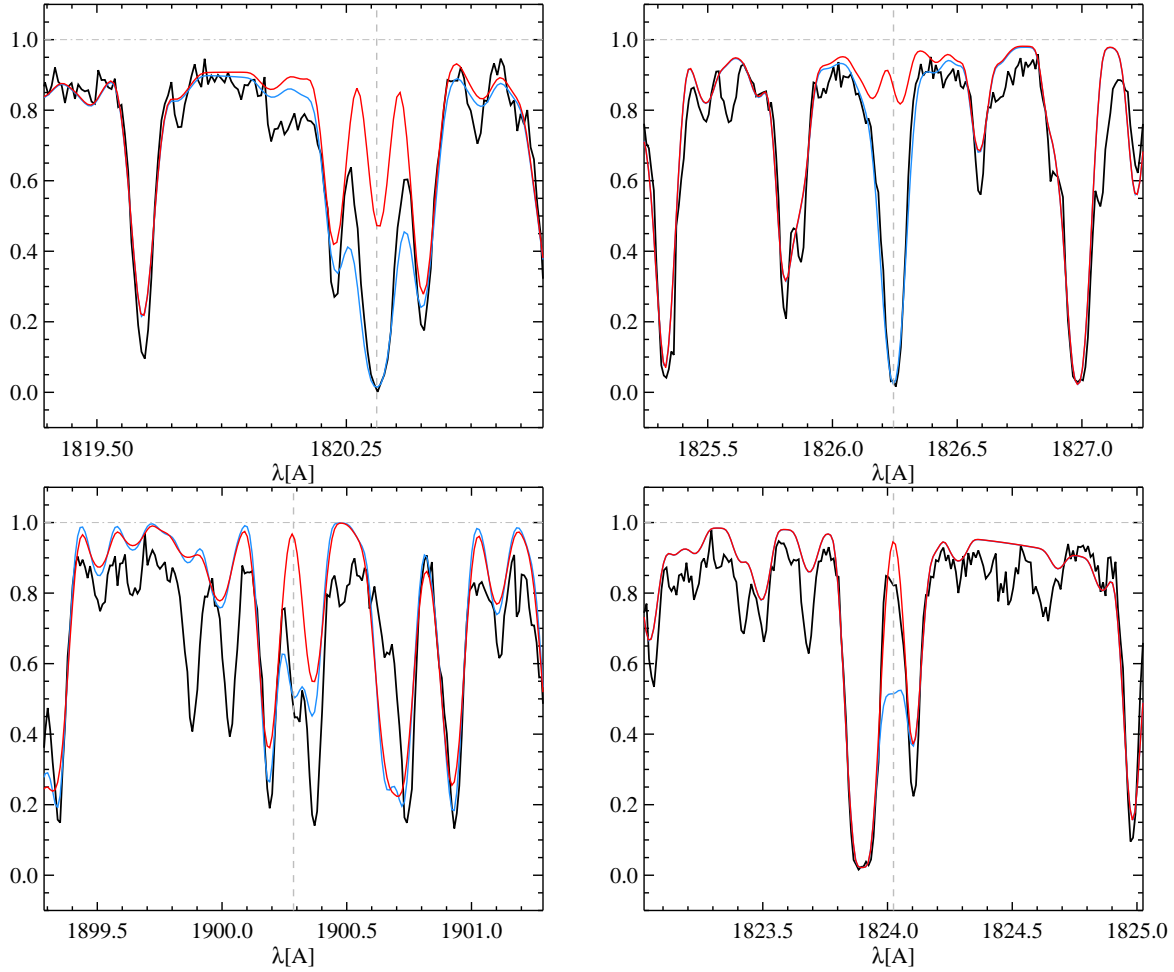


Figure 3.8: This figure shows the observation (in black), the calculated model with $\log(n_S/n_H) = -4.50 \pm 0.98$ (in blue), and without sulfur (in red). *Top:* S I UV multiplet (2) at 1807.311, 1820.341 (Left), and 1826.244 Å (Right), *Bottom left:* UV multiplet (1) at 1900.286 Å, *Bottom right:* A relatively strong S II line at 1824.024 Å.

in our line list at this temperature, despite the fact that the Saha equation predicts it to be the dominant state of ionization in the line forming region of the atmosphere (see Table 3.3). The second most important state of ionization is Ca II which is consistent with our database, but the absence of Ca III occurs because the majority of these lines arise from relatively high energy levels (~ 28 eV).

In order to determine the abundance of this element, we modeled the Ca II UV multiplet (11) at 1814 Å and found $\log(n_{Ca}/n_H) = -5.4$ for this element. These lines all arise from low lying energy levels (~ 3 eV) and have “C” $\log gf$ of roughly -1 . However, the best-fitting models for several different Ca II lines result in slightly different abundances. Using this dispersion together with the uncertainties discussed in section 3.3.3, the overall error for this value is of the order of 0.26 dex. For better illustration, we modeled a few other Ca II lines: UV multiplet (4) at 1838 Å, UV multiplet (3) at 2131 Å, A UV multiplet (9) at 2197 Å. Figure 3.9 shows the model and the observation.

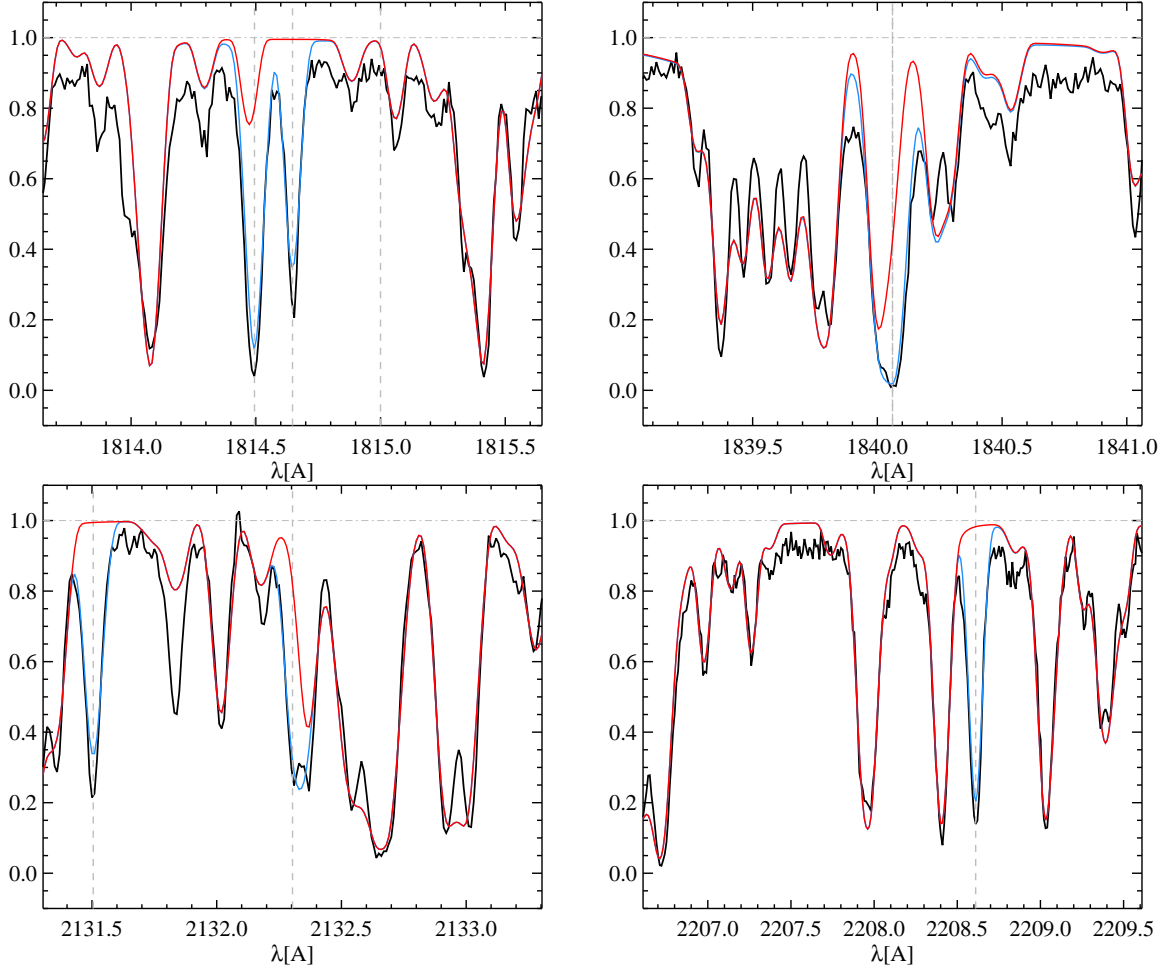


Figure 3.9: This figure shows the observation (in black), the calculated model with $\log(n_{\text{Ca}}/n_{\text{H}}) = -5.40 \pm 0.26$ (in blue), and without calcium (in red). *Top Left:* Ca II UV multiplet (11) at 1807.337 to 1814.647 Å, *Top Right:* A UV multiplet (4) at 1838.008 to 1840.060 Å, *Bottom left:* A UV multiplet (3) at 2128.750 to 2132.304 Å, *Bottom right:* A UV multiplet (9) at 2197.786 to 2208.610 Å.

3.4.10 Scandium, Z=21

In the linelist selected here, there are only 18 Sc II lines, of which none are deeper than 0.8 of the continuum. The Saha equation predicts Sc II to be the dominant ionization state which is consistent with our database. However, the results of the Saha equation also shows that Sc III should have almost half as much population as Sc II but it is completely absent from the linelist. None of the available lines are blend-free and strong enough for proper abundance determination of this element. However, we could find an upper limit of $\log(n_{\text{Sc}}/n_{\text{H}}) = -9.50$ for this element using the UV multiplet (1) at 2552 and 2563 Å. The two lines and best-fitting models are shown in Figure 3.10. Since there is not enough information provided about the uncertainty on the oscillator strength value for the lines we used here, we can assume the uncertainty on the upper limit we find to be of the order of 0.3 dex (see §3.3.3).

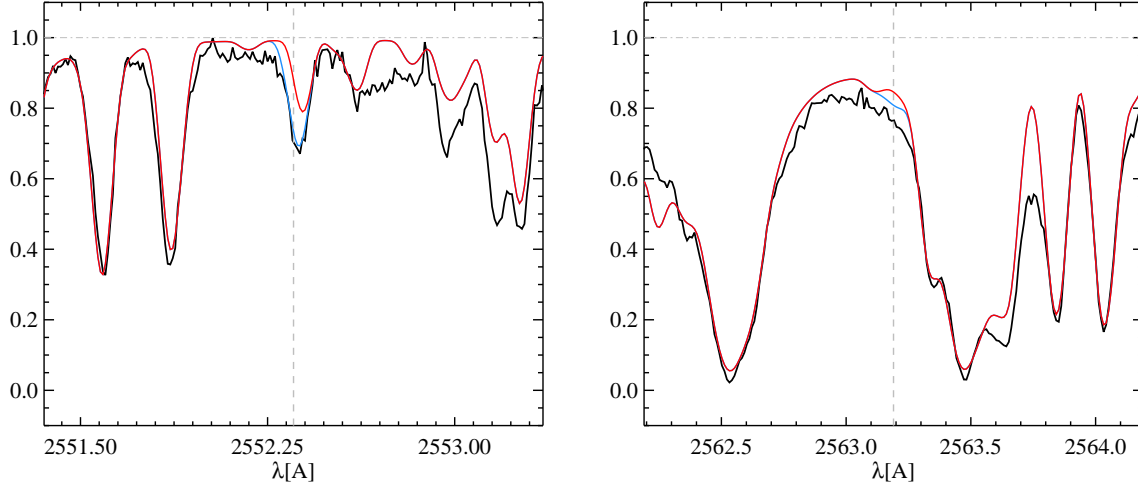


Figure 3.10: This figure shows the observation (in black), the calculated model with $\log(n_{\text{Sc}}/n_{\text{H}}) = -9.50 \pm 0.30$ (in blue), and without scandium (in red). UV multiplet (1) at 2552.354 Å (*Left*) and 2563.189 Å (*Right*).

3.4.11 Titanium, $Z=22$

In the subset of the VALD database used here, there are 465 Ti II lines and 25 Ti III lines. There are no Ti III lines and 21 Ti II lines that have a depth equal or greater than 0.8 of the continuum. According to the Saha equation, Ti II should be the dominant state of ionization at this temperature (see Table 3.3). This is somewhat consistent with our database, however, the Saha equation also predicts a small contribution from Ti III ionization state but our database has no representatives of this state, mostly because the majority of Ti III lines arise from high excitation energy levels (~ 9 eV).

In order to estimate the abundance for this element we modeled Ti II UV multiplet (16) at 2862 Å and found $\log(n_{\text{Ti}}/n_{\text{H}}) = -6.60$. This line arises from a low lying energy level of ~ 1 eV and a “B+” $\log gf$ of roughly -0.5 and it is suitable for our purpose. There is a slight difference between the abundances that result in the best fit among Ti II lines shown in Figure 3.11. This dispersion together with the uncertainties described in section 3.3.3 yields an error of the order of 0.18 dex. We also illustrated the modeled spectrum using the following; UV multiplet (16) at 2851 Å, and UV multiplet (14) at 2877 Å, and a triplet in between 1642 Å to 1830 Å window.

3.4.12 Vanadium, $Z=23$

In our subset of VALD database, there are 446 V II and 16 V III lines overall. Among them, there are no V III lines and only 7 V II lines that have a depth equal or greater than 0.8 of the continuum. The Saha equation predictions shows that V II is the dominant ionization state at this temperature. The database reflects this results.

We determined the abundance of vanadium using the V II UV multiplet (12) at 2880 Å and found $\log(n_{\text{V}}/n_{\text{H}}) = -7.2$. This is a resonance line (~ 0.3 eV) with a “B” $\log gf$ value of approximately -1.0 . As shown in Figure 3.12, V II lines are best fit with slightly different

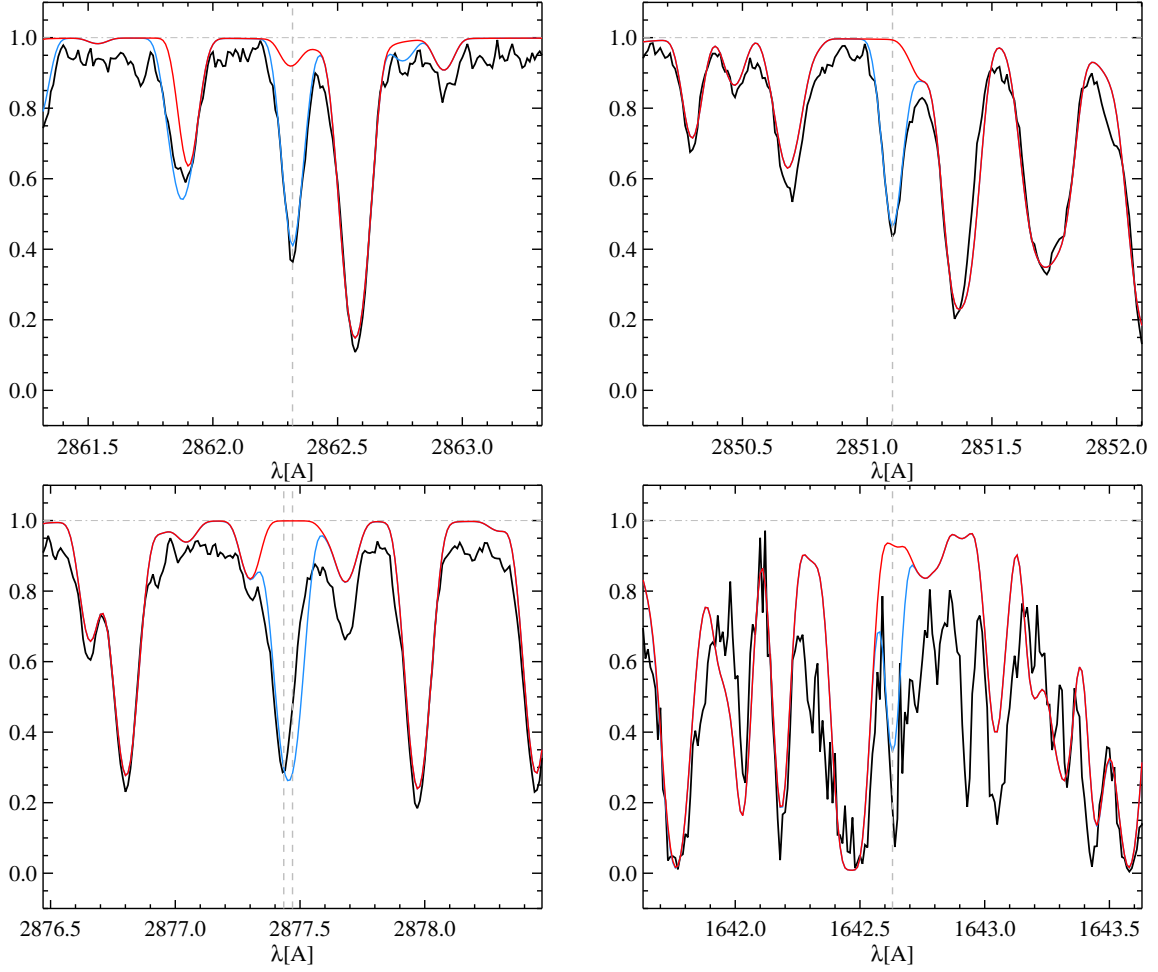


Figure 3.11: This figure shows the observation (in black), the calculated model with $\log(n_{\text{Ti}}/n_{\text{H}}) = -6.60 \pm 0.18$ (in blue), and without titanium (in red). *Top:* Ti II UV multiplet (16) at 2862.319 Å (*left*), and 2851.101 Å (*Right*), *Bottom left:* A UV multiplet (14) at 2877.434 Å, *Bottom right:* triplet of Ti II at 1642.630, 1650.623, 1830.463 Å.

abundances. From this dispersion together with the uncertainties discussed in section 3.3.3, we estimated an overall error of 0.26 dex. For better illustration we also modeled a V II UV multiplet (18) in 1636 Å to 1643 Å window. Figure 3.12 shows the observations and modeled lines.

3.4.13 Chromium, $Z=24$

In the subset of VALD database used here, there are overall 38 Cr I, 2140 Cr II lines and 87 Cr III lines. Among these, there are no Cr I or Cr III lines, and only 106 Cr II lines that have a depth which is equal or greater than 0.8 of the continuum. This is reflected in the results of the Saha equation which predicts that at this temperature, Cr II is the dominant state of ionization.

To determine the abundance, we modeled one of the Cr II multiplets at 1718 Å and found $\log(n_{\text{Cr}}/n_{\text{H}}) = -5.65$. This line arises from a relatively low lying energy state (~ 4 eV) and has

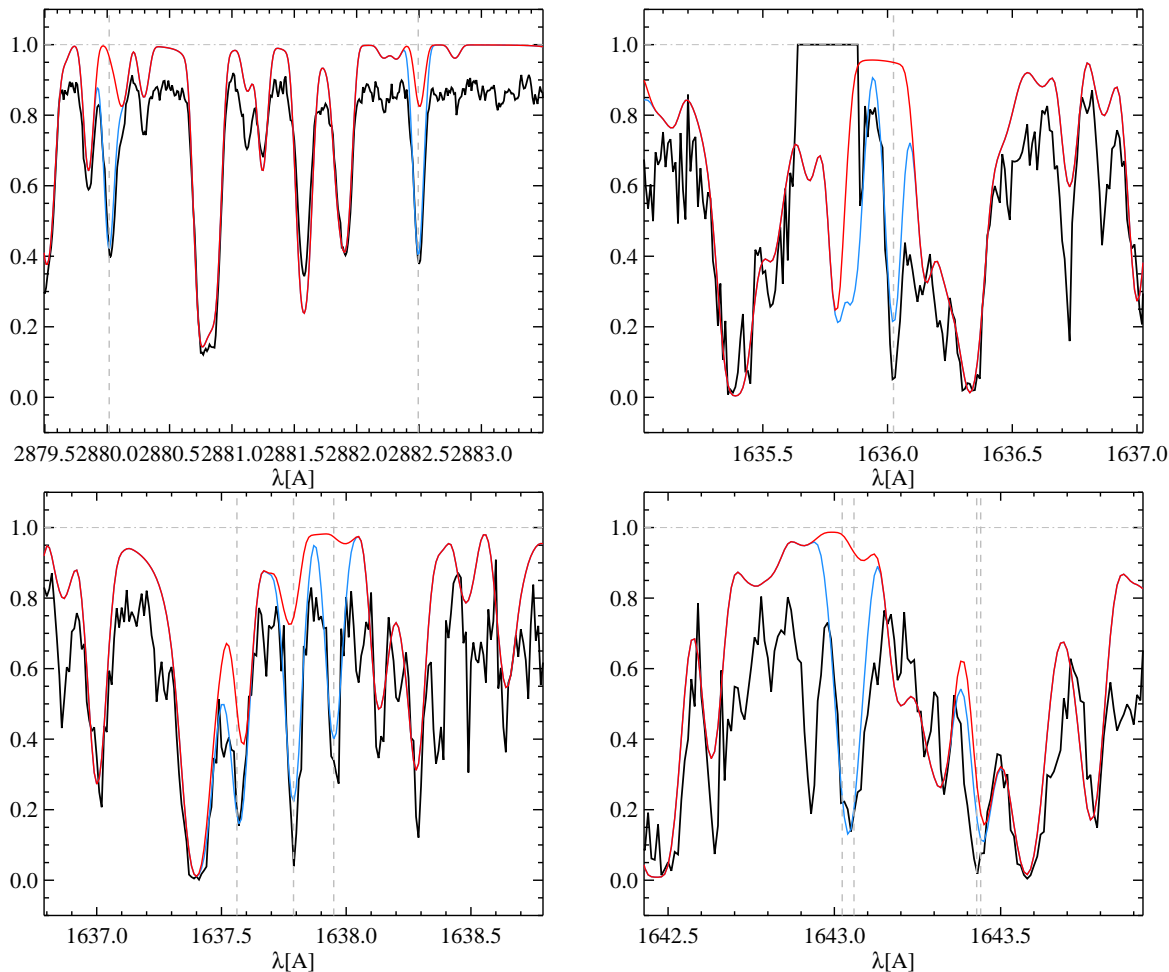


Figure 3.12: This figure shows the observation (in black), calculated model with $\log(n_V/n_H) = -7.2 \pm 0.26$ (in blue) and without vanadium (in red). *Top left:* V II UV multiplet (12) at 2880.016, 2882.494 Å, *Top right:* UV multiplet (18) at 1636.023 Å, *Bottom:* UV multiplet (18) at 1637.562 Å (*Left*), 1643.059 Å (*Right*).

an oscillator strength of roughly -0.5 , the accuracy of which is not specified by NIST.

Due to absence of strong and blend-free chromium lines in other states of ionization, we could not determine whether there is a dispersion in between the best-fitting abundance values for different ionization states. However, we modeled a few other Cr II lines for the purpose of confirmation and better illustration (see Figure 3.13), and we find that the abundance that results in the best-fitting model in each one of these lines is slightly different. The overall uncertainty of this value, including the uncertainties discussed in section 3.3.3, is of the order of 0.31 dex. In Figure 3.13 we have shown the model and observation for a few other lines: a part of a Cr II UV multiplet in between 2858–62 Å window, a small window of a Cr II UV multiplet at 1898 Å, together with a rather weak but unblended Cr II line at 1899 Å, and also a small window of another UV multiplet around 1732 Å.

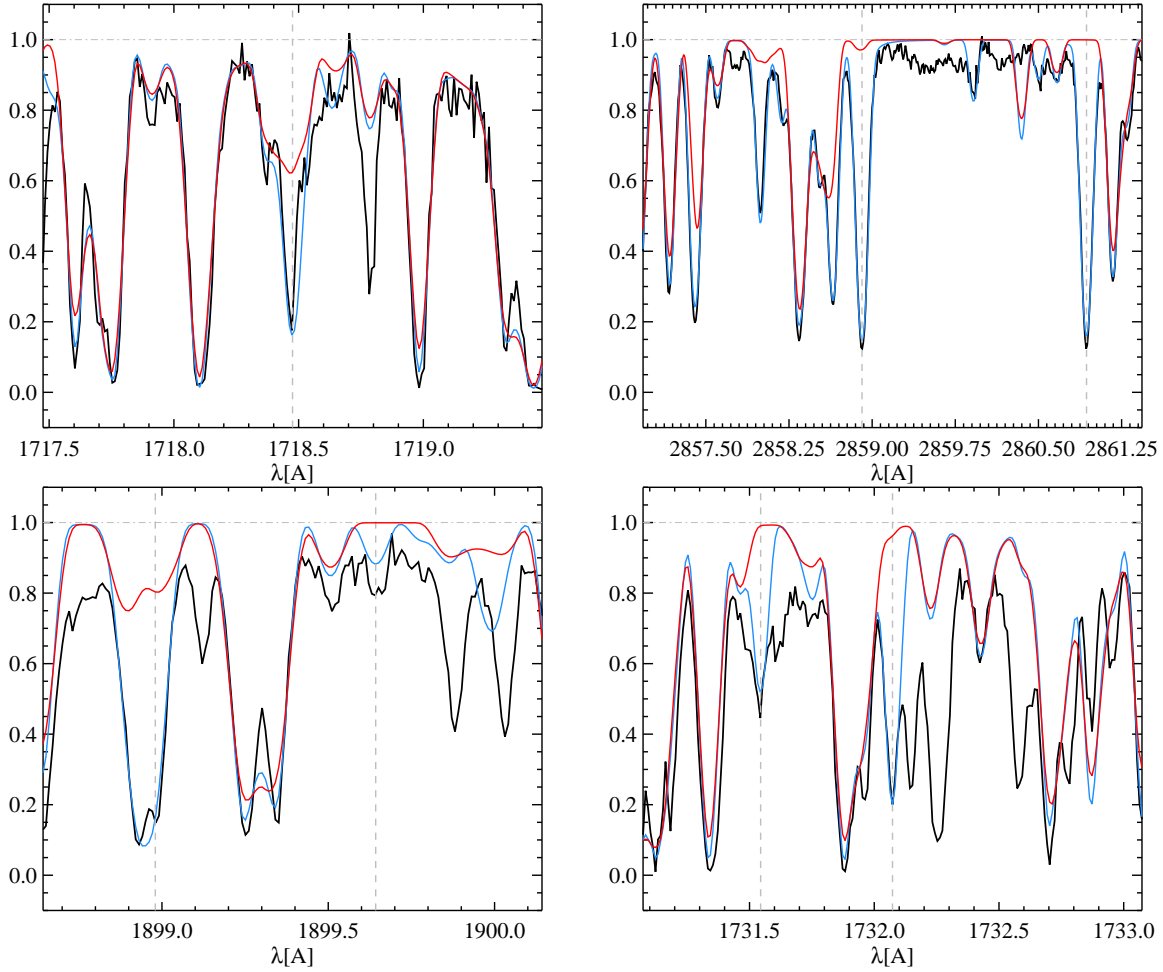


Figure 3.13: This figure shows the observation (in black), calculated model with $\log(n_{\text{Cr}}/n_{\text{H}}) = -5.65 \pm 0.31$ (in blue) and without chromium (in red). *Top left:* A part of a Cr II multiplet at 1718.475 Å, *Top right:* A small part of a Cr II UV multiplet at 2860.933, 2862.570, 2858.908 Å, *Bottom left:* Cr II UV multiplet at 1898.980 Å, together with a rather weak but unblended Cr II line at 1899.642 Å, *Bottom right:* A part of another UV multiplet at 1732.073 Å.

3.4.14 Manganese, $Z=25$

In the database selected here, there are 27 Mn I lines, 1550 Mn II lines, and 3 Mn III lines. Among these, there are no Mn I or Mn III lines and 62 Mn II lines that have depth that is equal or greater than 0.8 of the continuum. The fact that Mn II is the dominant ionization state in our linelist is consistent with the prediction of the Saha equation shown in Table 3.3.

We modeled a part of an Mn II UV multiplet at 1868.585 Å. We found the abundance of $\log(n_{\text{Mn}}/n_{\text{H}}) = -5.90$. This line has a relatively low excitation energy (~ 2 eV) and a $\log gf$ of roughly -1.5 , the accuracy of which is not determined by NIST. For better illustration and re-confirmation of this value, we also modeled a strong Mn II resonance line at 2576 Å (“A⁺⁺” $\log gf \sim 0.4$), A small window of an Mn II UV multiplet at 1714 Å, and a resonance Mn I line at 2798 Å. These lines and their best-fitting models are shown in Figure 3.14. Note that

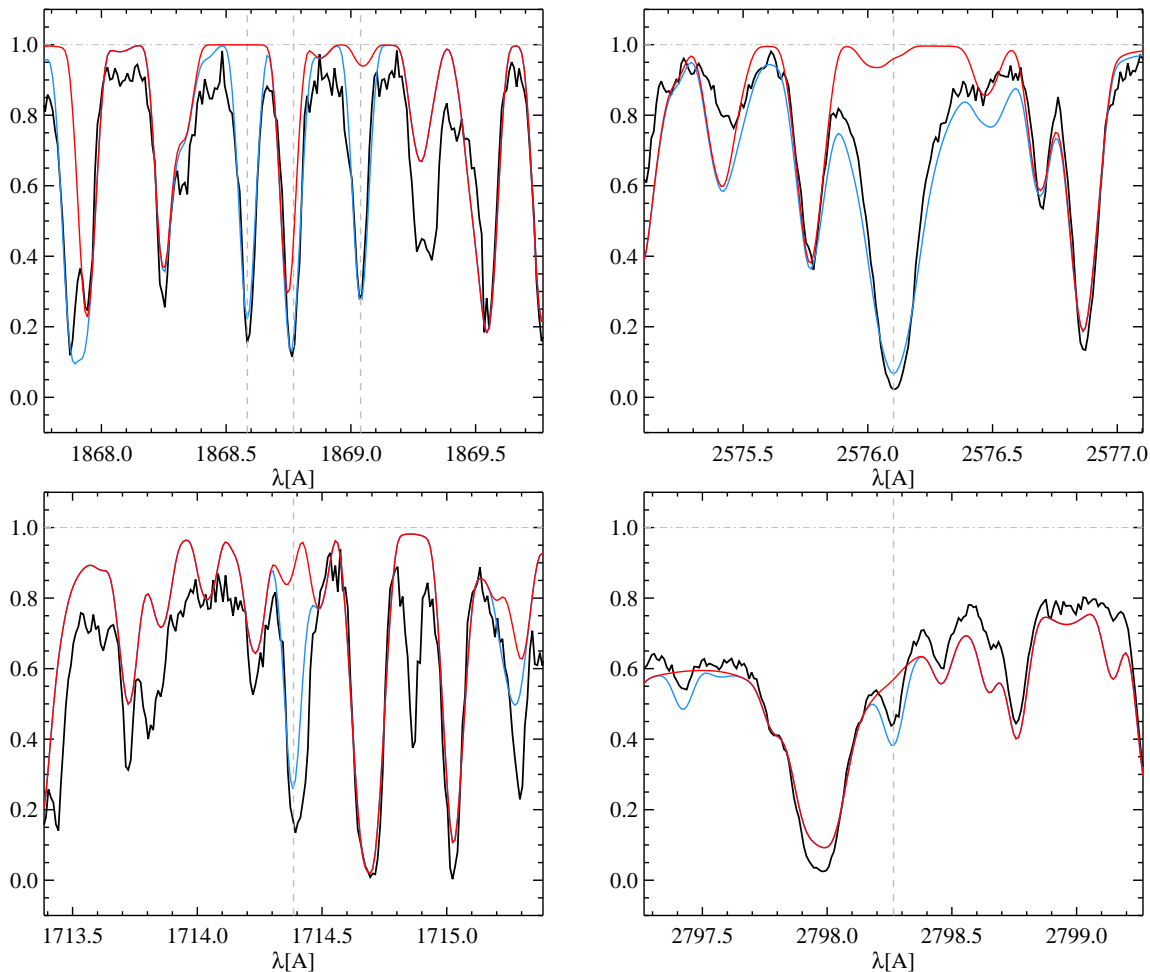


Figure 3.14: This figure shows the observation (in black), calculated model with $\log(n_{\text{Mn}}/n_{\text{H}}) = -5.90 \pm 0.22$ (in blue) and without manganese (in red). *Top left:* A part of an Mn II UV multiplet at 1868.585 Å, *Top right:* A strong Mn II resonance line at 2576.103 Å, *Bottom left:* A small window of an Mn II UV multiplet at 1714.385 Å, *Bottom right:* A resonance strong Mn I at 2798.266 Å.

the best-fitting models presented in Figure 3.14, are all modeled using the same abundance. However, it is evident from the goodness of the fits, that this value is uncertain. Together with the uncertainties discussed in section 3.3.3, we estimate an overall error of 0.22 dex for the measured abundance.

3.4.15 Iron, $Z=26$

The line list selected here, contains 1107 Fe I lines, 5797 Fe II lines, and 421 Fe III lines in total. Among them there are 29 Fe I lines, 1038 Fe II lines, one Fe III line that have a depth that is equal or greater than 0.8 of the continuum. There is a clear dominance in Fe II which is consistent with the results of the Saha equation at this temperature (see Table 3.3).

We estimated the abundance of $\log(n_{\text{Fe}}/n_{\text{H}}) = -3.75$ using a small window of a Fe II UV

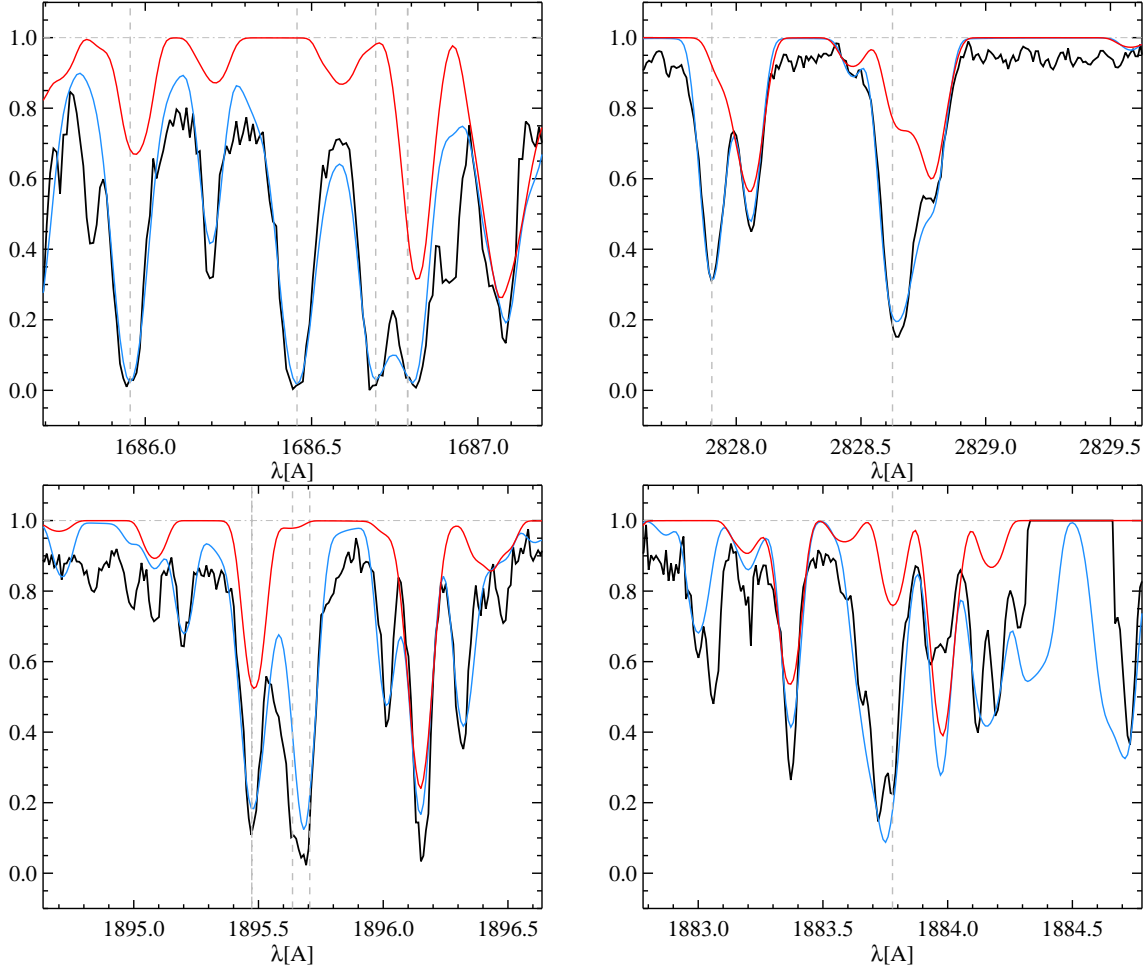


Figure 3.15: This figure shows the observation (in black), calculated model with $\log(n_{\text{Fe}}/n_{\text{H}}) = -3.75 \pm 0.24$ (in blue) and without iron (in red). *Top left:* A small window of a Fe II UV multiplet at 1685.954 Å, *Top right:* One window of an Fe II UV multiplet at 2828.626 Å, *Bottom left:* A part of an Fe III multiplet at 1895.473 Å, *Bottom right:* A strong resonance Fe I lines at 1883.778 Å.

multiplet at 1685 Å. For better illustration, we also modeled the following: one window of an Fe II UV multiplet at 2828 Å, a part of an Fe III multiplet at 1895 Å, a strong resonance Fe I lines at 1883 Å. Figure 3.15 shows these lines and their best-fitting models using the same abundance. However, it is evident that this abundance does not result in the best-fitting model for all of the ionization states. The overall uncertainty associated with this abundance, due to both the difference ionization states and the uncertainties discussed in section 3.3.3 is of the order of 0.24 dex.

3.4.16 Cobalt, $Z=27$

In our selected line list, there are 41 Co I lines, 746 Co II lines, and 27 Co III lines overall. Among them, there are no Co I and Co III, and 66 Co II lines that have depth equal or greater than 0.8 of the continuum. The dominance of Co II is consistent with the prediction of the Saha

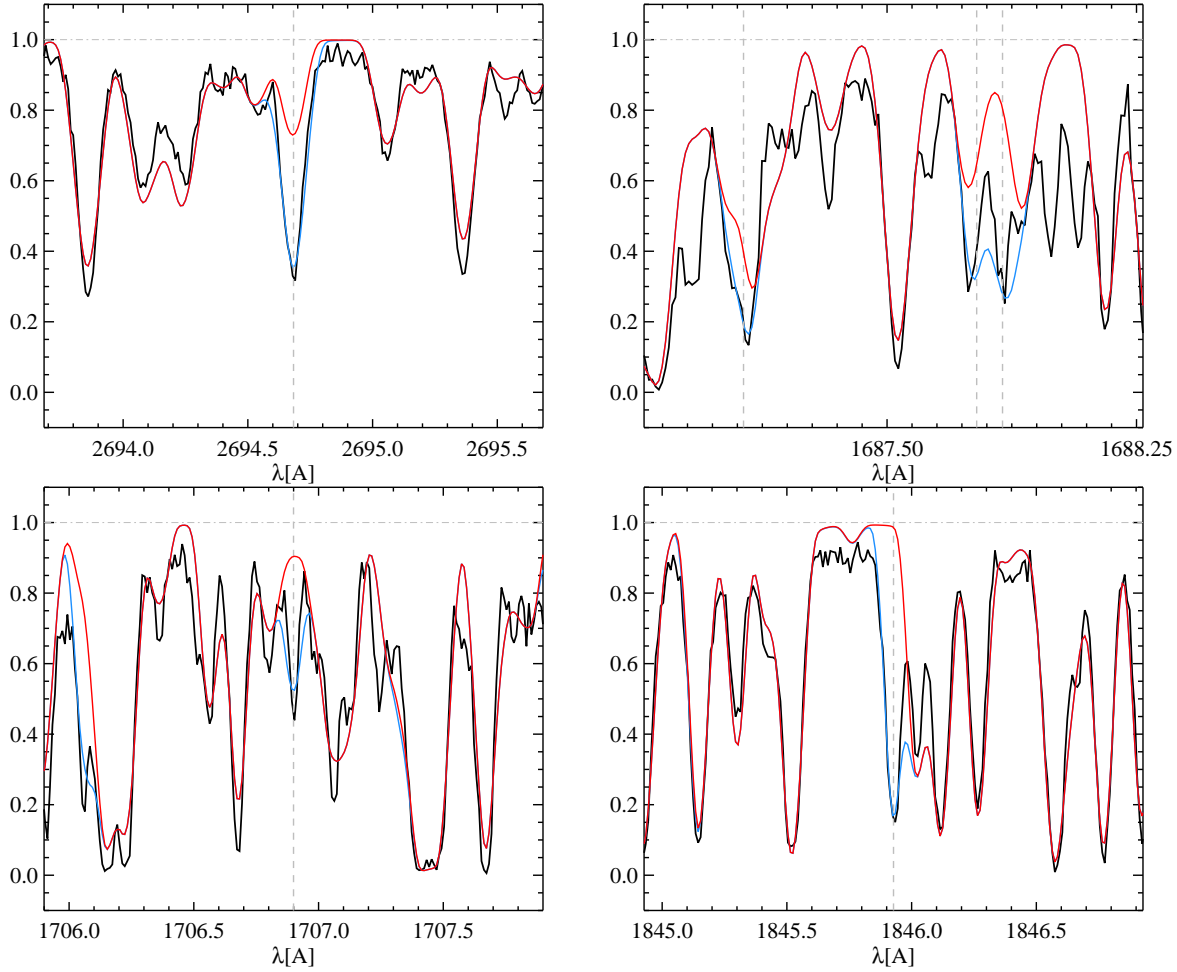


Figure 3.16: This figure shows the observation (in black), calculated model with $\log(n_{\text{Co}}/n_{\text{H}}) = -6.50 \pm 0.12$ (in blue) and without cobalt (in red). *Top left*: A small window of a Co II UV multiplet at 2694.683 Å, *Top right*: A small part of a Co II UV multiplet at 1687.847 Å, *Bottom left*: A small part of a Co II UV multiplet at 1706.899 Å, *Bottom right*: A small part of a Co II UV multiplet at 1845.927 Å

equation at this temperature (see Table 3.3).

We find the abundance of $\log(n_{\text{Co}}/n_{\text{H}}) = -6.50$ for this element through modeling a small window of a Co II UV multiplet at 2694 Å. These lines have low excitation energy (~ 1 eV) and a “C+” $\log gf$ value of -0.5 . We also modeled the a small part of the following Co II UV multiplets for better illustration; 1687 Å, 1706 Å, 1845 Å. These lines and their best fitting models using the same abundance are shown in Figure 3.16. There are no other strong and blend free lines available in any other state of ionization so it is not possible for us to determine whether there is any dispersion associated with that. However, from the figure it appears that there a slight difference between the abundance that results in the best-fitting models even among Co II lines. The overall error, including the uncertainties discussed in section 3.3.3, is of the order of 0.12 dex.

3.4.17 Nickel, $Z=28$

The selected database here contains 204 Ni I, 658 Ni II, and 175 Ni III lines overall. However, only 6 Ni I, 136 Ni II and no Ni III lines that have depth equal or greater than 0.8 of the continuum. The dominance of Ni II is consistent with the results of the Saha equation (see Table 3.3).

We modeled a strong resonance Ni II line at 1703.410 Å and found $\log(n_{\text{Ni}}/n_{\text{H}}) = -5.05$. The $\log gf$ value for this line is estimated to be -1.1 but there is no information on NIST about its accuracy. We confirmed this value by also modeling: I) a resonance Ni I line at 2320 Å, with “C” $\log gf$ of roughly 0.8, II) a strong Ni I line at 2321 Å, with “E” $\log gf$ of roughly 0.5, III) a small window of an Ni II multiplet at 2312 Å IV) a very strong Ni II line at 1900 Å. For the last two, there is no information on NIST regarding the inaccuracies of their measurements. Figure 3.17 shows these lines and their best-fitting models using the same abundance. It appears that the exact same abundance can not reproduce all the ionization states of nickel perfectly well. We estimate the overall uncertainty on this abundance, taking into account the uncertainties discussed in section 3.3.3, to be of the order of 0.36 dex.

3.4.18 Copper, $Z=29$

In the selected linelist here, there are 21 Cu I lines and 29 Cu II lines. Among these lines, there are only 13 Cu II lines that are equal or deeper than 0.8 of the continuum. The Saha equation predict Cu II as the dominant state of ionization at this temperature and in the line forming region which is consistent with the database used here.

We modeled the strong Cu II line at 2148.983 Å and found $\log(n_{\text{Cu}}/n_{\text{H}}) = -7.00$ for copper. This line arises from a relatively low energy of ~ 2 eV and has a $\log gf$ of -0.5 , the accuracy of which is not provided by NIST. We also modeled the Cu II line at 2189 Å ($E=3.2$ eV), and Cu I lines at 2165 Å ($E=0.0$ eV), 2230 Å ($E=1.4$ eV). The observation and models are shown in Figure 3.18. It appears that the abundance that results in the best-fitting model for Cu I lines is slightly different ($\log(n_{\text{Cu}}/n_{\text{H}}) = -7.2$). Taking into account the uncertainties discussed in section 3.3.3, the overall uncertainty associated with this value is of the order of 0.21 dex.

3.4.19 Zinc, $Z=30$

In the subset of the VALD list selected here, there are 9 zinc lines in total. There is only one Zn I lines with the depth of roughly 0.9 of the continuum. There are three Zn II and five Zn III lines present that in the strongest case are 0.1 of the continuum. The Saha equation predicts Zn II as the dominant ionization state at this temperature which is not consistent with our database (Table 3.3). This is mostly due to the fact that majority of Zn II lines have fairly high excitation energies of about ~ 6 eV. the NIST database does not provide much information about this matter either.

Despite lack of unblended lines, we used the lines of Zn I at 2138.5730 and Zn II at 2557.948 Å, and found a value of $\log(n_{\text{Zn}}/n_{\text{H}}) = -6.70$ for this element. The proper estimate of the error on this value requires more clean lines which we do not have, also there is not enough information available about the accuracy of the oscillator strength on the lines we used to model this

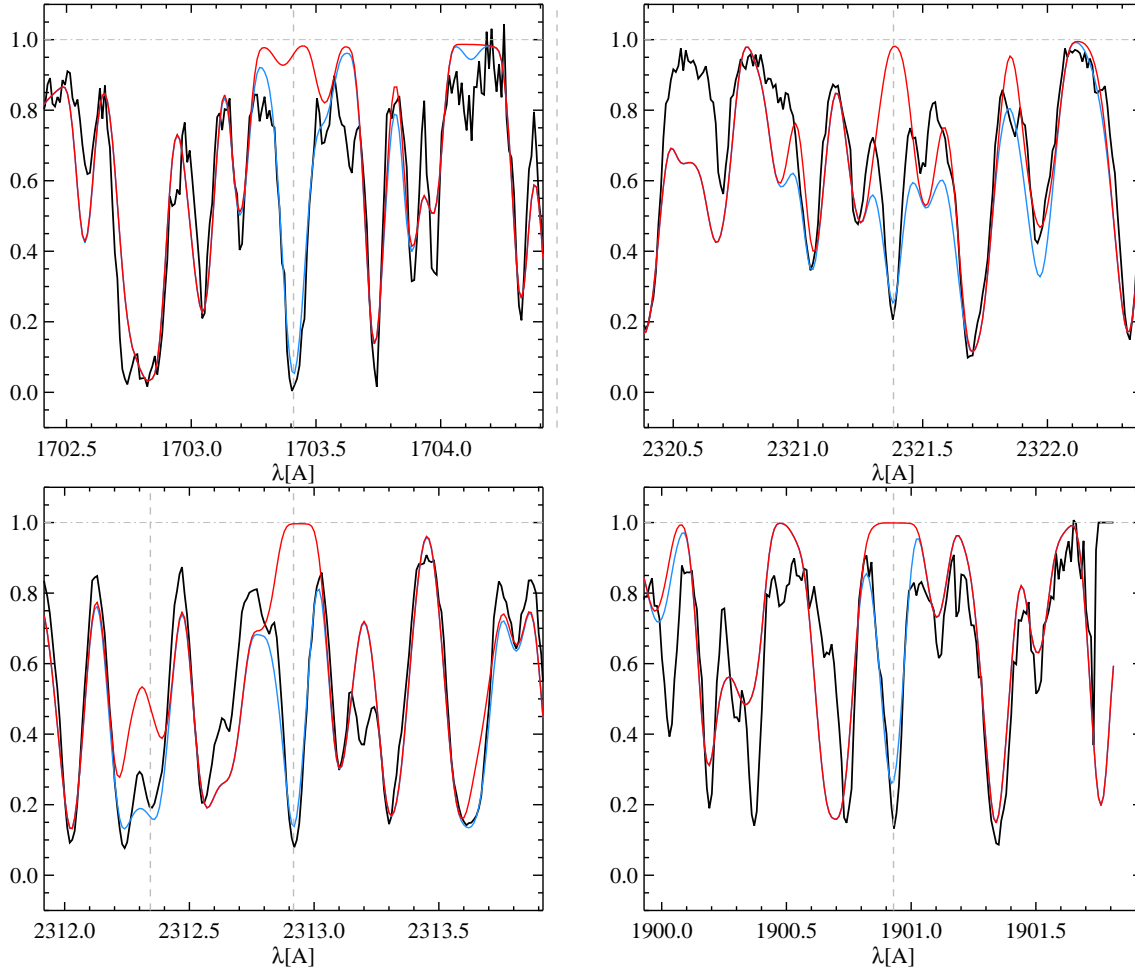


Figure 3.17: This figure shows the observation (in black), calculated model with $\log(n_{\text{Ni}}/n_{\text{H}}) = -5.05 \pm 0.36$ (in blue) and without nickel (in red). *Top left*: a strong resonance Ni II line at 1703.410 Å, *Top right*: A resonance Ni I line at 2320.034 Å and a strong Ni I line at 2321.383 Å, *Bottom left*: A small window of an Ni II multiplet at 2312.917 Å together with a strong Ni II line at 2312.315 Å, *Bottom right*: A very strong Ni II line at 1900.929 Å.

line, therefore, the uncertainty on this upper limit is assumed to be of the order of 0.3 dex (see §3.3.3). Figure 3.19 shows the observation and models.

3.4.20 Yttrium, $Z=39$

In the subset of VALD list selected here, there are 5 Y II and 4 Y III lines and none of them have a depth that is greater than 0.8 of the continuum. According to the Saha equation, Y II should be the dominant state of ionization which despite the rarity of Y lines seems to be the case in our database. However, the Y II lines were too weak to be of any use for abundance determination.

We modeled two Y III lines around 2367 Å, and 2414 Å, and found $\log(n_{\text{Y}}/n_{\text{H}}) = -7.90$.

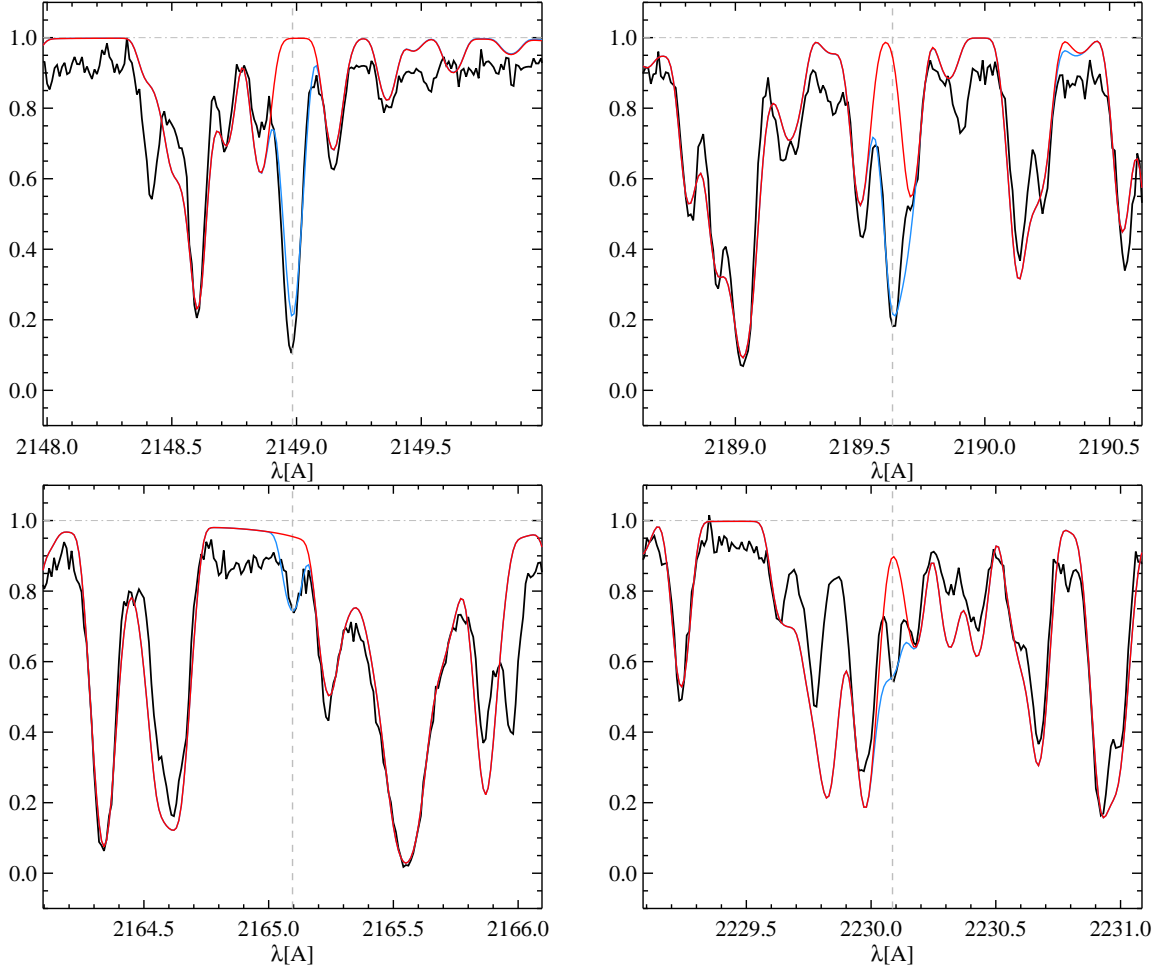


Figure 3.18: This figure shows the observation (in black), calculated model with $\log(n_{\text{Cu}}/n_{\text{H}}) = -7.00 \pm 0.21$ (in blue) and without copper (in red). *Top left:* A strong unblended Cu II line at 2148.983 Å, *Top right:* A strong unblended Cu II line at 2189.629 Å, *Bottom left:* An unblended Cu I line at 2165.095 Å, *Bottom right:* a relatively weak and blended Cu I line at 2230.085 Å.

These line are both resonance lines ($E=0.0$ eV) and they have $\log gf$ values close to -0.2 . There is no information on NIST on the accuracy of these values. The dispersion between the best-fitting abundance values can not easily be determined because there is not a noticeable dispersion between the two available lines that we modeled, and because lines of other ionization states for this element are not clean or easy to model. Therefore, due to lack of available information, the uncertainty is assumed to be of the order of 0.3 dex (see section 3.3.3). Figure 3.20 shows the observation and the models.

3.4.21 Zirconium, $Z=40$

In our selected linelist, there are 58 Zr II lines and 20 Zr III lines and none of them are deeper than 0.8 of the continuum. According to the Saha equation dominant states of ionization are

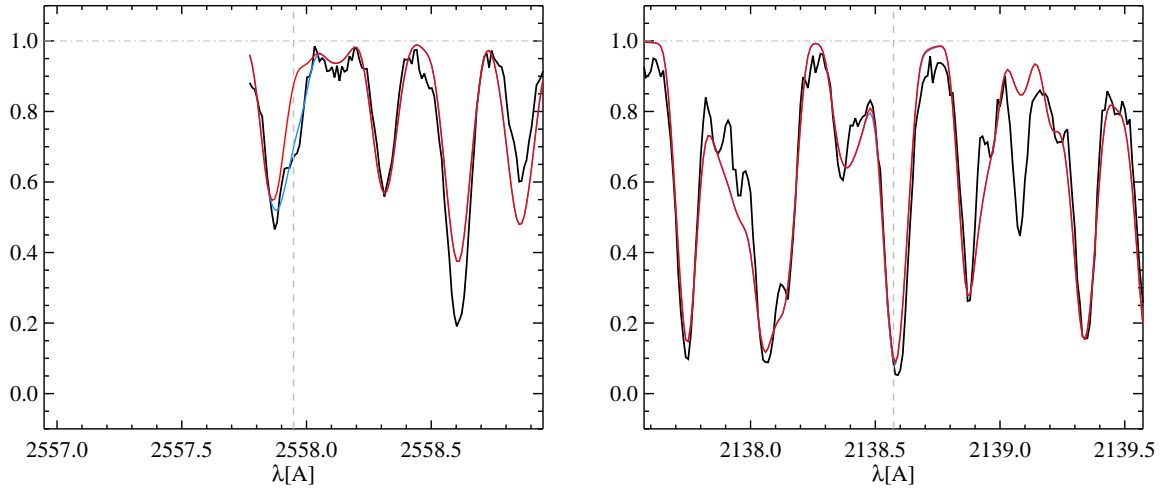


Figure 3.19: This figure shows the observation (in black), calculated model with $\log(n_{\text{Zn}}/n_{\text{H}}) = -6.70 \pm 0.30$ (in blue) and without zinc (in red). *Left*: This shows a Zn II line at 2557.948 Å which illustrates that this value is also an upper limit upon increase of which the model will no longer fit the observation properly. *Right*: Zn I line at 2138.573 Å, in which if we add any more abundance to zinc, it will appear as an excess absorption on top of what already looks like a relatively good fit.

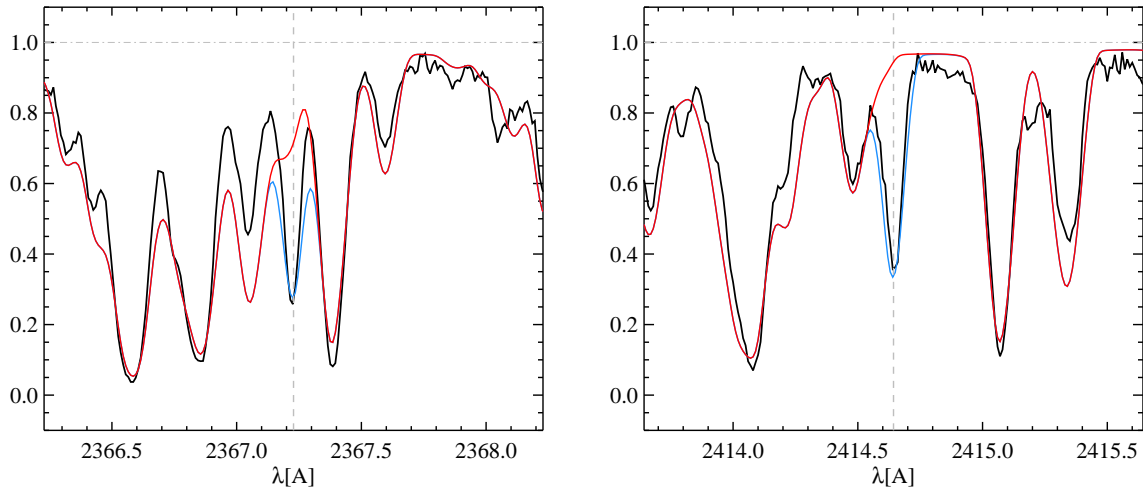


Figure 3.20: This figure shows the observation (in black), calculated model with $\log(n_{\text{Y}}/n_{\text{H}}) = -7.90 \pm 0.30$ (in blue) and without yttrium (in red). Both line are relatively clean Y III lines at *Left*: 2367.228 Å, and *Right*: 2414.643 Å.

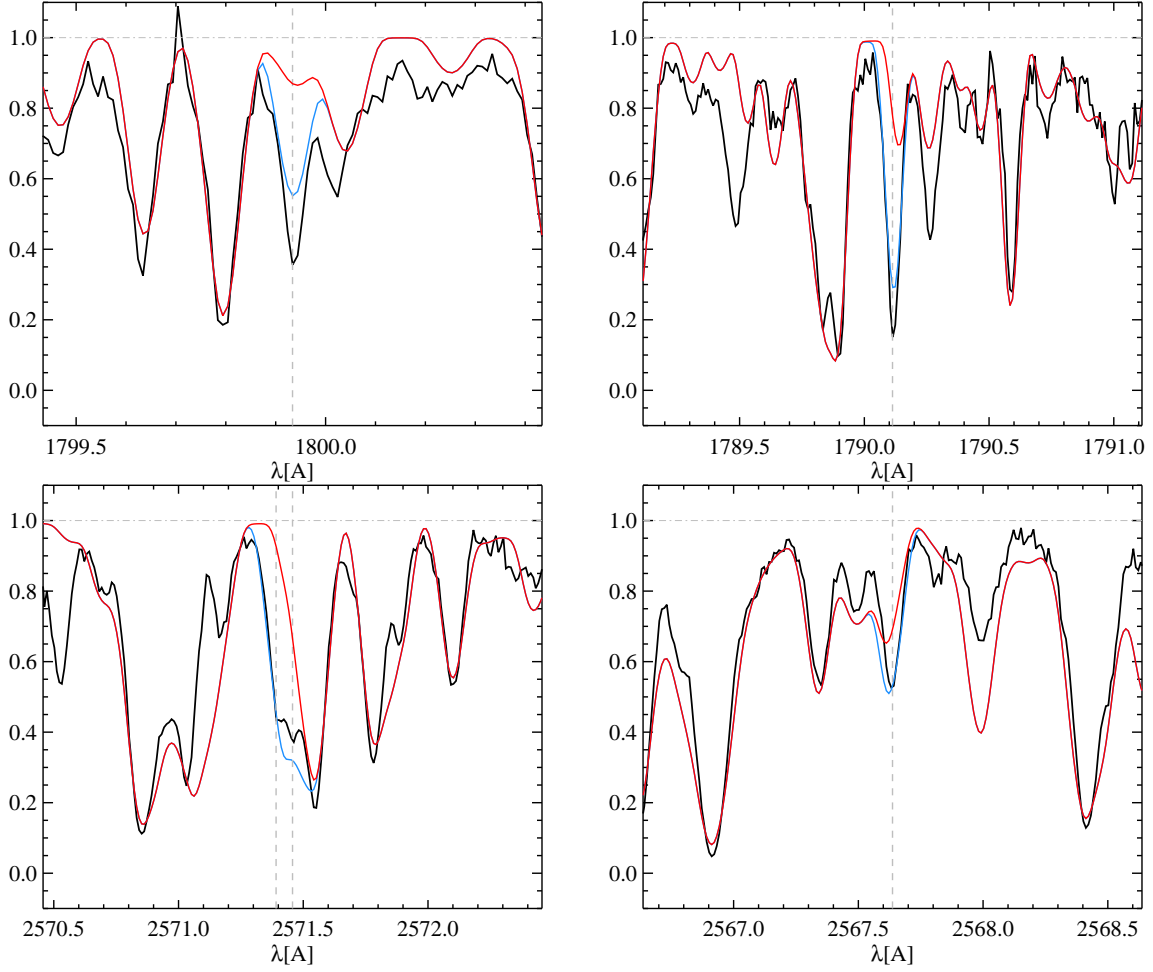


Figure 3.21: This figure shows the observation (in black), calculated model with $\log(n_{\text{Zr}}/n_{\text{H}}) = -8.30 \pm 0.29$ (in blue) and without zirconium (in red). *Top left*: A strong unblended Zr III at 1798.047 Å, *Top right*: A moderately strong Zr III line at 1790.113 Å, *Bottom left*: A blended Zr II line at 2571.391, 2571.457 Å, *Bottom right*: A resonance blended Zr II line at 2567.637 Å.

Zr II and Zr III respectively with minor to no contribution from other states (see Table 3.3).

We modeled a resonance unblended Zr III line at 1798 Å with $\log gf$ of almost zero for which no accuracy is provided by NIST. We found $\log(n_{\text{Zr}}/n_{\text{H}}) = -8.30$. We also modeled the moderately strong Zr III line at 1790 Å ($E=0.1$ eV) a blended Zr II line at 2568 Å ($E=0.1$ eV), a blended Zr II resonance line at 2567 Å. These lines and models are shown in Figure 3.21. The plots shows that different states of ionization are best fit with a slightly different abundance. The overall uncertainty associated with this value, including the discussions of section 3.3.3, is of the order of 0.29 dex.

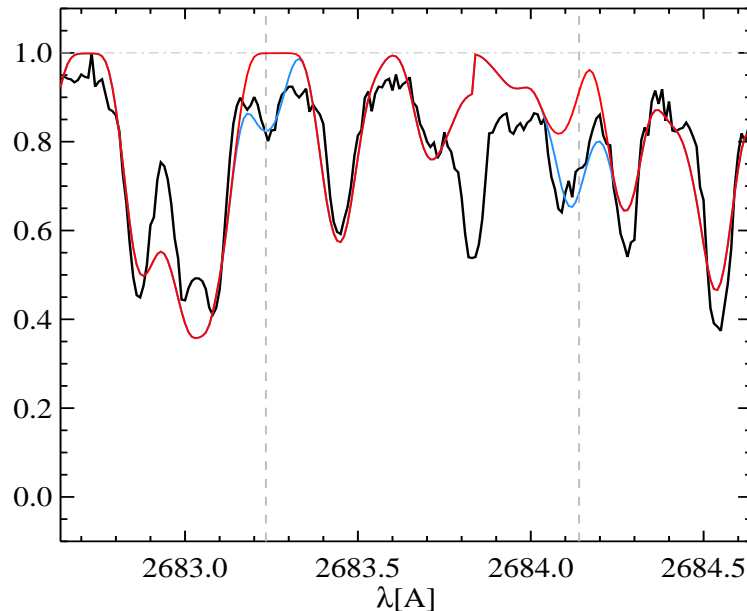


Figure 3.22: This figure shows the Mo II lines at 2683.234, 2684.140 Å (in black), calculated model with $\log(n_{\text{Mo}}/n_{\text{H}}) = -9.00 \pm 0.30$ (in blue) and without molybdenum (in red).

3.4.22 Molybdenum, $Z=42$

There are 17 Mo II lines in the selected list here and none of them are deeper than 0.8 of the continuum. Mo II is the dominant state of ionization according to the Saha equation (see table 3.3). Even though there are not many lines available, we have made use of the two relatively weak but unblended Mo II lines in the 2683–84 Å window and found $\log(n_{\text{Mo}}/n_{\text{H}}) = -9.00$ for the abundance of this element. This feature has an excitation energy of around 1.5 eV and $\log gf$ close to zero. There is no information regarding the accuracy of these measurements in the NIST database. The uncertainty could not be determined because we did not have access to enough clean and unblended lines in order to estimate the dispersion in between them (or even various states of ionization). Therefore, the uncertainty for this value comes from what was discussed in section 3.3.3 and is of the order of 0.3 dex. The line and model is shown in Figure 3.22.

3.4.23 Ruthenium, $Z=44$

Among the 45 Ru II lines present in the selected VALD list, there are no unblended lines that are strong enough to serve the purpose of abundance determination. Instead, we used a resonance multiplets of Ru II at 1896.464, 1897.461, 1875.578 Å, and 1877.201 Å ($E=0.1$ eV) to estimate an upper limit for the abundance of this element $\log n_{\text{Ru}}/n_{\text{H}} \leq -10.50$. All these lines have a $\log gf$ of zero but NIST does not provide any information on their accuracy. The uncertainty on this value can not be determined due to lack of clear lines, however following the discussions in section 3.3.3, it is affected by an uncertainty of the order of 0.3 dex.

3.4.24 Rhodium, $Z=45$

Among the 7 Rh II lines present in the selected VALD list, there are no lines with depth greater than 0.8 of the continuum. There are no unblended lines that can be used for abundance determination. Instead, we used the line at 1637.905, 1668.758 Å to estimate an upper limit for the abundance of this element $\log n_{\text{Rh}}/n_{\text{H}} \leq -10.0$. These two lines arise from a relatively low lying energy level ($E \sim 0.3$ eV) and $\log gf$ of zero. NIST does not have any information on the accuracy of this value. The uncertainty could not be determined because we did not have access to enough clean and unblended lines in order to estimate the dispersion in between them (or even various states of ionization). The assumed uncertainty on this value would be of the order of 0.3 dex as discussed in section §3.3.3.

3.4.25 Tin, $Z=50$

In the VALD list used here, there are 7 Sn II lines and the strongest of them is almost half of the continuum level. Due to lack of clean and unblended lines, we only modeled the resonance line at 1757 Å, to determine the abundance and found $\log(n_{\text{Sn}}/n_{\text{H}}) = -8.8$. The $\log gf$ of this line is roughly -0.5 but NIST does not provide any information on the accuracy. The uncertainty associated with this value is not easy to determine due to absence of enough clean and unblended lines for a noticeable dispersion (or even in various states of ionization). However, the fit presented here is not perfectly recreating the observation. We varied the abundance to higher and lower values but we did not achieve a perfect match. The two values which are just below or above the perfect match give us a difference of 0.6 in the abundance which corresponds to twice the reasonable fitting uncertainty. Thus overall, the uncertainty on this abundance, including the 0.1 dex discussed in section 3.3.3, is of the order of 0.4 dex. Figure 3.23 shows the observation and model.

3.4.26 Barium, $Z=56$

In the subset of VALD selected here, there are only 3 Ba II lines. The strongest of them is almost 0.4 of the continuum. The Saha equation predicts Ba III to be the dominant ionization state at this temperature but that is not the case in our database (see Table 3.3). This is mostly due to the fact that majority of Ba III lines in the wavelength range studied here arise from a fairly highly excited state at about ~ 17 eV.

We modeled the two blended lines of Ba II at 2304 Å, and 2335 Å and managed to find an upper limit of $\log(n_{\text{Ba}}/n_{\text{H}}) \leq -9.65$ for this element. The NIST database does not provide any information on the accuracy of the $\log gf$ values for these two lines but according to the VALD list they are both close to 1.2. The error on this value can not be estimated due to lack of enough clean and unblended lines. However, the error of 0.3 dex is applicable as discussed in section 3.3.3. Figure 3.24 shows the observation and the models.

3.4.27 Ytterbium, $Z=70$

In the VALD list selected here, there are 4 Yb II and 1 Yb III lines, none of which are deeper than 0.8 of the continuum. The Saha equation predicts that at this temperature, Yb II and Yb III,

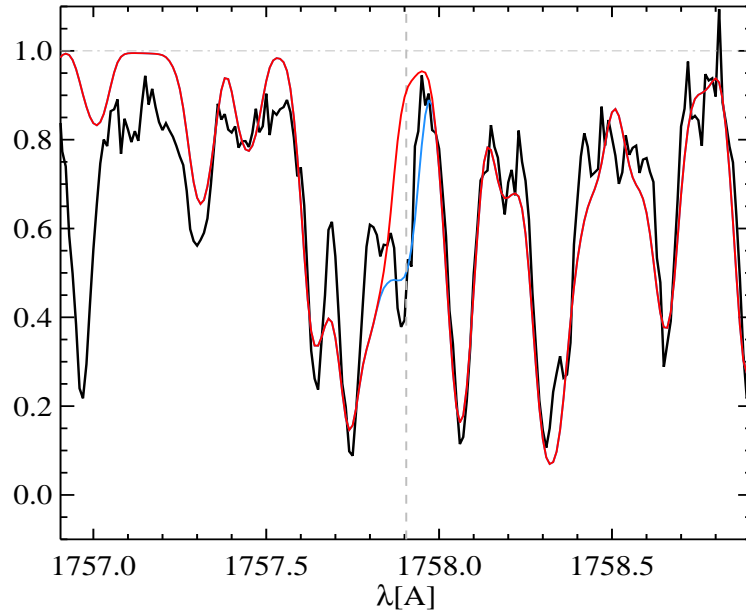


Figure 3.23: This figure shows the Sn II line at 1757.905 Å (in black), calculated model with $\log(n_{\text{Sn}}/n_{\text{H}}) = -8.8 \pm 0.4$ (in blue) and without tin (in red).

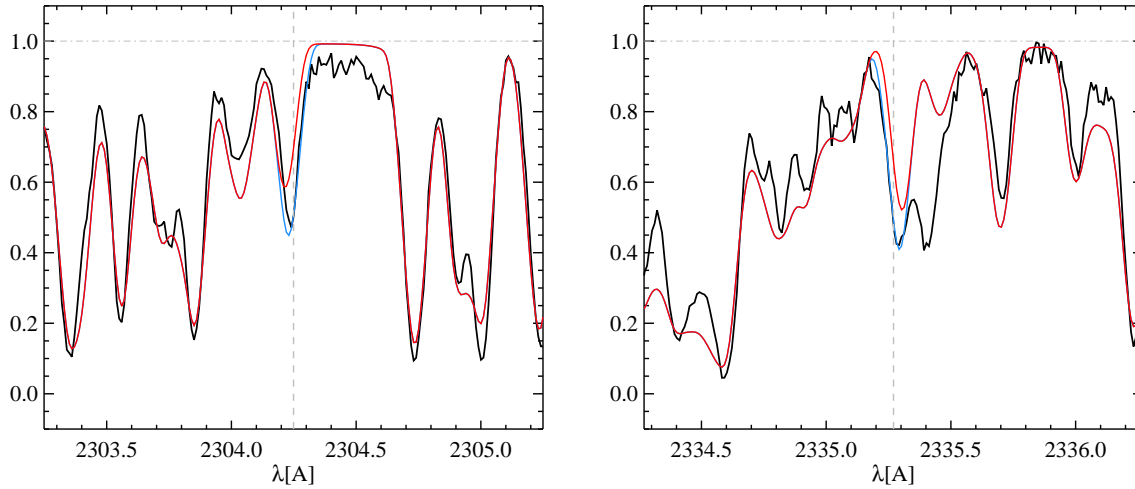


Figure 3.24: This figure shows the observation (in black), calculated model with $\log(n_{\text{Ba}}/n_{\text{H}}) = -9.65 \pm 0.30$ (in blue) and without barium (in red). Both lines are Ba II, *left*: one at 2304.249 Å, and *right*: the other at 2335.270 Å.

are both almost equally dominant (see Table 3.3).

Even though all of these lines are resonance lines, the majority of them are heavily blended. We used the only fairly unblended line Yb III at 1873 Å, and determined the abundance of $\log(n_{\text{Yb}}/n_{\text{H}}) = -9.00$. It is a resonance line with $\log gf$ value of -0.6 , for which NIST does not provide any information on its accuracy. The uncertainty could not be determined because we did not have access to enough clean and unblended lines in order to estimate the dispersion in between them (or even various states of ionization). The overall uncertainty is of the order of

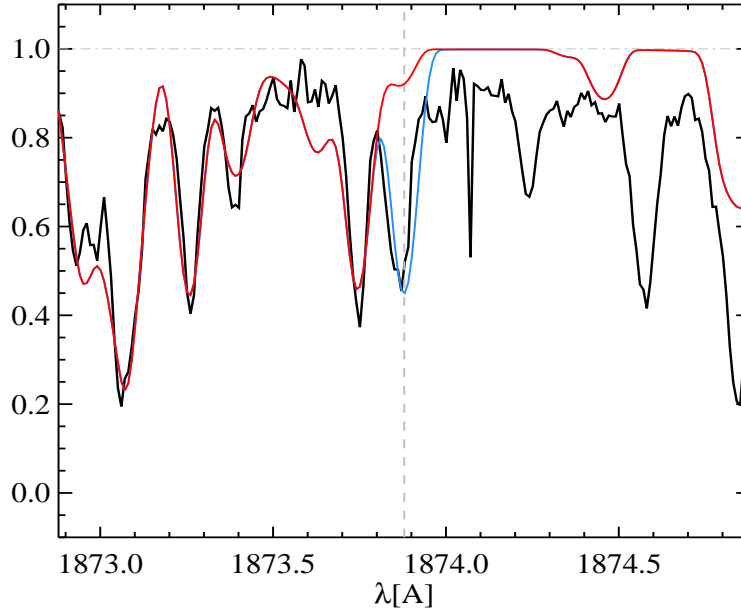


Figure 3.25: This figure shows the Yb III at 1873.879 Å (in black), calculated model with $\log(n_{\text{Yb}}/n_{\text{H}}) = -9.00 \pm 0.30$ (in blue) and without ytterbium (in red).

0.3 dex, based on the considerations of Section 3.3.3.

3.4.28 Osmium, Z=76

This lines of this element are barely detectable in the spectrum, even though there are 21 lines in the VALD list. We used the Os II line at 2563.163 Å to determine an upper limit of -12.0 for this element. The strongest line is almost 0.3 times the depth of the continuum but heavily blended that is virtually impossible to model this line. The uncertainty on this value is of the order of 0.3 dex as discussed in section 3.3.3.

3.4.29 Platinum, Z=78

In the subset of VALD list selected here there are 22 Pt II lines and none of them are deeper than 0.8 of the continuum. There was no clean and unblended Pt lines in our sample. The Saha equation predicts Pt II as the dominant state of ionization which is consistent with our database (Table 3.3). Despite the lack of good lines, we still used a small window of a Pt II UV multiplet at 1777 Å ($E \sim 0.59$ eV, $\log gf \sim 0.70$), and a small window of another multiplet at 1883 Å ($E \sim 1.65$ eV, $\log gf \sim 1.2$) to determine an upper limit of $\log(n_{\text{Pt}}/n_{\text{H}}) \leq -9.50$ for this element. NIST does not provide any information regarding the accuracy of the $\log gf$ values for these two lines. Figure 3.26 shows the observation and the models at these wavelengths. The uncertainty could not be determined because we did not have access to enough clean and unblended lines in order to estimate the dispersion in between them (or even various states of ionization). However, the uncertainty of 0.3 dex, discussed in section 3.3.3, is applicable to this value.

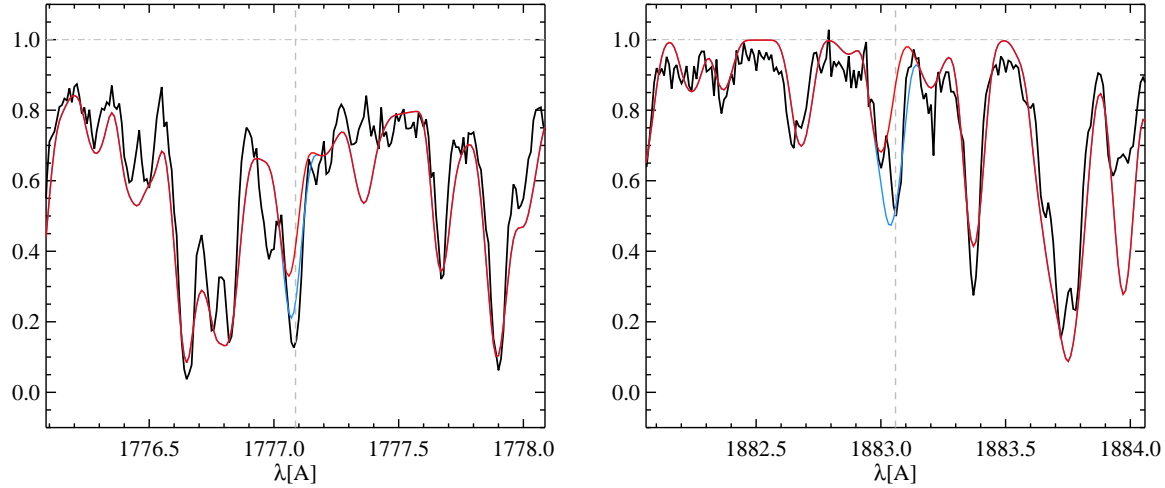


Figure 3.26: This figure shows the observation (in black), calculated model with $\log(n_{\text{Pt}}/n_{\text{H}}) = -9.50 \pm 0.30$ (in blue) and without platinum (in red). Both lines belong to Pt II at *left*: 1777.086 Å and *right*: 1883.058 Å.

3.4.30 Gold, Z=79

Among the six Au II lines present in the selected VALD list, there are no unblended lines that we can use to determine the abundance of gold. Instead, we used the line at 1749.756 Å to estimate an upper limit for the abundance of this element $\log(n_{\text{Au}}/n_{\text{H}}) \leq -9.00$. This line arises from a relatively low lying energy level (~ 2 eV) and $\log gf$ of zero. NIST does not provide any information about the accuracy of this value. The Saha equation also predicts Au II as the dominant state of ionization which is consistent with what we extract from our database. The uncertainty is 0.3 dex from the sources discussed in section 3.3.3.

3.4.31 Mercury, Z=80

In the subset of VALD list there is only one Hg II line that occurs at 1649.937 Å. This line is a resonance lines and has $\log gf$ of ~ 0.3 and a depth that is 0.6 that of the continuum. The NIST database does not provide information on the accuracy of this oscillator strength. The Saha equation predicts a much greater contribution from Hg II at this temperature (see Table 3.3) which is not consistent with the database we have. This is mainly due to the fact that majority of Hg II lines arise from high excitation states of about ~ 10 eV.

The one available line is strong enough for us to determine the abundance. We find the value of $\log(n_{\text{Hg}}/n_{\text{H}}) = -9.20$ but due to lack of enough clean lines we can not assign a proper error to this value. The 0.3 dex error from all the sources discussed in section 3.3.3 is still applicable. Figure 3.27 shows the observation and models.

3.4.32 Lead, Z=82

Among the six Pb II lines present in the selected VALD list, there are no unblended lines that we can use to determine the abundance of lead. Instead, we used the lines at 1682.127 and

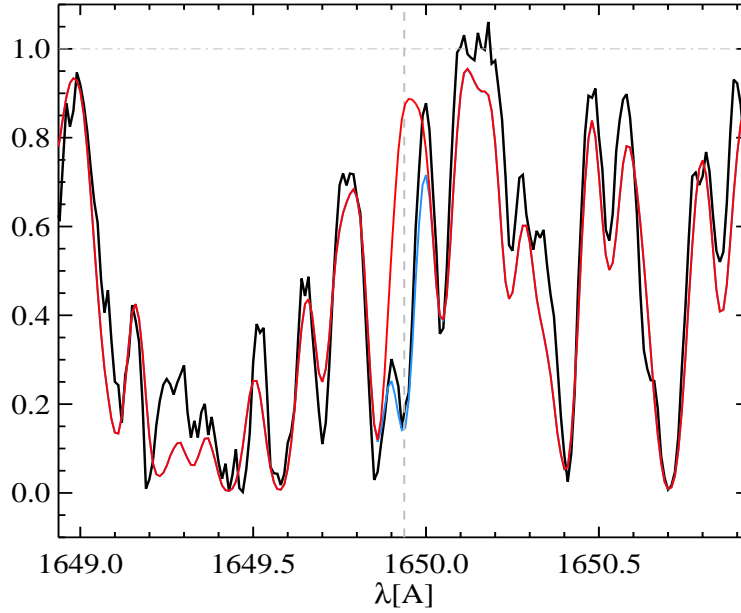


Figure 3.27: This figure shows the line at 1649.937 Å (in black), calculated model with $\log(n_{\text{Hg}}/n_{\text{H}}) = -9.20 \pm 0.30$ (in blue) and without mercury (in red).

1726.803 Å to estimate an upper limit for the abundance of this element $\log(n_{\text{Pb}}/n_{\text{H}}) \leq -10.00$. Both of these lines are resonance lines and they have $\log gf$ of -0.5 and zero, respectively. The NIST database does not provide any information about the accuracy of these values. The error on this abundance measurement is therefore 0.3 dex from all the sources discussed in section 3.3.3.

3.4.33 The Missing Lines

Up to this point, we have done the spectrum synthesis from which we determined the abundances of several elements using the atomic data provided in the VALD database. However, the spectrum of HD72660 still shows some relatively strong lines that are missing from the calculated model (see e.g. 1660.04 Å, 1655.97 Å, 1160.04 Å, 1712.07 Å, 1732.30 Å, 1751.21 Å, 1874.55 Å, 1874.25 Å, 2847.20 Å, etc. in Appendix C).

We first investigated the possibility of these missing lines existing in the VALD list but with incorrect $\log gf$ values. There are several ways to extract data from the VALD database. For this purpose, we used the “Extract All” option which extracts all transitions for all lines of a given element within a certain wavelength interval. For some of the strongest missing features, we extracted a short list within a small matching wavelength interval. Even though the resulting list contained a few good candidate lines for the unidentified features, the change in the oscillator strength that was required to achieve a good fit was not plausible. Although we found a few good coincidences, in all cases no reasonable change in oscillator strength would lead to a good fit. Therefore, we did not continue this investigation any further.

The hydrogen Lyman series also can not be a possible reason for missing lines since it does not occur in the wavelength window studied here. We suspect that most of the remaining strong unidentified features are high-excitation lines of abundant ions, perhaps usually of iron peak

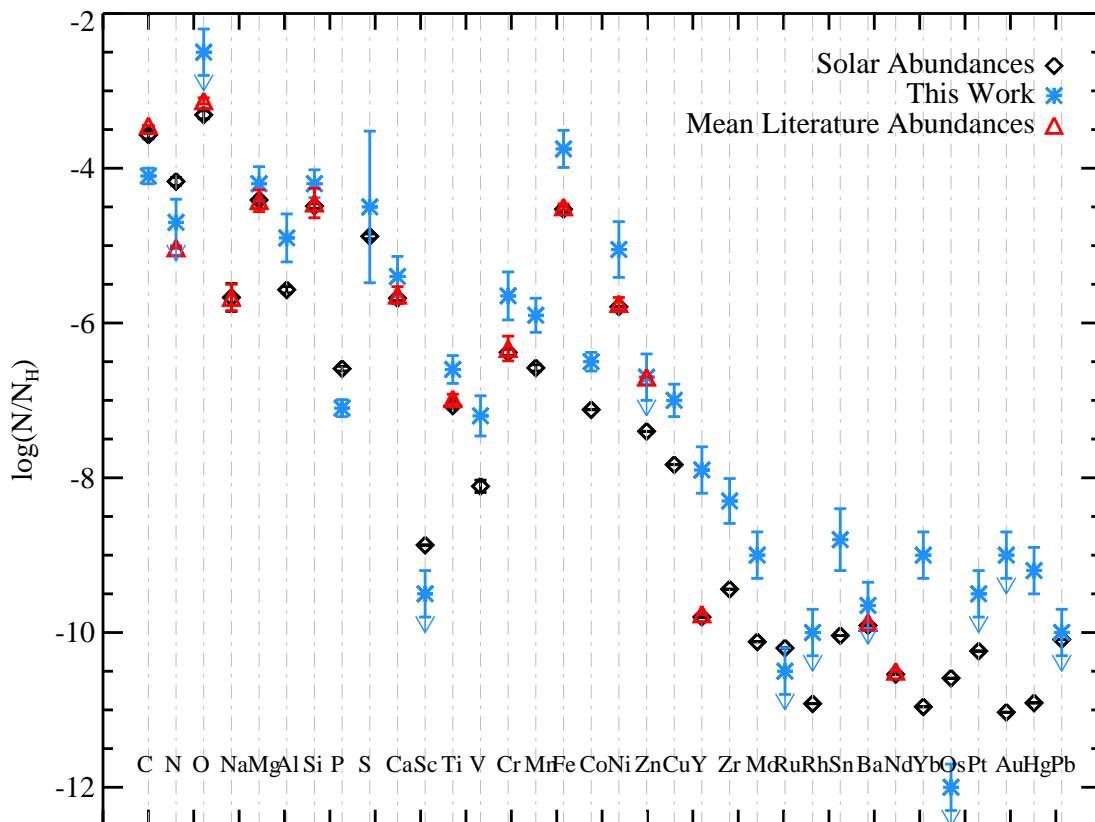


Figure 3.28: This figure shows a comparison between the solar abundances of 29 elements and the abundances obtained from this work and the literature. Note that the literature values are the mean taken from Table 3.1. The arrows represent upper limits.

elements, that simply lack oscillator strengths. The proper identifications of these lines as well as the possible correction to the oscillator strength values, can be the focus of a future work.

3.5 Discussion & Conclusion

3.5.1 Comparison with Literature

This work presents a detailed UV spectral synthesis for HD72660. It is important to compare the outcome of this new approach with previous work. The results of this study are listed in Table 3.2, and shown graphically in Figure 3.28. In this project, we investigated the abundance of 32 elements covering atomic numbers from $Z=6$ -82. We attempted to derive an abundance for every single element that we investigated but in eleven cases, we had to settle for an upper limit. These elements include: Nitrogen (-4.7 , see §3.4.2), Oxygen (-2.5 , see §3.4.3), Scandium (-9.5 , see §3.4.10), Zinc (-6.7 , see §3.4.19), Ruthenium (-10.5 ,

see §3.4.23), Rhodium (−10.0, see §3.4.24), Barium (−9.65, see §3.4.26), Osmium (−12.0, see §3.4.28), Platinum (−9.5, see §3.4.29), Gold (−9.0, see §3.4.30), Lead (−10.0, see §3.4.32).

The upper limits we find for O, Zn, Rh, Pt, Au are higher than solar whereas that of N, Sc, Ru, and Os are lower than solar and exceptionally Ba, Pb are almost solar (see Figure 3.28).

There are two elements, sodium and neodymium, that have been studied in the optical spectra [34] and their abundances are listed in table 3.1. In case of sodium, the majority of the transition that occur in the wavelength range studied here are in the form of Na III, Na IV, Na VI, and Na VII. However, their excitation energies range from 51 eV to 143 eV which is very high for them to occur in our spectrum. The element neodymium does not have any useful transitions in our wavelength window.

Table 3.1 provide a list of elemental abundances found in the literature for this particular target. Most of these abundance that have been reported before are almost solar (see Figure 3.28). Aside from sodium and neodymium, there are 13 elements that are revisited in this work: C, N, O, Mg, Si, Ca, Ti, Cr, Fe, Ni, Zn, Y, Ba.

Our results show that carbon is the only element for which we find a sub-solar abundance. We find a higher abundance for Ti, Cr, Fe, Ni, Zn, Y compared to their solar value which is almost equal to their literature values. We find that the abundances of Mg, Si, Ca are almost equal to their literature or solar value. For barium and nitrogen we already described the upper limits above.

There are 12 new elements that we investigated in this work with detailed synthesis for the first time and managed to find a value for their abundance. They include the following: Al, P, S, V, Mn, Co, Cu, Zr, Mo, Sn, Yb, Hg. We find that all of these element have abundances higher than solar except for phosphorous which is less than solar. Sulfur also has a very large error bar so it is rather difficult to comment on whether or not it is higher or lower than solar value.

The purpose of this project, as described in §3.1, was to revisit the abundance analysis and spectrum synthesis in the UV. The task has been accomplished and our result, on average, suggest slightly higher abundances compared to the results of previous studies.

The high abundance that we find for elements such as mercury, together with an atmospheric excess of elements such as manganese, yttrium, zirconium, platinum, suggest that this star may belong to a category of stars known as “mercury-manganese (Mn-Hg)” type star.

On the other hand, our results clearly indicate the presence of lanthanides which are a series of chemical elements with atomic number 57 through 71. They are chemically similar to scandium and yttrium, and they are also referred to as “rare earth elements”. Our results include a few of these rare earth elements and they show a very high abundance: Y ($Z=39$, $\log(n_Y/n_H) = -7.9$), Yb ($Z=70$, $\log(n_{Yb}/n_H) = -9.0$) and also from optical windows Nd ($Z=60$, $\log(n_{Nd}/n_H) = -10.5$). Showing an evidence for the presence of lanthanides can put this star into another category known as “Am” type stars. This can provide a supporting argument for what was suggested by [36]: HD72660 may represent a transition object in between a late-B type Hg-Mn star and Am type stars.

3.5.2 Further considerations and future work

One of the important phenomena that needs to be taken into consideration is the presence of stellar winds. One of the numerous stellar wind indicators in a spectrum is blue-shifted excess

absorption in the wings of resonance lines [15, 16]. We have modeled resonance lines of Mn II at 2576.103 Å, Mg II at 2802.705 Å, and 2795.528 Å, Si II 1808.0126, 1816.928, 1817.45 Å, and they appear to be the strongest such lines present in regions for which we have data and that we can model confidently. All of these lines are modeled reasonably well (see Figures 3.14, 3.4, 3.6, respectively) and neither one of them show an excess blue wing absorption. Modeling with a data covering a larger wavelength window, could further clarify this situation. In any case, evidence of detectable (mixed) stellar wind in this star is absent.

In a calm atmosphere of a slowly rotating star like HD72660 ($v \sin i \sim 6 \text{ km s}^{-1}$), some heavier elements sink under the force of gravity through the ambient hydrogen and they drift downwards into the stellar interior. This process is known as “diffusion”. However, in some cases like HD72660, we observe a large abundance of heavy elements and lower abundance of lighter elements in the atmosphere. This suggests that there must be another phenomena to counteract the effects of downward diffusion. This kind of abundance anomaly can occur when radiation pressure from the stellar interior, reverses the downward drift of the low-abundance elements. This phenomenon is known as “radiative levitation” which can operate particularly effectively in slowly rotating stars.

The over-abundance of heavy elements we observe in the atmosphere of HD72660 can be potentially explained by radiative levitation in this star. In a way, it mirrors the phenomenon observed by Hill & Landstreet [8], that even most normal but slowly rotating A0V stars seem to have overabundance of some heavy elements such as Zr, Ba and La.

The evolution on the main sequence and later stages, are greatly influenced by the structure and processes such as separation and complex mixing that occur in the stellar interior and envelopes, thus study of chemical abundances in a star can provide powerful tools to investigate these processes. Obtaining accurate measurements of the relative abundances of as many elements as possible is an essential first step to interpreting the information content of stellar chemistry. In this work we show that spectrum synthesis in the ultraviolet wavelength window makes a useful contribution to understanding sharp-line A-type stars such as HD72660

3.6 Acknowledgement

SSG acknowledges support from the Department of Physics and Astronomy of the University of Western Ontario. SSG and JDL acknowledge financial support for this work from the Natural Sciences and Engineering Council of Canada. This work is based on observations made with the STIS/NUV-MAMA instrument on board Hubble Space Telescope (HST). The data presented in this paper were obtained from the Mikulski Archive for Space Telescopes (MAST). STScI is operated by the Association of Universities for Research in Astronomy, Inc., under NASA contract NAS5-26555. Support for MAST for non-HST data is provided by the NASA Office of Space Science via grant NNX13AC07G and by other grants and contracts.

Table 3.1: HD72660 - Summary of Literature Abundances ($\log N/N_H$). (1) Varenne [33] with $v_{\text{ sini}}=6 \text{ km s}^{-1}$, $\xi=2.5 \text{ km s}^{-1}$, (2) Landstreet et al. [21, and unpublished] with $v_{\text{ sini}}=5.0\pm0.5$ and $\xi=2.3\pm0.3$ for the published work and $v_{\text{ sini}}=5.6 \text{ km s}^{-1}$, $\xi=2.3 \text{ km s}^{-1}$ for the unpublished work in the optical, (3) Varenne & Monier [34] with $v_{\text{ sini}}=10\pm2 \text{ km s}^{-1}$, for which superscripts u and o mean that the value is obtained from UV or Optical lines, respectively. (4) Wahlgren & Leckrone [37] with $v_{\text{ sini}}=6.0\pm0.5$ and $\xi=2.0$ whose results imply a typical abundance in the range of +1.0 to +1.5 dex, with respect to the solar values.

Species	(1)	(2)	(3)	(4)
C	-3.45		$\leq -4.45^u$	
N			$\lesssim -5.03^u$	
O	-3.13 ± 0.04		-3.64 ± 0.15^o	
Na	-5.67 ± 0.17		-4.91 ± 0.18^o	
Mg	-4.42 ± 0.14	-3.55	-3.97	
Si	-4.45 ± 0.19	-4.20 ± 0.11	-3.89 ± 0.15^o & $\lesssim -4.45^u$	
Ca	-5.64 ± 0.11		-5.56 ± 0.15^o	
Ti	-6.98 ± 0.06	-6.72	-6.10 ± 0.10^o	
Cr	-6.33 ± 0.16	-6.09 ± 0.10	-5.47^o & $\sim -6.03^u$	
Fe	-4.5 ± 0.04	-4.35 ± 0.12	-3.80 ± 0.05^o & $\sim -4.5^u$	
Ni	-5.75 ± 0.08	-5.17	-4.91^o	
Zn		-8.20	$\sim -6.70^u$	
Y	-9.76			
Mo				-8.92
Ba	-9.87	-8.60	-8.47^o	-8.81
Nd	-10.50			

Table 3.2: This table shows the abundances determined in this work for every element studied, solar abundances from Scott et al. [32, I & II], Grevesse et al. [9] and Asplund et al. [1], and the wavelengths used to determine these values. The sign \downarrow means the given value is an upper limit.

Species	$\log(N/N_H)$	$\log(N/N_H)_\odot$	Unblended Lines Wavelengths[Å]
C	-4.10 ± 0.10	-3.57 ± 0.05	1656.928, 1657.379, 1657.907, 1657.008, 1658.121, 1751.823
N	-4.70 ± 0.30 (\downarrow)	-4.17 ± 0.05	1745.252, 1745.260, 1742.729, 1742.719
O	-2.50 ± 0.30 (\downarrow)	-3.31 ± 0.05	1641.305, 1868.655
Mg	-4.20 ± 0.22	-4.41 ± 0.04	1827.935, 2852.126, 2795.528, 2802.705
Al	-4.90 ± 0.31	-5.57 ± 0.04	1719.442, 1721.244, 1721.271, 1766.381, 1769.133
Si	-4.20 ± 0.18	-4.49 ± 0.03	1808.012, 1816.928, 1817.451, 1770.629, 1853.152
P	-7.10 ± 0.11	-6.59 ± 0.03	1774.949, 1782.829, 1787.647, 1858.871, 1859.401, 2135.469, 2136.182, 2149.142
S	-4.50 ± 0.98	-4.88 ± 0.03	1807.311, 1820.341, 1826.244, 1706.360, 1707.13, 1900.286
Ca	-5.40 ± 0.26	-5.68 ± 0.03	1807.337-1814.647, 1838.008-1840.060, 2128.750-2132.304, 2197.786-2208.610
Sc	-9.50 ± 0.30 (\downarrow)	-8.87	2552.354, 2563.189
Ti	-6.60 ± 0.18	-7.07 ± 0.04	1642.630, 1650.623, 1830.463, 2877.434, 2851.101, 2862.319
V	-7.20 ± 0.26	-8.11 ± 0.08	1636.023, 1637.562, 1643.059, 2880.016, 2882.494
Cr	-5.65 ± 0.31	-6.38 ± 0.04	1718.475, 1732.073, 1898.980, 1899.642, 2860.933, 2862.570, 2858.908,
Mn	-5.90 ± 0.22	-6.58 ± 0.04	1714.385, 1868.585, 2798.266, 2576.103
Fe	-3.75 ± 0.24	-4.53 ± 0.04	1685.954, 1883.778, 1895.473, 2828.626
Co	-6.50 ± 0.12	-7.12	1687.847, 1706.899, 1845.927, 2694.683
Ni	-5.05 ± 0.36	-5.79	1703.410, 1900.929, 2320.034, 2321.383, 2312.917
Cu	-7.00 ± 0.21	-7.83	2148.983, 2165.095, 2189.629, 2230.085
Zn	-6.70 ± 0.30 (\downarrow)	-7.40	2138.573, 2557.948
Y	-7.90 ± 0.30	-9.80	2367.228, 2414.643
Zr	-8.30 ± 0.29	-9.44	1798.047, 1790.113, 2568.871, 2567.637
Mo	-9.00 ± 0.30	-10.12	2684.139
Ru	-10.5 ± 0.30 (\downarrow)	-10.20	1896.464, 1897.461, 1875.578, 1877.201
Rh	-10.0 ± 0.30 (\downarrow)	-10.92	1637.905, 1668.758
Sn	-8.80 ± 0.40	-10.04	1757.905
Ba	-9.65 ± 0.30 (\downarrow)	-9.91	2304.249, 2335.270
Yb	-9.00 ± 0.30	-10.96	1873.879
Os	-12.0 ± 0.30 (\downarrow)	-10.59	2563.163
Pt	-9.50 ± 0.30 (\downarrow)	-10.24	1777.086, 1883.058
Au	-9.00 ± 0.30 (\downarrow)	-11.03	1749.756
Hg	-9.20 ± 0.30	-10.91	1649.937
Pb	-10.00 ± 0.30 (\downarrow)	-10.09	1682.127, 1726.803

Table 3.3: The percentile ionization ratios directly measured from the Saha equation. Note that n_{tot} is the total number density in every state ($n_{tot} = n_0 + n_1 + n_2 + n_3$). Note that this table shows the calculations at two different regions; *left column*: The region where the continuum and weak lines are formed ($\tau \sim 0.3$ near the short wavelength and ~ 1.0 near the long wavelength end of the data, $T \sim 9600\text{K}$, $n_e \sim 2.71 \times 10^{14}$). and *right column*: The region where line core of strong line are formed ($\tau = 3 \times 10^{-4}$, $T \sim 6900\text{K}$, $n_e \sim 1.35 \times 10^{12}$), respectively. [14].

Species	$\tau \sim 0.2-1.0$				$\tau \sim 3 \times 10^{-4}$			
	[I] // n_{tot}	[II]/ n_{tot}	[III]/ n_{tot}	[IV]/ n_{tot}	[I]/ n_{tot}	[II]/ n_{tot}	[III]/ n_{tot}	[IV]/ n_{tot}
C	7.19	92.80	3.62×10^{-5}	6.89×10^{-23}	11.71	88.29	3.98×10^{-8}	1.26×10^{-33}
N	54.99	45.00	1.25×10^{-7}	3.37×10^{-26}	90.81	9.19	2.48×10^{-12}	1.37×10^{-38}
O	67.05	32.95	3.80×10^{-10}	4.66×10^{-32}	91.42	8.57	7.05×10^{-16}	5.07×10^{-47}
Mg	2.92×10^{-2}	90.96	9.00	5.11×10^{-34}	9.81×10^{-3}	99.03	0.95	2.04×10^{-49}
Al	0.05	99.55	0.39	3.33×10^{-9}	7.21×10^{-3}	99.98	6.41×10^{-3}	9.08×10^{-15}
Si	0.17	99.16	0.67	4.93×10^{-11}	6.96×10^{-2}	99.89	3.52×10^{-2}	3.99×10^{-17}
P	0.89	99.06	4.40×10^{-2}	1.51×10^{-11}	1.05	98.95	4.64×10^{-4}	1.18×10^{-17}
S	3.75	96.24	1.81×10^{-3}	8.82×10^{-15}	4.17	95.82	3.45×10^{-6}	1.36×10^{-22}
Ca	8.93×10^{-4}	17.85	82.15	1.19×10^{-17}	2.47×10^{-4}	33.20	66.79	3.84×10^{-26}
Sc	3.75×10^{-3}	33.45	66.55	9.85×10^{-6}	1.30×10^{-3}	64.10	35.89	5.14×10^{-9}
Ti	9.47×10^{-3}	53.52	46.47	1.19×10^{-6}	3.15×10^{-3}	85.55	14.44	9.81×10^{-11}
V	1.77×10^{-2}	73.85	26.13	1.16×10^{-7}	4.62×10^{-3}	96.02	3.98	1.97×10^{-12}
Cr	2.26×10^{-2}	87.75	12.23	1.09×10^{-8}	5.19×10^{-3}	99.32	0.67	3.07×10^{-14}
Mn	3.94×10^{-2}	92.43	7.53	9.33×10^{-10}	1.18×10^{-2}	99.39	0.59	1.04×10^{-15}
Fe	7.02×10^{-2}	96.02	3.91	1.08×10^{-9}	2.54×10^{-2}	99.74	0.23	3.77×10^{-15}
Co	0.11	97.68	2.21	7.21×10^{-11}	0.038	99.87	8.42×10^{-2}	4.21×10^{-17}
Ni	0.13	98.95	0.92	5.89×10^{-12}	4.08×10^{-2}	99.94	2.04×10^{-2}	9.10×10^{-19}
Cu	0.14	99.52	0.33	4.50×10^{-13}	4.53×10^{-2}	99.95	2.69×10^{-3}	1.15×10^{-20}
Zn	0.26	99.45	0.28	0.00	0.19	99.80	6.8×10^{-3}	0.00
Y	0.14	99.52	0.33	4.50×10^{-13}	4.53×10^{-2}	99.95	2.69×10^{-3}	1.15×10^{-20}
Zr	7.25×10^{-3}	40.00	59.98	3.62×10^{-4}	2.80×10^{-3}	73.47	26.52	3.58×10^{-7}
Mo	3.18×10^{-2}	82.40	17.56	1.58×10^{-6}	9.07×10^{-3}	98.78	1.21	3.37×10^{-11}
Ru	5.62×10^{-2}	97.81	2.13	8.38×10^{-9}	1.55×10^{-2}	99.89	9.36×10^{-2}	6.13×10^{-14}
Rh	6.79×10^{-2}	99.28	0.65	4.10×10^{-10}	1.92×10^{-2}	99.96	1.50×10^{-2}	4.63×10^{-16}
Sn	6.34×10^{-2}	94.83	5.10	1.42×10^{-8}	1.77×10^{-2}	99.35	0.63	1.11×10^{-13}
Ba	3.68×10^{-5}	2.20	97.80	0.00	3.38×10^{-6}	2.08	97.92	0.00
Yb	1.43×10^{-3}	24.08	75.91	1.10×10^{-3}	4.31×10^{-4}	45.69	54.29	6.67×10^{-7}
Os	0.17	98.05	1.79	1.98×10^{-6}	7.53×10^{-2}	99.85	6.98×10^{-2}	6.67×10^{-11}
Pt	0.31	99.41	0.27	7.88×10^{-9}	0.18	99.81	4.99×10^{-3}	3.01×10^{-14}
Au	0.43	99.54	2.59×10^{-2}	6.63×10^{-11}	0.28	99.71	1.89×10^{-4}	3.90×10^{-17}
Hg	0.94	98.84	0.21	0.00	1.09	98.90	3.5×10^{-3}	0.00
Pb	6.09×10^{-2}	83.37	16.57	4.04×10^{-9}	0.019	98.07	1.90	1.49×10^{-14}

Bibliography

- [1] Asplund, M., Grevesse, N., Sauval, A. J., & Scott, P. 2009, *ARA&A*, 47, 481
- [3] Aerts, C., Puls, J., Godart, M., & Dupret, M.-A. 2009, *Communications in Asteroseismology*, 158, 66
- [3] Aerts, C., Puls, J., Godart, M., & Dupret, M.-A. 2009, *Communications in Asteroseismology*, 158, 66
- [4] Aurière, M., Wade, G. A., Lignières, F., et al. 2010, *A&A*, 523, AA40
- [5] Borra, E. F., & Landstreet, J. D. 1980, *ApJS*, 42, 421
- [6] Cantiello, M., Langer, N., Brott, I., et al. 2009, *Communications in Asteroseismology*, 158, 61
- [7] Cowley, C. R. 1996, *M.A.S.S., Model Atmospheres and Spectrum Synthesis*, 108, 223
- [8] Hill, G. M., & Landstreet, J. D. 1993, *A&A*, 276, 142
- [9] Grevesse, N., Scott, P., Asplund, M., & Sauval, A. J. 2014, arXiv:1405.0288
- [10] Kramida, A., Ralchenko, Yu., Reader, J. and NIST ASD Team, 2014, NIST Atomic Spectra Database (version 5.2), [Online]. Available: <http://physics.nist.gov/asd> [Saturday, 24-Jan-2015 16:37:16 EST]. National Institute of Standards and Technology, Gaithersburg, MD
- [70] Kupka, F., Piskunov, N., Ryabchikova, T. A., Stempels, H. C., & Weiss, W. W. 1999, *A&AS*, 138, 119
- [100] Kupka, F. G., Ryabchikova, T. A., Piskunov, N. E., Stempels, H. C., & Weiss, W. W. 2000, *Baltic Astronomy*, 9, 590
- [71] Kurucz, R. L. 1970, *SAO Special Report*, 309,
- [14] Kurucz, R. L. 1979, *ApJS*, 40, 1
- [15] Lamers, H. J. G. L. M. 1981, *IAU Colloq. 59: Effects of Mass Loss on Stellar Evolution*, 89, 181
- [16] Lamers, H. J. G. L. M., Gathier, R., & Snow, T. P., Jr. 1982, *ApJ*, 258, 186

- [39] Wade, G. A., Bagnulo, S., Kochukhov, O., et al. 2001, *A&A*, 374, 265
- [40] Wade, G. A., Folsom, C. P., Petit, P., et al. 2014, arXiv:1407.3991
- [19] Landstreet, J. D. 1982, *ApJ*, 258, 639
- [20] Landsman, W. B. 1993, *Astronomical Data Analysis Software and Systems II*, 52, 246
- [21] Landstreet, J. D., Kupka, F., Ford, H. A., et al. 2009, *A&A*, 503, 973
- [74] Landstreet, J. D. 1988, *ApJ*, 326, 967
- [23] Landstreet, J. D., Barker, P. K., Bohlender, D. A., & Jewison, M. S. 1989, *ApJ*, 344, 876
- [24] Monier, R., Dubaj, D., & Richard, O. 2003, SF2A-2003: Semaine de l'Astrophysique Francaise, 605
- [25] Nieva, M.-F., & Simón-Díaz, S. 2011, *A&A*, 532, AA2
- [26] Nordlund, A., & Stein, R. F. 1995, *Liege International Astrophysical Colloquia*, 32, 75
- [99] Piskunov, N. E., Kupka, F., Ryabchikova, T. A., Weiss, W. W., & Jeffery, C. S. 1995, *A&AS*, 112, 525
- [28] Przybilla, N., Nieva, M.-F., & Butler, K. 2011, *Journal of Physics Conference Series*, 328, 012015
- [101] Piskunov, N., & Kupka, F. 2001, *ApJ*, 547, 1040
- [104] Ryabchikova, T. A., Piskunov, N. E., Kupka, F., & Weiss, W. W. 1997, *Baltic Astronomy*, 6, 244
- [31] Scott, P., Asplund, M., Grevesse, N., Bergemann, M., & Sauval, A. J. 2014, arXiv:1405.0287
- [32] Scott, P., Grevesse, N., Asplund, M., et al. 2014, arXiv:1405.0279
- [33] Varenne, O. 1999, *A&A*, 341, 233
- [34] Varenne, O., & Monier, R. 1998, *Ultraviolet Astrophysics Beyond the IUE Final Archive*, 413, 289
- [35] Shorlin, S. L. S., Wade, G. A., Donati, J.-F., et al. 2002, *A&A*, 392, 637
- [36] Wahlgren, G. M., & Leckrone, D. S. 2009, *Bulletin of the American Astronomical Society*, 41, #408.05
- [37] Wahlgren, G. M., & Leckrone, D. S. 2008, *Contributions of the Astronomical Observatory Skalnaté Pleso*, 38, 463
- [38] Woodgate, B. E., Kimble, R. A., Bowers, C. W., et al. 1998, *PASP*, 110, 1183
- [39] Wade, G. A., Bagnulo, S., Kochukhov, O., et al. 2001, *A&A*, 374, 265
- [40] Wade, G. A., Folsom, C. P., Petit, P., et al. 2014, arXiv:1407.3991

Chapter 4

IR Spectroscopy of AGB Stars in the Galactic Bulge

4.1 Introduction

In the dust (and gas) budget of the galaxy, stars on the Asymptotic Giant Branch (AGB) play a major role [see 37, 31, 34, for reviews about various aspects of AGB phase]. During this stellar phase, stars with initial masses between $\sim 0.8\text{--}8\text{ M}_{\odot}$ lose much of their mass through a dust-driven wind, and eventually end up as slowly cooling white dwarfs with core masses between $\sim 0.5\text{--}1.4\text{ M}_{\odot}$ [see e.g. 45, 55]. In fact, while the details are not well understood, the evolution of the star in this phase is thought to be dominated by mass loss from the surface rather than nuclear burning in the interior. The mass-loss process on the AGB is thought to be initiated by stellar pulsations which transport material high above the photosphere while it cools down, allowing small dust particles to nucleate and grow. Radiation pressure rapidly accelerates these dust grains and the gas is dragged along. This results in slow ($5\text{--}20\text{ km s}^{-1}$), massive ($10^{-8}\text{--}10^{-4}\text{ M}_{\odot}\text{ yr}^{-1}$) outflows which last for some 10^6 yr , amounting to $0\text{--}0.07\text{ M}_{\odot}$ of dust (and $0.3\text{ to }7\text{ M}_{\odot}$ of gas) [89, 26].

As a result of this mass loss, the IR spectral appearance of AGB stars – as well as their evolutionary ‘daughters’, the post-AGB objects and planetary nebulae – is dominated by the dust ejected during the AGB phase. Previous space-based studies (*IRAS* and *ISO*) have revealed a large variety of dust materials in these types of objects, including aluminium-oxides [58, 7], magnesium-iron oxides [7, 67], and various crystalline and amorphous silicates [for a review on *ISO* results see 1]. However, while there is some observational evidence that these compositional variations are related to the mass-loss rate, the origin of these variations and the physical and chemical processes driving this complexity are not well understood.

Stardust forms through chemical nucleation and growth in cool ($\sim 1000\text{ K}$), dense ($\sim 10^8\text{ cm}^{-3}$) gas. Theoretical studies on dust formation have a long history in astrophysics dating back to Salpeter [71] for stellar ejecta and Grossman & Larimer [30] for the solar nebula. These and subsequent studies [75, 48] rely on thermodynamic condensation sequences to predict the compounds formed and the fraction of mass locked up in them. For O-rich ejecta, these thermodynamic studies predict that dust formation starts with the formation of very refractory oxides (aluminium-oxide, spinel) at a temperature of $\sim 1500\text{ K}$. Through a variety of gas-solid and

solid-solid interactions, these compounds are then transformed into calcium-aluminium silicates when the out-flowing gas cools further. At about 1200 K, the majority of the silicon will condense first as magnesium-rich olivine (forsterite, Mg_2SiO_4), which reacts with excess gaseous silicon to transform into pyroxene (enstatite, MgSiO_3).

There is qualitative confirmation of these predictions for dust formation in stellar ejecta. Several observations, mostly IRAS/LRS and *ISO/SWS* have revealed the presence of many different dust compounds in O-rich AGB stars [86, 64, 77, 87, 79, 21, 7, 67, 6] and many – but not all – of these compounds are part of the theoretical condensation sequence. Indeed, AGB stars with high mass-loss rates show copious amounts of silicates, including crystalline olivines and pyroxenes. The spectra of AGB stars with low mass-loss rates, on the other hand, only show evidence for spinel, aluminium-oxide and magnesium-iron oxides [6, 46]. This difference in spectral structure of AGB stars is thought to reflect the rapid “freeze-out” of the dust condensation sequence, a term used to indicate that the densities in the dust formation zone are too low for certain condensation reactions to occur, and therefore the dust condensation sequence stops at an intermediate step.

Thus, studying a sample of similar stars but with different mass-loss rates is a powerful way to probe the dust condensation sequence observationally, as the freeze-out will occur at different densities and therefore stop the condensation sequence at different intermediate steps. The galactic bulge offers an interesting opportunity to select such a sample, and the sensitivity of the *Spitzer* Space Telescope allows to study galactic bulge AGB stars in great detail.

The homogeneity and completeness of our sample can be ensured by carefully selecting stars which have been detected by the ISOGAL survey [63]. ISOGAL is the second largest survey program performed with the *ISO* satellite [47] and provides a point source catalog in 5 wavelength bands and includes near-infrared [DENIS, 20], 7 and 15- μm photometry. This survey covered about 16 square degrees in the inner galaxy down to a sensitivity of 10 – 20 mJy in the mid-infrared and $\sim 10^5$ sources were detected which are mostly AGB stars, red giants and YSOs. The survey is complete for sources which are brighter than 9 magnitudes at 7- μm and 8 magnitudes at 15- μm [63].

An interesting subset are those ISOGAL sources from fields in the “intermediate” Galactic bulge ($|l| < 2^\circ$ and $|b| \approx 1^\circ - 4^\circ$). Stars at these latitudes in the direction of the bulge are believed to belong to the bulge stellar population which only shows a small range in masses. These giants have evolved from a population of stars of $\approx 1.5 - 2 M_\odot$ [29, 6]. Omont et al. [62] and later Ojha et al. [60] demonstrated that all sources detected in these fields are AGB stars or stars at the tip of the Red Giant Branch, and that the ISOGAL $K_{s,0} - [15]$ colours can be translated into mass-loss rates (see Fig. 4.1). Radiative transfer modelling of a subset of ISOGAL sources for which ISOCAM CVF (5–17- μm) data were available [6] showed that the lowest mass-loss rates detected are $\gtrsim 10^{-8} M_\odot \text{ yr}^{-1}$. As the ISOGAL sample is complete in terms of magnitudes, it is also complete for the lowest mass-loss rates ($\gtrsim 10^{-8} M_\odot \text{ yr}^{-1}$); therefore, AGB stars from the Galactic bulge which are detected in the ISOGAL sample cover the full range of mass-loss rates. It starts from the onset of dusty mass loss ($\sim 10^{-8} M_\odot \text{ yr}^{-1}$) and covers up to the mass-loss rates of $\sim 10^{-4} M_\odot \text{ yr}^{-1}$ associated with the so-called super-wind phase in OH/IR type AGB stars [see e.g. 84].

With all the stars in these fields originating from about $1.5 M_\odot$ stars, the main difference between these objects is their age on the AGB, and colour-magnitude diagrams of these stars as the one presented in Fig. 4.1 effectively correspond to the evolutionary track on the AGB for

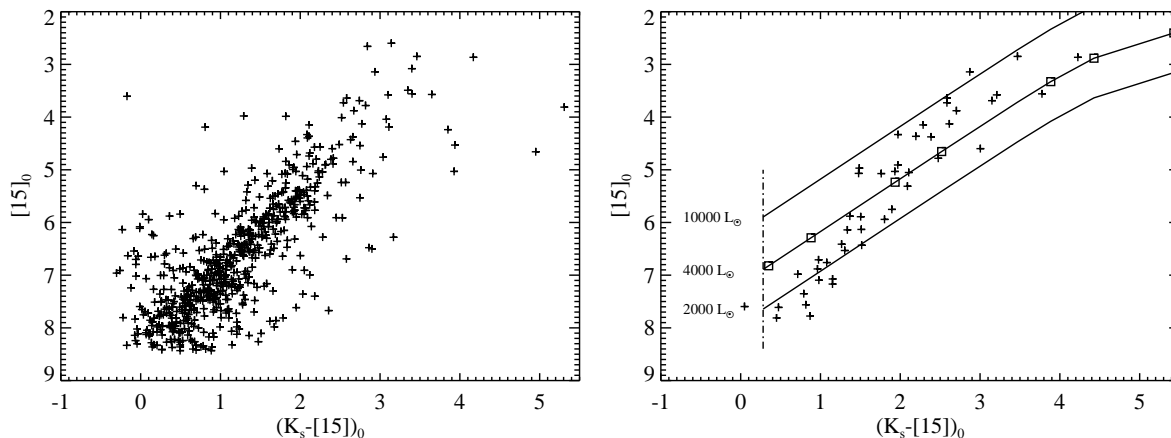


Figure 4.1: $[15]/K_{s,o}-[15]$ colour-magnitude diagrams for all sources detected in our selected ISOGAL fields (left panel) showing a linear sequence of increasingly redder colours (and thus mass-loss rates) for brighter $15\text{-}\mu\text{m}$. The right panel shows the representative sample that we have selected. For comparison, we show three tracks corresponding to AGB stars with luminosities of 2000, 4000, and 10,000 L_{\odot} (bottom, middle and top curve respectively) and with mass loss rates increasing from 10^{-9} to $3 \times 10^{-6} \text{ M}_{\odot}\text{yr}^{-1}$ (squares on the 4000 L_{\odot} track indicate mass-loss rates of 10^{-9} , 10^{-8} , 5×10^{-8} , 10^{-7} , 5×10^{-7} , 10^{-6} and $3 \times 10^{-6} \text{ M}_{\odot}\text{yr}^{-1}$). The tracks were obtained using a mixture of amorphous silicate and aluminium-oxide dust [see 24, 25, for the radiative transfer models]. The vertical dot-dashed line represents a track of increasing luminosity without mass loss. Note that the six OH/IR stars in our sample that were selected from IRAS have no corresponding 2MASS and ISOGAL fluxes and are therefore not shown in this CMD (Figures Taken From [6], with permission)

a 1.5 M_{\odot} star, characterized by varying luminosities and mass-loss rates [see e.g. 23]. These fields therefore offer unique opportunities to study the evolution of 1.5 M_{\odot} stars and their circumstellar material as they evolve on the AGB.

Here, we present a first analysis of *Spitzer* observations of a sample of AGB stars, selected from these bulge fields. This sample is the core of an observational program whose main scientific goal is to study the variations in the dust composition as a function of mass loss rate and other fundamental stellar parameters. We present the selection criteria and the sample of stars in § 4.2. The *Spitzer-IRS* observations and the data reduction steps are detailed in § 4.3. In § 4.4, we describe the strong and variable emission of interstellar dust that contaminates our observations. In § 4.5, we describe the spectra, and focus in particular on the “naked stars” – objects without dust emission. These prove particularly useful to characterize the contribution of the star and the molecular layers to the infrared spectra, and to assess the effect of interstellar extinction in § 4.6. We characterize our sample in § 4.7 and present the resulting dust emission spectra in § 4.8. We summarize our findings in § 4.9.

Table 4.1: Basic data for our sample of galactic bulge AGB stars.

ID	Object ^a	RA [J2000]	Dec [J2000]	<i>b</i> [deg]	<i>l</i> [deg]	<i>J</i> [mag]	<i>H</i> [mag]	<i>K_s</i> [mag]	[7] [mag]	[15] [mag]	AOR key
c32-1	J174117.5-282957	17:41:17.50	-28:29:57.5	1.037	359.874	9.702	7.872	6.996	5.36	4.42	10421504
c32-2	J174122.7-283146	17:41:22.70	-28:31:47.0	1.005	359.858	3.47	1.54	10421504
c32-3	J174123.6-282723	17:41:23.56	-28:27:24.2	1.041	359.922	10.715	8.993	8.245	7.57	6.98	10422784
c32-4	J174126.6-282702	17:41:26.60	-28:27:02.2	1.034	359.933	11.557	9.285	7.895	5.44	3.83	10421504
c32-5	J174127.3-282851	17:41:27.26	-28:28:52.1	1.016	359.908	10.008	8.306	7.304	5.78	4.40	10421504
c32-6	J174127.9-282816	17:41:27.88	-28:28:17.1	1.019	359.918	9.569	7.828	7.016	6.30	5.24	10421504
c32-7	J174128.5-282733	17:41:28.51	-28:27:33.8	1.024	359.929	9.580	7.968	7.107	6.41	5.34	10421504
c32-8	J174130.2-282801	17:41:30.15	-28:28:01.3	1.015	359.926	11.353	9.662	8.880	7.77	7.44	10422784
c32-9	J174134.6-282431	17:41:34.60	-28:24:31.4	1.032	359.984	10.902	9.137	8.163	5.97	4.87	10421504
c32-10	J174139.5-282428	17:41:39.48	-28:24:28.2	1.017	359.994	9.528	7.801	6.874	5.34	4.00	10421504
c32-11	J174140.0-282521	17:41:39.94	-28:25:21.2	1.008	359.982	9.630	7.977	7.143	6.09	4.15	10421504
c32-12	J174153.3-281638	17:41:55.27	-28:16:38.7	1.037	0.135	9.610	7.739	6.785	5.61	3.91	10421504
c32-13	J174157.6-282237	17:41:57.53	-28:22:37.7	0.977	0.055	9.852	8.272	7.438	6.74	5.18	10421504
c32-14	J174158.8-281849	17:41:58.73	-28:18:49.2	1.007	0.111	10.160	8.415	7.348	5.57	3.85	10421504
c32-15	J174203.7-281729	17:42:03.69	-28:17:29.9	1.003	0.139	10.262	8.501	7.398	5.38	3.96	10421504
c32-16	J174206.85-281832	17:42:06.86	-28:18:32.4	0.984	0.131	9.641	7.893	6.878	4.82	3.12	10421504
c35-1	J174917.0-293502	17:49:16.96	-29:35:02.7	-1.019	359.859	10.869	9.157	8.199	7.40	6.49	10421248
c35-2	J174924.1-293522	17:49:23.99	-29:35:22.2	-1.044	359.868	10.466	9.030	8.417	7.55	7.33	10421248
c35-3	J174943.7-292154	17:49:43.65	-29:21:54.5	-0.989	0.097	10.810	8.889	7.970	6.97	6.23	10421248
c35-4	J174948.1-292104	17:49:48.05	-29:21:04.8	-0.996	0.117	11.401	9.520	8.560	7.75	7.11	10421248
c35-5	J174951.7-292108	17:49:51.65	-29:21:08.7	-1.008	0.122	10.829	9.043	8.116	7.39	6.24	10421248
Ogle-1	J175432.0-295326	17:54:31.94	-29:53:26.5	-2.156	0.176	8.906	7.623	6.957	6.00	4.49	10422528
Ogle-2	J175456.8-294157	17:54:56.80	-29:41:57.4	-2.137	0.387	8.827	7.438	6.757	5.81	4.48	10422528
Ogle-3	J175459.0-294701	17:54:58.98	-29:47:01.4	-2.186	0.318	10.422	8.530	7.287	4.88	2.98	10422528
Ogle-4	J175511.9-294027	17:55:11.90	-29:40:27.8	-2.171	0.436	10.422	9.254	8.841	8.17	7.89	10423040
Ogle-5	J175515.4-294122	17:55:15.41	-29:41:22.8	-2.190	0.429	10.005	8.770	8.271	7.79	7.21	10423040
Ogle-6	J175517.0-294131	17:55:16.97	-29:41:31.9	-2.196	0.430	9.371	8.339	7.839	7.65	7.71	10423040
Ogle-7	J175521.7-293912	17:55:21.70	-29:39:13.0	-2.192	0.472	8.56	...	10423040
NGC 6522-1	J180234.8-295958	18:02:34.78	-29:59:58.9	-3.722	0.950	8.177	6.894	6.146	4.66	3.22	10421760
NGC 6522-2	J180238.8-295954	18:02:38.72	-29:59:54.6	-3.734	0.958	9.411	8.327	7.780	7.31	5.83	10421760
NGC 6522-3	J180248.9-295430	18:02:48.90	-29:54:31.0	-3.722	1.054	9.574	8.485	7.969	7.62	6.61	10422016
NGC 6522-4	J180249.5-295853	18:02:49.44	-29:58:53.4	-3.759	0.992	9.932	8.953	8.512	8.15	7.64	10422272
NGC 6522-5	J180259.6-300254	18:02:59.51	-30:02:54.3	-3.824	0.951	9.070	7.880	7.391	6.79	4.86	10421760
NGC 6522-6	J180301.6-300001	18:03:01.60	-30:00:01.1	-3.807	0.997	9.773	8.661	8.219	7.94	7.69	10422272
NGC 6522-7	J180304.8-295258	18:03:04.80	-29:52:59.3	-3.760	1.105	9.888	8.792	8.395	8.02	7.89	10422272
NGC 6522-8	J180305.3-295515	18:03:05.25	-29:55:15.9	-3.780	1.072	8.714	7.620	7.098	6.49	5.11	10421760
NGC 6522-9	J180305.4-295527	18:03:05.33	-29:55:27.8	-3.782	1.070	9.293	8.243	7.810	7.54	6.49	10422016
NGC 6522-10	J180308.2-295747	18:03:08.11	-29:57:48.0	-3.809	1.040	9.470	8.360	7.777	7.16	6.21	10422016
NGC 6522-11	J180308.6-300526	18:03:08.52	-30:05:26.5	-3.873	0.930	8.077	7.064	6.437	5.85	4.41	10421760
NGC 6522-12	J180308.7-295220	18:03:08.69	-29:52:20.4	-3.767	1.121	9.492	8.417	7.878	7.40	6.02	10421760
NGC 6522-13	J180311.5-295747	18:03:11.47	-29:57:47.2	-3.820	1.047	9.353	8.200	7.535	6.53	5.39	10421760
NGC 6522-14	J180313.9-295621	18:03:13.88	-29:56:20.9	-3.816	1.072	9.407	8.398	7.978	7.70	6.96	10422016
NGC 6522-15	J180316.1-295538	18:03:15.99	-29:55:38.3	-3.817	1.086	9.752	8.744	8.276	7.90	7.43	10422272
NGC 6522-16	J180323.9-295410	18:03:23.84	-29:54:10.7	-3.830	1.121	9.536	8.543	8.082	7.59	6.51	10422016
NGC 6522-17	J180328.4-295545	18:03:28.36	-29:55:45.4	-3.856	1.106	8.999	7.879	7.291	6.74	5.13	10421760
NGC 6522-18	J180333.3-295911	18:03:33.26	-29:59:11.5	-3.900	1.065	9.832	8.795	8.357	8.06	7.15	10422016
NGC 6522-19	J180334.1-295958	18:03:34.07	-29:59:58.8	-3.909	1.055	8.658	7.520	6.967	6.50	5.15	10421760
IRAS-17251	IRAS-17251-2821	17:28:18.50	-28:23:55.8	3.492	358.414	10423296
IRAS-17276	IRAS-17276-2846	17:30:48.31	-28:49:01.9	2.801	358.367	6080768
IRAS-17323	IRAS-17323-2424	17:35:26.00	-24:26:32.0	4.310	2.613	10423808
IRAS-17347	IRAS-17347-2319	17:37:46.28	-23:20:52.8	4.442	3.826	6080000
IRAS-17413	IRAS-17413-3531	17:44:43.45	-35:32:34.3	-3.281	354.260	6081280
IRAS-18042	IRAS-18042-2905	18:07:24.40	-29:04:48.0	-4.191	2.266	10424576

^aReferences:Omont et al. [63], Ojha et al. [60], Blommaert et al. [6].

Note: The [7] and [15] magnitudes are taken from the ISOGAL catalogue and have uncertainties of typically 0.15 mag [72].

The 2MASS *J*, *H* and *K_s* magnitudes have uncertainties in the order of 0.03 mag, also included is the Spitzer-IRS observing date.

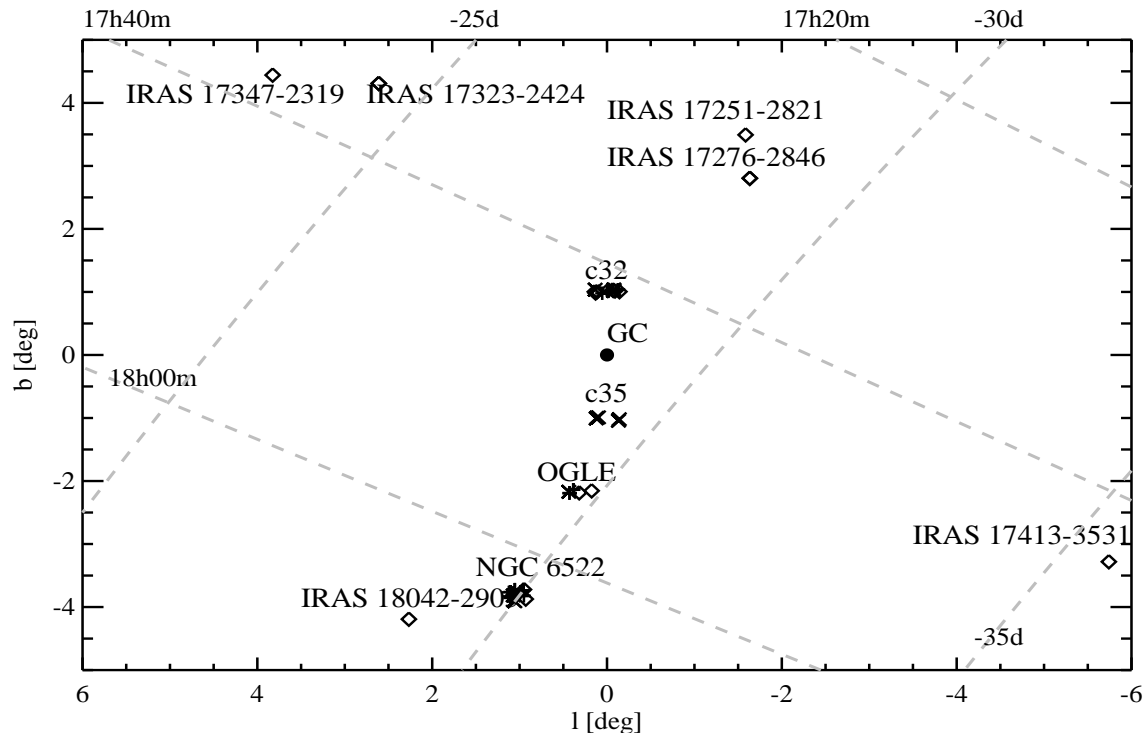


Figure 4.2: The location of our targets in galactic coordinates. Note that targets in c32 and c35 are at roughly the same angular distance (about one degree) to the galactic centre.

4.2 The sample selection

ISO/SWS studies of nearby O-rich AGB stars have revealed the presence of at least 5 distinct dust components in the wavelength range 8–27- μm [see e.g. 7], and several more features at wavelengths longer than 30- μm [an overview can be found in 1]. Typically, oxide dust dominates the spectra of stars with low mass-loss rates; while high mass-loss rate objects exhibit strong silicate emission. From these differences in the dust composition and given the range in mass-loss rates for these objects, we estimate that we need a sample of ~ 15 sources per logarithmic bin in mass-loss rate to fully sample these variations in a statistically significant way.

Ojha et al. [60] and Blommaert et al. [6] showed that the $K_{s,o} - [15]$ colour is a good tracer for mass-loss rates for AGB stars in the ISOGAL fields (see also Fig. 4.1). We therefore selected our targets based on their $K_{s,o} - [15]$ colour. We included sources with $K_{s,o} - [15]$ values close to zero to ensure that we can trace the dust at the onset of mass loss. From the Bulge fields in the ISOGAL sample (c32, c35, the OGLE field and NGC 6522), we thus selected 47 sources. We also included OH/IR stars to represent the highest mass-loss rates on the AGB. Since the super-wind phase is extremely short (less than 10,000 years), OH/IR stars are rare in the ISOGAL bulge fields and we therefore have included 6 OH/IR stars detected with *IRAS*, to complete our sample on the high mass-loss rate end. These OH/IR stars were selected from the same latitude range as our ISOGAL sources and have similar luminosities as the Miras in our sample. Thus, we expect that these OH/IR stars belong to the same population. Our

final sample of 53 sources then cover ~ 4 orders of magnitude in mass-loss rate ($10^{-8} - 10^{-4} M_{\odot} \text{ yr}^{-1}$). The complete list of our sample targets is presented in Table 4.1; their position in galactic coordinates is indicated in Fig. 4.2.

We also obtained ground-based J , H , K_s , and L -band photometry as well as spectroscopic observations (PRW on the ANU 2.3-m telescope at *Siding Spring* Observatory) to accurately determine the pulsation phase and to have consistent photometry for composing spectral energy distributions. A monitoring program is performed in the K-band to establish pulsational periods of the AGB variables. These ground based data will be described in a separate paper.

4.3 Observations and data reduction

We observed our targets with the Infrared Spectrograph [IRS, 39] on board the *Spitzer* Space Telescope [127] as part of a General Observer program (GO-1, program ID 3167, P.I. J. Blommaert) and a Director’s Discretionary Time program (program ID 1094, P.I. F. Kemper). Table 4.1 lists the unique Astronomical Observation Request (AOR) key for all observations.

All targets were observed using the IRS Staring Mode observing template at low resolution ($\lambda/\Delta\lambda \sim 60 - 125$). We covered the entire wavelength range (5.2–38- μm) by observing each target with the Short-Low module (SL, 5.2–14- μm) and the Long-Low module (LL, 14.0–38- μm). Using this template, each target is observed at two different nod positions within each of the different IRS sub-slits (SL1, SL2, LL1, LL2). Furthermore, we obtained at least 3 individual exposures for each nod position in order to reliably identify cosmic rays. We reduced the *Spitzer*-IRS observations using the SMART package [40] and custom IDL routines, starting from the pipeline level of Basic Calibrated Data (BCD; S18.18 products). The data reduction process involves removing bad pixels; subtracting background emission from the images; extracting the spectra; correcting for instrumental fringes; flux calibration and scaling of the modules, trimming the order edges and rebinning.

We first used IRSclean to treat rogue pixels using the campaign rogue masks as well as the bad pixel maps associated with each individual exposure. When necessary, we also used the routine `irsclean_mask` to flag additional bad pixels. We then co-added the cleaned images for each nod using a weighted average [see 40].

The next step in the data reduction process is subtraction of the background emission due to interstellar dust. For many of our targets, this is quite a challenging aspect since the galactic bulge is a very crowded region with a highly structured and varying background. Indeed, most of our observations exhibit strong background emission with many spectral features that furthermore show significant wavelength-dependent variations on small spatial scales – often even within the IRS low-resolution slit (see Fig. D.1 and § 4.4). In several cases, a proper characterization of this background emission and its variation is further complicated by the contamination of other sources in the slit. We removed this background using a combination of methods described in details in Appendix D. Note that in the slit before extraction or calibration, the background level is of the order of typically 100e/pix while the source is 1000 e/pix, so that can introduce up to 10% uncertainty to the final spectra.

For each sub-slit, we then extracted the spectrum using optimal extraction [73] in the SMART data reduction package. Using an earlier version of the IRS calibration files, we noticed that optimal extraction resulted in spurious features near 17.4 and 18.9- μm (in the

LL2 data) for sources that are slightly offset from the nominal position. These can be residuals of background subtraction or due to imperfections in the relative spectral response function (RSRF) for offset sources. The most recent (S18.18) RSRF and flux calibration files largely solve this problem, although a few targets still show weak artifacts near these wavelengths. An additional problem for sources that are slightly offset from the nominal position, is that there is often a mismatch (in some cases of up to 20%) between the flux levels of the two different nods of the SL1 sub-slit after optimal extraction. These discrepancies can be largely removed by generating a customized point spread function corresponding to the specific offset position [see 73, for more details]. We thus generated these “on-the-fly” point spread functions for all sources showing such a mismatch.

The extracted spectra often exhibit instrumental fringes in the LL1 sub-slit. We used the `IRSfringe` routine to remove these as much as possible; however, weak fringe residuals remain in a few spectra.

For most of our targets, the extracted spectra for the different orders and modules have comparable flux levels in adjacent (or overlapping) wavelength ranges; in some cases, small flux differences (typically a few percent) are present within nods as well as in adjacent modules. We scaled the nods to their common median, and adjacent modules to the median in overlapping ranges, using the flux in the SL1 module (where most of our targets reach their peak flux) as a reference. Many spectra still show a few spikes at this point resulting from cosmic ray hits or insufficient bad pixel removal. We removed those points from our spectra, and also trimmed the edges of each sub-slit spectrum. Finally, we rebinned the data to a single spectrum with a constant resolving power of 120. The resulting full 5–38- μm spectra are shown in Appendix G, along with earlier *IRAS* and *ISO* photometry data. The spectra overall show a reasonable correspondence with these earlier measurements. We also compared our spectra to those available from the Cornell Atlas of *Spitzer-IRS* sources [CASSIS, 50]. The agreement is very good; in several cases, our detailed inspection of the processing issues has resulted in a somewhat better data quality.

In the spectra of OH/IR targets, the 10- μm feature appears in absorption due to the presence of an optically thick circumstellar dust shell. The spectra is presented later in Figure 4.11 in § 4.7 along with the rest of the sample however these targets are excluded from the study presented in this paper.

4.4 Interstellar emission towards the galactic bulge

Although the focus of our research program is on dust formation in AGB stars, our observations serendipitously include a large number of interstellar emission spectra in the general direction of the galactic bulge. In fact, we have more and better spectra of this interstellar emission than we have AGB observations. For each staring mode observation, our target will only be visible in one of the orders at a time, but the other order still contains a spectrum of the interstellar emission at a slightly offset location. We thus applied our background fitting (see § 4.3) to each of the orders for each observations. We extracted calibrated interstellar emission spectra from these background fits using CUBISM [78].

Fig. 4.3 shows the average interstellar emission for each of the four bulge fields. All spectra show a thermal dust continuum; for the OGLE field and NGC 6522, this continuum reaches

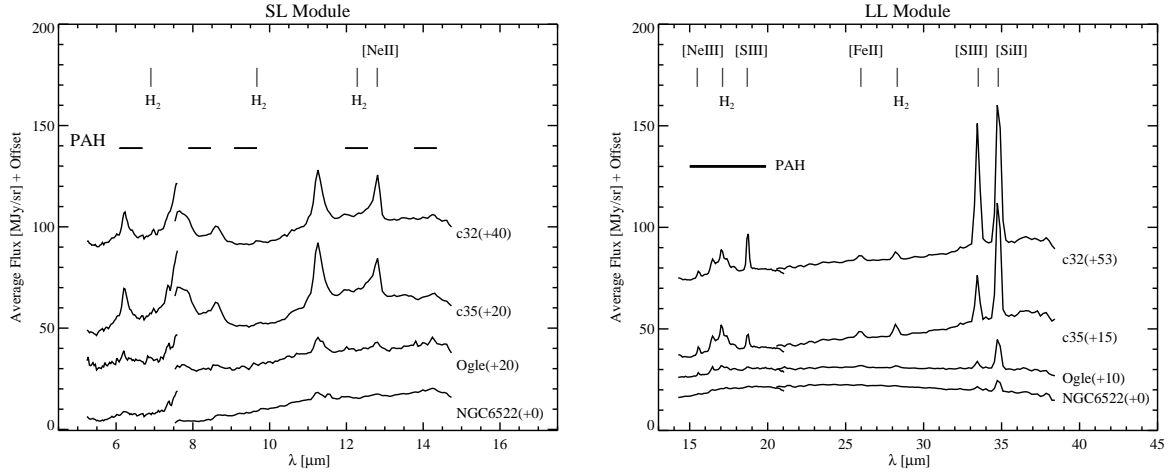


Figure 4.3: The (average) interstellar emission spectra for each of the fields. Note how the spectra reveal significant changes in the excitation conditions for the interstellar gas and dust for the different fields as one moves away from the galactic centre. Note that depending on telescope pointing accuracy, there can be mismatch between SL2/SL1, SL1/LL2, or LL2/LL1.

its maximum between 20 and 30- μm ; for c32 and c35 on the other hand, the continuum is still rising up to 35- μm (and it is not clear what happens at longer wavelengths). Superposed on this dust continuum is emission from polycyclic aromatic hydrocarbons [PAHs, see e.g. 66, 81], exhibiting their usual features at 6.2, 7.7, 8.6, 11.2 and 12.7- μm , as well as plateau emission between 15–20- μm with additional features at 16.4 and 17.4- μm . The spectra also reveal several atomic emission lines: [Ne II] at 12.8- μm ; [Ne III] at 15.5- μm ; [S III] at 18.7 and 33.5- μm ; [Fe II] at 25.99- μm and [Si II] at 34.8- μm . In addition, several H_2 lines (at 6.90, 9.66, 12.27, 17.03 and 28.2- μm) are present as well. A very weak silicate emission feature at 9.7- μm may be present, most notably in the spectra of c32 and c35 (see Tielens [81] for a review on PAHs in the ISM or Kemper et al. [44] for a comparison to LMC).

A first look at the variations in these interstellar spectra reveals different local excitation conditions. This can be inferred for example from the changes in the [S III](33.5- μm)/[Si II](34.8- μm) line flux ratio. At the same time, the characteristics of the PAH emission change quite dramatically, from very weak emission in NGC 6522 to very strong features (and pronounced 15–20- μm emission) when moving in closer to the galactic centre. This suggests that most of the interstellar emission originates from material in the bulge itself, rather than from the interstellar medium in the solar neighborhood. An in-depth analysis of these interstellar spectra will be presented elsewhere.

4.5 Stellar and molecular contributions

The target spectra show a great variety in the appearance of spectral features; it is interesting to note that most spectra are dominated by features that are typically found in an oxygen-rich environment (e.g. H_2O , SiO) while the typical carbon-rich species (e.g. HCN , C_2H_2 , etc.) are not evidently present. Longward of 10- μm , most of our spectra show various emission fea-

tures originating from circumstellar dust (see § 4.8.2). To obtain the pure dust emission spectra from these observations, we need a good knowledge of the underlying emission and absorption characteristics from the AGB star and the surrounding warm molecular layers [see e.g. 82, 7]. For an AGB photosphere at the mid-IR wavelengths studied here, continuum opacity is dominated by H^- , and in that case, the resulting IR continuum can be represented analytically by a modified blackbody function [19]. However, many of these objects have significant amounts of water in their extended photospheres or in dense molecular layers. Since water has a near-continuous opacity in the mid-IR, the continuum is often effectively determined by these water layers. In addition, molecular features (most notably of SiO) can have a profound effect on the shape of the dust features, especially near $10\text{-}\mu\text{m}$. Thus, a detailed inventory and discussion of the molecular content in these targets is appropriate. We will give particular attention to those targets that do not show obvious dust emission and are therefore “naked stars”. A good understanding of the properties of these objects will be of great help in obtaining the dust spectra for the other targets.

We point out here that some of our observations at the same time reveal the clear imprint of interstellar extinction as well, most visibly so as weak absorption around $10\text{-}\mu\text{m}$ in the spectra of our naked stars. Extinction has the potential to dramatically affect our analysis of the resulting dust spectra since many minerals in the circumstellar environment of AGB stars also exhibit features around $10\text{-}\mu\text{m}$. This greatly complicates our analysis. As will become clear, a good knowledge of the molecular bands is helpful to quantify the effect of extinction (see § 4.6), and is thus also facilitated by the study of our naked stars.

4.5.1 Molecular bands: Inventory

Previous space-based missions have revealed that O-rich AGB stars are surrounded by warm layers that are rich in molecules. The most commonly detected molecules in the near-IR to mid-IR range are H_2O , OH, CO, CO_2 , SiO and SO_2 [see e.g. 43, 9, 70, 90, 91, 18, 41, 57, 1], and most of those are also prominently present in our *Spitzer* spectra (see Fig. 4.4). The only exception is CO since the fundamental of CO (at $4.6\text{-}\mu\text{m}$) is not covered by IRS. At the resolution of our IRS spectra, detailed line profiles are somewhat smeared out, but the molecular bands often leave a noticeable and recognizable footprint in the spectra of our target stars.

The most important molecular component in these spectra is water vapor. In the wavelength range presented in Fig. 4.4, water reveals its presence by a fairly sharp drop in the flux near $6.5\text{-}\mu\text{m}$ corresponding to a strong increase in the water opacity. At longer wavelengths and at the low resolution of our observations, the variations in the water opacity can result in a broad emission-like feature centered around $10\text{-}\mu\text{m}$ (see Fig. 4.6) in pure water absorption spectra. A good characterization of the water absorption over the entire spectrum (but in particular under the $10\text{-}\mu\text{m}$ dust feature) is thus crucial for dust studies.

The SiO fundamental mode will also affect the dust spectra. SiO is a very abundant molecule in the atmospheres of AGB stars [61]. Models show that significant amounts of SiO are formed in stellar atmospheres with effective temperatures of ~ 4000 K and less [1]. SiO is also a primary constituent for oxygen-rich dust and can be considered a prerequisite for dust production [52, and references therein]. At the typical temperatures for the AGB atmospheres and molecular layers, SiO appears as a deep and broad absorption band with a clear band head

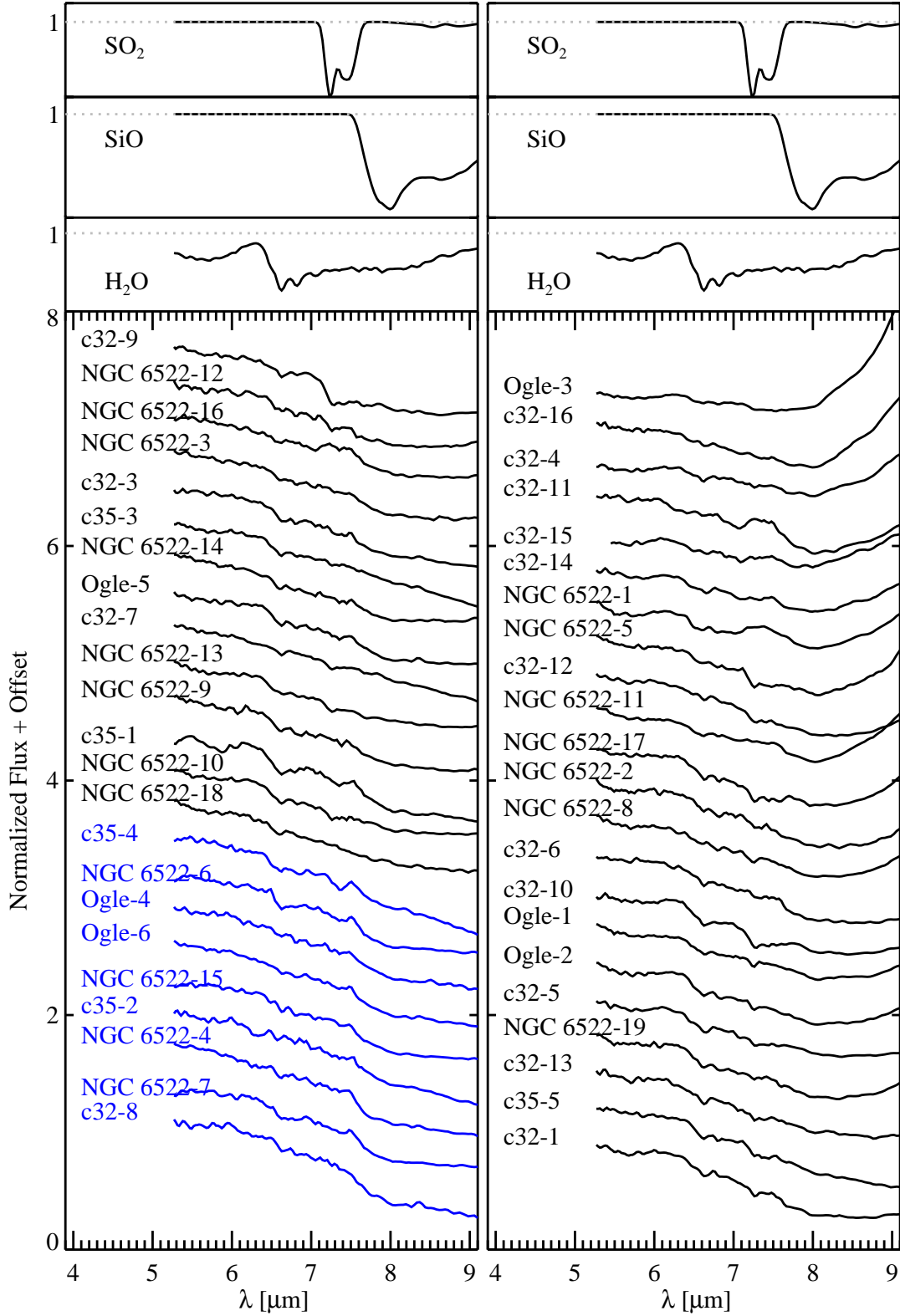


Figure 4.4: All our target spectra in the wavelength range $5\text{--}9\text{-}\mu\text{m}$, showing the main molecular bands. The spectra are normalized to the flux at $6\text{-}\mu\text{m}$, and are shown in order of increasing flux ratio at $10\text{-}\mu\text{m}$ to $6\text{-}\mu\text{m}$ (see § 4.6, This ratio is taken from the fully corrected spectra and is the same as Fig. 4.15). Stars that we have classified as naked stars are shown in blue. For comparison, the top panel shows a few model spectra for the three most common molecular species (H_2O , SiO and SO_2).

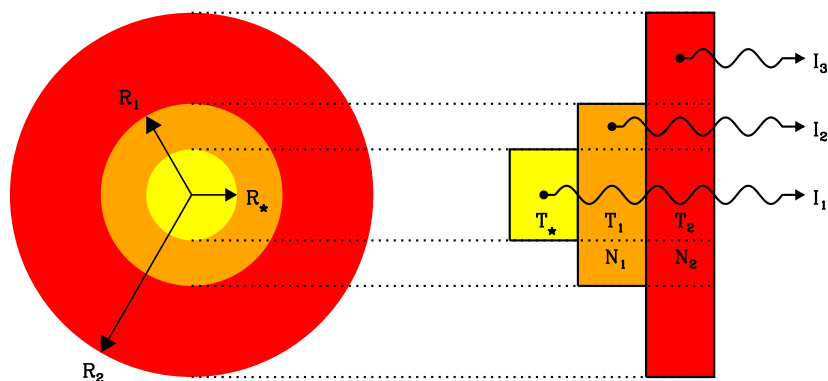


Figure 4.5: This figure illustrates how plane-parallel slab models can be used as an approximation to a spherical geometry when analyzing the molecular bands around AGB stars. The leftmost slab (yellow) represents the stellar photosphere; the other two slabs are molecular layers characterized by their own temperature and column densities of contributing species. Radiative transfer is calculated along the three indicated rays. Changing the size of the layers changes the relative importance of emission to absorption. Figure taken from Cami [8] (with permission).

at $7.55\text{-}\mu\text{m}$, and with a red wing that can extend to $10\text{--}12\text{-}\mu\text{m}$. SiO can therefore significantly alter the profile of dust features in the $10\text{-}\mu\text{m}$ region (see Fig. 4.4).

One molecular band that does not affect the dust spectrum much is the SO_2 ν_3 band at $7.3\text{-}\mu\text{m}$. This band has been detected in the *ISO/SWS* spectra of some oxygen-rich AGB stars [91], and can appear in absorption or in emission. Even at the low resolution of our observations, a close inspection of the spectra in Fig. 4.4 clearly show the weak presence of this band in some of our targets – sometimes in absorption (e.g. NGC 6522-17), sometimes in emission (e.g. c32-11). The SO_2 band is relatively narrow and ends at about $7.7\text{-}\mu\text{m}$, which is well before the onset of dust features. SO_2 emission or absorption will thus not affect the resulting dust spectra much, but may make it harder to characterize the onset of the SiO band which is in the middle of the SO_2 band.

Finally, we should note that our observations also include the wavelength range in which CO_2 exhibits its bending mode around $15\text{-}\mu\text{m}$, as well as several strong combination bands at 13.48 , 13.87 and $16.18\text{-}\mu\text{m}$ that have been observed in O-rich AGB stars [42, 11, 56, 43, 9, 69]. At the low resolution of our observations, these bands are not easily detected; but are nonetheless weakly present in some targets.

4.5.2 Molecular bands: Models

It is clear from Fig. 4.4 that there is a considerable variation in the relative strengths and precise shapes of these molecular bands in our sample. Therefore, it does not seem adequate to use a single template spectrum as an approximation to the spectrum of the photosphere and the molecular layers, as is often necessarily done [e.g. 77] in similar studies. A better approach may be to use model spectra that reproduce the observed molecular bands shortward of the

onset of dust emission ($\sim 8.5\text{-}\mu\text{m}$), and predict the shape of the spectrum underlying the dust features. We investigate such an approach here.

For our purposes, we assume that the molecular layers are spherically symmetric, since only 1-6% of CSEs are estimated to be non-spherical among the entire population of single or binary AGB stars [65]. We then approximate this spherical geometry by plane-parallel slabs that are located in front of a background represented by an Engelke function (see Fig. 4.5).

Such models have been used successfully to reproduce mid-IR spectra of AGB stars [see e.g. 90, 91, 11, 7, 57] and are computationally cheap. Water opacity plays a key role in our targets. It has been shown [90, 7] that at least two layers containing water vapor are required to properly reproduce the observations, owing to the high opacity of water and temperature gradients in the photosphere and the circumstellar environment. We thus include two water layers in our models. we also added SiO to each of the layers. Each layer is then fully characterized by the temperature T_{mol} , the column densities N of water and SiO, and the radius R ; increasing the radius will result in a larger weight for the emission component [see e.g. 11] and is required to reproduce emission features in the spectrum. Optical depths for each component are as described in SpectraFactory [12].

By changing the parameters of the slab model, we can reproduce a wide variety of infrared spectra. In its simplest form (with one slab only), the model already illustrates how a dense layer of water determines almost the entire mid-IR continuum (see Fig. 4.6). Indeed, if the water column density is high enough, the resulting spectrum is largely independent of the background flux due to the high water opacity over a large wavelength range. The main effect of such an opaque water layer is thus to lower the colour temperature of the apparent IR continuum [7, 40]; but note also the appearance of a broad feature around $10\text{-}\mu\text{m}$ in these pure absorption spectra that could easily be misinterpreted as a dust emission feature (see Fig. 4.6).

4.5.3 Modelling the naked stars

To get a feeling for the typical stellar and molecular parameters (i.e. temperatures, column densities and IR colour temperatures) corresponding to the infrared spectra of our AGB stars, we first apply our model to naked stars – stars that have no dust emission in their infrared spectra. However, the interplay of spectral features due to water, SiO and interstellar extinction make it surprisingly hard to determine whether or not an object is a naked star by just visually inspecting the spectrum.

Here, we therefore adopt a slightly different working definition for a naked star. We will call a star in our sample a naked star, if its (extinction-corrected) IR spectrum can be well reproduced by our two-slab model containing water and SiO. This is not straightforward though, since extinction towards our targets is not well established, and an extinction-corrected IR spectrum is thus not easily obtained. In practice, we therefore included an extinction correction in our models (with the A_K value as an additional model parameter). A naked star is then an object whose IR spectrum can be reproduced by our extinction-corrected two-slab model, provided that the best-fitting A_K value is reasonable. Applying this approach on our entire sample, we found that out of fifty three AGB stars in our sample only nine of them qualify as naked stars since they result in reasonable A_K values with acceptable fits. The implications for extinction are further discussed in Sect. 4.6.

Table 4.2: The resulting best-fit parameters for our naked star models, and literature values for the extinction.

Object	<i>a</i>	<i>b</i>	A_K [mag]		<i>d</i>	<i>e</i>	Layer 1				Layer 2		
			T_\star [K]	R_\star [$\times 10^{13}$ cm]			T [K]	$\log(N_{H_2O})$ [cm $^{-2}$]	$\log(N_{SiO})$ [cm $^{-2}$]	T [K]	$\log(N_{H_2O})$ [cm $^{-2}$]	R/R $_\star$ [R=R $_1$ =R $_2$]	
c32-8	0.51		0.78	0.43	0.52	4500	1.45	1800	17.4	22.0	1700	16.0	1.00
c35-2	0.54		0.87	0.43	0.54	2500	2.44	1600	16.0	22.0	500	16.0	1.00
c35-4	0.55		1.02	0.79	0.92	2500	2.88	1400	16.0	22.0	500	21.2	1.00
Ogle-4		0.30	0.26	0.06	0.25	2800	2.04	2000	16.0	22.0	500	16.0	1.00
Ogle-6		0.30	0.27	0.15	0.25	2800	2.58	1000	16.0	21.4	500	17.6	1.00
NGC 6522-4	0.18		0.17	0.15	0.27	3500	1.84	1900	16.0	22.0	500	16.0	1.00
NGC 6522-6	0.16		0.17	0.00	0.10	2500	2.33	1100	18.9	22.0	500	16.0	1.00
NGC 6522-7	0.06		0.15	0.07	0.14	4300	1.54	1000	16.0	22.0	600	18.9	1.00
NGC 6522-15	0.06		0.14	0.01	0.10	2500	2.31	1200	18.9	22.0	1100	16.0	1.00

^aSchultheis et al. [73]^bSumi [80]^cGonzalez et al. [28]^dThis work; determined from the best-fit slab models and adopting the galactic center extinction law.^eThis work; from the method described in § 4.6.4

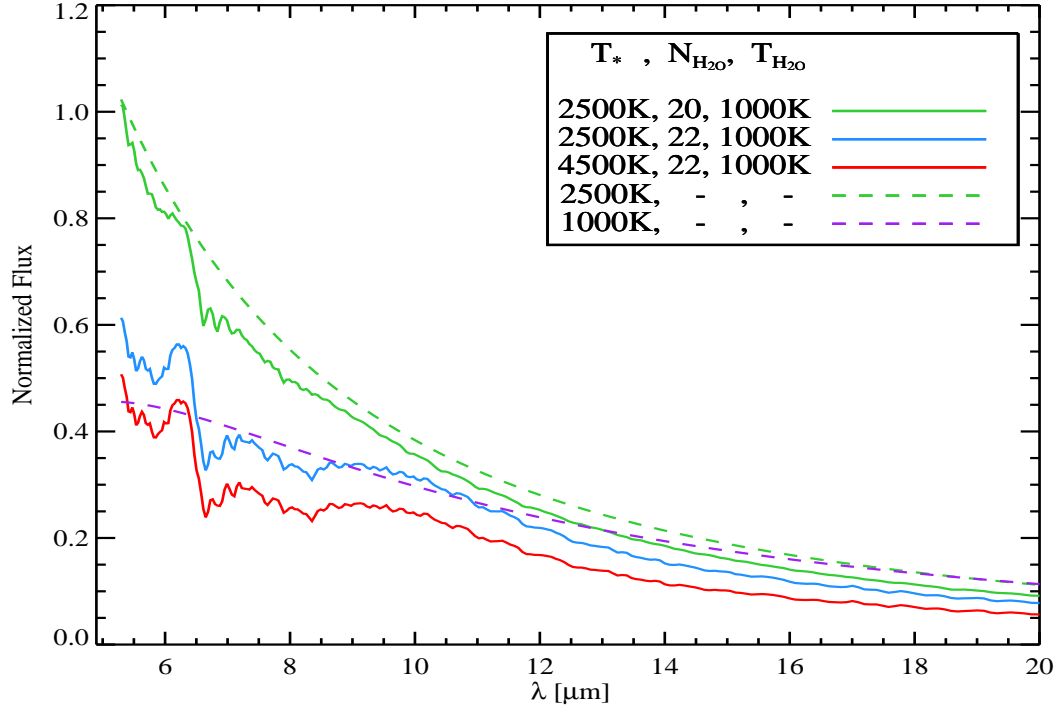


Figure 4.6: The infrared model spectra of three different slab models that only differ in their effective temperature and in the amounts of water. All models include a ($T = 1000$ K) layer of only water vapor. The green model represents pure absorption (I_1 in Fig. 4.5) with only moderate amounts of water. This is the only model where the overall shape of the spectrum is similar to a blackbody at the object’s effective temperature (in this case 2500 K, green dashed line). When only increasing the amount of water, we obtain the blue model. In this case, the shape of the spectrum looks more like a 1000 K blackbody (dashed purple line) – the temperature of the water layer. In the red model, we have changed the effective temperature but it looks almost identical to the blue model: the water layer hides the stellar photosphere. Note that the spectra are normalized to their own maximum.

In principle, our slab model has 10 free parameters: the temperature of the (Engelke) blackbody background (T_*); for each of the two layers a temperature T_{mol} , a size R , and column densities $N_{\text{H}_2\text{O}}$ and N_{SiO} for water and SiO respectively; and finally the extinction value A_K . We imposed constraints on the temperature structure: the inner molecular layer cannot have a higher temperature than T_* , and similarly the second layer cannot be warmer than the first layer. Since we do not see obvious emission features from cool molecular material, we did not include the third ray I_3 that is being emitted from the second layer only. It is as though we set the second layer to be the same extent as the first layer. During a first run, we furthermore realized that all best-fitting solutions essentially had no detectable SiO in the second layer. We thus removed N_{SiO} as a parameter in the second layer.

For each set of parameters, we first de-reddened the observed spectrum using the model A_K value (see §4.6). We then created our model spectrum by calculating radiative transfer along each of the rays depicted in Fig. 4.5. Note that for our first run, we used all three rays;

for the final run only I_1 and I_2 (since $R_2 = R_1$). A full model spectrum is then obtained by summing a linear combination of these rays. We used a non-negative least squares algorithm [NNLS, see e.g. 49] to determine the scale factors that minimize the χ^2 when comparing the final model spectrum to the observed (and de-reddened) spectrum. These scale factors really set R_\star and R . Note that we only used the 6–14- μm wavelength range for calculating the χ^2 value. Shortward of 6- μm , there is potential contribution from the tail of a CO absorption band which is not included in our models. The longer wavelengths do not contain much in terms of distinct molecular spectral features. Therefore, by restricting ourselves to the SL(6–14- μm) modules, we avoid possible difficulties originating from a poor overlap between SL and LL modules. Finally, rather than calculating models for each grid point in the entire parameter space, we used an adaptive mesh algorithm that starts from a coarse grid covering the entire parameter space, and then reduces the step size at each iteration while centering the region of interest at the minimum in the χ^2 hypersurface; the algorithm stops when all parameters have reached their desired step size and the χ^2 minimum is centered in the region of interest.

We varied all parameters on a fixed grid except the layer size(R) which was left free and we determined by other means. Temperatures were changed in steps of 100 K. The background temperature T_\star was set to vary between 2500 K and 4500 K; the temperature of the molecular layers T_{mol} between 500 K and 2500 K (but subject to the constraints detailed above). We considered molecular column densities between $N = 10^{16}$ and $N = 10^{22} \text{ cm}^{-2}$, and varied $\log N$ with a step size of 0.1. Finally, we varied the extinction value A_K between 0 and 1 in steps of 0.01.

4.5.4 Modelling results

The nine naked star spectra and their best-fitting model are shown in Figs. 4.7 and 4.8, and Table 4.2 lists the corresponding model parameters¹. Note that there is a considerable variation in the appearance of even these naked star spectra. In all cases, we can reproduce the observations reasonably well; in some cases though, there is some mismatch, most notably at the longer wavelengths corresponding to the LL1 module. While part of the discrepancy may point to remaining calibration issues, these clearly indicate shortcomings in our (simple) models, e.g. by producing too much water emission longward of 20- μm in several objects. A key result from our modelling is that we do indeed find that in all cases, the spectra are best represented by models that include high column densities and high temperatures for SiO.

As can be seen from Table 4.2, our best-fitting models represent a fairly wide range of stellar temperatures T_\star (2500 K < T_\star < 4500 K). However, we caution that these may not be well determined. As explained above and demonstrated in Fig. 4.6, the presence of water can significantly alter the shape (and corresponding colour temperature) of the IR continuum, and as a consequence, all information about the stellar continuum radiation is lost.

In few cases, we find that stars include a very thick water layer (e.g. c35-4), we must conclude that the stellar temperatures in those cases are ill-determined. Similarly, in those cases, the column densities for SiO are not well determined for the same reasons. SiO is clearly present in our spectra and shows up most clearly at its band head at 7.55- μm . This indicates a high temperature, and from the depth of the band we can also infer that the column

¹Note that we will discuss our results for the extinction values in §6.

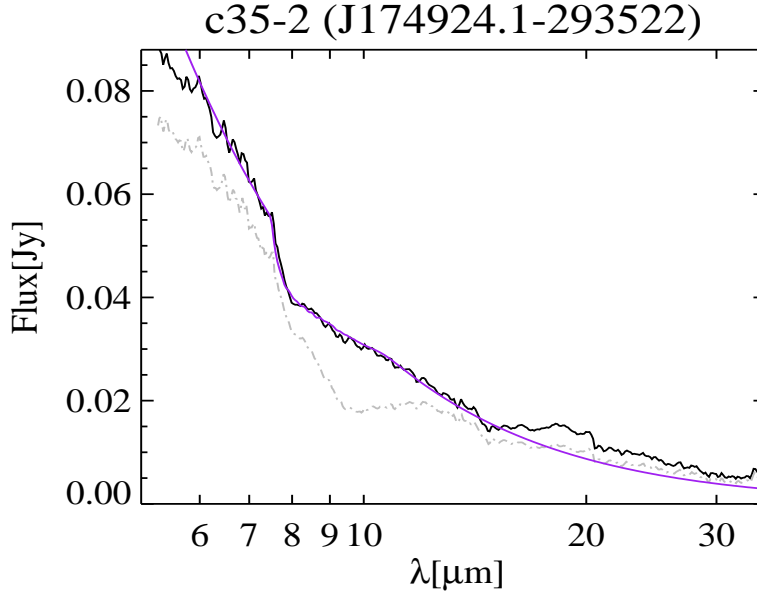


Figure 4.7: The raw *Spitzer-IRS* spectrum of c35-2 (grey), and the extinction-corrected spectrum (black) adopting a galactic centre extinction law with $A_K = 0.49$. The best-fitting model is shown in purple. Note the clear signature of interstellar extinction at $9.7\text{-}\mu\text{m}$ (silicate absorption) in the original spectrum.

density must be high, but accurate values cannot be obtained for these objects with our simple models.

4.6 Interstellar Extinction

Interstellar extinction can leave a significant spectral imprint especially in the $10\text{-}\mu\text{m}$ region where many minerals exhibit characteristic resonances. We selected our targets from fields covering the galactic bulge that are typically characterized as having low extinction, and with most of the extinction originating from “local” interstellar material rather than from regions within the bulge itself. However, we found that the effect of extinction on our target spectra is not negligible, and this is most easily ascertained by studying the naked stars. In several cases, this is clear and unambiguous from the appearance of an absorption feature around $9.7\text{-}\mu\text{m}$ in the spectra. The best examples are e.g. c35-2 and c35-4 (see Figs. 4.7 and 4.8) where the spectra show the clear water absorption near $6.5\text{-}\mu\text{m}$ and the SiO band head near $7.55\text{-}\mu\text{m}$ that are typical for O-rich AGB stars, but in addition also exhibit a broad absorption band with the deepest absorption occurring near $9.7\text{-}\mu\text{m}$. Clearly, this is not some other molecular absorption band, and the feature cannot be due to warm circumstellar dust either. Thus, interstellar extinction is clearly affecting our observations and needs to be corrected for. For other sources, the effect of extinction is more subtle and hard to establish visually.

Since interstellar extinction can also significantly affect the resulting dust spectra of our target AGB stars, we have taken great care in characterizing extinction in our different fields. We have done this by using the naked stars in our sample, and comparing different approaches

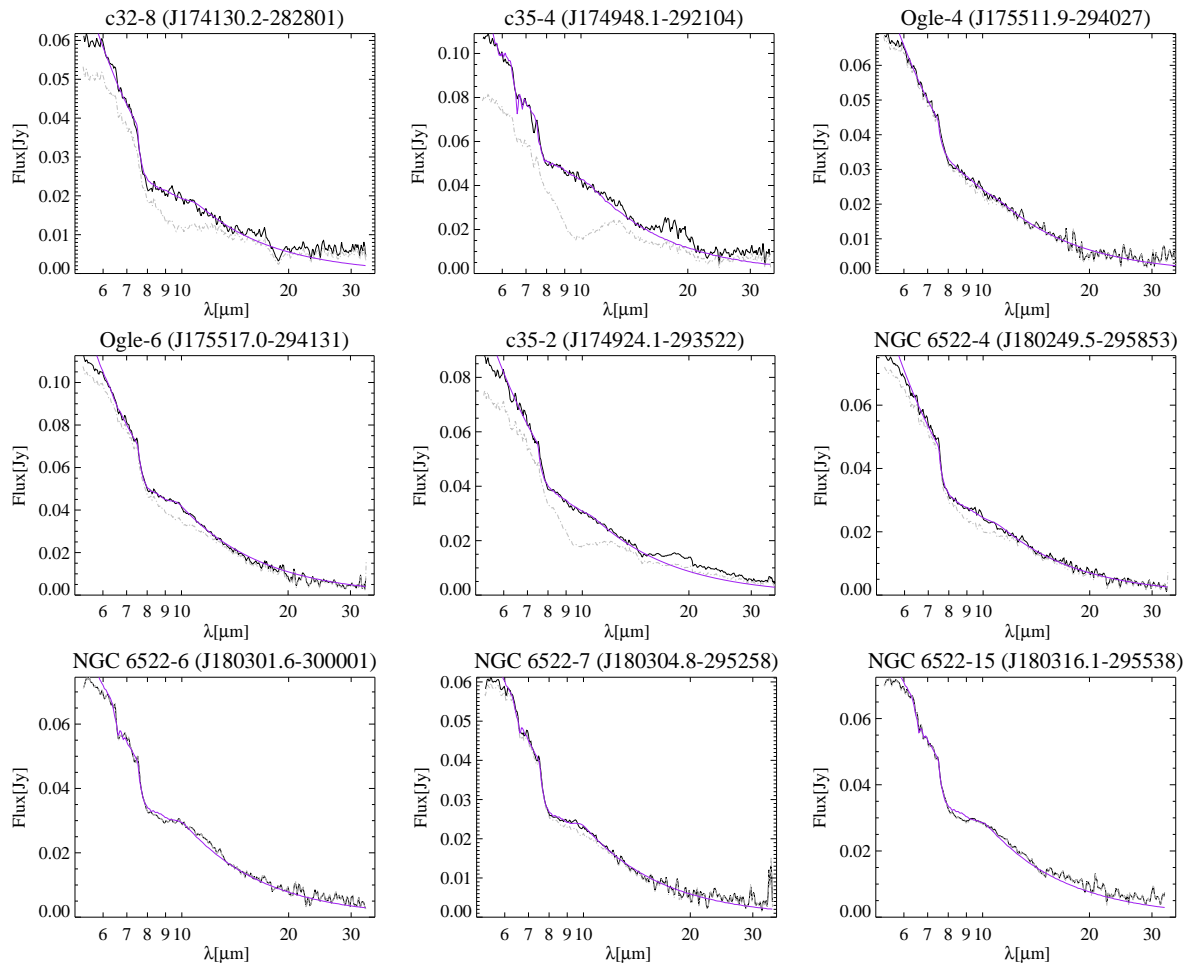


Figure 4.8: The nine naked star spectra and their best-fitting models. The original, uncorrected spectrum is shown in gray and the best-fitting extinction-corrected spectrum in black. The best-fitting stellar and molecular model spectrum is shown in purple.

to determine extinction in these lines of sight. We then use these results to estimate extinction for our remaining targets as well.

4.6.1 The IR extinction curve

The spectral shape of the extinction curve in the IR is discussed in great detail by Chiar & Tielens [13]. These authors construct two slightly different extinction laws: one that is appropriate for the “local” ISM, and another for the material toward the galactic centre (GC). Indeed, it is well known that the IR extinction toward the GC has a somewhat different shape than the extinction in the local ISM [54]; moreover, there is more silicate per unit of visual extinction towards the GC compared to the local ISM, resulting in a stronger $10\text{-}\mu\text{m}$ feature in the GC extinction curve. These extinction laws are consistent with earlier work by Lutz et al. [54] and Indebetouw et al. [38]. On the other hand, Román-Zúñiga et al. [68] found small differences with Chiar & Tielens [13], indicating that the extinction law in the near- and mid-IR may vary

slightly as a function of environment.

It is not clear a priori whether the extinction in the sightlines toward our targets is mainly due to dust in the local ISM or rather originates from material within the galactic bulge and we have thus considered both possibilities in this work. The extinction curves by Chiar & Tielens [13] are presented as A_λ/A_K (i.e. normalized to extinction in the K -band) and cover the IR up to $27\text{-}\mu\text{m}$. Since our spectra contain data up to $38\text{-}\mu\text{m}$, we extrapolated the extinction curves to $38\text{-}\mu\text{m}$ by fitting a straight line longward of $27.0\text{-}\mu\text{m}$ in the log-log plane of A_λ/A_K vs λ , using the same slope as the extinction curve between $23\text{--}27\text{-}\mu\text{m}$.

With the extinction curves expressed as A_λ/A_K , we then still need a good estimate of the amount of extinction toward each of our targets (we will use A_K here).

4.6.2 Literature A_K values

The literature offers several extinction maps to estimate A_K values based on the position of a target in the Galactic Bulge. For our fields, especially the work by Schultheis et al. [73] and Sumi [80] are relevant. More recently, also Gonzalez et al. [28] produced an extinction map for the galactic bulge. The corresponding A_K values for all three sources are listed in Table 4.2. Where necessary, we used the relations provided by Cardelli et al. [12] to obtain A_K values.

It is clear from Table 4.2 that the most reddened targets are those in c32 and c35 and the least reddened field is NGC 6522 with the OGLE field intermediate between those two. However, there is considerable disagreement (up to a factor of 2.5) between these sources about the actual A_K value for an individual target, and it is not clear which value is the best to use for our purposes. Thus, alternative ways are required to determine the extinction in our targets.

4.6.3 A_K values from the slab models

Since the amount of extinction is in principle encoded in our observations, we also investigated how we could determine the A_K values from the spectra themselves.

As described in Sect. 4.5, we included A_K as a free parameter when modelling the naked stars. For each set of model parameters we considered, we furthermore compared the slab model to two different spectra: one where we applied the GC extinction curve, and one where we applied the local ISM law. For all naked stars, we found much better overall model fits when using the GC extinction curve. Moreover, the resulting best-fitting A_K values we obtain when using the GC extinction curve are generally better in agreement with some of the available literature values. Clearly, this indicates that for our purposes, the GC extinction law is more appropriate to use than the local ISM law. We have therefore adopted the GC extinction law from Chiar & Tielens [13] for all targets in our sample.

When comparing the model A_K values to the available literature values, we also find that the objects in c32 and c35 are subject to the most severe extinction, and that NGC 6522 is far less affected. However, for individual targets our derived value can be very close to either of the literature sources, or take on a very different value altogether. It is important to realize that the uncertainties on our derived A_K values are significant though: there is a fairly large range in A_K values around the best-fitting value over which the associated spectral changes can be

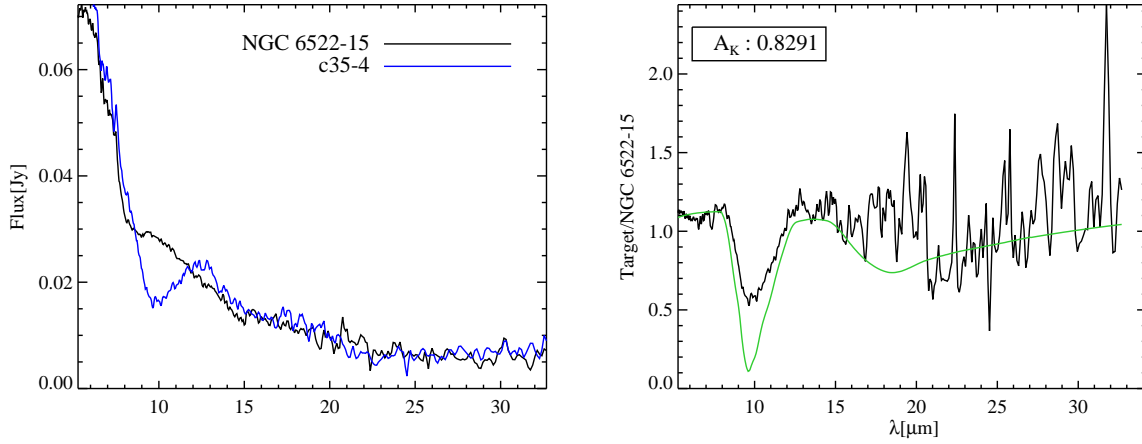


Figure 4.9: (*Left*) The *Spitzer-IRS* spectrum of the reddened naked star c35-4 (blue) compared to the least reddened naked star NGC 6522-15 (black). (*Right*) The result of dividing the spectrum of c35-4 by NGC 6522-15 (black). The green curve is the GC extinction curve by Chiar & Tielens [13].

accommodated by changing the properties of the molecular layers. Thus, also our models tell us that it is very difficult to disentangle the effect of low extinction from molecular features.

4.6.4 A model-independent approach

Finally, we tried to more directly determine the A_K values from our observations without using models for the stellar and molecular contributions. The basic premise for this approach is fairly simple. Denoting with I_ν^1 the specific intensity originating from a given naked star, and similarly using I_ν^2 to describe the intensity originating from a second naked star, the fluxes F_ν^1 and F_ν^2 that we observe from these stars, scale with $I_\nu^1 e^{-\tau_\nu^1}$ and $I_\nu^2 e^{-\tau_\nu^2}$ respectively, where τ_ν^1 represents the optical depth of the interstellar material in the line of sight toward star 1, and τ_ν^2 towards star 2. In § 4.6.3, we investigate the two extinction laws (Local and Galactic) and we verify that, between the two, Galactic extinction law works better for all of our targets. , we can write that $\tau_\nu^1 = \tau_1 \tau_\nu$ and $\tau_\nu^2 = \tau_2 \tau_\nu$.

Dividing the observed spectra of two naked stars, we then find that

$$\frac{F_\nu^1}{F_\nu^2} \propto \frac{I_\nu^1}{I_\nu^2} e^{-(\tau_\nu^1 - \tau_\nu^2)} = \frac{I_\nu^1}{I_\nu^2} e^{-\tau_\nu(\tau_1 - \tau_2)} \quad (4.1)$$

Thus, if the intrinsic spectra for our naked stars were identical ($I_\nu^1 = I_\nu^2$), the quotient spectra can be used to determine the amount of differential extinction ($\tau_1 - \tau_2$), provided the spectral shape (τ_ν) of the extinction law is known. Note that the intrinsic spectra for our naked stars are indeed overall fairly similar. We have verified this similarity by normalizing each naked star spectra to their flux at 6- μm and overplotting them on top of each other. As pointed out in § 4.5, they all show a similar spectral fingerprint of a hot ($T \approx 1000$ K) and dense layer of water vapor which, despite different central star temperatures (T_*), determines much about the shape of the spectrum over the entire wavelength range covered here.

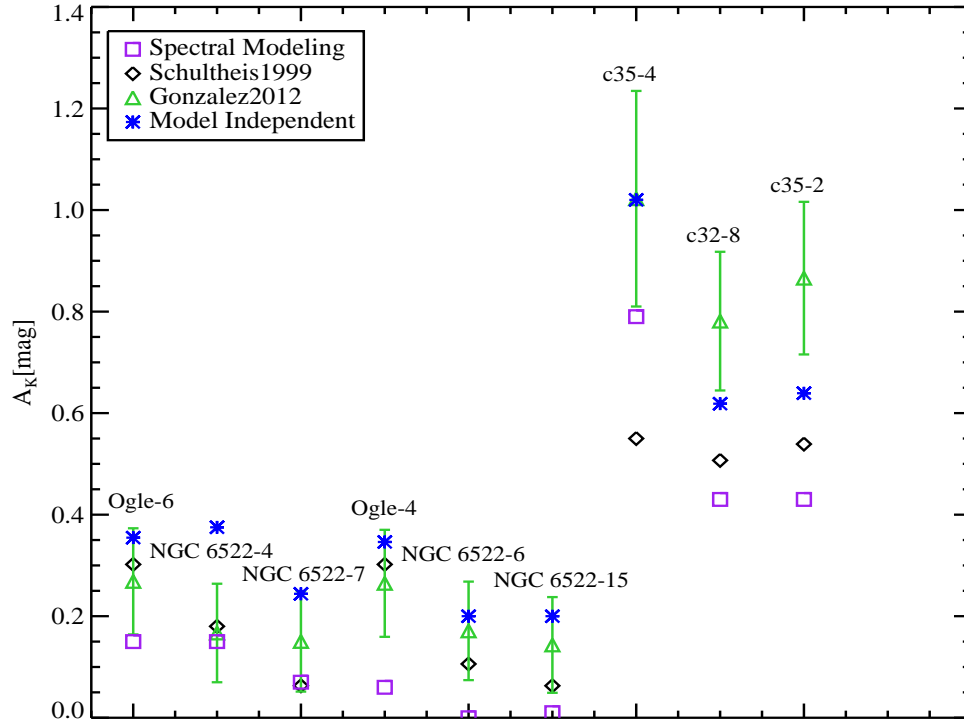


Figure 4.10: Extinction values (A_K) for our naked stars from different sources and methods.

Fig. 4.9 shows an example of the resulting quotient spectrum after dividing two naked star spectra. In practice, the water signature in two different objects is not exactly the same, and some water residuals do show – small scale features as well as broad trends due to differences in IR colour temperature between the objects. Nonetheless, most water spectral features especially at the shorter wavelengths have disappeared. Other spectral features due to SiO and SO₂ are confined to small wavelength ranges and easily recognized. What stands out most, is the result of differential extinction between the two naked stars; as can be seen from the Figure, the quotient spectrum closely resembles the Chiar & Tielens [13] GC extinction law, especially around the 10- μ m silicate absorption.

We then used this approach to determine A_K values as follows. First, we determined that NGC 6522-15 is the naked star with the lowest amount of extinction. Indeed, when using this spectrum as a reference, all other naked stars show absorption in their quotient spectra at the wavelength of the interstellar silicate absorption feature. Therefore, all other naked stars must be subject to more interstellar extinction than NGC 6522-15. Note that this also agrees with the literature values by Schultheis et al. [73] and Gonzalez et al. [28].

For each of the remaining naked stars, we then created a set of extinction-corrected spectra, using A'_K values (the \prime indicating that these may not reflect “true” A_K values) ranging from 0 to 1 mag in steps of 0.01, and we divided each corrected spectrum by the reference spectrum (NGC 6522-15). The resulting set of quotient spectra change in appearance from typically showing absorption near 9.7- μ m (when under-corrected) to showing emission at the

same wavelength (when over-corrected). A flat spectrum indicates a “perfect” extinction correction. We quantified this by calculating the linear Pearson correlation coefficient between the quotient spectra and the Chiar & Tielens [13] GC extinction curve in wavelengths between $8\text{-}\mu\text{m}$ and the maximum available wavelength in each case; correlation coefficients for our quotient spectra then typically change from positive values (for under-correction) to negative values (over-correction). We then simply determined the A'_K value corresponding to a correlation coefficient of 0. In the process, we noticed that sometimes strong SiO band can interfere somewhat with this process; we therefore used SiO model spectra [12] to divide out any SiO residuals before calculating the correlation coefficient.

Note that the procedure outlined above only determines the *relative* extinction between the target and the reference spectrum (NGC 6522-15) to the point where both spectra contain identical extinction spectral features. The *actual* A_K value for the target is in principle given by $A_K = A'_K + A_K^{\text{NGC 6522-15}}$. To obtain A_K values for our naked stars using the determined A'_K values, we could simply adopt a set value for $A_K^{\text{NGC 6522-15}}$. However, as is clear from Table 4.2, the literature offers quite different extinction values for this source. To reduce the sensitivity of our extinction values to a single source, we instead opted to calibrate our A'_K sequence by using all available extinction values for all our naked stars (literature values as well as our own slab model results). We determined that setting $A_K^{\text{NGC 6522-15}} = 0.10$ results in the lowest absolute deviation between A_K values determined with this method and the weighted average of all other available values. Note that this value is within the uncertainty obtained using the Gonzalez et al. [28] maps (who found $A_K^{\text{NGC 6522-15}} = 0.14 \pm 0.09$).

The resulting A_K values for our naked stars are listed in Table 4.2; Fig. 4.10 shows a graphical comparison between the extinction values. In most cases, there is a good agreement between these values and the results from our spectral modelling; and often, they are also close to one of the literature values. Since the A_K values determined here are based on the individual spectra directly and are thus model-independent, we deem them to be somewhat more reliable than the other values, and we thus adopt these A_K values for the remainder of this paper.

Armed with a good characterization of the extinction towards our naked stars, we can now better assess what extinction values to use for our dusty targets. Since the different fields have somewhat different extinction characteristics, it is insightful to evaluate our results per field. To furthermore get a feeling for the small scale variability, it is also helpful to consider the *Spitzer-IRAC* $8\text{-}\mu\text{m}$ images of our fields; these are from the GLIMPSE II survey [15] or from the work by Uttenthaler et al. [83]. The IRAC $8\text{-}\mu\text{m}$ images are particularly sensitive to the emission of PAHs in the $7.7\text{-}\mu\text{m}$ PAH band; these may thus give some information on the small scale variability of interstellar dust. The details of this study are shown in Appendix E and the results are tabulated in Table 4.4 along with all other relevant extinction values.

4.7 The Full Spitzer-IRS spectra

At this point, we have obtained the final *Spitzer-IRS* spectra for all targets in our sample, and we show these in Figure 4.11. As we showed already in Fig. 4.4, the spectra are dominated, shortward of $8\text{-}\mu\text{m}$, by molecular features originating from the stellar photosphere and warm molecular layers. Circumstellar dust shows up quite clearly at longer wavelengths (most no-

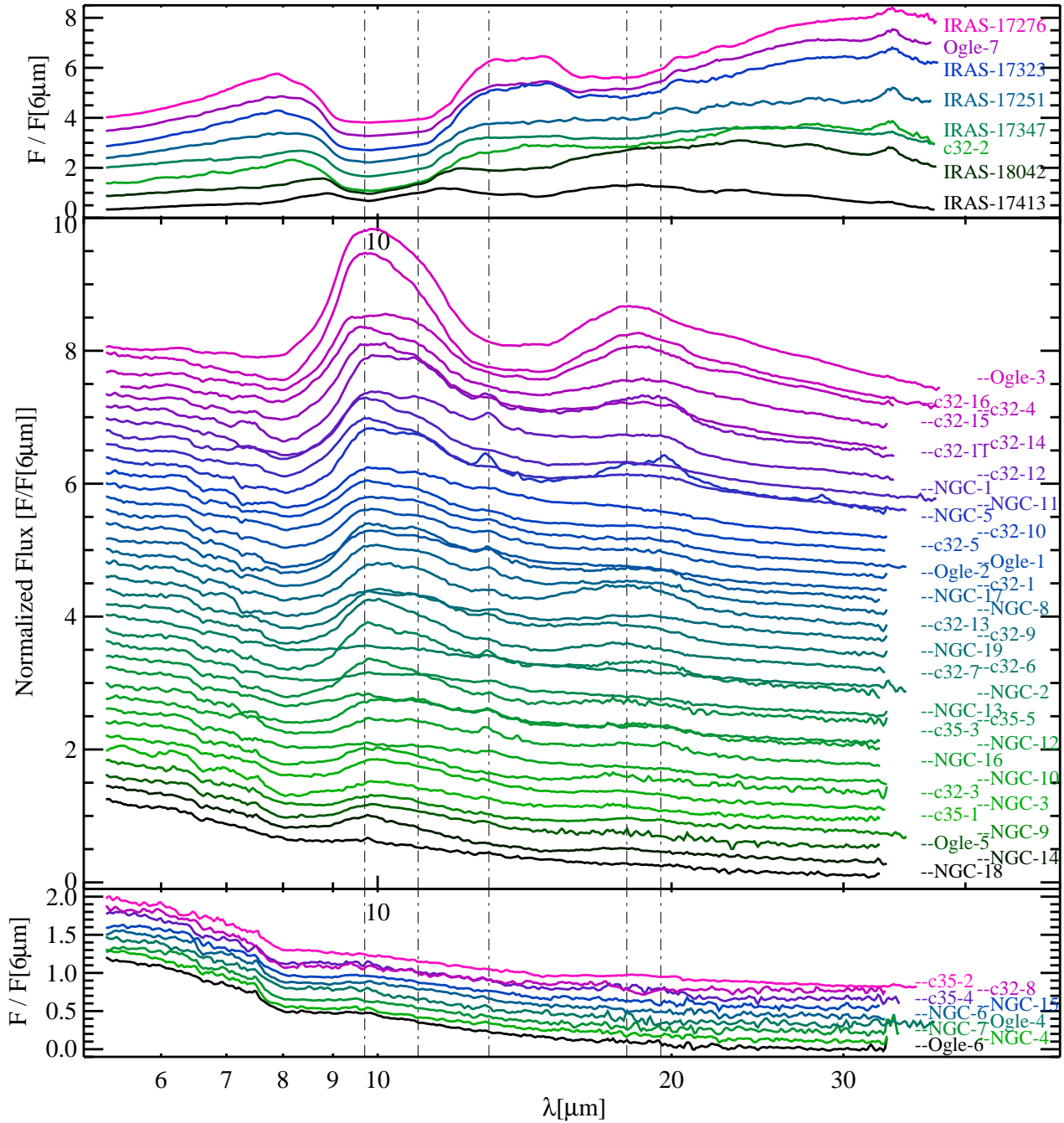


Figure 4.11: The full extinction-corrected *Spitzer-IRS* spectra of OH/IR stars (*top*), dusty targets (*middle*) and naked stars (*bottom*). The spectra at longer wavelengths are trimmed in cases where data seemed too noisy thus unreliable. The spectra are colour coded for better illustration. The spectra are normalized to their flux at $6\text{-}\mu\text{m}$ and are sorted as a function of increasing $10/6\text{-}\mu\text{m}$ flux ratio except for the dusty targets (*middle*) where the spectra are sorted as a function of increasing mass loss rates (listed in table 4.4). Shortward of $9.7\text{-}\mu\text{m}$, the molecular features are present with no clear trend however this figure represents a sequence of increasing dust optical depth (See text for more details). Note: Due to lack of space in this plot, we exceptionally used NGC as a short form of NGC 6522.

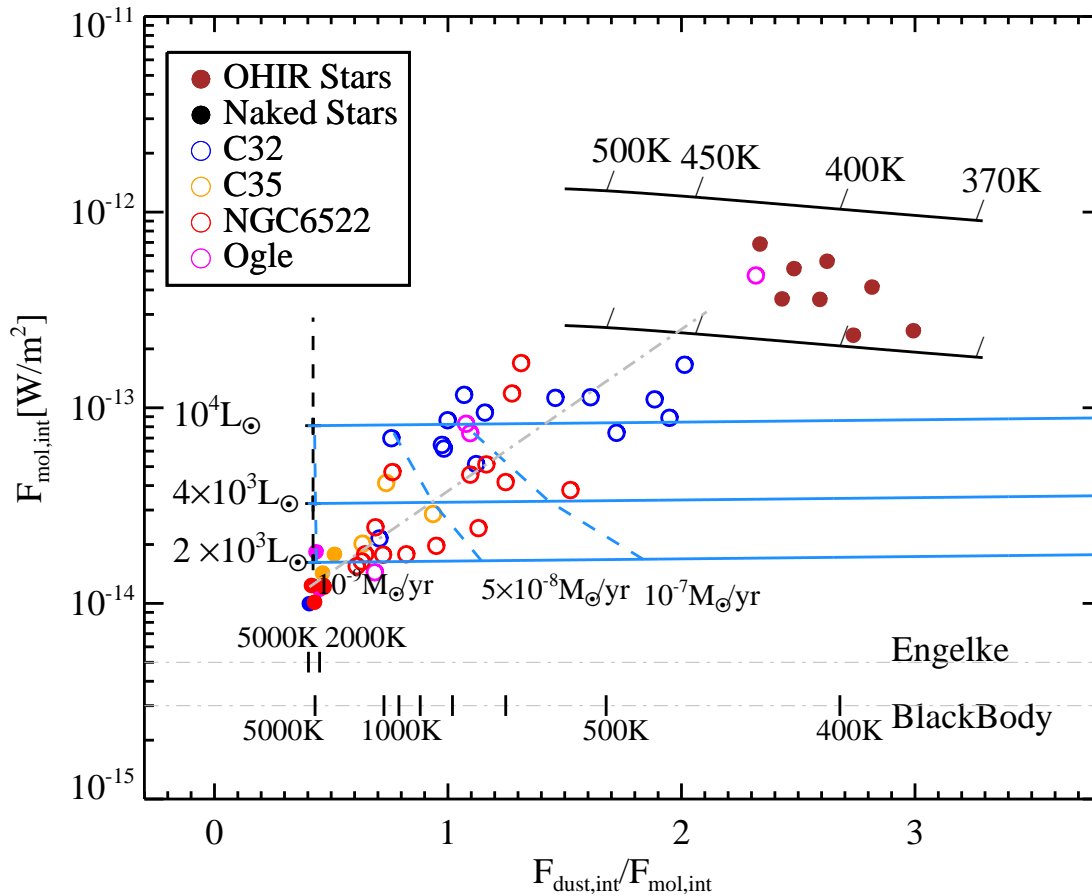


Figure 4.12: F_{mol} as a function of $F_{\text{dust}}/F_{\text{mol}}$ for all objects in our sample. The black vertical dashed line on the left represents the locus for dust-free AGB stars for various luminosities at the distance of the galactic bulge. The solid blue lines represent models for such AGB stars (at 2000, 6000 and 10,000 L_{\odot}) surrounded by optically thin dust shells (of pure silicates) with increasing mass-loss rates; the blue dashed lines are lines of constant mass loss rate (assuming a dust-to-gas ratio of 0.005). The solid black lines on top represent pure blackbody emitters at $L = 2000L_{\odot}$ (lower) and $10,000L_{\odot}$ (upper) as an approximation of extremely optically thick dust shells. At the bottom, we have indicated the expected $F_{\text{dust}}/F_{\text{mol}}$ values for respectively an Engelke function and for pure blackbodies with varying effective temperatures. The grey dash-dotted line is a least absolute deviation fit to the data points (excluding the OH/IR stars). See text for details.

tably e.g. in the 10- μm emission complex), and there is a fairly large range in the amount of dust emission relative to the “naked star” spectra in our sample. The OH/IR stars on top represent the most extreme cases where only dust emission (and self-absorption) is present.

It is instructive to quantify the amount of dust and stellar emission and compare those to simple models for AGB stars with mass loss. We therefore define F_{mol} as the integrated flux between 5–8- μm (where molecular bands are present, but no dust features) and F_{dust} as the integrated flux between 8–30- μm (the range with most conspicuous dust features and dust

continuum). Note though that F_{dust} and F_{mol} both include a contribution from the stellar photosphere and molecular layers; at the same time, F_{mol} will not correspond to molecular bands for the optically thick OH/IR stars.

Fig. 4.12 shows how the integrated dust-free continuum flux F_{mol} changes as a function of the relative amount of dust emission ($F_{\text{dust}}/F_{\text{mol}}$) for the stars in our sample. In essence, this figure is similar to the colour-magnitude diagram in Fig. 1, but it is derived purely from the *Spitzer* spectra. Compared to the naked stars (lower left of the diagram), our dusty targets follow a trend characterized by more dust emission ($F_{\text{dust}}/F_{\text{mol}}$) for higher stellar fluxes (F_{mol}), as was expected for our sample based on Fig. 1.

For comparison, we also show several models in Fig. 4.12. First, we indicate the locus for naked AGB stars at the distance of galactic bulge (assumed to be 8.5 kpc). For this, we have used an Engelke function with an effective temperature of 3000 K for the stellar continuum and calculated F_{mol} and F_{dust} for luminosities between ~ 2000 and $\sim 10,000 L_{\odot}$. This appears as the straight dashed line on the left side of the plot close to where naked stars are located. Note that changing the effective temperature (within reasonable limits for AGB stars) will primarily shift the line up or down.

We have also included a series of models for optically thin dust shells with increasing mass-loss rates, following the same approach as Schutte & Tielens [74]. All our models include only MgFeSiO_4 silicate dust, i.e. olivine with equal iron and magnesium content (with optical constants from Dorschner et al. 17); we have verified though that the results for other minerals are very similar. We calculated the emerging dust flux for total mass loss rates ranging from $10^{-9} M_{\odot} \text{yr}^{-1}$ to $10^{-6} M_{\odot} \text{yr}^{-1}$ and assuming a dust-to-gas ratio of 0.005, as in Blommaert et al. [6]. We added this dust flux to the central stellar flux (for three different luminosities: $L=2000$, 4000 and $10,000 L_{\odot}$). This results in nearly horizontal curves representing objects with the same stellar luminosities, but increasing mass loss rates (and thus increasing dust emission).

As mass loss rates increase, the dust will eventually become optically thick, and these models will not be applicable. An approximation for extremely optically thick dust shells (represented by the OH/IR stars) is shown in Fig. 4.12, where we have represented the optically thick dust shells by pure blackbody radiators of differing effective temperatures T_{dust} ; two such curves are shown with luminosities of 2000 and $10,000 L_{\odot}$ respectively, that bracket the OH/IR stars in our sample. The downward trend for decreasing dust T_{dust} reflects that a smaller fraction of the dust emission is occurring in the $5\text{--}8\text{-}\mu\text{m}$ range; such a trend is also apparent in our OH/IR stars, whose decreasing dust colour temperatures can also be ascertained from Fig. 4.11.

Comparing our targets (excluding now the OH/IR stars) to these models clearly indicates that our sample corresponds to a sequence of increasing luminosities and increasing mass-loss rates, albeit with a large scatter. We quantified this trend by performing a least absolute deviation fit to the data points (excluding the OH/IR stars); the best fit is indicated by the dashed line in Fig. 4.12 and is given by the relation:

$$\log F_{\text{mol}} = -14.25 + 0.83 \frac{F_{\text{dust}}}{F_{\text{mol}}} \quad [\text{W} \cdot \text{m}^{-2}] \quad (4.2)$$

In the optically thin limit, each point on this line corresponds to a unique combination of stellar luminosity and mass loss rate (when assuming a constant effective temperature of 3000 K), and we can thus use this to determine a $\dot{M} - L$ relation for our sample (see Fig. 4.12). Note that \dot{M} represents the total mass loss rate as opposed to the dust mass loss rate ($\dot{M}_{\text{tot}} = \dot{M}_{\text{dust}}/0.005$).

From a detailed comparison to our model curves, we find that

$$\log \dot{M} = 1.37 \log\left(\frac{L}{L_{\odot}}\right) - 12.28 \quad [\text{M}_{\odot} \cdot \text{yr}^{-1}] \quad (4.3)$$

The \dot{M} and L values are listed in Table 4.4. In Fig. 4.12, the lines that represent constant mass loss rate (blue dashed lines), are nearly perpendicular to the best-fitting line. Additionally, increasing mass loss rates at constant luminosities result in almost horizontal lines (blue solid lines), allowing every intersection with the best-fitting line to be traced back to its corresponding luminosity. Therefore, by projecting every data point on to the best-fitting line, we can estimate its corresponding luminosity which using Eq. 4.3 can lead to a rough estimate of the mass loss rate.

Note that under several assumption, this method be treated as a tool to estimate stellar luminosities and mass-loss rates directly from the *Spitzer-IRS* spectrum of an AGB star. These assumptions include, modeling constraints such as stellar temperature, selective dust mineral, constant grain size, spherical grain shape and spherical symmetry in the outflow).

The location of our targets in this diagram compared to simple approximate models assures that our sample represents a sample of AGB stars at the distance of Galactic bulge, with increasing luminosities and mass loss rates as we first envisioned, and is thus appropriate for studying the dust condensation sequence as a star climbs the AGB.

4.8 The Dust Spectra

We now turn our attention to the dust. Here, we will only discuss a fairly basic characterization of the dust properties in our sample in terms of spectral components, and in terms of their classification following the well-known Silicate Emission (SE) index [77]. Most of our discussion does not apply to the OH/IR stars, and we will therefore largely ignore them for the remainder of this paper. A much more detailed analysis will be presented in future papers.

4.8.1 Extracting the dust spectra

In order to study the spectroscopic properties of the dust alone, we need to be able to somehow separate the dust from the stellar (and molecular gas) component, and extract the pure dust spectra from the *Spitzer* observations. This, however, is not straightforward, and small errors on the stellar component can have an enormous impact on the dust spectra, especially for those targets with little dust emission.

An often used method to extract the dust spectra from IR AGB star spectra is to adopt a template spectrum for the underlying stellar contribution, scale to the observed spectrum at a key wavelength, and subsequently subtract the template from the observed spectrum. The residual is then the dust spectrum. A widely used template in this context was discussed first by Sloan & Price [77]. These authors studied IRAS-LRS observations of five bright naked giants, and found that they could approximate these spectra starting from an Engelke function with an effective temperature of $T_{\text{eff}} = 3240$ K. To this continuum, they added an SiO absorption band with a depth of 15%, where the band profile was taken from the median absorption profile in

their naked giants. This same template was then used for all O-rich AGB stars in their sample, and scaled to the observations by minimizing the χ^2 over the wavelength range 7.67–8.58- μm .

It is clear from our work on the naked stars in §4.5 that a single template model cannot reliably reproduce all our naked stars. This already shows from the clear variations in the extinction-corrected spectra directly (see Fig. 4.8). When modelling these naked stars, we furthermore also used an Engelke function as the basis for our IR continuum, but we find very different effective temperatures than 3240 K (see Table 4.2); moreover, we found that the IR continuum is often dominated by the presence of an opaque water layer which lowers the IR colour temperature and produces broad features.

In Appendix F, we show how such a template compares to all of the dusty target spectra in our sample. In this case, the template is an Engelke function with $T_{\text{eff}} = 3240$ K to which we have added a single SiO absorption layer ($T_{\text{SiO}} = 2000$ K; $N_{\text{SiO}} = 10^{22} \text{ cm}^{-2}$) such that the resulting SiO absorption band has a depth of 15%. We scaled this template to the flux around 8- μm . For a few spectra (e.g. c32-1, c32-3), this template compares reasonably well to the observations at shorter wavelengths, but in most cases, the template only matches the observed spectrum near the wavelengths used for scaling and does not reproduce the stellar/molecular contribution at all – not in terms of the spectral features, but not even in terms of the shape of the continuum (e.g. c32-4 or OGLE-3). Moreover, any underlying spectral features due to water (which are often broad and present over the entire observed wavelength ranges) are not included in this template. It is thus not clear how reliable the extracted dust spectrum can be when adopting such a template, and it is worth it to consider some alternatives.

An appealing alternative would be to directly use some of the ten naked star spectra as templates for the underlying stellar contribution. However, the large variations in the spectral features and continuum slope for the naked stars requires some caution. We have tried such an approach by finding the naked star that contains the most similar spectral features to the dusty spectra in the 5–8- μm range. We then accounted for the continuum variations by first dividing out the naked star continuum (using a blackbody at the appropriate temperature) and multiplying the result by a blackbody of the appropriate temperature to match the dusty target. In some cases, this method works quite well; in others, there is much less correspondence. However, despite the obvious appeal in having an observed spectrum as the underlying template, this method has a several drawbacks.

First and foremost the existing noise in the naked star spectra will introduce significant noise to the extracted dust spectra (see Appendix F). Moreover, there is often a mismatch in the depth of SiO absorption feature between the two spectra affects the onset wavelength of the resulting dust profile. Interestingly, we also found that in a few cases the strength of the resulting 13- μm feature is reduced since some of our template naked star spectra show an emission bump resembling that of a 13- μm feature (see Figure 4.8). We have confirmed that this feature, unlike the small bump around 14- μm , is not introduced by discontinuities between the SL and LL module. It is not clear though whether these weak bumps are instrumental artefacts or real spectral features (see § 4.8.2 for further discussion).

Given these issues, we tried out yet another approach. Encouraged by our success in reproducing the 5–14- μm spectra of the naked stars with two-slab models in § 4.5, we considered using the same models to fit each of our dust target spectra, by minimizing the χ^2 in the dust-free wavelength range 5–8- μm , and then extending that model to the longer wavelengths. If this method works, it has the clear advantage that it provides a noise-free template for each

target on an individual basis. However, this is a significantly smaller wavelength range, and thus it is not guaranteed that the results are representative for the full wavelength range.

To test the reliability of this approach, we determined the best-fitting model parameters for all our naked stars again, but this time only using the 6–8.5- μm range; we then constructed full spectra from the best-fitting parameters. In Fig. 4.13, we show how these models (6–8.5- μm) compare to the original best-fitting naked star models (6–14- μm). In general, both models are fairly similar. However, the only potential problem in using short wavelength range models (6–8.5- μm) is the under-representation of the naked star flux around 10- μm .

Thus, by using models determined from fitting the 6–8.5- μm region as templates, there is a risk that we introduce artefacts in the resulting dust spectra. The shape of these artefacts is clear from Fig. 4.13: a fairly narrow emission feature around 9.5- μm (e.g. OGLE-6, NGC 6522-4), or alternatively a broad feature starting around 8- μm and sometimes extending up to 20- μm (e.g. c35-2, NGC 6522-7) or a combination of the two (e.g. NGC 6522-18). In the worst case (e.g. NGC 6522-18), these show up at a strength of about the 20% of the stellar flux level but in other cases, these artefacts are not very prominent (typically $\sim 5\%$ of the flux).

Appendix F shows a comparison between the best-fitting 6–8.5- μm model and the template from Sloan & Price [77] and the observed naked star templates, for all our targets. In most cases, the differences between the different approaches for the resulting dust spectra are negligible. The most pronounced differences occur on the blue edge of the 10- μm dust complex, and they are most pronounced for the objects with low amounts of dust emission (e.g. c35-1) or lowest stellar colour temperature (e.g. OGLE-3)

In Conclusion, the modelling method amongst all, provides a much better reproduction of the molecular features and the overall shape of the continuum. We thus adopted the modelling method to subtract the stellar and molecular contribution from the data, and to extract the dust spectra. It is clear though that there would be some benefit in having more reliable underlying template spectra for these objects.

4.8.2 A spectral inventory

The extracted dust spectra of all our targets are shown in Fig. 4.15 and reveal a diversity of spectral features. The dust composition (as traced by the spectral features) furthermore appears to be quite different for stars with low mass-loss rates (bottom) and high mass-loss rates (top). Table 4.3 provides a general description of a few key components by which we can characterize our entire sample. Note that the peak position of the features can be variable between the specified range as well as their overall shape. Some features are more round compared to some other that appear more triangularly shaped.

In the following, we offer a more detailed description of the spectral features and discuss the the variations in our sample. To guide the eye in the following discussion, we show in Fig. 4.14 the particularly rich spectrum of NGC 6522-5, as well as dust scattering efficiencies for various minerals that we discuss here.

The 10- μm region

All our targets exhibit clear dust emission around 10- μm . For the targets in the top part of Fig. 4.15, the 10- μm feature is smooth and roundish, and peaks at 9.7- μm – characteristic

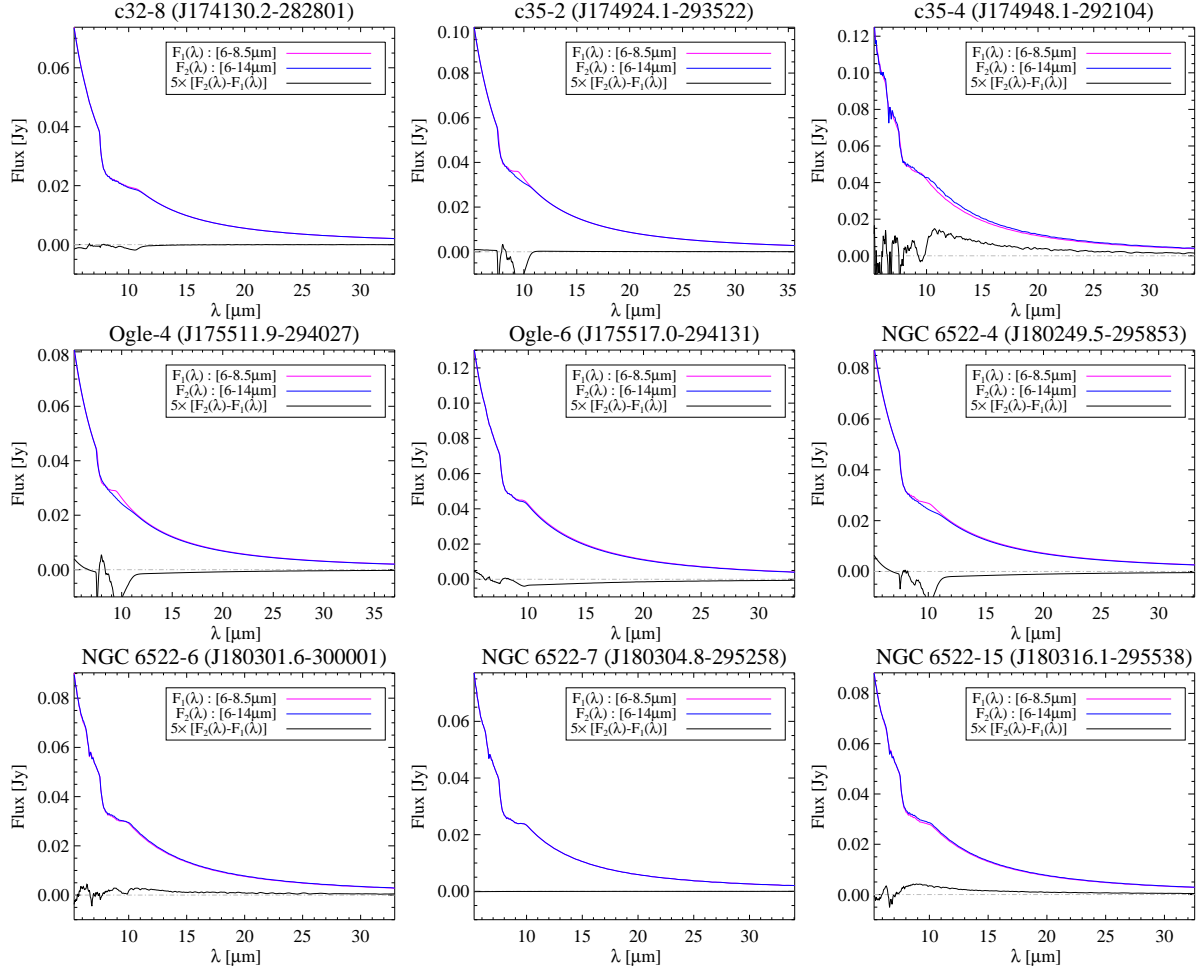


Figure 4.13: A comparison of different model spectra for the naked stars: models obtained from fitting the 6–14- μm range (blue), and from fitting only the 6–8.5- μm range (magenta). The two models are virtually indistinguishable between 6 and 8.5- μm , and in almost all cases, correspond to roughly the same stellar parameters. The black curve shows the residual difference between the two models. Note that the residuals are scaled ($\times 5$) for clarity.

of amorphous silicates. The second emission band commonly associated with such minerals, at 18- μm , also appears quite clearly in those spectra. Thus, for the objects near the top, the dust emission is largely due to amorphous silicates. However, there are clear variations in the precise shape of the 10- μm emission feature even for those “silicate” sources. For some targets, a shoulder appears at slightly longer wavelengths. As we further move down the sequence in Fig. 4.15, the character of the band changes significantly. In some sources, the 10- μm complex becomes much more sharply peaked (e.g. c32-6, c35-5, NGC 6522-14), and as we approach the bottom part of the Figure, emission in this range looks very different from the smooth silicate profiles at the top. Clearly, the dust composition in those targets must be different.

Differences in the dust composition as a function of mass loss rate have been observed before for samples of nearby, bright AGB stars [e.g. 7, 33]. However, for those samples, the

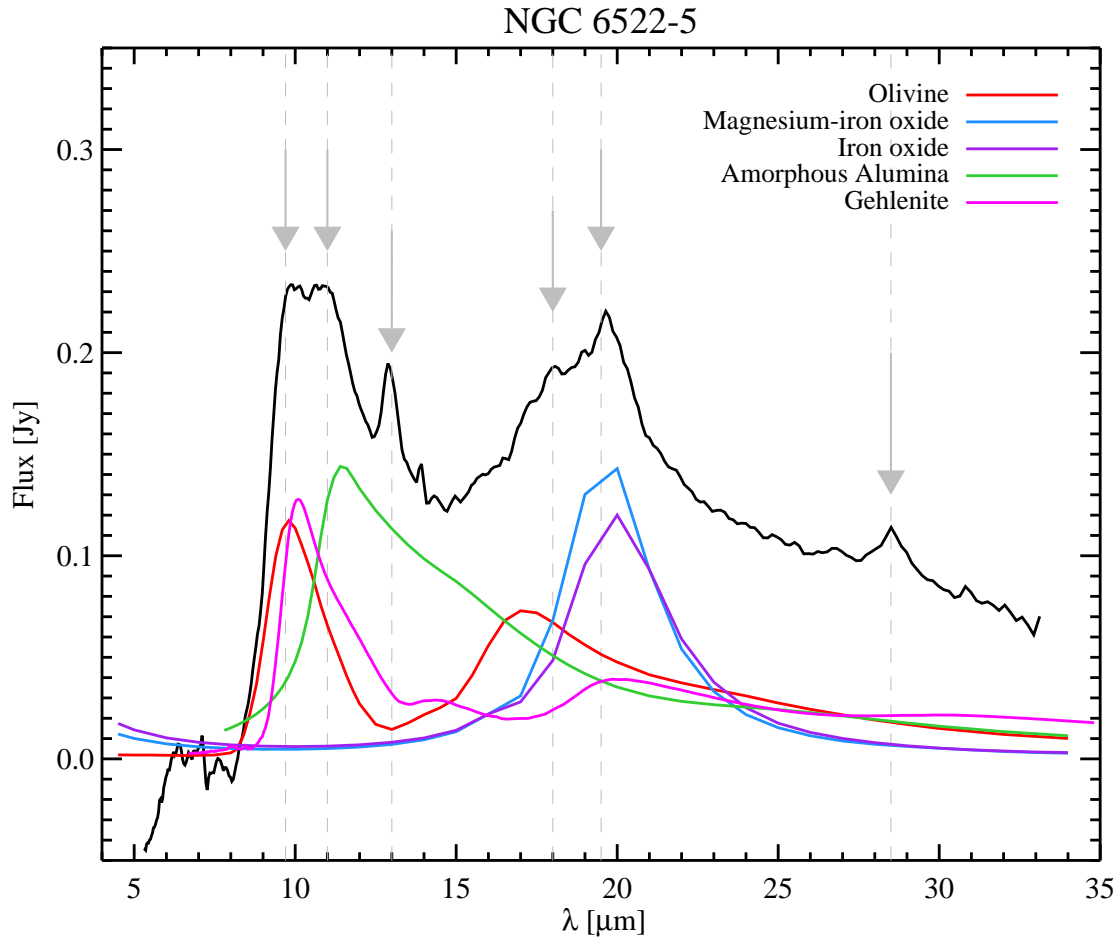


Figure 4.14: This figure shows the dust spectrum of target NGC 6522-5 which seems to have a particularly rich variety of dust features; some of those are indicated with arrows. For comparison, we also show the dust scattering efficiencies for some minerals that have been proposed as carriers for these dust features: silicates (the olivine MgFeSiO_4 is shown in red [17]), gehlenite ($\text{Ca}_2\text{Al}_2\text{SiO}_7$; magenta [59]), Alumina (Al_2O_3 [2]), iron oxide (FeO , purple [32]) and magnesiowüstite (MgFeO , blue [32]).

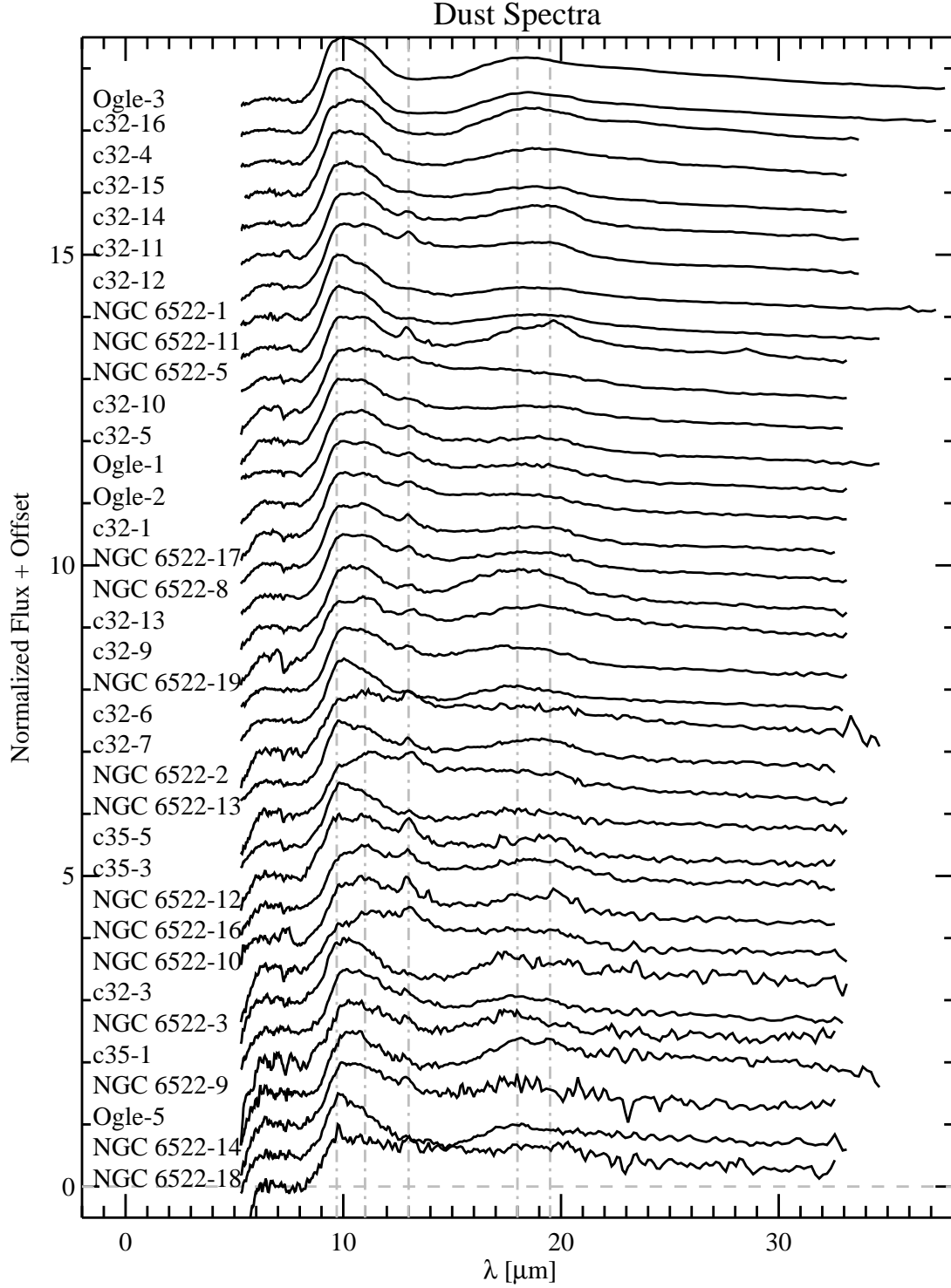


Figure 4.15: This figure shows the final dust spectra sorted based on increasing mass loss rate. Mass loss rates are estimated using equation 4.3. Overall as we go from bottom to top, different features show noticeable variations in terms of strength, shape and peak wavelength (see text for more details).

targets with the lowest mass-loss rates show a first emission peak at $11\text{-}\mu\text{m}$ and an overall dust spectrum that resembles emission from alumina (Al_2O_3 ; see Fig. 4.14). This $11\text{-}\mu\text{m}$ feature had already been detected in Mira variables observed with the Infrared Astronomical Satellite's Low Resolution Spectrometer (IRAS-LRS) by Little-Marenin & Little [53], who proposed crystalline olivine to be the carrier of this feature. Begemann et al. [2] and Miyata et al. [58] on the other hand related the $11\text{-}\mu\text{m}$ feature to amorphous alumina oxide grains. Cami [7] shows, based on *ISO-SWS* spectra, that this feature peaks at $11.1\text{-}\mu\text{m}$, while crystalline olivines peak at slightly longer wavelengths ($11.3\text{-}\mu\text{m}$), thus corroborating the assignment to amorphous alumina. In our sample that we present here though, there is not a single target where the emission peaks at $11\text{-}\mu\text{m}$, or where the dust spectrum resembles pure alumina. However, many spectra show a clear emission bump at $11\text{-}\mu\text{m}$, and this alumina may certainly be a contributing component.

There may be various other components that contribute to the $10\text{-}\mu\text{m}$ emission complex. Of particular interest in the studies of dust condensation are mellilites – a group of sorosilicates that are also commonly found in CAIs (Ca and Al-rich inclusions) in primitive chondrites. In meteorites, these mellilites form a solid solution between the Al-rich endmember called gehlenite ($\text{Ca}_2\text{Al}_2\text{SiO}_7$) and the Mg end member åkermanite ($\text{Ca}_2\text{MgSi}_2\text{O}_7$). In their analysis and modelling of a sample of O-rich AGB stars, Heras & Hony [33] found that including gehlenite significantly improved the quality of the resulting fit both in the 10 and $20\text{-}\mu\text{m}$ regions. Note that these authors used the optical constants from Mutschke et al. [59].

Chihara et al. [14] presented IR absorption spectra of the entire mellilite solid solution series between åkermanite and gehlenite. For all components, there are several peaks noticeable, including in the $9\text{--}13\text{-}\mu\text{m}$ region, but also at 14 , 15 , 17 , 19 , 21 , 24 , 30 , 37 and $60\text{-}\mu\text{m}$. In the $10\text{-}\mu\text{m}$ region, the gehlenite sample shows a spectrum that is quite different from Mutschke et al. [59], and shows a broad flat-topped, trapezoidal $10\text{-}\mu\text{m}$ feature with several small peaks superposed. The pure åkermanite on the other hand shows a much narrower $10\text{-}\mu\text{m}$ profile with sharp and prominent peaks at 10.3 , 10.7 , and $11.7\text{-}\mu\text{m}$. It is not clear how much these minerals could contribute to the spectra of our targets though; in addition to the $10\text{-}\mu\text{m}$ range, all mellilites also show strong features between 20 and $30\text{-}\mu\text{m}$, where our spectra show little to no spectral structure.

The $13\text{-}\mu\text{m}$ feature – the first condensate?

Many, but not all, of our dust spectra also show the clear presence of the so-called $13\text{-}\mu\text{m}$ feature. Vardya et al. [86] were the first to discover this feature when they studied IRAS-LRS spectra of about 20 Miras. They attributed the feature to some sort of silicate. The feature was later associated with oxygen-rich AGB stars [76]. Recently, several candidates have been proposed to be the carrier of the $13\text{-}\mu\text{m}$ feature. The 3 main candidates are corundum (crystalline Al_2O_3), spinel (MgAl_2O_4), and silicon dioxide (SiO_2) [see 16, and references therein]. Recently, Zeidler et al. [92] measured the optical constants of some of these minerals, and favor oblate corundum grains as the carriers for the $13\text{-}\mu\text{m}$ feature.

In our sample, this feature is found in many of our targets. However, we also noticed that our naked stars OGLE-4 and NGC 6522-18 may exhibit this feature. The best example is OGLE-4, where a weak feature at $13\text{-}\mu\text{m}$ appears at about the 2.6σ level, with a width and profile similar to the $13\text{-}\mu\text{m}$ feature in our dusty targets (e.g. NGC 6522-5). If this is indeed

the same 13- μm feature, it could indicate that the carrier of that feature is really the very first dust species to condense in the environment of O-rich AGB stars – maybe even in stars that otherwise produce no noticeable dust at all. Further confirmation of this detection would be desirable.

The band at 19.5- μm

A broad and sharply peaked feature at 19.5- μm (sometimes also called the 20- μm feature) is often seen in O-rich AGB stars. Little-Marenin & Little [53] and Goebel et al. [27] already detected and described it in their IRAS-LRS spectra. Following earlier work by Begemann et al. [3], Henning et al. [32] suggested that magnesium-iron oxides (magnesiowüstite) could indeed be responsible for the strong emission seen near 19- μm in some oxygen-rich stars that lack the broad silicate features. Indeed, laboratory spectroscopy of magnesium-iron oxides in the mid-IR show a single absorption band in the 15–20- μm range; the precise peak wavelength shows a strong dependence on the Mg/Fe ratio: pure FeO peaks at 20- μm ; as the Mg content increases, the peak shifts to shorter wavelengths. Observations with *ISO/SWS* yielded many more spectra of much higher quality; based on such observations, Cami [7] and Posch et al. [67] independently confirmed the good correspondence between the astronomical observations and laboratory spectra of Fe-rich MgFeO ($\text{Mg}_{0.1}\text{Fe}_{0.9}\text{O}$). A few more objects were discussed by Van Malderen [85], and Heras & Hony [33].

In our sample, there is far less evidence for the presence of this band. The 19- μm feature appears clearly in the spectrum of NGC 6522-5, but is not obviously present in the other targets; further analysis will have to confirm whether or not the band is possibly weakly present in other targets. For NGC 6522-5, the peak position is consistent with earlier studies, i.e. we find that the best correspondence with the laboratory measurements occurs for magnesiowüstite with a 10% Mg fraction ($\text{Mg}_{0.1}\text{Fe}_{0.9}\text{O}$, [32]).

The band at 28.5- μm

We only observe the 28.5- μm feature in one of our sources (NGC 6522-5). On first sight, this feature may resemble enstatite however, we have compared it to the feature that is identified as enstatite in Jones et al. [39] and verified that they are not the same neither in terms of shape nor the peak wavelength. We have over-plotted and investigated the dust scattering efficiency for enstatite and did not find a match there either. There is a possibility that this feature is due to a crystalline grain but its actual carrier is not yet fully confirmed.

4.8.3 Variations in the dust composition

In Fig. 4.15, we show the extracted dust spectra (normalized to the peak of the dust emission) sorted as a function of increasing mass loss rate. These mass loss rates were estimated from Eq. (4.3).

Compared to similar sequences obtained for nearby AGB stars [e.g. 7, 33], there are some similarities, but also very clear differences in the variations that we see in the dust spectra. Indeed, these studies showed a clear difference between objects with low mass-loss rates whose spectra are dominated by oxide type dust (as seen through 11- μm , 13- μm and 19- μm features),

Table 4.3: This table provides a list of a few key features that characterize all our spectra and is sorted based on increasing mass loss rate. Note that symbols such as Δ & \bigcirc are used when the profile has a noticeable triangular or round appearance. In cases where it is not easy to determine the actual shape of the profiles individually, we have used \checkmark to denote the presence of the features. Note also the actual peak wavelength of these features can be slightly variable throughout our sample (e.g. $\lambda_{peak} \in [9.7-10.3], [10.8-11.2], [12.8-13.2]\mu m$).

Identifier	$\lambda_{peak} \sim 9.7\&18\mu m$	$\lambda_{peak} \sim 11\mu m$	$\lambda_{peak} \sim 13\mu m$	$\lambda_{peak} \sim 19.5\mu m$	$\lambda_{peak} \sim 28.5\mu m$
NGC 6522-14	Δ	\checkmark	\checkmark
Ogle-5	\checkmark	\checkmark	\checkmark
NGC 6522-9	\checkmark	\checkmark	\checkmark	\checkmark	...
c35-1	\checkmark	\checkmark	\checkmark	\checkmark	...
NGC 6522-3	\checkmark	\checkmark	\checkmark
c32-3	\checkmark	...	\checkmark	\checkmark	...
NGC 6522-10	\checkmark	\checkmark	\checkmark
NGC 6522-16	\checkmark	\checkmark	\checkmark	\checkmark	...
NGC 6522-12	\checkmark	\checkmark	\checkmark	\checkmark	...
c35-3	\checkmark	\checkmark	\checkmark
c35-5	\checkmark	\checkmark	\checkmark
NGC 6522-13	...	\checkmark	\checkmark	\checkmark	...
NGC 6522-2	\checkmark	\checkmark	\checkmark
c32-7	...	\checkmark	\checkmark	\checkmark	...
c32-6	\checkmark	...	\checkmark	\checkmark	...
NGC 6522-19	\checkmark	\checkmark	\checkmark
c32-9	\checkmark	\checkmark	\checkmark	\checkmark	...
c32-13	\checkmark	\checkmark	\checkmark	\checkmark	...
NGC 6522-8	\checkmark	\checkmark	\checkmark
NGC 6522-17	\checkmark	\checkmark	\checkmark
c32-1	\checkmark	\checkmark	\checkmark	\checkmark	...
Ogle-2	\checkmark	\checkmark	\checkmark	\checkmark	...
Ogle-1	\checkmark	\checkmark	\checkmark	\checkmark	...
c32-5	\checkmark	\checkmark	\checkmark	\checkmark	...
c32-10	\checkmark	\checkmark	\checkmark
NGC 6522-5	\checkmark	\checkmark	\checkmark	\checkmark	\checkmark
NGC 6522-11	\checkmark	\checkmark	\checkmark
NGC 6522-1	\checkmark	\checkmark	\checkmark	\checkmark	...
c32-12	\checkmark	\checkmark	\checkmark
c32-11	\checkmark	\checkmark	\checkmark
c32-14	\checkmark	\checkmark	\checkmark	\checkmark	...
c32-15	\checkmark	\checkmark	...	\checkmark	...
c32-4	\checkmark	\checkmark	...	\checkmark	...
c32-16	\bigcirc
Ogle-3	\bigcirc	\checkmark	...

and Mira variables with higher mass-loss rates whose spectra show primarily silicate emission (broad and smooth 10 and 18- μm bands). Fig. 4.15 reveals a somewhat more chaotic picture for our target stars. The spectra of objects with high mass-loss rates (the top spectra in Fig. 4.15) show the broad silicate emission bands, but there are no clear objects in our sample whose spectra are characteristic of the oxide dominated dust. For instance, we see no single spectrum that is dominated by an alumina-like dust emission profile. Similarly, as noted above, the 19- μm band attributed to MgFeO is only clearly visible in one object (NGC 6522-5) which happens to have a fairly high mass-loss rate.

It is also interesting to note that the 13- μm feature appears in most of our spectra, although there seems to be no clear trend regarding the strength of this feature as a function of mass loss rate. There are objects with both high and low mass-loss rates where the 13- μm feature is absent or very weak.

Thus, while our sample does show clear variations in the spectral content of our targets, these variations are not easy to interpret. It seems that spectra dominated by oxide dust are underrepresented in our sample, and there is no clear one to one relation between mass-loss rates and dust composition as traced from the spectra.

4.8.4 The SE classification of our targets

We can also study variations in our dust spectra (and a possible sequence in the dust composition) in a different way – by determining the so-called Silicate Emission (SE) index, first discussed by Sloan & Price [77] who worked out the SE classification based on IRAS-LRS observations of a sample of O-rich AGB stars. These authors used simple flux measurements at 10, 11, and 12 μm to characterize the shape of the 10 μm dust profiles, and divided their spectra into 8 different SE classes defined as

$$\text{SE} = 10(F_{11}/F_{12}) - 7.5. \quad (4.4)$$

Sloan & Price [77] argue that stars that belong to the first SE class (SE1) show a very broad 11 μm feature associated with alumina dust. Moving towards higher classes, this feature gradually becomes narrower and the peak position shifts towards shorter wavelengths. Stars that belong to the highest SE class (SE8), show a feature that peaks around 9.7 μm associated with amorphous silicate dust. Thus, the SE classes can be understood as a sequence in dust composition that is related to changes in mass-loss rate.

Fig. 4.16 shows the SE classes for all targets in our sample. All targets cluster around the power-law line described by [77]; however, it is immediately clear that class SE1 is absent and class SE2 is only represented by two targets, in fact most of our targets are in classes SE5 or higher. This seems to confirm our conclusions from studying the dust spectra in Fig. 4.15 where we found that no target seems to correspond to a pure oxide dust spectrum.

When we determined the SE classes, we used the dust spectra obtained by subtracting a detailed model of the underlying stellar and molecular contributions. This is different from Sloan & Price [77] who used the same template model for all their objects (see § 4.8.1). We have therefore repeated our classification, but this time using dust spectra obtained by subtracting the same template. While there are small differences in the resulting classification, those are details and the overall conclusion remains the same: the lower SE classes are missing or underrepresented in our sample.

Table 4.4: Extinction values for all our targets as well as SE classification. Note that naked stars (NS) do not belong to any SE class. The CC abbreviation refers to the method of using Correlation Coefficient.

Identifier	A_K [mag] (S99 and S04) ^a	A_K [mag] (Modeling)	A_K [mag] (G12) ^b	A_K [mag] (CC)	A_K [mag] (Final)	SE Index	$\log(L/L_\odot)$	$\log \dot{M}[M_\odot/\text{yr}]$ (This Work)	$\log \dot{M}[M_\odot/\text{yr}]$ [60]
c32-1	0.571		0.797±0.136		0.581	5	4.02	-6.97	-6.03
c32-3	0.518		0.772±0.128		0.528	8	3.45	-7.53	-7.83
c32-4	0.518		0.772±0.128		0.528	7	4.08	-6.55	-5.30
c32-5	0.507		0.780±0.136		0.517	6	4.09	-6.87	-5.84
c32-6	0.507		0.780±0.136		0.517	8	3.91	-7.06	-6.90
c32-7	0.507		0.781±0.136		0.517	4	3.95	-7.21	-6.91
c32-8	0.507	0.57	0.781±0.136	0.518	0.520	NS			
c32-9	0.507		0.772±0.130		0.517	5	3.93	-7.06	-5.62
c32-10	0.507		0.743±0.127		0.517	5	4.04	-6.86	-5.86
c32-11	0.497		0.770±0.133		0.507	6	3.97	-6.66	-5.79
c32-12	0.528		0.781±0.136		0.538	5	4.08	-6.70	-5.85
c32-13	0.476		0.730±0.135		0.486	6	3.84	-7.01	-6.36
c32-14	0.507		0.775±0.133		0.517	7	4.08	-6.64	-5.53
c32-15	0.518		0.762±0.142		0.528	7	4.02	-6.56	-5.55
c32-16	0.550		0.790±0.145		0.560	9	4.16	-6.48	-5.40
c35-1	0.602		0.923±0.169		0.600	6	3.42	-7.60	-6.90
c35-2	0.539	0.49	0.865±0.150	0.539	0.540	NS			
c35-3	0.624		1.033±0.210		0.920	5	3.74	-7.37	-6.54
c35-4	0.550	0.87	1.022±0.212	0.920	0.920	NS			
c35-5	0.581		0.972±0.217		0.920	7	3.56	-7.34	-6.39
Ogle-1	0.302		0.252±0.103		0.238	5	4.00	-6.93	-6.35
Ogle-2	0.302		0.260±0.107		0.242	5	3.97	-6.95	-6.54
Ogle-3	0.302		0.260±0.105		0.242	8	4.33	-6.32	-5.29
Ogle-4	0.302	0.18	0.264±0.105	0.246	0.246	NS			
Ogle-5	0.302		0.268±0.104		0.254	6	3.22	-7.66	-9.18
Ogle-6	0.302	0.21	0.268±0.104	0.254	0.254	NS			
NGC 6522-1	0.127		0.171±0.098		0.285	8	4.17	-6.70	-5.94
NGC 6522-2	0.111		0.166±0.097		0.275	5	3.50	-7.22	-6.93
NGC 6522-3	0.155		0.152±0.098		0.155	6	3.35	-7.57	-8.39
NGC 6522-4	0.180	0.27	0.166±0.097	0.275	0.275	NS			
NGC 6522-5	0.106		0.171±0.097		0.100	6	3.70	-6.84	-6.39
NGC 6522-6	0.160	0.10	0.171±0.097	0.100	0.100	NS			
NGC 6522-7	0.063	0.18	0.150±0.098	0.144	0.144	NS			
NGC 6522-8	0.090		0.148±0.097		0.130	6	3.84	-6.98	-7.04
NGC 6522-9	0.090		0.148±0.097		0.130	7	3.35	-7.63	-8.58
NGC 6522-10	0.106		0.143±0.094		0.100	3	3.50	-7.51	-7.93
NGC 6522-11	0.095		0.177±0.098		0.100	7	4.09	-6.77	-7.03
NGC 6522-12	0.063		0.147±0.099		0.144	4	3.40	-7.40	-7.24
NGC 6522-13	0.106		0.143±0.094		0.100	3	3.80	-7.33	-6.85
NGC 6522-14	0.085		0.143±0.094		0.100	9	3.30	-7.66	-10.00
NGC 6522-15	0.063	0.11	0.143±0.094	0.100	0.100	NS			
NGC 6522-16	0.063		0.142±0.096		0.100	4	3.35	-7.49	-7.91
NGC 6522-17	0.085		0.143±0.095		0.100	5	3.75	-6.98	-6.83
NGC 6522-18	0.106		0.141±0.098	0.12	0.157	5			
NGC 6522-19	0.099		0.141±0.098		0.12	6	3.79	-7.06	-7.29

^aS99: Schultheis et al. [73], S04: Sumi [80]

^bG12: Gonzalez et al. [28]

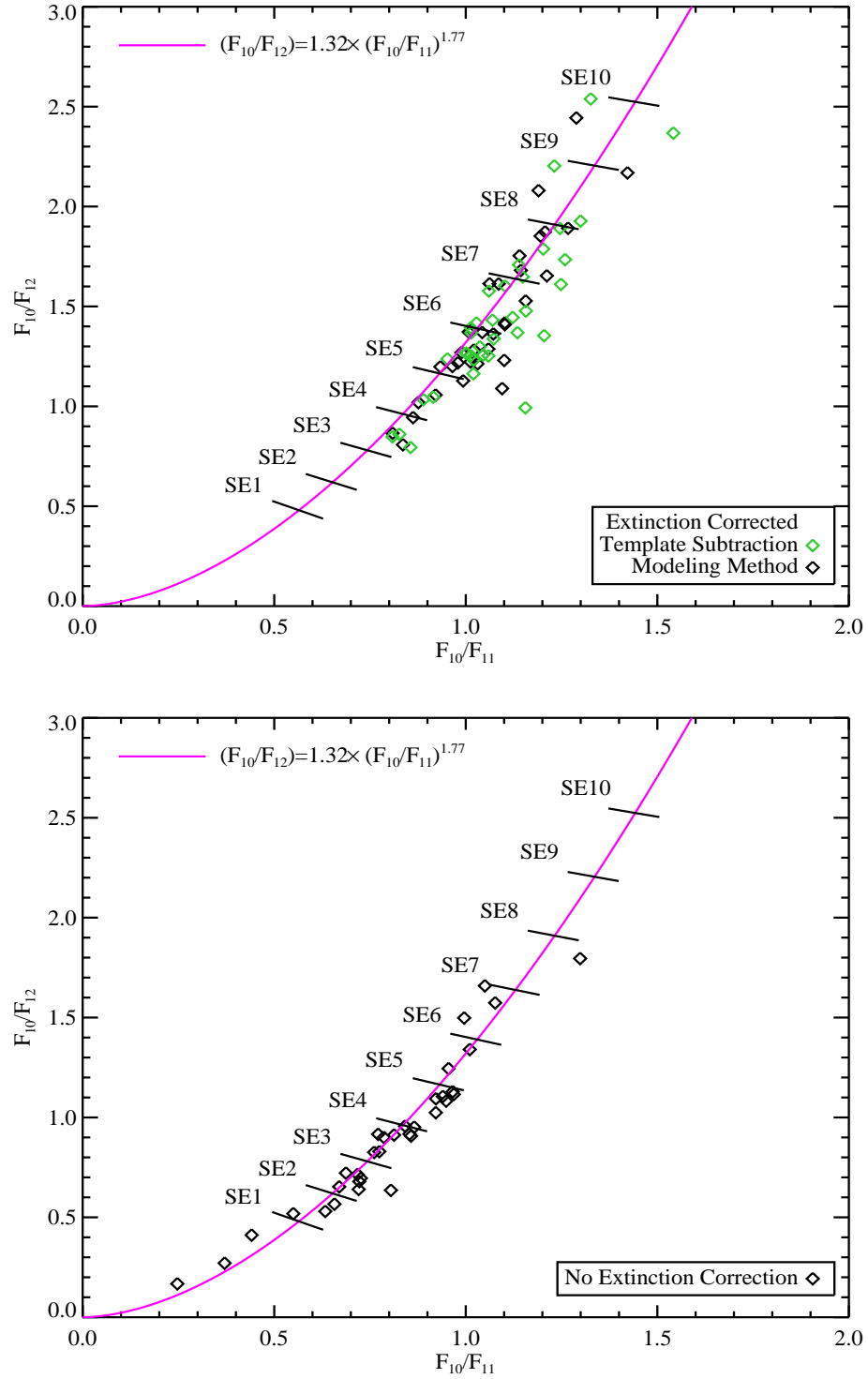


Figure 4.16: The SE classification for our sample after applying an extinction correction (*top*) and without applying an extinction correction (*bottom*). Flux ratios for our targets are indicated with the black diamonds; the green symbols indicate ratios obtained when using a similar stellar template as Sloan & Price [77]. The solid curve indicates the power law through the classes derived by Sloan & Price [77] and the SE classes themselves are separated by grey lines (dashed and dotted for better illustration).

This result is somewhat surprising, given the goal of this program and our careful sample selection. Either something must have gone wrong in the sample selection, or alternatively, our conclusions indicate that the dust around the AGB stars in the galactic bulge might be somewhat different than the dust composition in the solar neighbourhood. It is clear though that a first contributing factor is certainly extinction. Indeed, at the time of our sample selection, reliable quantitative information about extinction towards our targets was scarce, and there was no reason to assume large variations in extinction values from one line of sight to another; our sample selection was thus based on sampling a color-magnitude diagram that was not corrected for extinction. The effect of extinction on our SE classification is illustrated in the bottom panel of Fig. 4.16, where we show the classes obtained without performing an extinction correction. In this case, we find a much more uniform coverage of the different SE classes. One could thus easily dismiss our “missing classes” conclusions as due to these extinction effects and improper sample selection.

However, this cannot be the main or only reason for this effect. Indeed, it is important to realize here that we did select some of the bluest targets possible (see Fig. 4.2 and our discussion in § 4.2); and even in the presence of extinction, this selection ensured that we have about 9 naked stars in our sample. If extinction would systematically shift our targets to the higher SE classes, we should not have found any naked stars in our sample either.

Thus, we have to entertain the possibility that the absence of the SE classes represents a real effect, possibly due to different conditions in the galactic bulge (e.g. lower metallicity). If proven correct, this could offer valuable insights into the dust condensation around O-rich AGB stars; follow-up work relating to this question will be the topic of further research.

4.9 Summary & Conclusions

We have obtained *Spitzer-IRS* spectra for a sample of AGB stars in the Galactic Bulge with targets that were selected based on their $(K_s - [15])_0$ colour in order to cover the full range of low to high mass loss rates on the AGB. Strong and variable background emission in the crowded bulge fields complicates data reduction, and our targets suffer from interstellar extinction.

Using a subset of naked stars in our sample, we compared different methods to quantify and correct the interstellar extinction in our fields, and adopted extinction values derived from a model-independent analysis of the naked stars. From these naked star values, and from literature results as well as IRAC images, we estimated the extinction towards our dusty targets as well, and de-reddened our observations.

We constructed a *Spitzer-IRS* based colour-magnitude diagram, and used this to estimate luminosities and mass-loss rates for our targets. With these, we can characterize our sample, and confirm that it indeed corresponds to AGB stars at the distance of the Galactic bulge (~ 8.5 kpc) covering the entire range of mass-loss rates expected on the AGB. We modeled the underlying stellar and molecular spectral contributions between 5-8- μ m, and used these results to construct the stellar and molecular model spectra over the entire *Spitzer-IRS* wavelength range; these models were then subtracted from the observations to obtain the dust spectra.

A first analysis of the dust spectra by carrying out a spectral inventory and by determining the SE classification for our targets shows that our sample shows clear variations in the dust composition, but these changes are not clearly related to changes in the mass-loss rates. Due to

extinction, the lower SE classes (corresponding to spectra dominated by oxides) are somewhat underrepresented in our sample. The detection of a $13\text{-}\mu\text{m}$ band in two of our naked stars entertains the possibility of this feature being among the first dust grains to condense out.

Further work on this sample of spectra will include detailed modelling of the spectra, studying the relation with metallicity and comparison with pulsational properties obtained from ground-based data.

Acknowledgments

SSG and JC acknowledge support from an NSERC Discovery Grant and a start-up grant from the Department of Physics and Astronomy at Western University. FK is being supported by grant NSC100-2112-M-001-023-MY3 from the National Science Council. This research has made use of the SIMBAD database, operated at CDS, Strasbourg, France; and of NASA's Astrophysics Data System Bibliographic Services.

This work is based on observations made with the *Spitzer* Space Telescope, which is operated by the Jet Propulsion Laboratory, California Institute of Technology under a contract with NASA. The IRS was a collaborative venture between Cornell University and Ball Aerospace Corporation funded by NASA through the Jet Propulsion Laboratory and Ames Research Centre. SMART was developed by the IRS Team at Cornell University and is available through the *Spitzer* Science Centre at Caltech. This publication makes use of data products from the Two Micron All Sky Survey, which is a joint project of the University of Massachusetts and the Infrared Processing and Analysis Centre/California Institute of Technology, funded by the National Aeronautics and Space Administration and the National Science Foundation.

Bibliography

- [1] Aringer B., Jørgensen U.G., Langhoff S.R., Hron J., 2000, In: Wing R.F. (ed.), *The Carbon Star Phenomenon*, vol. 177 of *IAU Symposium*, p. 520
- [2] Begemann B., Dorschner J., Henning T., et al., 1997, *ApJ* 476, 199
- [3] Begemann B., Henning T., Mutschke H., Dorschner J., 1995, *Planet. Space Sci.* 43, 1257
- [4] Beichman C.A., Neugebauer G., Habing H.J., Clegg P.E., Chester T.J. (eds.), 1988, Infrared astronomical satellite (IRAS) catalogs and atlases. Volume 1: Explanatory supplement, vol. 1
- [1] Blommaert J.A.D.L., Cami J., Szczerba R., Barlow M.J., 2005, *Space Science Reviews* 119, 215
- [6] Blommaert J.A.D.L., Groenewegen M.A.T., Okumura K., et al., 2006, *A&A* 460, 555
- [7] Cami J., 2002, *Ph.D. Thesis, University of Amsterdam*
- [8] Cami J., 2012, Database-Driven Analyses of Astronomical Spectra, pp. 267–285
- [9] Cami J., Justtanont K., de Jong T., et al., 1997, In: Heras A.M., Leech K., Trams N.R., Perry M. (eds.), *The first ISO workshop on Analytical Spectroscopy*, vol. 419 of *ESA Special Publication*
- [12] Cami J., van Malderen R., Markwick A.J., 2010, *ApJS* 187, 409
- [11] Cami J., Yamamura I., de Jong T., et al., 2000, *A&A* 360, 562
- [12] Cardelli J.A., Clayton G.C., Mathis J.S., 1989, In: Allamandola L.J., Tielens A.G.G.M. (eds.), *Interstellar Dust*, vol. 135 of *IAU Symposium*, p. 5P
- [13] Chiar J.E., Tielens A.G.G.M., 2006, *ApJ* 637, 774
- [14] Chihara H., Koike C., Tsuchiyama A., 2007, *A&A* 464, 229
- [15] Churchwell E., Brian B., Bania T., et al., 2005, *Spitzer Proposal* p. 20201
- [16] DePew K., Speck A., Dijkstra C., 2006, *ApJ* 640, 971
- [17] Dorschner J., Begemann B., Henning T., Jaeger C., Mutschke H., 1995, *A&A* 300, 503

- [18] Duari D., Cherchneff I., Willacy K., 1999, *A&A* 341, L47
- [19] Engelke C.W., 1992, *AJ* 104, 1248
- [20] Epchtein N., Deul E., Derriere S., et al., 1999, *A&A* 349, 236
- [21] Fabian D., Posch T., Mutschke H., Kerschbaum F., Dorschner J., 2001, *A&A* 373, 1125
- [22] Felli M., Testi L., Schuller F., Omont A., 2002, *A&A* 392, 971
- [23] Girardi, L., Williams, B. F., Gilbert, K. M., et al. 2010, *ApJ*, 724, 1030
- [24] Groenewegen, M. A. T. 1993, Ph.D. Thesis,
- [25] Groenewegen, M. A. T. 1995, *A&A*, 293, 463
- [26] Girardi, L., Marigo, P., Bressan, A., & Rosenfield, P. 2013, *ApJ*, 777, 142
- [27] Goebel J.H., Bregman J.D., Witteborn F.C., 1994, In: *American Astronomical Society Meeting Abstracts*, vol. 26 of *Bulletin of the American Astronomical Society*, p. 1455
- [28] Gonzalez O.A., Rejkuba M., Zoccali M., et al., 2012, *A&A* 543, A13
- [29] Groenewegen M.A.T., Blommaert J.A.D.L., 2005, *A&A* 443, 143
- [30] Grossman L., Larimer J.W., 1974, *Rev Geophys Spac Phys* 12, 71
- [31] Habing H.J., 1996, *A&AR* 7, 97
- [32] Henning T., Begemann B., Mutschke H., Dorschner J., 1995, *A&AS* 112, 143
- [33] Heras A.M., Hony S., 2005, *A&A* 439, 171
- [34] Herwig F., 2005, *ARA&A* 43, 435
- [40] Higdon, S. J. U., Devost, D., Higdon, J. L., et al. 2004, *pasp*, 116, 975
- [39] Houck J.R., Roellig T.L., van Cleve J., et al., 2004, *ApJS* 154, 18
- [37] Iben I., Renzini A., 1983, *ARA&A* 21, 271
- [38] Indebetouw R., Mathis J.S., Babler B.L., et al., 2005, *ApJ* 619, 931
- [39] Jones, O. C., Kemper, F., Sargent, B. A., et al. 2012, *mnras*, 427, 3209
- [40] Jones H.R.A., Pavlenko Y., Viti S., Tennyson J., 2002, *MNRAS* 330, 675
- [41] Jørgensen U.G., Jensen P., Sørensen G.O., Aringer B., 2001, *A&A* 372, 249
- [42] Woods, P. M., Sloan, G. C., Gordon, K. D., et al. 2011, arXiv:1108.1715
- [43] Justtanont K., Feuchtgruber H., de Jong T., et al., 1998, *A&A* 330, L17

- [44] Kemper, F., Woods, P. M., Antoniou, V., et al. 2010, *pasp*, 122, 683
- [45] Kalirai, J. S., Hansen, B. M. S., Kelson, D. D., et al. 2008, *ApJ*, 676, 594
- [46] Karovicova I., Wittkowski M., Ohnaka K., et al., 2013, *A&A* 560, A75
- [47] Kessler M.F., Steinz J.A., Anderegg M.E., et al., 1996, *A&A* 315, L27
- [48] Kozasa T., Sogawa H., 1997, *Ap&SS* 255, 437
- [49] Lawson C.L., Hanson R.J., 1974, Solving least squares problems. Prentice-Hall Series in Automatic Computation, Englewood Cliffs: Prentice-Hall, 1974
- [50] Leboutteiller V., Barry D.J., Spoon H.W.W., et al., 2011, *ApJS* 196, 8
- [73] Leboutteiller V., Bernard-Salas J., Sloan G.C., Barry D.J., 2010, *pasp* 122, 231
- [52] Lebzelter T., Posch T., 2001, *Information Bulletin on Variable Stars* 5089, 1
- [53] Little-Marenin I.R., Little S.J., 1990, *ApJ* 99, 1173
- [54] Lutz D., Feuchtgruber H., Genzel R., et al., 1996, *A&A* 315, L269
- [55] Marigo, P. 2013, IAU Symposium, 281, 36
- [56] Markwick A., Millar T., 2000, *A&A* 359, 1162
- [57] Matsuura M., Yamamura I., Cami J., Onaka T., Murakami H., 2002, *A&A* 383, 972
- [58] Miyata T., Kataza H., Okamoto Y., Onaka T., Yamashita T., 2000, *ApJ* 531, 917
- [59] Mutschke H., Begemann B., Dorschner J., et al., 1998, *A&A* 333, 188
- [60] Ojha D.K., Omont A., Schuller F., et al., 2003, *A&A* 403, 141
- [61] Olofsson H., 2005, In: Wilson A. (ed.), *ESA Special Publication*, vol. 577 of *ESA Special Publication*, pp. 223–228
- [62] Omont A., Ganesh S., Alard C., et al., 1999, *A&A* 348, 755
- [63] Omont A., Gilmore G.F., Alard C., et al., 2003, *A&A* 403, 975
- [64] Onaka T., de Jong T., Willems F.J., 1989, *A&A* 218, 169
- [65] Politano, M., & Taam, R. E. 2011, *ApJ*, 741, 5
- [66] Peeters E., Hony S., Van Kerckhoven C., et al., 2002, *A&A* in press
- [67] Posch T., Kerschbaum F., Mutschke H., Dorschner J., Jäger C., 2002, *A&A* 393, L7
- [68] Román-Zúñiga C.G., Lada C.J., Muench A., Alves J.F., 2007, *ApJ* 664, 357
- [69] Ryde N., Eriksson K., Gustafsson B., 1999, *A&A* 341, 579

- [70] Ryde N., Eriksson K., Gustafsson B., Lindqvist M., Olofsson H., 1998, *Ap&SS* 255, 301
- [71] Salpeter E.E., 1974, *ApJ* 193, 579
- [72] Schuller F., Ganesh S., Messineo M., et al., 2003, *A&A* 403, 955
- [73] Schultheis M., Ganesh S., Simon G., et al., 1999, *A&A* 349, L69
- [74] Schutte W.A., Tielens A.G.G.M., 1989, *ApJ* 343, 369
- [75] Sedlmayr E., 1989, In: *IAU Symp. 135: Interstellar Dust*, vol. 135, p. 467
- [76] Sloan G.C., Levan P.D., Little-Marenin I.R., 1996, *ApJ* 463, 310
- [77] Sloan G.C., Price S.D., 1995, *ApJ* 451, 758
- [78] Smith J.D.T., Armus L., Dale D.A., et al., 2007, *pasp* 119, 1133
- [79] Speck A.K., Barlow M.J., Sylvester R.J., Hofmeister A.M., 2000, *A&AS* 146, 437
- [80] Sumi T., 2004, *mnras* 349, 193
- [81] Tielens A.G.G.M., 2008, *ARA&A* 46, 289
- [82] Tsuji T., Ohnaka K., Aoki W., Yamamura I., 1997, *A&A* 320, L1
- [83] Uttenthaler S., Stute M., Sahai R., et al., 2010, *A&A* 517, A44
- [84] van Loon, J. T., Marshall, J. R., Matsuura, M., & Zijlstra, A. A. 2003, *mnras*, 341, 1205
- [85] Van Malderen R., 2003, *Ph.D. Thesis, University of Leuven*
- [86] Vardya M.S., de Jong T., Willems F.J., 1986, *ApJ Lett.* 304, L29
- [87] Waters L.B.F.M., Molster F.J., de Jong T., et al., 1996, *A&A* 315, L361
- [127] Werner M.W., Roellig T.L., Low F.J., et al., 2004, *ApJS* 154, 1
- [89] Willson L.A., 2000, *ARA&A* 38, 573
- [90] Yamamura I., de Jong T., Cami J., 1999a, *A&A* 348, L55
- [91] Yamamura I., de Jong T., Onaka T., Cami J., Waters L.B.F.M., 1999b, *A&A* 341, L9
- [92] Zeidler S., Posch T., Mutschke H., 2013, *A&A* 553, A81

Chapter 5

Summary & Open Questions

During their early main sequence lives, the A- and B-type stars undergo various nucleosynthesis processes that results in production of new elements. These elements are brought up to the atmosphere over time via radiation pressure or convection. The abundance of the elements plays a crucial role in the way the chemistry of the stellar photosphere develops in the next stages of evolution such as AGB phase.

In this work we presented a reliable method to determine the atmospheric abundances of early type stars in the ultraviolet window. We presented two comprehensive lists of such determinations in two different stars, as a conclusive proof that the adopted synthesis tool in the ultraviolet range, is indeed reliable and usable for future work. This can involve surveys of large number of stars covering larger wavelength windows for potentially more new elements.

Next, we shifted our focus from early stars to evolved stars. The two stars that are studied in chapters 2 & 3 will eventually evolve into the stars that are studied in chapter 4. The importance of this study arises from the fact that, over the entire AGB evolution, stars return over 80% of their initial mass back to the the ISM [124], and this way they contribute greatly to the chemistry of ISM. As a result of this extensive mass loss, each star forms a large circumstellar envelope surrounding the star. The radiation pressure from the central star is absorbed by the dust and will be re-radiated in the infrared region of the electromagnetic spectrum. Therefore Infrared observations of dust allow us to address long existing yet still open questions.

One of the key questions that is yet to be answered, is how exactly dust forms. While there is some qualitative observational correspondence between detected dust species and theoretical condensation sequences, many minerals that are part of the condensation sequence have not been observationally confirmed yet, and at the same time, observations have revealed the presence of minerals that were not expected based on the dust condensation sequence. Furthermore, silicates are primarily seen in amorphous form, whereas dust formation theories predict that they should form in a crystalline structure at the temperatures where they supposedly condense out. Why this is not the case is not clear. Several studies have previously addressed the condensation of dust along AGB [18, 10], but were necessarily carried out using inhomogenous samples of targets which makes the results hard to interpret. An intriguing related question is which dust species drive the mass loss rate. Recently, it was shown that radiation pressure on silicate grains does not provide a sufficient force to drive the outflow. There is little doubt that the stellar wind is driven by radiation pressure on dust, but if silicates (the most abundant dust grains in most O-rich AGB stars) cannot drive the outflow, then what dust component can?

A related problem is that we may not even know very well what the dust spectra of these AGB stars look like. To obtain the dust spectra, we need to subtract a good template for the stellar atmosphere and the surrounding molecular layers. No such good and reliable templates are available though. A key role in this problem is played by water. Water is abundantly present in AGB CSEs, and has a large opacity over a large wavelength range. Water thus strongly determines how the IR “pseudo-continuum” appears. However, to date there is no model for a spherical and optically thick shell of water surrounding an AGB star, and thus it is not even clear how reliable our “observed” dust spectra are.

Additionally, the relation between the stellar properties, the warm molecular layers and dust formation is not yet well understood. Do the warm molecular layers play a role in the formation of dust ? How do different parameters within the molecular layer (such as temperature and column density or composition) affect the sequence of dust formation or its chemistry ?

Many of these problems can be addressed by observations carried out by Spitzer Space Telescope. In chapter 4, we have presented a unique and homogeneous sample of AGB stars. We extracted the infrared spectra and modeled the warm molecular layers. The modeling of the dust spectra is the focus of future work which can help answer some of the questions mentioned above.

After modeling the dust spectra, one can sort the sample based on increasing mass loss rate in order to extract an “observational condensation sequence” which can further be compared to the theoretical condensation sequence for possible correlations. The remaining fundamental questions about the detailed processes involved in the dust nucleation will need an in depth study which is not addressed in this thesis.

Bibliography

- [1] Blommaert, J. A. D. L., Cami, J., Szczerba, R., & Barlow, M. J. 2005, *Space Sci. Rev.* , 119, 215
- [2] Becker, S. A. 1981, *ApJ*, 248, 298
- [3] Becker, S. A., & Iben, I., Jr. 1979, *ApJ*, 232, 831
- [4] Becker, S. A., & Iben, I., Jr. 1980, *ApJ*, 237, 111
- [5] Busso, M., Gallino, R., & Wasserburg, G. J. 1999, *ARA&A* , 37, 239
- [6] Bowers, P. F., & Hagen, W. 1984, *ApJ* , 285, 637
- [7] Boyer, M. L., Srinivasan, S., van Loon, J. T., et al. 2011, Why Galaxies Care about AGB Stars II: Shining Examples and Common Inhabitants, 445, 473
- [8] Benjamin, R. A., Churchwell, E., Babler, B. L., et al. 2003, *PASP* , 115, 953
- [9] Bethe, H. A. 1939, *Physical Review*, 55, 434
- [10] Blommaert, J. A. D. L., Vanhollebeke, E., Cami, J., et al. 2007, Why Galaxies Care About AGB Stars: Their Importance as Actors and Probes, 378, 164
- [11] Bernath, P. F. 1995, *Spectra of Atoms and Molecules*, Oxford University Press, Inc., ISBN 0-19-507598-6
- [12] Cami J., van Malderen R., Markwick A.J., 2010, *ApJS* 187, 409
- [13] Caputo, D. P., Speck, A. K., Barlow, M. J., et al. 2008, *Bulletin of the American Astronomical Society*, 40, 196
- [14] Cameron, A. G. W. 1955, *ApJ*, 121, 144
- [15] Chaboyer, B., & Kim, Y.-C. 1995, *ApJ* , 454, 767
- [16] Carbon, D. F., Chiar, J. E., & Goorvitch, D. 2003, *Astrophysics of Dust*, 58
- [17] Caughlan, G. R. 1965, *ApJ*, 141, 688
- [18] Cami, J. 2002, Ph.D. Thesis,

- [19] Charbonnel, C. 1994, *A&A* , 282, 811
- [20] Clayton, D. D. 1968, New York: McGraw-Hill, 1968,
- [21] Carroll, B. W., & Ostlie, D. A. 1996, Institute for Mathematics and Its Applications,
- [22] Decin, L., De Beck, E., Brünken, S., et al. 2010, *A&A*, 516, AA69
- [23] Dirks, U., Schirrmacher, V., & Sedlmayr, E. 2008, *A&A* , 491, 643
- [24] Dotter, A., Chaboyer, B., Jevremović, D., et al. 2007, *aj* , 134, 376
- [25] De Beck, E., Decin, L., de Koter, A., et al. 2010, *A&A* , 523, AA18
- [26] Schöier, F. L. 2007, Why Galaxies Care About AGB Stars: Their Importance as Actors and Probes, 378, 216
- [27] Ford, K. E. S., Neufeld, D. A., Schilke, P., & Melnick, G. J. 2004, *ApJ*, 614, 990
- [28] Fowler, W. A. 1986, Highlights of Modern Astrophysics: Concepts and Controversies, 3
- [29] Fazio, G. G., Hora, J. L., Allen, L. E., et al. 2004, *ApJS* , 154, 10
- [30] Foukal, P., Fröhlich, C., Spruit, H., & Wigley, T. M. L. 2006, *Nature* , 443, 161
- [31] Gray, D. F. 2008, The Observation and Analysis of Stellar Photospheres, by David F. Gray, Cambridge, UK: Cambridge University Press, 2008,
- [32] Gaunt, J., A. 1930, *Phil. Trans. Roy. Soc. Lond. Ser. A* , 229, 163
- [33] Gielen, C., Cami, J., Bouwman, J., Peeters, E., & Min, M. 2011, *A&A*, 536, AA54
- [34] Girardi, L., Bressan, A., Bertelli, G., & Chiosi, C. 2000, *A&As* , 141, 371
- [35] Gilroy, K. K., & Brown, J. A. 1991, *ApJ* , 371, 578
- [36] García-Lario, P., Manchado, A., & Pottasch, S. R. 1993, European Southern Observatory Conference and Workshop Proceedings, 46, 129
- [37] Gérard, E., & Le Bertre, T. 2006, *aj* , 132, 2566
- [38] Gilman, R. C. 1969, *ApJl* , 155, L185
- [39] Houck J.R., Roellig T.L., van Cleve J., et al., 2004, *ApJS* 154, 18
- [40] Higdon, S. J. U., Devost, D., Higdon, J. L., et al. 2004, *PASP* , 116, 975
- [41] Harris, M. J., Fowler, W. A., Caughlan, G. R., & Zimmerman, B. A. 1983, *ARA&A*, 21, 165
- [42] Herwig, F., Bloeker, T., & Driebe, T. 2000, *memsai* , 71, 745
- [43] Herwig, F., Bloeker, T., Schoenberner, D., & El Eid, M. 1997, *A&A* , 324, L81

- [44] Herwig, F. 2004, *ApJ* , 605, 425
- [45] Herwig, F. 2005, *ARA&A* , 43, 435
- [46] Hayashi, C. 1966, *ARA&A* , 4, 171
- [47] Habing, H. J., & Olofsson, H. 2004, *Springer-Verlag* , 1, 402
- [48] Hartmann, L., & MacGregor, K. B. 1980, *ApJ* , 242, 260
- [49] Höfner, S., Gautschi-Loidl, R., Aringer, B., & Jørgensen, U. G. 2003, *A&A* , 399, 589
- [50] Höfner, S. 2011, Why Galaxies Care about AGB Stars II: Shining Examples and Common Inhabitants, 445, 193
- [53] Höfner, S. 2007, Why Galaxies Care About AGB Stars: Their Importance as Actors and Probes, 378, 145
- [52] Habing, H. J. 1996, *A&Ar* , 7, 97
- [53] Höfner, S., & Andersen, A. C. 2007, *A&A* , 465, L39
- [54] Iben, I., Jr., & Renzini, A. 1983, *ARA&A*, 21, 271
- [55] Iben, I., Jr. 1975, *ApJ*, 196, 549
- [56] Iben, I., Jr. 1968, *ApJ* , 154, 581
- [57] Iben, I., Jr. 1965, *ApJ* , 141, 993
- [58] Imbriani, G., Costantini, H., Formicola, A., et al. 2004, *A&A* , 420, 625
- [59] Iben, I., Jr. 1967, *ARA&A* , 5, 571
- [60] Justtanont, K., Khouri, T., Maercker, M., et al. 2012, *A&A*, 537, AA144
- [61] Jones, T. W., & Merrill, K. M. 1976, *ApJ* , 209, 509
- [62] Kramers, H. A. 1923, *Phil. Mah.* 46, 836
- [63] Kholopov, P. N. 1987, General Catalogue of Variable Stars.. The fourth edition containing information on variable stars discovered and designated till 1982. Volume III: Constellations Pavo-Vulpecula. P. N. Kholopov (Editor-in-Chief). Nauka, Moscow, USSR. 368 pp. (1987). In Russian and English.,
- [64] Karakas, A. I. 2011, Asymmetric Planetary Nebulae 5 Conference, 144
- [65] Kippenhahn, R. 1965, *Mitteilungen der Astronomischen Gesellschaft Hamburg*, 19, 53
- [66] Kippenhahn, R., & Weigert, A. 1990, *Stellar Structure and Evolution*, XVI, 468 pp. 192 figs.. Springer-Verlag Berlin Heidelberg New York. Also Astronomy and Astrophysics Library,

- [67] Kučinskas, A. 1998, *Baltic Astronomy*, 7, 495
- [68] Kemper, F., Waters, L. B. F. M., de Koter, A., & Tielens, A. G. G. M. 2001, *A&A* , 369, 132
- [100] Kupka, F. G., Ryabchikova, T. A., Piskunov, N. E., Stempels, H. C., & Weiss, W. W. 2000, *Baltic Astronomy*, 9, 590
- [70] Kupka, F., Piskunov, N., Ryabchikova, T. A., Stempels, H. C., & Weiss, W. W. 1999, *A&As*, 138, 119
- [71] Kurucz, R. L. 1970, *SAO Special Report*, 309,
- [72] Roberts, J. D., Caserio, M. C., 1977, *Basic Principles of Organic Chemistry*, second edition. W. A. Benjamin, Inc. , Menlo Park, CA.
- [73] Lebouteiller V., Bernard-Salas J., Sloan G.C., Barry D.J., 2010, *PASP* 122, 231
- [74] Landstreet, J. D. 1988, *ApJ*, 326, 967
- [75] Le Bertre, T., Winters, J. M., & Sedlmayr, E. 1998, *IAU Symposium*, 191, 306P
- [76] Lattanzio, J. C. 2002, *nar* , 46, 469
- [77] Larson, R. B. 1969, *MNRAS* , 145, 271
- [78] Larson, R. B. 1969, *MNRAS* , 145, 271
- [79] Mihalas, D. M. 1982, *Stellar atmospheres..* D. M. Mihalas. Translated from the English edition. Mir, Moskva. Part I. 352 pp. Part II. 424 pp. (1982). In Russian. -,
- [80] Marengo, M., Evans, N. R., Matthews, L. D., et al. 2011, arXiv:1112.0619
- [81] Murray, N. 2011, *ApJ*, 729, 133
- [82] Minamidani, T., Tanaka, T., Mizuno, Y., et al. 2011, *aj*, 141, 73
- [83] McDonald, I., Zijlstra, A. A., Sloan, G. C., & Matsuura, M. 2011, *Why Galaxies Care about AGB Stars II: Shining Examples and Common Inhabitants*, 445, 241
- [84] McDonald, I., Sloan, G. C., Zijlstra, A. A., et al. 2010, *ApJl* , 717, L92
- [85] Meixner, M., Gordon, K. D., Indebetouw, R., et al. 2006, *aj* , 132, 2268
- [86] Mitalas, R. 1988, *ApJ* , 325, 476
- [87] Mauron, N., & Huggins, P. J. 2006, *A&A* , 452, 257
- [88] Mestel, L. 1974, *memsai* , 45, 397
- [89] Molster, F. J., Yamamura, I., Waters, L. B. F. M., et al. 1999, *Nature* , 401, 563

- [90] Neilson, H. R., Langer, N., & Cantiello, M. 2011, 9th Pacific Rim Conference on Stellar Astrophysics, 451, 327
- [91] Neufeld, D. A., González-Alfonso, E., Melnick, G., et al. 2011, *Astrophys. Lett.* , 727, LL29
- [92] Niyogi, S. G., & Speck, A. 2009, American Institute of Physics Conference Series, 1170, 155
- [93] Ojha, D. K., & Omont, A. 2003, The Proceedings of the IAU 8th Asian-Pacific Regional Meeting, Volume 1, 289, 121
- [94] Omont, A., Gilmore, G. F., Alard, C., et al. 2003, *A&A* , 403, 975
- [95] PuŁEcka, M., Schmidt, M. R., & Szczerba, R. 2005, ESA Special Publication, 577, 457
- [96] Pols, O. R., Tout, C. A., Lattanzio, J. C., & Karakas, A. I. 2001, Evolution of Binary and Multiple Star Systems, 229, 31
- [97] Persi, P., Ferrari-Toniolo, M., Grasdalen, G. L., & Spada, G. 1980, *A&A* , 92, 238
- [98] Pijpers, F. P., & Habing, H. J. 1989, *A&A* , 215, 334
- [99] Piskunov, N. E., Kupka, F., Ryabchikova, T. A., Weiss, W. W., & Jeffery, C. S. 1995, *A&As*, 112, 525
- [100] Kupka, F. G., Ryabchikova, T. A., Piskunov, N. E., Stempels, H. C., & Weiss, W. W. 2000, *Baltic Astronomy*, 9, 590
- [101] Piskunov, N., & Kupka, F. 2001, *ApJ* , 547, 1040
- [102] Posch, T., Kerschbaum, F., Mutschke, H., Dorschner, J., Jaumlger, C. 2002, *A&A* , 393, L7
- [103] Popper, D. M. 1980, *ARA&A* , 18, 115
- [104] Ryabchikova, T. A., Piskunov, N. E., Kupka, F., & Weiss, W. W. 1997, *Baltic Astronomy*, 6, 244
- [106] Renzini, A., & Fusi Pecci, F. 1988, *ARA&A* , 26, 199
- [106] Renzini, A., & Fusi Pecci, F. 1988, *ARA&A* , 26, 199
- [107] Schaller, G., Schaerer, D., Meynet, G., & Maeder, A. 1992, *A&As* , 96, 269
- [108] Schirmacher, V., Woitke, P., & Sedlmayr, E. 2003, *A&A*, 404, 267
- [109] Speil, J. 2006, Journal of the American Association of Variable Star Observers (JAAVSO), 35, 88
- [110] Sipahi, E. 2012, *na*, 17, 377

- [111] Smith, V. V., & Lambert, D. L. 1986, *ApJ*, 311, 843
- [112] Schwarzschild, M., Hárm, R. 1965, *ApJ*, 142, 855
- [113] Sedlmayr, E. 1989, *Interstellar Dust*, 135, 467
- [114] Skrutskie, M. F., Schneider, S. E., Stiening, R., et al. 1997, *The Impact of Large Scale Near-IR Sky Surveys*, 210, 25
- [115] Spitzer, L., Jr. 1968, *Nebulae and Interstellar Matter*, 1
- [116] Salpeter, E. E. 1952, *ApJ*, 115, 326
- [117] Tenenbaum, E. D., Woolf, N. J., & Ziurys, L. M. 2007, *ApJl*, 666, L29
- [118] Tenenbaum, E. D., Apponi, A. J., Ziurys, L. M., et al. 2006, *ApJl*, 649, L17
- [119] Templeton, M., Willson, L. A., & Foster, G. 2008, *Journal of the American Association of Variable Star Observers (JAAVSO)*, 36, 1
- [120] Thomas, H.-C. 1967, *zap*, 67, 420
- [121] Truong-Bach, Nguyen-Q-Rieu, Omont, A., Olofsson, H., & Johansson, L. E. B. 1987, *A&A*, 176, 285
- [122] Ueta, T., Speck, A. K., Stencel, R. E., et al. 2006, *Astrophys. Lett.*, 648, L39
- [123] van Loon, J. T., Groenewegen, M. A. T., de Koter, A., et al. 1999, *A&A*, 351, 559
- [124] Villaver, E., García-Segura, G., & Manchado, A. 2007, *Why Galaxies Care About AGB Stars: Their Importance as Actors and Probes*, 378, 345
- [125] de Vries, B. L., Klotz, D., Lombaert, R., et al. 2011, *Why Galaxies Care about AGB Stars II: Shining Examples and Common Inhabitants*, 445, 621
- [126] von Weizsäcker, C. F., 1938, *ber Elementumwandlungen in Innern der Sterne II, Physikalische Zeitschrift*, 39, 633
- [127] Werner M.W., Roellig T.L., Low F.J., et al., 2004, *ApJS* 154, 1
- [128] Waterhouse, J. 1890, *Memorie della Societa Degli Spettroscopisti Italiani*, 18, 14
- [129] Whitelock, P. A. 2012, *Ap&SS*, 341, 123
- [130] Woitke, P. 2006, *A&A*, 460, L9
- [131] Winters, J. M., Le Bertre, T., Jeong, K. S., Nyman, L.-Å., & Epchtein, N. 2003, *A&A*, 409, 715
- [132] Waters, L. B. F. M., Cami, J., de Jong, T., et al. 1998, *Nature*, 391, 868
- [133] Willson, L. A. 2000, *ARA&A*, 38, 573
- [134] Yamamura, I., & de Jong, T. 2000, *ISO Beyond the Peaks: The 2nd ISO Workshop on Analytical Spectroscopy*, 456, 155

Appendix A

A.1 Stellar Evolution: A Comprehensive Description

A.1.1 Main Sequence Evolution

We start our description of stellar evolution at the point where stars start fusing hydrogen in their core. On the Hertzsprung-Russell (HR) diagram, stars that are fusing hydrogen into helium in their center are found on a locus known as the main sequence (MS).

Main Sequence Lifetime

Stars spend the longest period of their lifetime on the main sequence while their luminosity during this time slightly fluctuates. An estimate for MS lifetimes can be obtained from

$$\tau_H = \frac{E_H}{L} \quad (\text{A.1})$$

where E_H is the nuclear energy released by hydrogen fusion in the core. Since nuclear fusion produces energy through converting mass to energy, the higher the mass content of hydrogen is, the more fuel is available for fusion to occur therefore the more energy can be released. This yields a direct dependency between the energy and the total mass content of hydrogen and by extension the total mass of the star ($E_H \propto M_H \rightarrow E_H \propto M$).

For MS stars, there is a relation between mass and luminosity that is understood theoretically and confirmed observationally [103, see e.g.]. In general, it is found that ($L \propto M^\eta$) with η between 3 to 6 [For details see 66]; here we take an average value of $\bar{\eta} \approx 3.5$ [66]. Inserting these relations between mass-luminosity and mass-energy in equation A.1 we find,

$$\tau_H(M) \propto \frac{M}{M^\eta} \propto M^{1-\eta}$$

and given the average $\bar{\eta} \approx 3.5$, the time-scale on main sequence will then become;

$$\tau_H(M) \propto \frac{M}{M^{3.5}} \propto M^{-2.5}$$

The result shows an inverse relation between mass and timescale on main sequence which means that more massive stars spend less time on main sequence and vice versa meaning that

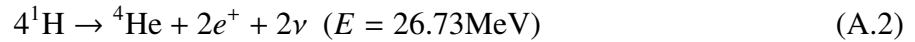
despite their larger amount of fuel, massive stars burn their fuel faster. In the case of our own sun ($1 M_{\odot}$), the timescale on main sequence is of the order of 10 Gyrs.

It is interesting to note that red dwarf stars with masses below $0.8M_{\odot}$ have lifetimes longer than the current age of the universe. Therefore, not a single red dwarf can have burned up all their hydrogen fuel yet [see e.g. 15].

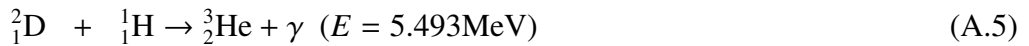
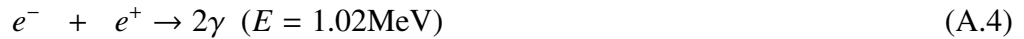
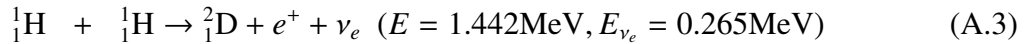
Main Sources of Energy Production

Stars on the main sequence produce energy through two mechanisms: the proton-proton chain (or *pp*-chain) and CNO cycle. In the case of low mass stars, the hydrogen fusing process takes place through *pp*-chain reaction whereas in intermediate mass stars it happens via CNO cycle [see Chapter 2 in 47]. In what follows we briefly describe both mechanisms.

The net effect of the proton-proton chain, as shown in equation A.2, is the conversion of four hydrogen atoms into helium accompanied by the release of 26.731 MeV of energy (corresponding to 0.71 percent mass defect). However, neutrinos carry away 2-30% of this energy; therefore depending on the exact reactions this value can change [see e.g. 20].



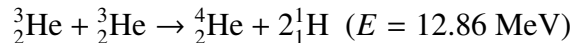
The question regarding the steps involved in *pp*-chain have first been addressed by von Weizsäcker [126] and Bethe [9]; in all cases, the first few reactions are:



The *pp*-reaction chain begins with the formation of deuterium (^2_1H or ^2_1D) releasing a positron and a neutrino (see Eq. A.3). Almost immediately, the positron annihilates with an electron and produces two gamma ray photons with a total energy of 1.02MeV (Eq. A.4). Thereafter, the combination of deuterium produced in step A.3 with another hydrogen nucleus will lead to the formation of ^3_2He (Eq. A.5).

From here on the ^4_2He can form through three possible paths (or branches). The branching of the proton-proton chain to any one of these three possibilities, depends on temperature and the ratio of helium to hydrogen abundance [see e.g. 20].

The pp I Branch:



One possible path is the fusion of two ^3_2He nuclei which leads to ^4_2He and two hydrogen nuclei accompanied by a 12.86 MeV energy release [20]. Since *pp* I begins with two ^3_2He nuclei, the reactions in Eq. A.3 and A.5 have to occur twice but this is not the case in the other two branches. The total energy liberated through this chain is $E=26.20 \text{ MeV}$.

The *pp* I Branch can operate in a pure hydrogen gas since all the required ingredients can be formed from a pure hydrogen environment [20]. The *pp* I Branch is dominant at low temperatures ($T/T_6 \lesssim 10, T_6 = T/(10^6 K)$) and since its rate of reaction depends directly on the

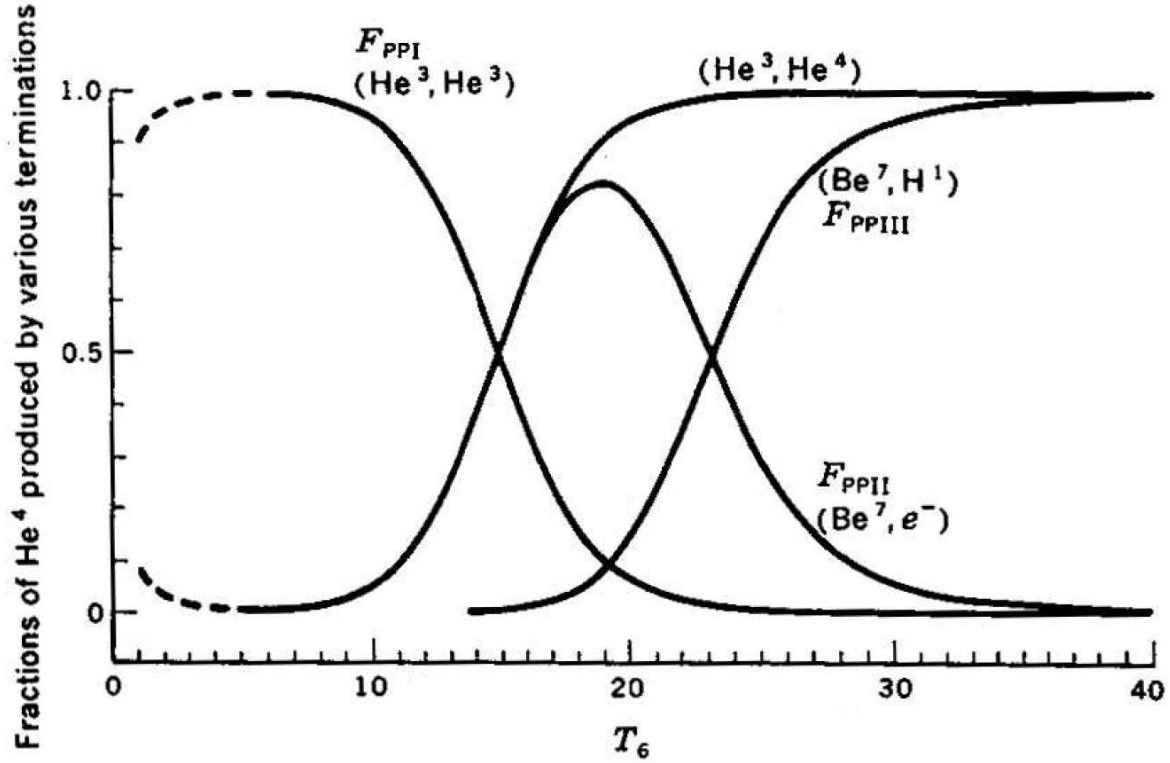
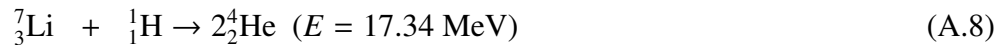


Figure A.1: This figure illustrates the fraction of ${}^4\text{He}$ produced via pp I, pp II or pp III Branch, as function of temperature in which $T_6 = T/(10^6 \text{ K})$ [20]. In lower temperatures, the abundance of ${}^3\text{He}$ is highest therefore pp I Branch dominates. At slightly higher temperature where the abundance of ${}^4\text{He}$ increases the probability of pp II Branch increases and in very high temperatures where the abundance of ${}^7\text{Be}$ grows, the pp III Branch becomes more dominant.

${}^3\text{He}$ abundance in the medium then at a given temperature the probability of pp I Branch will increase as the ${}^3\text{He}/{}^1\text{H}$ abundance ratio increases [20, 86].

The pp II Branch:



This branch starts with formation of ${}^4\text{Be}$ (Eq. A.6). This reaction can only take place if ${}^4\text{He}$ is already abundant. The existence of ${}^4_2\text{He}$ can be primordial or a product of the pp I chain [66]. For this branch to continue and dominate, ${}^4\text{Be}$ nuclei needs to capture an electron (Eq. A.7). ${}^4\text{Be}$ is more likely to combine with hydrogen (see pp III Branch), therefore the depletion of hydrogen can improve the chance of its reaction with electron (Eq. A.7). This branch is more dominant at high temperatures [see e.g. 20, 86]. The total energy liberated through this branch is $E=25.67 \text{ MeV}$.

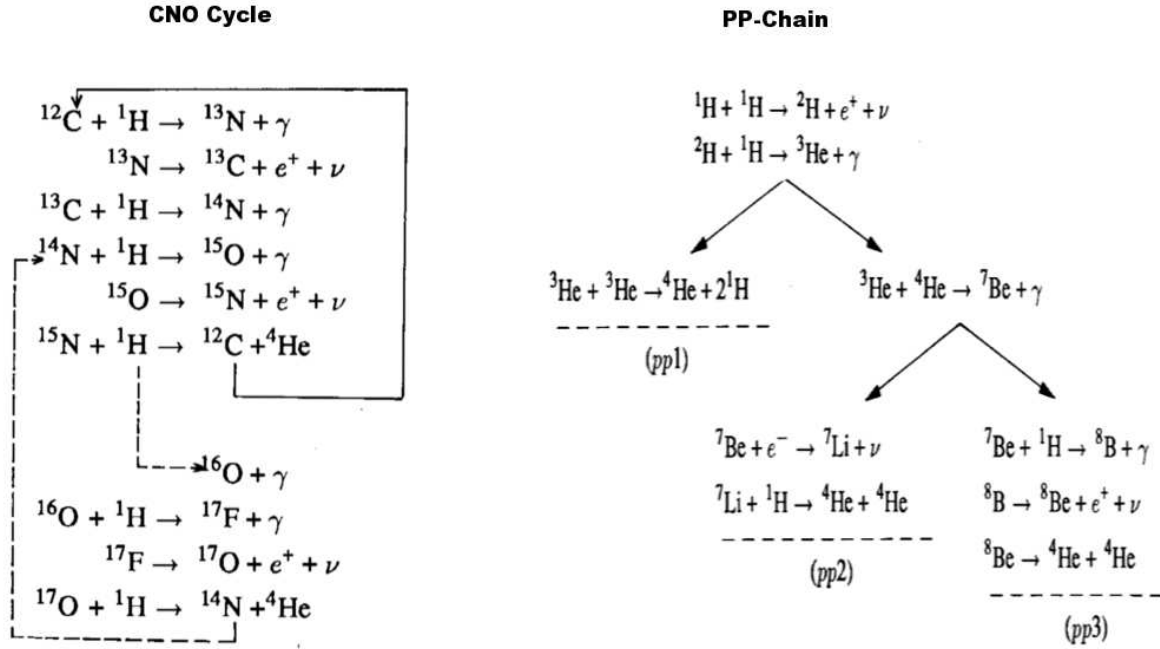
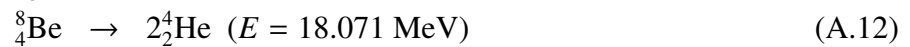
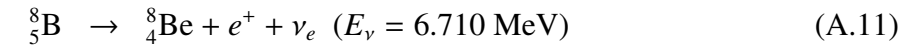
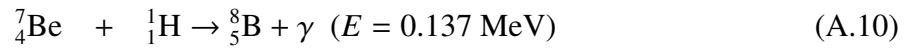
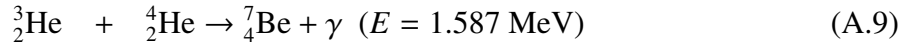


Figure A.2: *Left:* The reactions involved in the CNO cycle. *Right:* The reactions involved in *pp*-chain [66].

The pp III Branch:



This branch dominates over *pp* I and II branches at higher temperatures because at higher temperatures the rate of electron capture for ${}^7\text{Be}$ nuclei decreases because electrons will have higher kinetic energy thus less likely to successively react, therefore the likelihood of the reaction given in Eq. A.9 increases. The total energy liberated through this branch is $E=19.20$ MeV. A summary of the *pp* chain is shown in Figure A.2.

Another source of energy production is the CNO Cycle (a.k.a. Bethe-Weizsäcker Process) in which carbon, nitrogen and oxygen act as catalysts for the combination of four protons which will lead to formation of helium-4 [9]. The sequence of the CNO cycle reaction is shown in Figure A.2. The reaction ${}^{14}\text{N}(p,\gamma){}^{15}\text{O}$, is the bottleneck reaction of the CNO cycle and will cause the abundance of ${}^{14}\text{N}$ to exceed that of any other CNO nucleus [17]. When the CNO cycle reaches the reaction $({}^{15}\text{N}+{}^1\text{H})$ the cycle takes two possible paths (CNO bi-cycle). It can produce ${}^{12}\text{C}$ and repeat the main cycle (CNO-I), or (once out of every 10^4 cases) it can produce ${}^{16}\text{O}$ and enter a secondary cycle (CNO-II).

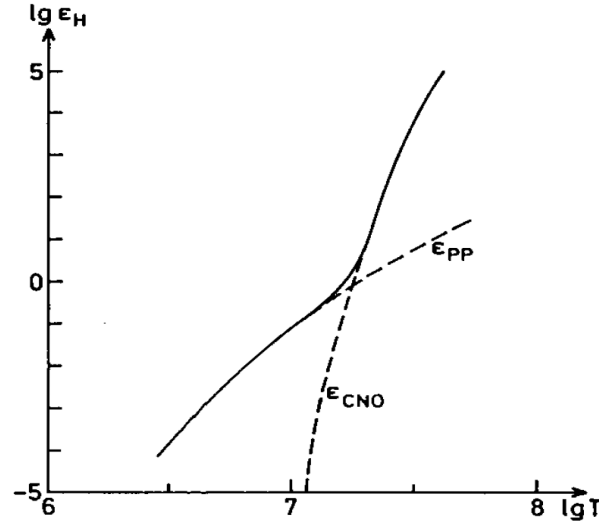


Figure A.3: This plot illustrates the contribution of the CNO cycle and pp -chain in energy production as a function of temperature. The CNO cycle dominates the pp chain at higher temperatures [66].

The CNO cycle is much more temperature dependent than the pp -chain, therefore the proton-proton chain dominates at lower temperatures while the CNO cycle takes over the energy generation at higher temperatures [66]. This is because unlike pp -chain, the reactions in CNO cycle start occurring at higher temperature ($\sim n$) and the rate of energy production rapidly increases with increasing temperature. Figure A.3 shows the contribution of each as a function of temperature.

From Main Sequence(MS) to Red Giant Branch(RGB)

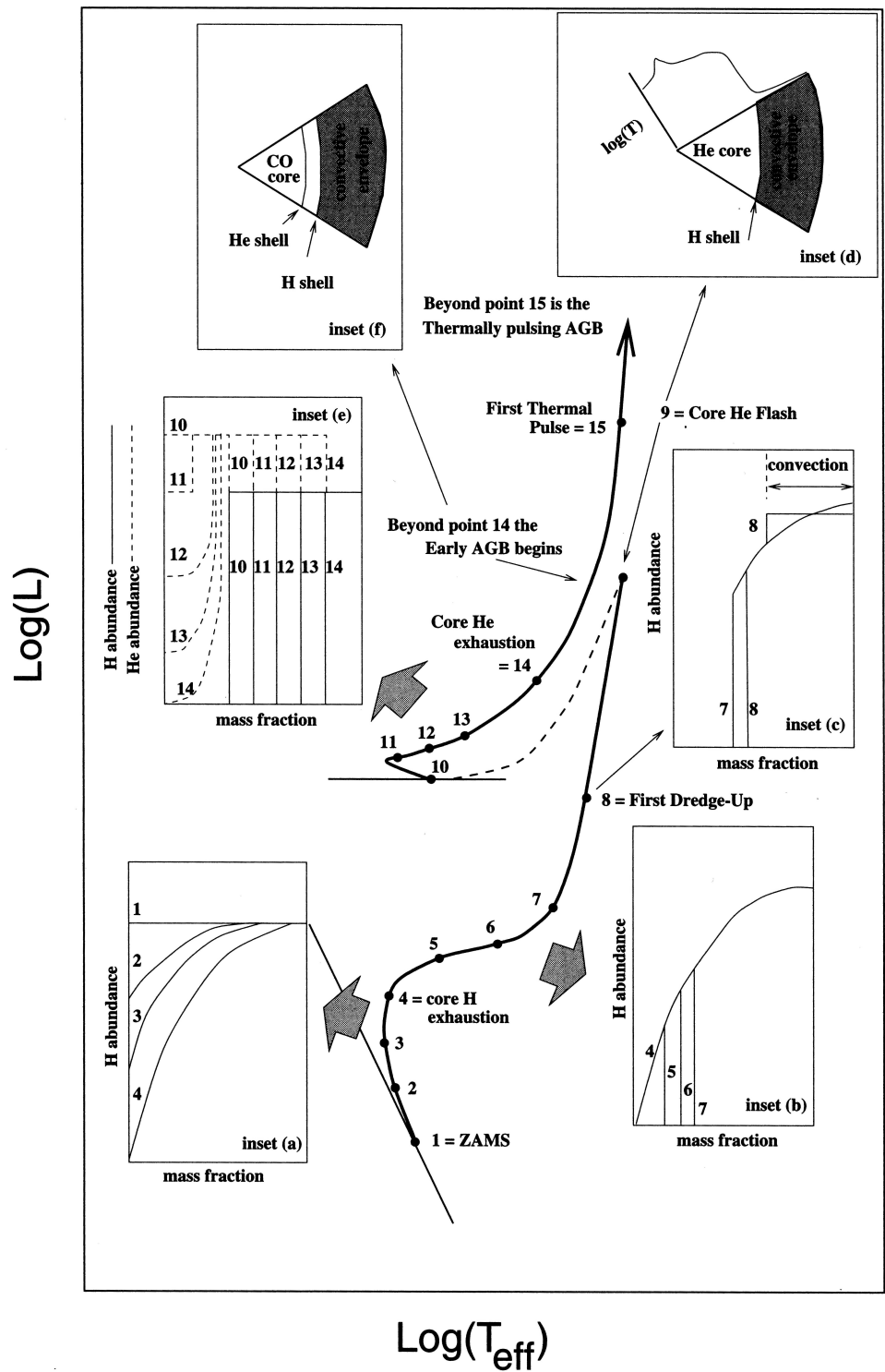
As discussed before, the core gradually heats up during MS evolution (Points 1–4 in Figures A.1.1 & A.4). Upon H exhaustion in the core, the core will further contract which will result in even higher temperatures.

As the core continues to shrink, the layers close to the core will also collapse and heat up, and reach H fusion temperatures; thus, at some point, H fusion is happening in a shell around the inactive He core.

In case of stars with $M \geq 2M_{\odot}$, the contraction of the core causes a gravitational energy release which dominates that of hydrogen core fusion. This causes the zigzag between points 4 and 5 in the evolutionary track shown in Figure A.4 which is missing from Figure A.1.1 in which case the star makes a smooth transit to hydrogen shell fusion.

As the hydrogen fuses in the shell, it adds more helium onto the embedded He-rich core causing its mean molecular mass to rise and at the same time the temperature increases due to contraction of the core. These two factors will increase the pressure at the base of the H-rich envelope causing it to expand. Once $\sim 10\%$ of the hydrogen has been converted to helium, this expansion becomes significant and drives the star off the main sequence.

The star will maintain its luminosity throughout this expansion because the expansion causes the temperature to decrease while the radius increases therefore from the well known



captionThe evolutionary track of a $1M_{\odot}$ star in the Hertzsprung-Russel diagram (Figure from Habing & Olofsson [47]).

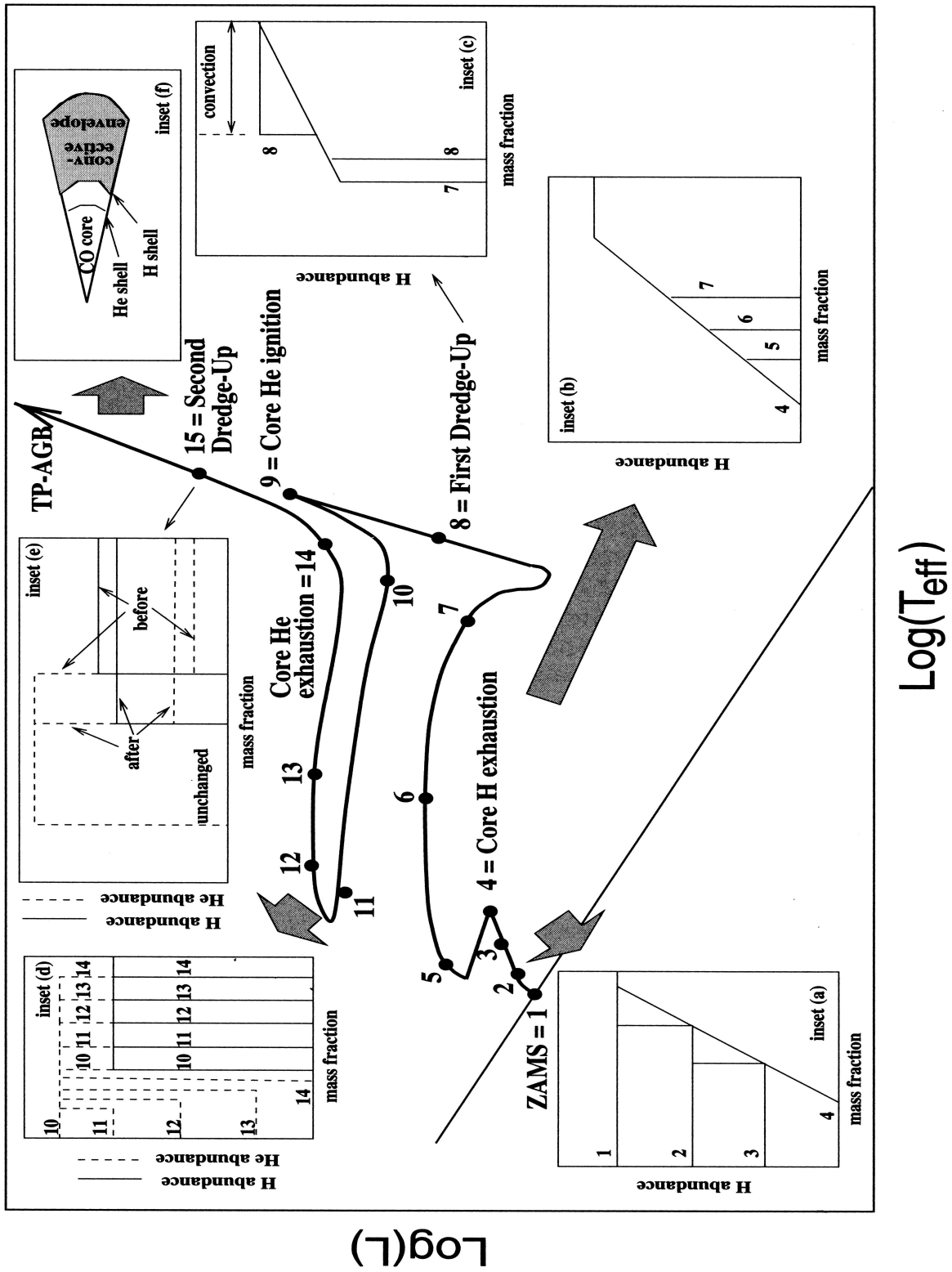


Figure A.4: The evolutionary track of a $5M_{\odot}$ star in the Hertzsprung-Russell diagram (Figure from Habing & Olofsson [47]).

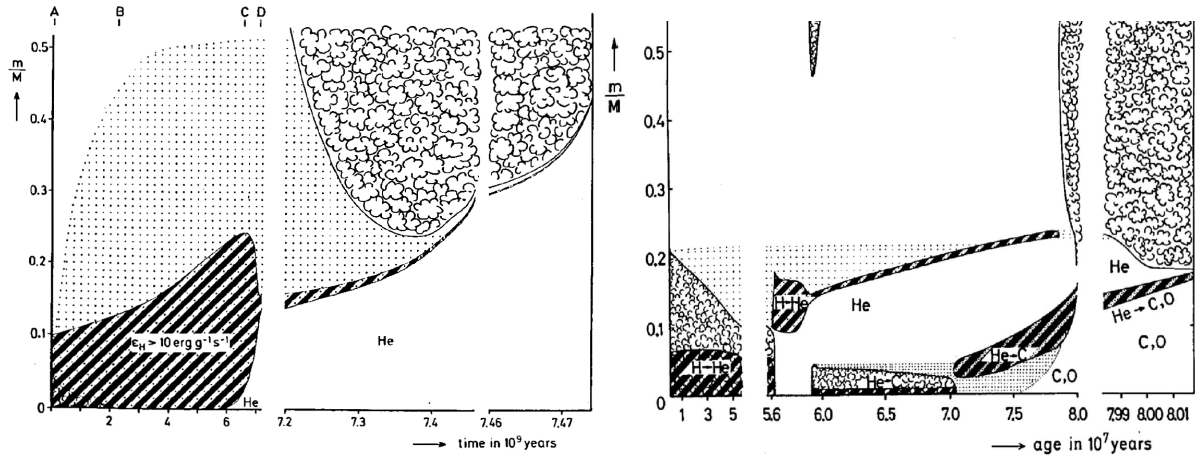


Figure A.5: This figure shows the evolution of interior structure of stars as it ages. The cloudy areas represent the convective regions, the hatched areas are regions where nuclear energy generation occurs. Dotted regions have variable chemical composition. *Left:* For a $1 M_{\odot}$ star [120]. *Right:* For a $5 M_{\odot}$ star [65].

relation $L = 4\pi r^2 \sigma T_{eff}^4$ the luminosity stays constant. Therefore the star moves almost horizontally across the HR diagram. This interval of horizontal movement on HR diagram is also called the sub-giant phase (Points 5–7 in Figures A.1.1 & A.4).

While the star crosses this phase, the mass of the core gradually increases from the surrounding burning shell. Once it reaches the Schrönberg-Chandrasekhar limit (a maximum mass limit for isothermal inactive core to be able to withhold an envelope), the core begins to contract however the core contraction happens on the Kelvin-Helmholtz time-scale which is relatively short, therefore it is unlikely to observe a star in this phase of its life. This results in a well-known gap in the HR diagram between the MS turn off point and the base of red giant branch called the Hertzsprung gap.

The expansion of the envelope continues until the Hayashi limit is reached – the theoretical locus for fully convective stars in the HR diagram. The Hayashi limit constrains the maximum radius to which the envelope can expand (Points 7 in Figures A.1.1 & A.4). This represents the base of the red giant branch (RGB).

As the star evolves toward the Hayashi line, the outer convective zone deepens until it eventually penetrates into the layers which are already enriched by nuclear fusion products (see Fig. A.5), but they are still above the active hydrogen fusing shell. These convective motions then bring up the nucleosynthesis products to the surface; a process generally known as ”dredge-up” and at this point ”first dredge-up” (point 8 in Figures A.1.1 & A.4). It is worthwhile to mention that this process only occurs as long as the star is convective, however when the star evolves further the core becomes more radiative gradually than convective therefore this process will cease.

The mixing elements during first dredge-up mostly include the CNO cycle products such as ^{13}C and ^{14}N . The dredge-up surface mixing process also causes the ^{12}C and other primordial elements on the surface to move down into the interior of the star. This results in a decrease of $^{12}\text{C}/^{13}\text{C}$ and $^{12}\text{C}/^{14}\text{N}$ surface abundance ratios.

Theoretical calculations show that for $1 M_{\odot}$ star, the $^{12}\text{C}/^{13}\text{C}$ ratio drops from ≈ 89 -90 to about

$\approx 20\text{-}25$ and the $^{12}\text{C}/^{14}\text{N}$ ratio decreases by a factor of 2.5 [see e.g. 59, 47] which is in good agreement with observations [see e.g. 59, 41, 35, 19, 5, and references therein for further details].

Upon reaching the Hayashi limit, the star becomes fully convective. Convective energy transport tends to be far more efficient than radiative diffusion. In this stage of evolution, the star's energy is directly related to the mass of the core which is continuously increased by the active hydrogen fusing shell. This energy is allowed to escape from the star much easier thus increasing the luminosity of the star. Therefore, the star will move up the HR diagram almost vertically into the Red Giant Branch (RGB).

From Red Giant Branch (RGB) to Horizontal Branch (HB):

As the star ascends the RGB branch, the inactive helium core continues to contract gravitationally. The core contraction results in temperature and density increase. However, if the initial mass of the star is lower than $1.8 M_{\odot}$, the pace at which density increases is higher than the pace of temperature increase. Thus at some point, the core becomes electron-degenerate before it can reach the helium ignition temperature and the degeneracy pressure will halt the contraction. One of the most important differences between degenerate matter and a non-degenerate (ideal) gas is the relation between temperature and pressure. Unlike an ideal gas for which pressure and temperature are directly related, in a degenerate gas the pressure is only very weakly dependent on temperature and mostly dependent on density. Thus temperature in the degenerate core increases while the pressure remain nearly unchanged.

The core continues to heat up until it reaches temperatures of about $\approx 10^8$ K when helium can ignite. With the onset of helium fusion the temperature rises, but since the core is degenerate and pressure is almost independent of temperature, there will be no stabilizing cooling expansion of the core. In turn, the higher temperatures result in a strong increase in the nuclear energy production since the He fusion reaction is very sensitive to temperature (see below). Thus, He fusion in degenerate conditions is a runaway process happening on very short timescales (few seconds); this phenomenon is therefore called the “helium flash” (Point 9 in Figure A.1.1). The helium flash ends when the temperature is high enough for thermal pressure to become dominant again (see Figure A.6); at that point, the core will expand and cool while the density will decrease. During the helium flash, there will be an enormous nuclear energy production. However, this energy is largely dissipated or absorbed by the stellar envelope. Therefore we do not observe a sharp luminosity peak during the helium flash.

In stars with masses greater than $1.8 M_{\odot}$ the core does not become electron-degenerate since the temperatures required for helium ignition will be reached before that (Point 9 in Figure A.4). The helium ignition starts in non-degenerate conditions, leading to helium fusion in a gentle manner.

Helium fusion (in both degenerate and non-degenerate conditions) occurs through a process known as the triple-alpha (3α) process. The 3α process converts three α particles (^4He) into one carbon nucleus (^{12}C). When the temperature of the contracting core reaches $\approx 10^8$ K, the

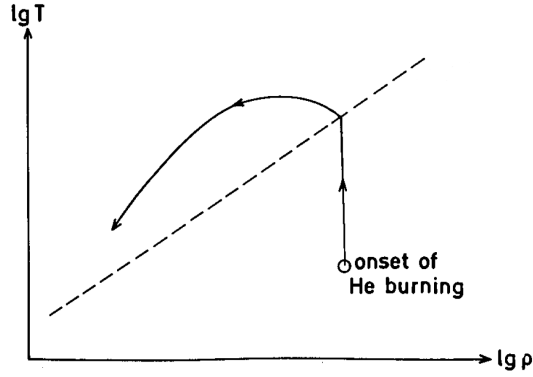
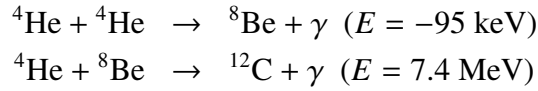
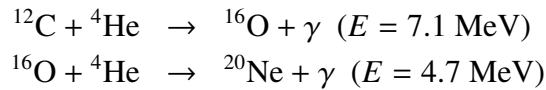


Figure A.6: This plot shows the change in central temperature versus central density during the helium flash. As long as the matter is degenerate (below the border dashed line), the temperature rises in constant density. As a result the star enters the non-degenerate regime followed by core expansion and density decreases. This will stabilize the helium fusion process [66].

following nuclear reactions set in [116];



${}^8\text{Be}$ is unstable against break up and decays into two α particles within the half-life of $\tau_{1/2}({}^8\text{Be}) \approx 3 \times 10^{-16} \text{ s}$. However ${}^8\text{Be}$ in its meta-stable ground state has a long enough lifetime to react with ${}^4\text{He}$ to form a stable ${}^{12}\text{C}$. Owing to a nuclear resonance, the indirect conversion of ${}^4\text{He}$ to ${}^{12}\text{C}$, involving the middle step of ${}^8\text{Be}$ formation, has a much higher probability than the direct conversion which involves a rather improbable three-body reaction of ${}^4\text{He}$. The triple-alpha process is very sensitive to the temperature: the nuclear reaction rates scale typically with T^{40} [66]. Once ${}^{12}\text{C}$ has been produced in the star, the following reactions also become possible [116];



Both low and intermediate mass stars that are fusing helium steadily in their core will settle down on the horizontal branch (HB) on the HR-diagram (Points 9-11 in Figures A.1.1 & A.4).

From Horizontal Branch (HB) to Asymptotic Giant Branch (AGB)

As helium gradually burns through the 3- α process in the core, the supply of helium goes down; once again, this leads to a slight drop in pressure and the core slowly goes through gravitational contraction to maintain hydro-static equilibrium. When the core runs out of He (Point 14 in Figures A.1.1 & A.4), the gradual contraction heats up the surrounding shell and switches on the shell burning process. As before, this results in an increase in luminosity and a decrease in effective temperature through expansion (Points 11-14 in Figures A.1.1 & A.4). The star has then reached the AGB phase [76], so called because it asymptotically touches the RGB.

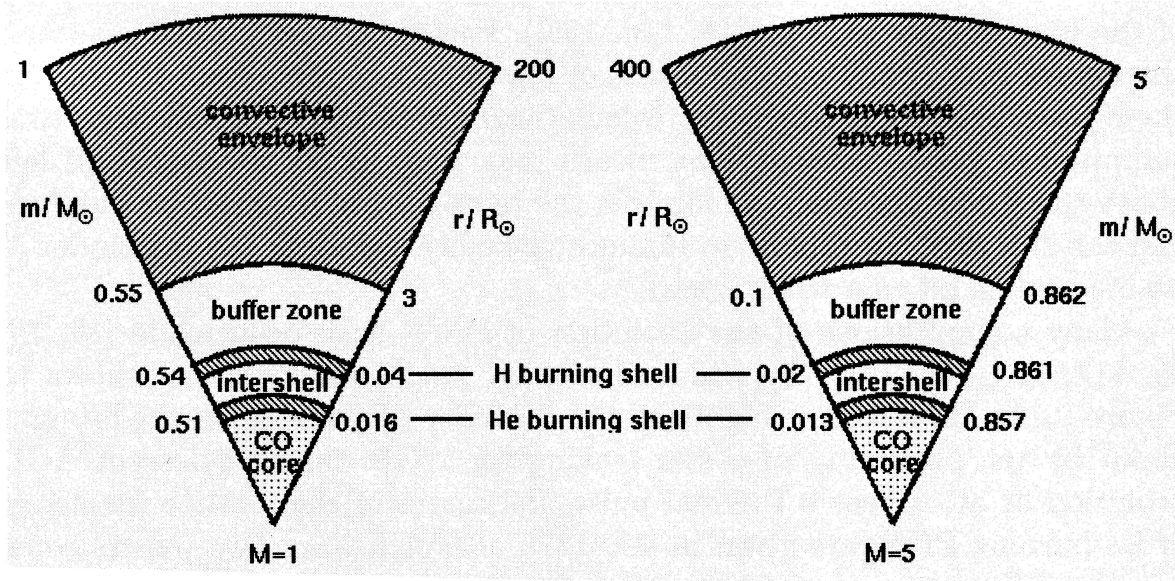


Figure A.7: The structure of a $1 M_\odot$ and $5 M_\odot$ E-AGB Stars [see Chapter 2 47]. In general terms, AGB stars are cool ($T=3000$ K) giants (typical $R=3 \times 10^{13}$ cm) with an inert, degenerate CO core, two burning shells (one He, one H) and large inactive convective envelopes.

Evolution on and beyond the Asymptotic Giant Branch (AGB)

When arriving onto the AGB, the stellar structure is roughly as follows (see Figure A.7). At the center is a dense and hot core consisting of carbon (^{12}C) and oxygen (^{16}O). This core is electron degenerate for similar reasons explain in case of He core. Further out is a He fusion shell that provides most of the luminosity in this phase and that adds mass to the core; further out is a H fusion shell, and the two are separated by a thin region called inter-shell zone which is primarily made out of pure helium. Around the hydrogen shell there is a radiative buffer zone which is surrounded by a much larger H-He envelope which is for the most part convective (see Fig. A.7).

At first, only the helium shell burns, and it adds more mass to the core and consumes the helium in the inter-shell zone thus reducing the mass in that region. The nuclear energy resulting from helium fusion will increase the temperature at the H/He interface to the point where hydrogen shell fusion can resume. This stage is sometimes referred to as the “double shell burning”.

In the case of intermediate mass stars with masses greater than $4 M_\odot$, convection penetrates through the inactive hydrogen fusing shell and into the inter-shell region above the active helium fusing shell [5]. It then brings the processed material on to the surface – the “second dredge-up” (Point 15 in Figure A.4). In those stars that undergo the second dredge-up, the surface abundances of ^{16}O and ^{14}N can be enhanced or decreased by a factor that depends on the initial composition and mass of the star [3, 47]. Also if the convective envelope reaches deep enough, then the abundance of ^{18}O and ^{22}Ne can similarly drop or increase depending on the stellar parameters [3].

The reason for this is that during the second dredge-up phase, the base of the convec-

tive envelope first reaches the region with variable hydrogen content and then extends to the hydrogen-exhausted core where the size of the hydrogen-exhausted core depends strongly on the initial composition (see Figures 11 and 12 in Becker & Iben [3])

The limit to which the base of the convective layer can penetrate depends strongly on the size of the hydrogen-exhausted core and the thickness of the helium fusing shell around it. The final enhancement or depletion of various elements will vary accordingly. If the base of convective zone layer reaches down to the helium-rich layer then the amount of helium that is dredged-up (ΔM_{He}) would be higher than other elements. Thus the abundance of heavier elements would decrease. Whereas if the base of the convective layer is able to reach deeper to hydrogen-exhausted core where reactions such as $^{14}\text{N}(\alpha, \gamma) ^{18}\text{F}(\beta^+, \gamma) ^{18}\text{O}$ or $^{18}\text{O}(\alpha, \gamma) ^{22}\text{Ne}$ has taken place, then the abundance of heavier elements such as ^{18}O and ^{22}Ne can be enhanced in the surface, respectively [3].

Note that the second dredge-up will not happen for stars with masses lower than a critical mass of $\approx 4 M_{\odot}$ (for solar metallicity) since the base of the convective layer does not penetrate the lower levels [47]. According to Becker & Iben [3], this critical mass value varies between 3.3 and 5.5 M_{\odot} since they found almost no change in surface abundance of stars within this range which means that convection barely reaches down and second dredge-up does not happen.

The He shell becomes thinner as more He is consumed. Eventually, this creates the conditions for a peculiar type of instability. This is due to thermal instabilities that were first described by Schwarzschild H arm [112], and that are particularly effective for thin shells that undergo nuclear fusion with a steep temperature dependency – such as the thin He shell that is now left. If the shell is thin enough, any perturbation will not lead to significant adjustments in the hydro-static structure of the star. Suppose a perturbation is introduced into such a shell that slightly increases its temperature. Following this rise in temperature there will be an increase in the rate of energy production in the helium shell (L_{He}), since the 3- α process has a very steep temperature dependency ($\epsilon \propto T^{40}$). This extra energy will then lead to further increases in the shell temperature thus leading to a thermal runaway (Beyond point 15 in Figures A.1.1 and A.4).

This process is referred to as “helium shell flash” or “thermal pulse” because it is somewhat similar to the runaway process that occurs during the helium core flash. However, this thermal instability happens in non-degenerate environment [112]. Thermal pulses typically last for $\sim 1,000$ years with inter-pulse periods of the order of 100,000 years.

Electron-degeneracy in the shell is not a necessary condition for a thermal pulse to occur but if the shell becomes degenerate at any point, the instability will be enhanced since pressure becomes independent of temperature [47].

Thermal pulses introduce a second stage of AGB evolution known as the thermally pulsing AGB (or TP-AGB). During every thermal pulse, the luminosity of the AGB star increases for a short period of time depending on the mass and composition of the star [47]. After a thermal pulse, the helium fusing shell switches off and the luminosity is only provided by hydrogen shell fusion. After a while, the hydrogen shell will dump enough mass to the underlying inter-shell region so that the double shell burning can restart and the whole cycle repeats.

As a result of helium shell flash, the inter-shell region becomes convective. Just like for

the first and second dredge-up, the convective layer will bring nucleosynthesis products to the surface in a series of events collectively referred to as “third dredge-up”. The major mixing elements are particularly ^{12}C and ^4He . One of the most important consequences of the third dredge-up is the formation of carbon stars. Stars start off with a C/O ratio below unity which makes them originally oxygen-rich. However, each third dredge-up episode, brings up more carbon to the surface and thus increases the C/O ratio until at some point this ratio exceeds unity and turns the star into a carbon (or C-rich) star. However, it is worthwhile to mention that the conversion from oxygen-rich star to carbon-rich star only occurs in intermediate mass stars, since the very massive stars convert carbon into nitrogen through further nuclear fusion in the core and very low mass stars lose all the material between core and surface through mass loss before the conversion can take place [47].

Theoretical models developed by Herwig et al. [43] show that for a $3 M_{\odot}$ star with $(Y, Z) = (0.28, 0.02)$, after seven thermal pulses the amount of dredged-up ^{12}C is up to $10^{-3} M_{\odot}$ and for ^{13}C it is $10^{-7} M_{\odot}$ (^{13}C -pocket). Herwig et al. [43] also find the inter-shell abundance of typically $(^4\text{He}/^{12}\text{C}/^{16}\text{O}) = (23/50/25)$ which indicates that in a case of a $3 M_{\odot}$ for example, the star becomes carbon rich after seven pulses.

In the case of extremely low metallicity ($0 \geq Z \geq 0.0001$) of the star, third dredge-up will also result in surface abundance enhancement of ^{16}O , ^{22}Ne , ^{23}Na , ^{25}Mg and ^{26}Mg [45]. The properties of the hydrogen shell in low metallicity stars is such that during the dredge-up, the temperature is high enough at the bottom of the convective layer so that protons can burn vigorously which can produce the above mentioned elements [44].

In addition to elements created by nuclear fusion, some nuclei can also be created by neutron capture and mixed to the surface through third dredge-up. In AGB stars, this happens through the so-called s-process. The s-process elements are produced in environments of sufficiently low neutron flux so that any neutron rich isotope that is formed will beta decay into a stable state before it can capture another neutron.

For sufficiently massive stars ($\gtrsim 5 M_{\odot}$), the base of the convective envelope can be hot enough for fusion to occur. This process is known as Hot Bottom Burning (or HBB) and it happens in inter-pulse phases. It is also referred to as “convective envelope burning”. The nucleosynthesis products of HBB are ^{13}C , ^{14}N and ^7Li . Due to the enhancement of ^{13}C which destroys ^{12}C that was transported down from the surface, one of the main effects of HBB is to delay or even prevent a star from becoming a carbon star [42].

A key ingredient in the evolution of AGB stars is that stellar winds reduce the mass of the envelope from the outside through mass loss (see Sec. A.1.2). Unlike most other phases in stellar evolution for which the amount and consumption rate of fuel determines the evolution, the AGB stellar evolution is characterized by rates at which material is removed from the outer layers of the star. At rates of 10^{-8} – $10^{-3} M_{\odot}$ per year (with mass loss rates increasing as stars climb the AGB), mass loss sets an AGB lifetime of $\approx 2 \times 10^6$ yr [54]. It is thought that near the tip of the AGB, AGB stars will experience a so-called superwind phase with mass-loss rates of up to $10^{-3} M_{\odot}/\text{yr}$, which effectively ejects the entire remaining stellar envelope in a short amount of time (~ 1000 years), and leads to the termination of AGB phase.

A.1.2 Post-AGB Evolution

After the superwind phase the star enters the post-asymptotic giant branch (Post-AGB) phase of evolution. The heavy mass loss rate during the superwind phase (SW) almost completely strips the star of its hydrogen-rich envelope. The deeper and hotter layers will gradually be exposed as the outer layers are expelled.

In the beginning of this process however, the central star is obscured by the remnants of the excessive mass loss during the superwind phase. In typically 100-1000 years, the circumstellar material becomes optically thin thus allowing the central star to be seen at optical wavelengths. The interval between the end of the superwind phase and this point is called the pre-planetary nebula phase.

The central star continues to get smaller and hotter until it is hot enough ($T \geq 10,000\text{K}$) to emit strong ultraviolet radiation to photo-ionize the surrounding material that were ejected during the superwind phase and is still expanding. The photo-ionized material will then emit in optical wavelengths, turning the object into a planetary nebula (PN).

Proto-planetary nebulae are observable from earth but not for a long duration. This is because the matter will become too dispersed that the radiation can no longer ionize it. The remnant is a white dwarf consisting of a degenerate core of carbon and oxygen.

The white dwarf remnant does not have any source of energy generated by fusion to support it against gravitational collapse except the electron degeneracy pressure which constrains the mass of the white dwarf to a maximum of $1.4M_{\odot}$ known as the Chandrasekhar limit. The white dwarf, once formed, is quite stable and continues to cool down on timescales of billions of years.

Mass loss & AGB circumstellar environments

A.1.3 Principles of the Mass Loss Process

Although many aspects of mass loss are understood qualitatively, there are still many details that remain unclear. In the most general terms, it is believed that stellar pulsations lift matter high above the photosphere where it cools down and forms molecules and dust grains. Radiation pressure on the dust grains then drives them outward, and the dust grains drag the gas along. This “pulsation-enhanced dust-driven wind scenario” is described in great detail in Höfner [50].

Stellar pulsation, in general terms, is the periodic contraction and expansion of the outer layers in order to maintain hydrostatic equilibrium. The mechanism that drives the pulsation in many types of pulsating variables is the κ -mechanism where κ is for opacity as a measure of transparency.

The UV radiation from the ISM is energetic enough to ionize the neutral hydrogen in the outer envelope as a result of which the opacity decreases in the outer envelope allowing the light to pass through. This will decrease the outward thermal pressure and cause the envelope to shrink. The density and temperature and opacity will increase as a result of compression. Therefore, the energy flux from inside of the star decreases since it can not escape the opaque region and this excess flux causes the envelope to expand. The expansion causes the opacity to drop so the cycle can continue.

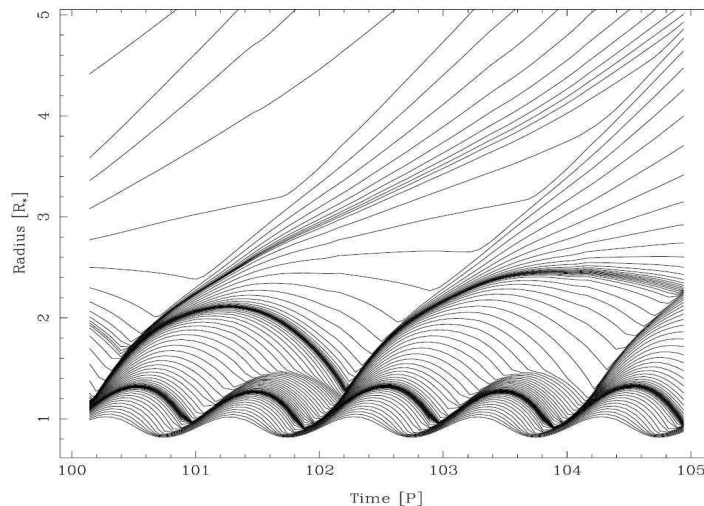


Figure A.8: This figure shows the movement of mass shells as a function of time. The pulses originating around periods 100, 102 and 104 trigger dust formation. The radiation will push these newly formed material away from the star therefore the density is not high enough for shocks around periods 101 and 103 to trigger dust formation.

These pulsations result in a periodic change in the luminosity of the star and since the luminosity of all AGB stars varies periodically and with large amplitudes, they are counted as pulsating stars.

Pulsating stars fall under the category of variable stars but not all variable stars are pulsators. AGB stars are classified as Miras (or Regular), semi-regular (SR) and irregular (L-type for slow irregular) [63]. The period of variation increases as the star evolves on the AGB phase thus Early-AGB stars tend to be semi-regulars and as they climb higher on the AGB they tend to be Mira variables.

E-AGB stars tend to be irregulars or semi-regulars with periods of typically 30 to 100 days; and higher up on the AGB we find the very regular Mira variables with periods of 100 days up to several years.

In every pulsation cycle, the outer layers are pushed away from the central star by expansion and they fall back inward on free-fall timescales. However, the in-falling material will encounter the material from a new expansion episode, and this will create a shock wave which provides a site for dust formation. Figure A.8 shows Radius versus Time which illustrates the movement of atmospheric layers during pulsations. The shocks created around periods 100, 102 and 104 result in dust formation and are thus pushed away by radiation pressure. On the other hand, the shocks created at periods 101 and 103 will not trigger dust formation due to insufficient density [49].

When in-falling material from previous pulse collides with the out-flowing material from the new pulse, there will be a density increase in the zone in which they collide. Additionally, according to models, after each shock wave there is a post-shock cooling process. A combination of these two factors contribute to the formation of molecules in these regions.

In this mixture of gas and dust, stellar radiation pressure will drive the dust grains away from the star. Dust grains transfer momentum to gas molecules through collision. As a result

the radiation pressure will accelerate the dust outwards and the dust will drag the gas along until the mixture of two reaches terminal velocity and sails into the interstellar medium as a slow (~ 15 km/s), but massive dust-driven outflow.

It is noteworthy that in some cases, very low outflow velocities ($\lesssim 5$ km/s) have been reported for AGB stars which can not be explained by a dust driven mechanism because low amounts of dust can form in these environments. The other possibility is the purely pulsation-driven mass loss but it's been thought for a long time that there is no evidence supporting this scenario [131].

The rate of mass loss increases as the star evolves toward greater luminosity, radius and lower effective temperature. Although mass loss processes can not be calculated from first principles, observational evidences suggest mass loss rates of $10^{-8} M_{\odot}$ for early AGB stars to some $10^{-3} M_{\odot}$ for the objects on the tip of AGB which for O-rich stars lead to the formation of OH/IR stars [54].

The heavy mass loss in the later stages of evolution gives rise to massive dust formation. The SiO molecules in the circumstellar environment are mostly consumed in the dust formation leaving the water molecules in the outer envelope to be split by the ultraviolet light from other stars which will lead to formation of hydroxyl(OH) molecule. The heat from the warm dust will excite this molecule and create OH maser emission lines. In addition to this, due to heavy mass loss, the circumstellar dust of these stars is optically thick making them undetectable in the optical range while giving them a strong IR excess. These stars are known as OH/IR stars.

A.1.4 Circumstellar Envelopes of AGB Stars

The extensive mass loss on the AGB results in the formation of an extended region containing a mixture of gas and dust – the circumstellar envelope (CSE). Close to the stellar surface, pulsation-induced shocks result in enhanced densities and warm (~ 500 - 1500 K) quasi-static layers known as the “dynamical atmosphere” (or MOLsphere) as shown in Figure A.9. This region is sometimes referred to as the inner CSE which usually starts around $1R_{*}$ and extends to about $R_{inner} \sim 5R_{*}$ [18].

The CSE of evolved stars can create a rich set of molecules and dust species making it one of the most remarkable chemical laboratories in the universe. Depending on the C/O ratio, metallicity, temperature and distance from the central star, different gas molecules can form. Several observations have been carried out to identify the chemical contents of the CSE. The results mostly indicate the presence of oxygen rich species such as SiO, H₂O, CO₂, SiS, CO, SO₂, SO, CS, CN, HCN, etc. whereas around carbon rich stars carbonaceous species are more abundantly detected such as H₂, CO, N₂, C₂H₂, HCN, etc. [95] and polycyclic aromatic hydrocarbons (PAH) only in handful of C stars [13]. However, there have been reports of few peculiar cases where a carbonaceous molecule (e.g. C₂H₂, HCN and CS [16] have been detected in the oxygen-rich circumstellar environment as well as the detection of an oxygen-rich molecule (e.g. water vapor) in CSE of carbon-rich AGB stars [91]. The different species leave different fingerprints on the spectra of these objects which helps astronomers identify them as either oxygen-rich or carbon-rich (see e.g. Figure A.10).

When the temperature of the expanding circumstellar gas drops down to 900-1400K, dust formation can begin if the density of the gas is sufficiently high. Dust grains absorb momentum from stellar radiation much more efficiently than molecules since they have larger cross section;

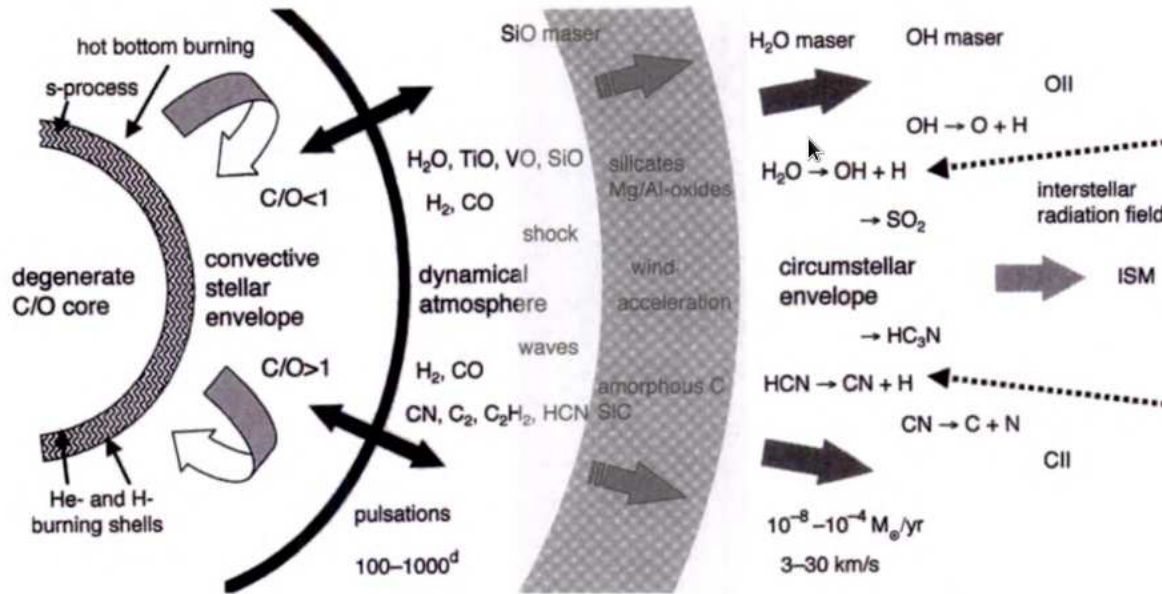


Figure A.9: Schematic diagram of the AGB stellar structure and the surrounding circumstellar envelope. It illustrates the chemical evolution of the stellar ejecta as it moves further away. The shocks occur in dynamical atmosphere and result in the formation of different molecules. Different dust species condense out and get accelerated by radiation pressure in the acceleration zone. The interstellar radiation will give rise to photo-chemistry in the CSE [see chapter one 47].

this will thus accelerate dust grains away from the star while they drag the gas with them through the “dust acceleration region”. This zone (intermediate CSE) extends to about $\sim 100R_*$ and down to temperatures as low as 100K [22].

When radiation pressure balances the drag, the outflow reaches the “terminal velocity” of typically $3\text{--}30 \text{ km s}^{-1}$ [47]. The terminal gas outflow velocity can be obtained from observations. The stellar parameters such as luminosity and dust parameters such as dust-to-gas ratio and average dust grain sizes, the dust condensation radius and to a lesser extent condensation temperature, can influence the terminal velocity of the outflow [67]. For example in two similar stars, one that has higher luminosity will result in a higher terminal velocity.

Although it is suggested that the radiation pressure on dust grains drives mass loss, calculations show that this method can not account for slow winds ($v < 10 \text{ km/s}$) of low mass loss rate stars ($\dot{M} < 10^{-6} M_{\odot}/\text{yr}$). In addition, dynamical models have shown that only solid Fe and Fe-rich silicate condensates can absorb sufficient momentum from radiation pressure to initiate the outflow. However, models predict only small amounts of these grains in the outflow thus they can not be the only driving force behind stellar mass loss [130]. For these cases, an additional mechanism (e.g. stellar pulsations) is required to accomplish the task [67].

At much larger distances, the interstellar radiation field can penetrate the outflow, resulting in photo-chemistry in the circumstellar envelope. The energy of the interstellar radiation is strong enough to photo-dissociate some of the species in the outer CSE and create radicals (e.g. C_2H and CN from parent species C_2H_2 and HCN , respectively [121]). This process does

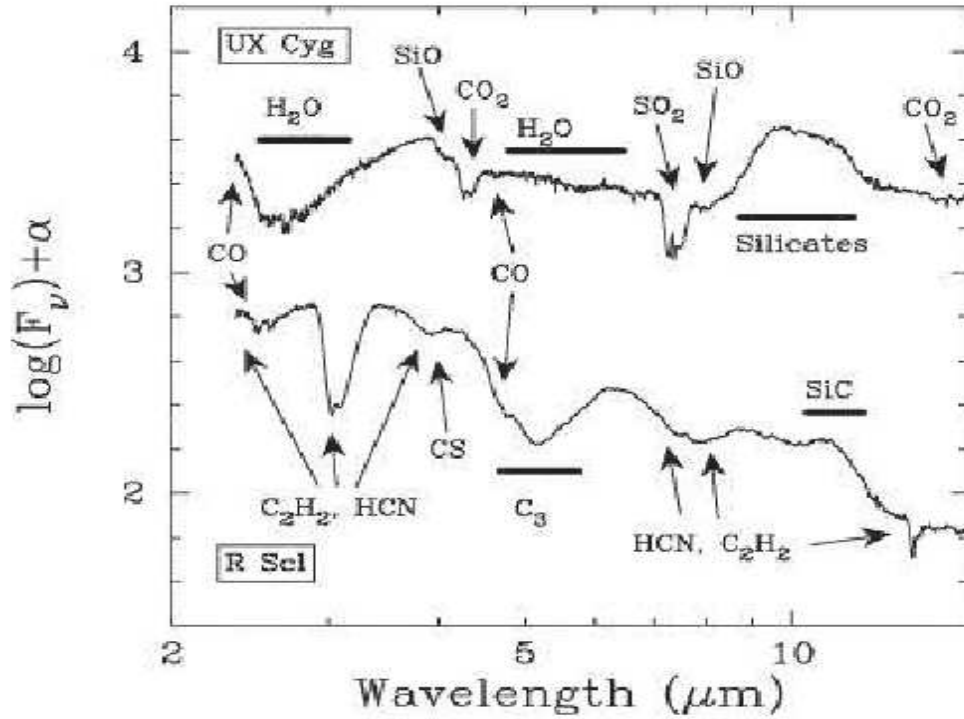


Figure A.10: This figure shows the difference between the spectral features in oxygen-rich and carbon-rich stars. The top spectrum belongs to UX Cyg and the lower one is R Scl, representing oxygen-rich and carbon-rich stars, respectively. CO is a common species between the two stars [134].

not happen in the inner regions since the inner CSE is shielded from the interstellar radiation by the outer CSE.

Finally, at large distances ($\approx 10^{18}$ cm from central star), the CSE merges with the ISM. This region (outer CSE) extends to $R_{\text{outer}} \sim 20,000 R_*$ and will reach temperatures as low as ~ 10 K [22].

A.1.5 Observational studies & Mass Loss

The observations of AGB stars include various sources such as photometry, interferometry, spectroscopy or even direct imaging. Here we briefly describe these methods and their corresponding results.

Previous infrared observational studies include near-infrared photometry such as the DENIS [94] and 2MASS [114] surveys or the Infrared Astronomical Satellite (IRAS) which observed infrared sources at 12, 25, 60, and 100 μm wavelengths. The Infrared Space Observatory (ISO) performed imaging and photometry between 2.5–240 μm and spectroscopy from 2 to 200 μm . The Spitzer Space Telescope (SST) which performed imaging and photometry between 3–160 μm and spectroscopy from 5 to 40 μm and spectrophotometry from 5–100 μm . The HIFI instrument on-board Herschel Space Telescope covers spectroscopy in far infrared for wavelengths between 157 to 212 μm and from 240 to 625 μm . In particular, the Short Wave-

length Spectrometer (SWS) and Long Wavelength Spectrometer (LWS) on-board ISO, have been a significant improvement over the previous studies since they carried out individual observation of a great number of evolved stars and revealed much about the chemical composition of the atmosphere and CSEs of evolved stars [see e.g. 1, for a review].

The O-rich or C-rich stellar atmosphere will result in very different chemical compositions for the CSEs. This is due to the fact that the first molecule that forms is the very stable carbon monoxide CO. This process is so efficient, and the molecule so stable, that in an oxygen-rich star, as good as all the carbon is locked up in CO molecule, and the excess oxygen will determine the rest of the chemistry (for molecules as well as dust grains). Conversely, in carbon stars, all the oxygen is locked up in CO, and thus the further chemistry is entirely driven by carbon. In addition to these two classes, ISO observations found a particular class of objects with “mixed chemistry” of O-rich and C-rich at the same time. In these cases the O-rich dust is found to be cool and highly crystalline while the C-rich dust is warm. These type of objects mostly belong to binary classes in which the O-rich dust is stored around the companion while in the meantime the star becomes a carbon star and gives rise to the carbon rich chemistry that follows (see e.g. Red Rectangle [132]).

Around O-rich AGB stars, infrared observations thus revealed the presence of H_2O , OH, CO, CO_2 , SO_2 and SiO gas as well as some dust features such as magnesiowüstite [$\text{Mg}_{1-x}\text{Fe}_x\text{O}$], alumina [Al_2O_3], and amorphous and crystalline silicates. For carbon stars, the IR inventory typically yields CO, CH, CS, SiS, HCN, C_3 , C_2H_2 gas in addition to SiC and MgS dust grains [see e.g. 1, 18, and references therein]. The search for more and new molecules and dust grains in circumstellar environments of evolved stars is certainly not a closed field of research and is still actively pursued.

Additionally, ISO satellite has performed another large mid-infrared survey using ISO-CAM. This survey is more generally known as ISOGAL survey in which 16 square degree of the Galactic plane is observed in mostly two wavelengths of 7 and $15\mu\text{m}$. This survey contains almost ~ 2000 sources. These observations combined with near-infrared observations of DENIS (I,J,K_s) provides a tool to study the nature of the objects observed at these wavelengths. Ojha & Omont [93] found that almost all of the ~ 2000 ISOGAL sources are AGB stars or on the tip of RGB.

Observations carried out by Spitzer Space Telescope have also provided us with valuable knowledge about AGB stars and their circumstellar envelope. For example, the strong infrared excess of AGB stars makes them a very valuable tool to study the structure of our own as well as other galaxies. The Infrared Array Camera (IRAC, Fazio et al. [29]) on-board Spitzer is particularly well suited for this task since it has a high sensitivity and covers a large areas in the sky. GLIMPSE [8] which covered 220 square degree of Galactic plane and SAGE [85] which mapped 50 square degree of the center of Large and Small Magellanic Clouds, are among two large surveys performed with IRAC. In addition, IRAC has four channels operating at 3.6, 4.5, 5.8 and $8\mu\text{m}$.

The SAGE (Surveying the Agents of Galaxy Evolution) program has imaged the small Magellanic cloud (SAGE-SMC) and large Magellanic cloud (SAGE-LMC) from 3.6 to $160\mu\text{m}$. Many AGB stars have been identified using the SAGE photometry. This study has also shown that C-rich AGB stars contribute the most to the interstellar dust even though they are fewer in numbers [7].

In Addition to all these above-mentioned observations, the Multiband Imaging Photometer

(MIPS) of the Space Infrared Telescope Facility (SIRTF) has imaged the parsec-sized dust shells around four carefully selected AGB stars in far-IR in order to study their circumstellar envelopes and mass loss mechanism. This survey is referred to as MIPS Infrared Imaging of AGB Dust-shells (MIRIAD). The first results of MIRIAD was the detection of a faint ($<5 \text{ MJyr}^{-1}$), extended ($\sim 400''$) far-IR nebula as well as an extended $\text{H}\alpha$ emission around one of the AGB stars (R Hya). This nebula is suggested to be due to a bow shock created by the interaction between stellar wind and interstellar medium [122].

Color-magnitude diagrams are also a useful tool to estimate the mass loss rate. Color-magnitude diagrams are analogous to HR-diagram since the magnitude is proportional to the luminosity and the color which is the difference between magnitude at two wavelengths is proportional to temperature. For instance, there is a increasing trend in the $(K_s - [15])/[15]$ color-magnitude diagram of the ISOGAL sample which corresponds to an increasing mass loss rates (ranging from 10^{-8} to $10^{-5} M_{\odot}/\text{yr}$).

The IRAS [12]-[25],[25]-[60] two-color diagram is also proven to be a valuable tool to study the mass loss rate. Garc'ia-Lario et al. [36] have found the best observational fit to the two color diagram to be:

$$[25] - [60] = -2.42 + 0.72e^{1.096([12]-[25])}$$

This sequence is referred to as Infrared Main sequence (IRMS) and it can be interpreted as an evolutionary sequence of mass and mass loss rate meaning that the more massive stars with higher mass loss rates are located in the upper part of the IRMS [36].

The spectroscopic observations of AGB stars also have allowed us to study the mass loss and circumstellar envelopes in great details. For instance, CO rotational line emissions and 21cm HI line and maser emission and radiative transfer models, have been used in the past to estimate the mass loss rates. In a few words, the general method involves the estimate of a total mass of the molecule from the line profile. Then by means of the typical outflow velocities for those species and the diameter to which they extend, one can find the timescales on which that amount of mass was lost and convert that to mass loss per year. In the following we briefly explain each method.

HI 21cm line emission : Molecular hydrogen (H_2) is an abundant species in the envelope of AGB stars. However, this molecule is quite difficult to observe since it has no allowed electric dipole transition and the quadrupole transitions only appear in infrared ranges which are not accessible from the ground. At larger distances the interstellar radiation can photo-dissociate the H_2 molecule and produce HI. The extent of HI in the envelope of AGB stars is quite large ($\sim 2\text{pc}$) which implies that HI is a better tool than any other molecule (e.g. CO) to study the mass loss rates over longer time-scales (up to $\sim 10^5 \text{yr}$).

The 21cm HI line in radio region of the spectrum was thought to be undetectable since it was too weak and contaminated by the Interstellar hydrogen along the same line of sight until the upgraded Nancay Radiotelescope (NRT) detected this line towards several AGB stars [37]. The emission line profile can be fitted with either a Gaussian or a rectangular from which the mass of the HI can be derived. Note that this estimated mass is usually underestimated because we do not take into account the interstellar contribution or self-absorption.

Even though the mass loss rates determined this way show a correlation with those obtained from other methods, they are still uncertain since the total mass of HI is not well determined [26].

CO line observations : After H_2 molecule, CO is the next most abundant molecule around AGB stars. The radiative transfer modeling of multi-transitional CO observations in radio regime are most commonly used and are also known to be the most accurate.

The line profile of CO have parabolic shape in optically thick cases and flat-topped or two-horned profile in optically thin or spatially resolved [25]. These line profiles can be fitted by a profile function which has the following general form;

$$T(v) = T_{MB,c} [1 - (\frac{v - v_{LSR}}{v_\infty})^2]^{\beta/2}$$

Where β is a measure for the shape of the profile, $\beta=2$ represents optically thick soft parabolic shape, $0 < \beta < 2$ lead to flat-topped shapes and negative β leads to two-horned profiles[25].

Through fitting the line profile with a parabola we can get an estimate of a few important parameters such as the expansion velocity of the CSE (v) and the brightness temperature at the center of the line ($T_{MB,c}$), the velocity of the star with respect to the local standard of rest (v_{LSR}) and optical thickness of the envelope (β) which will allow us to determine an analytic expression for the mass loss rate as a function of these parameters (The details of derivation are beyond the scope of this paper for further details see De Beck et al. [25]).

The average mass loss rate derived for AGB stars from this method is $\sim 2 \times 10^{-7} M_\odot \text{yr}^{-1}$ [26].

Maser emission : In addition to the two methods mentioned above maser emissions from H_2O , OH and sometimes SiO can also be used to determine mass loss rates for AGB stars. Bowers & Hagen [6] confirmed that the luminosity of OH maser as well as the ratio of H_2O to OH luminosities depend on the mass loss rate. This method is more useful for oxygen-rich stars ($C/O < 1$) since they can produce more H_2O molecules and thus more OH through photo-dissociation. Due to a strong dependence of maser line strength on chemistry, density, temperature and velocity of the gas, the mass loss rates estimated this way are more uncertain than CO line emission method [26].

Radiative transfer models : Another alternative method of mass loss determination is based on radiative transfer modeling of the observed spectral energy distributions of AGB stars [123, 26]. The details involved in the radiative transfer code are beyond the scope of this paper and can be found in van Loon et al. [123].

In order to estimate the mass loss rate using any of the above procedures, a commonly accepted model is adopted for the circumstellar envelope which involves few assumptions. The first basic assumption is that the circumstellar envelope is spherically symmetric produced by a constant mass loss rate which expands at constant velocity. In a region probed by the CO emission, the hydrogen is assumed to be in molecular form and CO is assumed to be in statistical equilibrium. This means that the rate of collisional excitation and de-excitation between CO and H_2 (para or ortho) molecules is the same where the ortho-to-para ratio is assumed to be 3 [26].

The obtained mass loss estimates are indeed uncertain. This uncertainty is increased in cases where the circumstellar model deviates from that of a standard model for instance in the presence of a bipolar outflow. The determination of the errors is not straightforward due to the large number of parameters involved. However, by fixing some parameters and varying a few, we can gain some insight about the sensitivity of the results on certain parameters (e.g. size of the envelope, temperature, etc.). Another way to estimate the uncertainties involved in mass

loss rates is to compare the values obtained through different procedures as explained above. They usually agree within 30% [26].

A combination of all these methods have provided us with a general picture about mass loss which is roughly spherical and suggests a time dependent outflow with typical velocities ranging from 5-30 km/s and mass loss rates between 10^{-8} to $10^{-3} M_{\odot}\text{yr}^{-1}$ [see e.g. 50].

A.2 Dust Formation in O-Rich CSEs

The study of dust formation is important due to several reasons. As mentioned before, it is believed that radiative pressure on dust grains is responsible for driving the massive outflows of the AGB stars. There has been many studies concerning which dust species initiate the outflows. In case of C-rich stars, the matter is almost satisfactorily resolved since radiation pressure on carbon dust grains (e.g. SiC, AMC) is sufficient to drive the outflow. However, for O-rich stars this matter is not very well resolved. Eventhough silicate dust is abundant in their envelopes, It has been confirmed that the radiative force on these grains is not sufficient to start the massive outflows. Even exceptionally large silicate grains can not be responsible for the initiation of the wind since these stars are very metal-poor to grow super-sized grains. There has been alternative possibilities speculated for initiation of the mass loss such as small amount of carbon grains [53], TiO_2 molecules [102], scattering on Al_2O_3 grains and the radiation pressure on water vapor which is abundant in molecular shells and also the presence of metallic Fe [84].

In particular, metallic iron was first suggested to account for the continuum emission observed between 5 and 8 μm in a group of OH/IR stars. Metallic iron has been considered as a wind driver because of its significant opacity compared to other dust species around O-rich stars which allows it to absorb momentum efficiently and drive the outflow [83] which eventually leads to dust formation.

The theory of dust formation was originally developed concerning the nucleation and condensation in the primitive solar nebula. The chondrules found in meteorites are believed to have formed in the primordial solar nebula where solids condensed from a low density, partially excited gas. The original condensation theories were developed under the assumption of thermal equilibrium which could, to a certain extent explain the chemistry and mineralogy of chondrites. However later on the observation of refractory compounds gave rise to the postulate of thermal disequilibrium processes.

According to the early theories of condensation, the solid particles can condense from a cool gas under certain conditions. Simply put, element X will remain gaseous if its vapor pressure P_v exceeds its partial pressure in the nebular gas, otherwise it will condense. In other words, for condensation to occur the ratio of the two pressures which is known as supersaturation ratio ($S = \frac{P_p}{P_v} > 1$) must be greater than one [47].

The assumption of thermal equilibrium however, is not applicable to the CSE of AGB stars since there are many temperature fluctuations in the AGB winds from several origins (e.g. stellar pulsations) where a temperature fluctuation of 20-60K can affect the rate of mass loss by 10-30% [23].

The formation of solid particle in a gaseous medium occurs in two steps. First the formation of critical clusters and second the growth of these clusters into macroscopic specimens [113].

The classical nucleation theory includes three different mechanisms for the formation of

critical clusters. First, *homomolecular homogenous nucleation*, which refers to the direct condensation from same kind of molecules. Second, *heteromolecular homogenous nucleation*, which refers to the formation of homogenous clusters by reacting with several different molecules. Third, *heterogenous nucleation*, which refers to the formation of clusters by chemical reaction or constructive collision with already existing species. The third method can be applied to astrophysical situations. One example can be the formation of silicate grains in M-type stars [113].

The grain formation can stabilize only if the created species do not evaporate as a result of temperature fluctuations in AGB winds. If this condition is met, the next step will be the growth of the grains. In this process, clusters will form a surface on which molecules are adsorbed.

The ad molecules (adsorbed molecules) will random walk until eventually they arrive at the least energetic lattice structure. This leads to the formation of a monocrystalline structure which grows further into polycrystalline and eventually amorphous grains. Such monotonic transition is expected to be seen in the AGB star outflows. The typical “amorphous” silicate or carbon grains that create the observed infrared excess, consist of monocrystalline cores with a polycrystalline shells and amorphous mantles [113]. However, there has been spectroscopic observation of AGB stars with large range of mass loss rates that can potentially be explained by the presence of crystalline silicate and crystalline alumina (Al_2O_3 -corundum), however this matter is still subject of debate.

The condensation of species, therefore happens in a sequence known as “condensation sequence”. This sequence is different for every specie and can vary strongly depending on the assumption of thermal equilibrium (LTE) or disequilibrium (non-LTE). Since the initiation of the sequence depends on the abundance of the required molecules, the non-LTE effects can strongly modify or even prohibit the sequence.

The initiation and continuation of the sequence also depends on the the temperature and density. The temperature must be around the condensation temperature for each specie (T_c) and the density must also be high enough for reactions to occur. If the density is too low, then the reactions will stop before the sequence is completed. This phenomenon is known as “freeze out” which is more likely to happen in stars with low mass loss rates [see e.g. 18].

Theories of thermodynamics predict that in O-rich stellar outflows, the first dust specie to condense is refractory oxides (e.g. aluminum oxide or alumina with $T_c \sim 1500\text{K}$). Through further gas-solid and solid-solid interactions, they get transformed into calcium-aluminum silicates. As the outflow cools down to about 1200K, silicon will condense into magnesium-rich olivine (forsterite, Mg_2SiO_4) and then through further interaction with remaining silicon it condenses into pyroxene(enstatite, MgSiO_3). This is the general condensation sequence predicted by theory. Parts of this sequence is shown in Figure A.11). In C-rich stars, the chemical pathway usually begins with acetylene (which is the most abundant) to a series of polycyclic aromatic hydrocarbons (PAHs) to macroscopic planar molecules which exhibit typical amorphous carbon emission feature.

Previous studies on this subject including ISO/SWS and IRAS/LRS have observationally examined the theory of dust condensation sequence. The results show that not all of the components predicted theoretically do actually appear observationally and some of the observed species are not a part of theoretical condensation sequence.

For example, in the oxygen-rich AGB environments, most of the dust is in the form of amorphous silicates [38, 61] although dust condensation theories predict a crystalline genesis

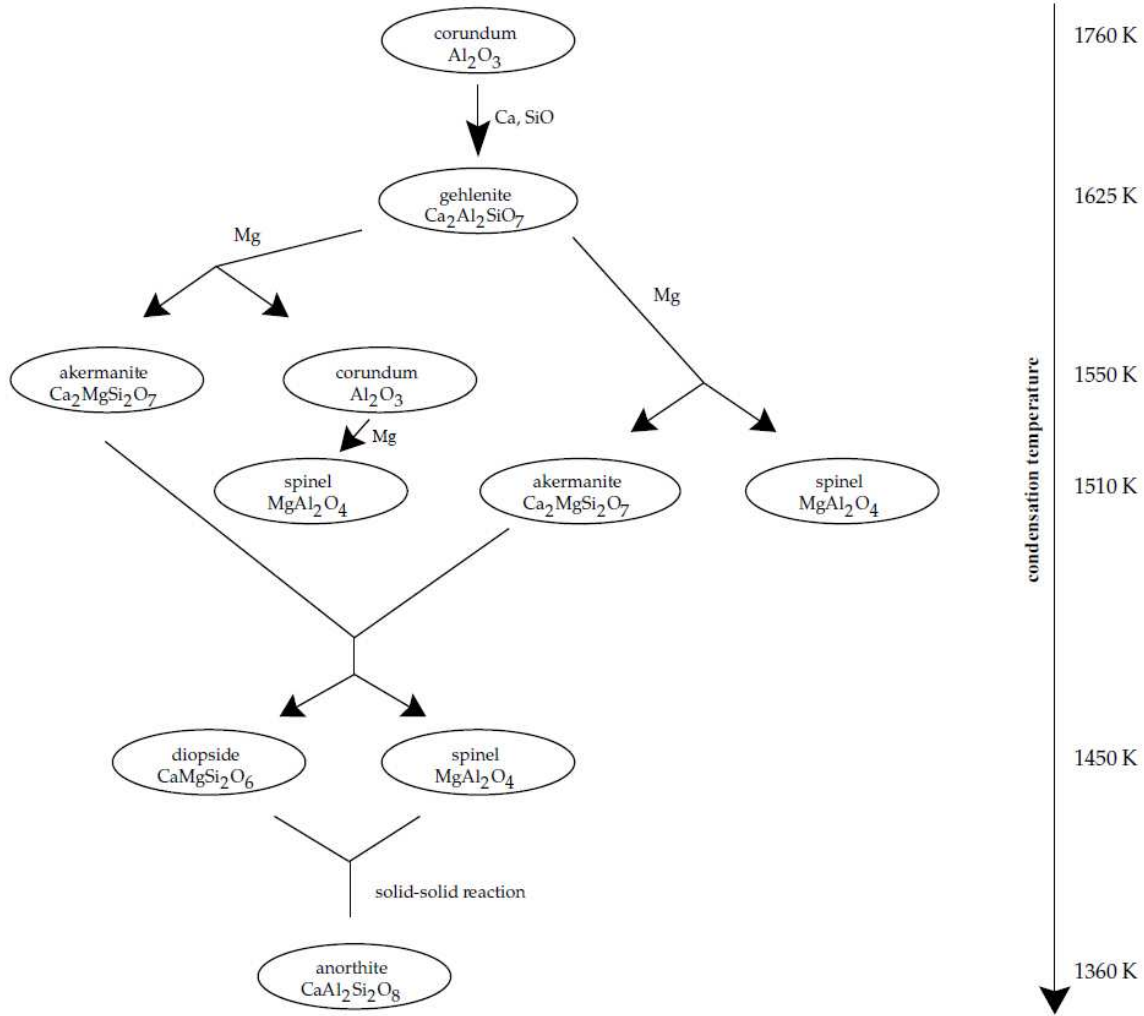


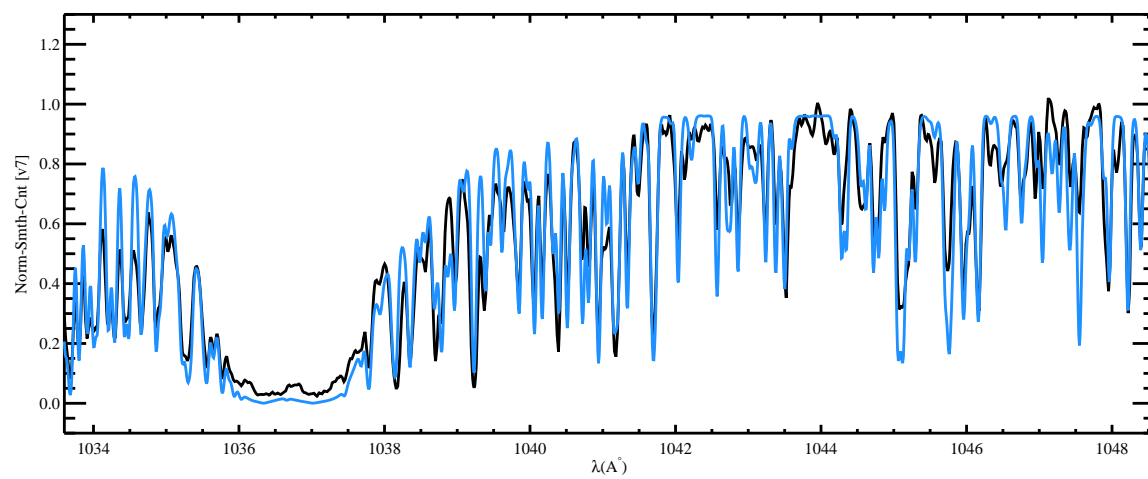
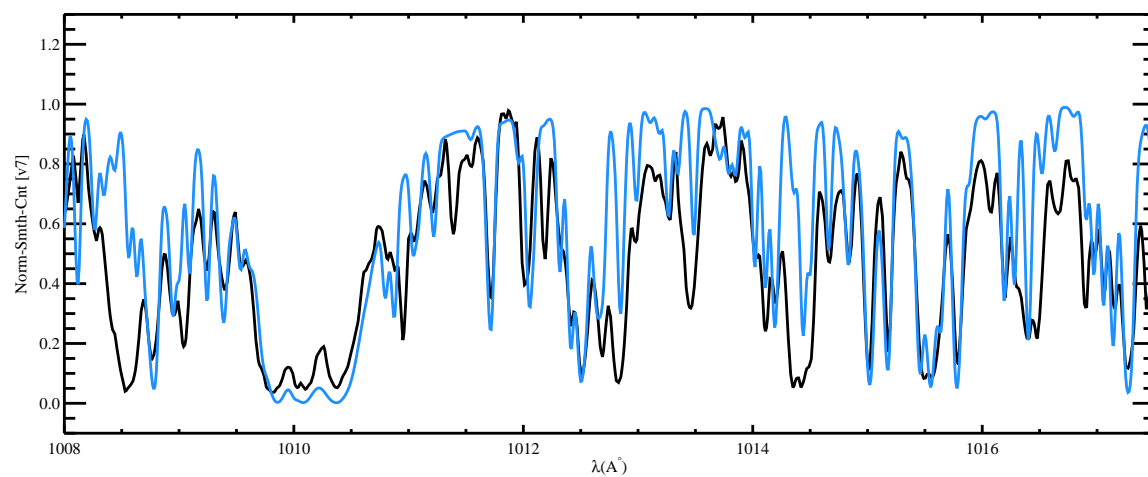
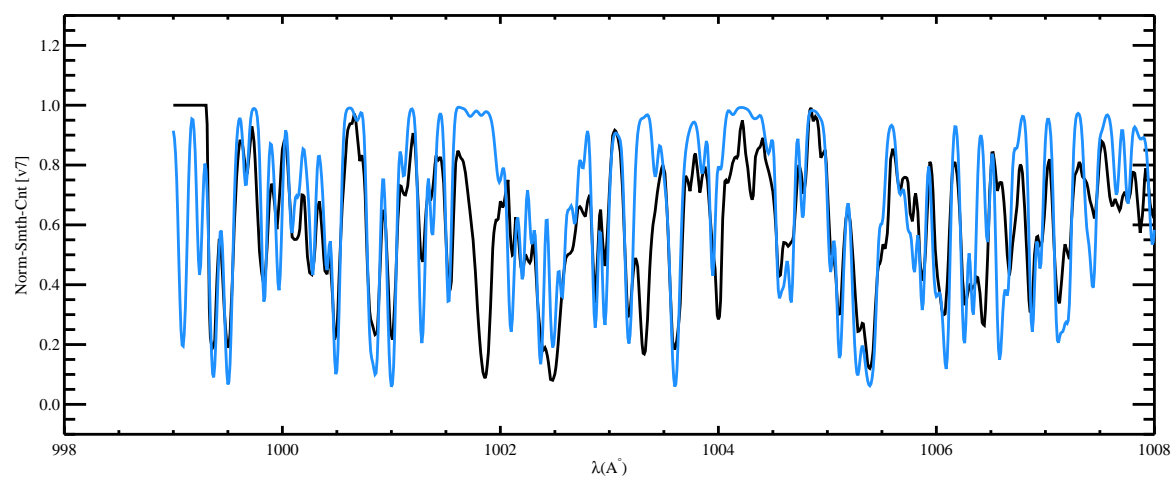
Figure A.11: This figure shows the formation sequence of Aluminum bearing condensates. [18]

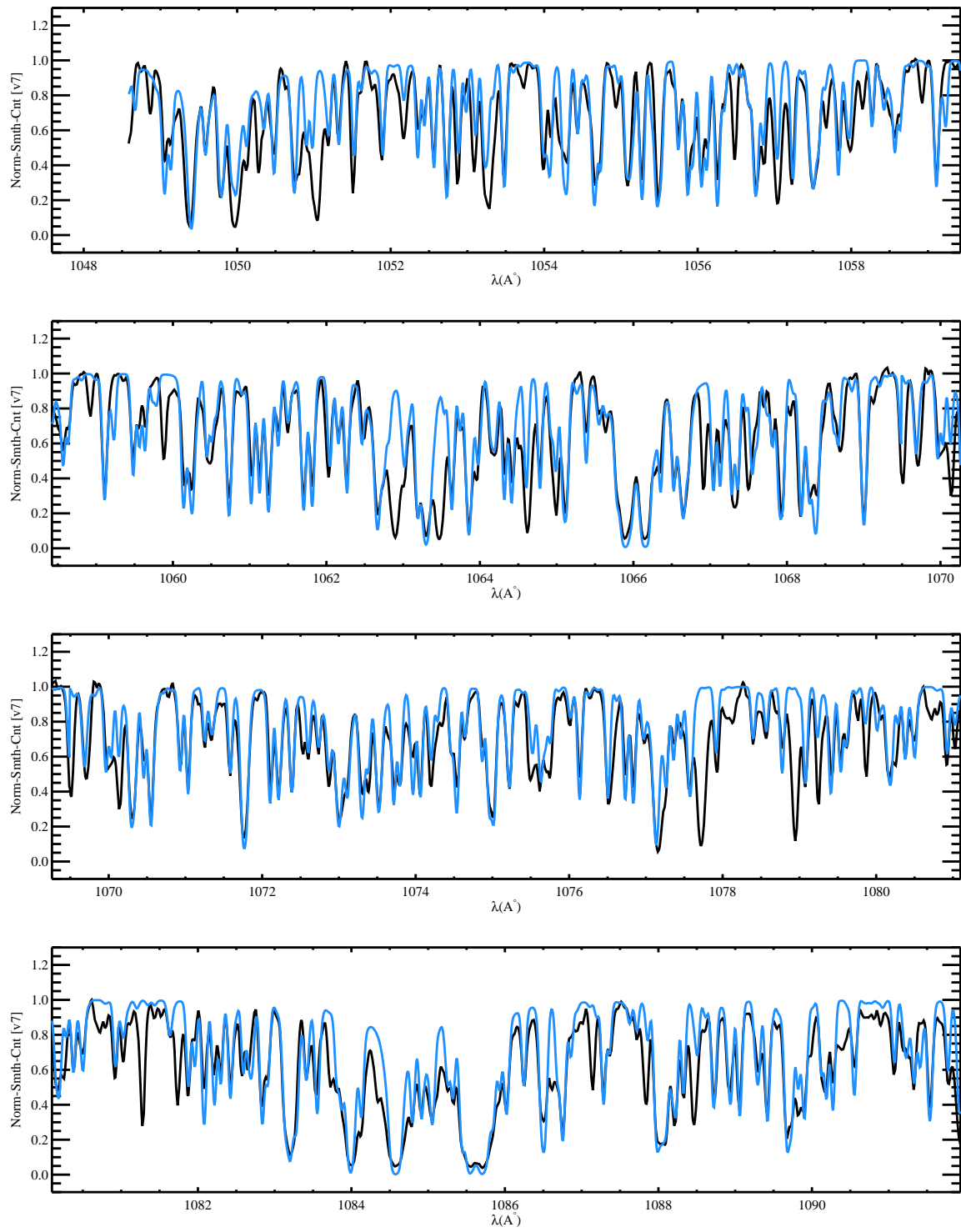
for these species. Only in the optically thick dust shells around AGB stars with high mass loss rates ($\sim 10^{-5}$ - $10^{-3} \text{ M}_\odot \text{ yr}^{-1}$, OH/IR stars), silicates appear in crystalline form [68]. Molster et al. [89] also report the observation of highly crystalline silicate dust in the surrounding disk of binary red-giant stars.

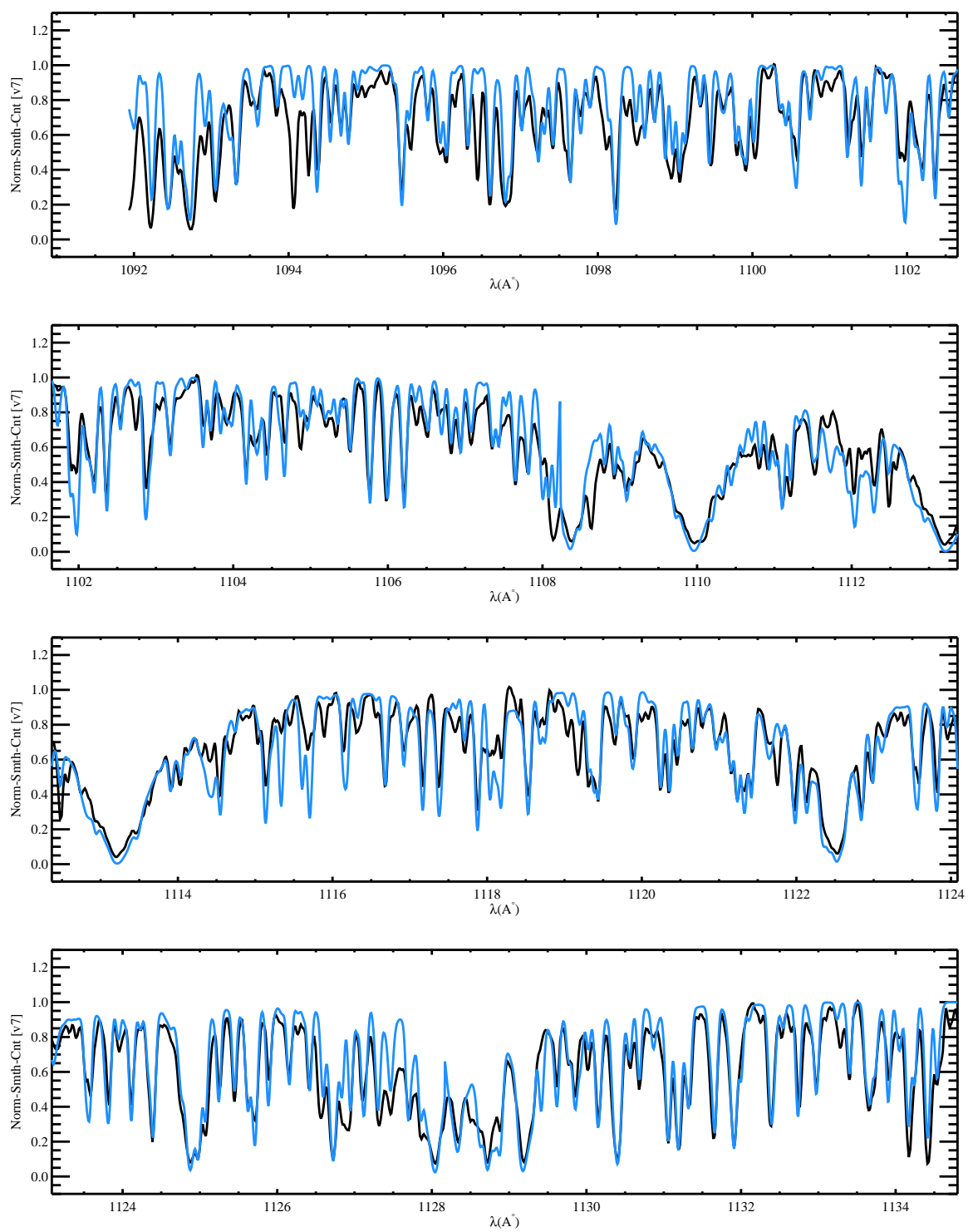
In general terms, what has been observed so far can be summarized as follows. The AGB stars with low mass loss rates exhibit mainly Alumina type dust because due to low density, the process of condensation will freeze out before it can complete the sequence. The high mass loss rate AGB stars are dominated with amorphous silicates. Those AGB stars that fall in neither extremes (intermediate mass loss), show a variety of dust features (e.g. $13\mu\text{m}$, $19.5\mu\text{m}$, etc.) which does not clearly correlate with mass loss rate but a correlation between $13\mu\text{m}$ and $19.5\mu\text{m}$ features have been reported [10].

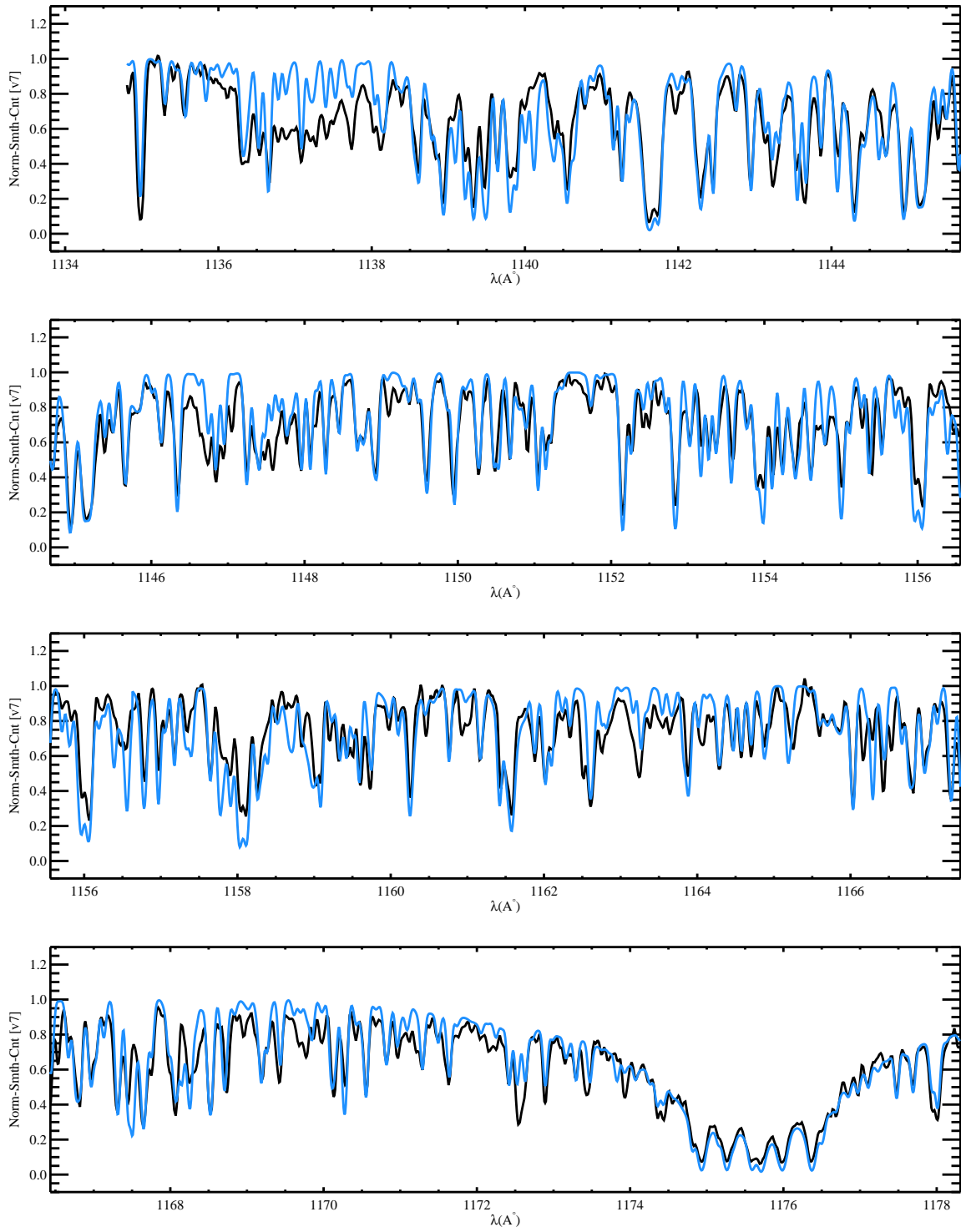
Appendix B

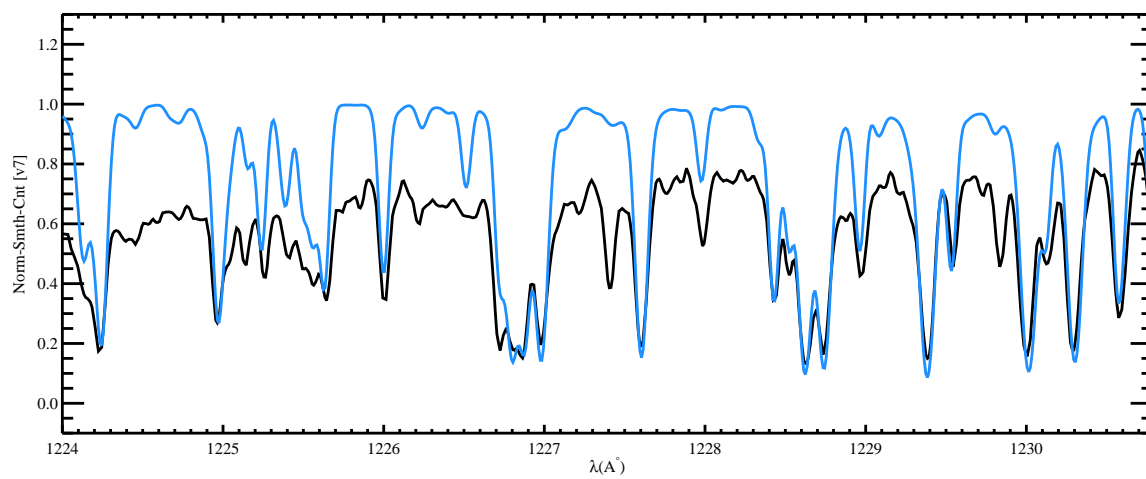
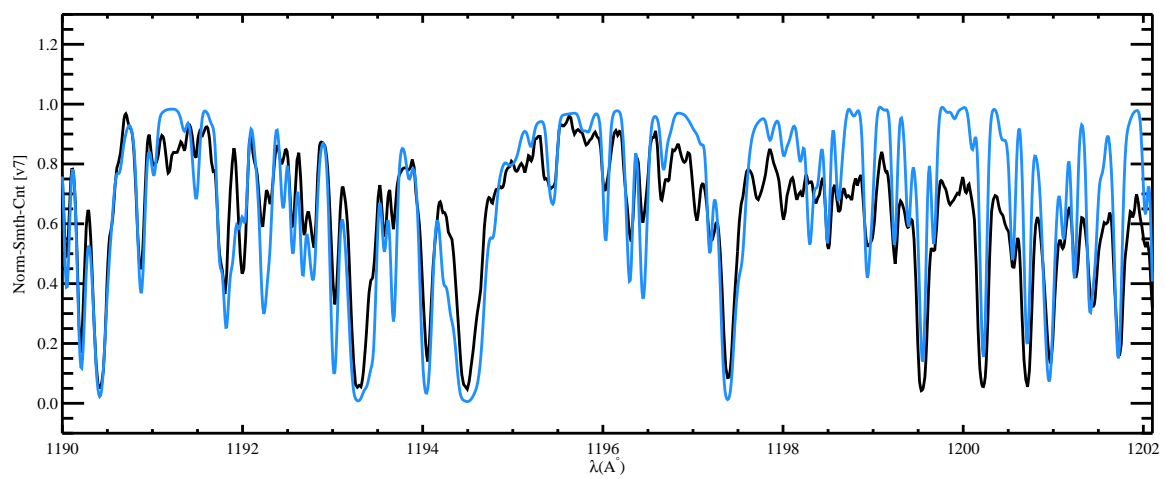
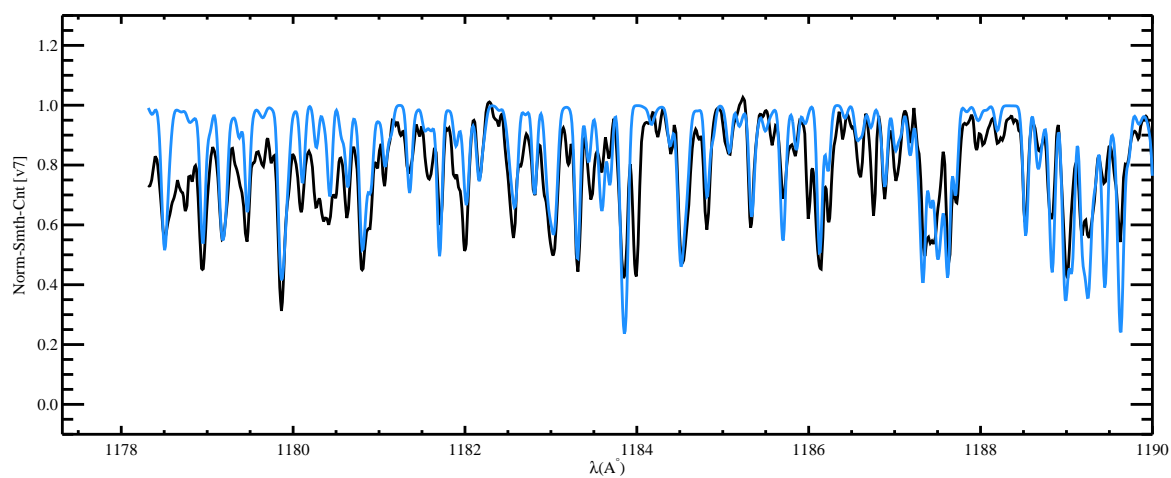
Iota Herculis Models

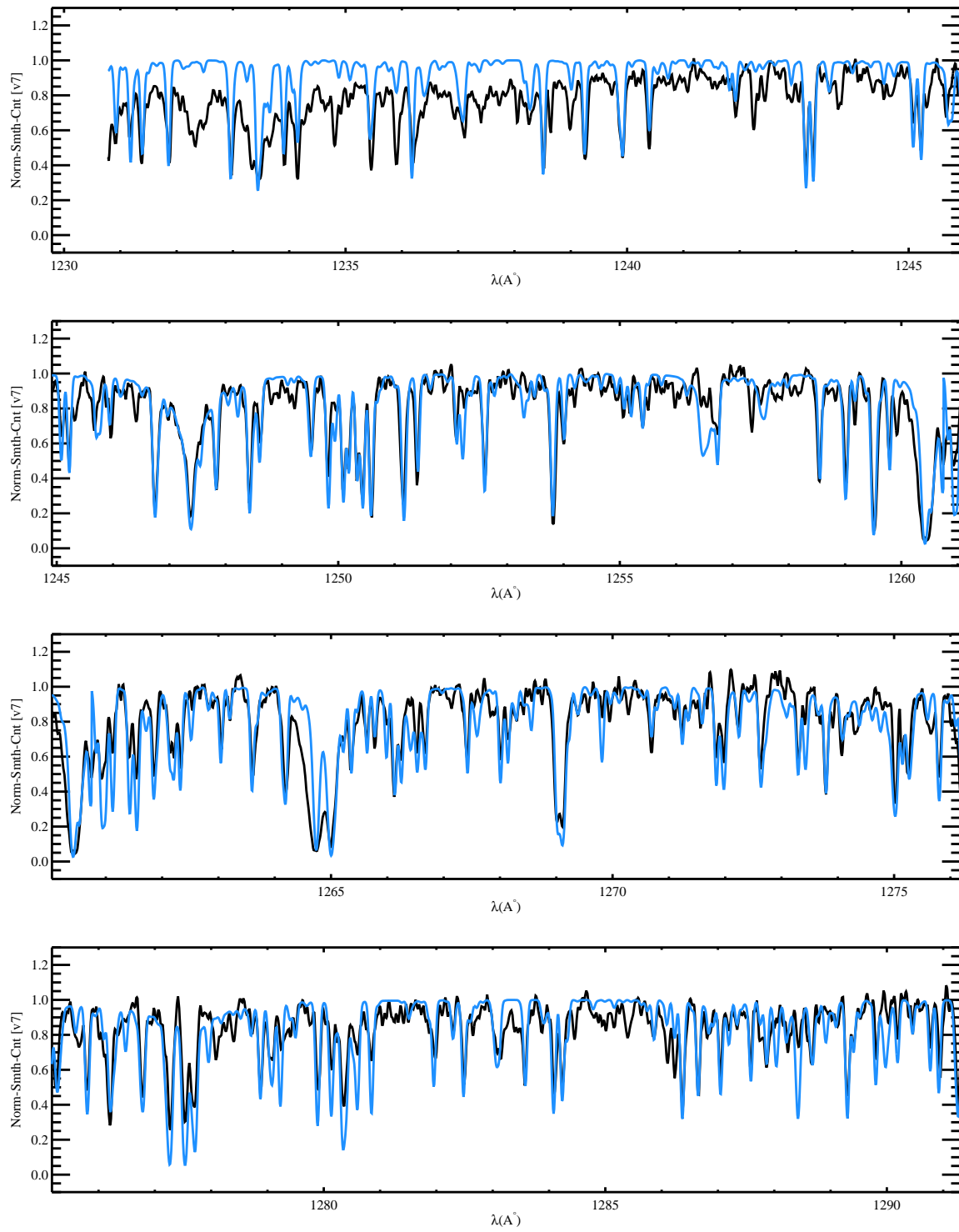


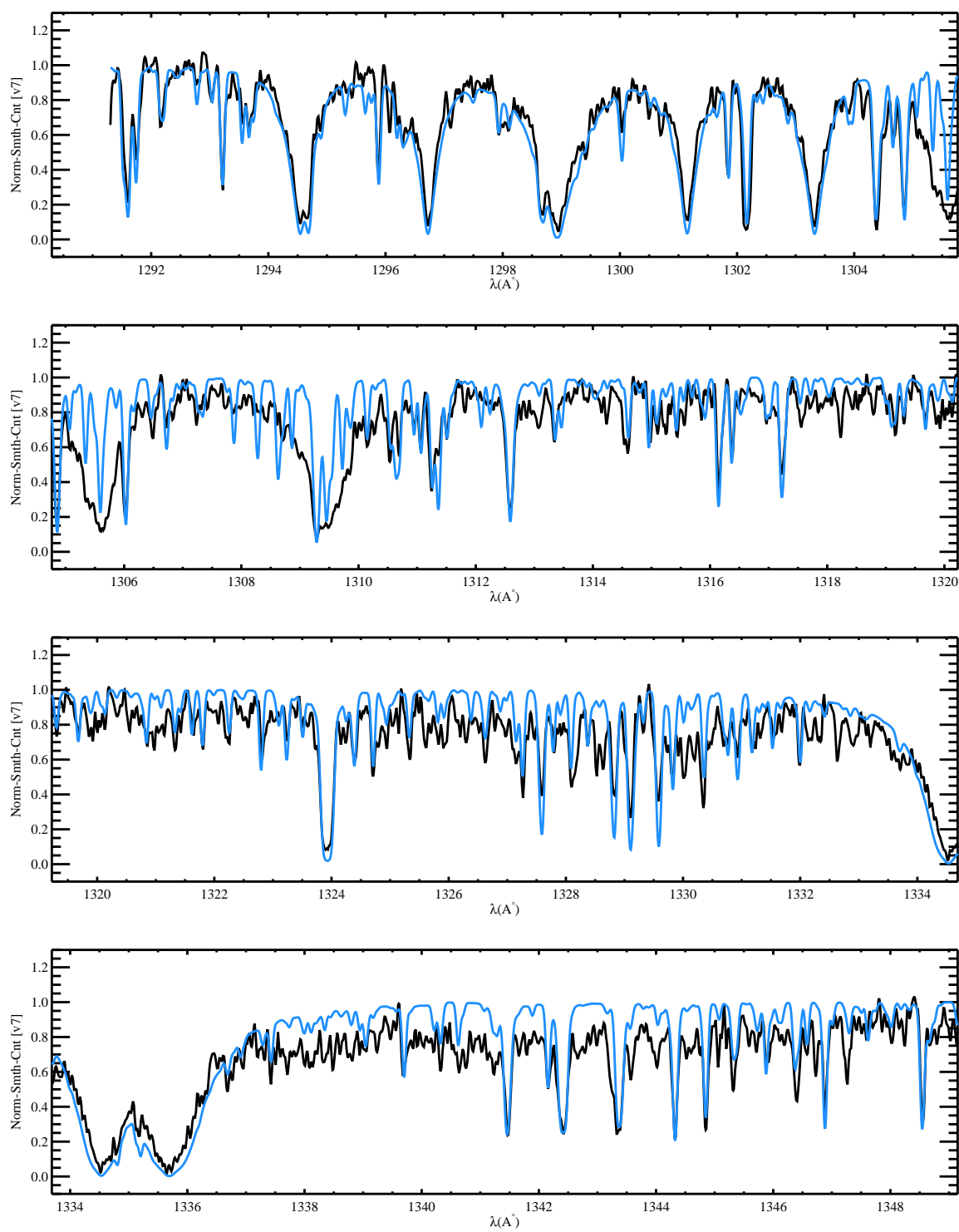


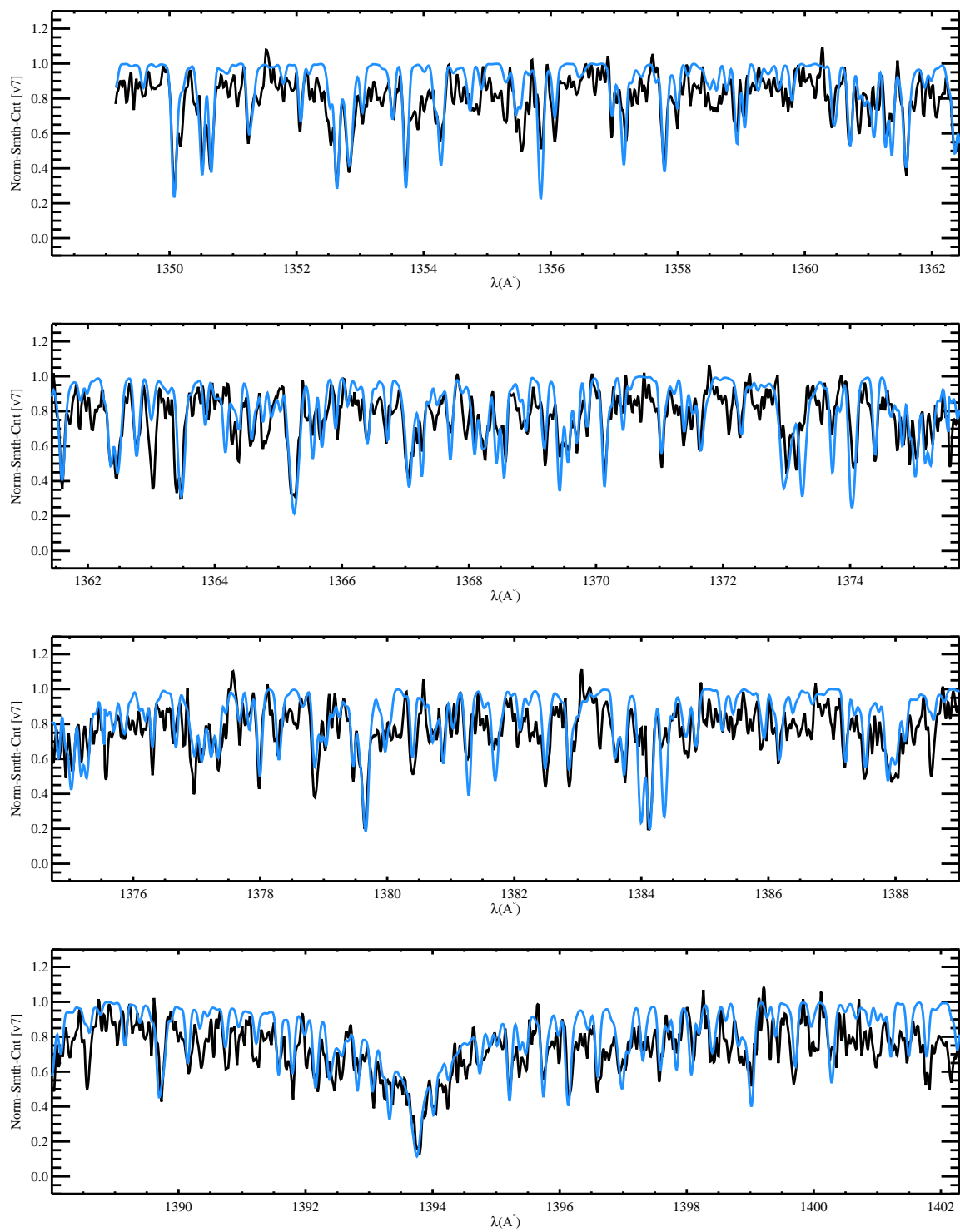


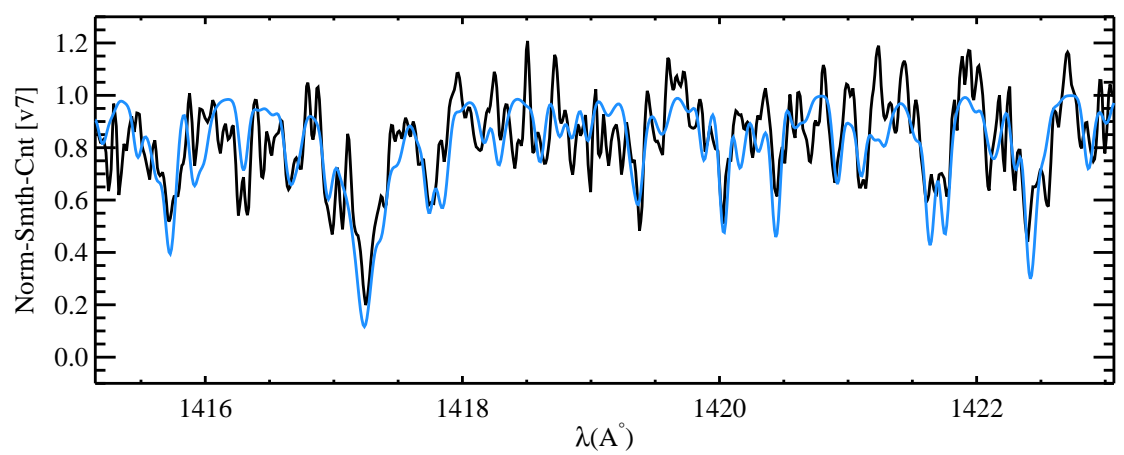
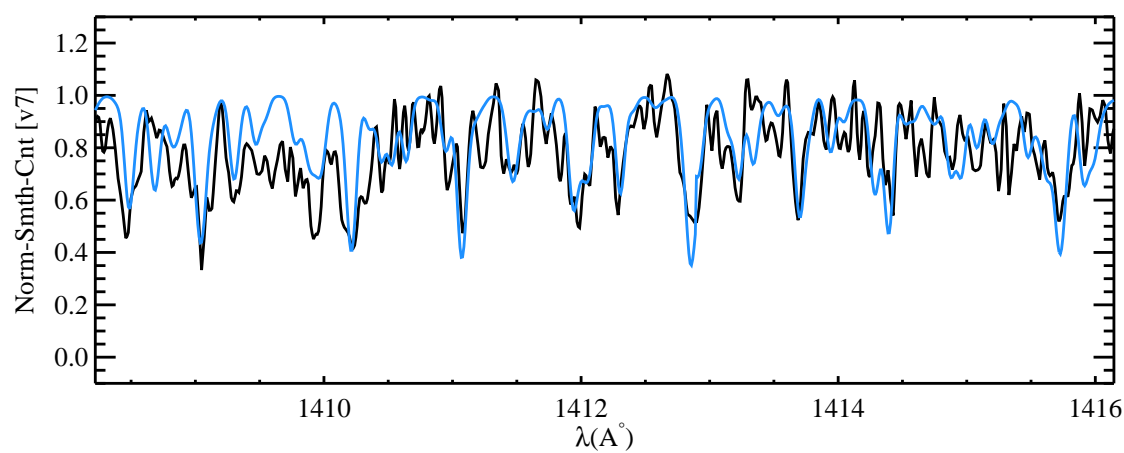
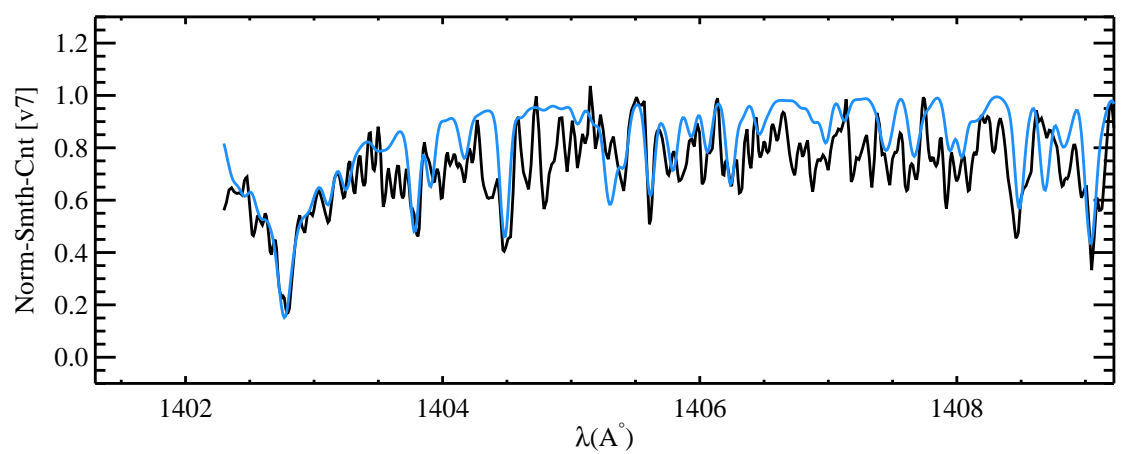


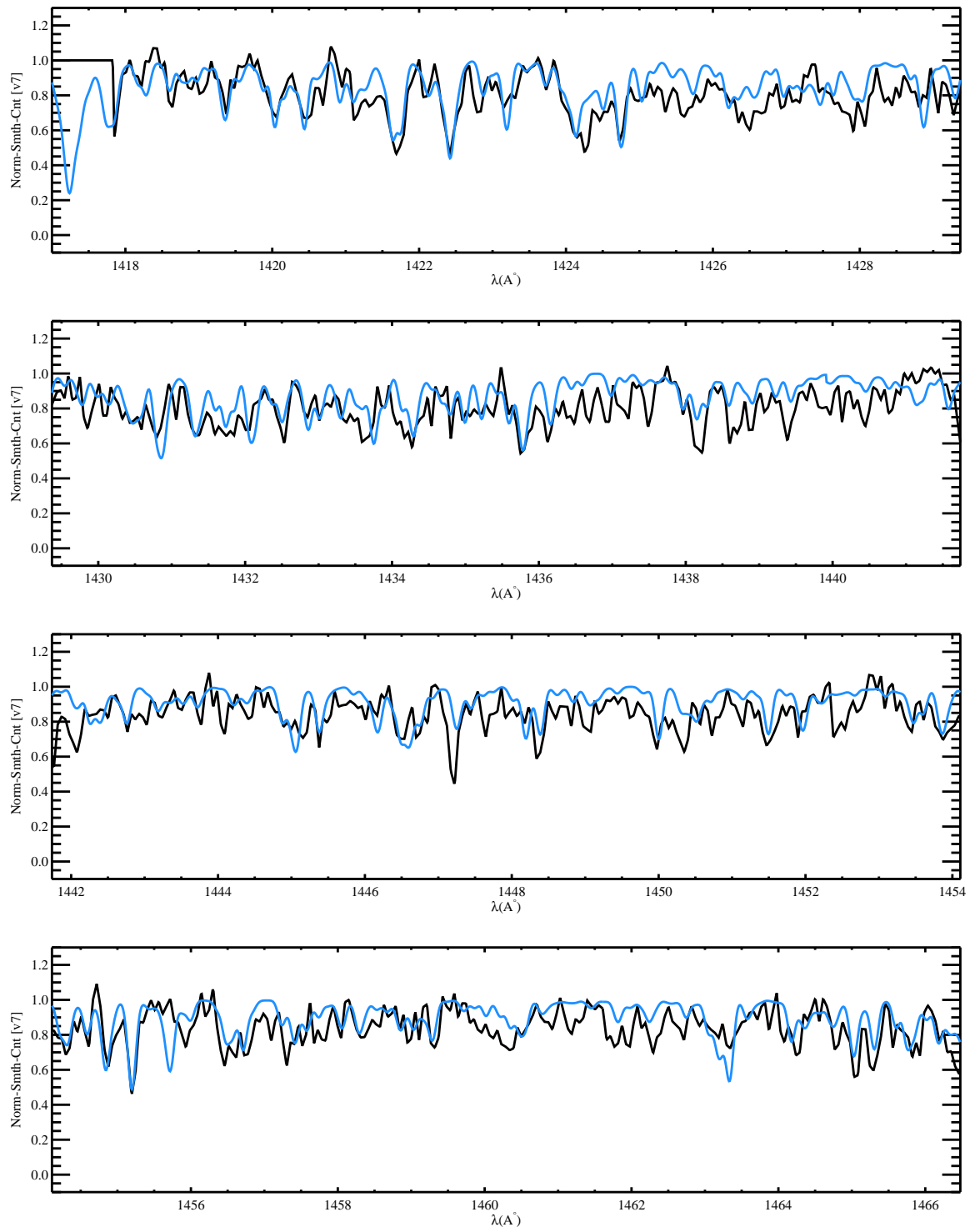






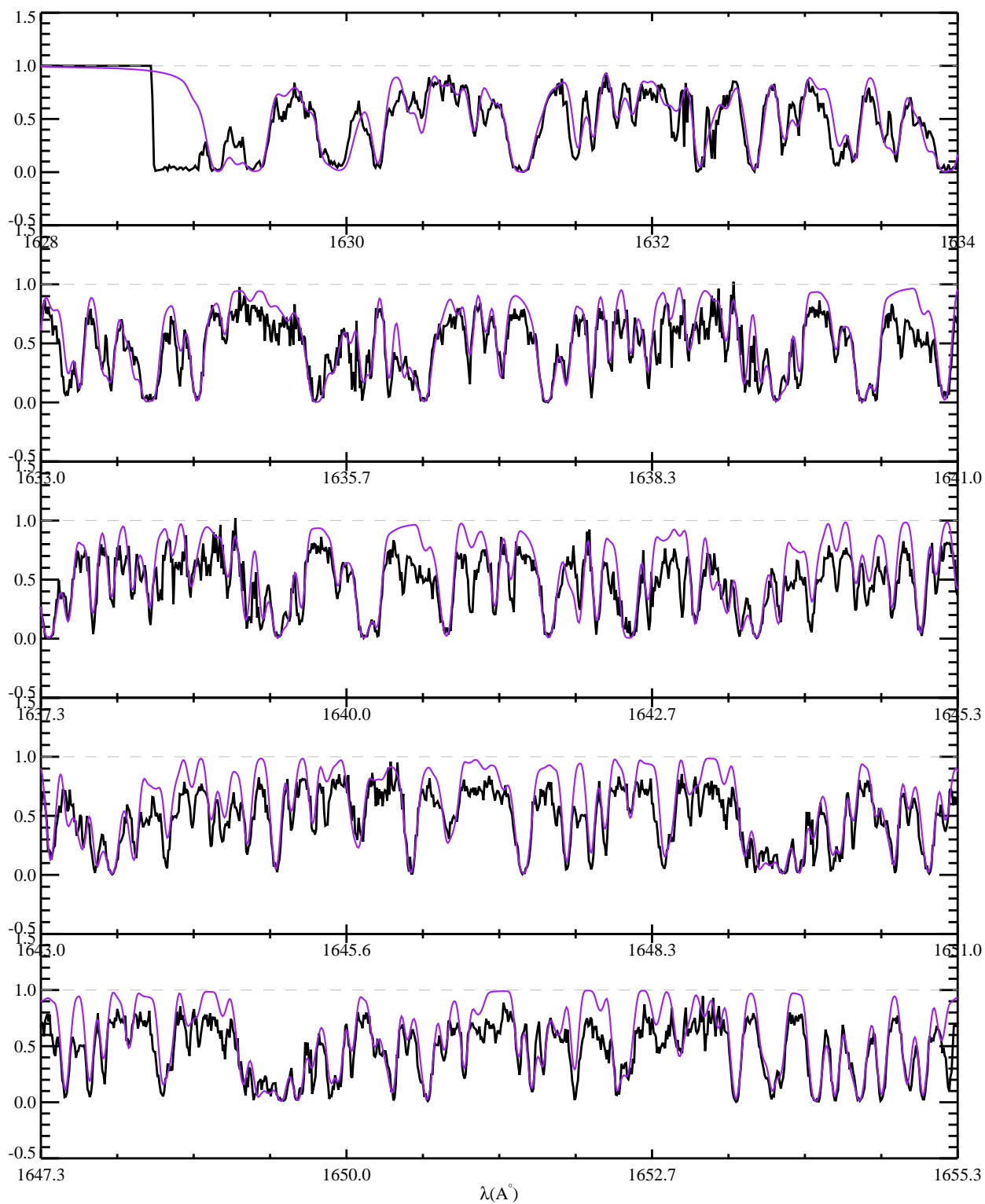


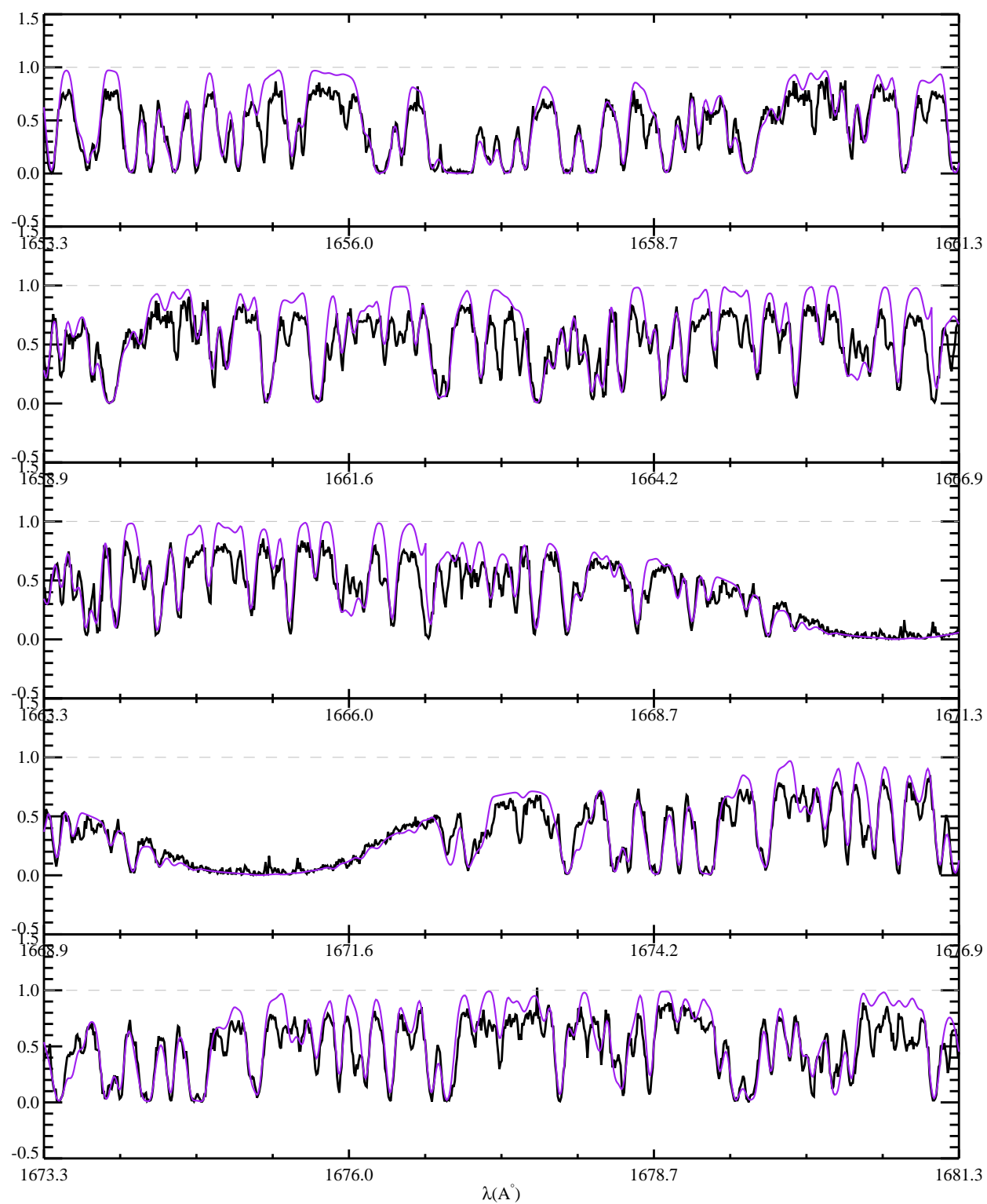


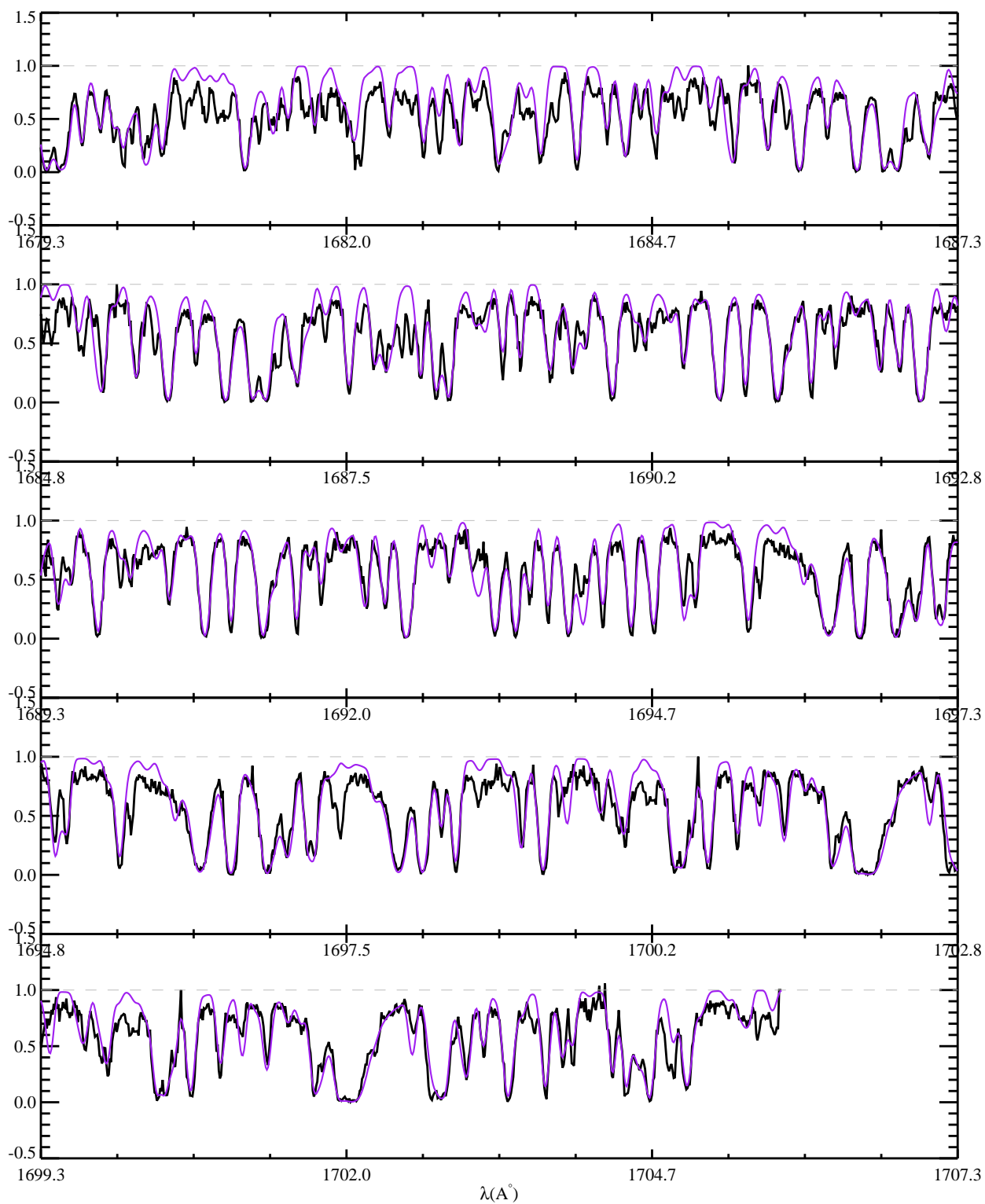


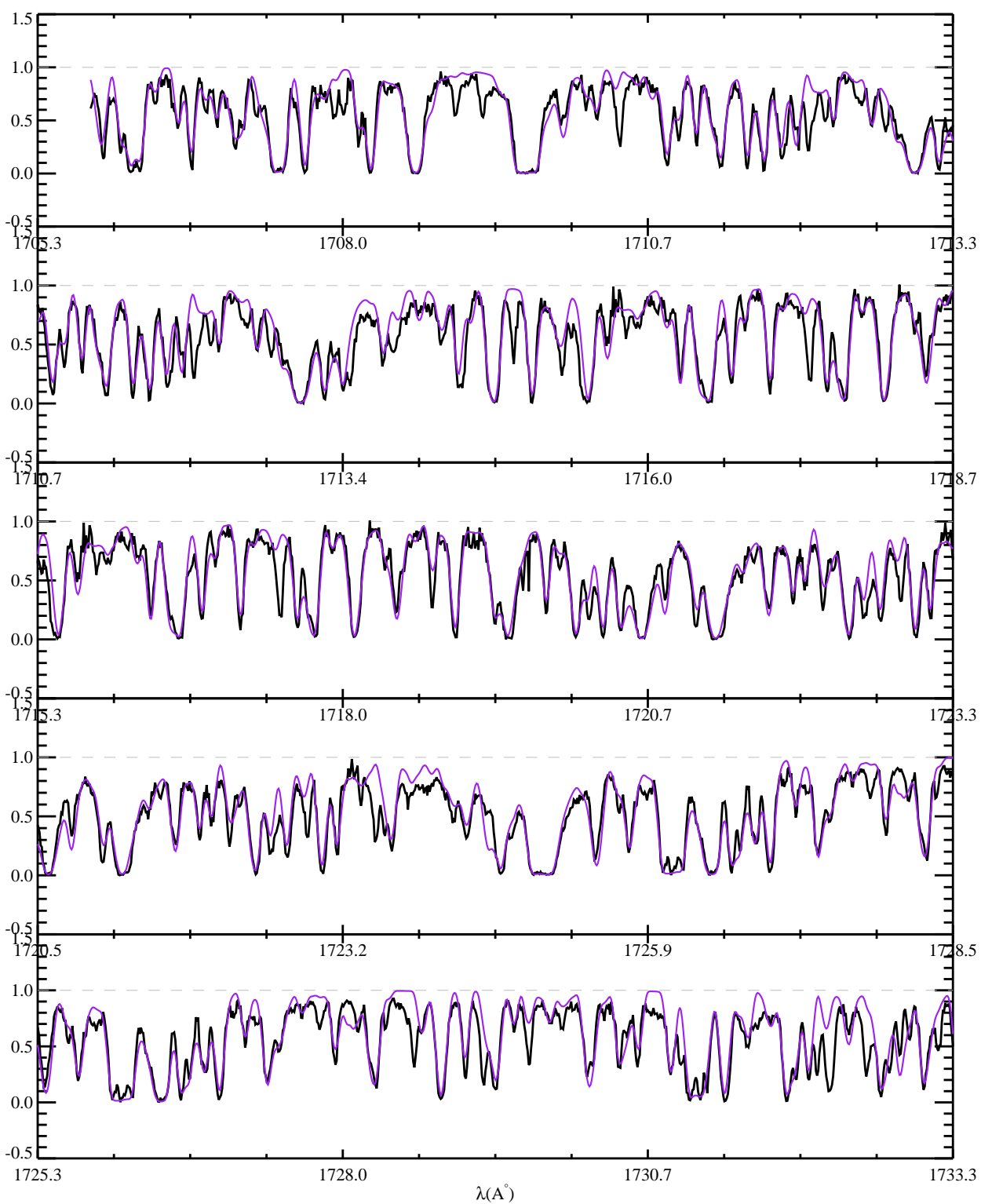
Appendix C

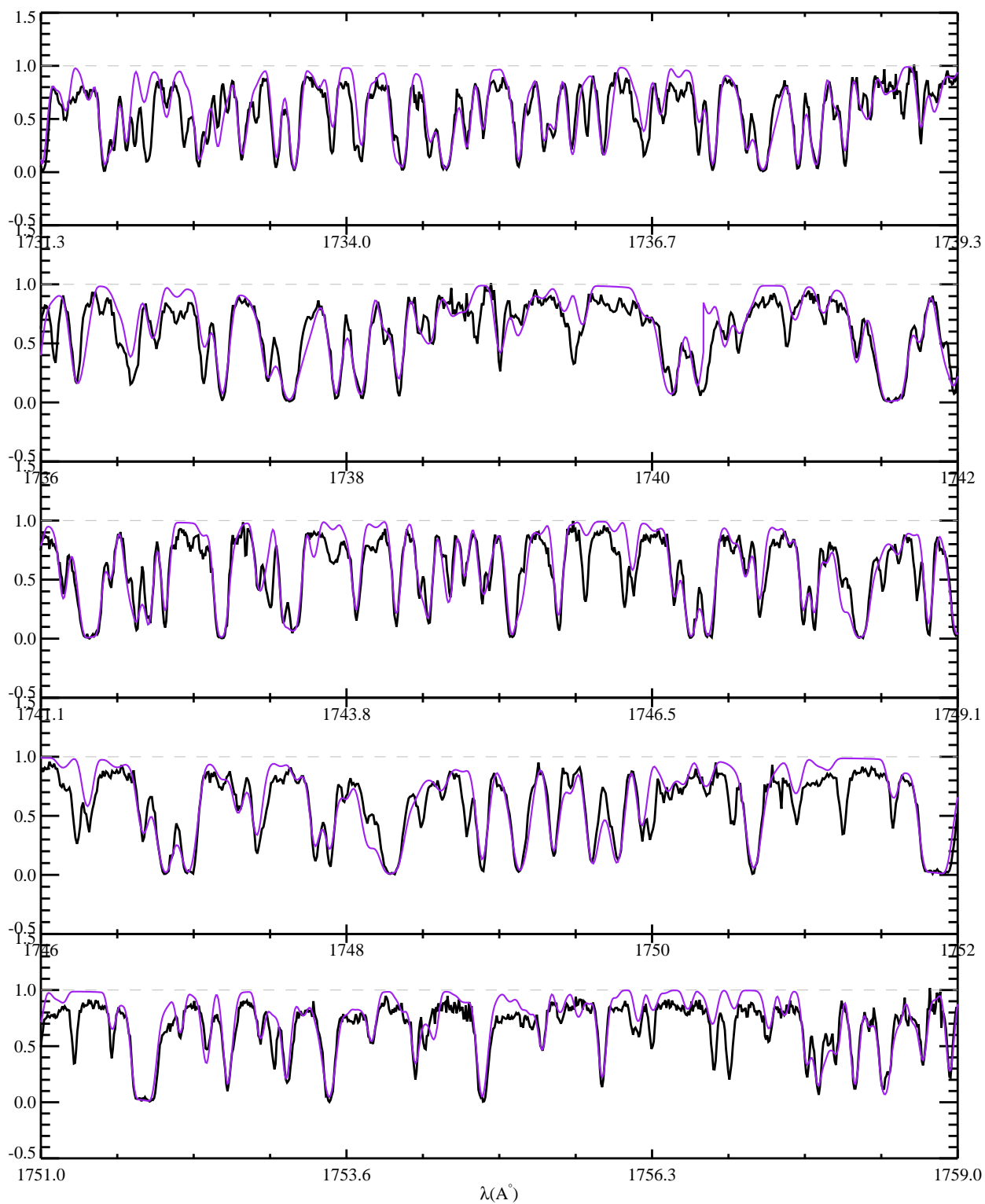
HD72660 Models

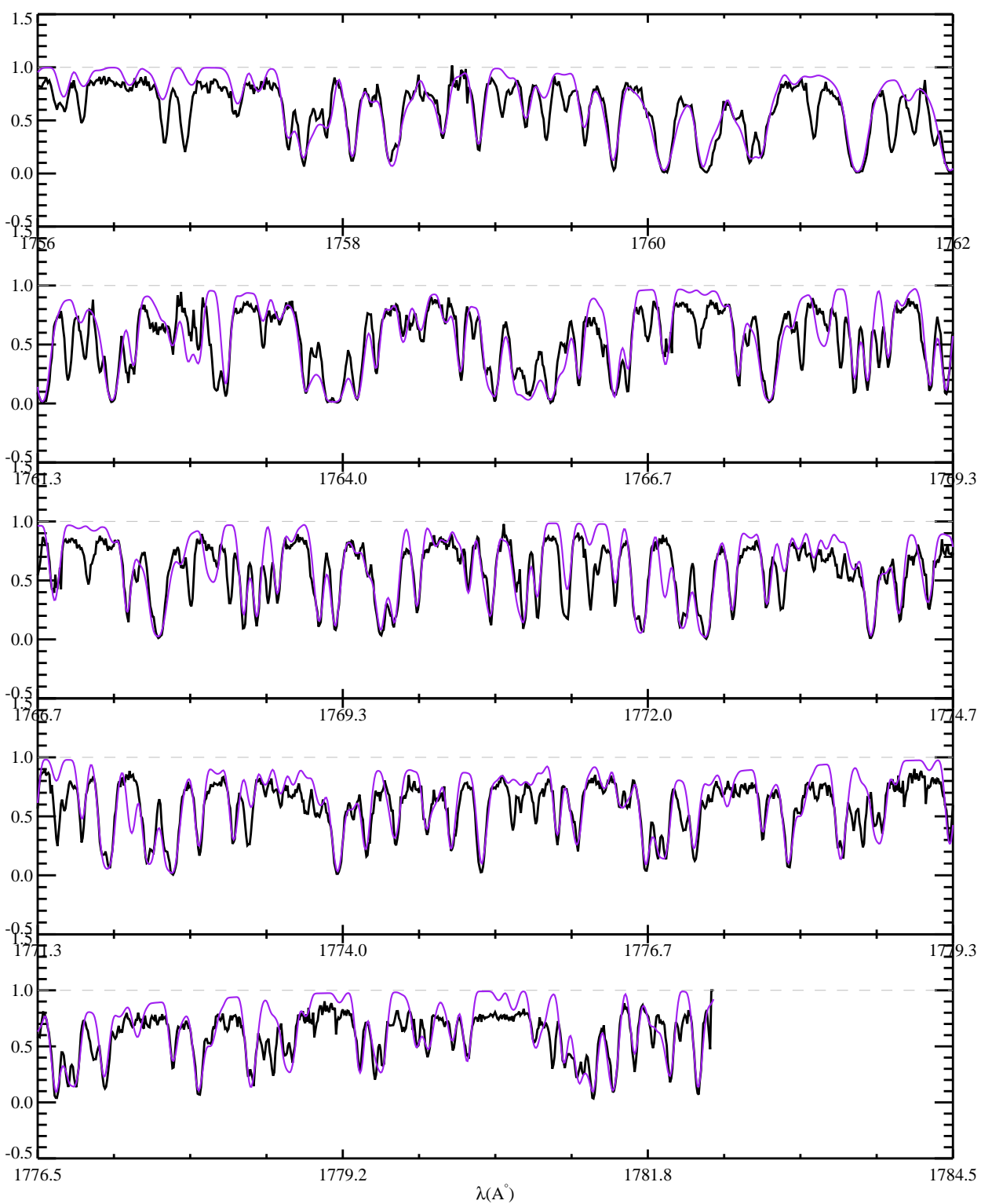


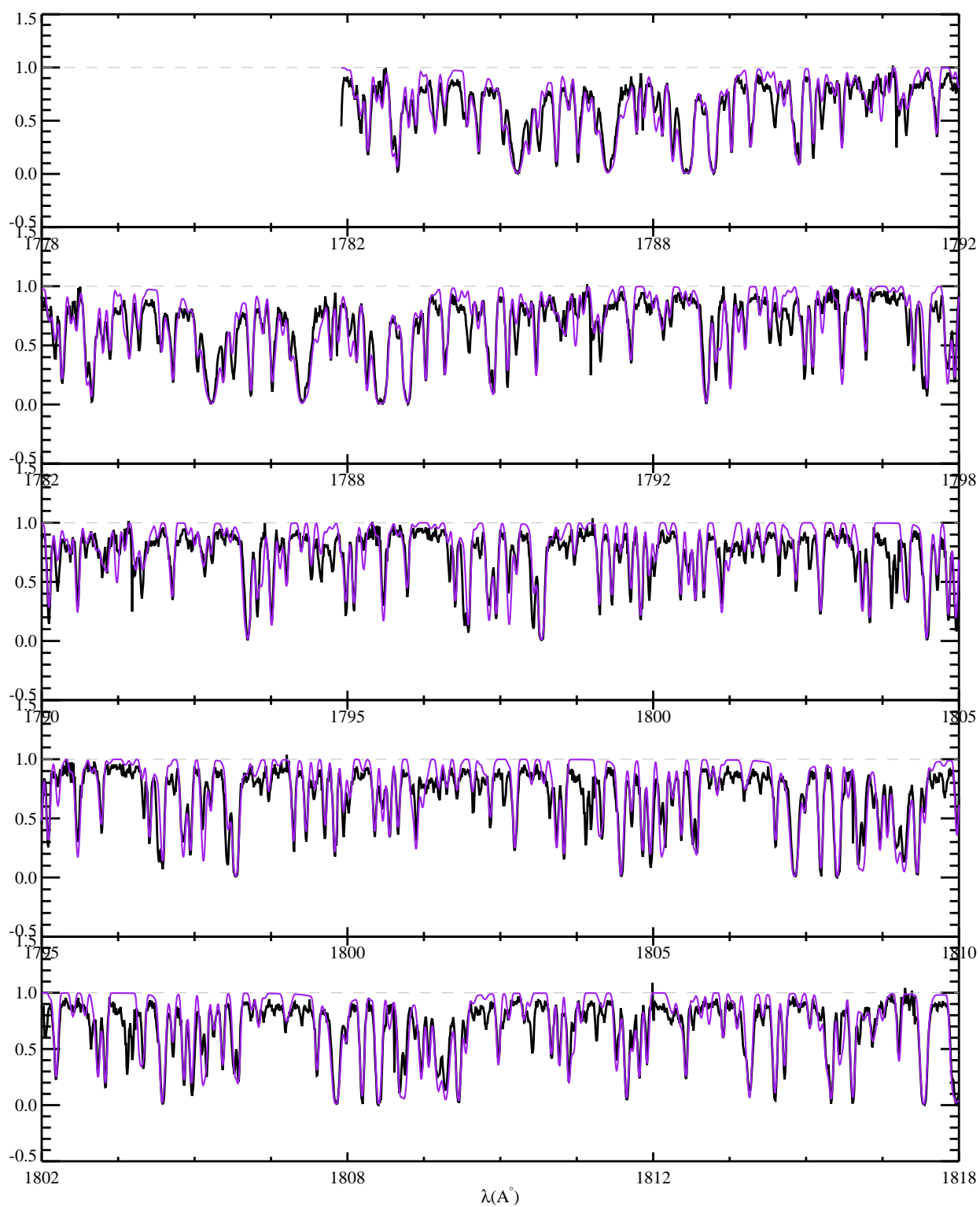


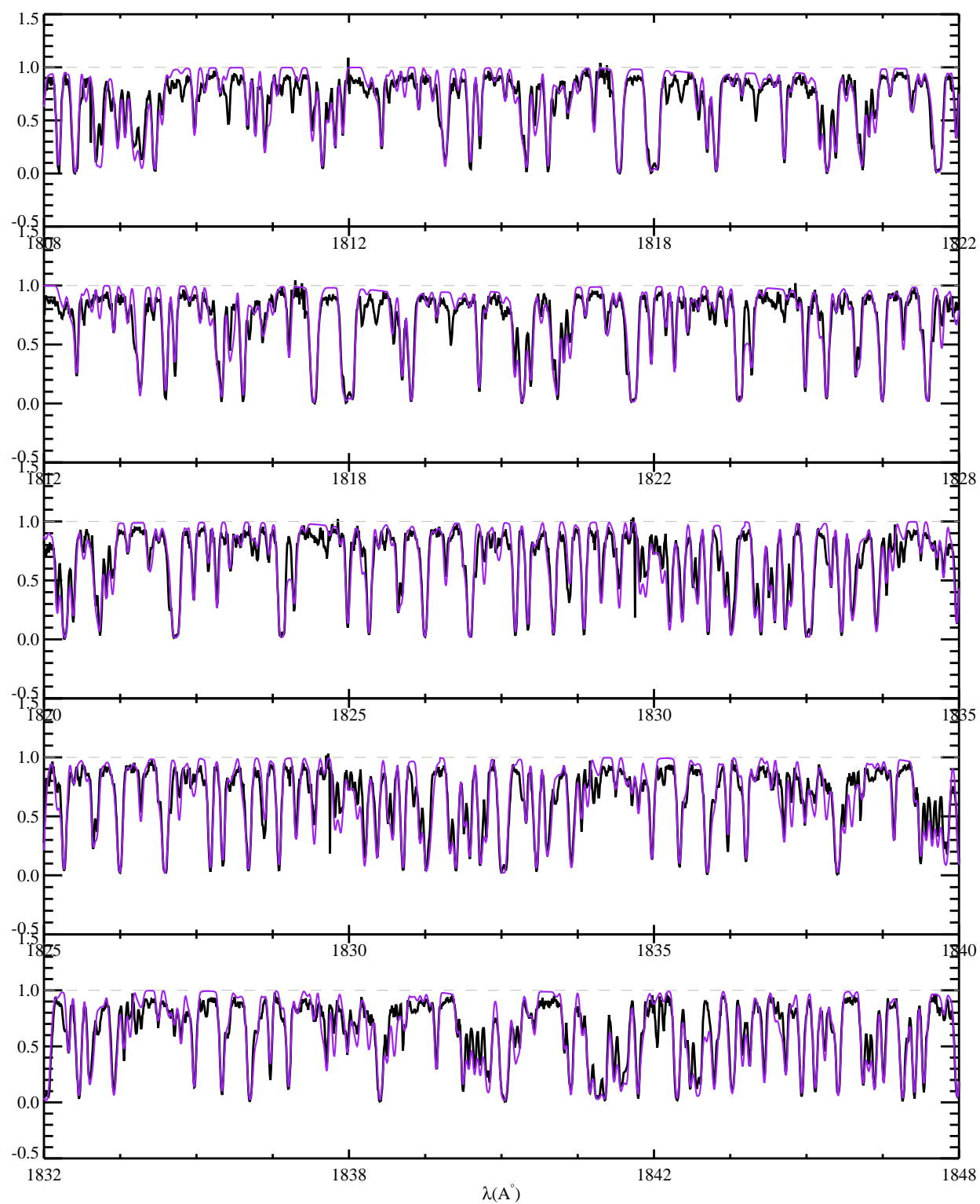


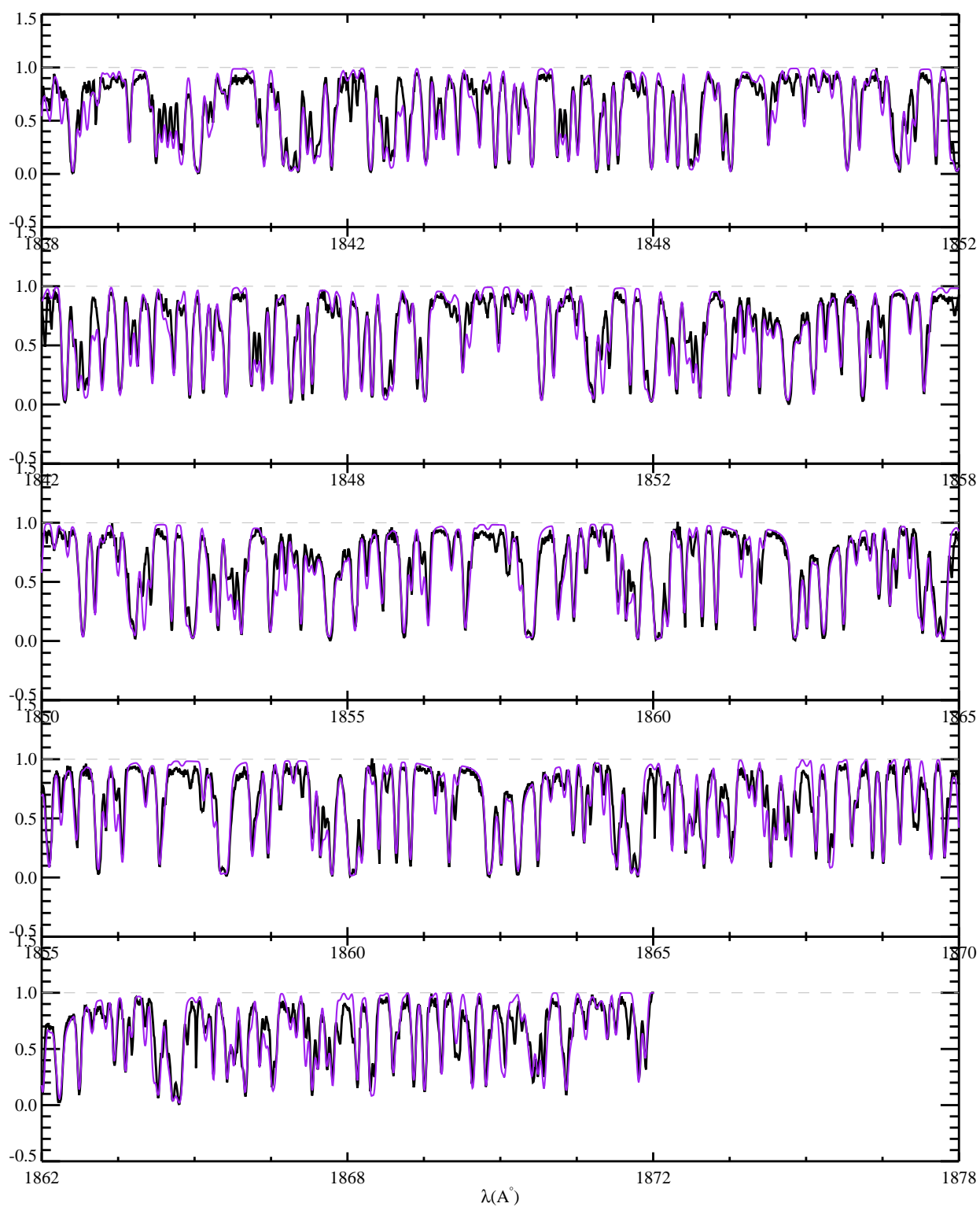


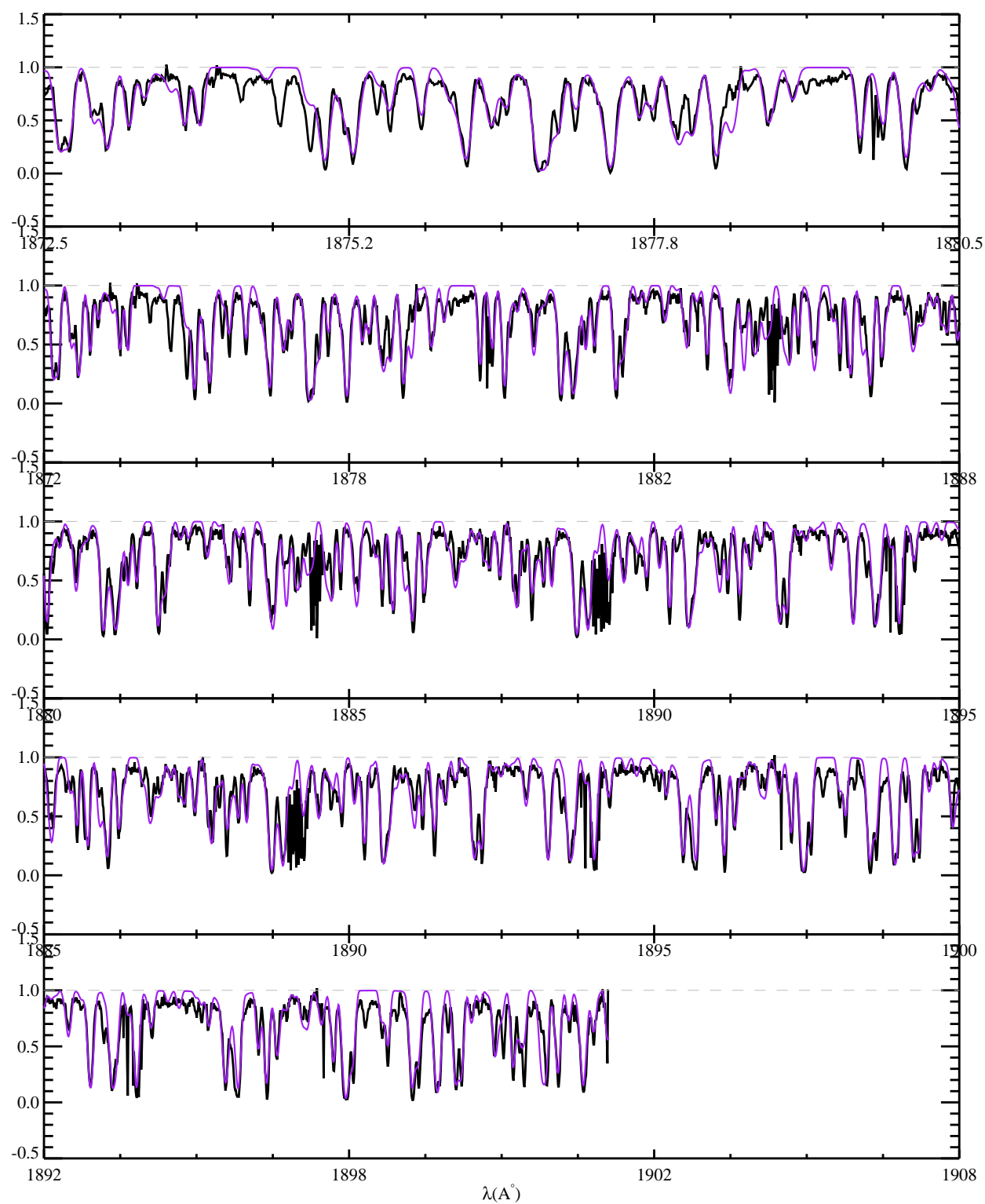


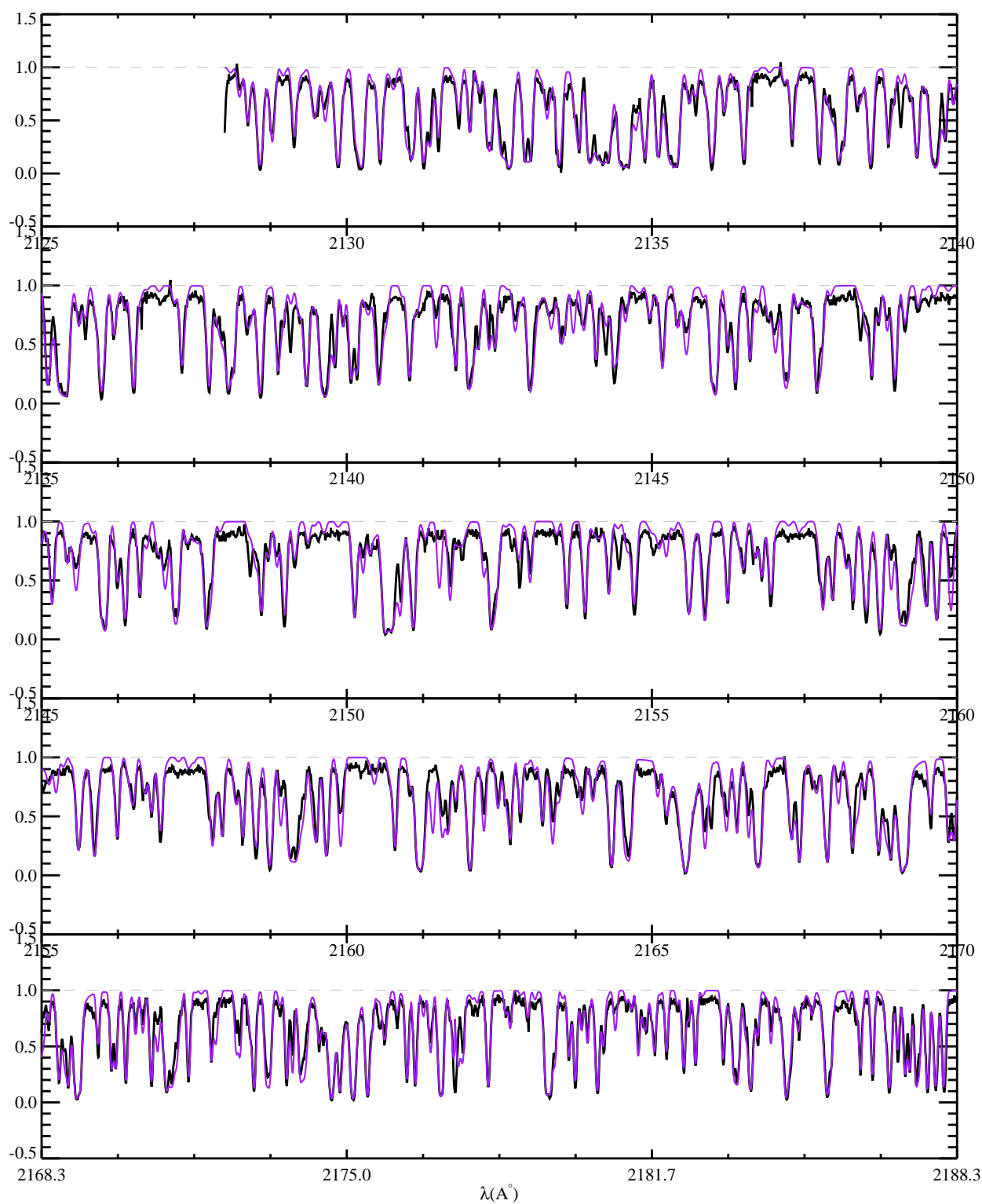


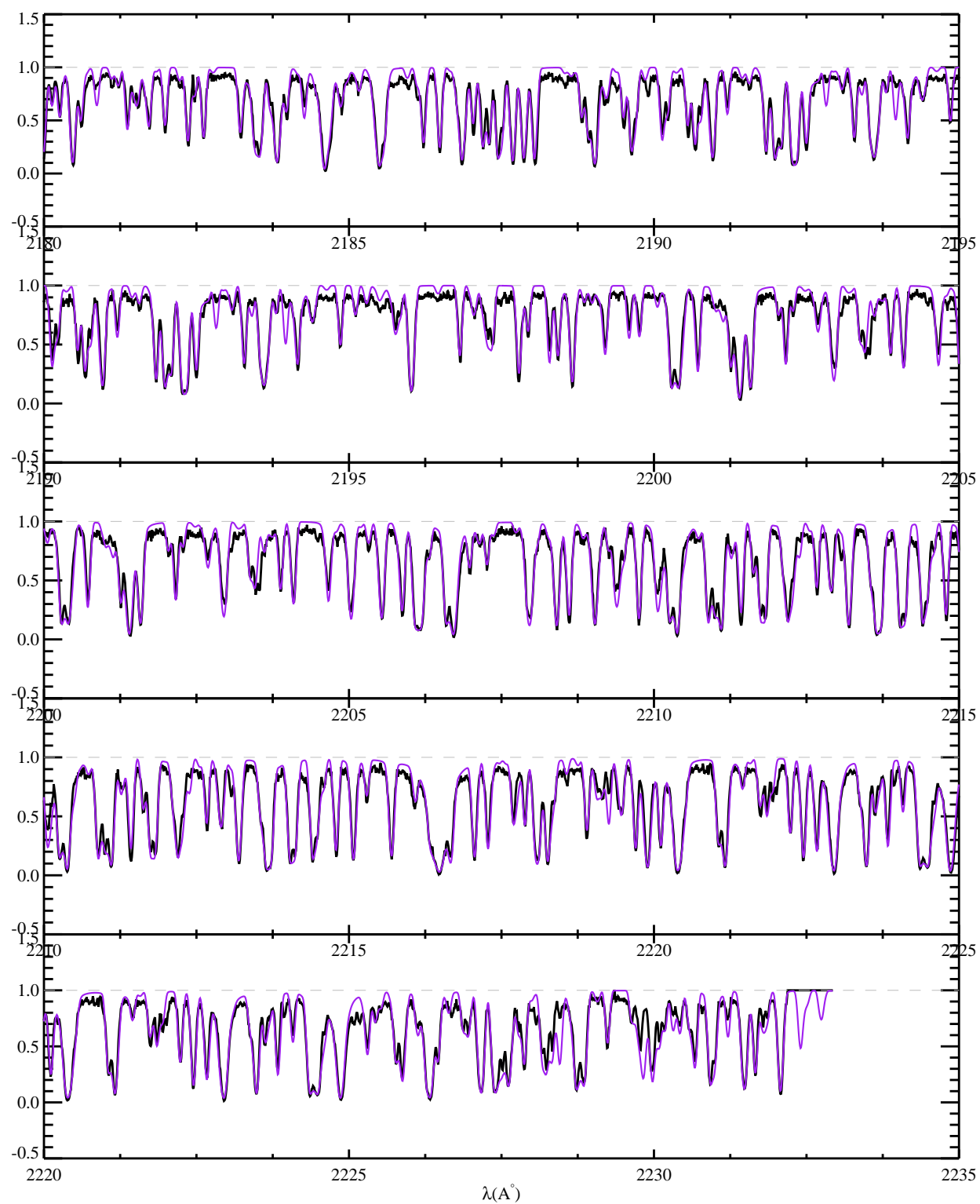


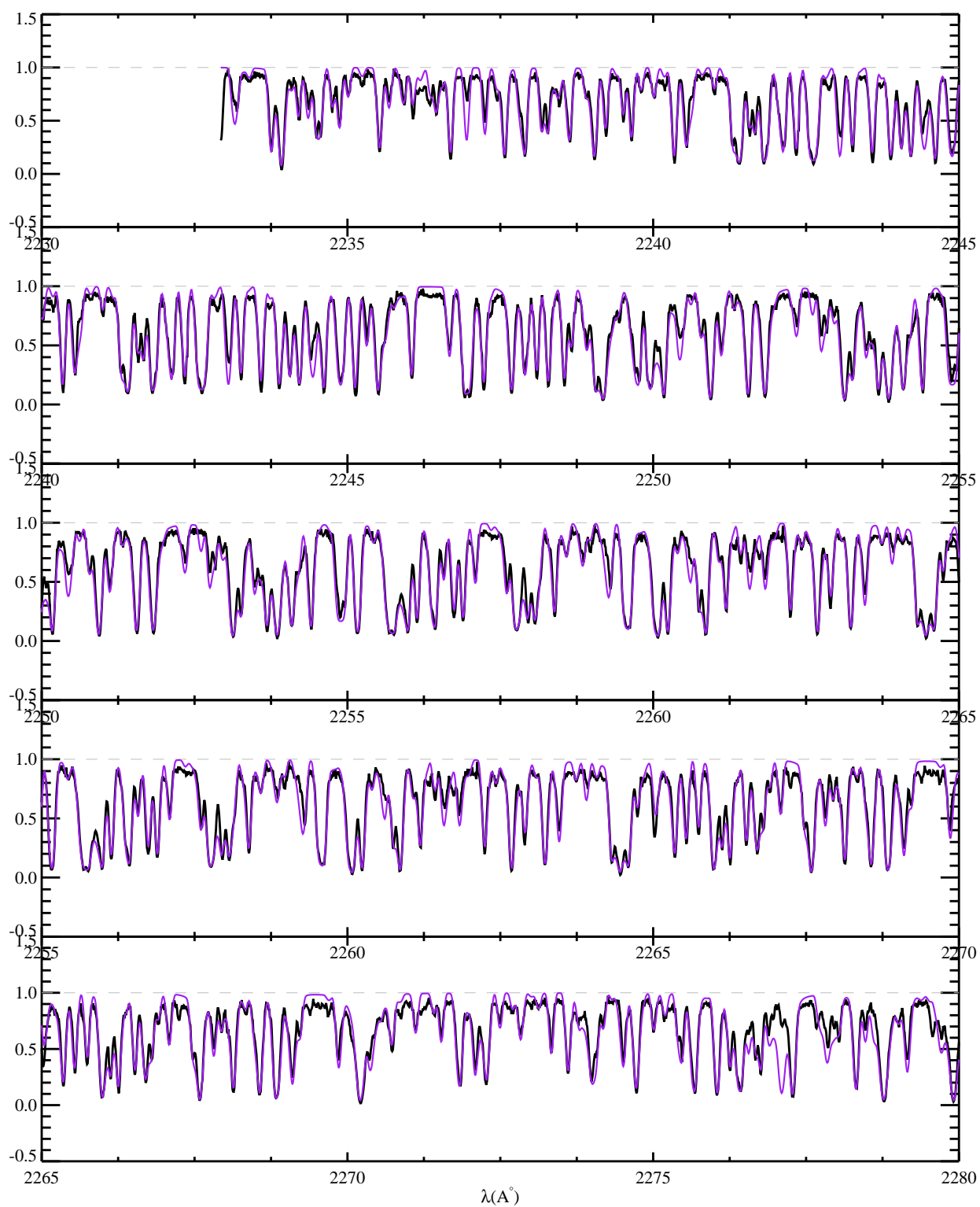


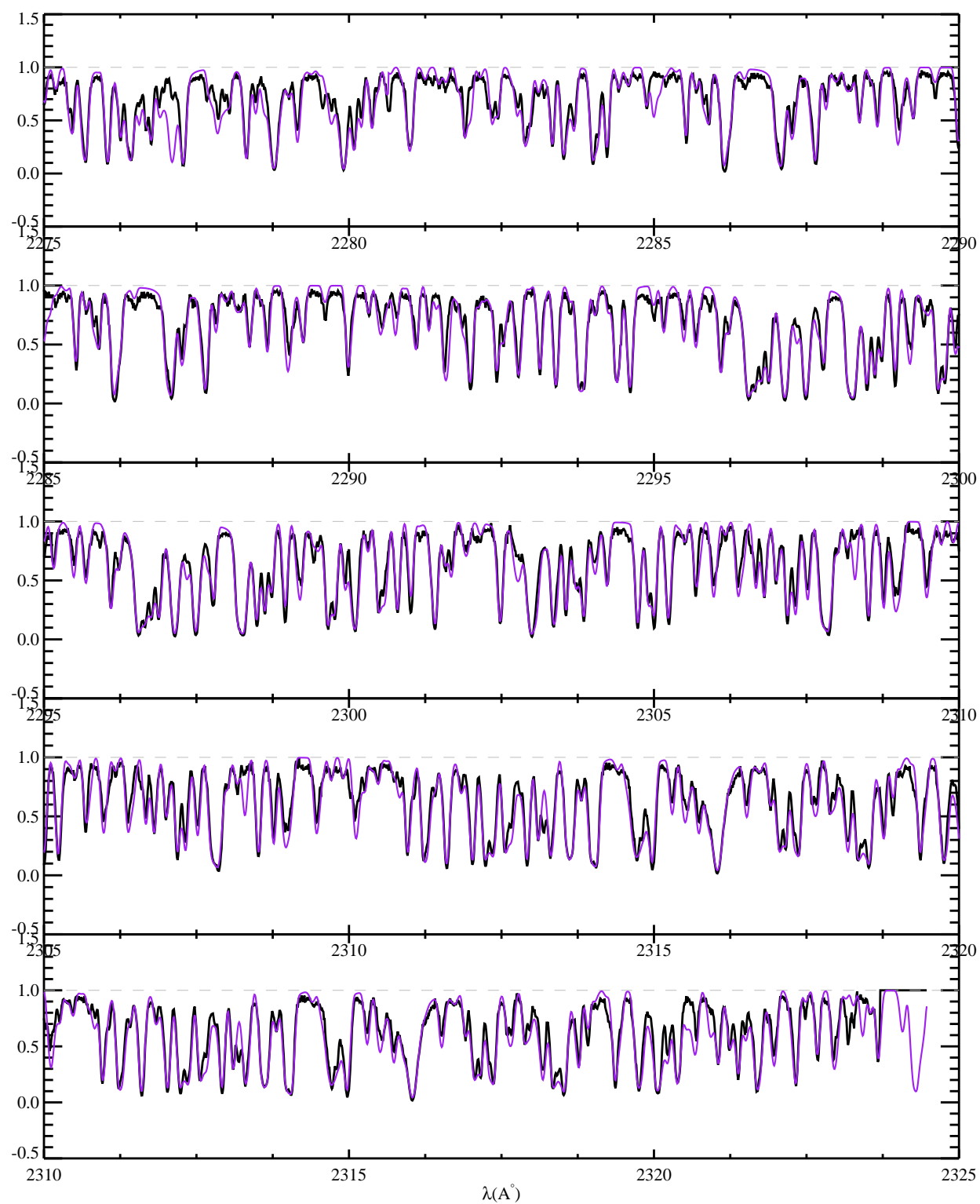


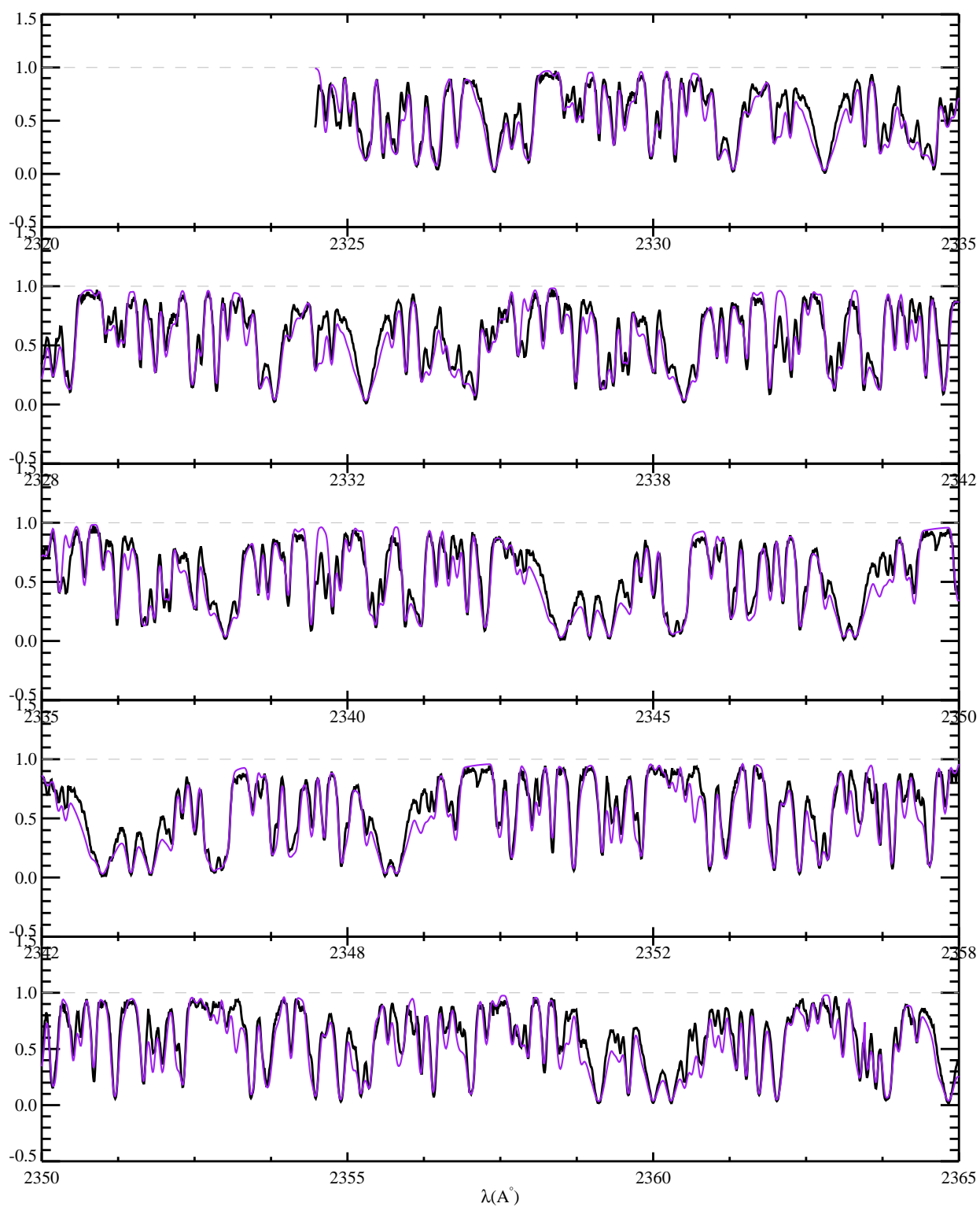


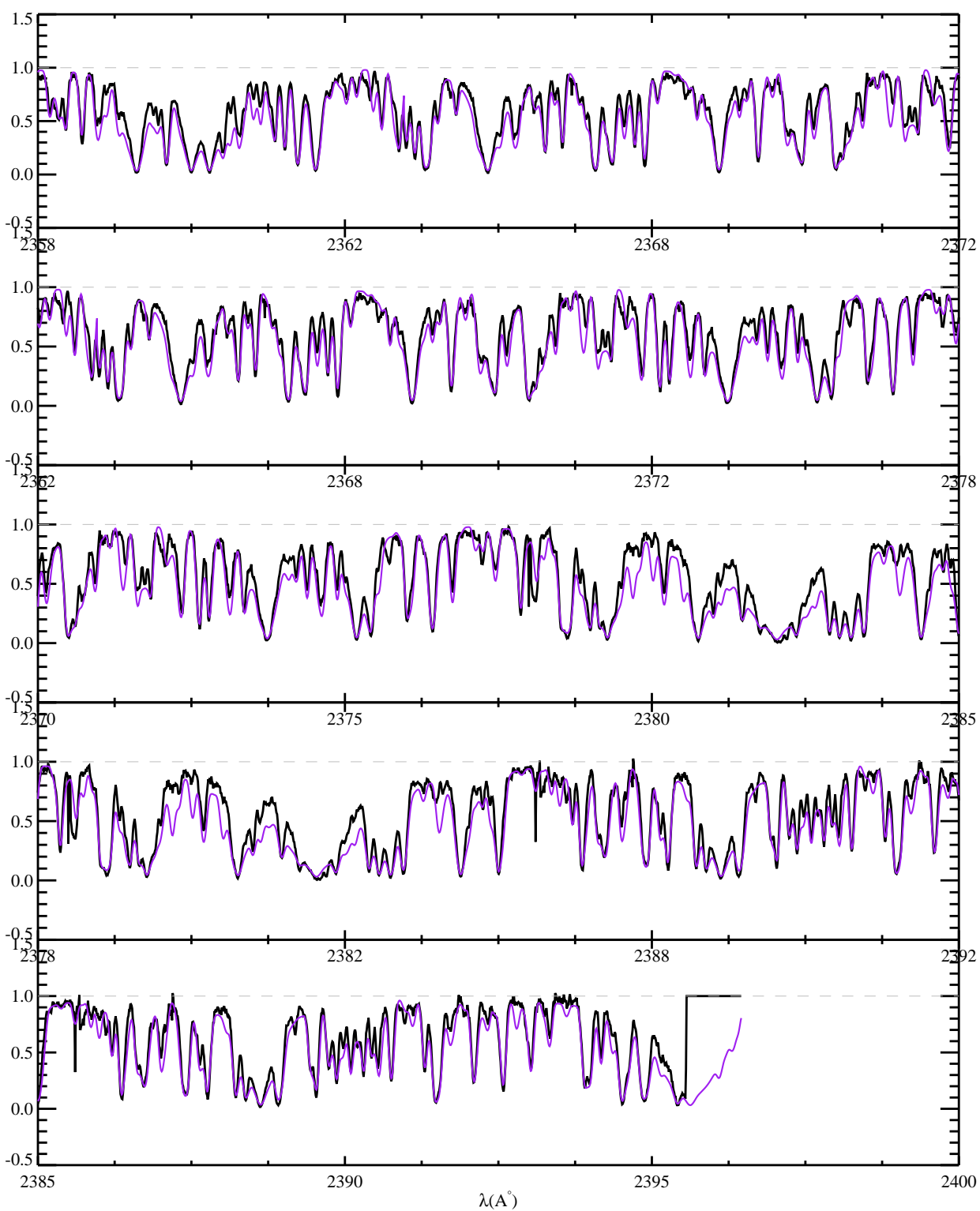


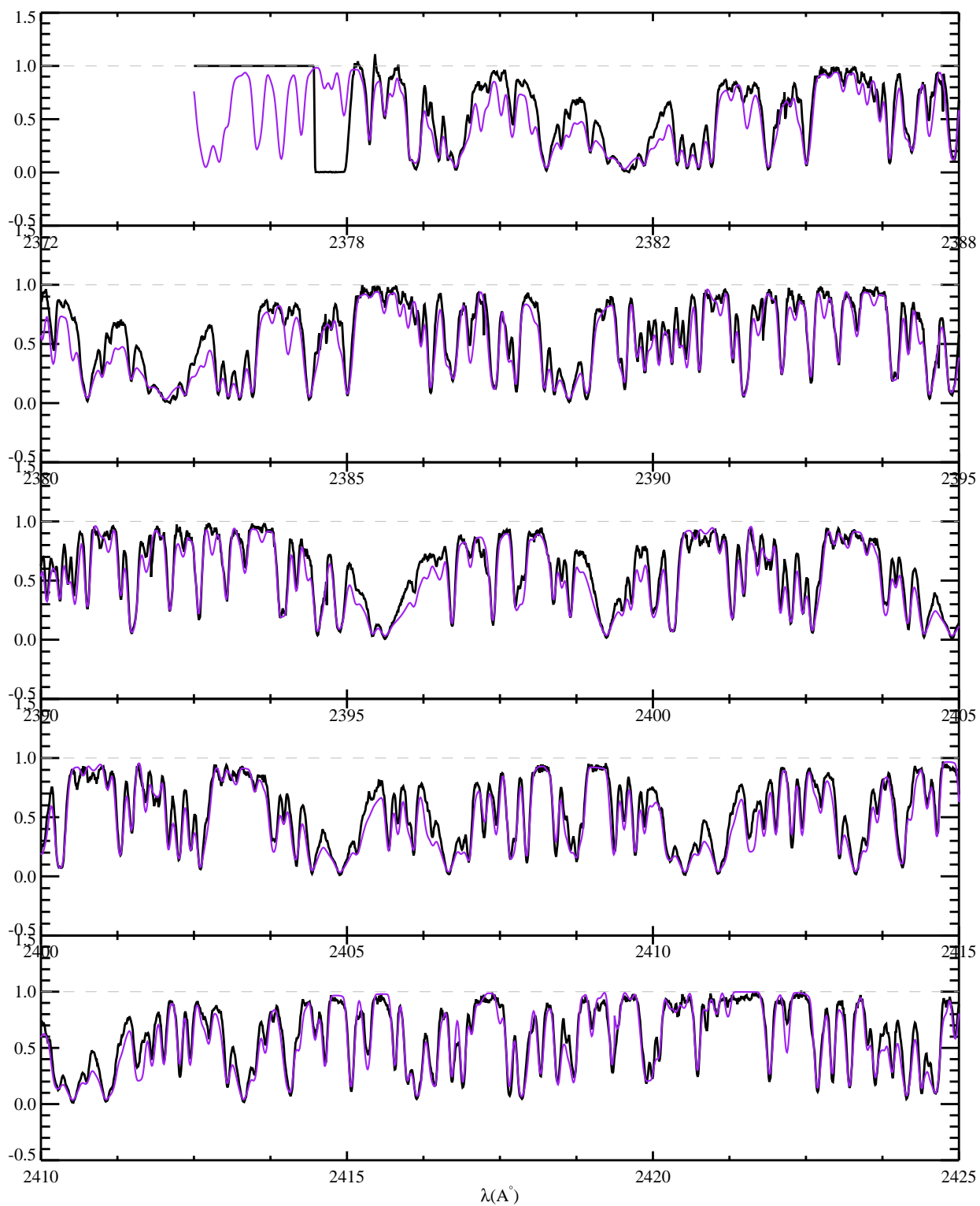


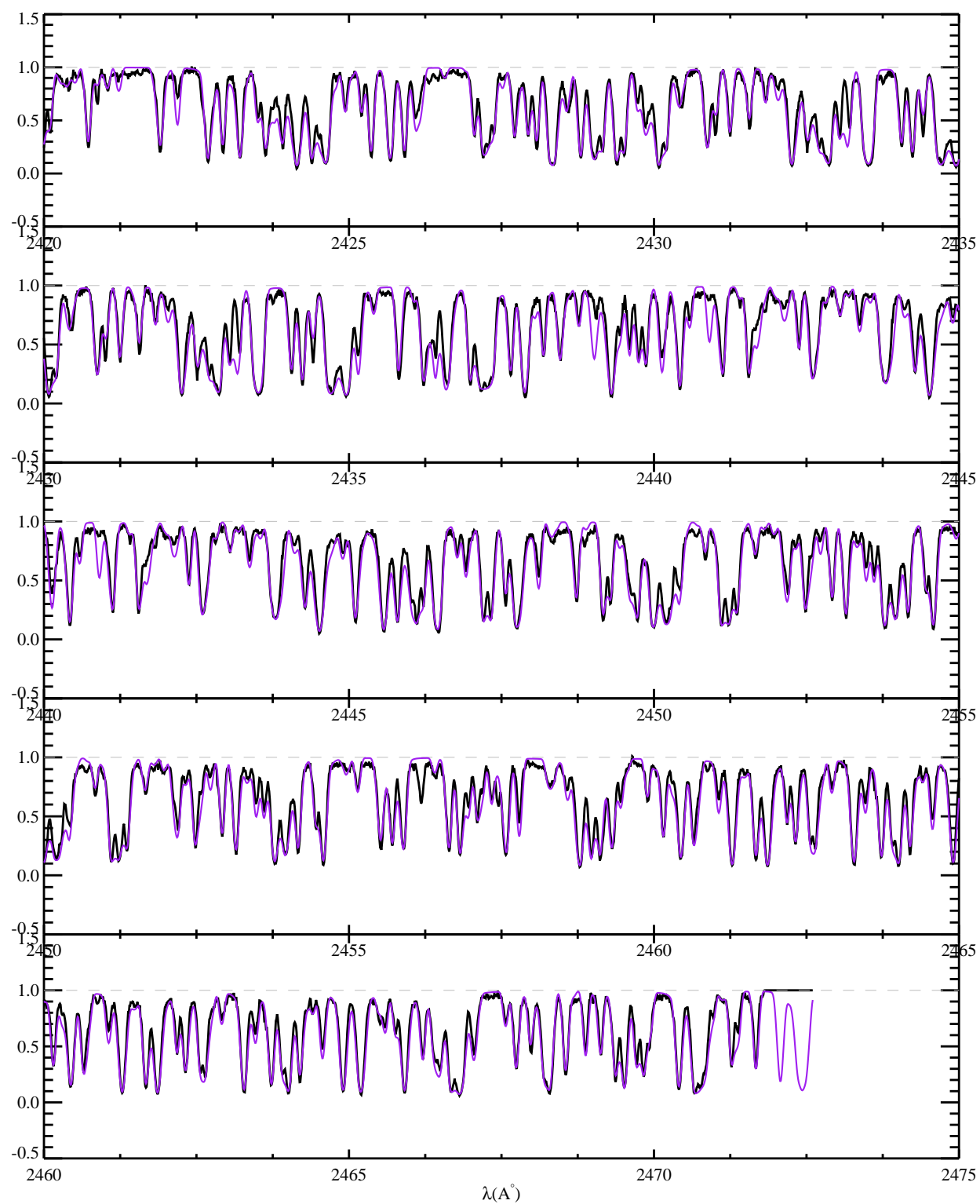


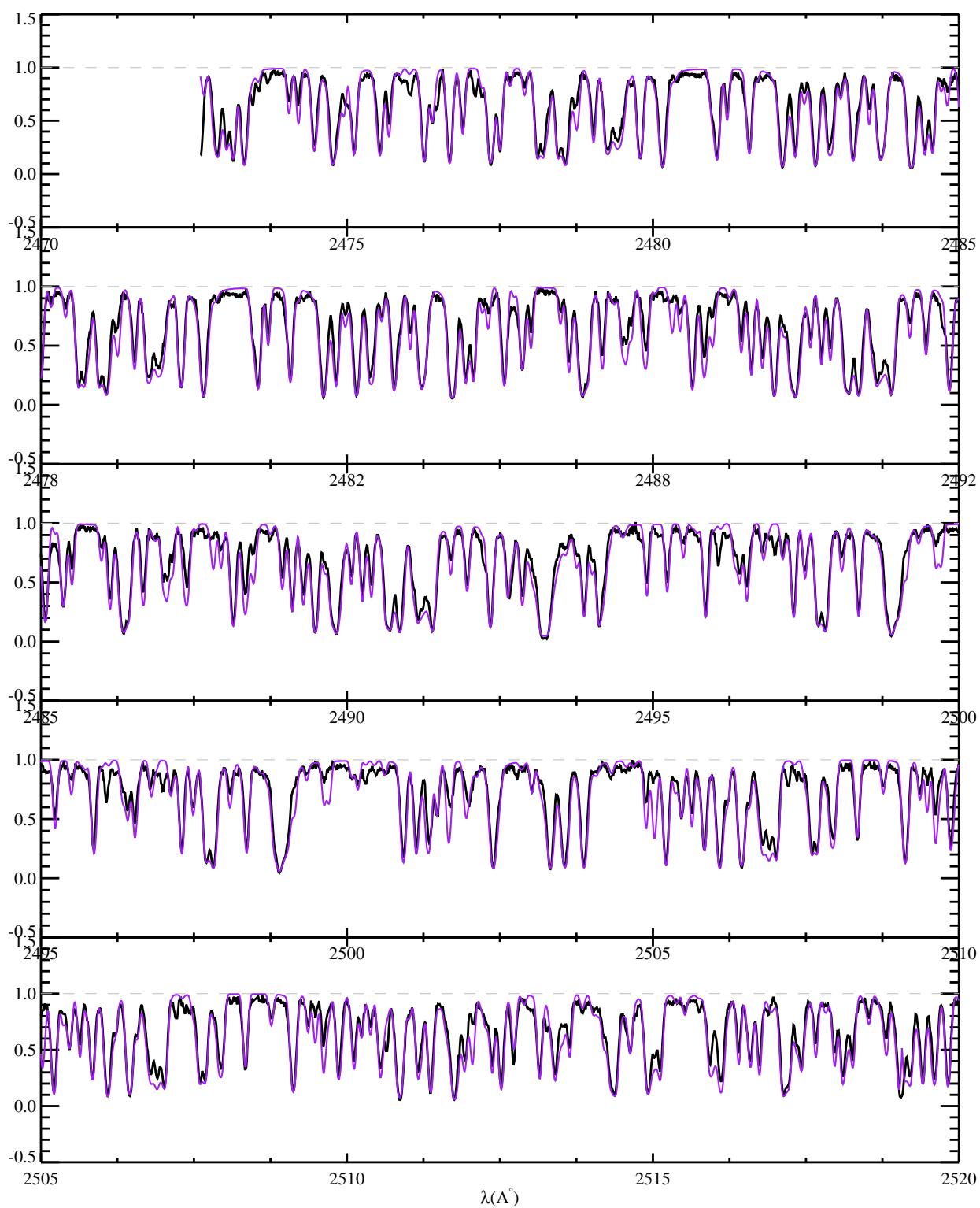


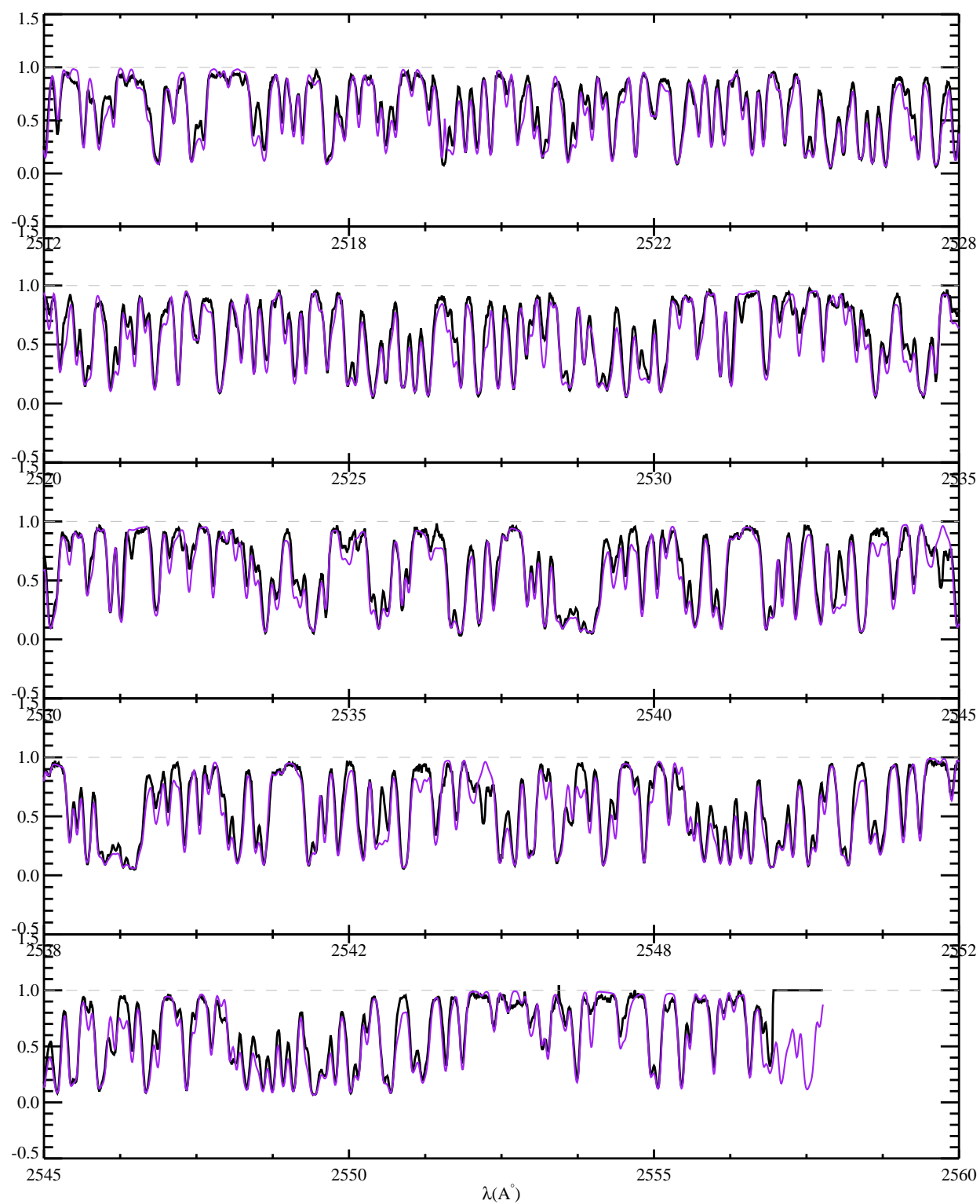


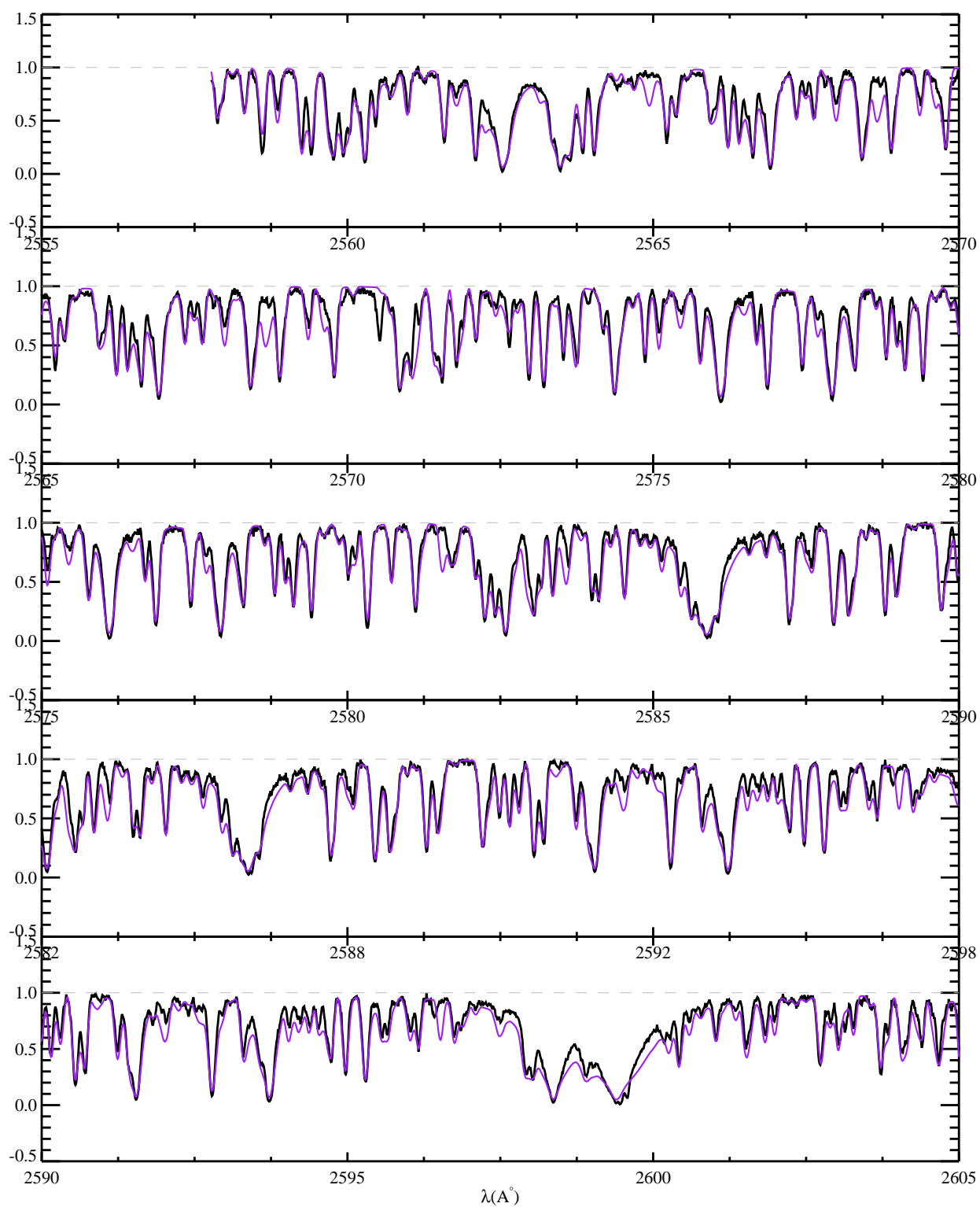


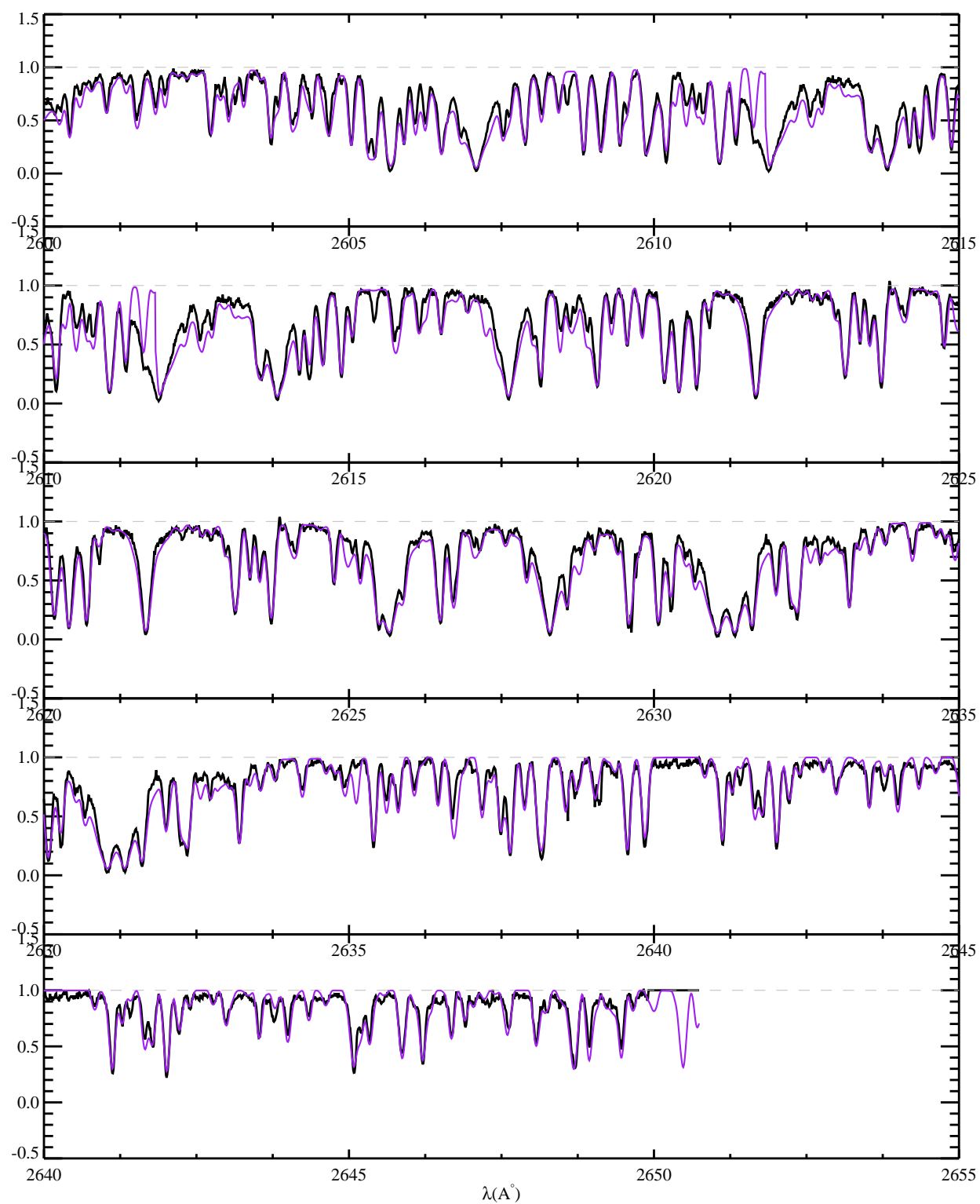


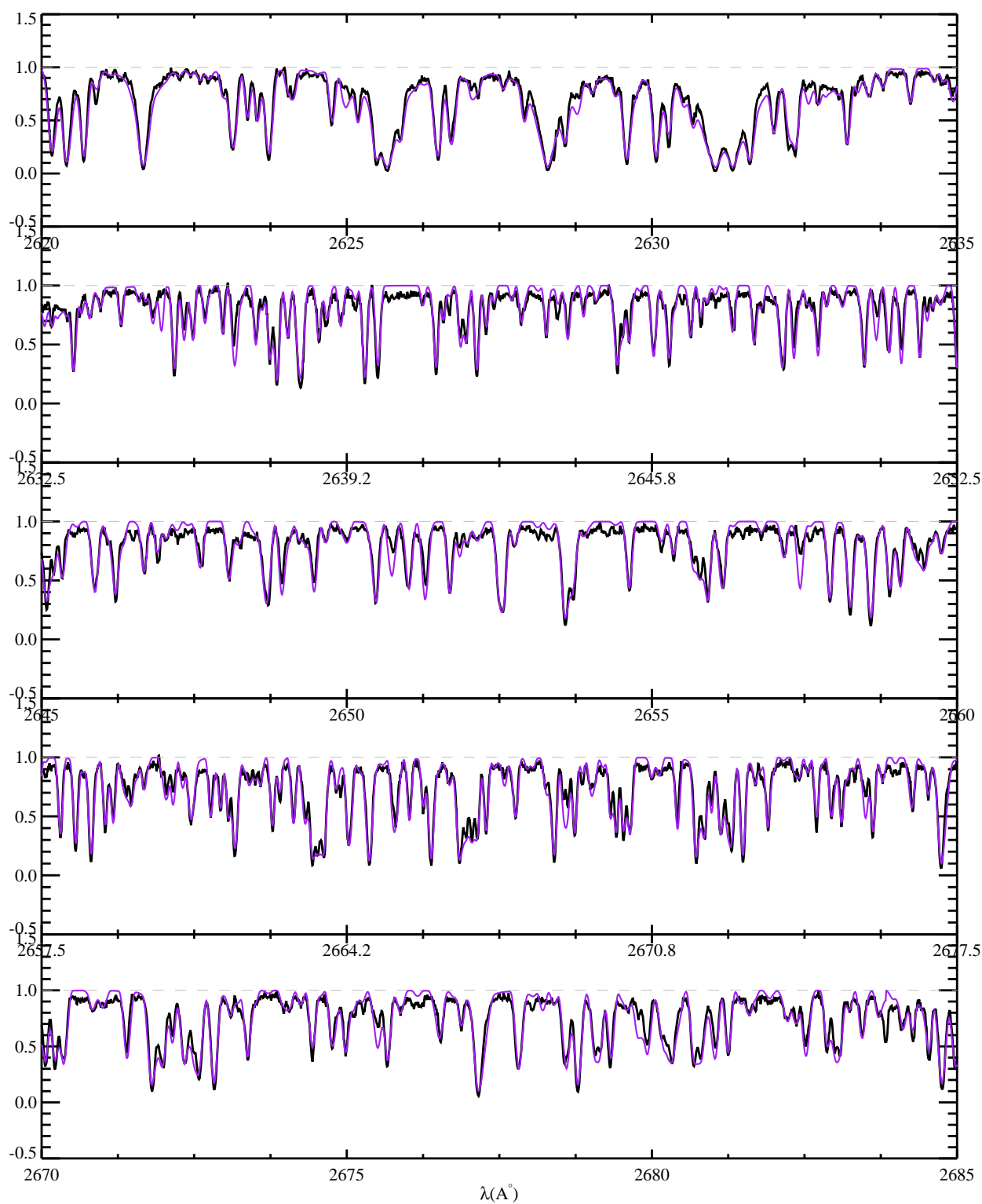


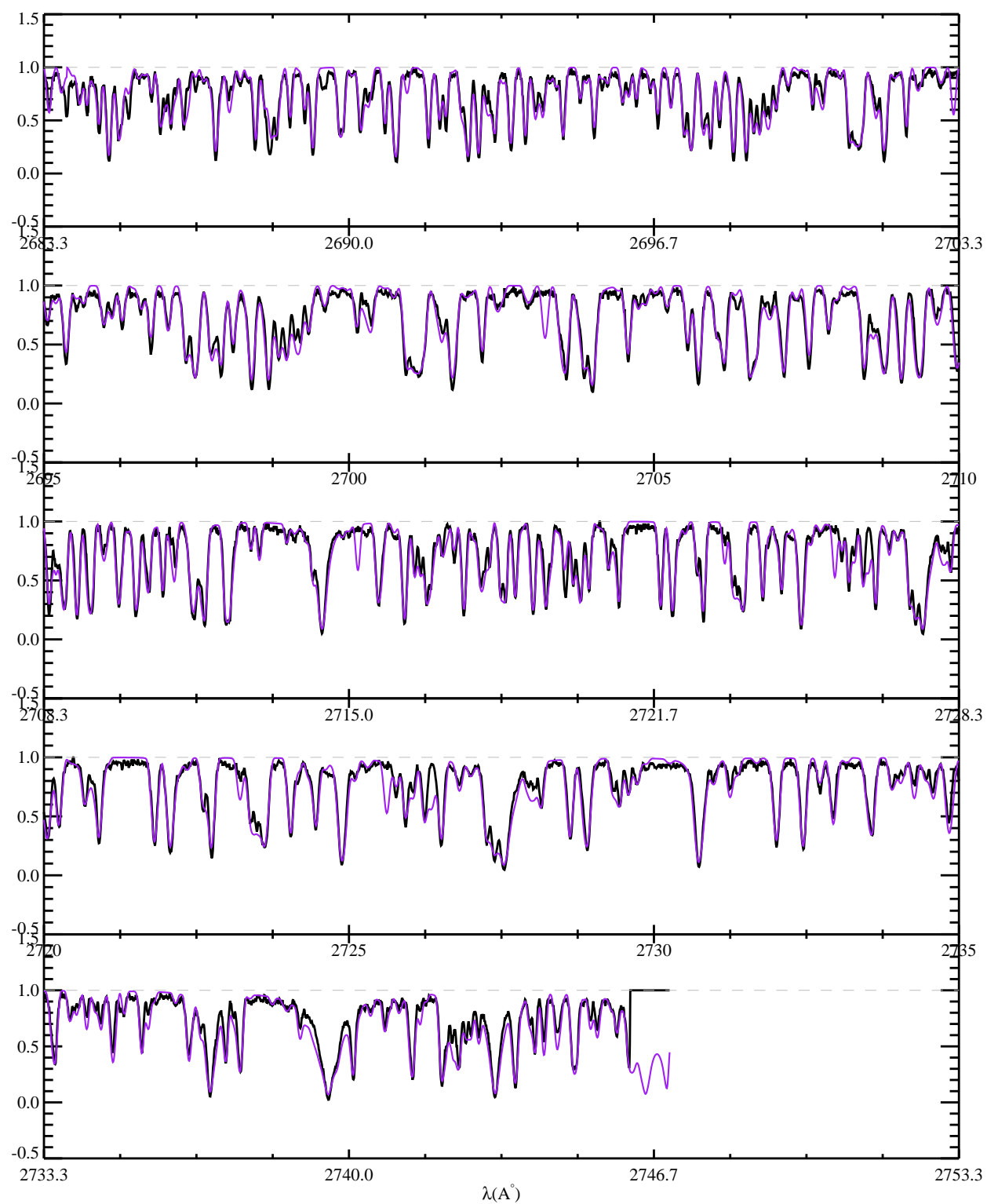


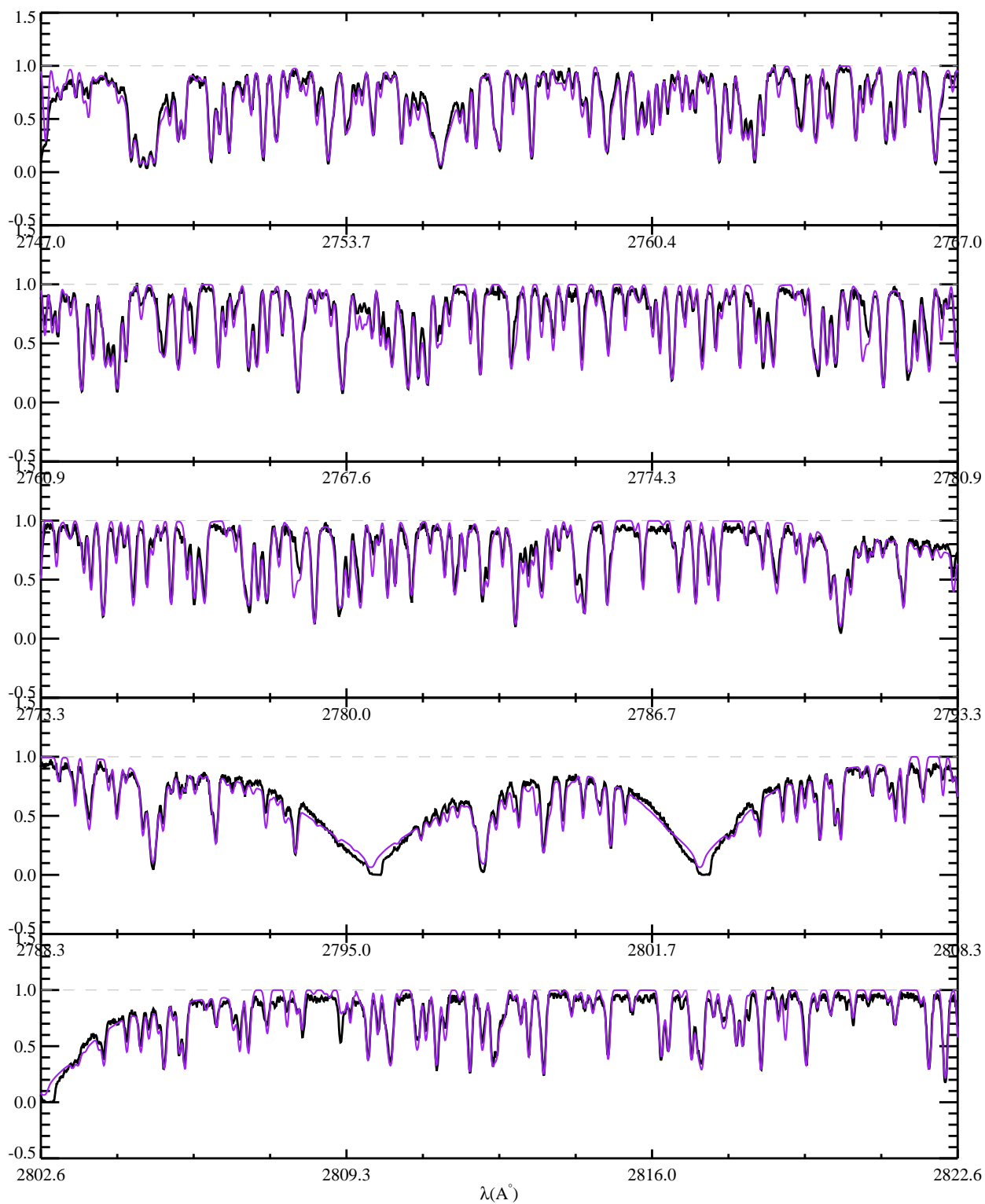


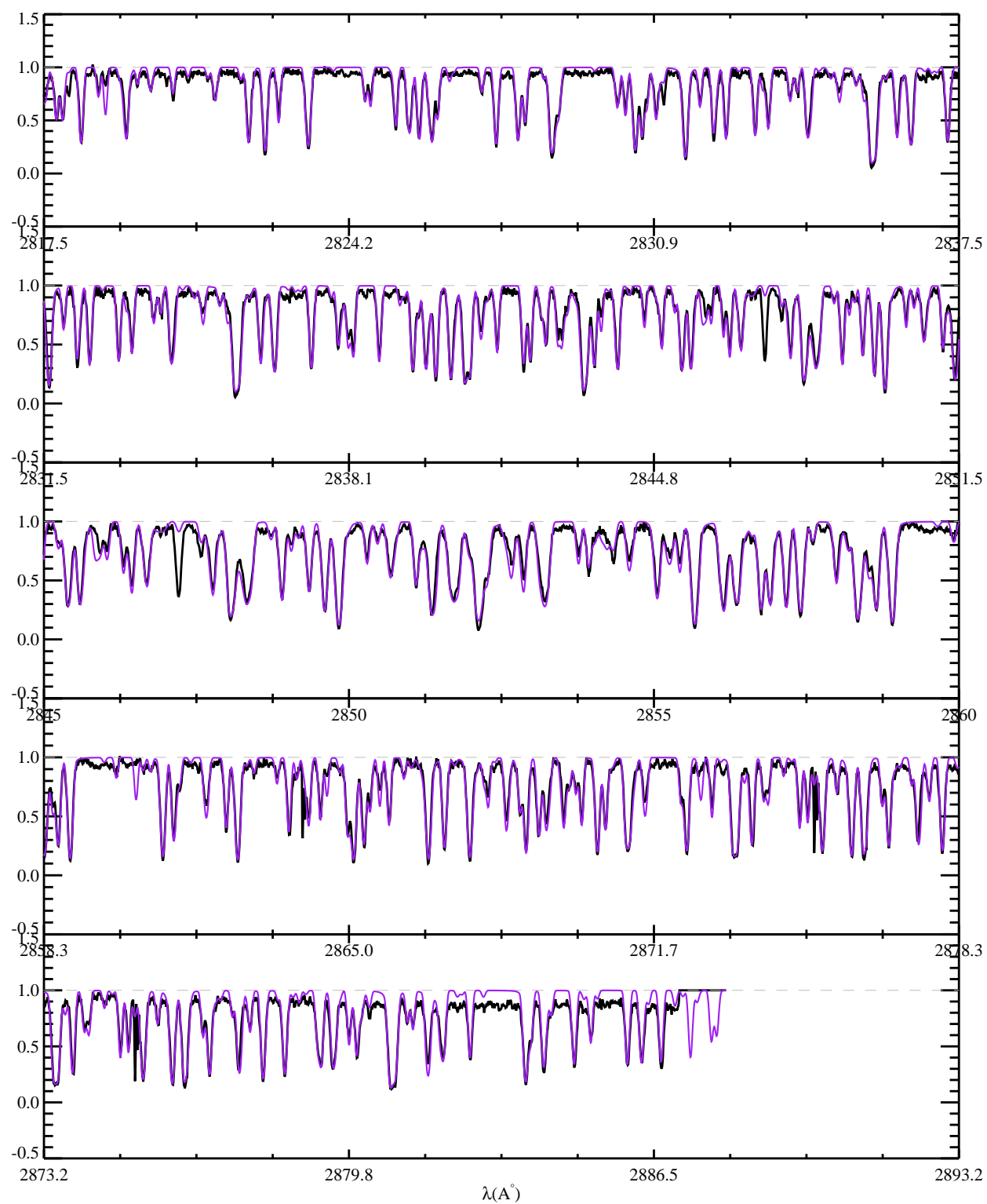












Appendix D

Background Removal

We compared different methods for removing the background emission. A standard background subtraction method for IRS staring observations is to perform a nod-by-nod subtraction of the images. This method works well if the background emission does not change much over the spatial scales corresponding to the distance between the nod positions. This method often yields good results. However, clear residuals are sometimes present (especially in c32 and c35) because of the significant spatial variations of the background emission. Other problematic cases in which nod-by-nod subtraction proves ineffective are those observations where a contaminating source happens to be located near one of the nod positions.

The optimal extraction routine [73] in the SMART data reduction package offers an appealing alternative. The program can trace multiple sources in the slit simultaneously, while representing the background emission and its variations in the spatial direction by a polynomial. For well-behaving backgrounds, this method furthermore yields the best possible signal-to-noise ratio on the extracted spectrum. However, the method assumes that the spatial variations at different wavelengths can be described by the same background equation. We find that clear background residuals are present in the final spectra of those targets with strong background emission whose spatial variations are very wavelength-dependent (such as shown in Fig. D.1). As the third and final alternative, we created a 2-dimensional model of the background emission by performing a least-absolute-deviation straight line fit to the background flux at each column in the raw images (i.e. roughly at each wavelength) independently, without taking into account the columns in which strong point sources are detected.

Additionally, we have visually looked for columns that contain weak sources and we masked them out manually. The use of least-absolute-deviation method ensures that little weight is given to such potential outliers in comparison with the strong and variable background features present.

The resulting background map generally represents the spectral as well as the spatial variations of the background emission quite well. We then subtracted this model from the raw images. This method generally works well, and no obvious background residuals are found in the extracted spectra. Moreover, the background maps can be used to study interstellar infrared emission toward the galactic bulge (see § 4.4).

In the end we extracted the background using either the SMART's polynomial subtraction or the two dimensional modelling (Detailed description is provided in Appendix G).

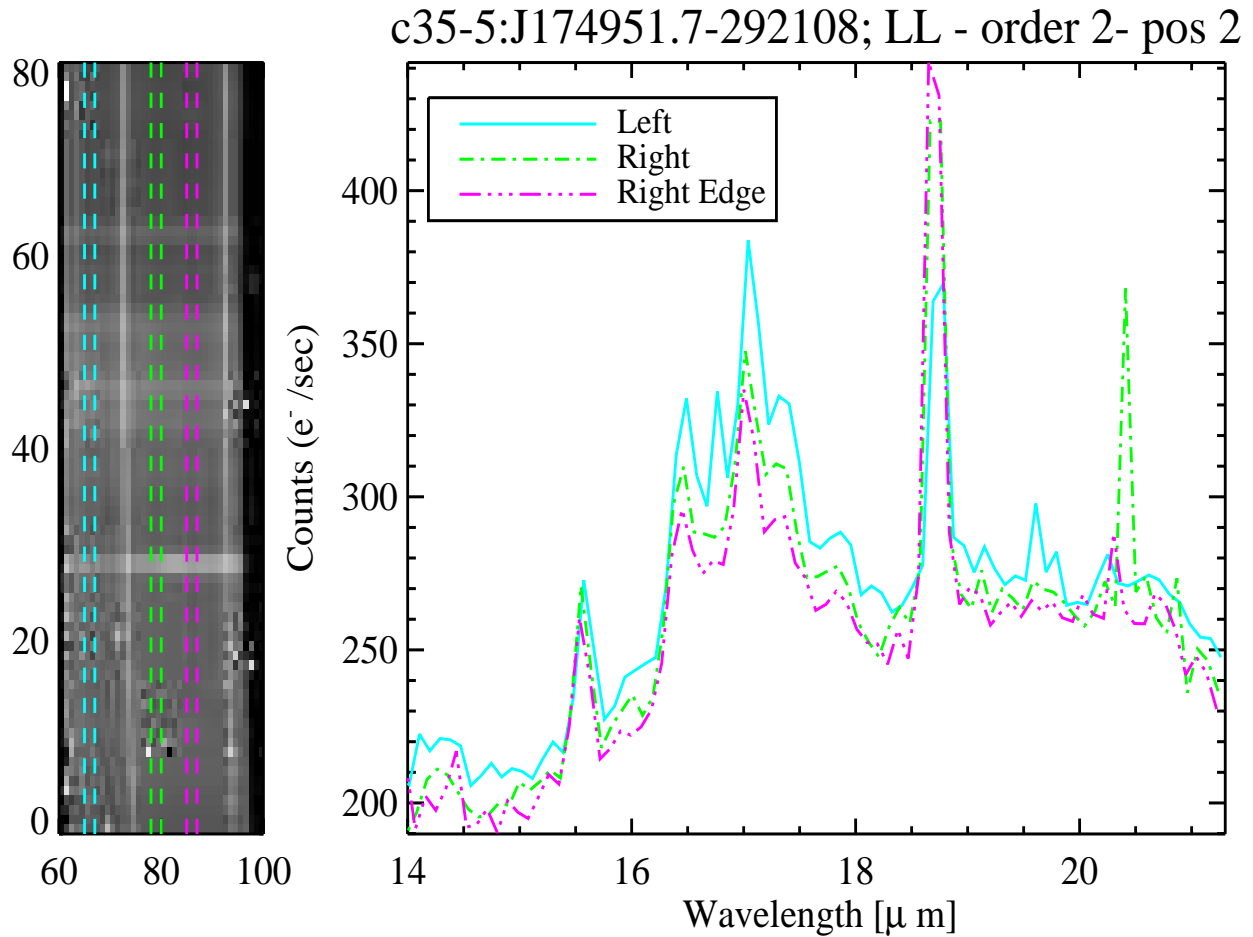


Figure D.1: This figure illustrates the strong background emission in our observations, and how this emission can vary significantly at small spatial scales (within the slit). (*Left*): The CCD image of the IRS observation corresponding to target c35-5 (LL, Order 2, Nod 2). Wavelength decreases from bottom to top. The dashed lines indicate three different spatial positions within the slit; the target trace can be seen between the green and the blue dashed lines. (*Right*): The background spectra corresponding to the spatial positions indicated on the image. All three show clear PAH emission between 16 and 18- μm as well as a strong [S III] line at 18.7- μm . Note how the intensity of the [S III] line increases from the left to the right, while the PAH emission weakens.

Appendix E

A_K Values

E.0.1 c32

Fig. E.1 shows the IRAC 8- μ m image for our targets in c32. The interstellar PAH emission is clearly patchy and variable even on these scales, and there is also some variation in the literature extinction values (see Table 4.4). Schultheis et al. [73] find that extinction values for our targets range from $A_K = 0.48$ to $A_K = 0.60$ with a median of $A_K = 0.51$; Gonzalez et al. [28] on the other hand find a range $A_K = 0.73 - 0.84$ with the median at $A_K = 0.78$. The variations in A_K furthermore appear to correspond qualitatively with the intensity of the PAH emission in the images: extinction is lowest (at $A_K = 0.48$ when using the Schultheis values) for c32-13 (left off centre) where little PAH emission is apparent; it is somewhat higher for most of the targets to the right (e.g. c32-10, $A_K = 0.51$), but clearly higher in regions with stronger 8- μ m emission (e.g. c32-16 on the left, $A_K = 0.55$; c32-2 on the right, $A_K = 0.60$). It is not a one-to-one correspondence though; for example, one would expect c32-14 and nearby c32-16 to have comparable extinction, but they are listed with $A_K = 0.51$ and $A_K = 0.55$ respectively. Similar trends are also apparent in the values from Gonzalez et al. [28], albeit with some subtle differences, and at much higher A_K values.

Unfortunately, we have only one naked star in this field (the object c32-8). Our best-fitting naked star model for this object corresponds to $A_K = 0.57$, and our more robust model-independent method yields $A_K = 0.52$ – very close to the $A_K = 0.51$ value found by Schultheis et al. [73] and much lower than the Gonzalez et al. [28] value ($A_K = 0.78$) for this object. It thus seems that the Schultheis et al. [73] values are better for our targets. Since Schultheis et al. [73] and Gonzalez et al. [28] find roughly the same range in A_K for our targets and roughly the same trends, our results indicate that for all targets in c32, we should use the Schultheis et al. [73] values. For consistency with our model-independent values though, we have added 0.01 to each of the Schultheis et al. [73] values ¹ (see Table 4.4).

E.0.2 c35

Five of our targets are located in the field c35, and also for this field, are clear variations in both the literature A_K values and the 8- μ m emission (see Fig. E.2). However, for this field there is

¹Note that a difference of 0.01 magnitudes in A_K results in spectral changes of less than 0.5% in the 10- μ m region; this is generally negligible.

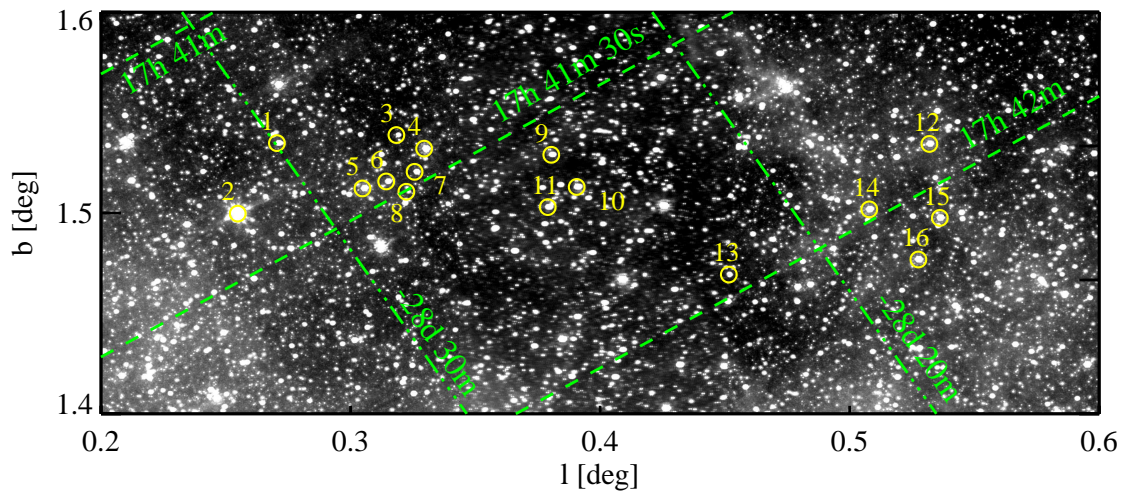


Figure E.1: The GLIMPSE II [15] 8- μ m IRAC image containing our targets in c32. The position of our targets is indicated, and the number corresponds to the ID in Table 4.1. Note that there is only one naked star in this field – object c32-8.

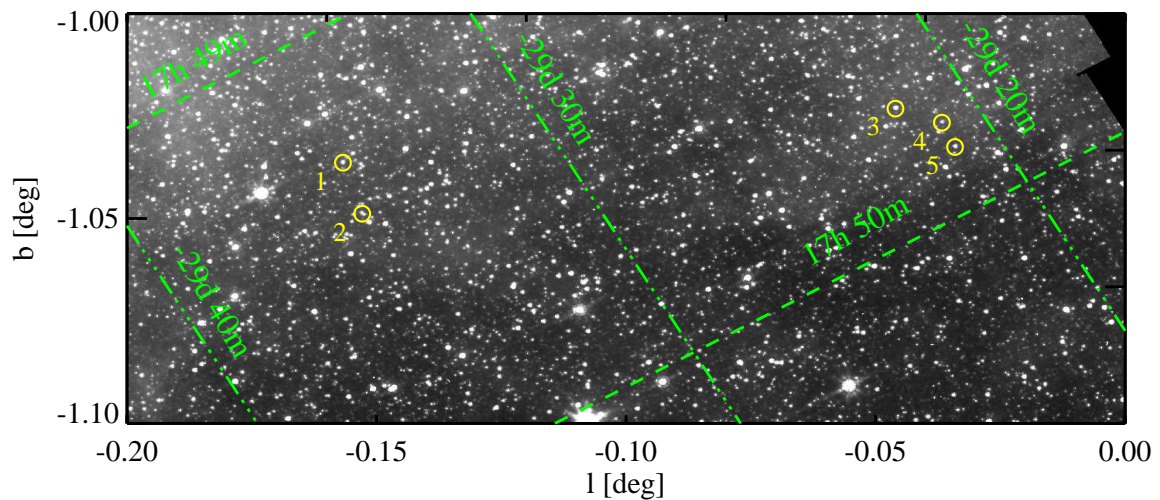


Figure E.2: The 8- μ m IRAC image [83] of our five targets in c35. The position of our targets is indicated, and the number corresponds to the ID in Table 4.1. Objects c35-2 and c35-4 are naked stars.

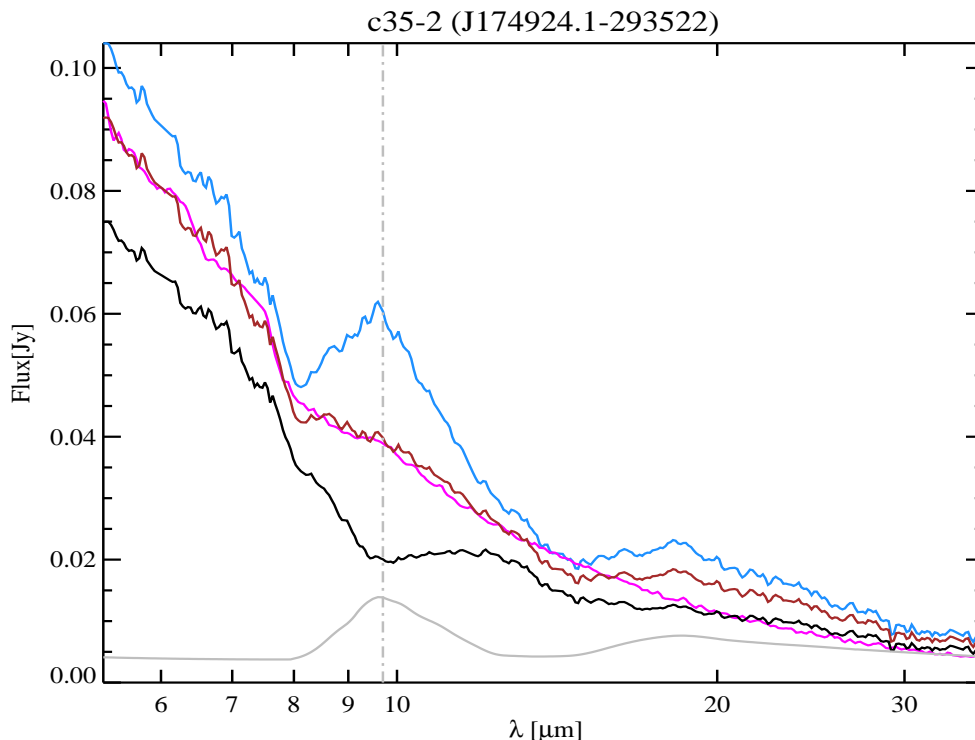


Figure E.3: The best-fitting model for target c35-2 using A_K values of 0.54 (model-independent, shown in brown) and 0.86 (Gonzalez et al. [28], shown in black). The green shows the raw spectrum without extinction correction and the Galactic centre extinction curve is also overplotted in grey. The best-fitting models are overplotted in blue (for $A_K=0.87$) and magenta (for $A_K=0.54$).

no clear correspondence between the two. Our targets are spatially clustered in two different locations (see Fig. E.2). The first group contains dust target c35-1 and naked star c35-2. For the latter, we determined that $A_K = 0.54$ using our model-independent method, in excellent agreement with Schultheis et al. [73] but much lower than the $A_K = 0.87$ value from Gonzalez et al. [28].

It is clear from the extinction-corrected spectra and also from our naked star models that the $A_K = 0.87$ value is far too high and results in a large over-correction, while the $A_K = 0.54$ value does not and furthermore results in good model fits as well (see Fig. E.3) and we thus adopt this value for c35-2. Rather than using the same value for nearby target c35-1, we note that both Schultheis et al. [73] and Gonzalez et al. [28] agree that the A_K value for c35-1 is roughly 0.06 magnitudes larger than those for c35-2; we thus adopt the $A_K = 0.60$ value for c35-1 as was done by [73] as well.

The second group contains three objects that are close to each other, in what appears to be the same patch of 8- μm emission. For naked star c35-4, our model-independent method this time yields $A_K = 0.92$, somewhat lower than the $A_K = 1.02$ value found in Gonzalez et al. [28] and significantly higher than the Schultheis et al. [73] value of $A_K = 0.55$. Indeed, using $A_K = 0.55$ appears to under-correct the spectrum in the interstellar 9.7- μm silicate feature (see Fig. E.4), and we thus adopt $A_K = 0.92$ as the proper value for c35-4. It is not clear though what to adopt

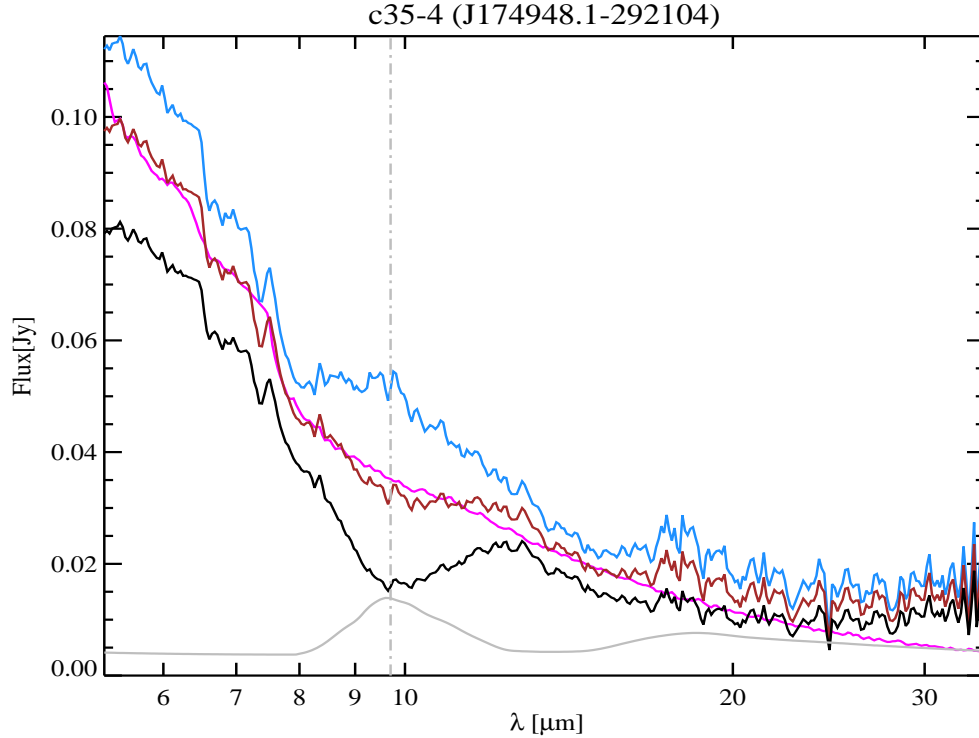


Figure E.4: This figure shows the raw spectrum of target c35-4 (in black) corrected for $A_K=0.55$ from Schultheis et al. [73] (in brown) and its corresponding best fit model (in magenta) and corrected spectrum using $A_K=0.92$ from model independent method (in blue). The Galactic centre extinction curve is also overplotted in grey.

for c35-3 and c35-5. While both Schultheis et al. [73] and Gonzalez et al. [28] find difference of about $\Delta A_K \approx 0.06$ magnitudes between the three objects, they disagree about which objects are most and least subject to extinction. Since this target is close to c35-3 and c35-5, and from the IRAC image, there is no clear change in the 8- μm emission between the three targets, we have applied the same A_K value to them as well.

E.0.3 Ogle

Fig. E.5 shows the IRAC 8- μm image covering our targets in the Ogle field. There is considerably less extinction towards our targets in the Ogle field than toward c32 or c35; and although the 8- μm image shows some variations in the 8- μm emission, extinction in this region is fairly homogeneous: for all our targets in the Ogle field, Sumi [80] obtain a value of $A_K = 0.302$ while [28] find a range between $A_K = 0.25 - 0.27$.

Ogle-4 and Ogle-6 are the two naked stars in this field. Unlike the naked stars in c32 and c35, the spectra for Ogle-4 and Ogle-6 do not reveal any obvious absorption feature near 9.7- μm at all, thus these targets offer a clear example of the ambiguity in determining the interstellar extinction. We can in fact reproduce these spectra quite well ($\chi^2_\nu = 0.69$ and 0.55 respectively) with our slab models without even applying an extinction correction (see Fig. E.6).

Using Gonzalez et al. [28] maps, we find A_K values of 0.264 ± 0.105 and 0.268 ± 0.104 and using

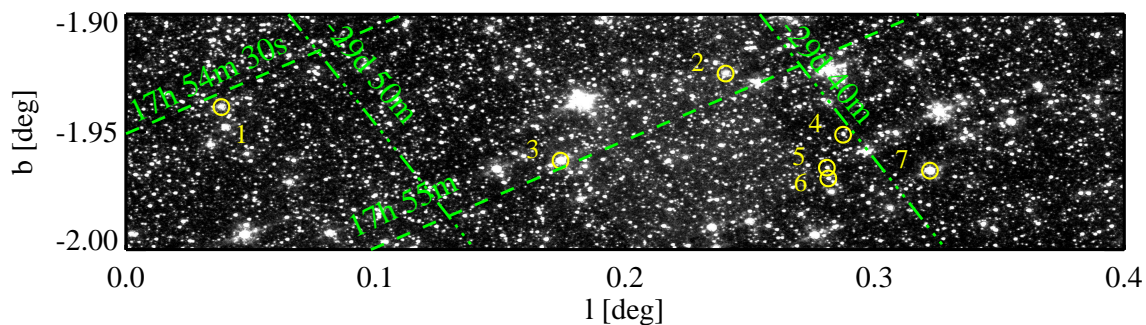


Figure E.5: The GLIMPSE II 8- μ m IRAC image [15] of our seven targets in the Ogle field. The position of our targets is indicated, with the number corresponding to the ID in table 4.1. The objects Ogle-4 and Ogle-6 are naked stars.

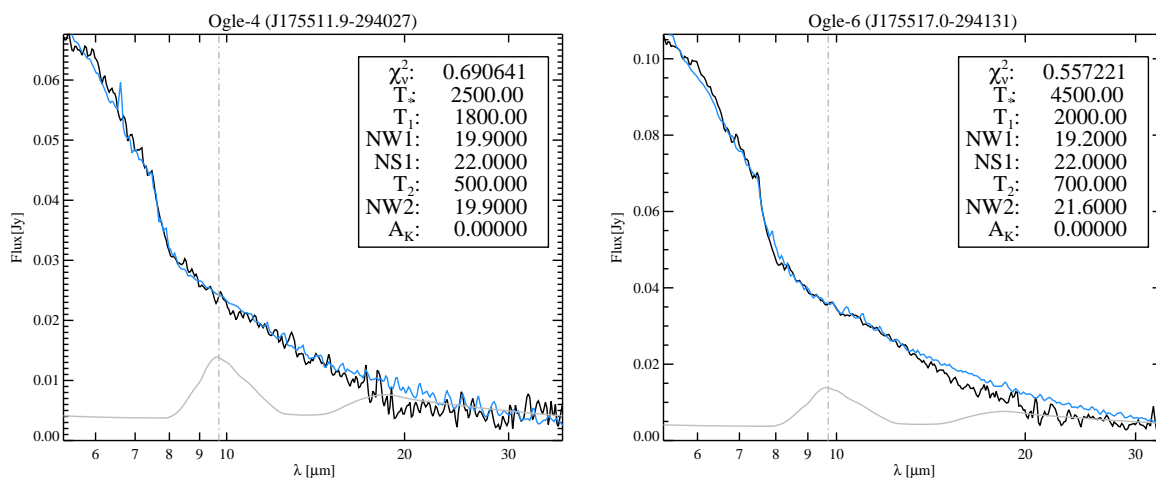


Figure E.6: This figure shows the best-fitting models for Ogle-4(left) and Ogle-6(right) when no extinction correction is applied at all (i.e. $A_K = 0$).

model-independent method, we find 0.246 and 0.254 for Ogle-4 and Ogle-6, respectively. The Gonzalez et al. [28] values show a marginal but consistent increasing trend in A_K (~ 0.05) between those targets in the field that have longitude difference of roughly $\sim 1^\circ$. This change will not affect the final spectra significantly but for consistency we have applied this trend to the targets of this field.

E.0.4 NGC 6522

Extinction in NGC 6522 is lower than the Ogle field, but with considerable variations – literature values range from $A_K = 0.06$ to $A_K = 0.18$ with a mean value of $A_K = 0.10$ for our targets in this field. Also the 8- μ m emission shows significant variations across the field (see Fig. E.7). From Gonzalez et al. [28] maps, we find a range from $A_K = 0.14$ to $A_K = 0.17$ with a mean

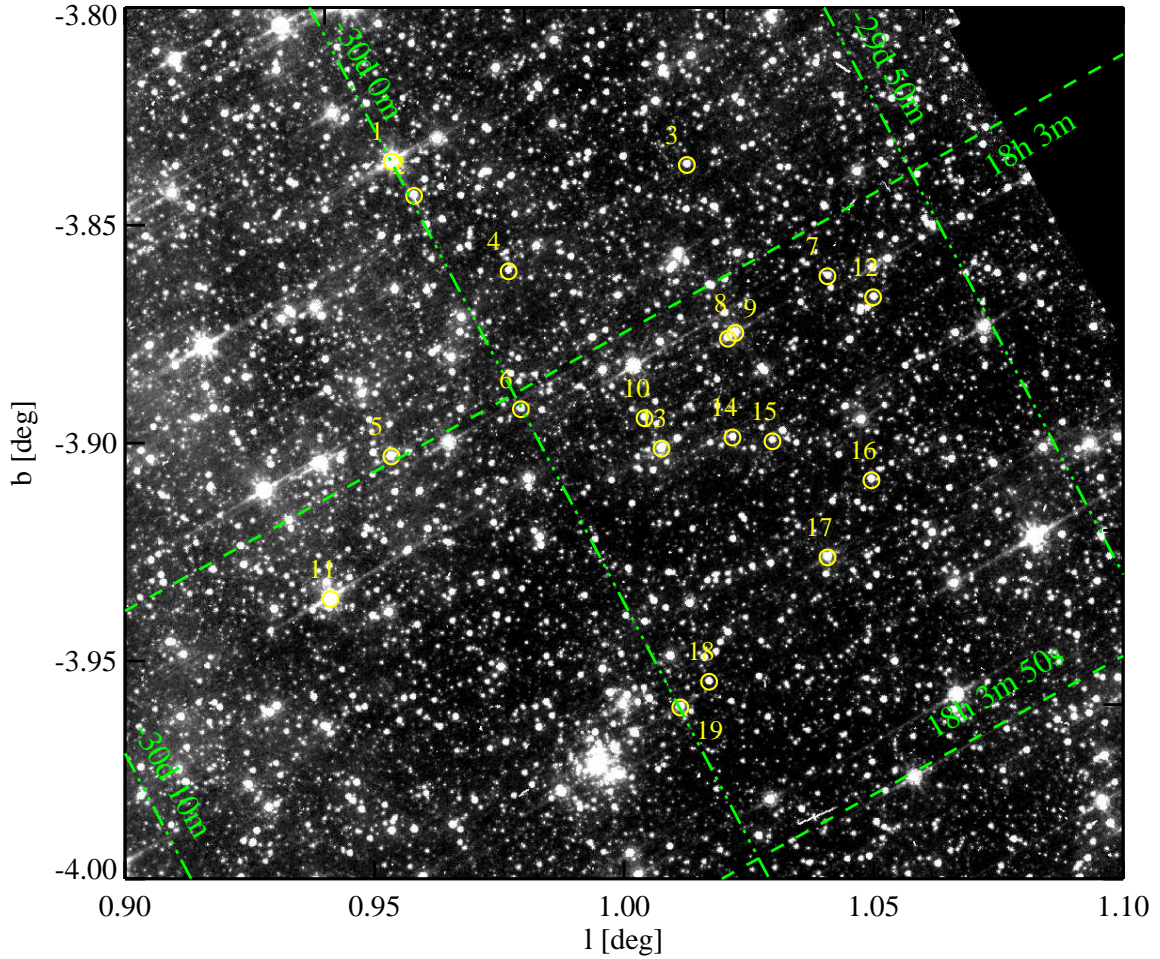


Figure E.7: The 8- μ m IRAC image [83] of our targets in NGC 6522. The position of our targets is indicated, with the number corresponding to the ID in table 4.1.

value of $A_K = 0.15$.

Targets NGC 6522-15 to NGC 6522-18 are all naked stars in this field. We have chosen the model independent values as final values for all naked stars. It is not immediately clear whether or not there is an overall trend between the A_K values of the targets in this field. In what follows we attempt to find local trends.

It appears from Gonzalez et al. [28] maps that targets NGC 6522-13, NGC 6522-17, NGC 6522-10, NGC 6522-14 and NGC 6522-16 have the exact same value as NGC 6522-15. It is also clear from IRAC image (Fig. E.7) that in the region in which this group of targets are located, the 8- μ m emission is not significantly variable and patchy. Our model independent method yields the value of 0.10 for NGC 6522-15 which indicates that Schultheis et al. [73] value of 0.063 is an underestimation for this region. We thus apply the value of 0.10 to this group of targets.

Targets NGC 6522-8 and NGC 6522-9 have the exact same A_K value which according to both literatures is slightly higher (~ 0.03) than that of NGC 6522-15. Thus for this two we have

added 0.03 to $A_K^{NGC\ 6522-15} = 0.10$.

Targets NGC 6522-7 and NGC 6522-12 are fairly close to one another and the literature values suggest equal values for both. NGC 6522-7 is a naked star for which we found $A_K=0.144$ from model independent method. This indicates that similar to NGC 6522-15, the value of 0.063 listed by Schultheis et al. [73] is an underestimation for this region. We used $A_K=0.144$ for these two targets.

The model independent value for naked star NGC 6522-6 yields 0.10 which points to an over estimation by 0.07 magnitudes in both literature values. Target NGC 6522-5 is located in the same region as NGC 6522-6 with the exact same A_K value according to Gonzalez et al. [28]. However, Schultheis et al. [73] estimate $A_K=0.106$ for NGC 6522-5 which is much closer to the value we find for this neighborhood through our model-independent method. Therefore, we concluded that $A_K=0.171$ which was estimated from Gonzalez et al. [28] maps is an over-estimation for both NGC 6522-5 and NGC 6522-6, instead we used $A_K = 0.10$ for both.

In case of target NGC 6522-2, the closest naked star is NGC 6522-4 which has the exact same A_K from Gonzalez et al. [28] maps but different values from Schultheis et al. [73]. Our model independent value for NGC 6522-4 is 0.275 and it shows a clear under-estimation in both literature values by roughly 0.1mag. Our modeled value for NGC 6522-4 is 0.27 which also points to the under-estimation in this region by both literatures. Since the IRAC image does not show a clear and significant difference in 8- μ m emission between NGC 6522-4 and NGC 6522-2 and also because Gonzalez et al. [28] maps estimate exact same values for both of them, we have used $A_K=0.275$ for both of them.

Targets NGC 6522-1 and NGC 6522-2 are located fairly nearby, therefore we can assume this underestimation holds true for NGC 6522-1 as well. However, both literature values for NGC 6522-1 estimate a value which is higher than NGC 6522-2 by roughly 0.01mag. Therefore, for NGC 6522-1 we added 0.01mag to $A_K^{NGC\ 6522-2}$ and used 0.285.

Target NGC 6522-3 has two literature values of $A_K = 0.152 \pm 0.098$ and $A_K = 0.155$ which are in reasonable agreement with each other. We have used an average value of $A_K = 0.153$ for this target. This target stands fairly alone in the field thus it is not possible to use any other target to re-examine the A_K value for NGC 6522-3 accordingly.

Gonzalez et al. [28] maps estimate the highest A_K value (0.177) for target NGC 6522-11 which is still not too different from that of NGC 6522-5 which is the closest target to it. We discussed that A_K in the region of NGC 6522-5 was over-estimated by Gonzalez et al. [28] and that Schultheis et al. [73] values are better representation of the correct extinction in these regions. It is not likely for extinction to change from 0.10 around NGC 6522-5 to 0.177 around NGC 6522-11 since any such dramatic change would have appeared clearly on the 8- μ m IRAC image shown in Fig. E.7. Therefore, we used $A_K=0.1$ for NGC 6522-11 as well. The final extinction values are listed in Table 4.4.

Targets NGC 6522-18 and NGC 6522-19 have similar A_K values according to both literatures. In Fig. E.7, they are located in a fairly isolated region in the field. For these two target we took the average literature value of $A_K=0.12$ which is the same for both.

Appendix F

In this appendix, we present different extraction methods used to obtain the dust spectrum (see §4.8.1). In Figures F.1 through F.6, the normalized spectrum of the dusty target is shown in black, the 5-8 μm range model for the dusty spectrum is shown in green, the scaled naked star that has the most similar features in 5-8 μm is shown in purple, and the template model used by Sloan & Price [77] is over-plotted in orange. In addition, the inset plots show the dust spectra that are obtained using each of these methods. The color of each resulting dust spectrum corresponds to the particular method of extraction.

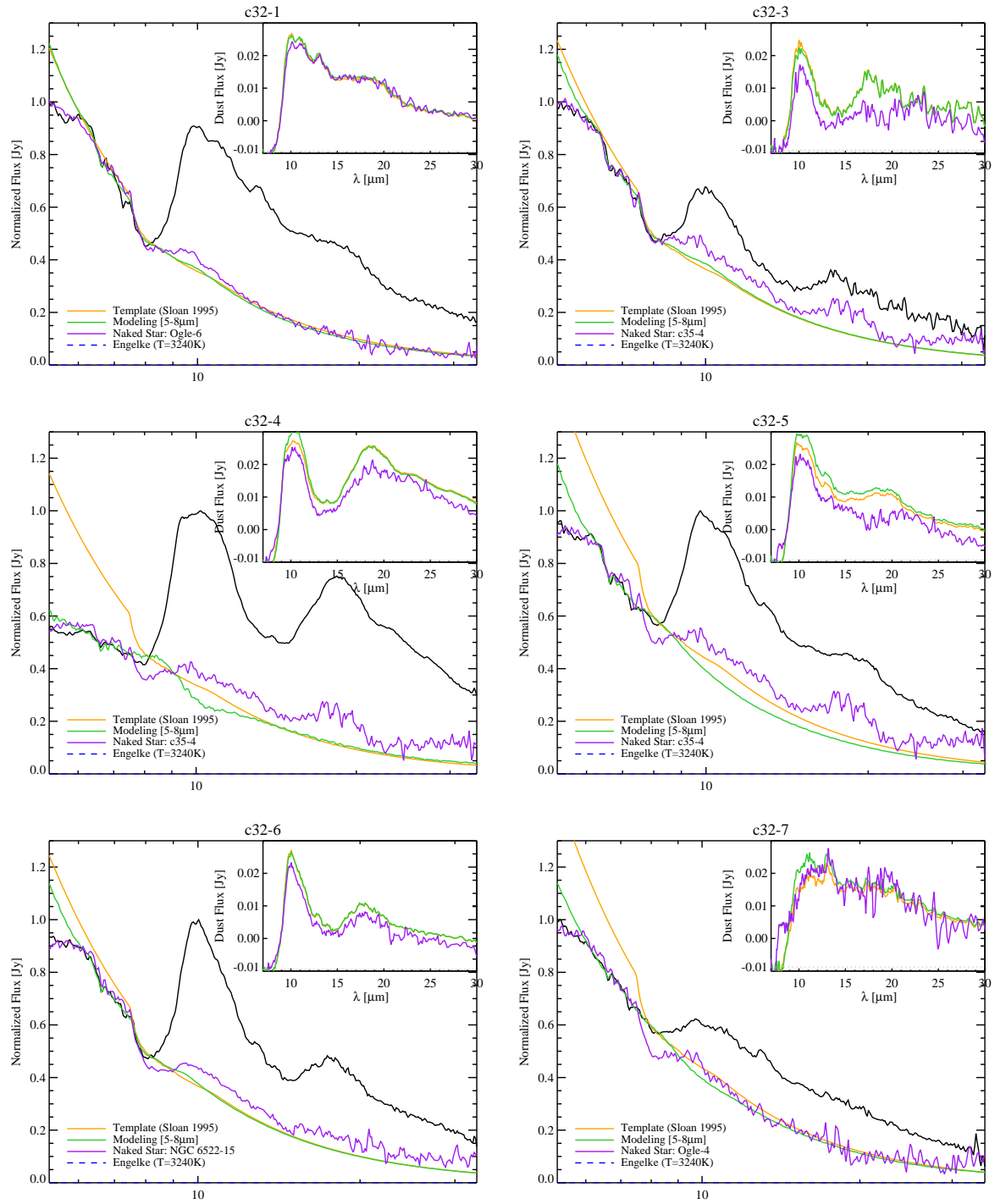


Figure F.1: Different dust extraction methods for naked stars c32-1, c32-3, c32-4, c32-5, c32-6 and c32-7. See text for more details.

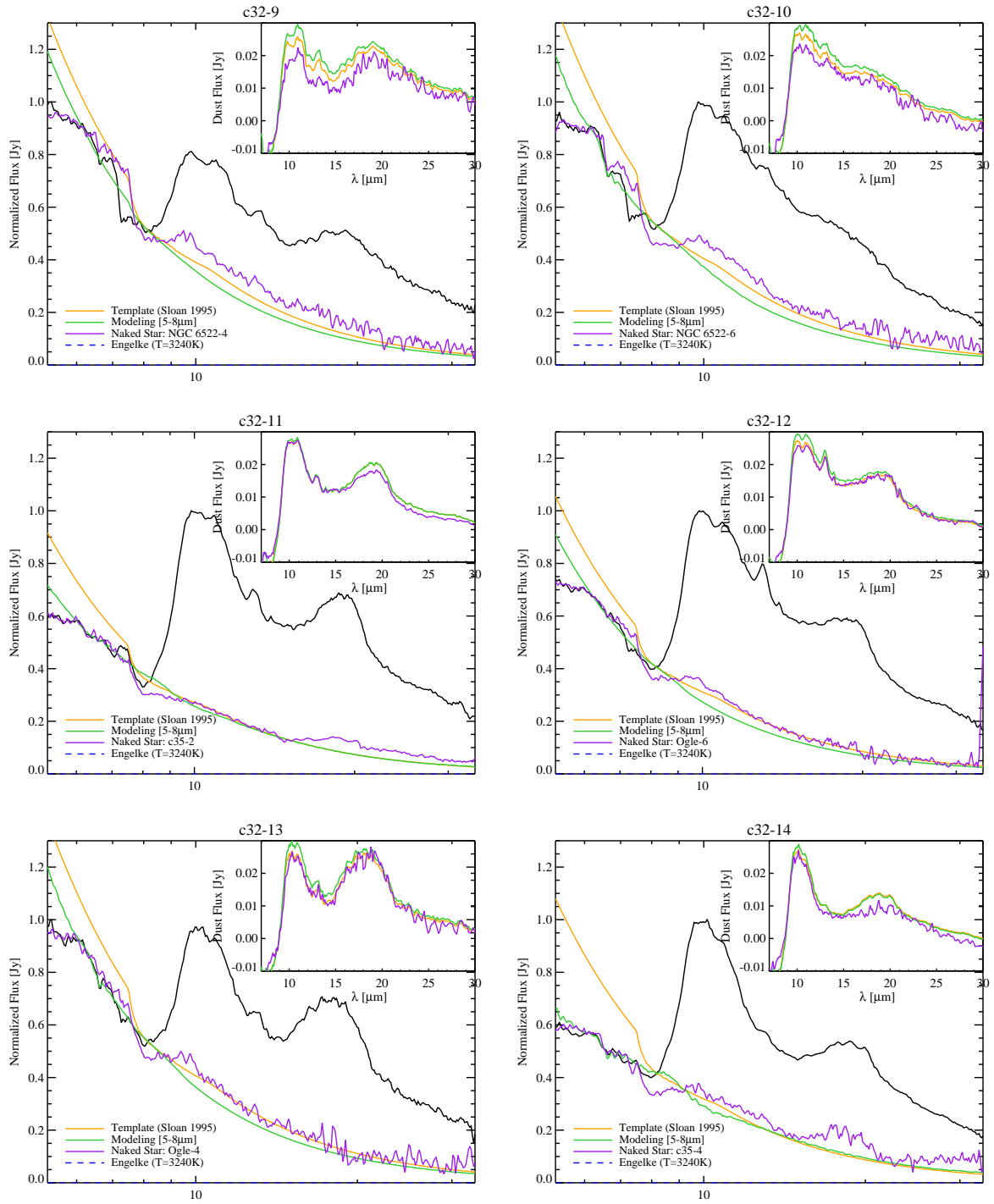


Figure F.2: Different dust extraction methods for naked stars c32-9, c32-10, c32-11, c32-12, c32-13 and c32-14. See text for more details.

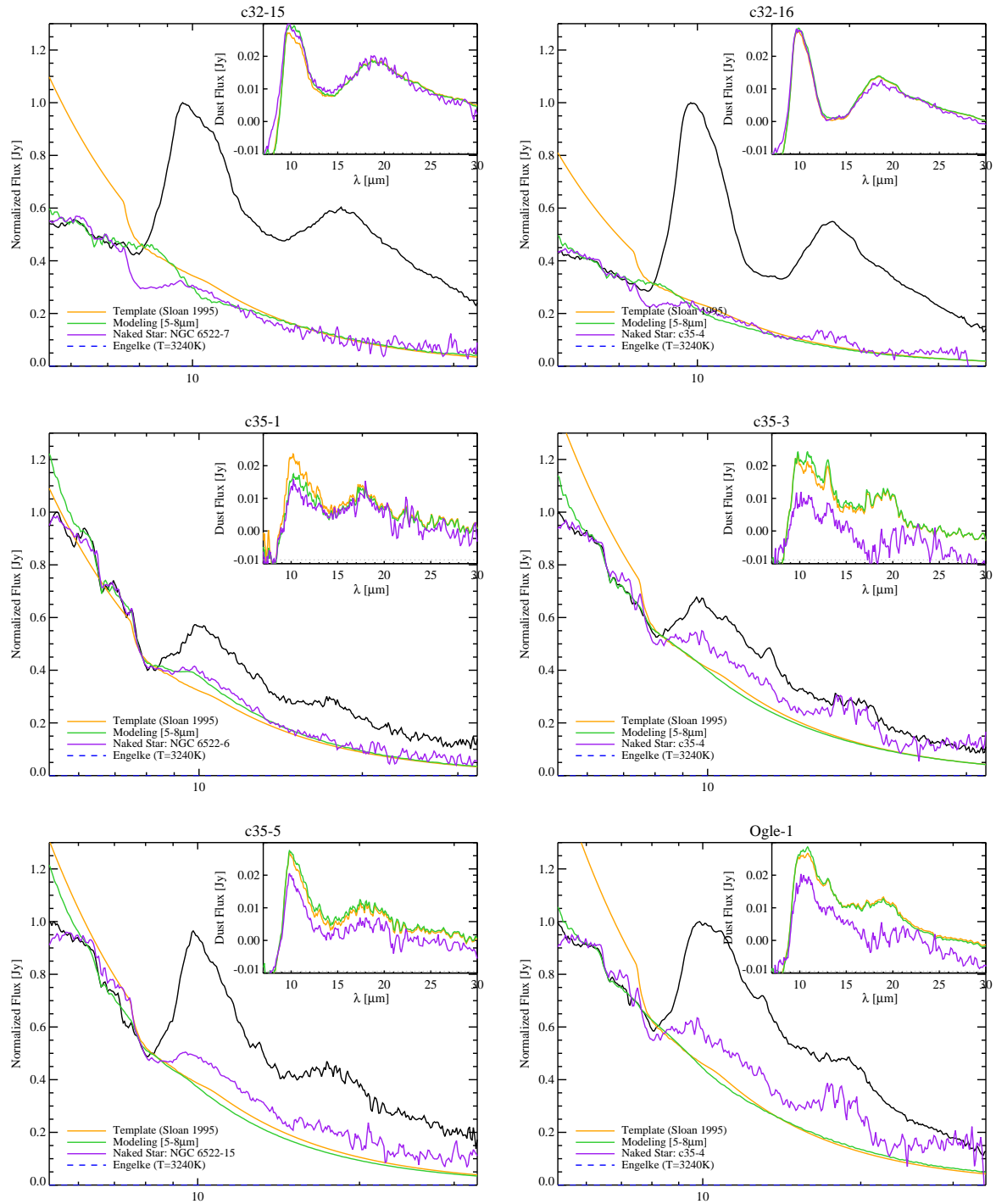


Figure F.3: Different dust extraction methods for naked stars c32-15, c32-16, c35-1, c35-3, c35-5 and Ogle-1. See text for more details.

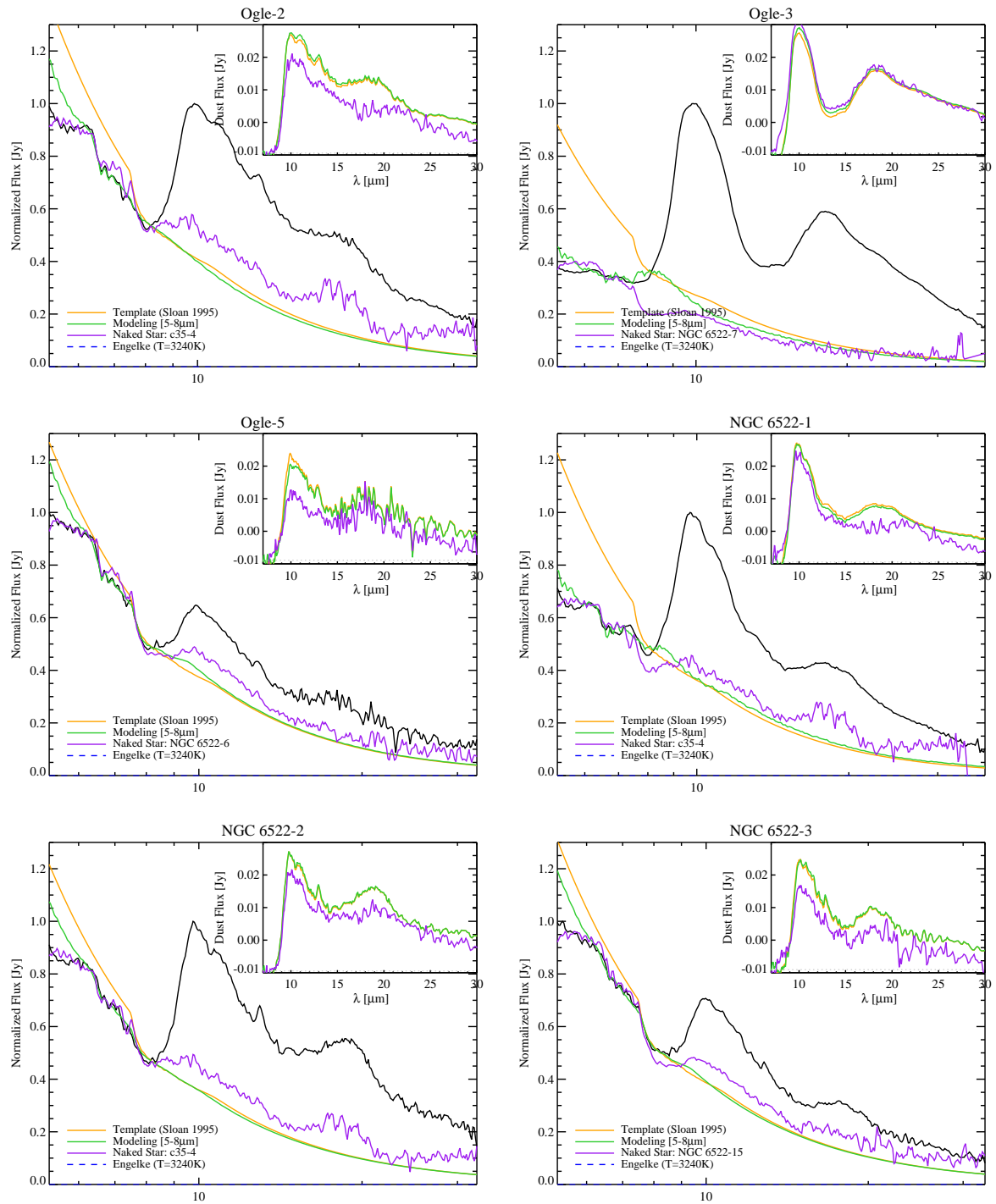


Figure F.4: Different dust extraction methods for naked stars Ogle-2, Ogle-3, Ogle-5, NGC6522-1, NGC6522-2, and NGC6522-3. See text for more details.

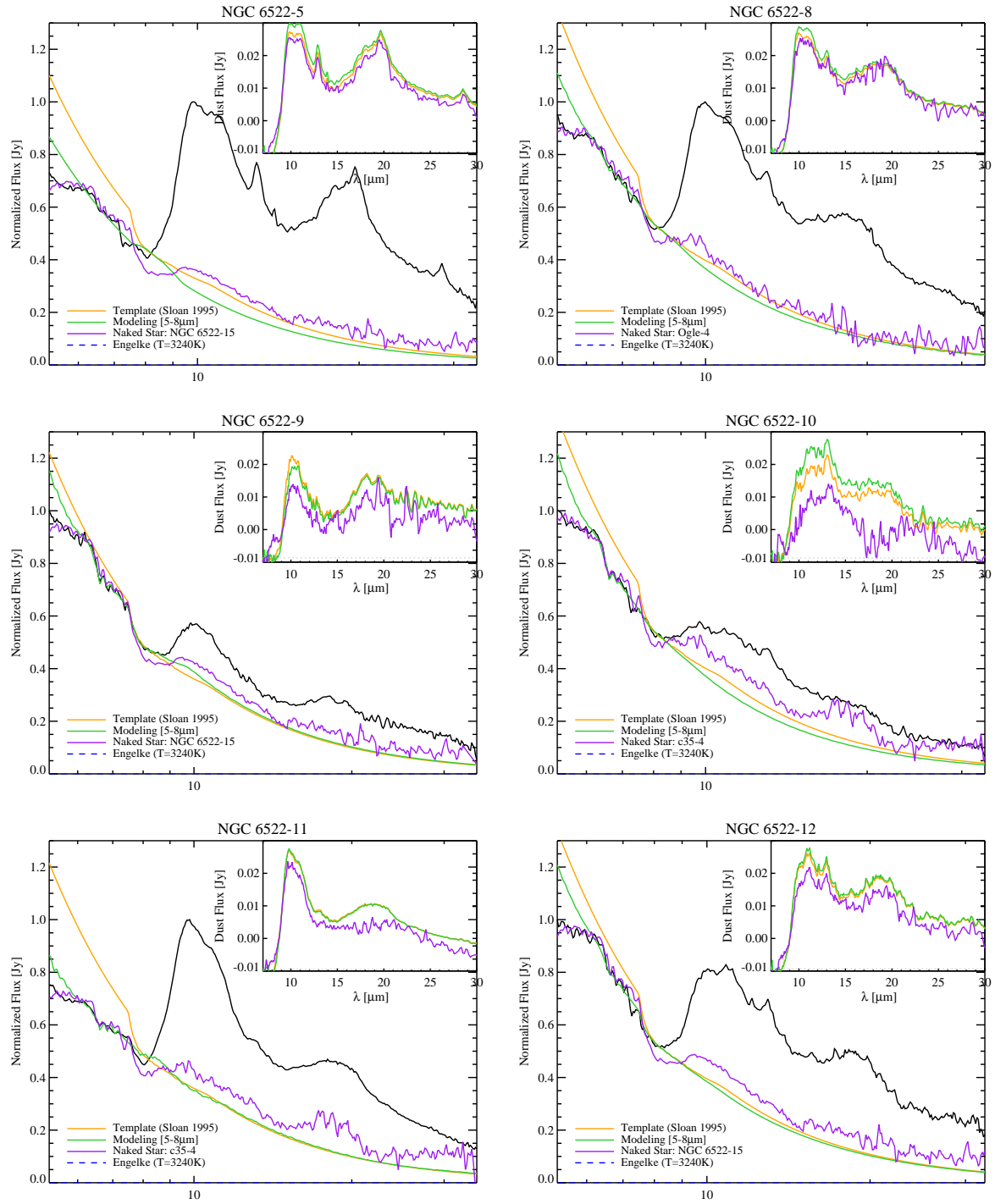


Figure F.5: Different dust extraction methods for naked stars NGC6522-5, NGC6522-8, NGC6522-9, NGC6522-10, NGC6522-11, and NGC6522-12. See text for more details.

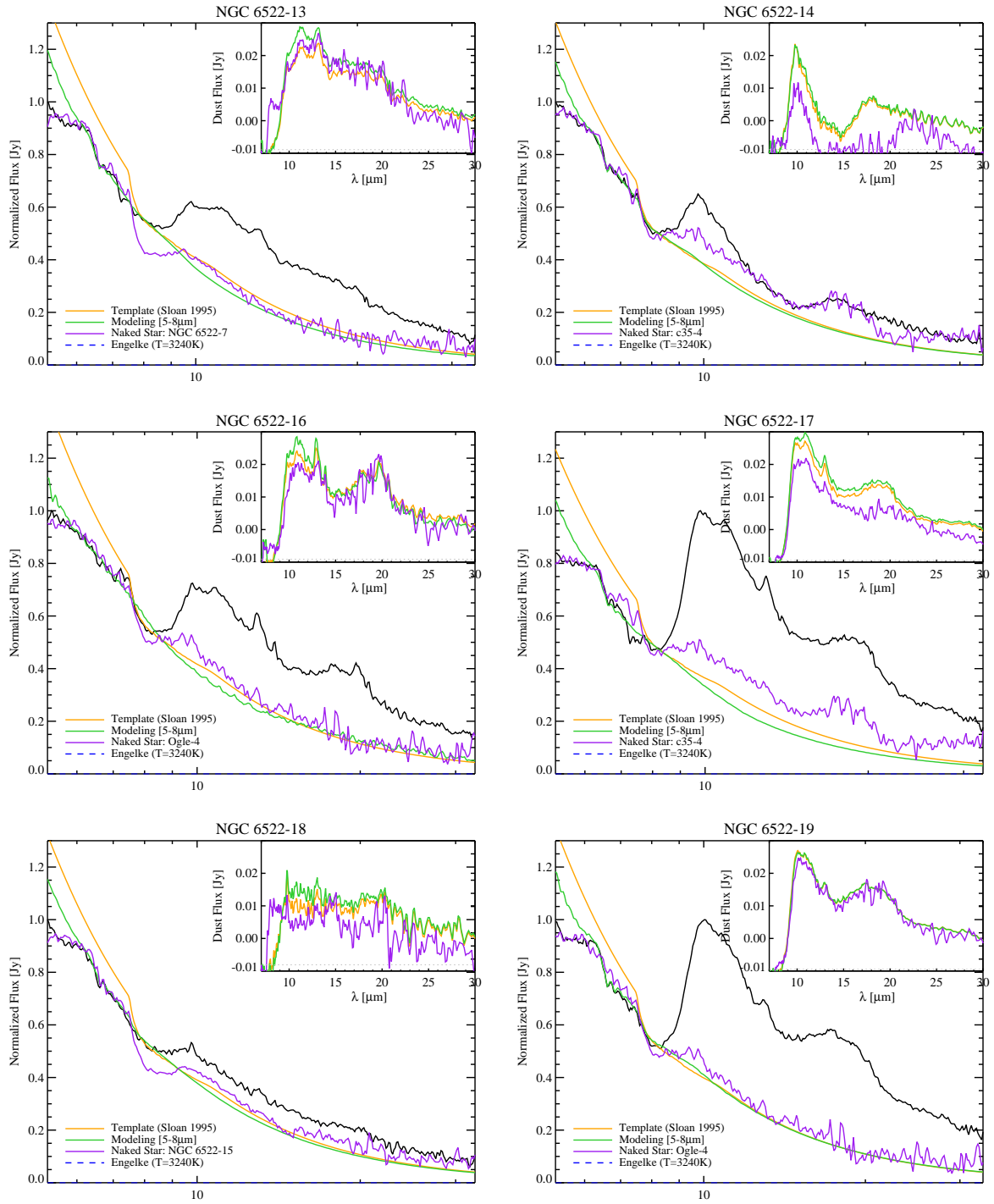


Figure F.6: Different dust extraction methods for naked stars NGC6522-13, NGC6522-14, NGC6522-16, NGC6522-17, NGC6522-18, and NGC6522-19. See text for more details.

Appendix G

In this appendix we present the final Spitzer-IRS spectra for our sample. In the text we discuss the general data reduction recipe that was applied to all the targets. However, in few exceptional cases slight modification to the general recipe was necessary. Here, we provide a brief per-target recipe that will allow the reader to achieve identical results.

In the following pages, the first plot (top) shows the extracted spectrum of each target. Note that the first and the second nod and module is distinguished by a certain color as shown in Table G.1.

In the second plot (bottom) on each page, we show the point spread functions for each nod and module after correction for the background. The observed point spread function is shown in black and our best fit point spread functions are shown in different colors depending on the number of sources detected in each of them. The caption of each figure shows the nod and module and its corresponding scale factor.

In most of our targets after extraction, there still appears a residual from insufficient bad pixel removal in form of unrealistic features (e.g. around $19.5\text{-}\mu\text{m}$ or $20.5\text{-}\mu\text{m}$). We have manually removed those features by masking (removing from the flux array) those points from our spectra. The two nods within each module have been scaled to their common median in all of our targets.

The photometry data from ISOGAL (7, $15\text{-}\mu\text{m}$), IRAC (3.6, 4.5, 5.8, $8\text{-}\mu\text{m}$) and MIPS ($24\text{-}\mu\text{m}$) are also over-plotted. In most cases the flux values we extract are in good agreement with the photometry values.

However, in some cases there appears to be a mismatch between the two. We do not have a clear reason that can explain these discrepancies in all targets. These occasional differences can

Module	Nod	Color
SL1	first	lime-green
SL1	second	magenta
SL2	first	red
SL2	second	sky blue
LL1	first	brown
LL1	second	purple
LL2	first	dark blue
LL2	second	orange

Table G.1: Colors used for each nod and module.

be introduced by a combination of error sources (e.g. instrumental, data processing, variability etc). The intrinsic variability of the star over time might be a plausible contributing factor to the discrepancies.

In the whole sample (except of OH/IR stars), we chose SL1 to be our reference module because it has the most reliable and the least noisy flux compared to other modules. We have also tried using other modules as references as well, but in some cases it alleviates and in some other cases it aggravates the discrepancies. The scale factors applied on the Long-Low modules range between $\sim 0.11 - 0.97$ and for SL2 they range between $\sim 0.85 - 1.5$. The typical offset between photometric data and spectroscopic data range between $\sim 0 - 2\text{Jy}$ in flux.

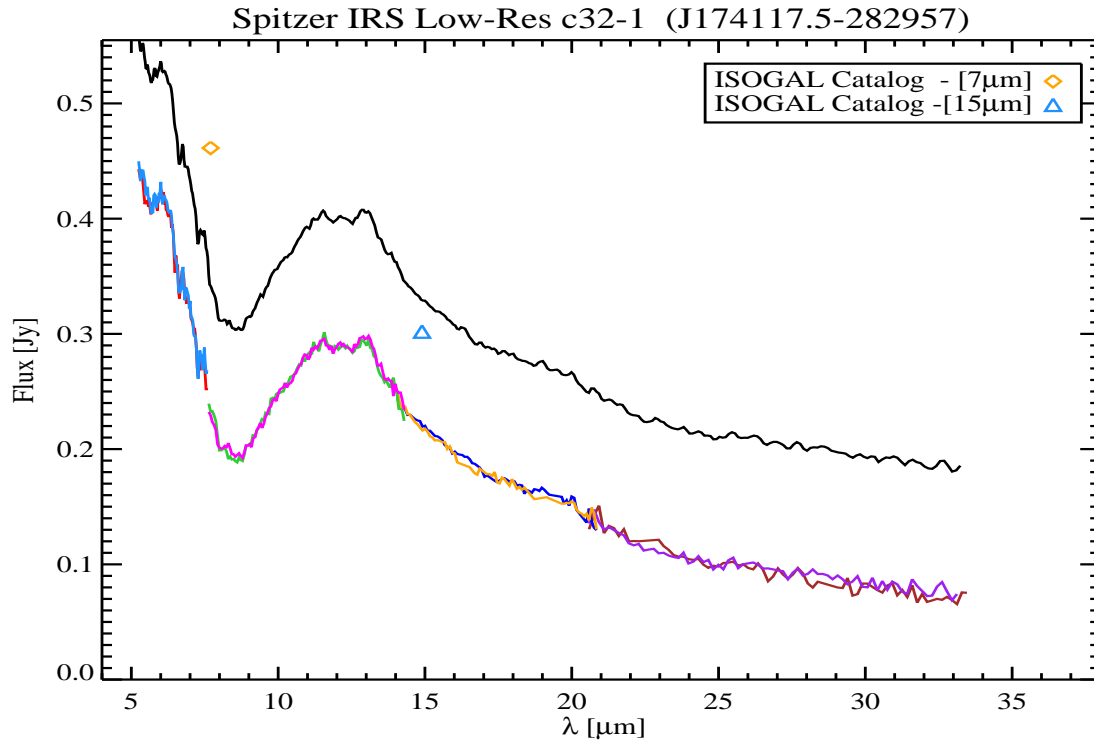


Figure G.1: **(c32-1)** Both nodes of the short low modules (SL1 & SL2) of this target contain only one target in the slit whereas in the long low module (LL1 & LL2) a second source appears very close to c32-1 (see Fig. G.2). The position of the extracted sources are shown in the Figure G.2. The spectrum shows residuals from insufficient bad pixel removal around 20.5- μ m which was properly masked. The background of this source is strong and variable with prominent PAH features. However, it can be properly modeled and corrected using the IDL program discussed in the text. In the obtained spectrum, there is a slight mismatch between long low and short low modules. We treated this mismatch by scaling the long low modules with respect to the short low modules. The scaling factors used are listed below.

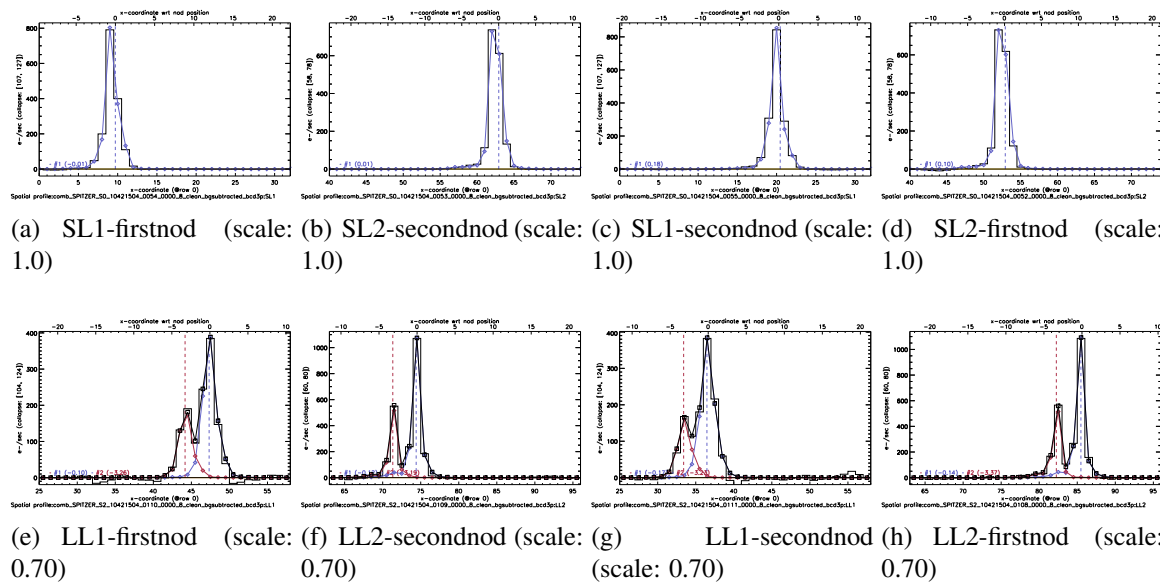


Figure G.2: SL and LL modules spatial profiles after subtraction of the background

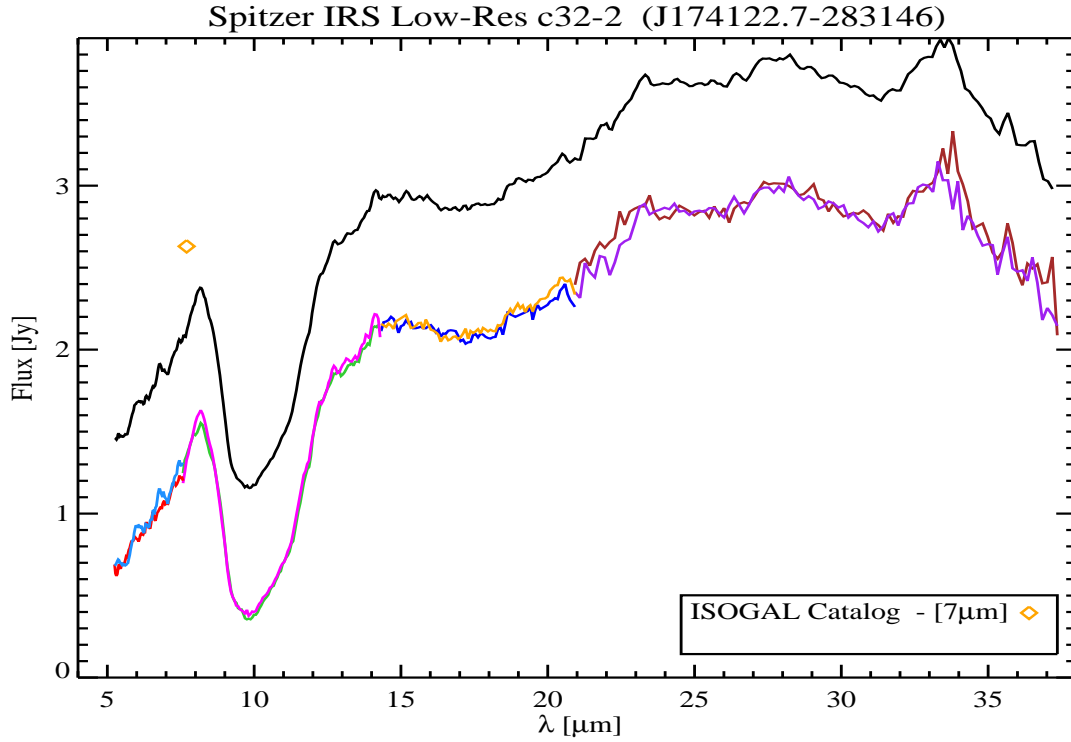


Figure G.3: (**c32-2**) The number of extracted sources in each nod and module is shown in Fig. G.4 along with their position. In the extracted spectrum, there was a mismatch between the two nods of the SL1 module. Specifically, close to the edges of the module this mismatch was more noticeable. In order to correct for that we have modified the point spread function in SMART by specifying new parameters for the central position and full-width-half-maximum(FWHM)of the PSF. The background of this target was strong and variable and quite similar to c32-1 since they are both in the field c32. The background for the long low modules was properly modeled by the program explained in the text but for the SL2 module we have subtracted the background assuming a first order polynomial within optimal extraction of SMART. Finally, The mismatch between the modules was corrected by scaling the short low modules with respect to long low modules, with the following scale factors.

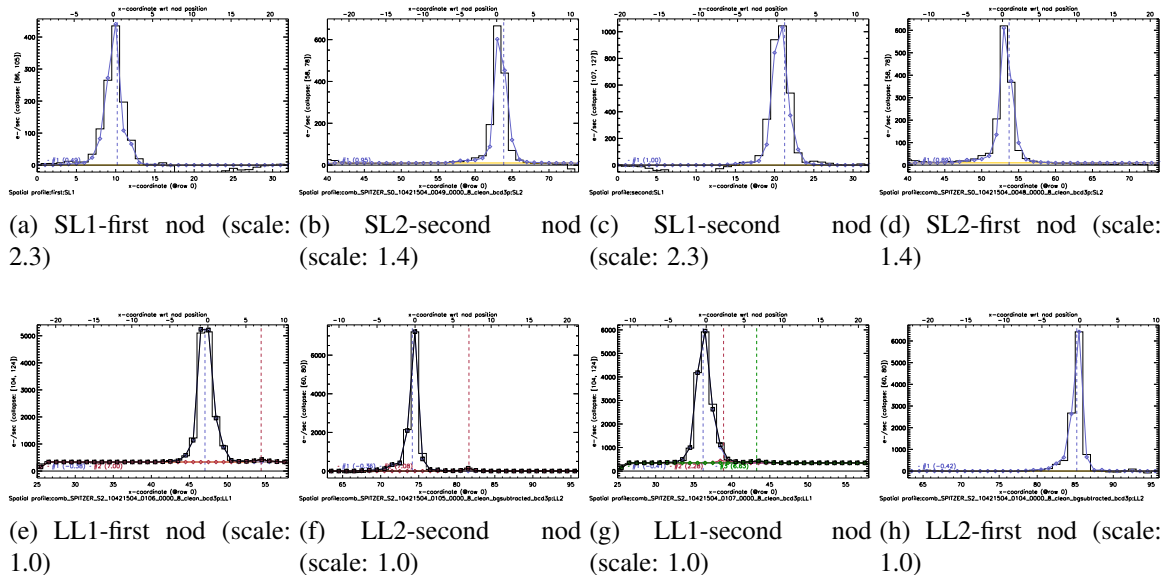


Figure G.4: SL and LL modules spatial profiles after subtraction of the background

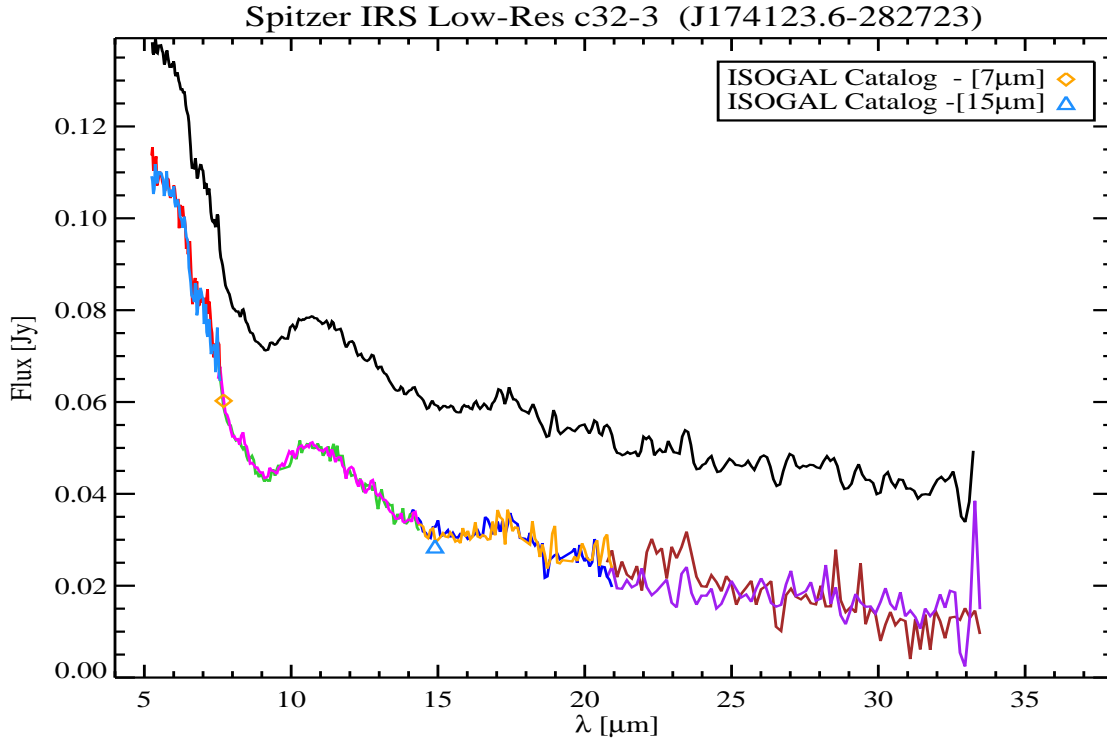


Figure G.5: **(c32-3)** As indicated in Figure G.6, the number of sources that have been extracted in each nod and module. There was a significant mismatch between the two nods of SL1 module which was corrected by modifying the point spread function(central position and FWHM). After extraction the residual features were masked properly (e.g. 19.5- μ m). This target is located in field c32 but the background is properly corrected through modeling except SL1 module. For this module, we have assumed a constant offset for the background (polynomial order zero) and performed the subtraction using optimal extraction within SMART. Finally, we scaled long low modules with respect to the short low modules using the following scale factors, in order to eliminate the mismatch between modules and obtain the continuum shown here.

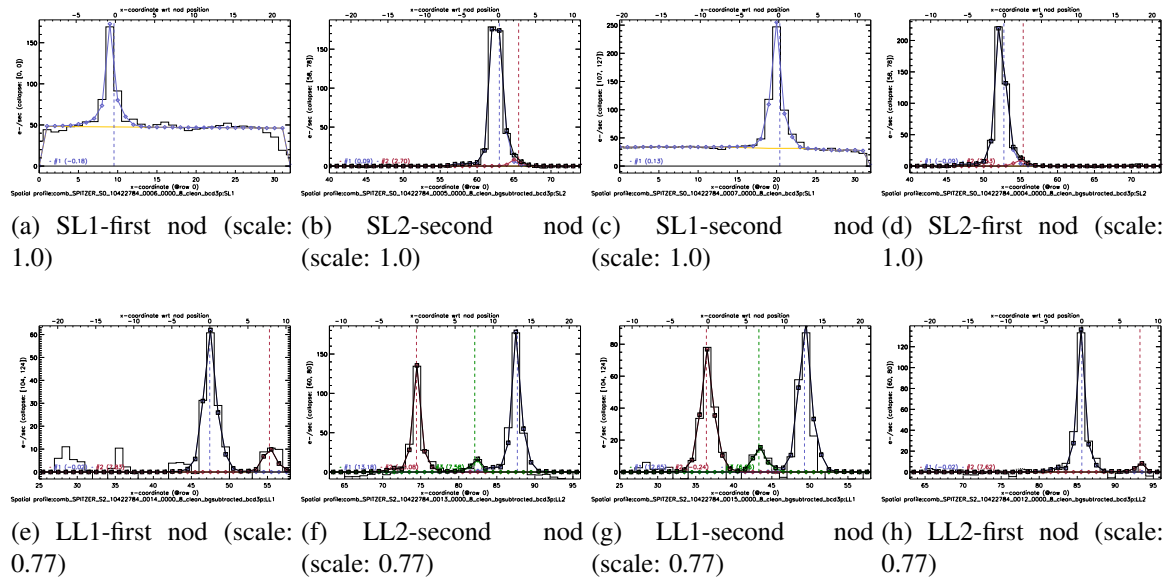


Figure G.6: SL and LL modules spatial profiles after subtraction of the background

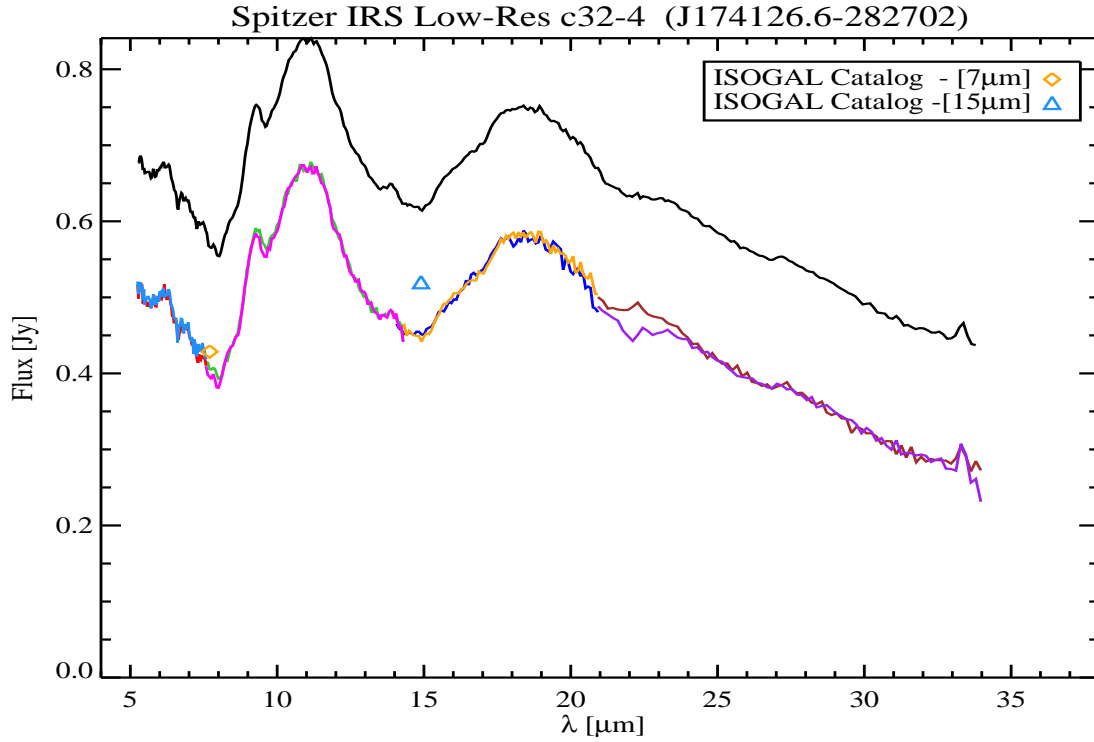


Figure G.7: (**c32-4**) All nodes of both modules (SL and LL) of this target contain only one source in the slit except first nod of SL2 module which contains a very faint second source (see Fig. G.8). The position of the extracted targets are shown in the figure G.8. The residuals we represent after extraction which were properly masked (e.g. 18.5- μ m). The background for this source is strong and variable but properly modeled and corrected. Finally, we applied the following scale factors on the corresponding module to eliminate the mismatch between modules and obtain the final continuum shown here.

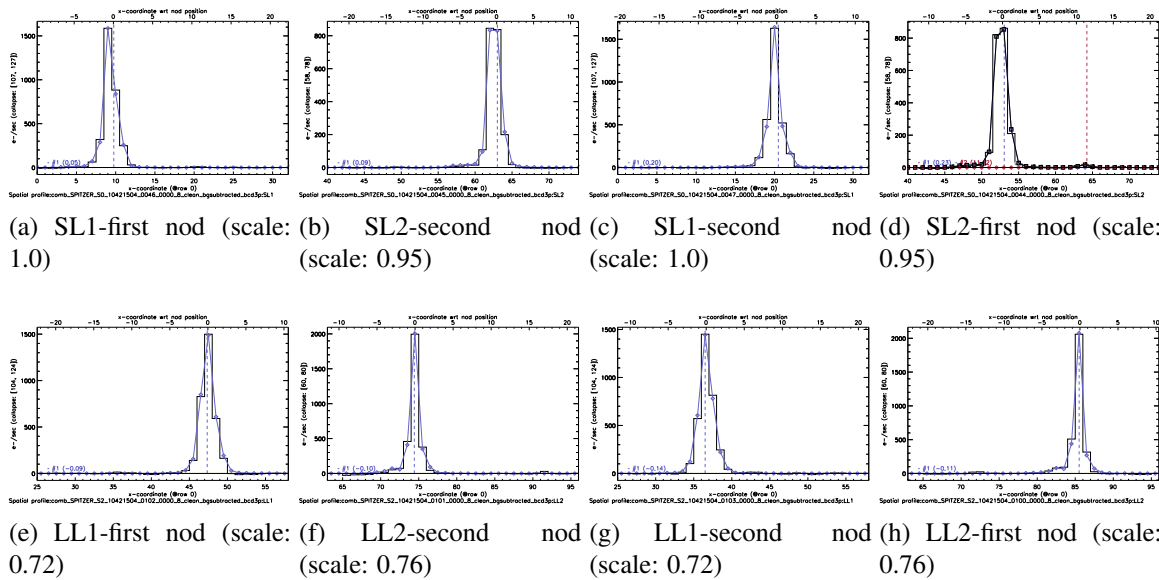


Figure G.8: SL and LL modules spatial profiles after subtraction of the background

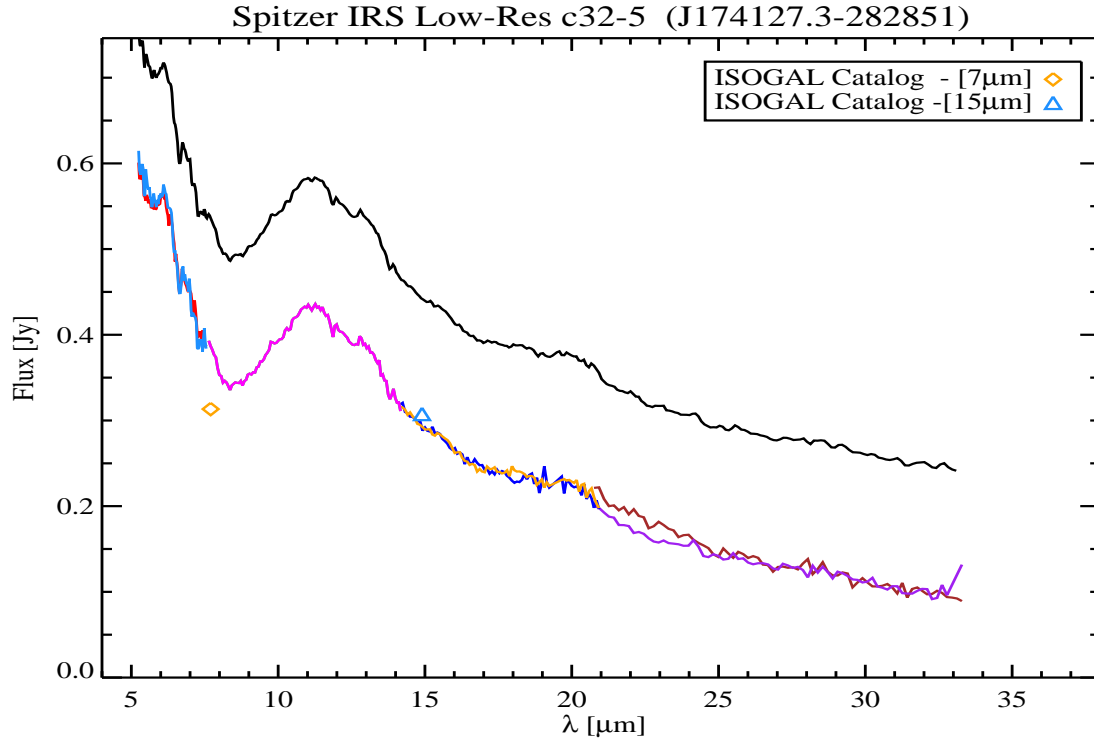


Figure G.9: **(c32-5)** This is the final spectrum of c32-5. Figure G.10 indicates the number of sources that have been extracted in each nod of each module. After extraction there was no obvious residuals left for us to remove manually. As shown in Figure G.10 the observation for the second nod of SL1 module did not contain any useful information to extract, therefore for this module, we only took into account the data in the first nod. The background for this source is strong and variable but properly modeled and corrected. Finally, we scaled the long low modules with respect to the short low in order to eliminate the mismatch between modules and obtain the continuum shown here.

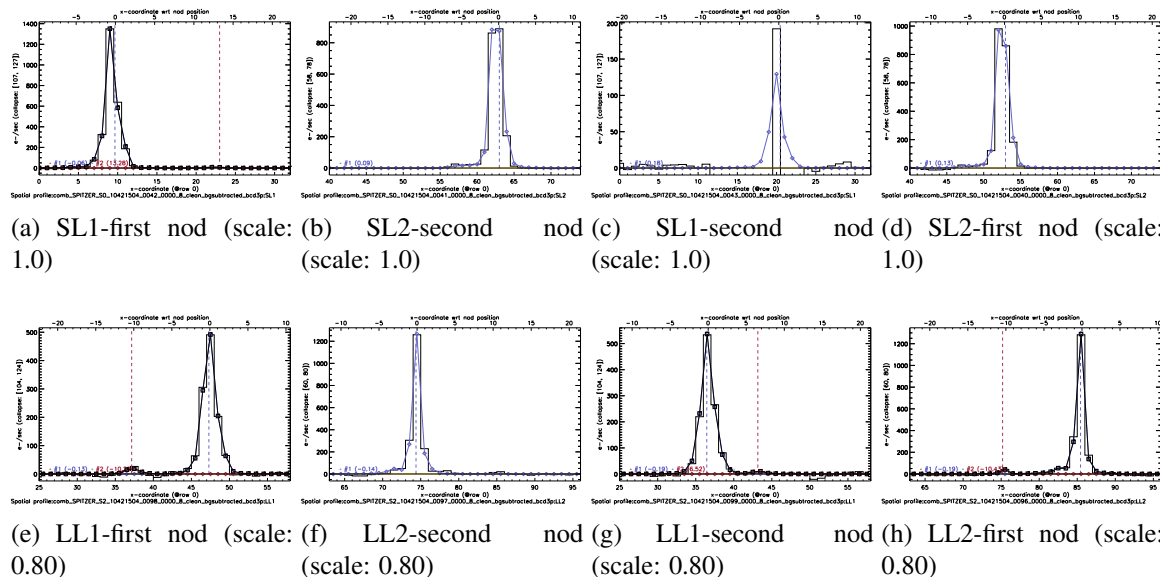


Figure G.10: SL and LL modules spatial profiles after subtraction of the background

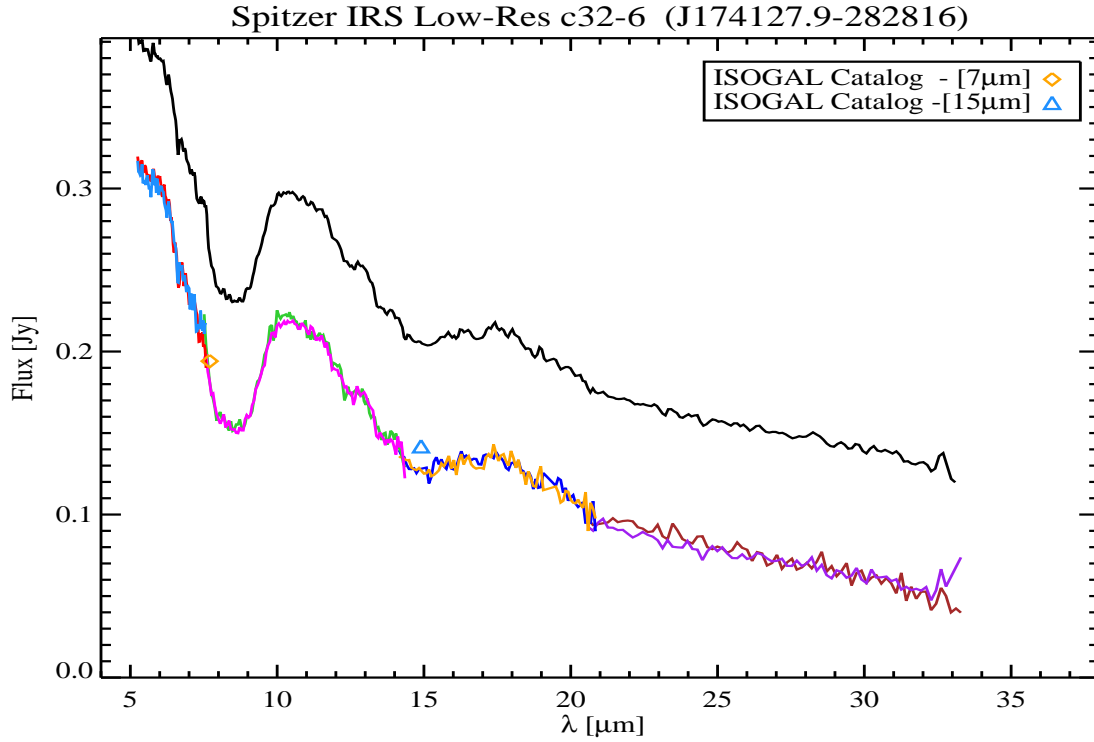


Figure G.11: **(c32-6)** This is the final spectrum of c32-6. Figure G.12 indicates the number of sources that have been extracted in each nod of each module. The mismatch between the nods of SL1 module was removed by modifying the point spread function (central position and FWHM). After extraction the residual features were masked (e.g. 19.5- μm). In all modules, the background could be corrected by means of modeling except the LL1 module, in which case we have subtracted the background assuming an order one polynomial (linear gradient) in manual optimal extraction within Smart. Finally, we scaled the long low modules with respect to the short low modules in order to eliminate the mismatch between modules and obtain the continuum shown here.

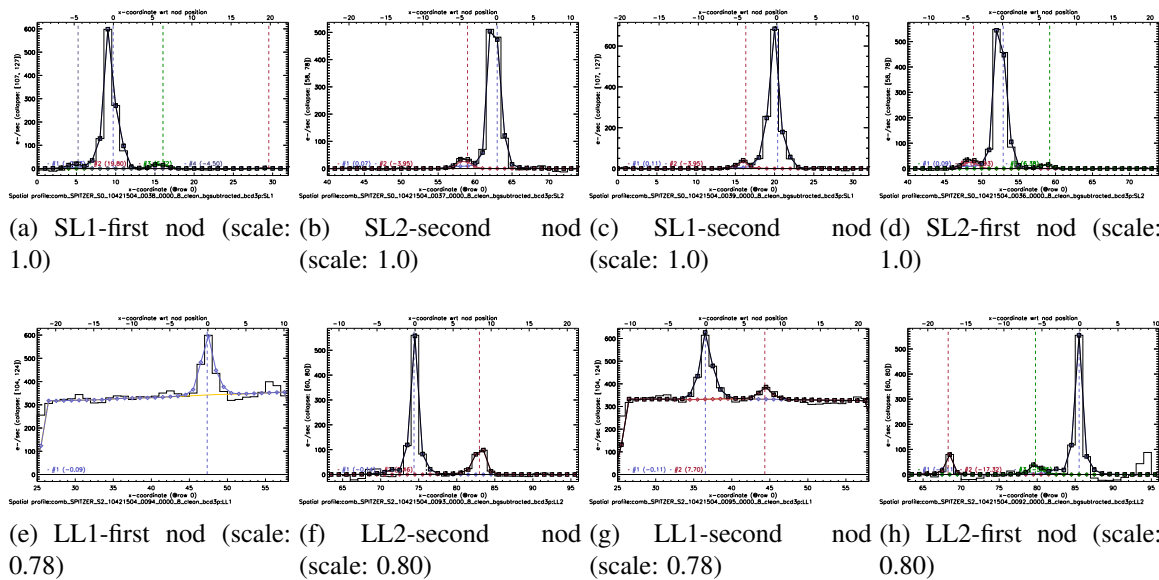


Figure G.12: SL and LL modules spatial profiles after subtraction of the background

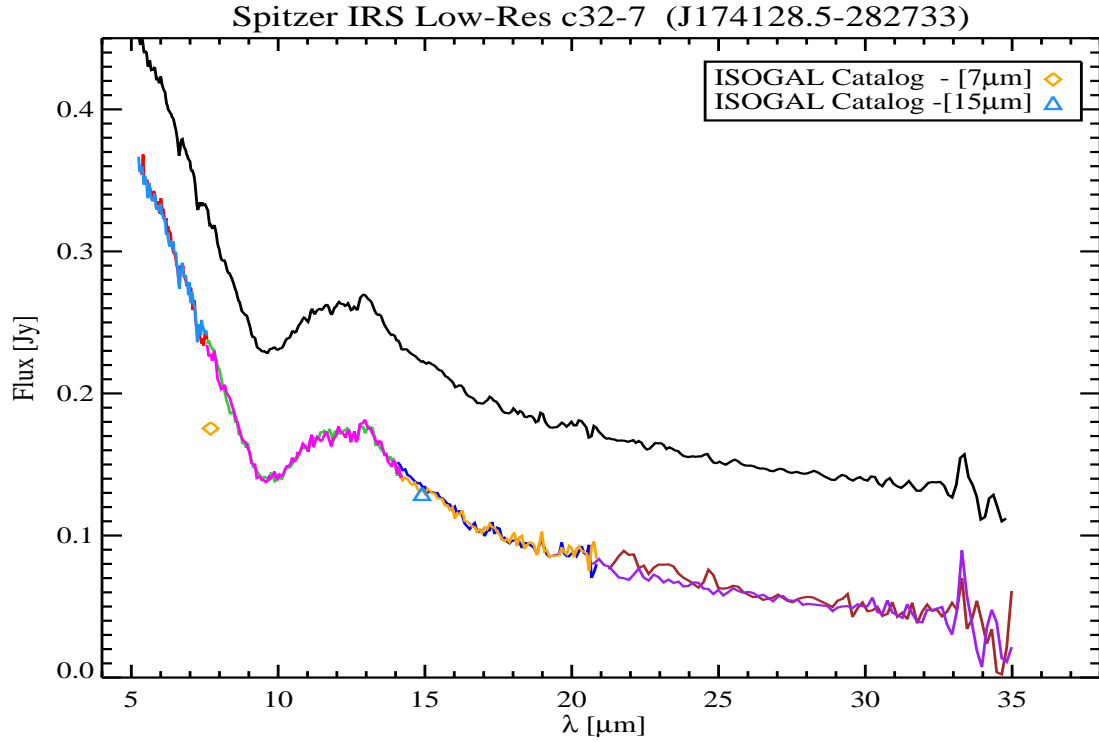


Figure G.13: (**c32-7**) This is the final spectrum of c32-7. Figure G.14 indicates the number of sources that have been extracted in each nod and module. There was a slight mismatch between the two nods of SL1 module which was removed by modifying the point spread function (central position and FWHM). After extraction the sharp and unrealistic residual features were masked (e.g. 19.5- μm). The background for this source is properly corrected through modeling. Finally, we applied the following scale factors on the corresponding module to eliminate the mismatch between modules and obtain the final continuum shown here.

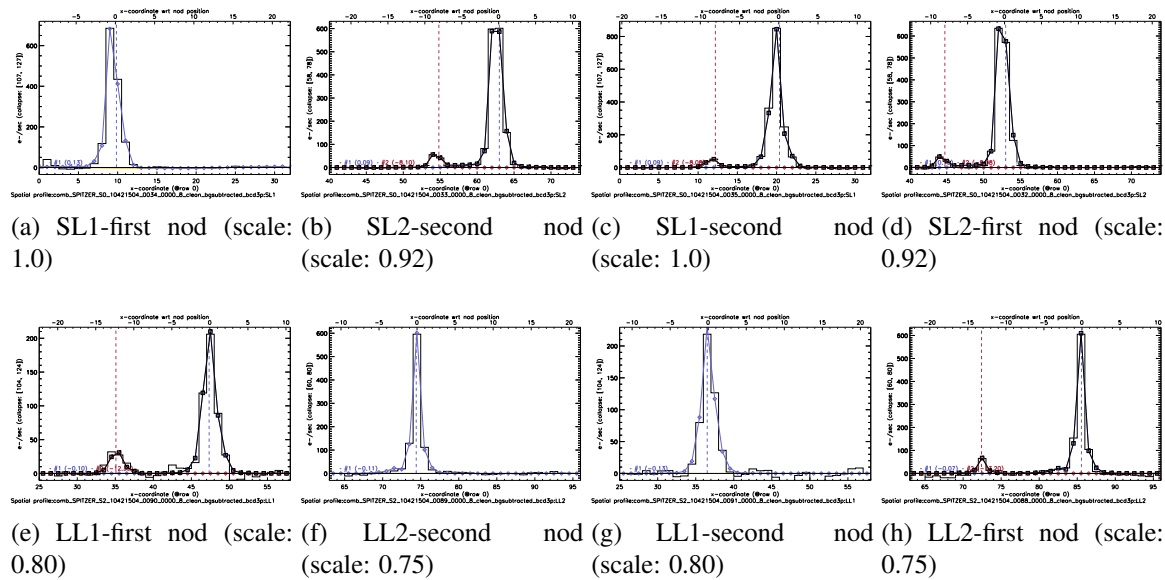


Figure G.14: SL and LL modules spatial profiles after subtraction of the background

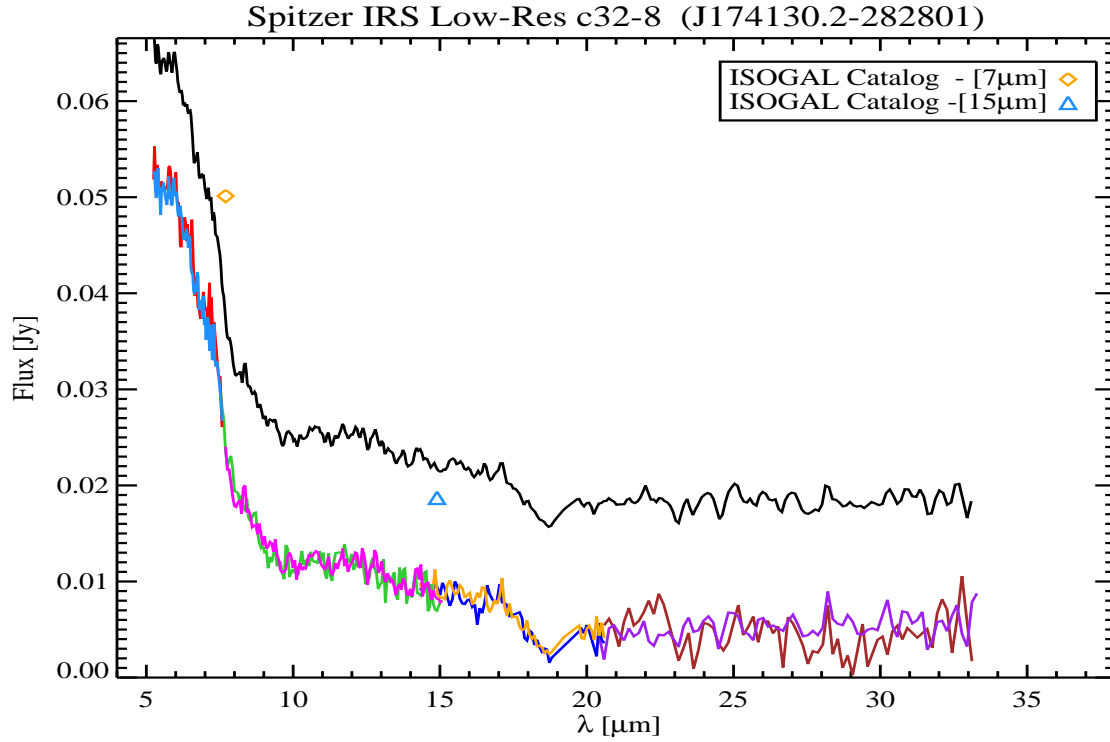


Figure G.15: (**c32-8**) This is the final spectrum of c32-8. Figure G.16 indicates the number of sources that have been extracted in each nod and module. There was a slight mismatch between the two nods of SL1 module which was removed by modifying the point spread function (central position and FWHM). After extraction there were no significant residuals to mask. The background is properly corrected through modeling. Finally, we scaled the long low modules with respect to the short low modules using the following scale factors, in order to eliminate the mismatch between them and obtain the continuum shown here.

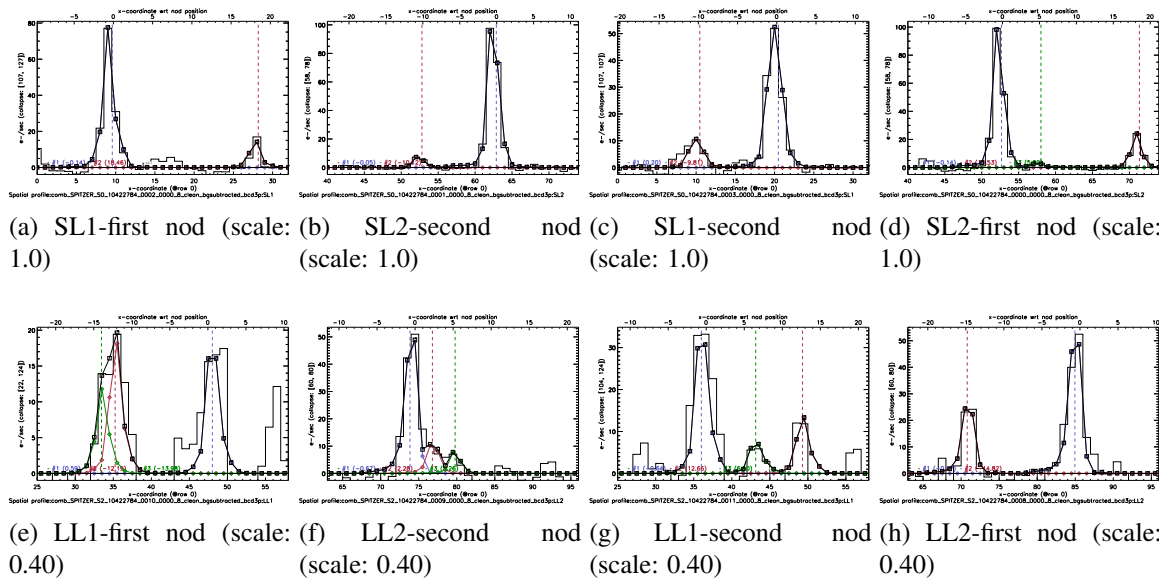


Figure G.16: SL and LL modules spatial profiles after subtraction of the background

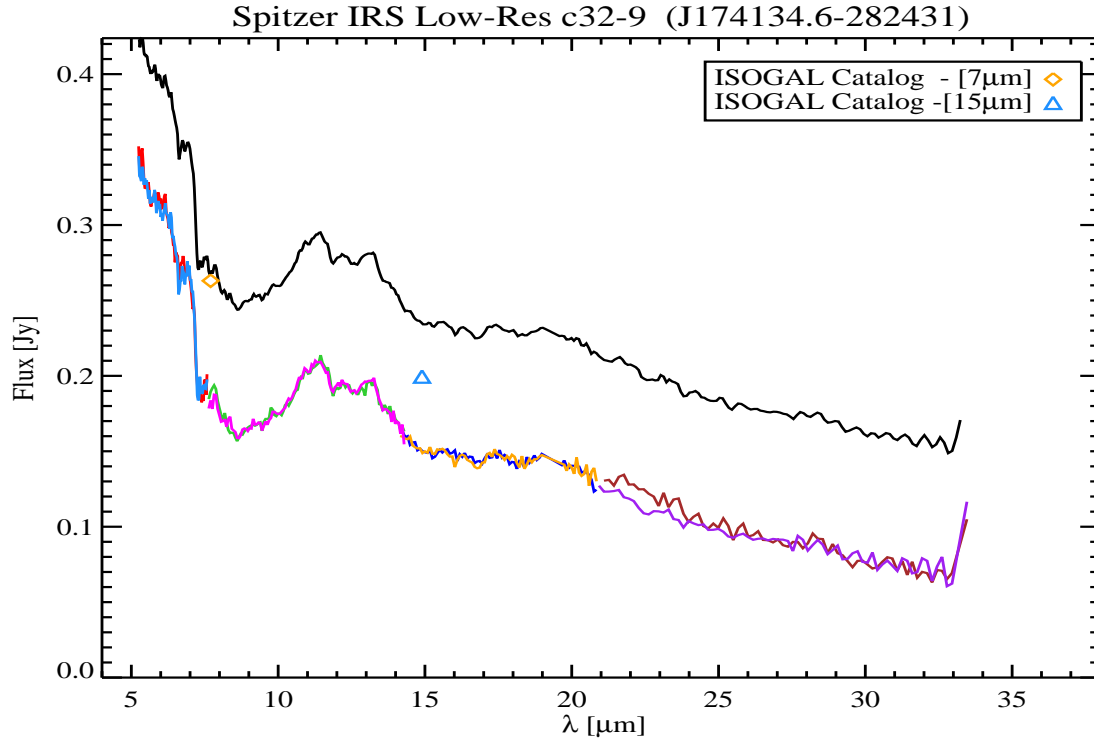


Figure G.17: (**c32-9**) This is the final spectrum of c32-9. Figure G.18 indicates the number of sources that have been extracted in each nod and module. There was a slight mismatch between the two nods of SL1 module which was removed by modifying the point spread function (central position and FWHM). After extraction the sharp and unrealistic residual features were masked (e.g. 19.5- μm). The background is properly modelled and corrected. Finally, we scaled the long low modules with respect to the short low modules using the following scale factors, in order to eliminate the mismatch between modules and obtain the continuum shown here.

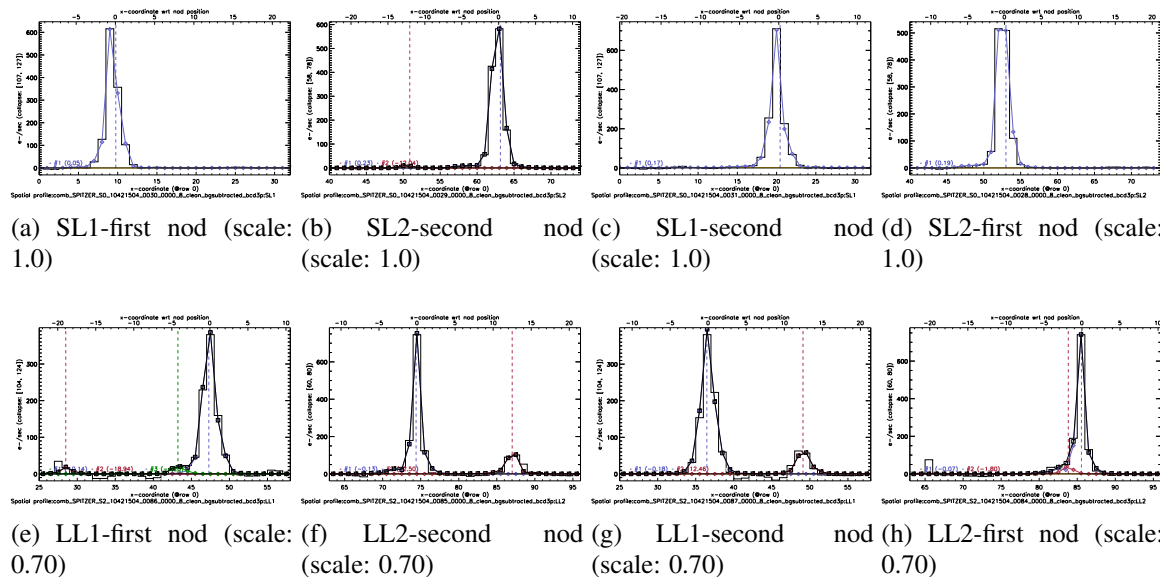


Figure G.18: SL and LL modules spatial profiles after subtraction of the background

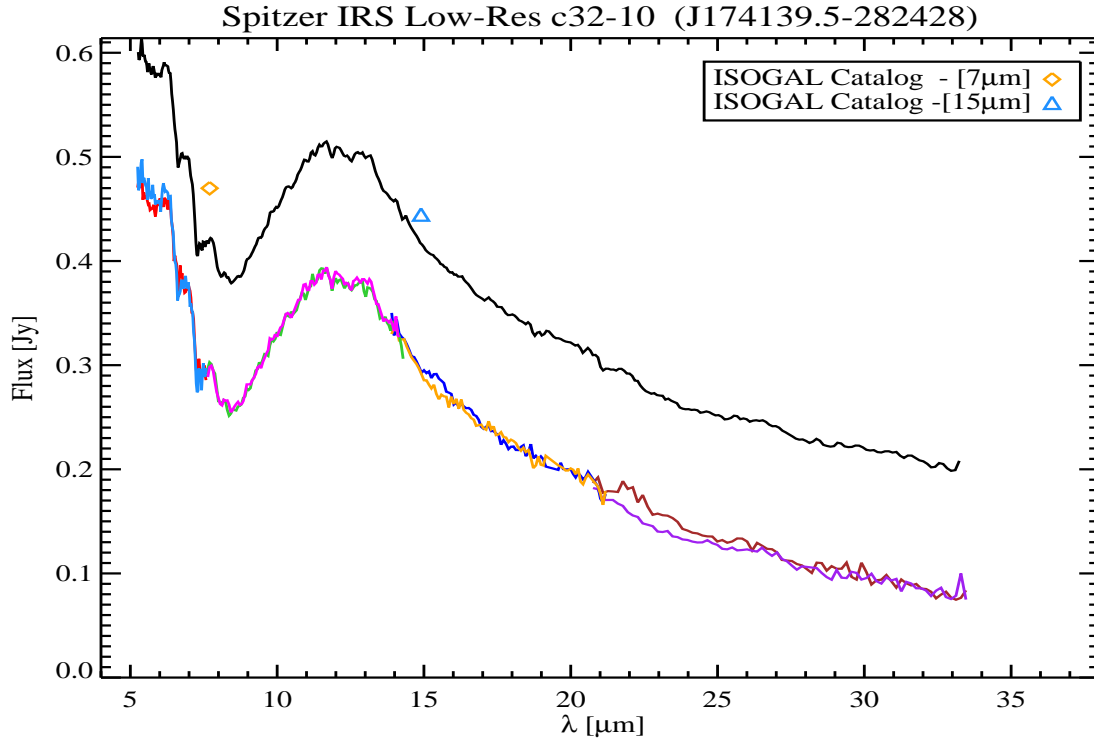


Figure G.19: **(c32-10)** This is the final spectrum of c32-10. Figure G.20 indicates the number of sources that have been extracted in each nod and module. There was a slight mismatch between the two nods of SL1 module which was removed by modifying the point spread function (central position and FWHM). After extraction the sharp and unrealistic residual features were masked (e.g. 19.5- μ m). The background for this source is properly corrected through modeling. Finally, we scaled all modules with respect to the SL1 module using the following scale factors, in order to eliminate the mismatch between modules and obtain the continuum shown here.

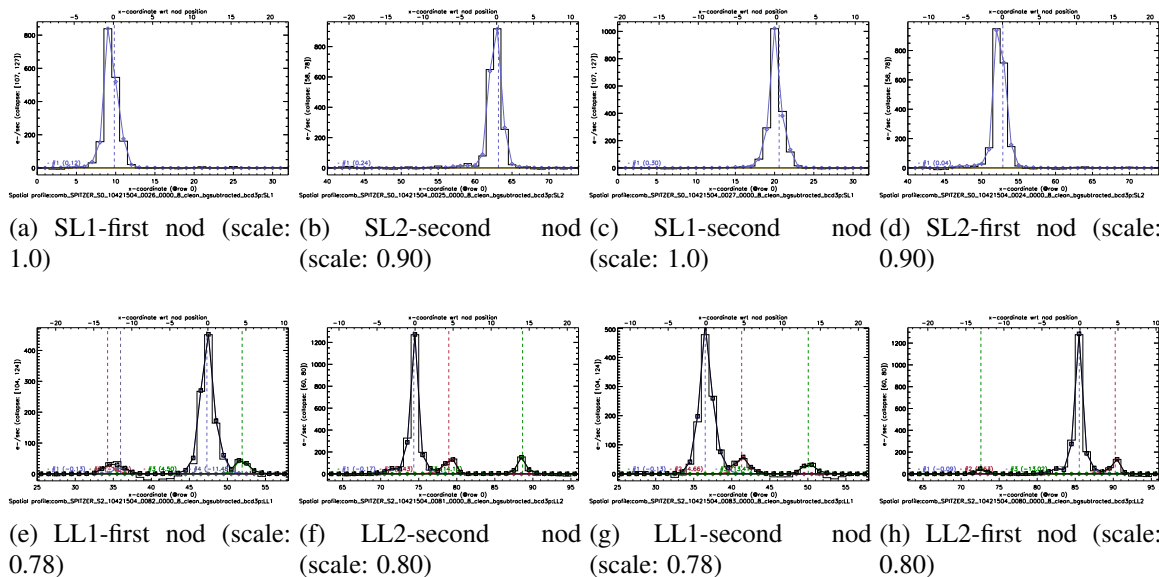


Figure G.20: SL and LL modules spatial profiles after subtraction of the background

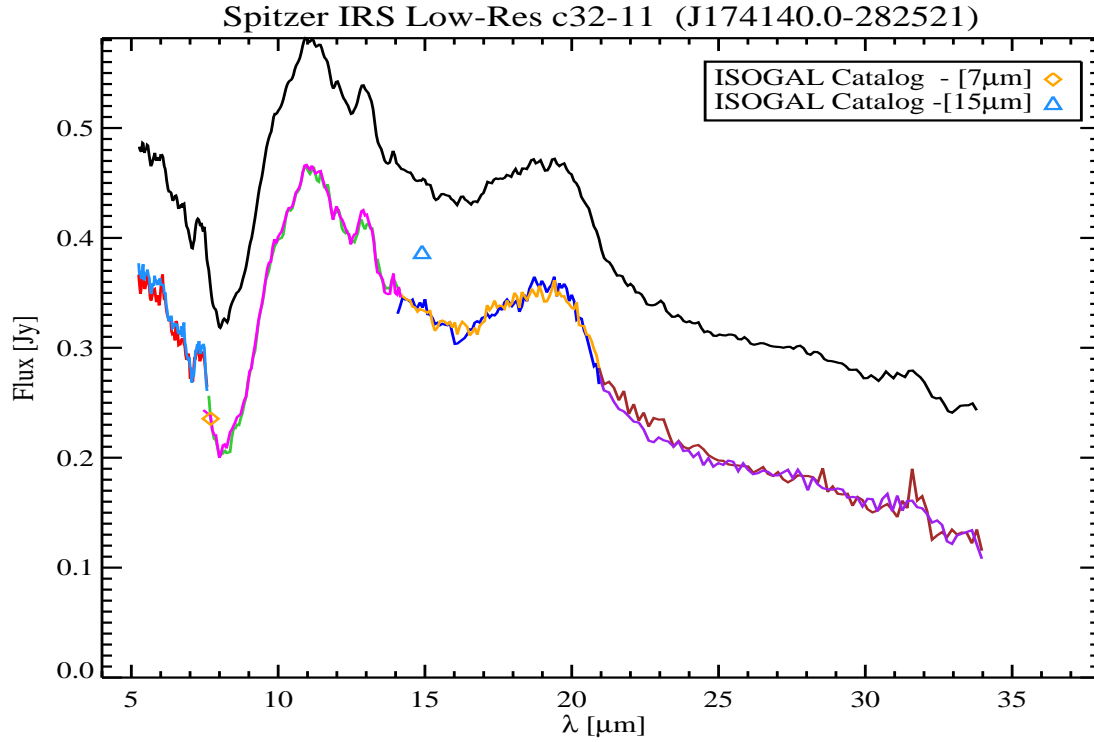


Figure G.21: **(c32-11)** This is the final spectrum of c32-11. Figure G.22 indicates the number of sources that have been extracted in each nod and module. There was a significant mismatch between the two nodes of SL1 module which was corrected by modifying the point spread function (central position and FWHM). After extraction there were no significant residuals to mask. The background for all modules is properly corrected through modeling except SL1 module. For this module, we have assumed a constant offset for the background (polynomial order zero) and performed the subtraction using optimal extraction within SMART. Finally, we scaled all modules with respect to the SL1 module using the following scale factors, in order to eliminate the mismatch between modules and obtain the continuum shown here.

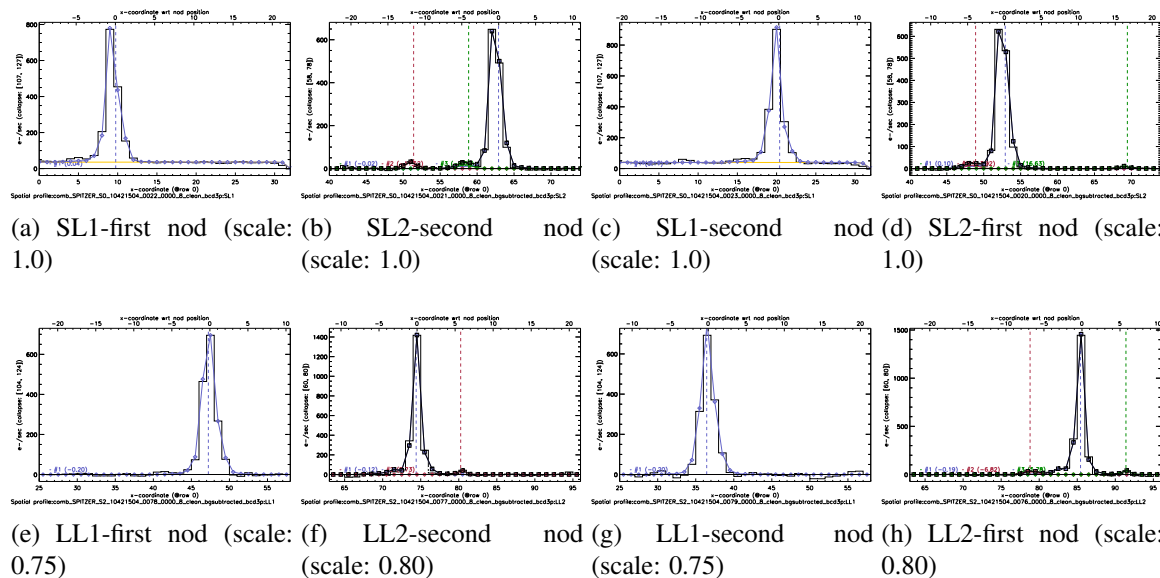


Figure G.22: SL and LL modules spatial profiles after subtraction of the background

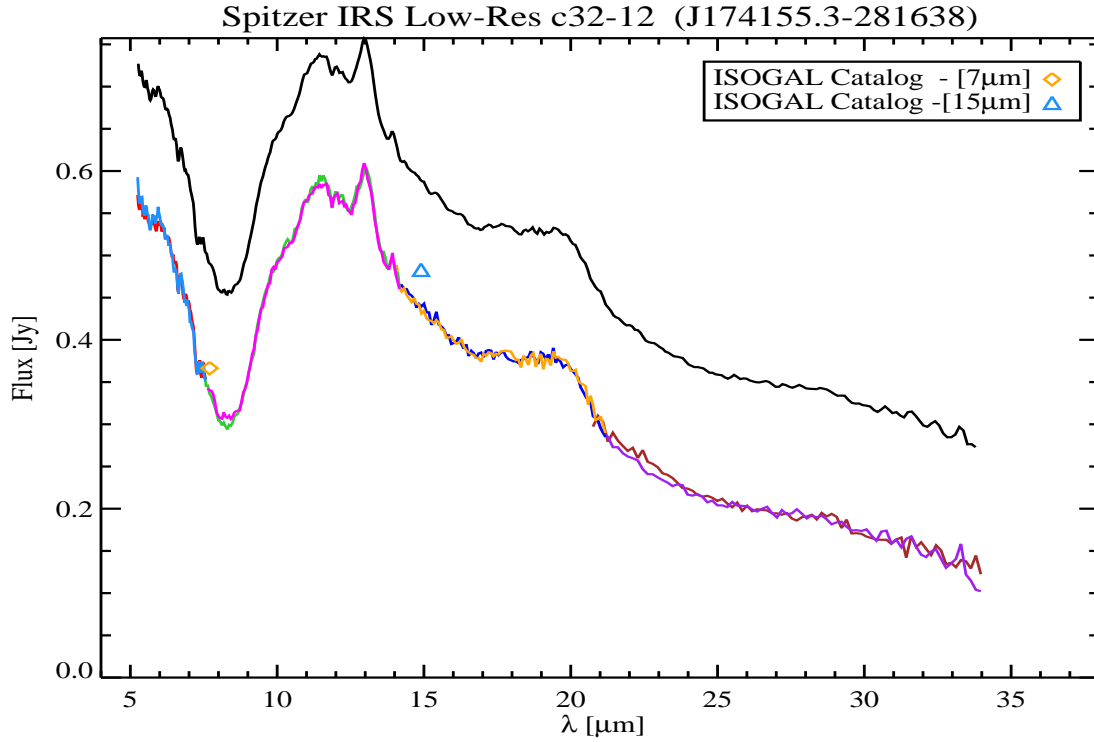


Figure G.23: **(c32-12)** This is the final spectrum of c32-12. Figure G.24 indicates the number of sources that have been extracted in each nod and module. There was a significant mismatch between the two nods of SL1 module which was removed by modifying the point spread function (central position and FWHM). After extraction there were no significant residuals to mask. The background is properly corrected through modeling. Finally, we scaled all modules with respect to the SL1 module using the following scale factors, in order to eliminate the mismatch between modules and obtain the continuum shown here.

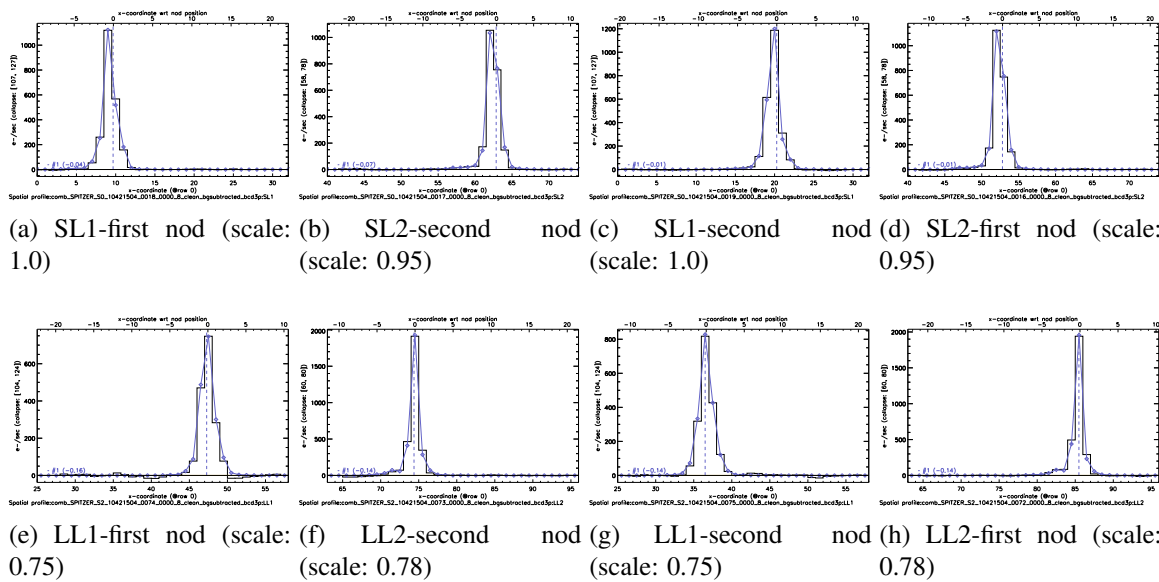


Figure G.24: SL and LL modules spatial profiles after subtraction of the background

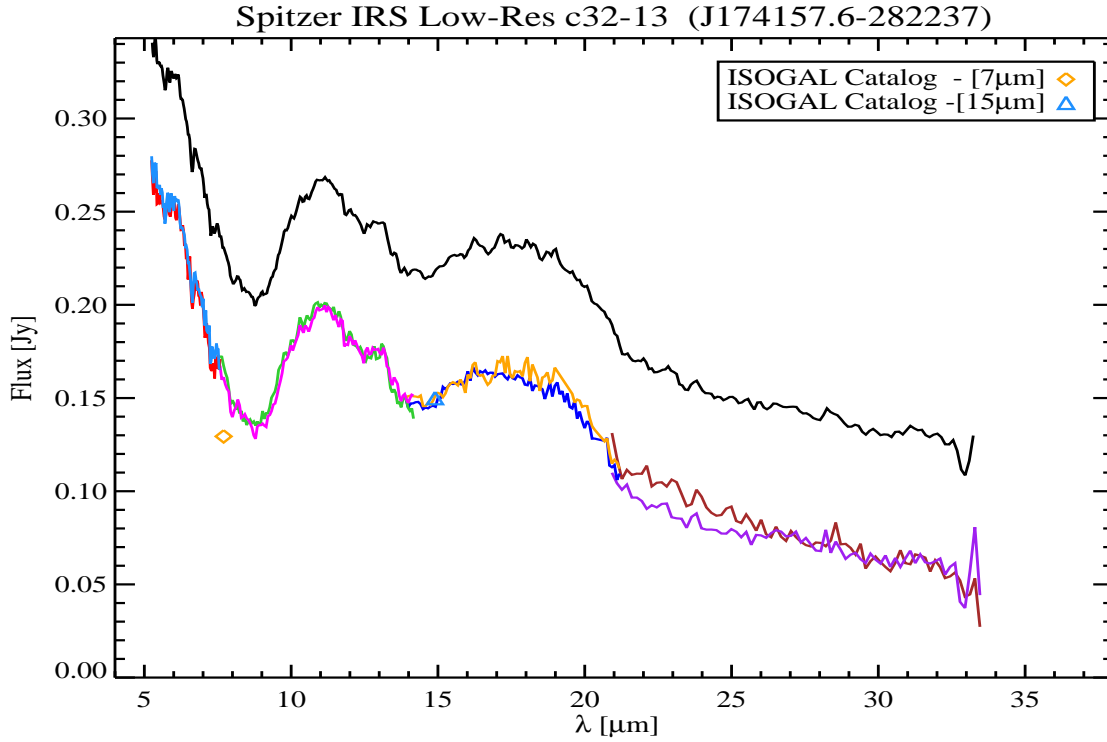


Figure G.25: (**c32-13**) This is final spectrum of c32-13. Figure G.26 indicates the number of sources that have been extracted in each nod and module. There was an extreme mismatch between the two nods of SL1 module which was corrected by modifying the point spread function (central position and FWHM). After extraction the residual features were masked properly (e.g. 19- μm). The background for all modules was properly corrected through modeling except LL2 module. For this module, we have assumed a constant offset for the background (polynomial order zero) and performed the subtraction using optimal extraction within SMART. Finally, we scaled all modules with respect to the SL1 module using the following scale factors, in order to eliminate the mismatch between modules and obtain the continuum shown here.

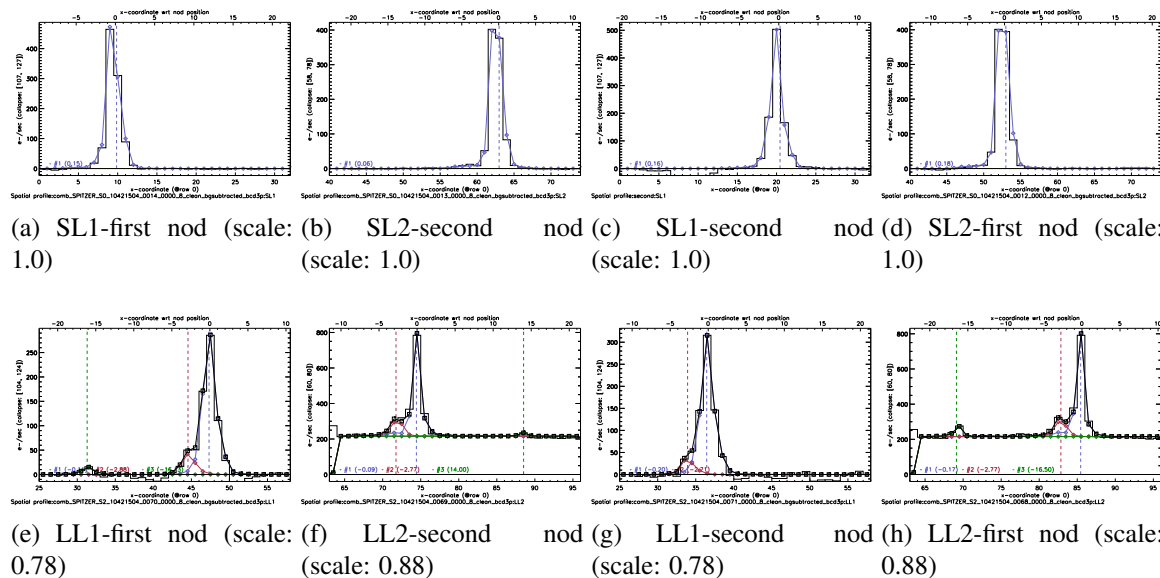


Figure G.26: SL and LL modules spatial profiles after subtraction of the background

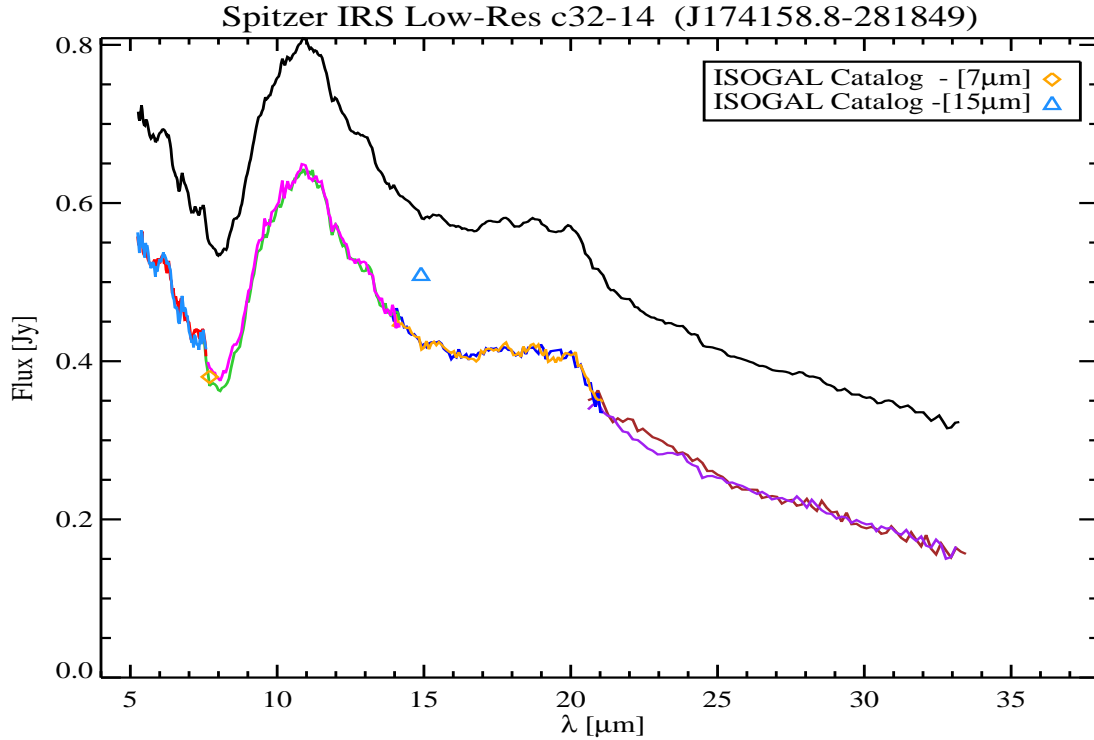


Figure G.27: **(c32-14)** This is the final spectrum of c32-14. Figure G.28 indicates the number of sources that have been extracted in each nod and module. There was an extreme mismatch between the two nods of SL1 module which was removed by modifying the point spread function (central position and FWHM). After extraction a few residual features were masked (e.g. 19.5- μm). The background for this source was properly corrected through modeling. Finally, we scaled long low modules with respect to the short low modules using the following scale factors, in order to eliminate the mismatch between modules and obtain the continuum shown here.

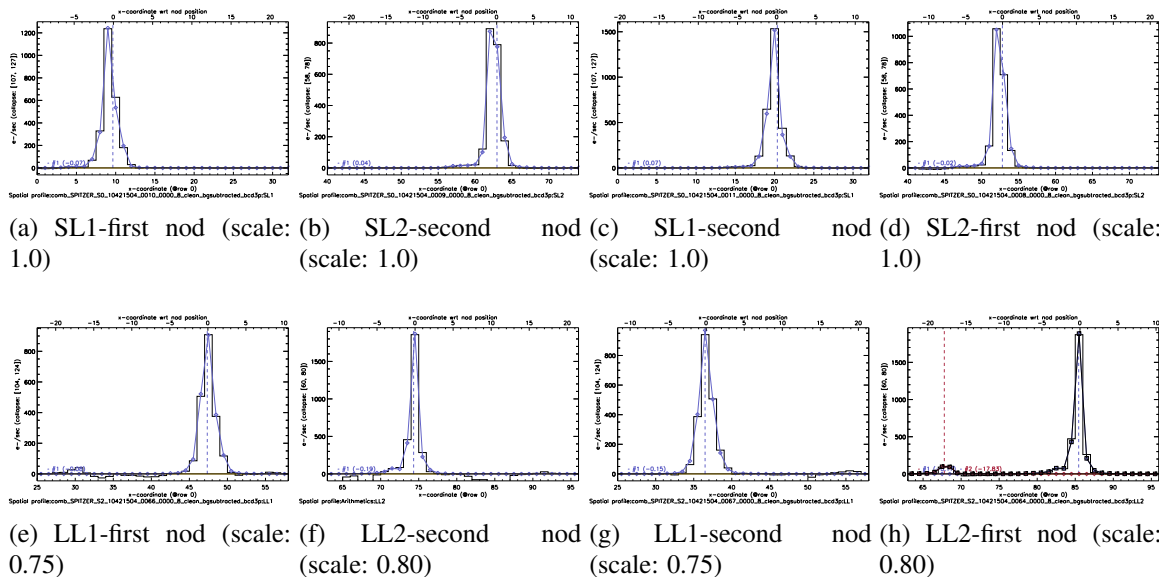


Figure G.28: SL and LL modules spatial profiles after subtraction of the background

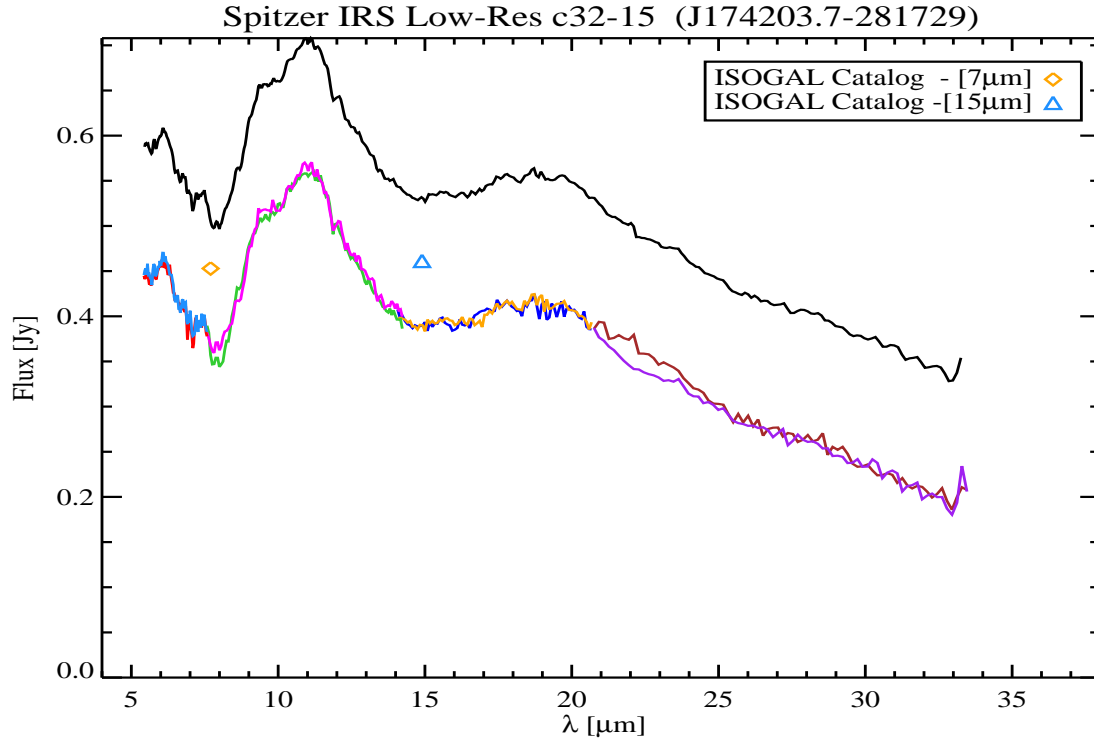


Figure G.29: (**c32-15**) This is the final spectrum of c32-15. Figure G.30 indicates the number of sources that have been extracted in each nod and module. There was a significant mismatch between the two nods of SL1 module which was removed by modifying the point spread function (central position and FWHM). After extraction the sharp and unrealistic residual features were masked (e.g. 19.5- μ m). The background for this source was properly corrected through modeling. Finally, we scaled long low modules with respect to the short low modules using the following scale factors, in order to eliminate the mismatch between modules and obtain the continuum shown here.

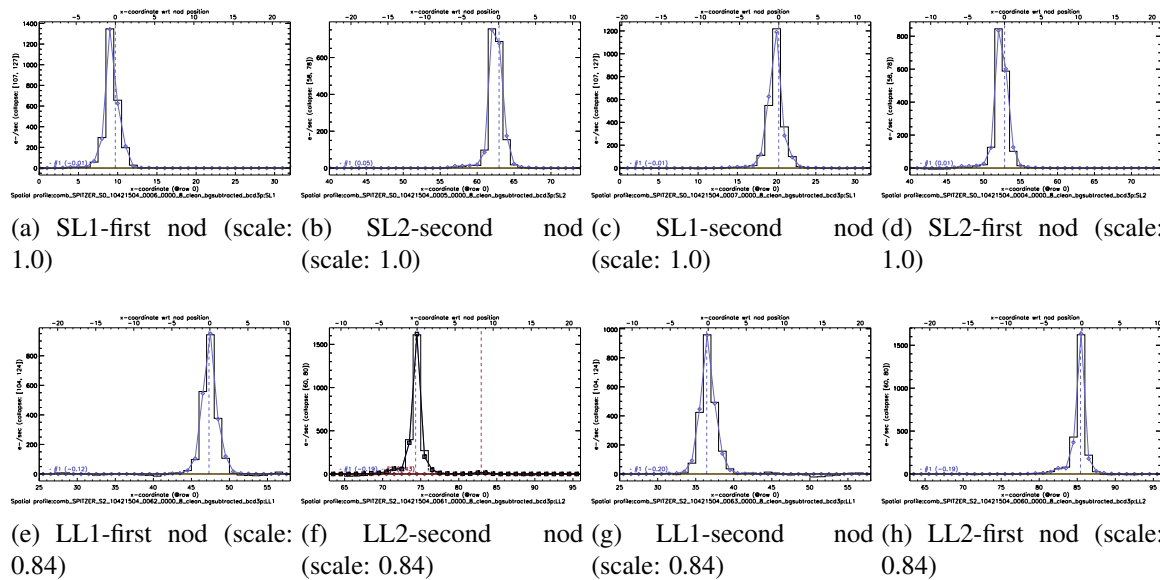


Figure G.30: SL and LL modules spatial profiles after subtraction of the background

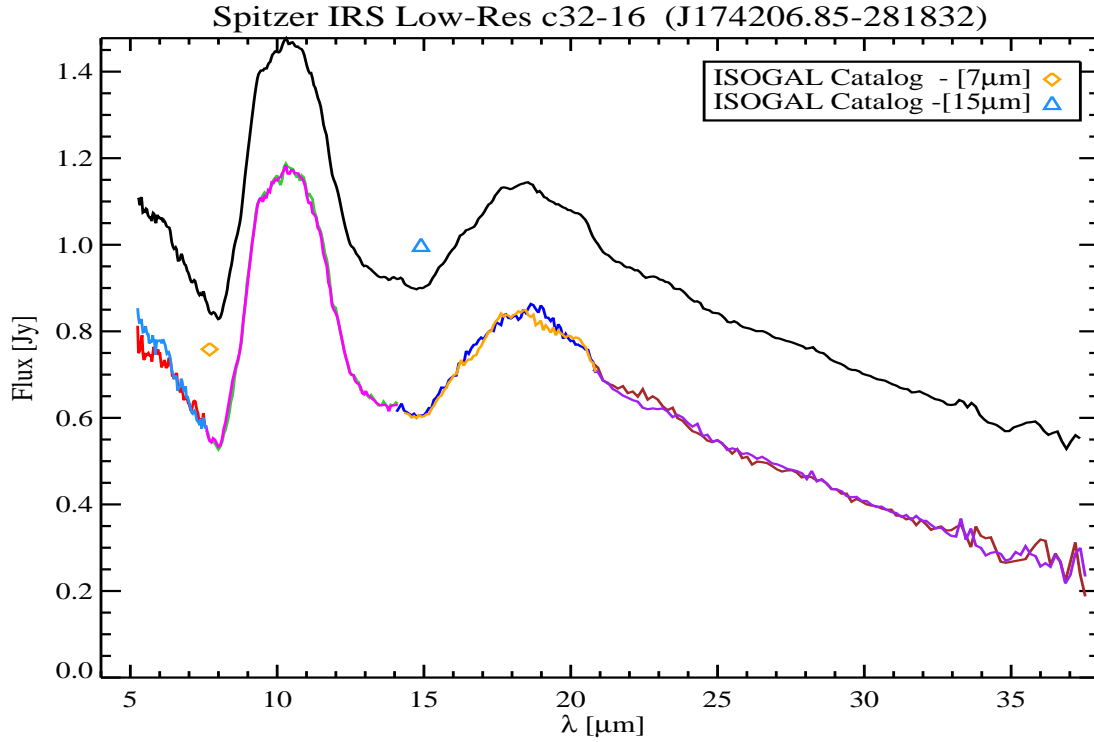


Figure G.31: **(c32-16)** This is the final spectrum of c32-16. Figure G.32 indicates the number of sources that have been extracted in each nod and module. There was a slight mismatch between the two nods of SL1 and SL2 modules which were removed by modifying the point spread function (central position and FWHM). After extraction there was no significant residual left to mask. The background for this source is properly corrected through modeling. Finally, we scaled all modules with respect to the SL1 module using the following scale factors, in order to eliminate the mismatch between modules and obtain the continuum shown here.

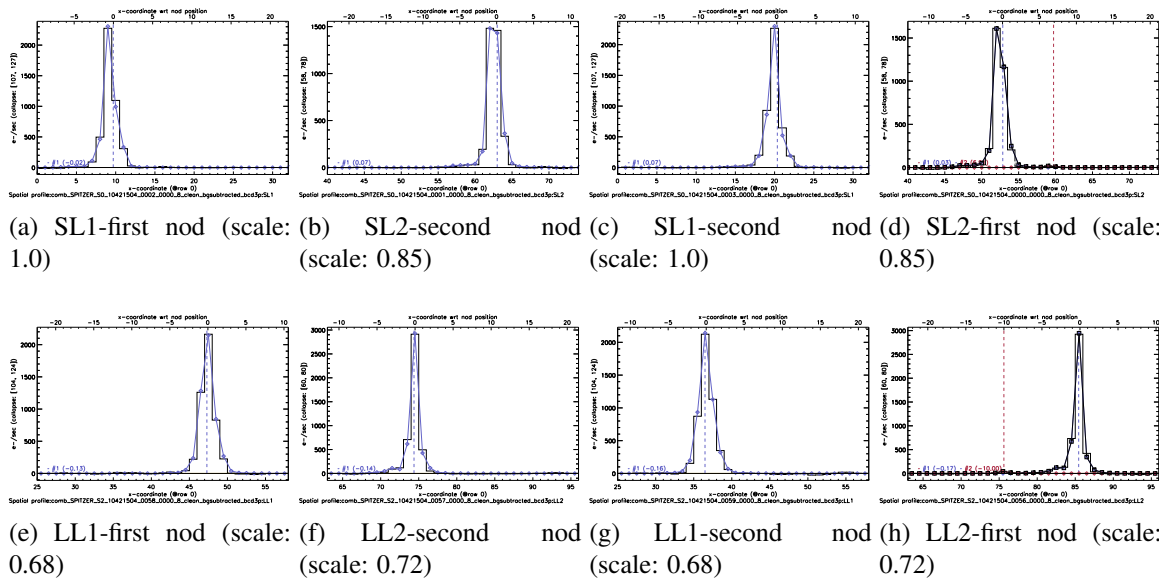


Figure G.32: SL and LL modules spatial profiles after subtraction of the background

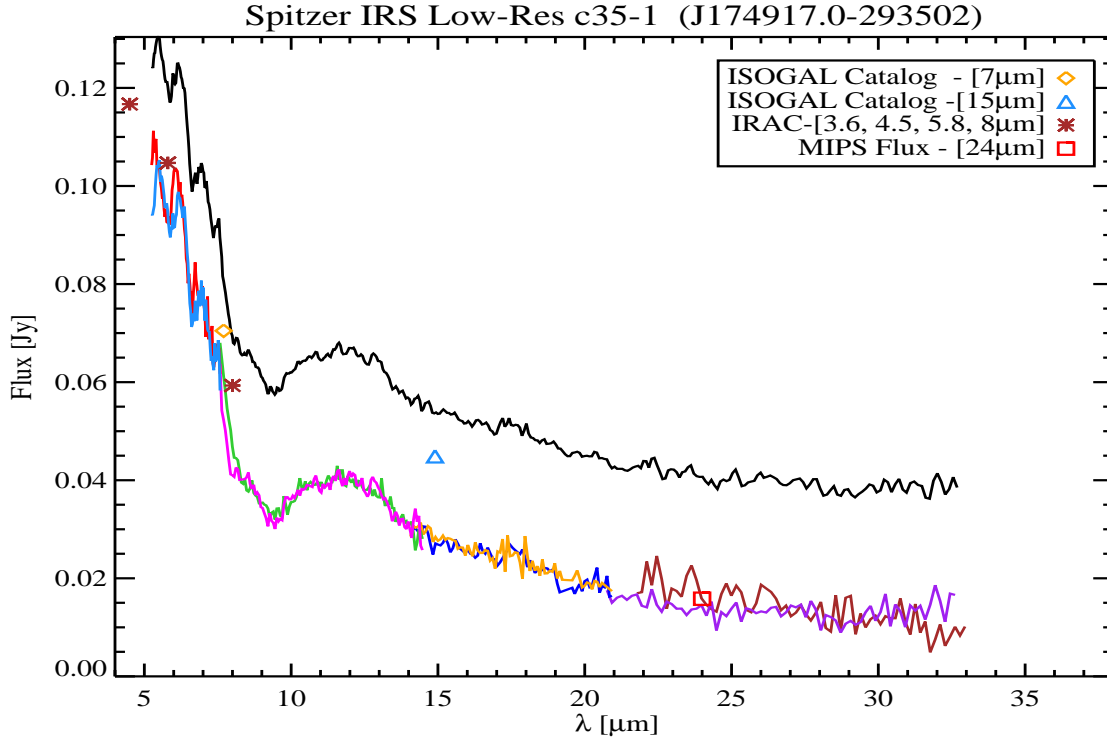


Figure G.33: (**c35-1**) This is the final spectrum of c35-1. Figure G.34 indicates the number of sources that have been extracted in each nod and module. After extraction the sharp and unrealistic residual features were masked (e.g. 19.5- μm). The strong and variable background with prominent PAH feature was properly modeled and corrected. Finally, we scaled long low modules with respect to the short low modules using the following scale factors, in order to eliminate the mismatch between them and obtain the continuum shown here.

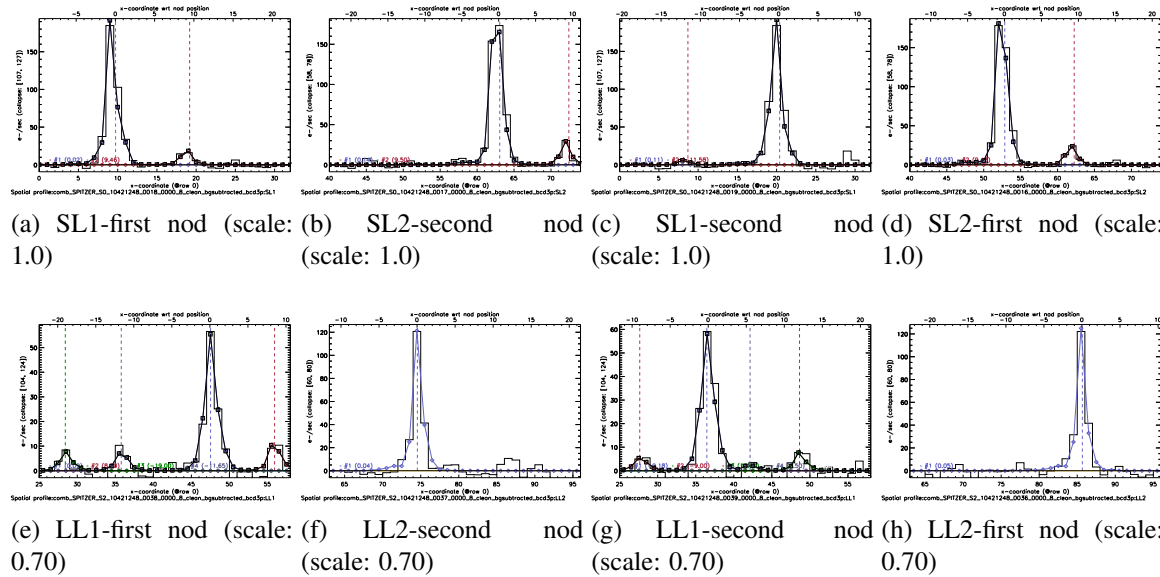


Figure G.34: SL and LL modules spatial profiles after subtraction of the background

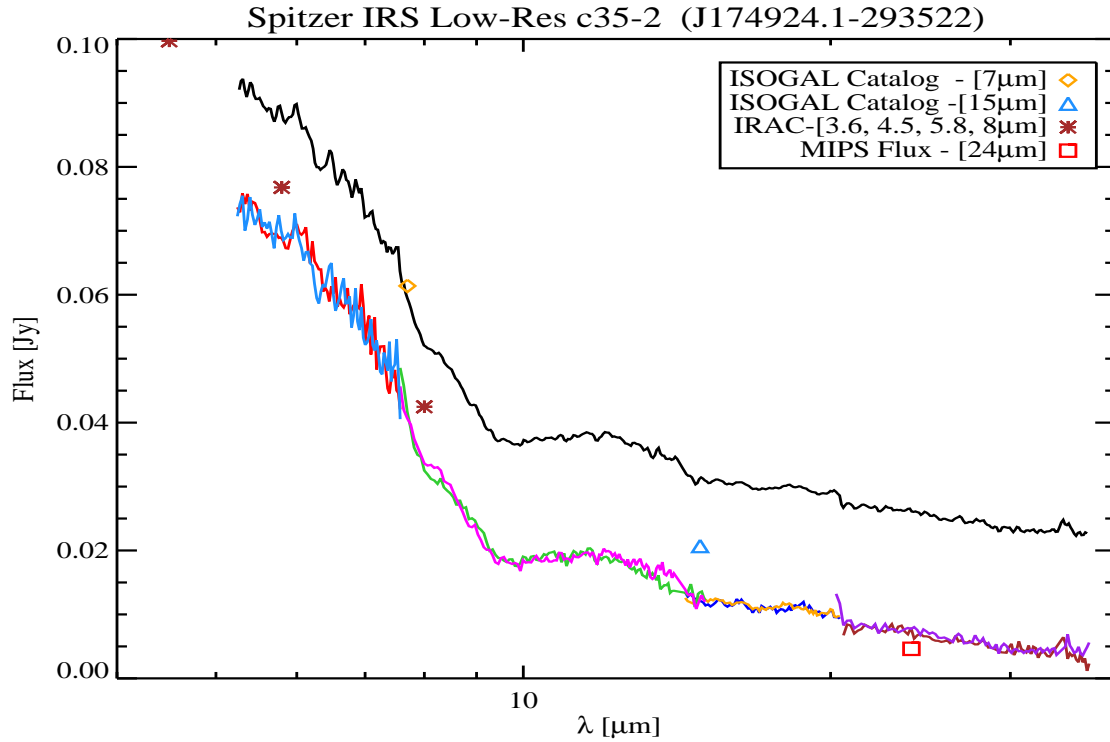


Figure G.35: (**c35-2**) This is the final spectrum of c35-2. Figure G.36 indicates the number of sources that have been extracted in each nod and module. After extraction the sharp and unrealistic residual features were masked (e.g. 19.5- μ m). The strong and variable background with prominent PAH feature was properly modeled and corrected. Finally, we scaled long low modules with respect to the short low modules using the following scale factors, in order to eliminate the mismatch between them and obtain the continuum shown here.

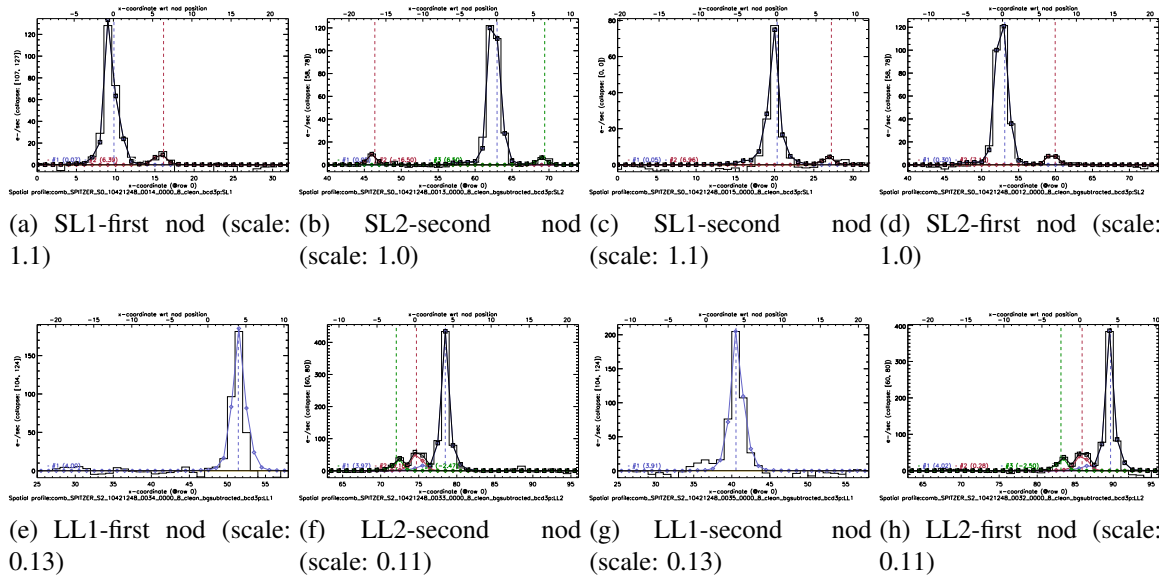


Figure G.36: SL and LL modules spatial profiles after subtraction of the background

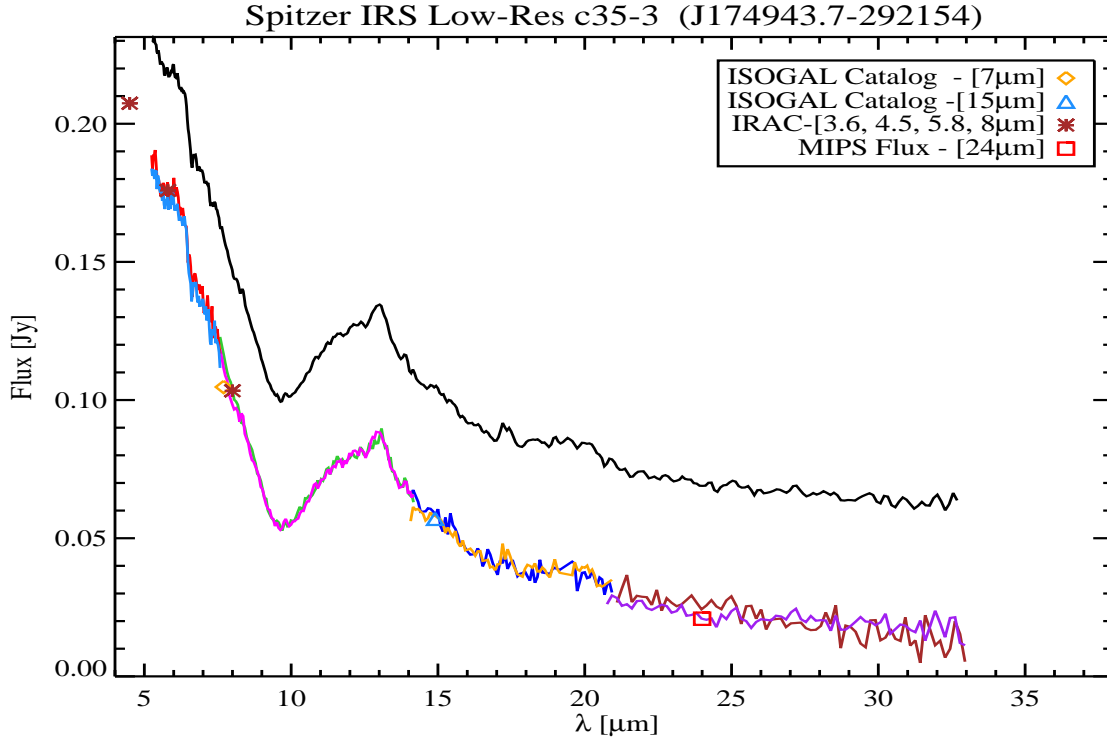


Figure G.37: (**c35-3**) This is the final spectrum of c35-3. Figure G.38 indicates the number of sources that have been extracted in each nod and module. After extraction the residual features were masked (e.g. 19.5- μ m). The strong and variable background with prominent PAH feature was properly modeled and corrected. Finally, we scaled long low modules with respect to the short low modules using the following scale factors, in order to eliminate the mismatch between modules and obtain the continuum shown here.

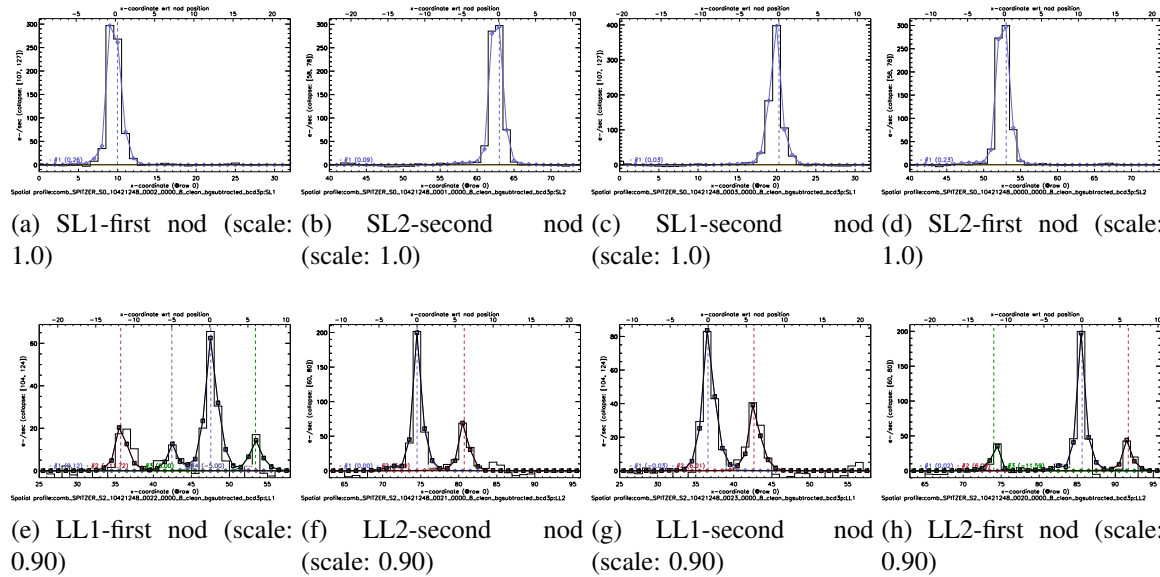


Figure G.38: SL and LL modules spatial profiles after subtraction of the background

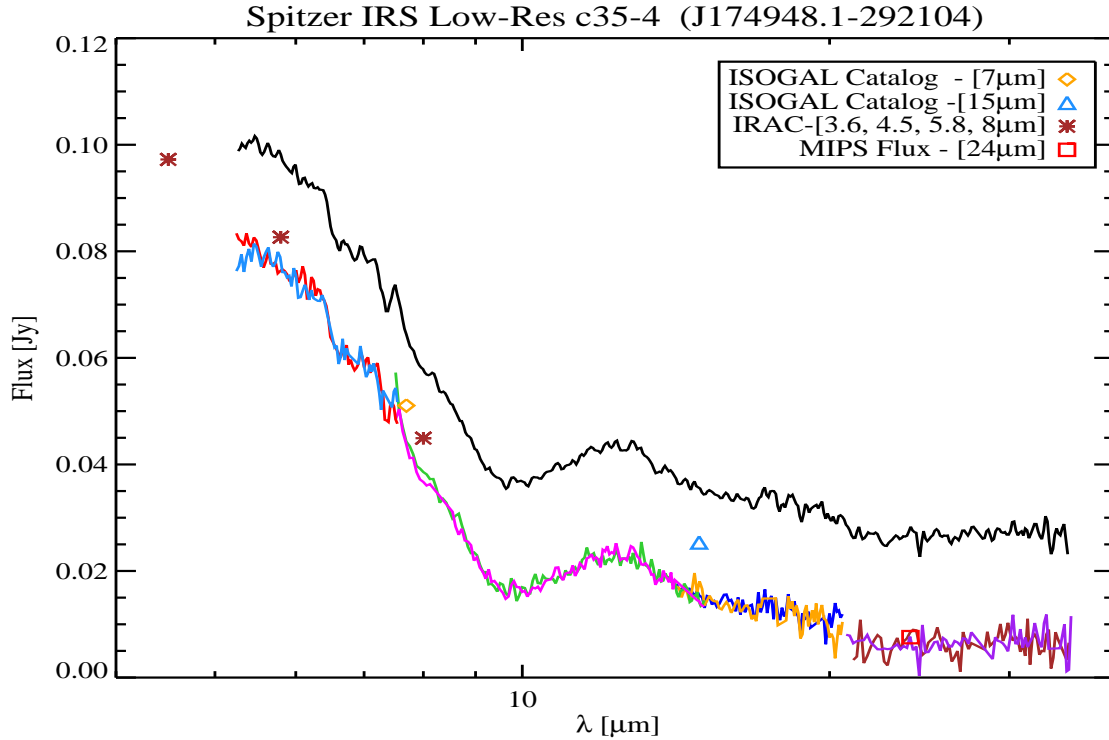


Figure G.39: **(c35-4)** This is the final spectrum of c35-4. Figure G.40 indicates the number of sources that have been extracted in each nod and module. There was a slight mismatch between the two nods of LL2 module which was removed by modifying the point spread function (central position and FWHM). After extraction the residual features were masked (e.g. 19.5- μm). The strong and variable background with prominent PAH feature was properly modeled and corrected. Finally, we scaled long low modules with respect to the short low modules using the following scale factors, in order to eliminate the mismatch between modules and obtain the continuum shown here.

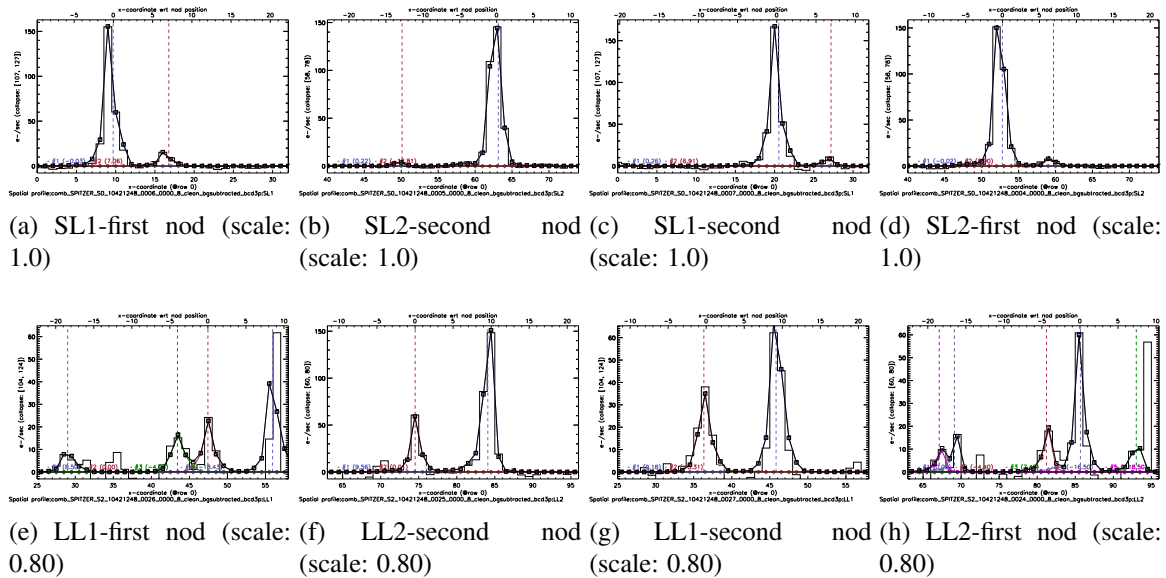


Figure G.40: SL and LL modules spatial profiles after subtraction of the background

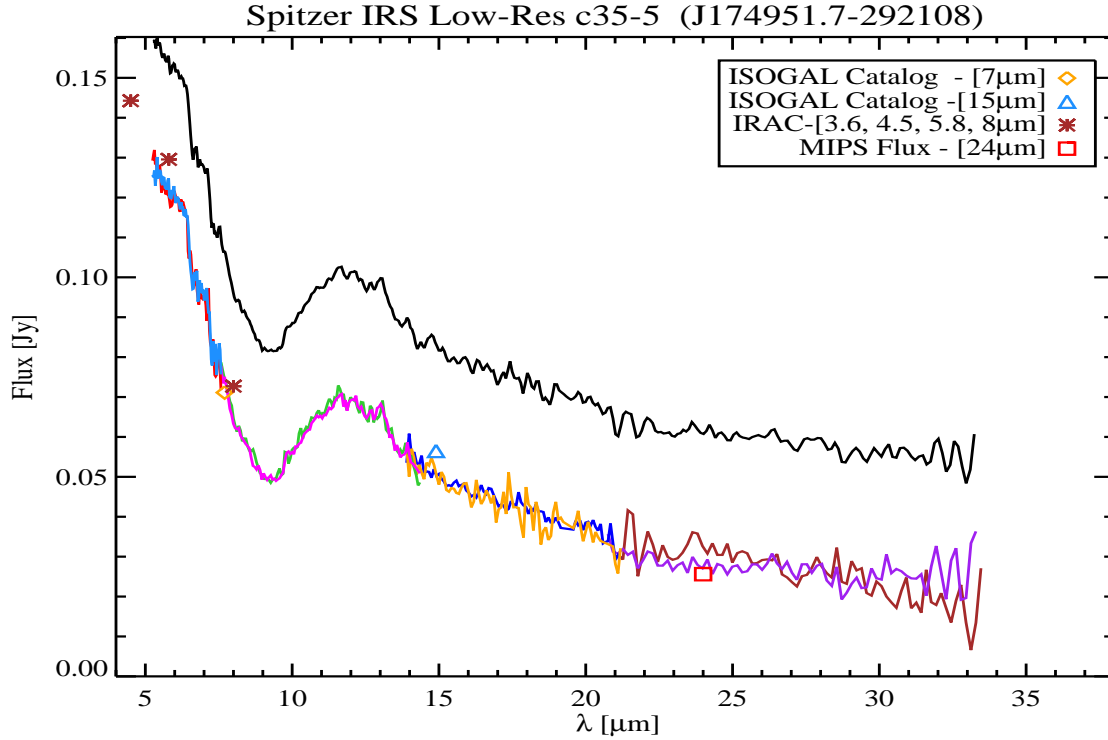


Figure G.41: (**c35-5**) This is the final spectrum of c35-5. Figure G.42 indicates the number of sources that have been extracted in each nod and module. After extraction, sharp residual features were masked (e.g. 19.5- μ m). The strong and variable background with prominent PAH feature was properly modeled and corrected. Finally, we scaled long low modules with respect to the short low modules using the following scale factors, in order to eliminate the mismatch between modules and obtain the continuum shown here.

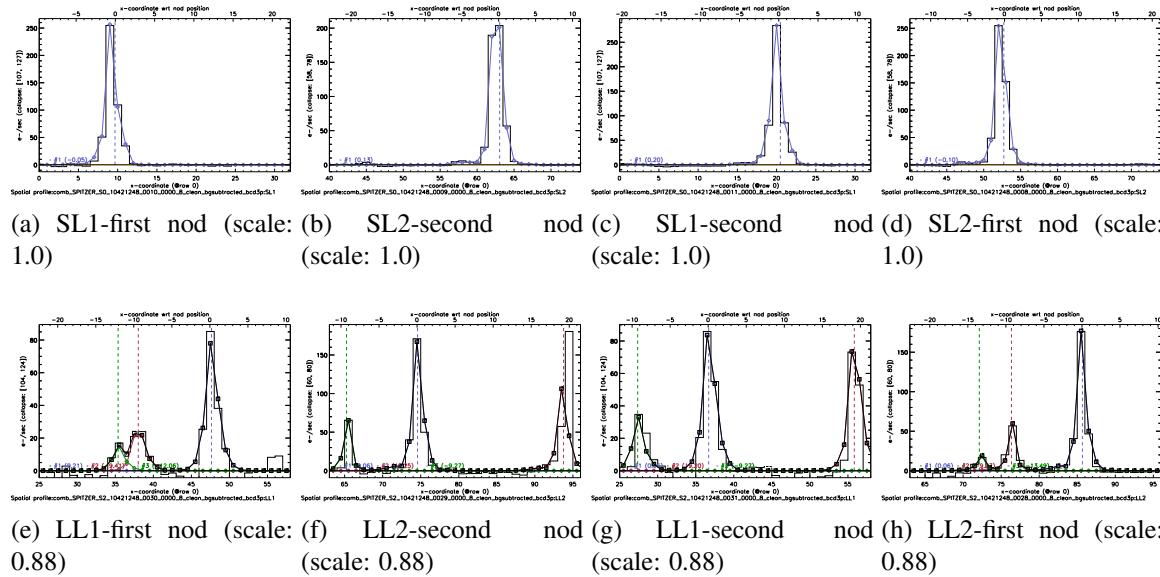


Figure G.42: SL and LL modules spatial profiles after subtraction of the background

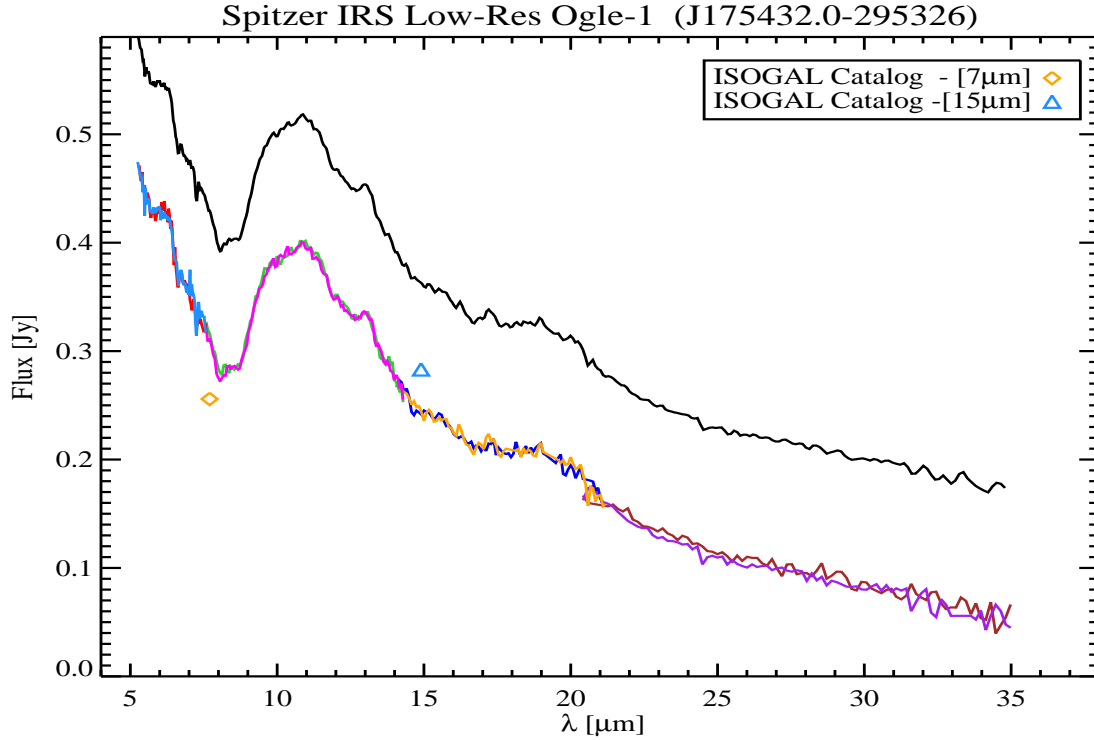


Figure G.43: **(Ogle-1)** This is the final spectrum of Ogle-1. Figure G.44 indicates the number of sources that have been extracted in each nod and module. After extraction the sharp and unrealistic residual features were masked (e.g. 19.5- μm). The strong and variable background for this source was properly corrected through modeling. Finally, we scaled long low modules with respect to the short low modules using the following scale factors, in order to eliminate the mismatch between modules and obtain the continuum shown here.

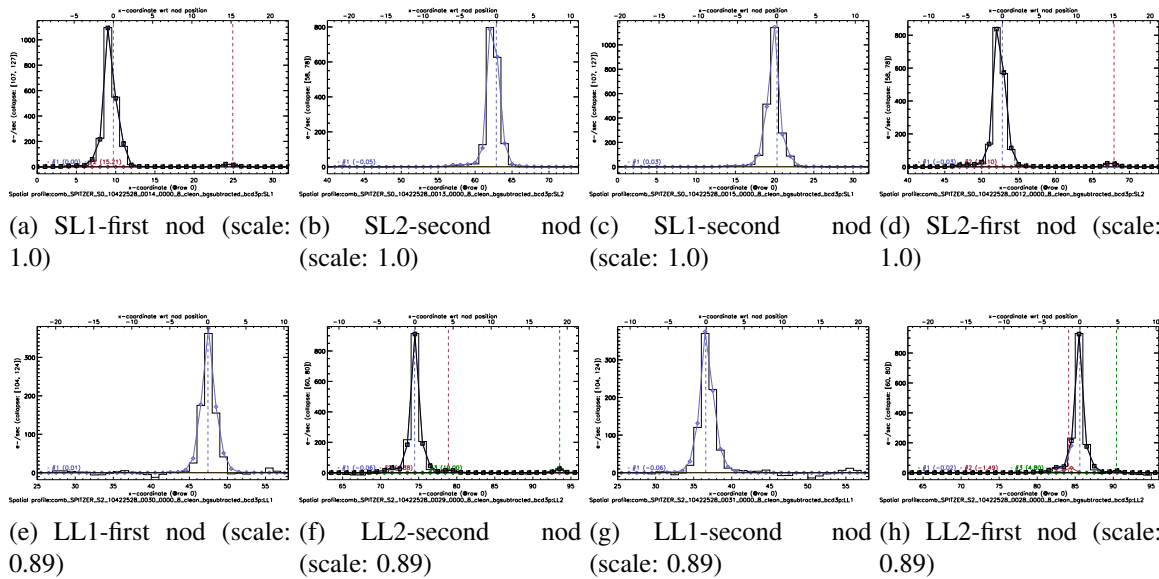


Figure G.44: SL and LL modules spatial profiles after subtraction of the background

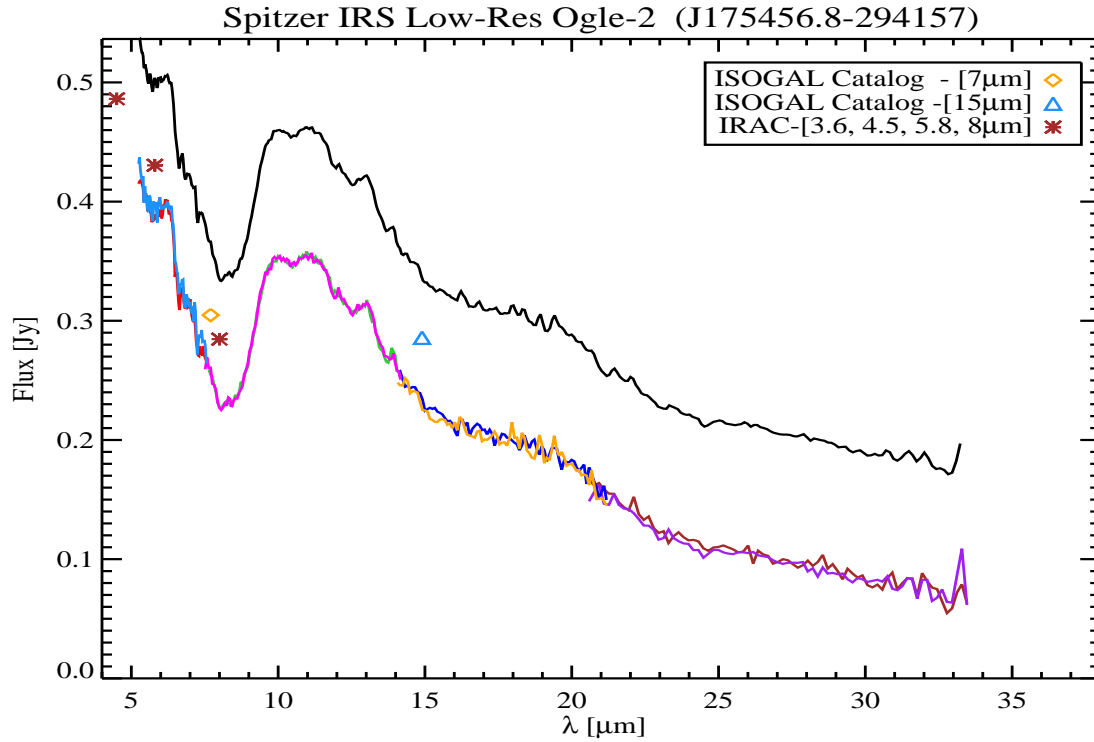


Figure G.45: (**Ogle-2**) This is the final spectrum of Ogle-2. Figure G.46 indicates the number of sources that have been extracted in each nod and module. After extraction the residual features were masked (e.g. 19.5- μm). The strong and variable background for this source was properly corrected through modeling. Finally, we scaled long low modules with respect to the short low modules using the following scale factors, in order to eliminate the mismatch between modules and obtain the continuum shown here.

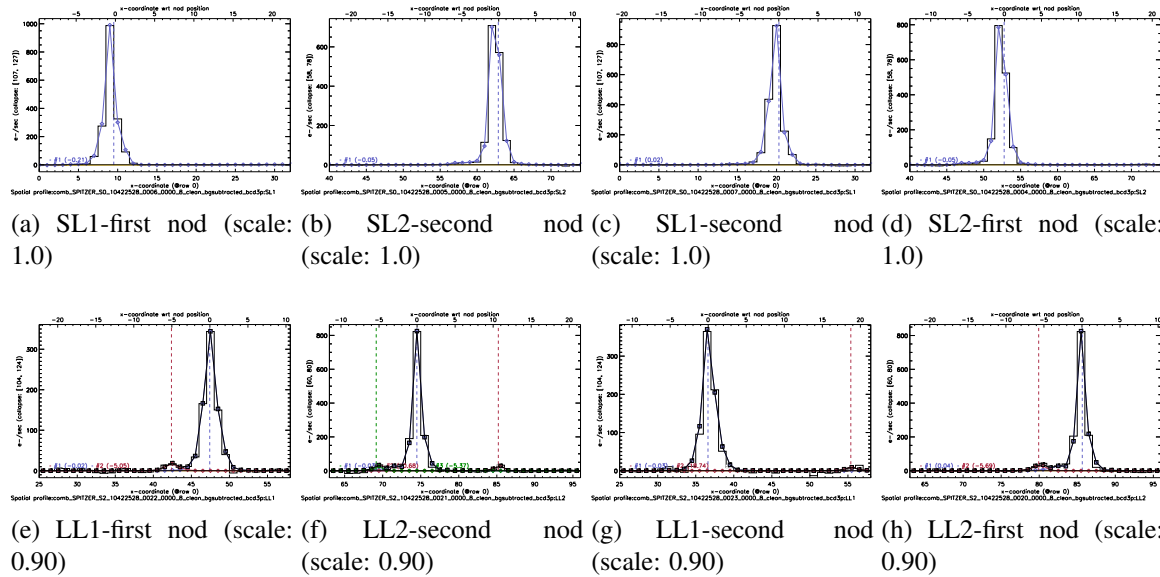


Figure G.46: SL and LL modules spatial profiles after subtraction of the background

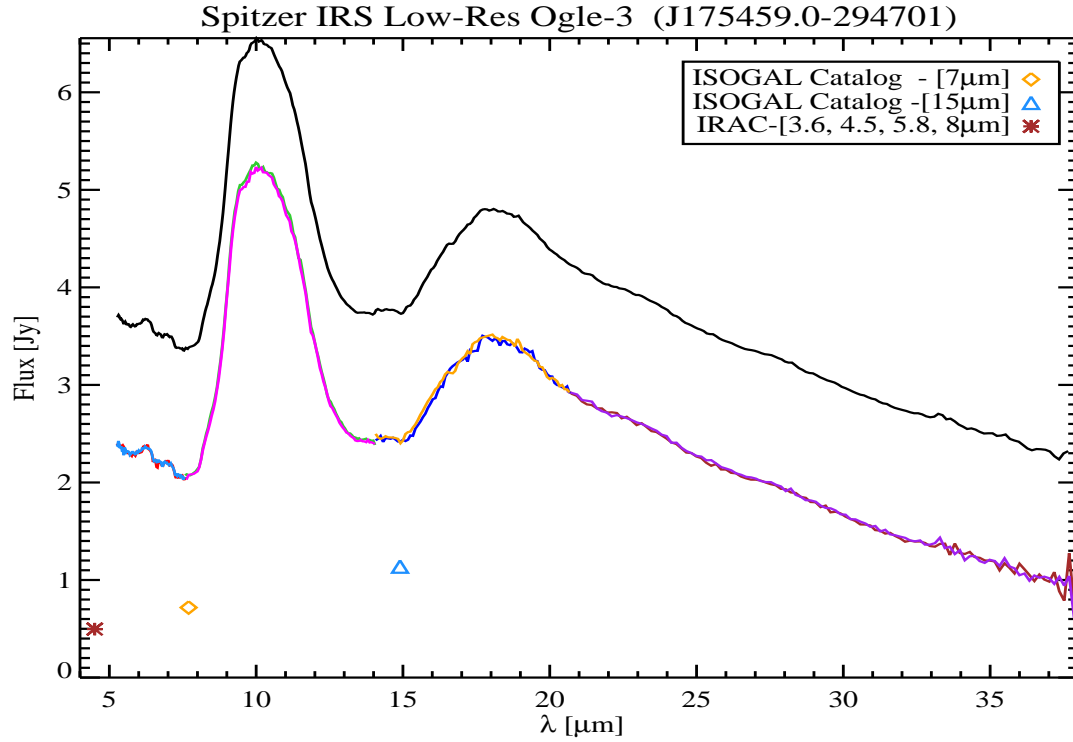


Figure G.47: (**Ogle-3**) This is the final spectrum of Ogle-3. Figure G.48 indicates the number of sources that have been extracted in each nod and module. After extraction the residual features were masked (e.g. 16.5- μm). The strong and variable background for this source was properly corrected through modeling. The only exception was the first nod of LL1 module which indicated strong background residuals, therefore we have also subtracted a constant offset (polynomial order zero) from the background after it has already been corrected through modeling. In this particular case, there was no mismatch between the modules therefore the continuum shown here was obtained without any further scaling.

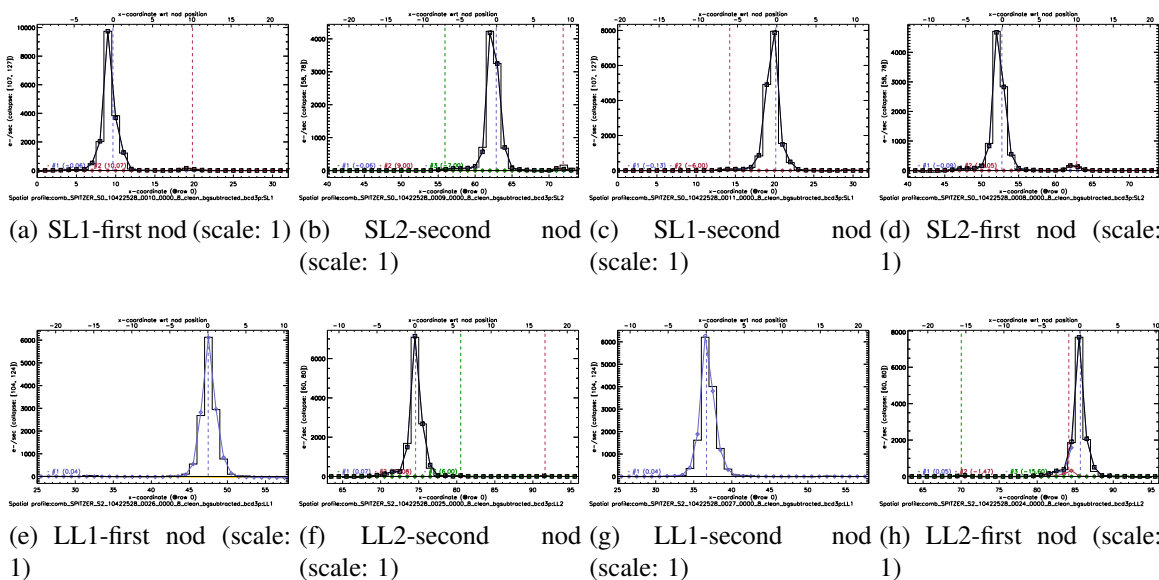


Figure G.48: SL and LL modules spatial profiles after subtraction of the background

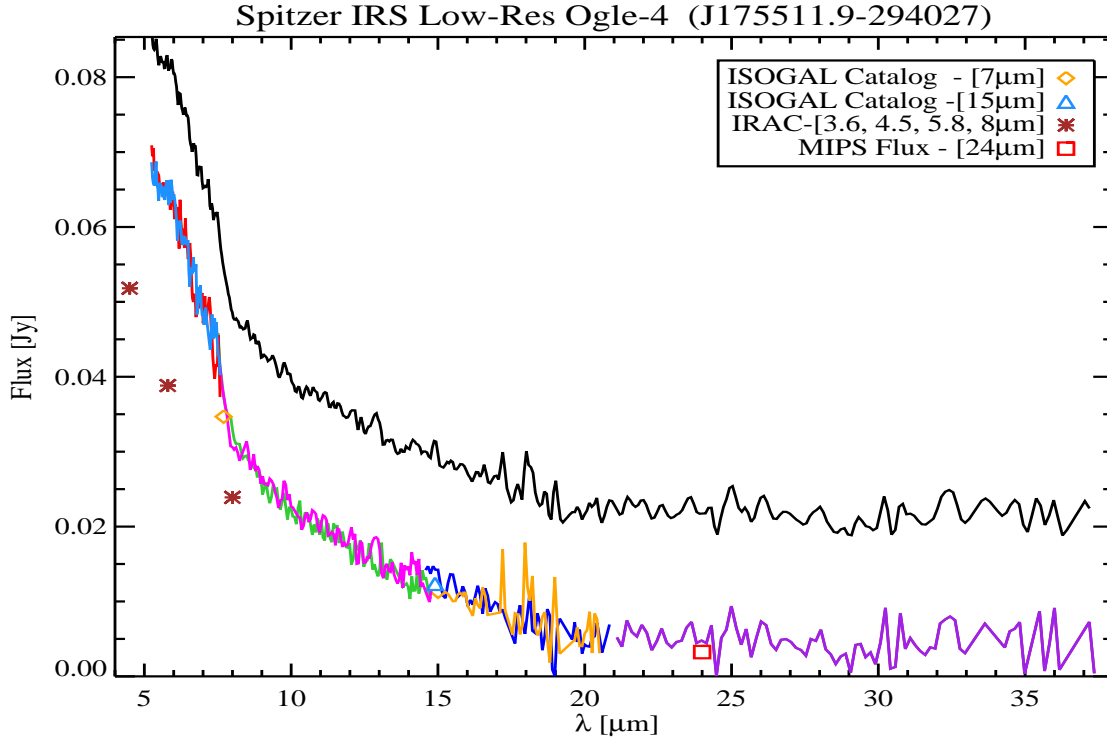


Figure G.49: **(Ogle-4)** This is the final spectrum of Ogle-4. Figure G.50 indicates the number of sources that have been extracted in each nod and module. After extraction, residual features were masked (e.g. 19.5- μm). The strong and variable background for this source was properly corrected through modeling. Finally, we scaled long low modules with respect to the short low modules using the following scale factors, in order to eliminate the mismatch between modules and obtain the continuum shown here.

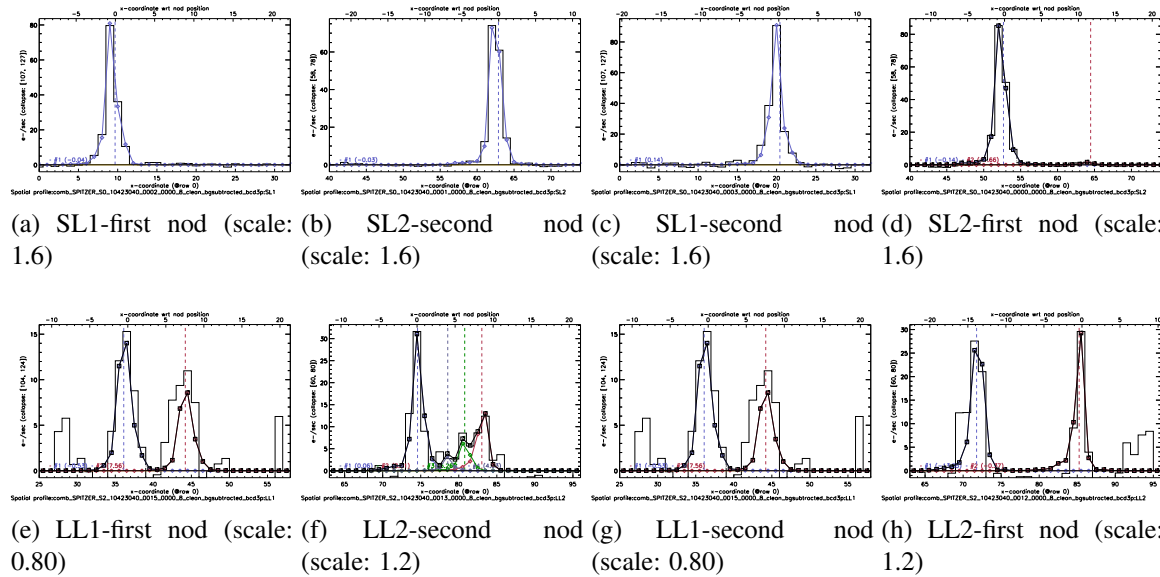


Figure G.50: SL and LL modules spatial profiles after subtraction of the background

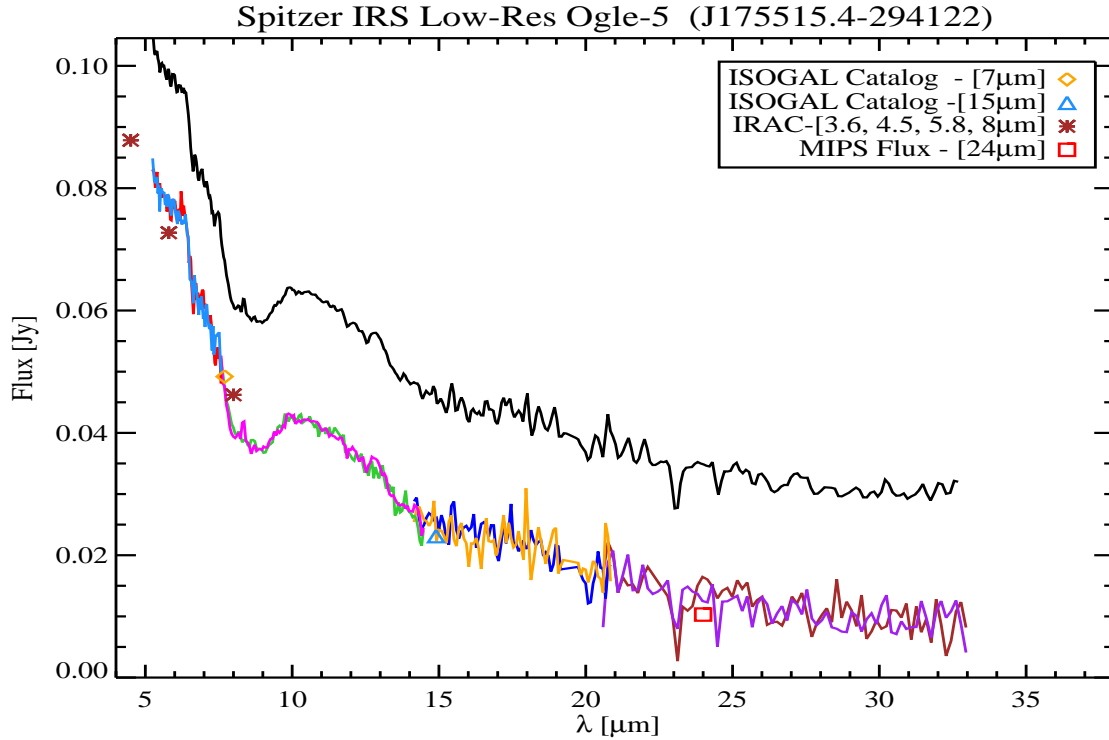


Figure G.51: (**Ogle-5**) This is final spectrum of Ogle-5. Figure G.52 indicates the number of sources that have been extracted in each nod and module. After extraction the sharp and unrealistic residual features were masked (e.g. 18- μ m). The strong and variable background for this source was properly corrected through modeling. In this particular case, there was no mismatch between the modules therefore the continuum shown here was obtained without any further scaling.

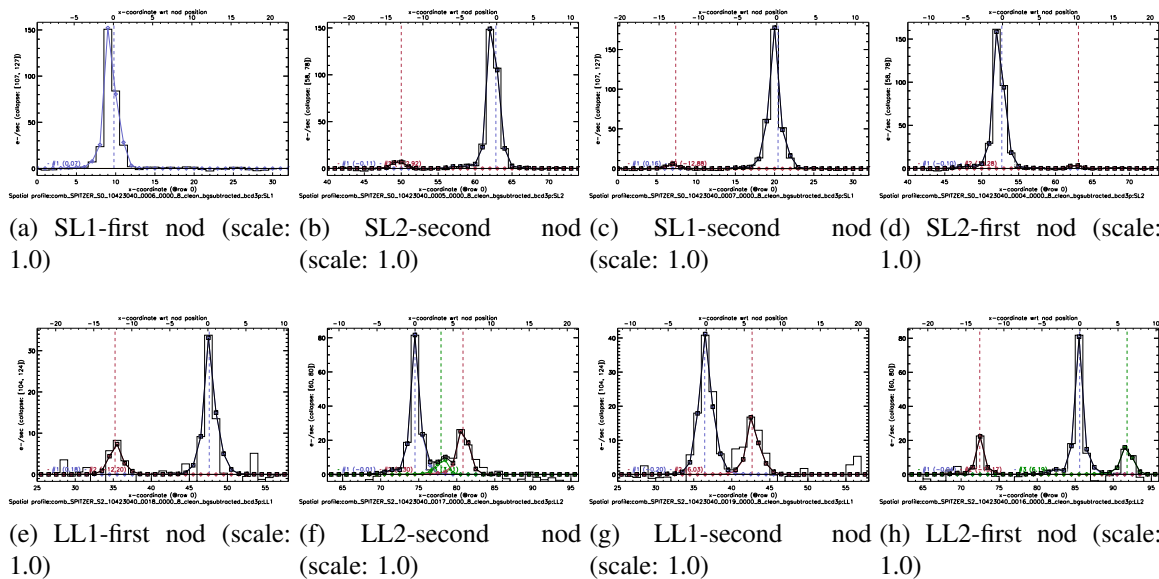


Figure G.52: SL and LL modules spatial profiles after subtraction of the background

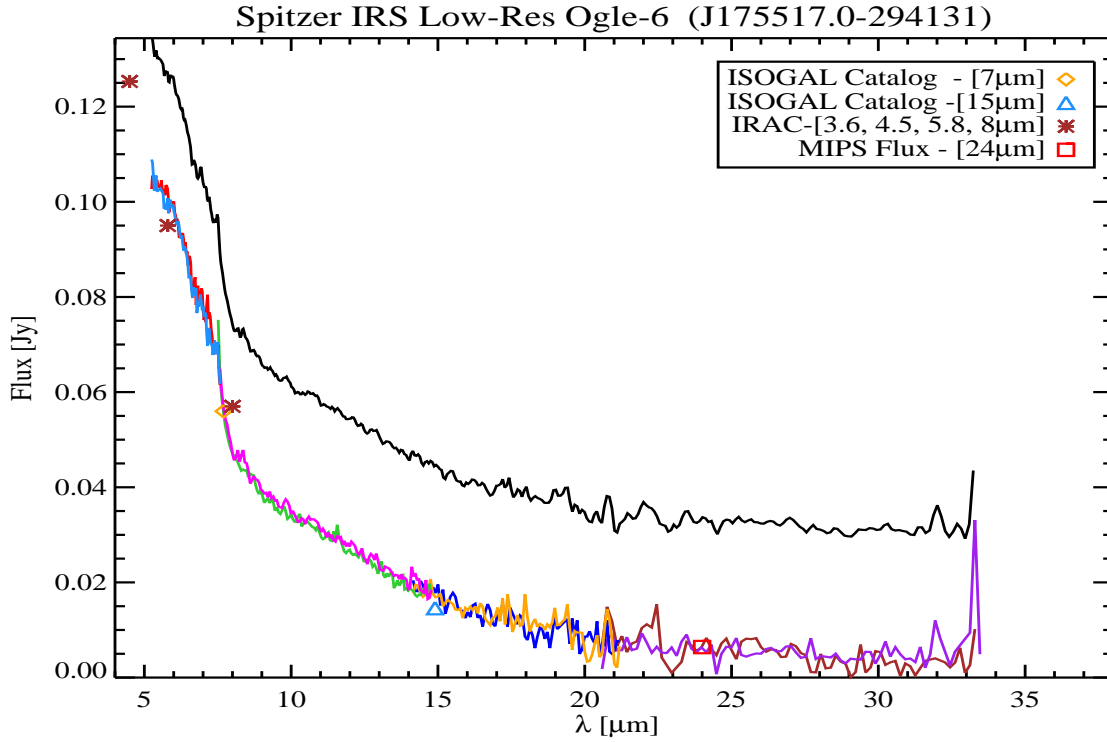


Figure G.53: (**Ogle-6**) This is the final spectrum of Ogle-6. Figure G.54 indicates the number of sources that have been extracted in each nod and module. After extraction the sharp and unrealistic residual features were masked (e.g. 19.5- μm). The background for this source is similar to other sources in field Ogle which was properly corrected through modeling. Finally, we scaled long low modules with respect to the short low module using the following scale factors, in order to eliminate the mismatch between modules and obtain the continuum shown here.

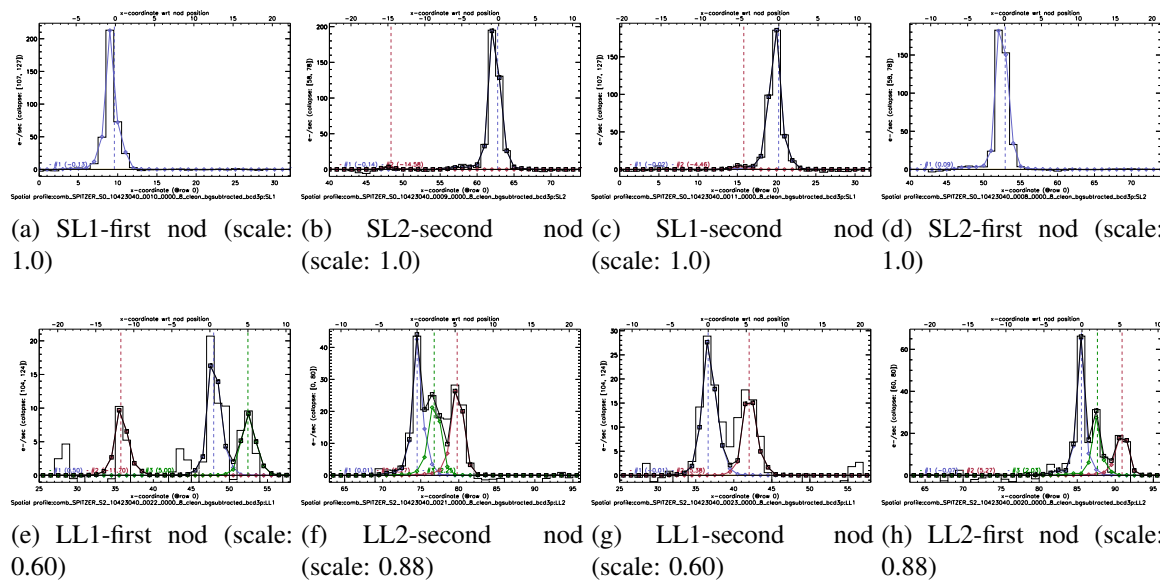


Figure G.54: SL and LL modules spatial profiles after subtraction of the background

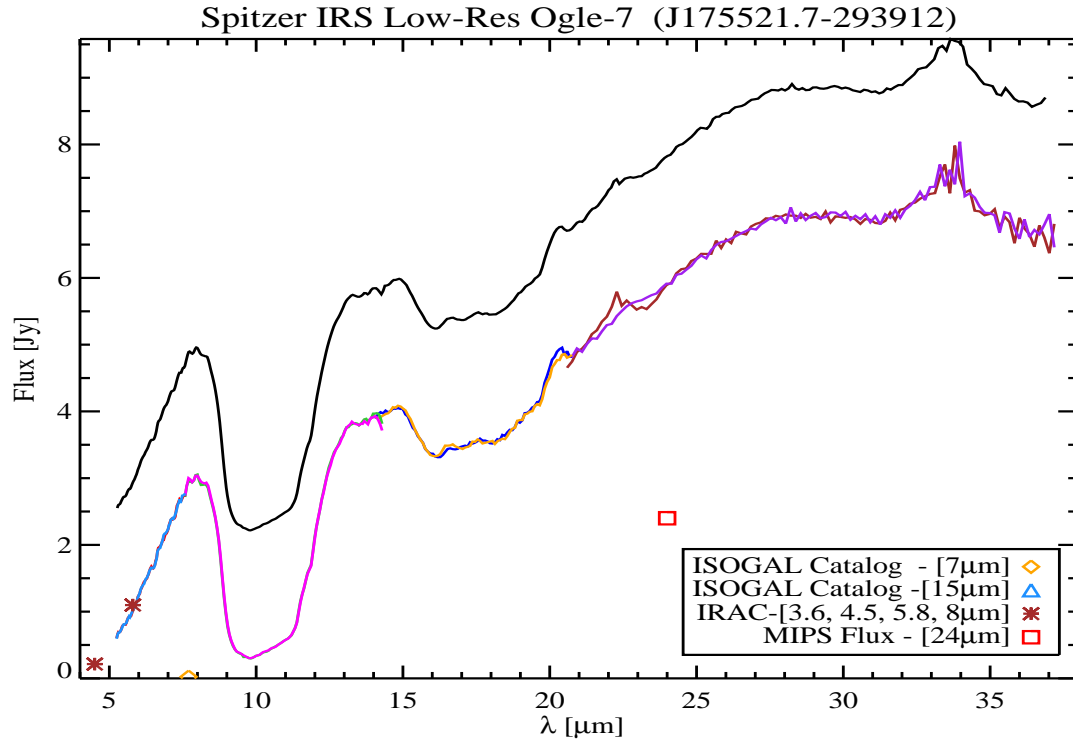


Figure G.55: (**Ogle-7**) This is the final spectrum of Ogle-7. Figure G.56 indicates the number of sources that have been extracted in each nod and module. After extraction, residual features were masked (e.g. 16.5- μm). The strong and variable background for this source was properly corrected through modeling. Finally, we scaled all modules with respect to the SL1 module using the following scale factors, in order to eliminate the mismatch between modules and obtain the continuum shown here.

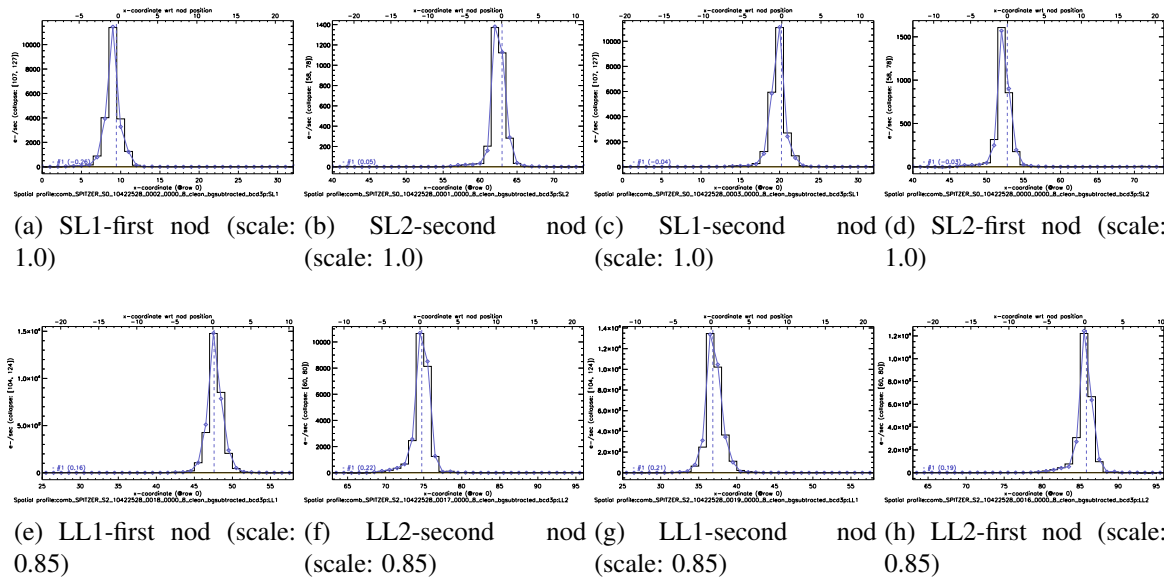


Figure G.56: SL and LL modules spatial profiles after subtraction of the background

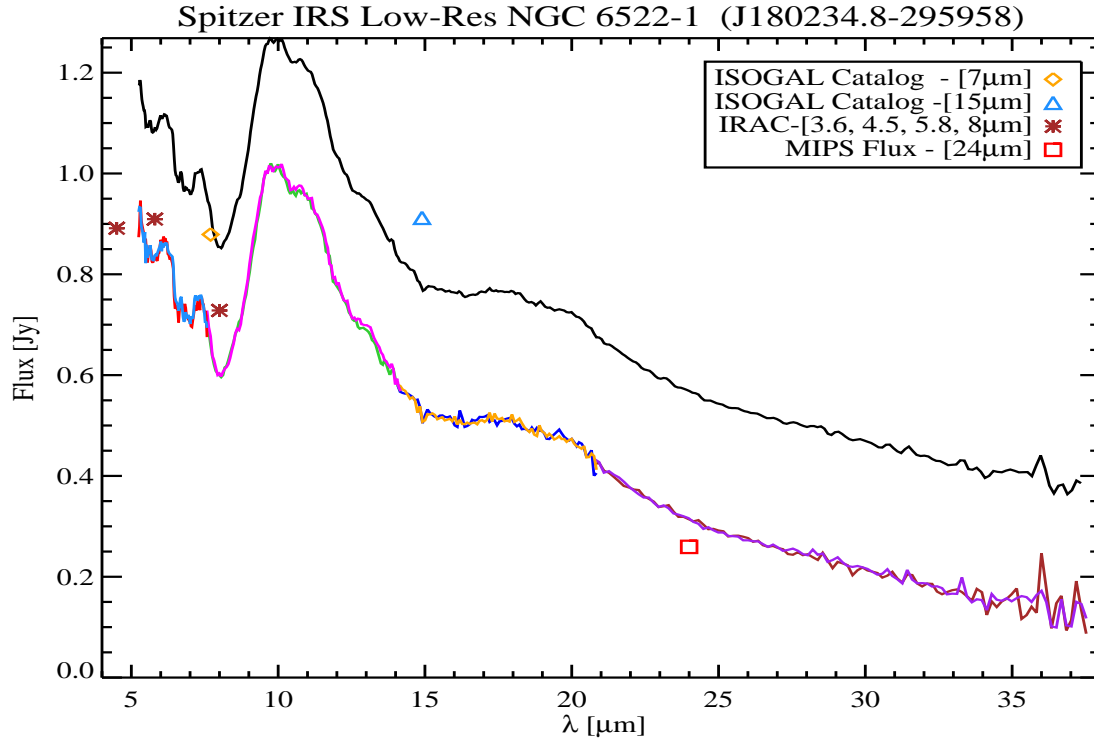


Figure G.57: (**NGC 6522-1**) This is the final spectrum of NGC 6522-1. Figure G.58 indicates the number of sources that have been extracted in each nod and module. After extraction the sharp and unrealistic residual features were masked (e.g. 19.5- μm). The background for this source is strong but it shows slightly less variation over the observed wavelength range, compared to other fields. This background was properly corrected through modeling. Finally, we scaled long low modules with respect to the short low modules using the following scale factors, in order to eliminate the mismatch between them and obtain the continuum shown here.

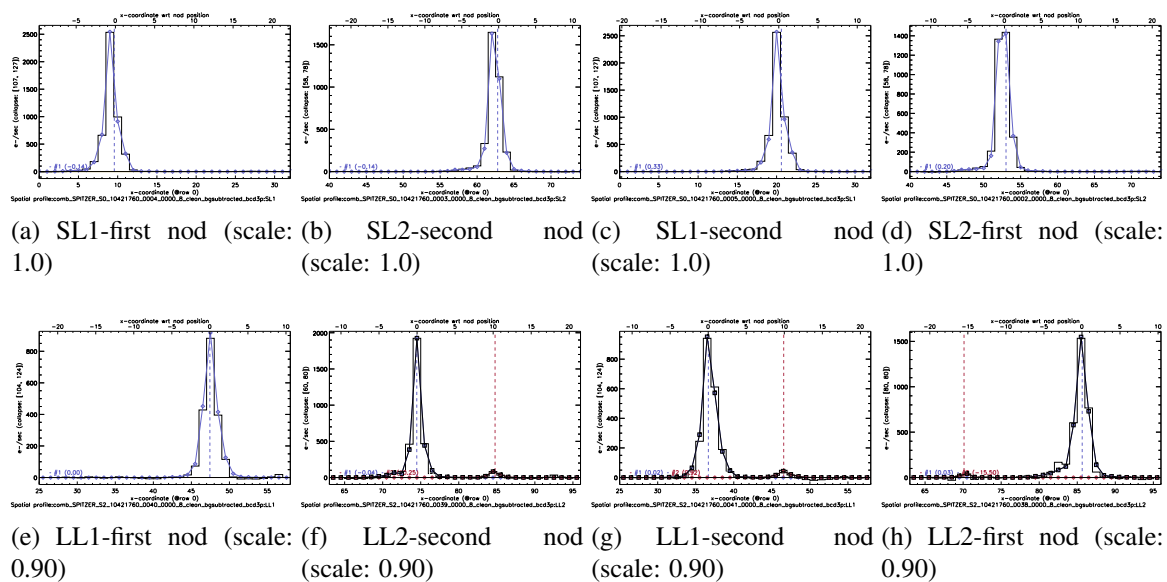


Figure G.58: SL and LL modules spatial profiles after subtraction of the background

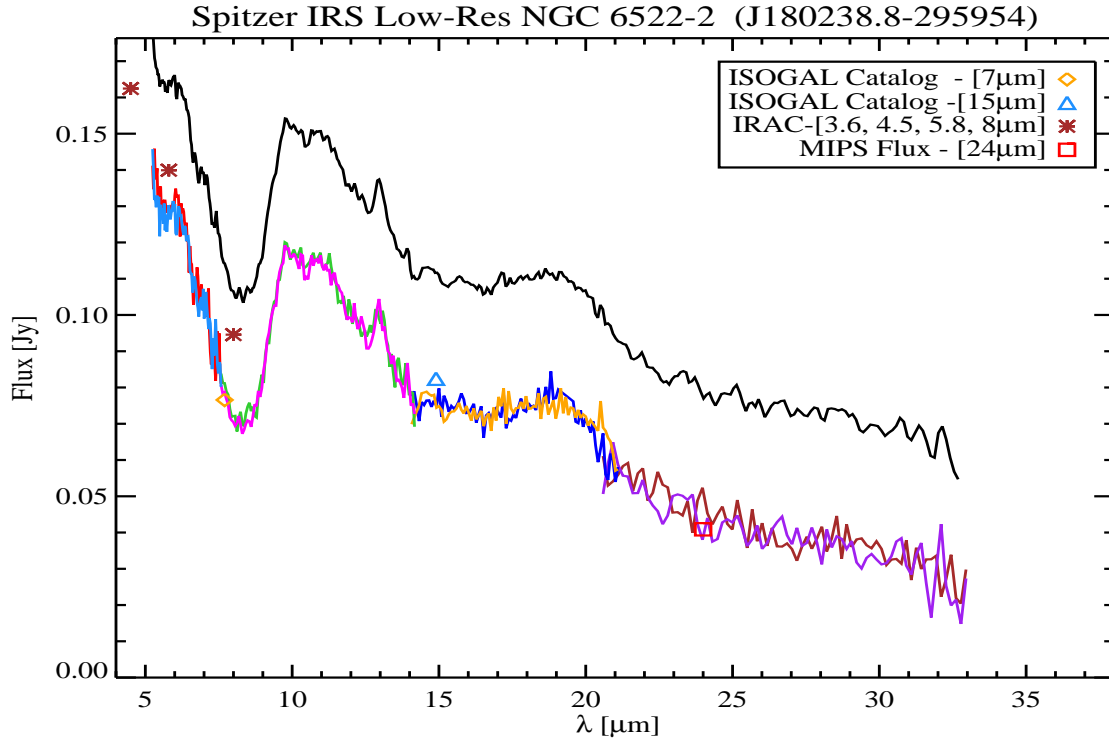


Figure G.59: (NGC 6522-2) This is the final spectrum of NGC 6522-2. Figure G.60 indicates the number of sources that have been extracted in each nod and module. There was a slight mismatch between the two nods of SL1 module which was removed by modifying the point spread function (central position and FWHM). After extraction the sharp and unrealistic residual features were masked (e.g. 19.5- μ m). This source is located in the field covering NGC6522 and its background is similar to that of NGC 6522-1 therefore it was similarly corrected through modeling. Finally, we scaled long low modules with respect to the short low modules using the following scale factors, in order to eliminate the mismatch between them and obtain the continuum shown here.

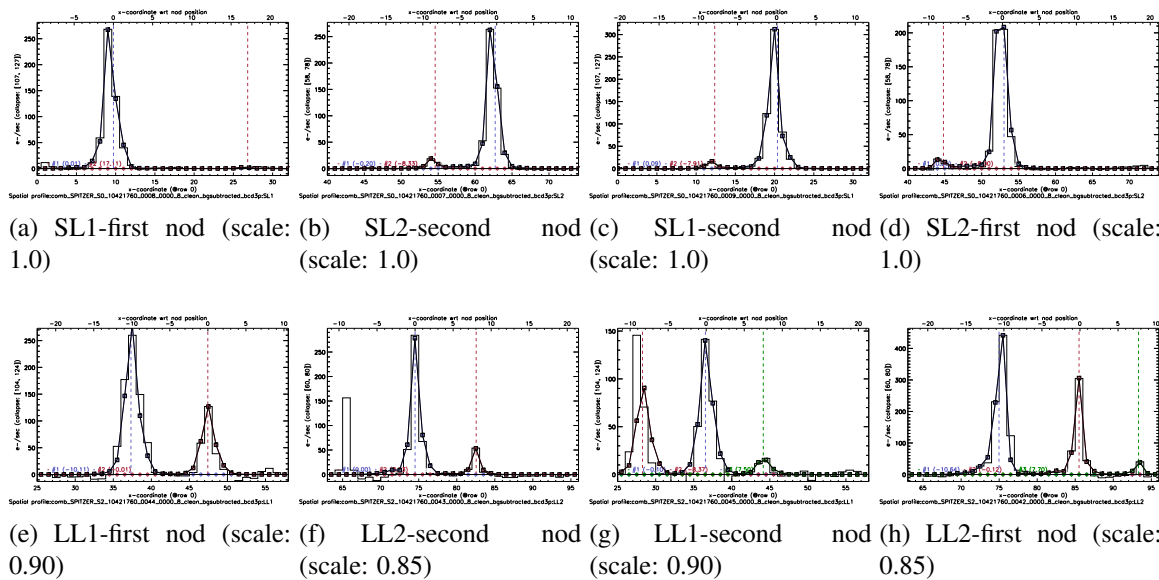


Figure G.60: SL and LL modules spatial profiles after subtraction of the background

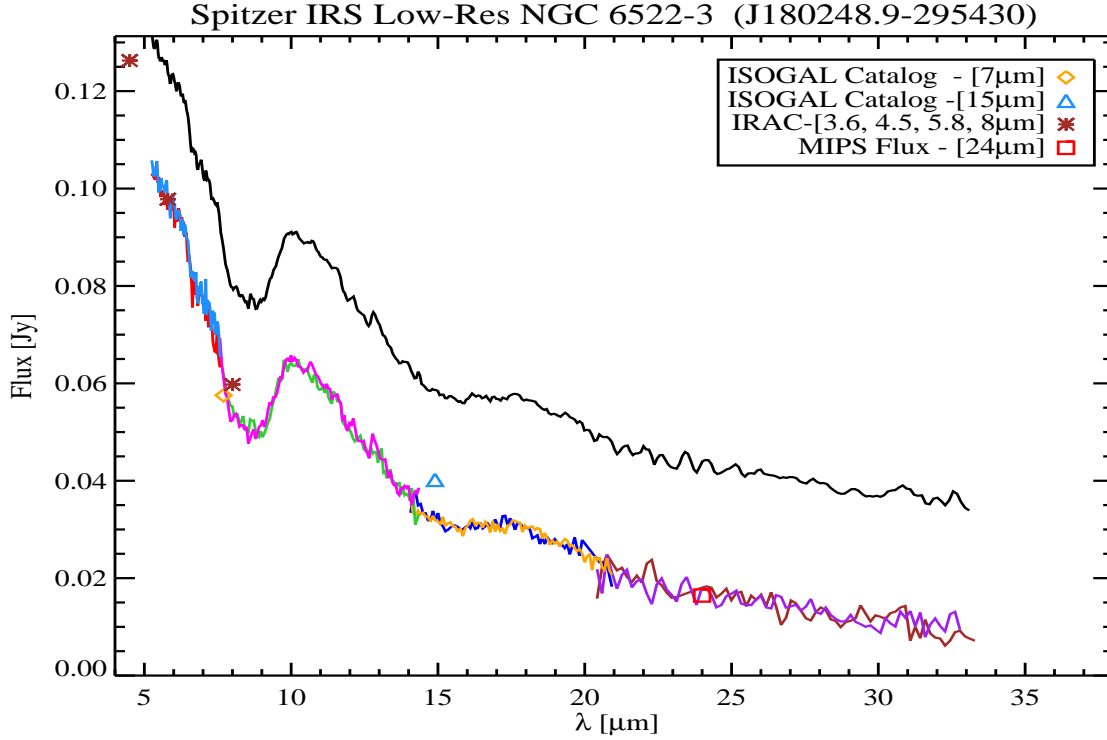


Figure G.61: (**NGC 6522-3**) This is the final spectrum of NGC 6522-3. Figure G.62 indicates the number of sources that have been extracted in each nod and module. After extraction the sharp and unrealistic residual features were masked (e.g. 20.5- μm). This source is located in the field covering NGC6522 and its background is similar to that of the rest of the field thus similarly it was corrected through modeling. Finally, we scaled long low modules with respect to the short low modules using the following scale factors, in order to eliminate the mismatch between them and obtain the continuum shown here.

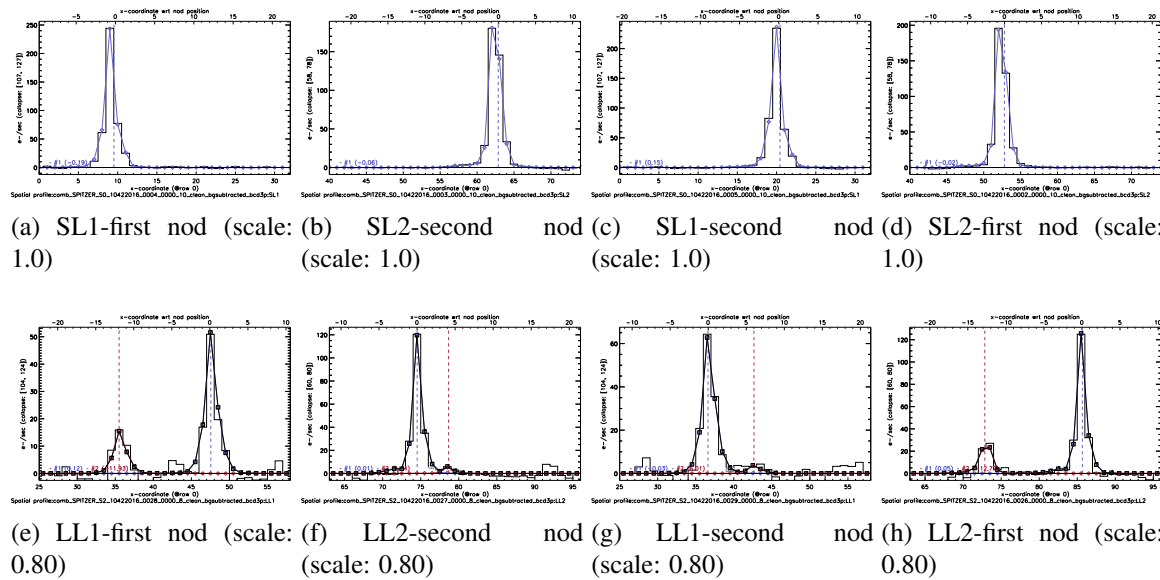


Figure G.62: SL and LL modules spatial profiles after subtraction of the background

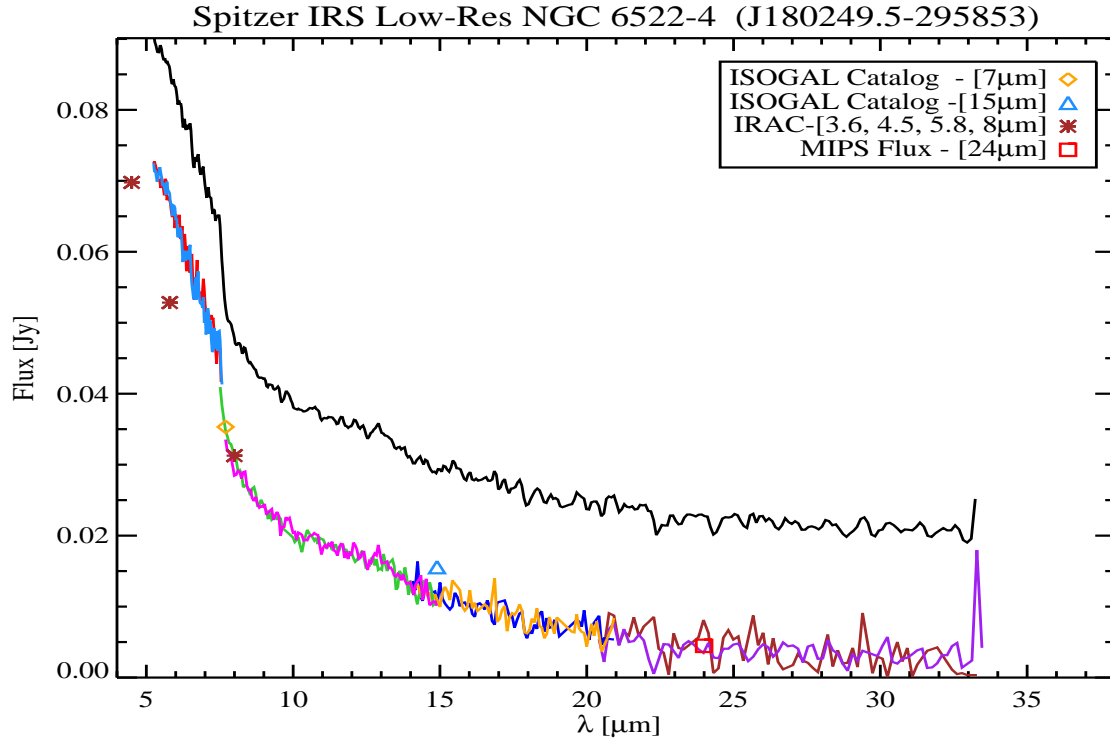


Figure G.63: **(NGC 6522-4)** This is the final spectrum of NGC 6522-4. Figure G.64 indicates the number of sources that have been extracted in each nod and module. There was a slight mismatch between the two nods of SL1 module which was removed by modifying the point spread function (central position and FWHM). After extraction, residual features were masked (e.g. 19.5- μ m). This source is located in the field covering NGC6522 and its background is similar to that of the rest of the field thus similarly it was corrected through modeling. Finally, we scaled all modules with respect to the SL1 module using the following scale factors, in order to eliminate the mismatch between them and obtain the continuum shown here.

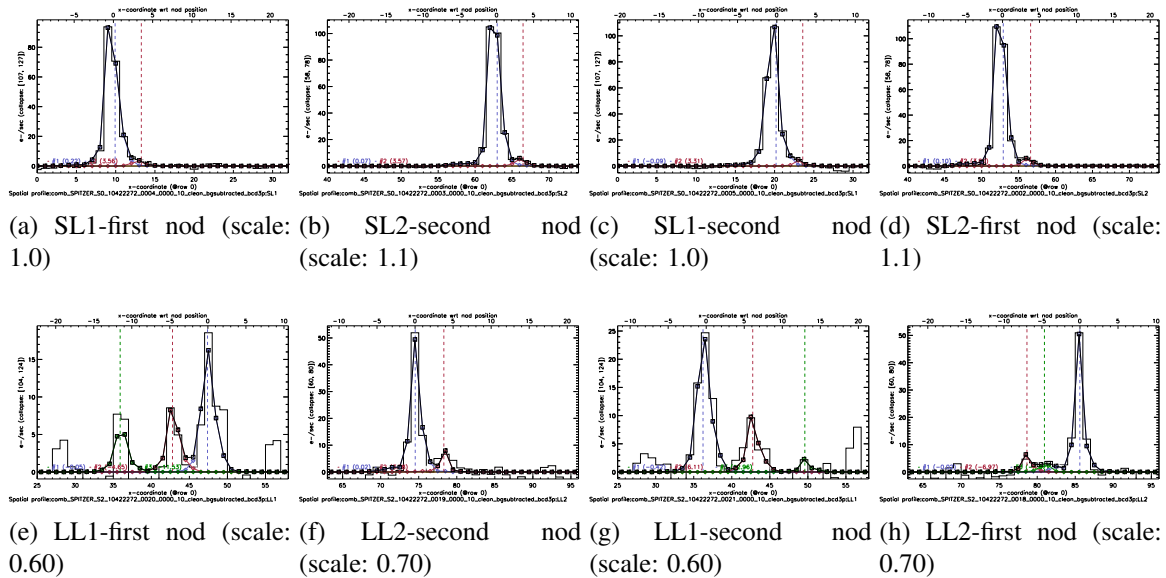


Figure G.64: SL and LL modules spatial profiles after subtraction of the background

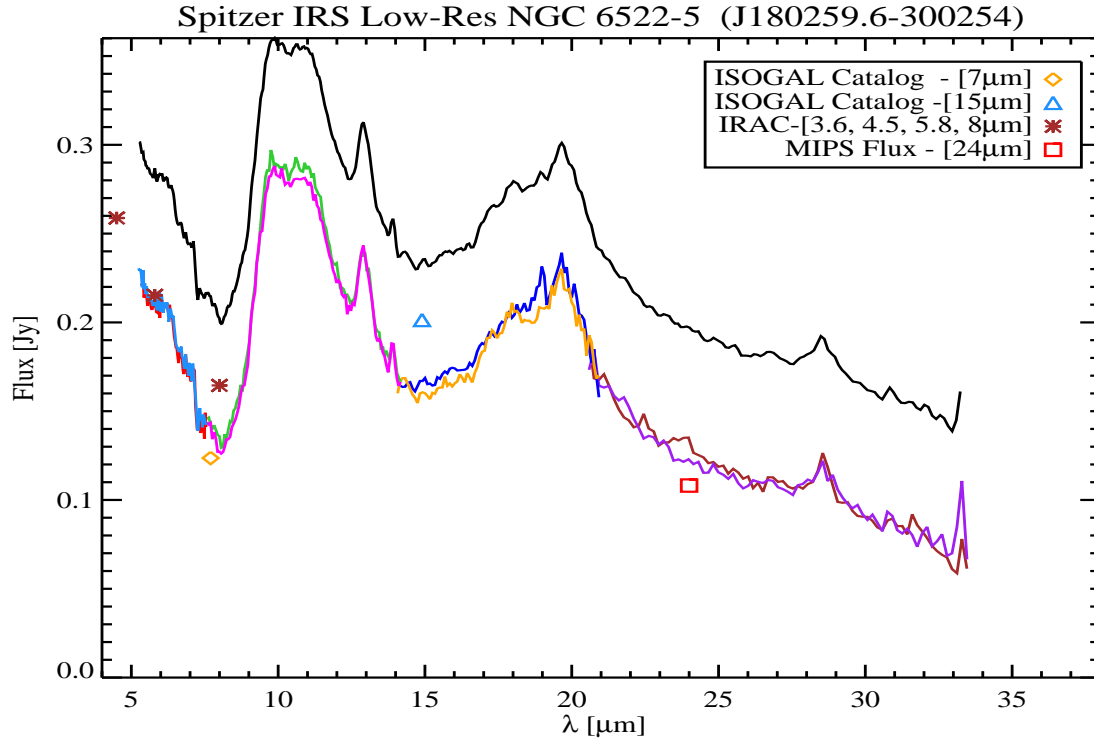


Figure G.65: (**NGC 6522-5**) This is the final spectrum of NGC 6522-5. Figure G.66 indicates the number of sources that have been extracted in each nod and module. After extraction the sharp and unrealistic residual features were masked (e.g. 19.5- μm). This source is located in the field covering NGC6522 and its background is similar to that of the rest of the field thus similarly it was corrected through modeling. Finally, we scaled long low modules with respect to the short low modules using the following scale factors, in order to eliminate the mismatch between them and obtain the continuum shown here.

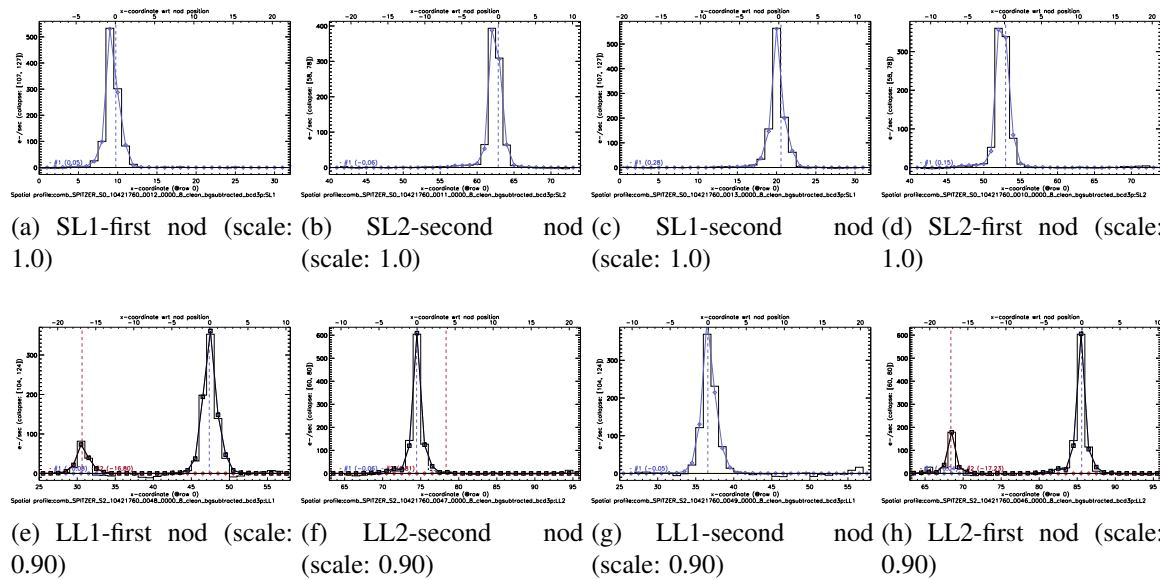


Figure G.66: SL and LL modules spatial profiles after subtraction of the background

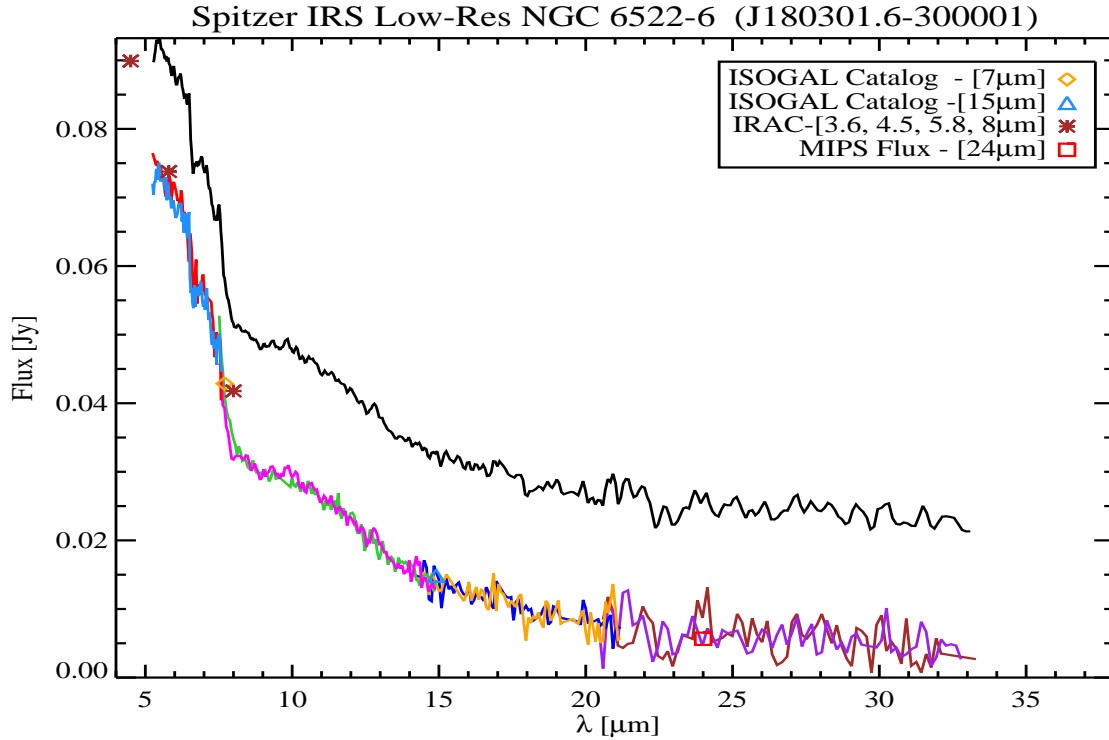


Figure G.67: (**NGC 6522-6**) This is the final spectrum of NGC 6522-6. Figure G.68 indicates the number of sources that have been extracted in each nod and module. After extraction, residual features were masked (e.g. 19.5- μ m). This source is located in the field covering NGC6522 and its background is similar to that of the rest of the field thus similarly it was corrected through modeling. Finally, we scaled long low modules with respect to the short low modules using the following scale factors, in order to eliminate the mismatch between them and obtain the continuum shown here.

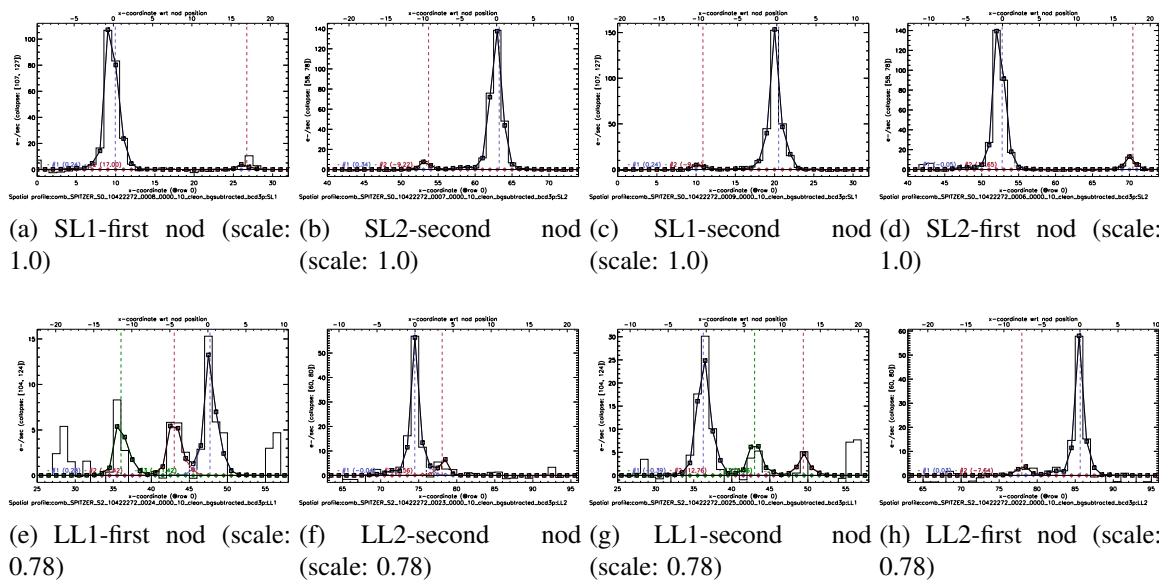


Figure G.68: SL and LL modules spatial profiles after subtraction of the background

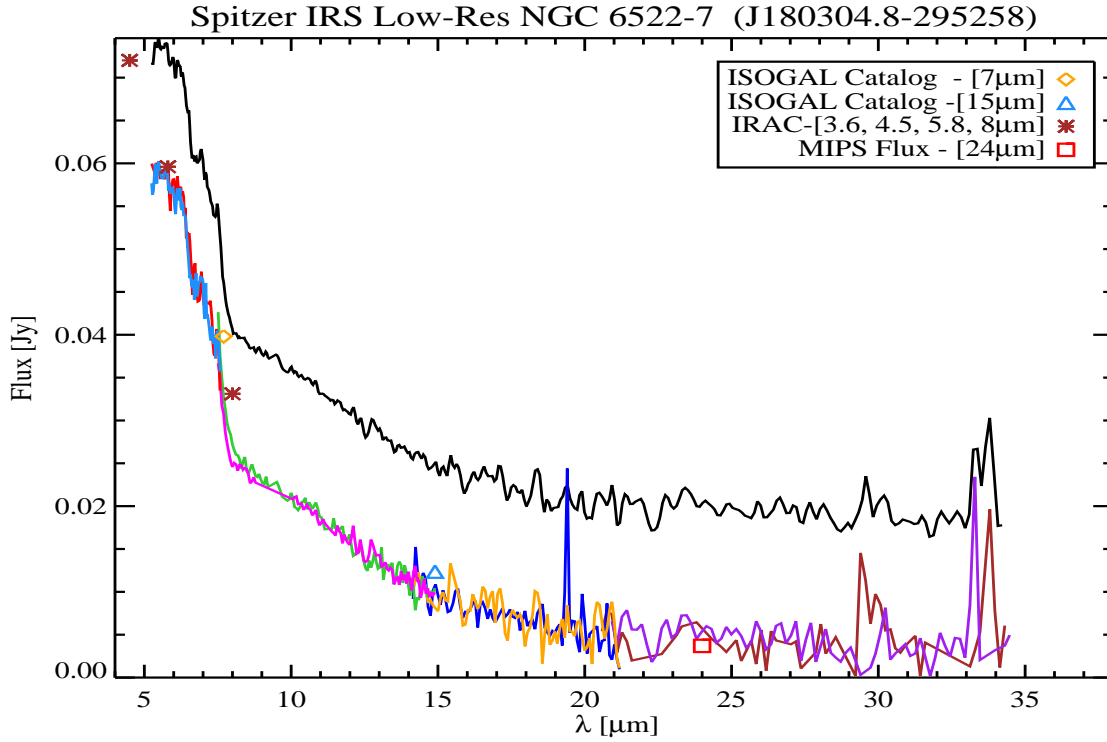


Figure G.69: (**NGC 6522-7**) This is the final spectrum of NGC 6522-7. Figure G.70 indicates the number of sources that have been extracted in each nod and module. There was a slight mismatch between the two nods of SL1 module which was removed by modifying the point spread function (central position and FWHM). After extraction, residual features were masked (e.g. 19.5- μm). This source is located in the field covering NGC6522 and its background is similar to that of the rest of the field thus similarly it was corrected through modeling. Finally, we scaled long low modules with respect to the short low modules using the following scale factors, in order to eliminate the mismatch between them and obtain the continuum shown here.

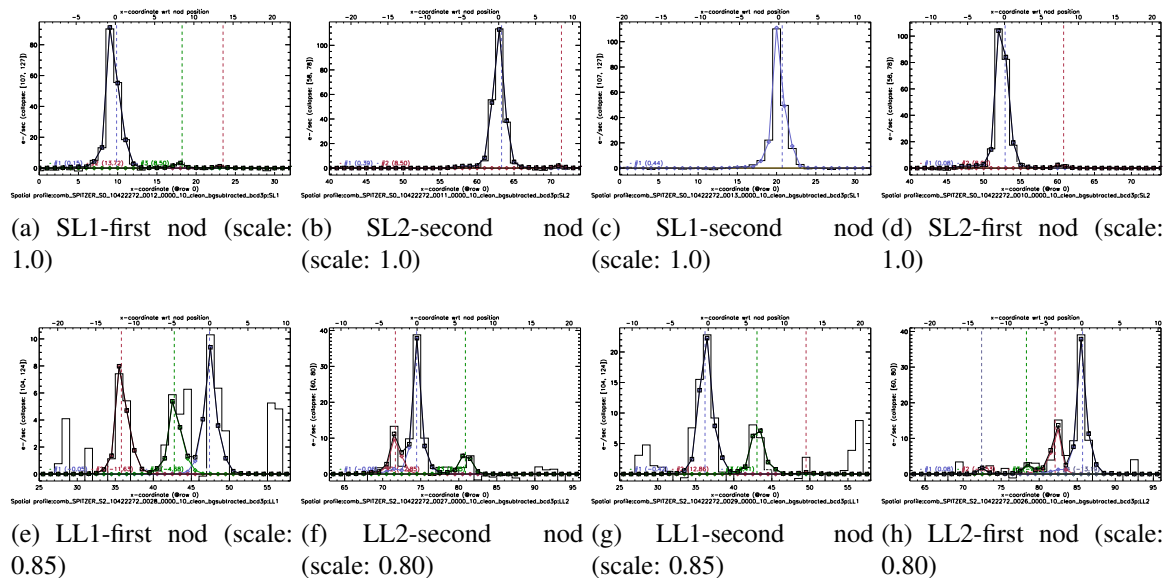


Figure G.70: SL and LL modules spatial profiles after subtraction of the background

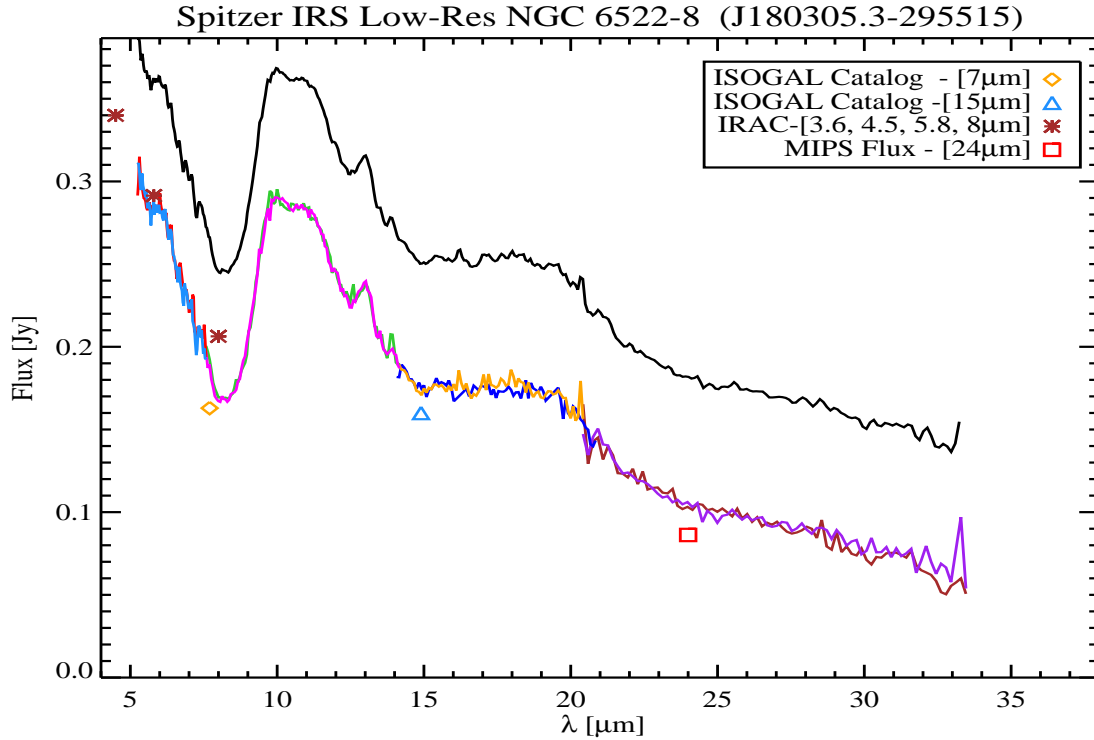


Figure G.71: (**NGC 6522-8**) This is the final spectrum of NGC 6522-8. Figure G.72 indicates the number of sources that have been extracted in each nod and module. There was a slight mismatch between the two nods of SL1 module which was removed by modifying the point spread function (central position and FWHM). After extraction the sharp and unrealistic residual features were masked (e.g. 19.5- μ m). This source is located in the field covering NGC6522 and its background is similar to that of the rest of the field thus similarly it was corrected through modeling. Finally, we scaled long low modules with respect to the short low modules using the following scale factors, in order to eliminate the mismatch between them and obtain the continuum shown here.

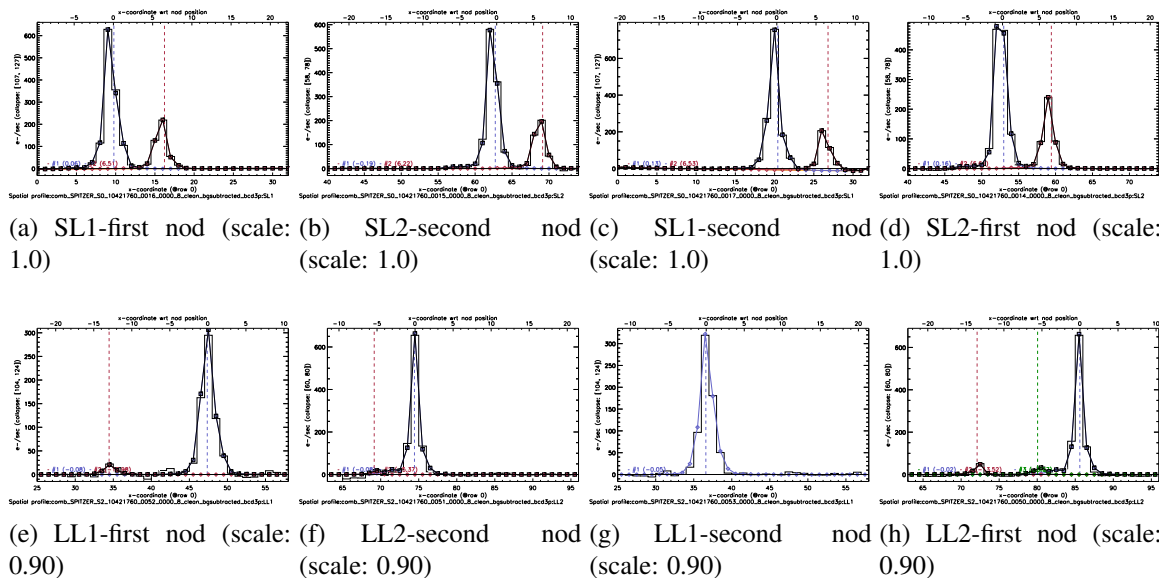


Figure G.72: SL and LL modules spatial profiles after subtraction of the background

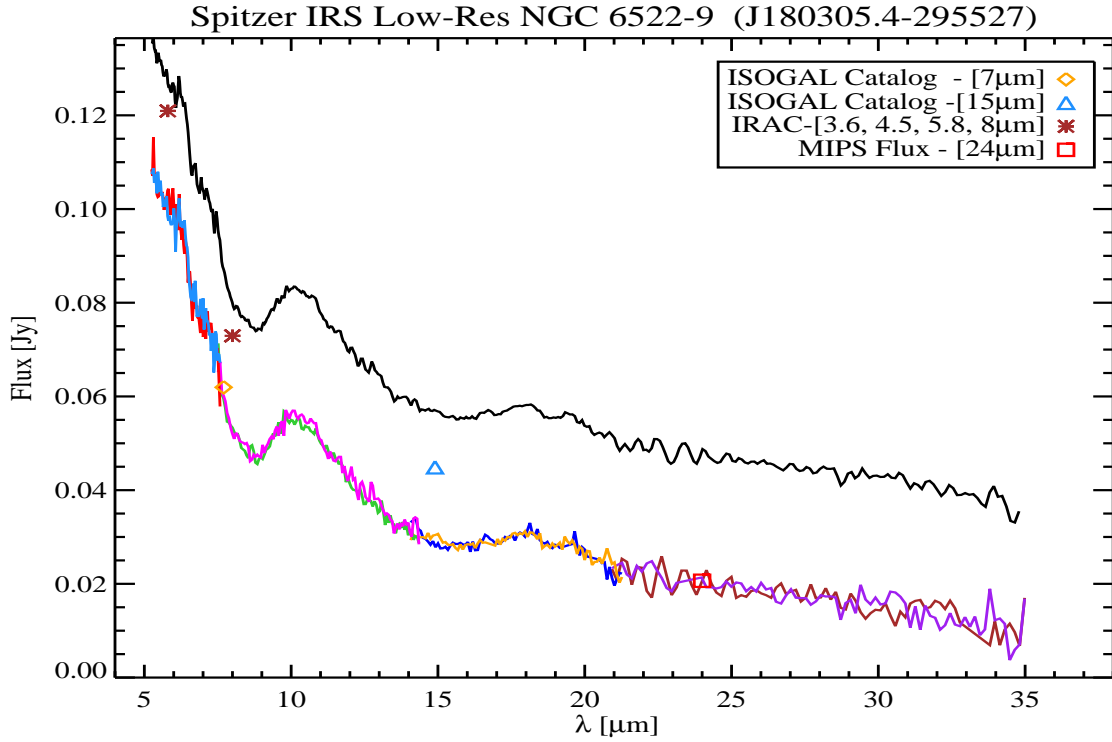


Figure G.73: (**NGC 6522-9**) This is the final spectrum of NGC 6522-9. Figure G.74 indicates the number of sources that have been extracted in each nod and module. After extraction the sharp and unrealistic residual features were masked (e.g. 19.5- μm). This source is located in the field covering NGC6522 and its background is similar to that of the rest of the field thus similarly it was corrected through modeling. Finally, we scaled long low modules with respect to the short low modules using the following scale factors, in order to eliminate the mismatch between them and obtain the continuum shown here.

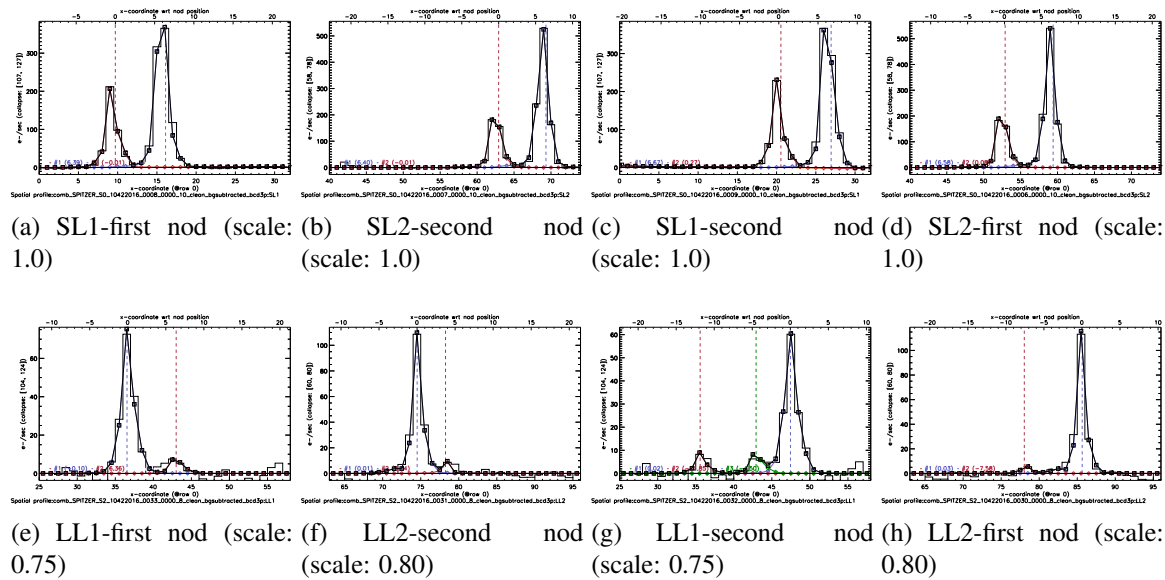


Figure G.74: SL and LL modules spatial profiles after subtraction of the background

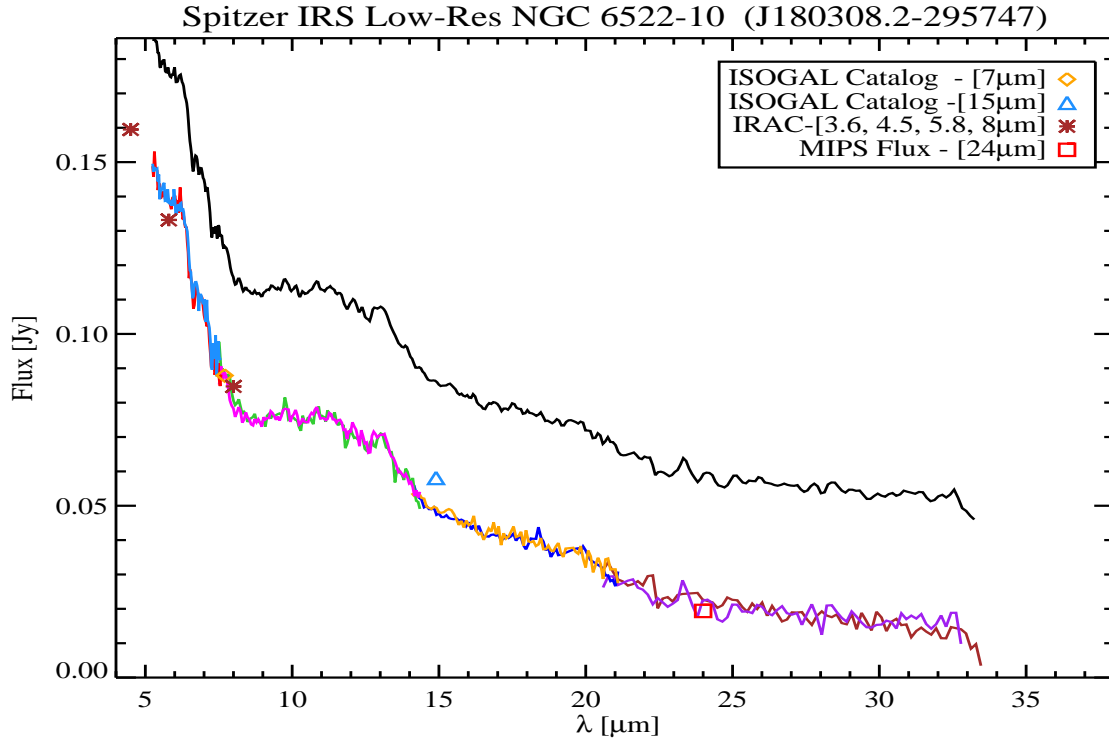


Figure G.75: (**NGC 6522-10**) This is the final spectrum of NGC 6522-10. Figure G.76 indicates the number of sources that have been extracted in each nod and module. After extraction the sharp and unrealistic residual features were masked (e.g. 19.5- μm). This source is located in the field covering NGC6522 and its background is similar to that of the rest of the field thus similarly it was corrected through modeling. Finally, we scaled long low modules with respect to the short low modules using the following scale factors, in order to eliminate the mismatch between them and obtain the continuum shown here.

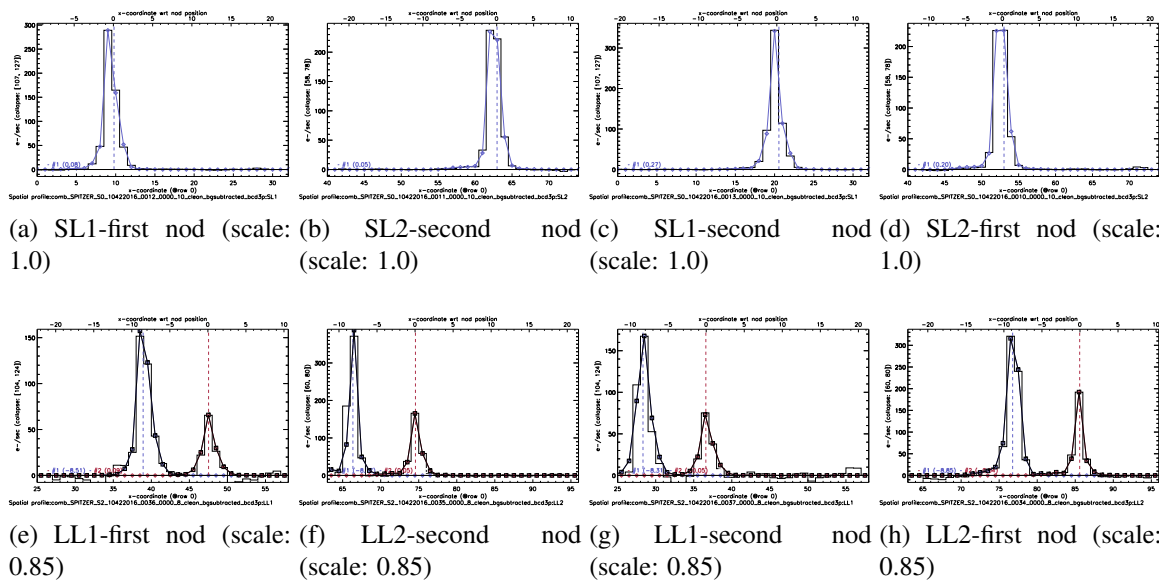


Figure G.76: SL and LL modules spatial profiles after subtraction of the background

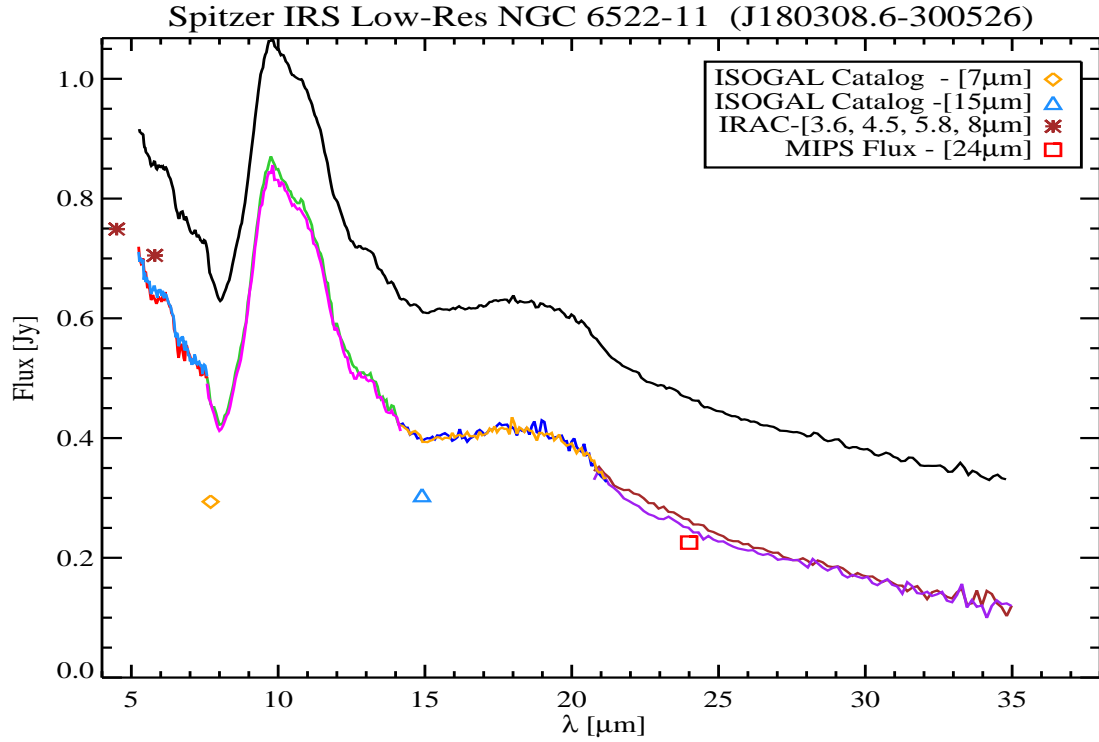


Figure G.77: (**NGC 6522-11**) This is the final spectrum of NGC 6522-11. Figure G.78 indicates the number of sources that have been extracted in each nod and module. There was a slight mismatch between the two nods of SL1 module which was removed by modifying the point spread function (central position and FWHM). After extraction the sharp and unrealistic residual features were masked (e.g. 19.5- μ m). This source is located in the field covering NGC6522 and its background is similar to that of the rest of the field thus similarly it was corrected through modeling. Finally, we scaled long low modules with respect to the short low modules using the following scale factors, in order to eliminate the mismatch between them and obtain the continuum shown here.

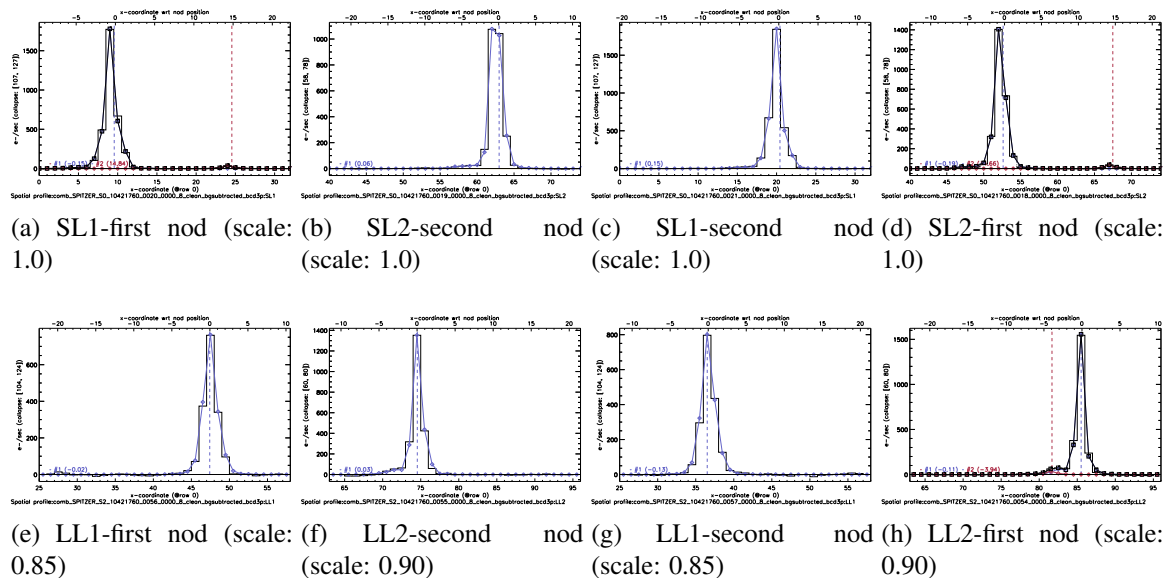


Figure G.78: SL and LL modules spatial profiles after subtraction of the background

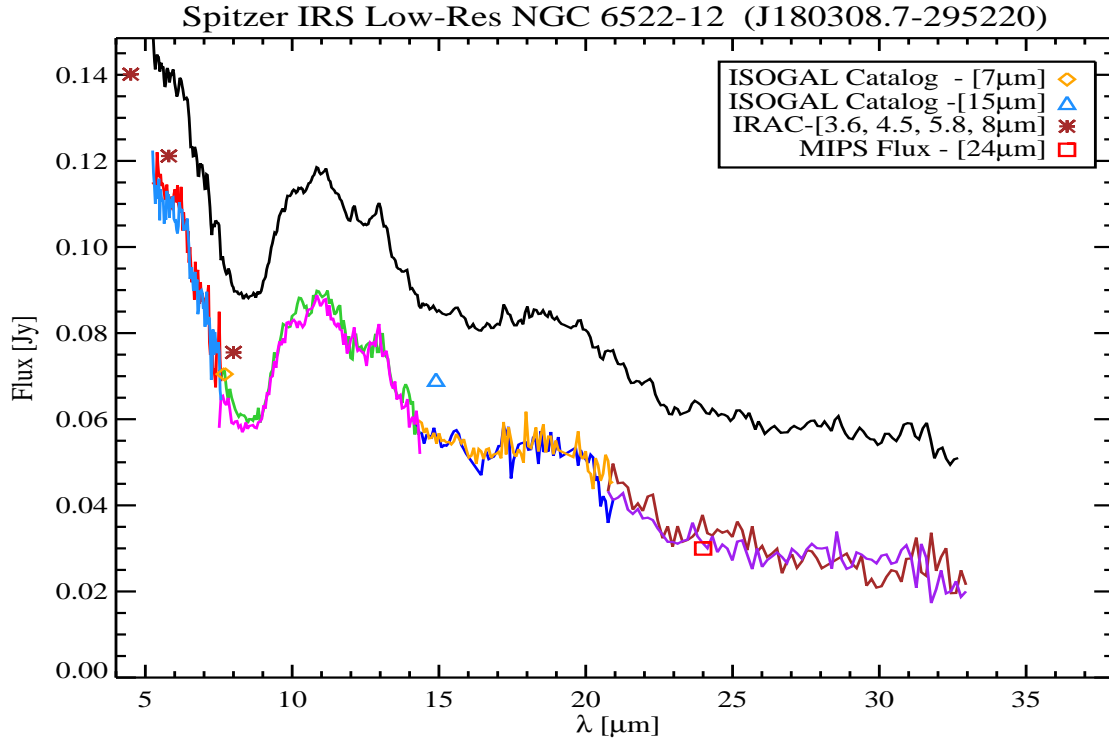


Figure G.79: (**NGC 6522-12**) This is the final spectrum of NGC 6522-12. Figure G.80 indicates the number of sources that have been extracted in each nod and module. There was a slight mismatch between the two nods of SL1 module which was removed by modifying the point spread function (central position and FWHM). After extraction the sharp and unrealistic residual features were masked (e.g. 19.5- μm). This source is located in the field covering NGC6522 and its background is similar to that of the rest of the field thus similarly it was corrected through modeling. Finally, we scaled long low modules with respect to the short low modules using the following scale factors, in order to eliminate the mismatch between them and obtain the continuum shown here.

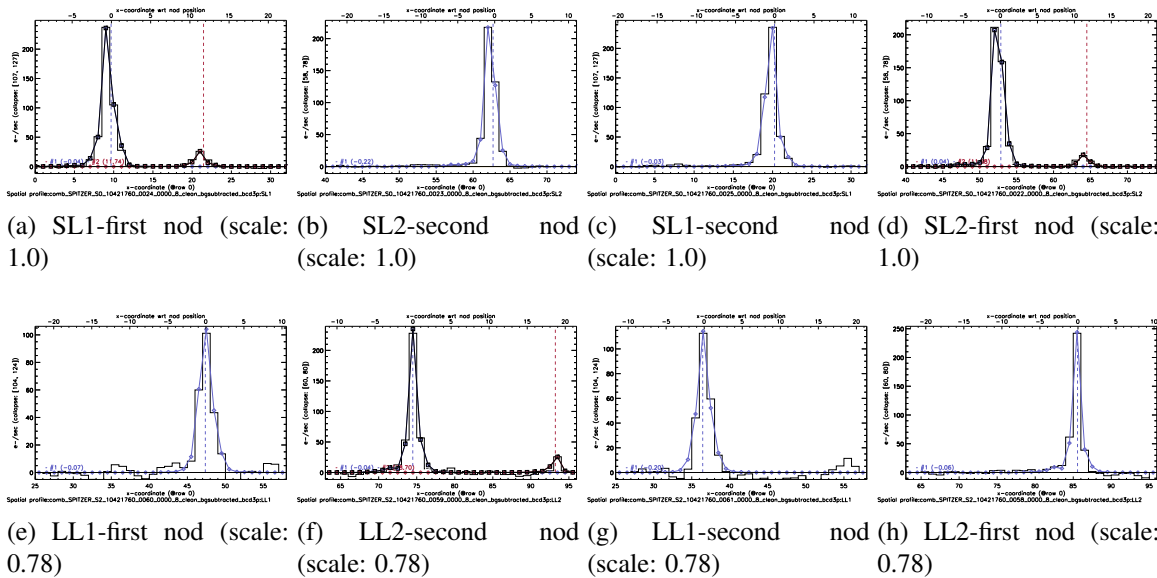


Figure G.80: SL and LL modules spatial profiles after subtraction of the background

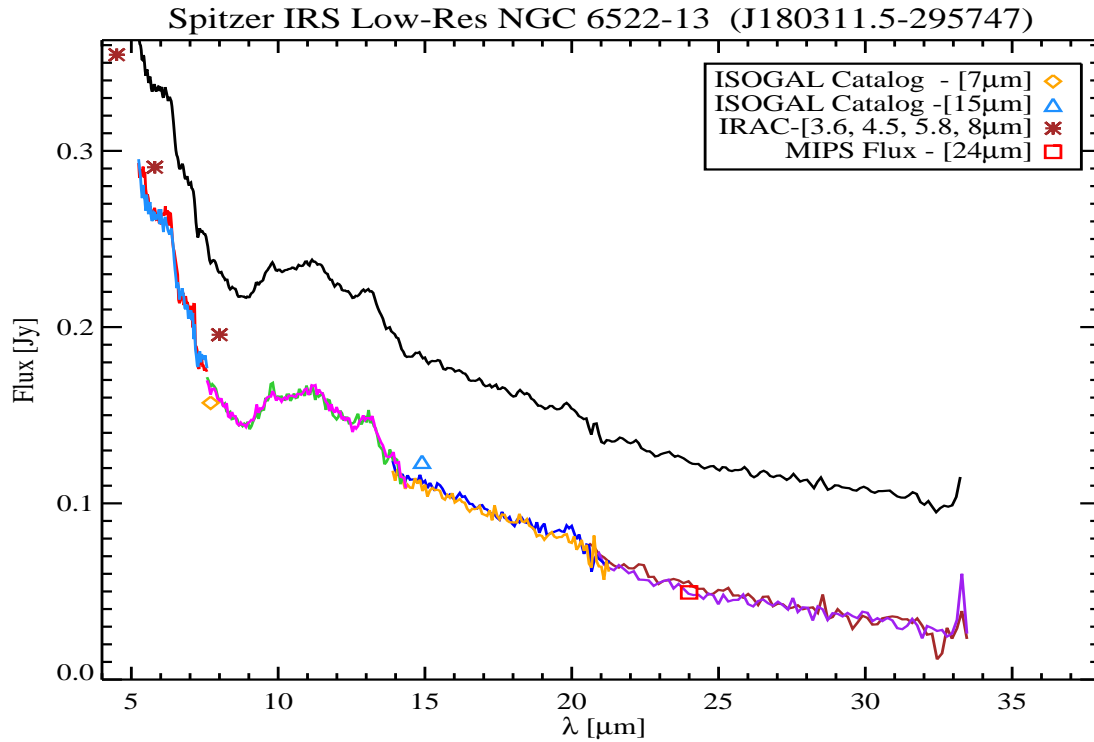


Figure G.81: (**NGC 6522-13**) This is the final spectrum of NGC 6522-13. Figure G.82 indicates the number of sources that have been extracted in each nod and module. After extraction the sharp and unrealistic residual features were masked (e.g. 19.5- μm). This source is located in the field covering NGC6522 and its background is similar to that of the rest of the field thus similarly it was corrected through modeling. Finally, we scaled long low modules with respect to the short low modules using the following scale factors, in order to eliminate the mismatch between them and obtain the continuum shown here.

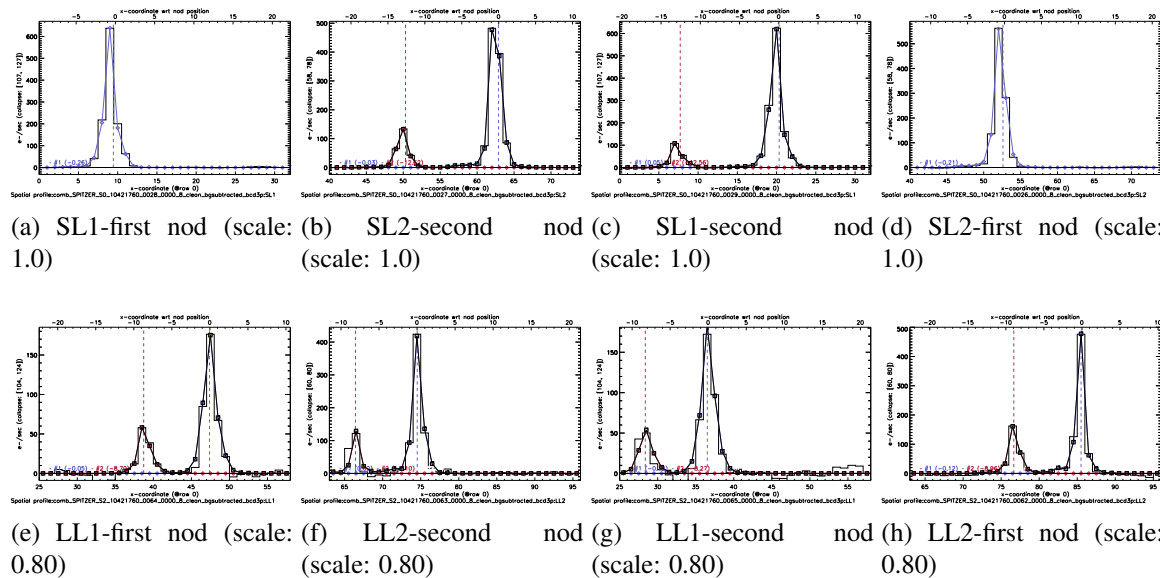


Figure G.82: SL and LL modules spatial profiles after subtraction of the background

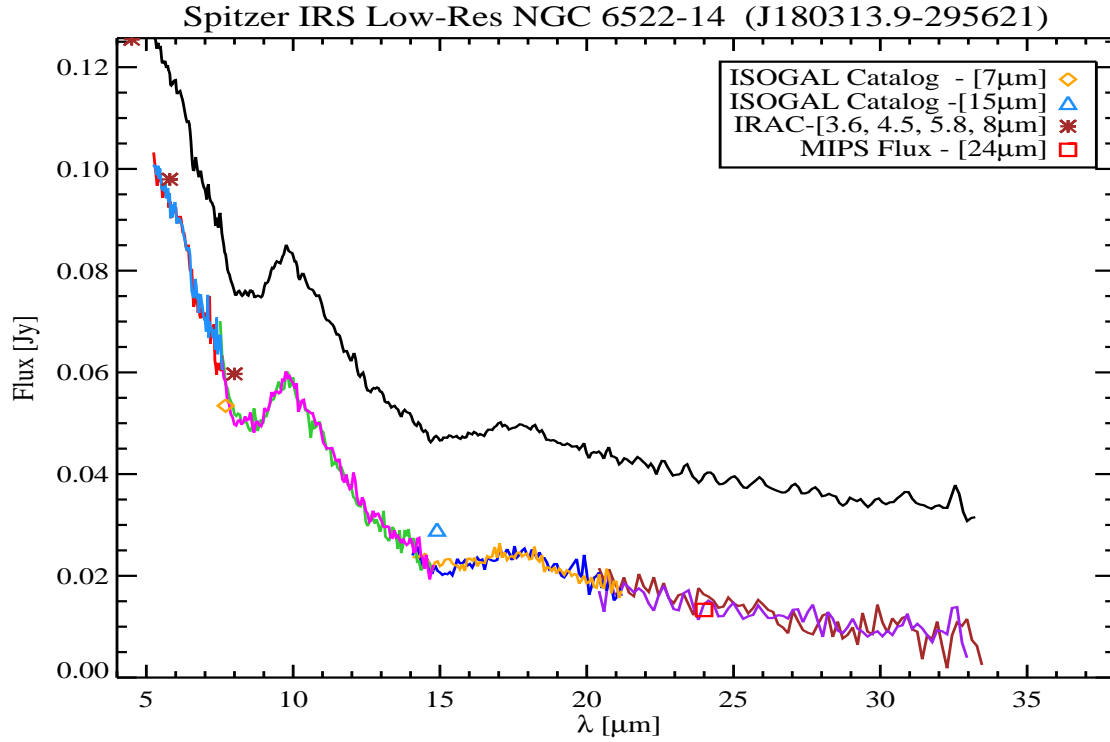


Figure G.83: (**NGC 6522-14**) This is the final spectrum of NGC 6522-14. Figure G.84 indicates the number of sources that have been extracted in each nod and module. After extraction the sharp and unrealistic residual features were masked (e.g. 19.5- μm). This source is located in the field covering NGC6522 and its background is similar to that of the rest of the field thus similarly it was corrected through modeling. Finally, we scaled long low modules with respect to the short low modules using the following scale factors, in order to eliminate the mismatch between them and obtain the continuum shown here.

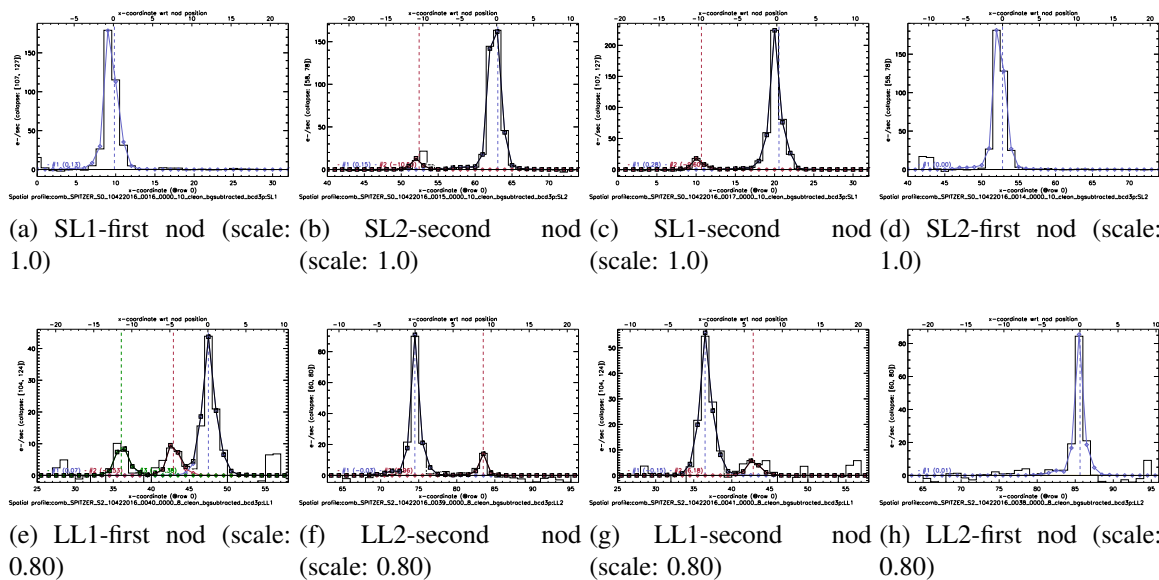


Figure G.84: SL and LL modules spatial profiles after subtraction of the background

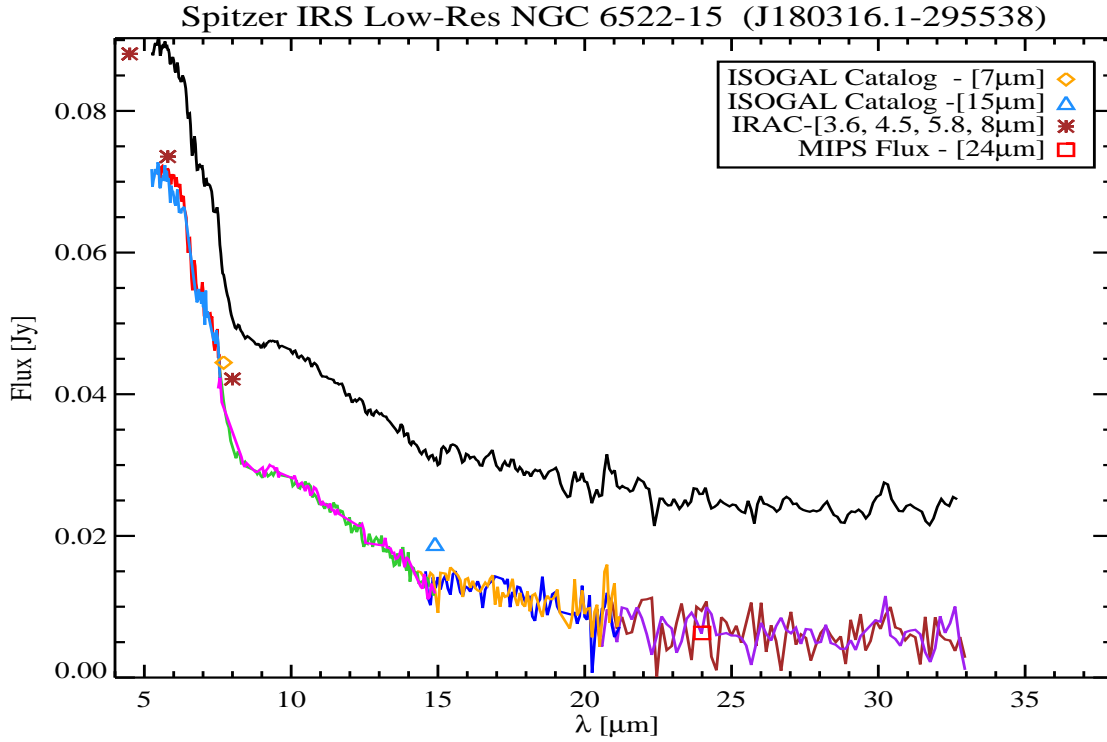


Figure G.85: (**NGC 6522-15**) This is the final spectrum of NGC 6522-15. Figure G.86 indicates the number of sources that have been extracted in each nod and module. There was a slight mismatch between the two nods of SL1 module which was removed by modifying the point spread function (central position and FWHM). After extraction, residual features were masked (e.g. 19.5- μm). This source is located in the field covering NGC6522 and its background is similar to that of the rest of the field thus similarly it was corrected through modeling. Finally, we scaled long low modules with respect to the short low modules using the following scale factors, in order to eliminate the mismatch between them and obtain the continuum shown here.

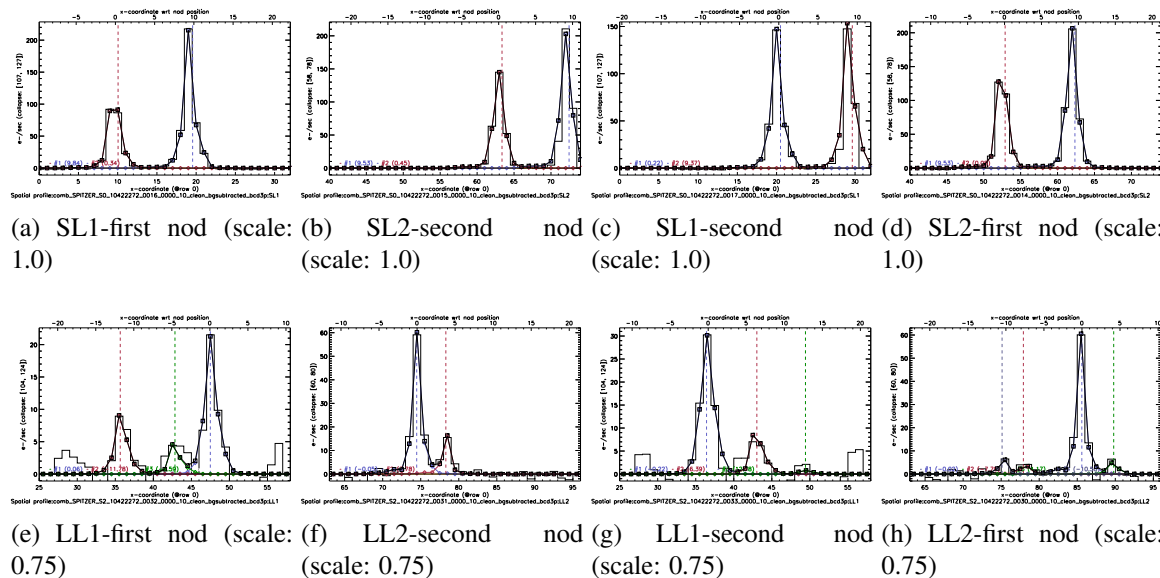


Figure G.86: SL and LL modules spatial profiles after subtraction of the background

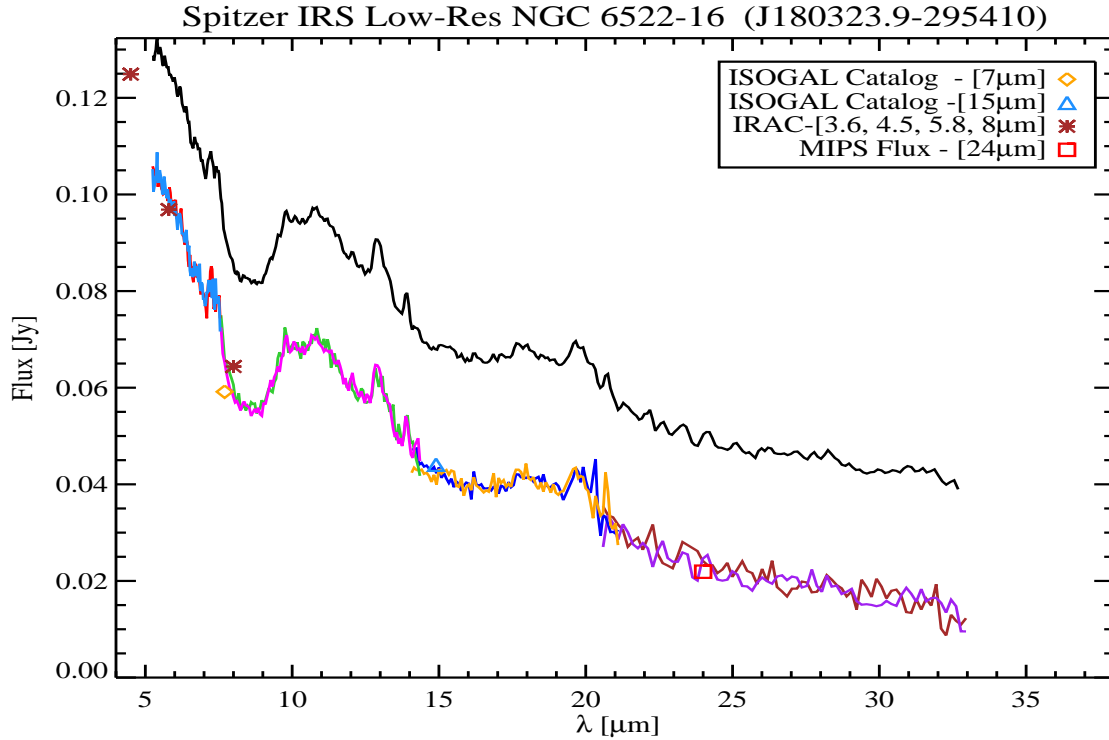


Figure G.87: **(NGC 6522-16)** This is the final spectrum of NGC 6522-16. Figure G.88 indicates the number of sources that have been extracted in each nod and module. There was a slight mismatch between the two nods of SL1 module which was removed by modifying the point spread function (central position and FWHM). After extraction the sharp and unrealistic residual features were masked (e.g. 19.5- μ m). This source is located in the field covering NGC6522 and its background is similar to that of the rest of the field thus similarly it was corrected through modeling. Finally, we scaled long low modules with respect to the short low modules using the following scale factors, in order to eliminate the mismatch between them and obtain the continuum shown here.

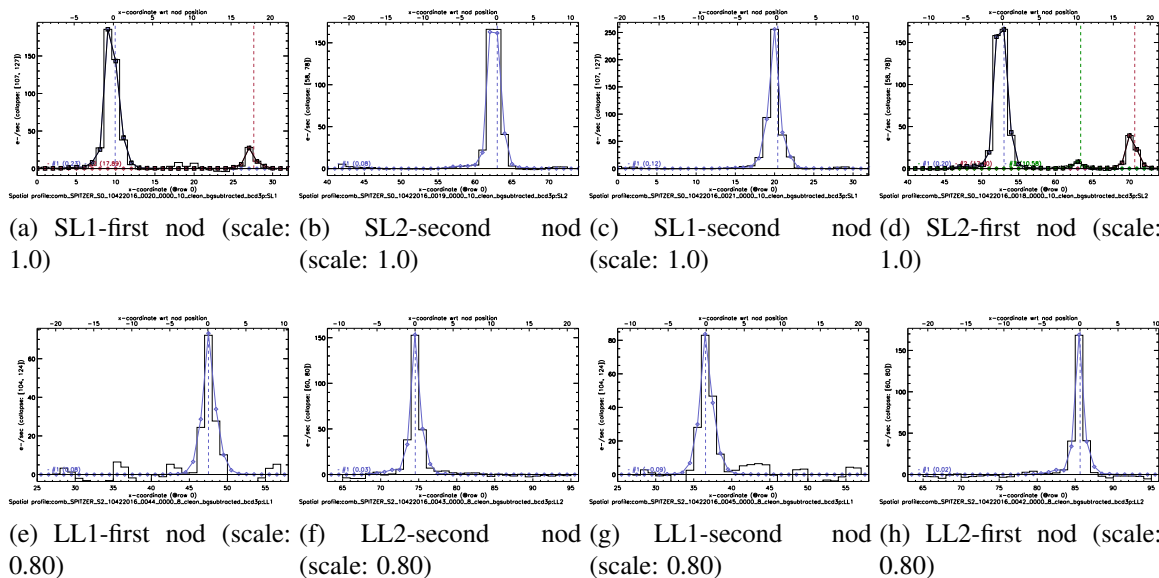


Figure G.88: SL and LL modules spatial profiles after subtraction of the background

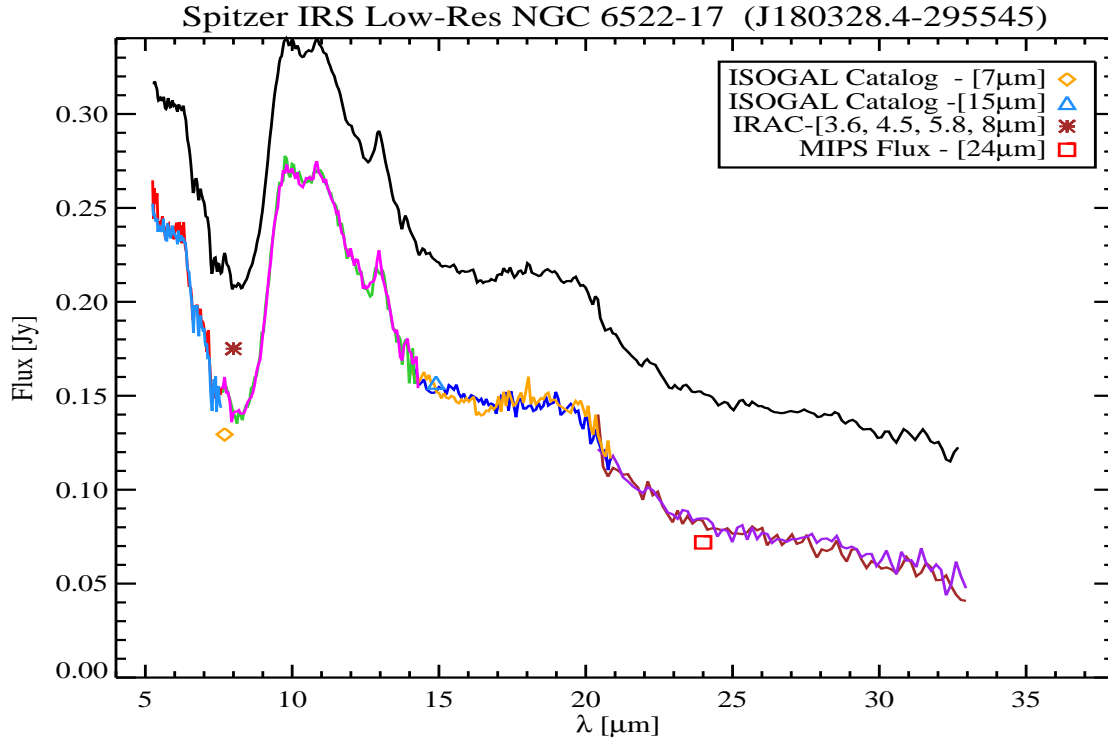


Figure G.89: (**NGC 6522-17**) This is the final spectrum of NGC 6522-17. Figure G.90 indicates the number of sources that have been extracted in each nod and module. After extraction the sharp and unrealistic residual features were masked (e.g. 19.5- μm). This source is located in the field covering NGC6522 and its background is similar to that of the rest of the field thus similarly it was corrected through modeling. Finally, we scaled long low modules with respect to the short low modules using the following scale factors, in order to eliminate the mismatch between them and obtain the continuum shown here.

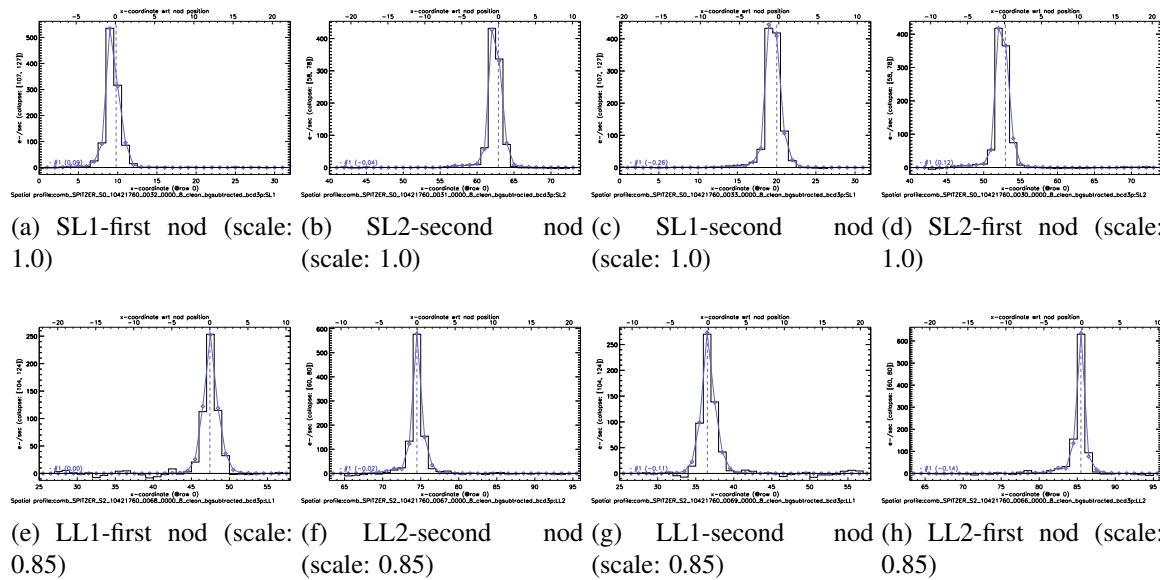


Figure G.90: SL and LL modules spatial profiles after subtraction of the background

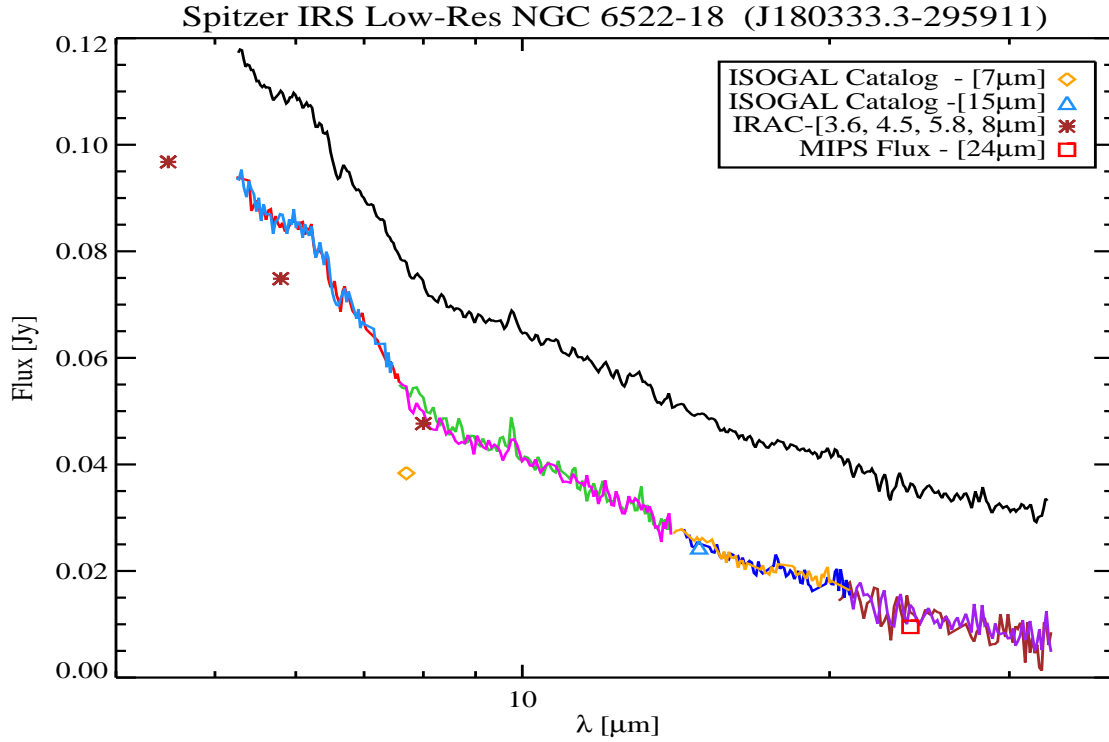


Figure G.91: (**NGC 6522-18**) This is the final spectrum of NGC 6522-18. Figure G.92 indicates the number of sources that have been extracted in each nod and module. After extraction, residual features were masked (e.g. 19.5- μ m). This source is located in the field covering NGC6522 and its background is similar to that of the rest of the field thus similarly it was corrected through modeling. Finally, we scaled long low modules with respect to the short low modules using the following scale factors, in order to eliminate the mismatch between them and obtain the continuum shown here.

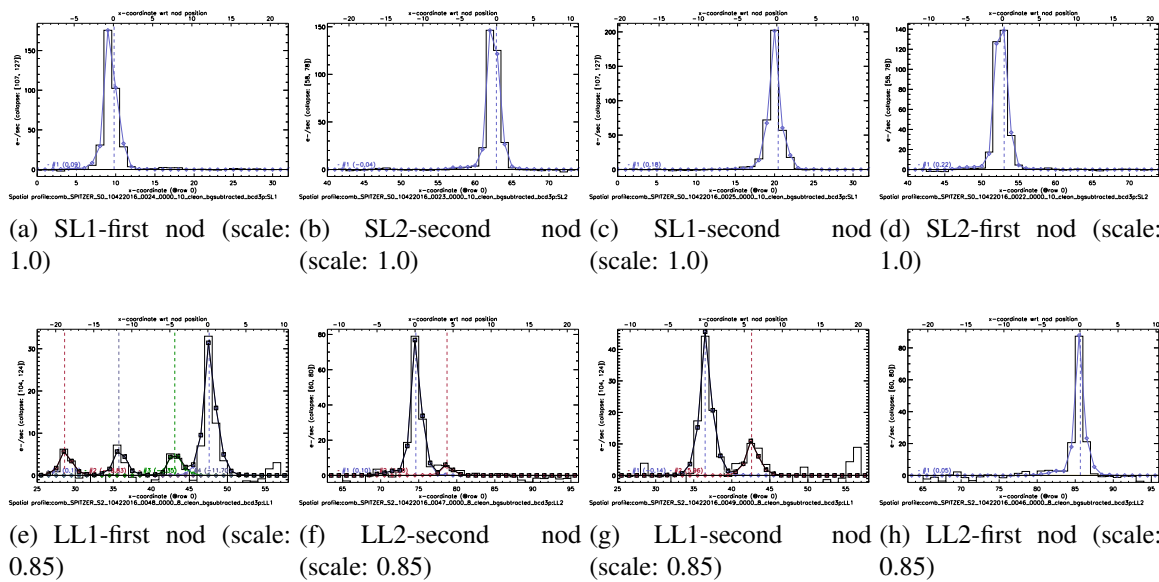


Figure G.92: SL and LL modules spatial profiles after subtraction of the background

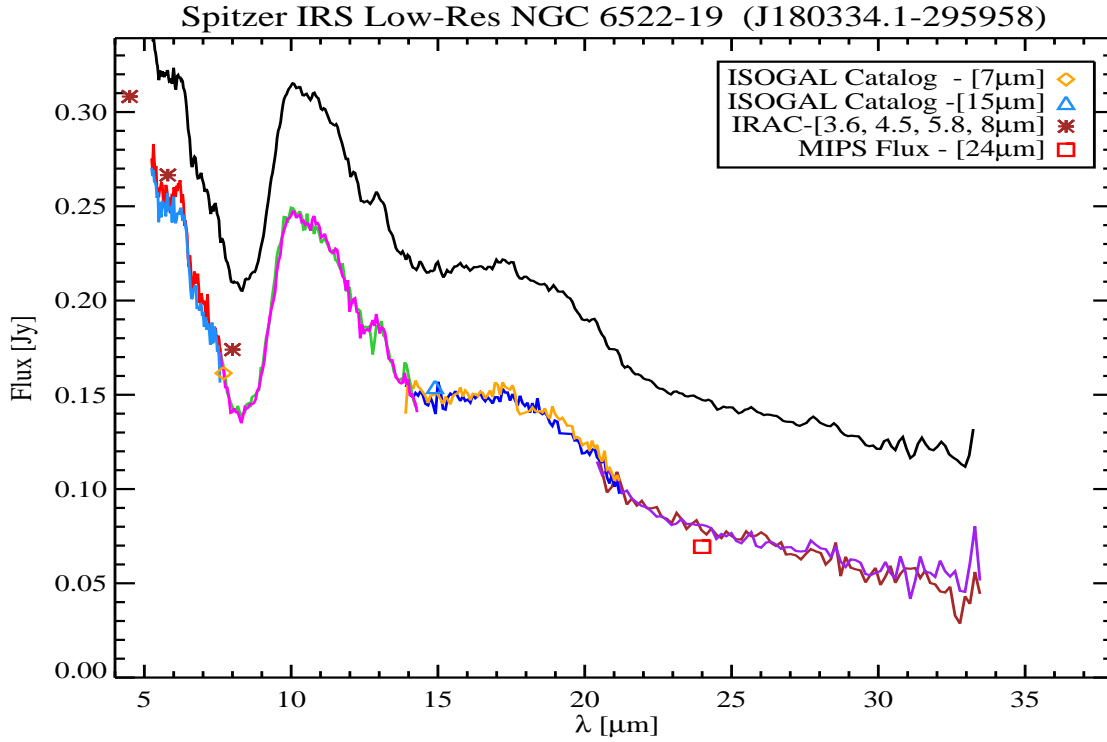


Figure G.93: (**NGC 6522-19**) This is the final spectrum of NGC 6522-19. Figure G.94 indicates the number of sources that have been extracted in each nod and module. After extraction the sharp and unrealistic residual features were masked (e.g. 19.5- μm). This source is located in the field covering NGC6522 and its background is similar to that of the rest of the field thus similarly it was corrected through modeling. Finally, we scaled long low modules with respect to the short low modules using the following scale factors, in order to eliminate the mismatch between them and obtain the continuum shown here.

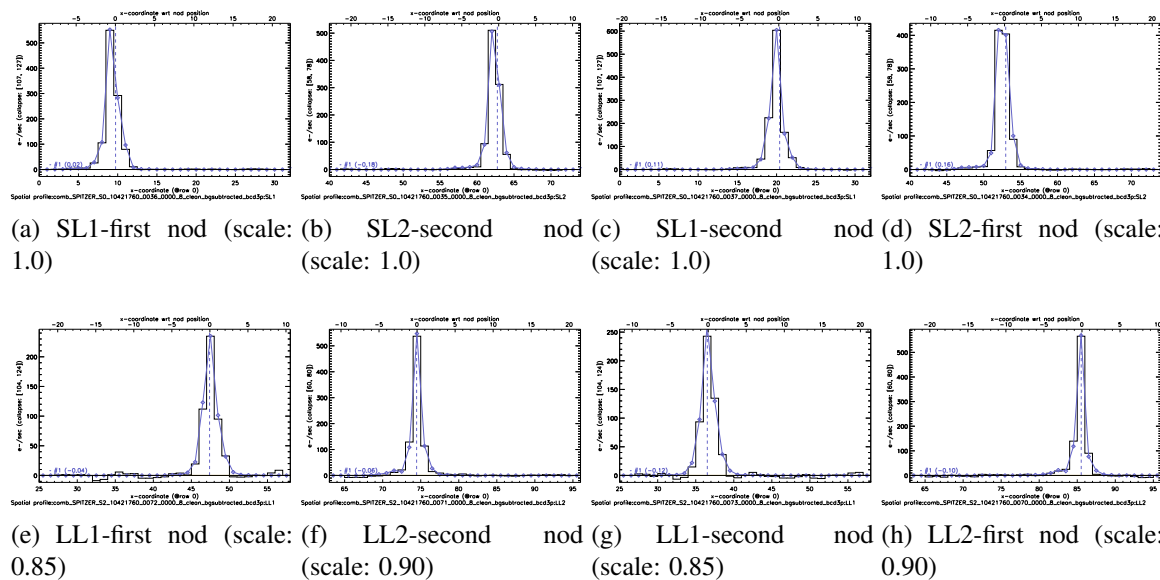


Figure G.94: SL and LL modules spatial profiles after subtraction of the background

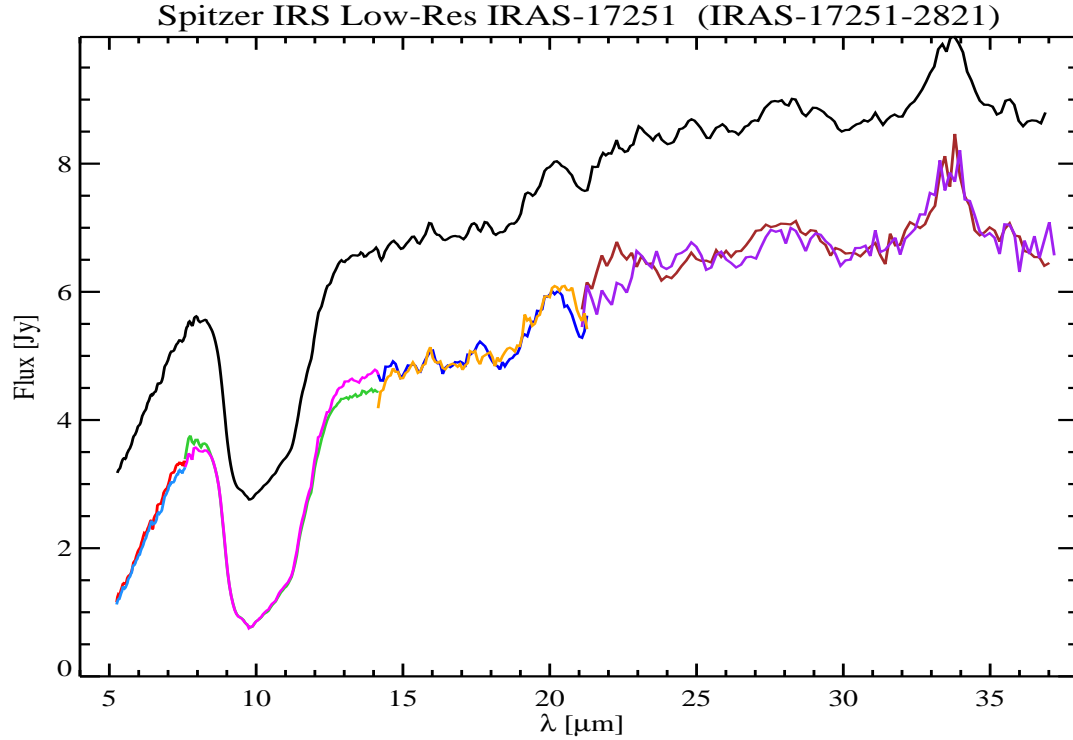


Figure G.95: **(IRAS-17251-2821)** This is the final spectrum of IRAS-17251-2821. Figure G.96 indicates the number of sources that have been extracted in each nod and module. After extraction, residual features were masked (e.g. $16.5\text{-}\mu\text{m}$). This background was corrected through modeling. Finally, we scaled all modules with respect to the SL1 modules using the following scale factors, in order to eliminate the mismatch between them and obtain the continuum shown here.

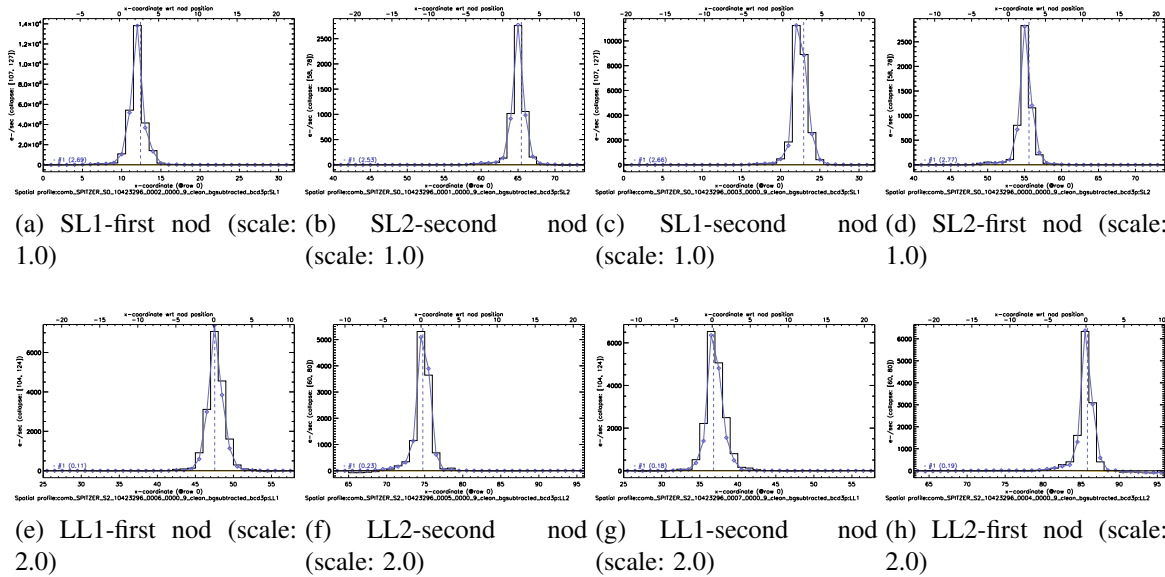


Figure G.96: SL and LL modules spatial profiles after subtraction of the background

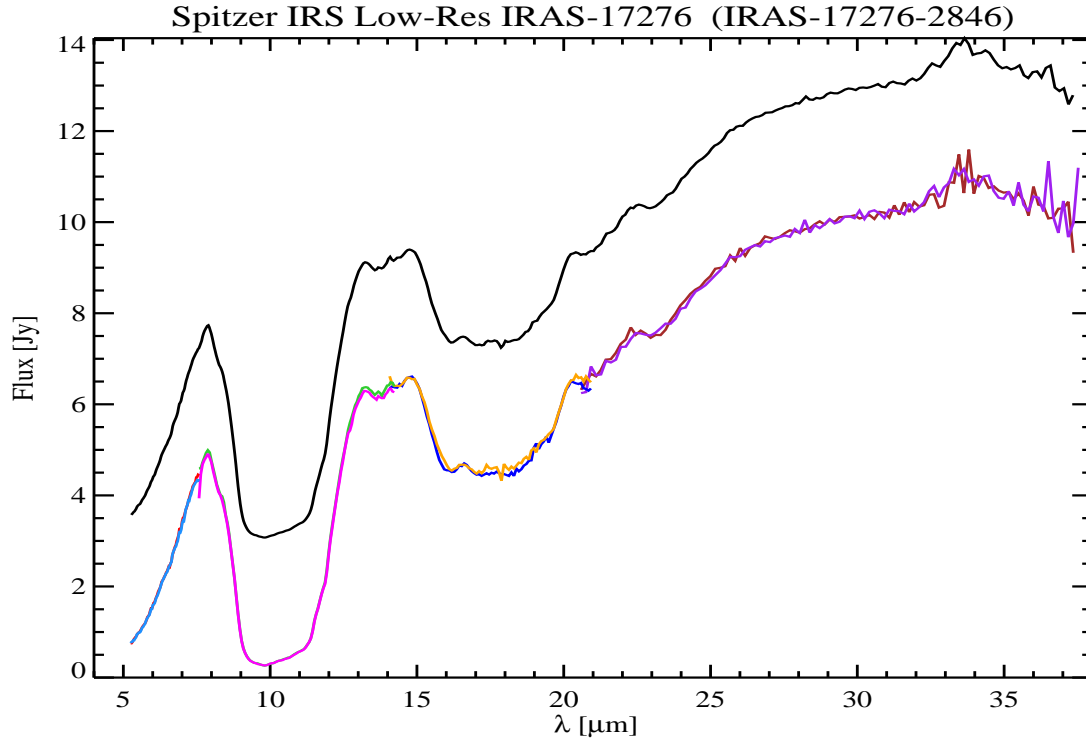


Figure G.97: **(IRAS-17276-2846)** This is the final spectrum of IRAS-17276-2846. Figure G.98 indicates the number of sources that have been extracted in each nod and module. After extraction, residual features were masked (e.g. 16.5- μm). The background was corrected through modeling except that, in the long low modules, there were residuals left from the background. We removed those residuals by further subtracting a constant offset (zeroth order polynomial). This particular case results in no mismatch between the modules therefore the continuum shown here is obtained without any further scaling.

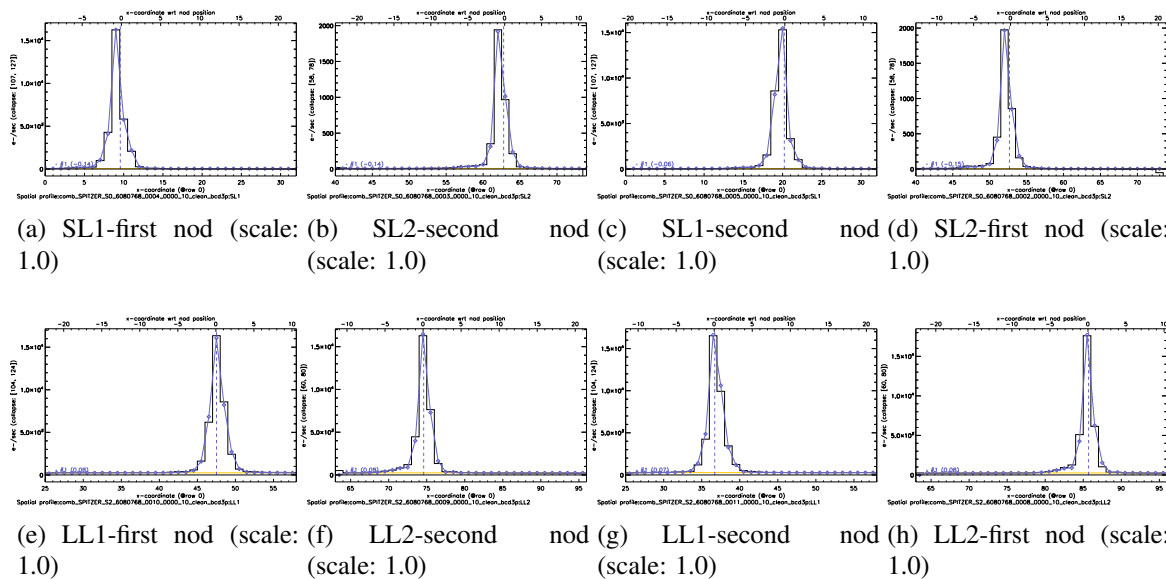


Figure G.98: SL and LL modules spatial profiles after subtraction of the background

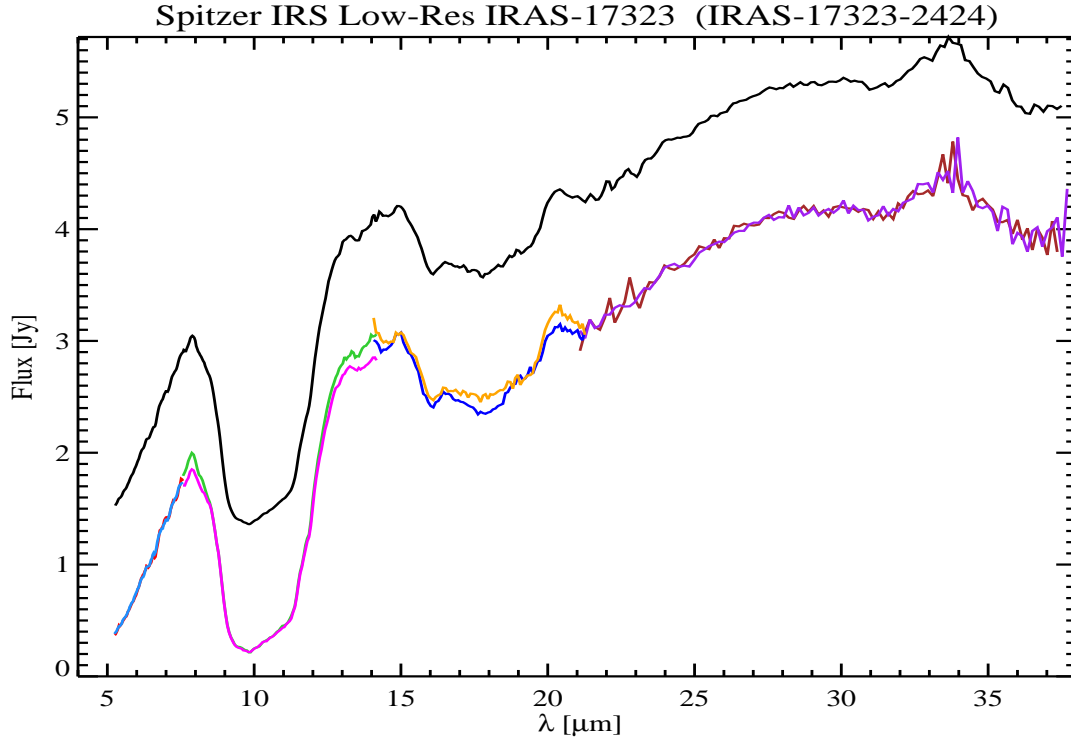


Figure G.99: **(IRAS-17323-2424)** This is the final spectrum of IRAS-17323-2424. Figure G.100 indicates the number of sources that have been extracted in each nod and module. After extraction, no significant residual was left to mask. The background was corrected through modeling. Finally, we scaled long low modules with respect to the short low modules using the following scale factors, in order to eliminate the mismatch between them and obtain the continuum shown here.

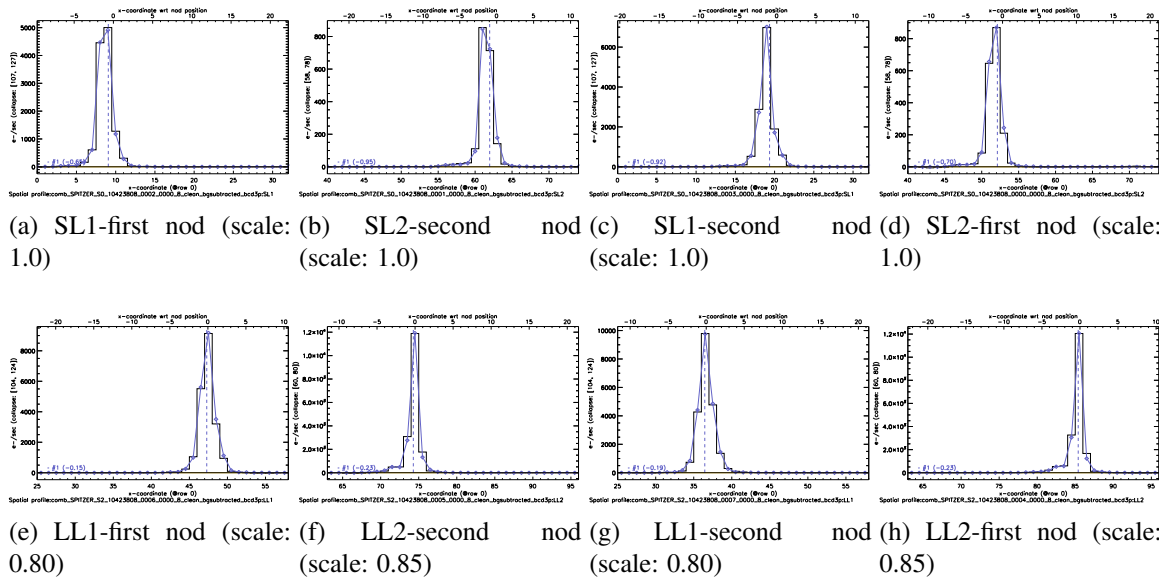


Figure G.100: SL and LL modules spatial profiles after subtraction of the background

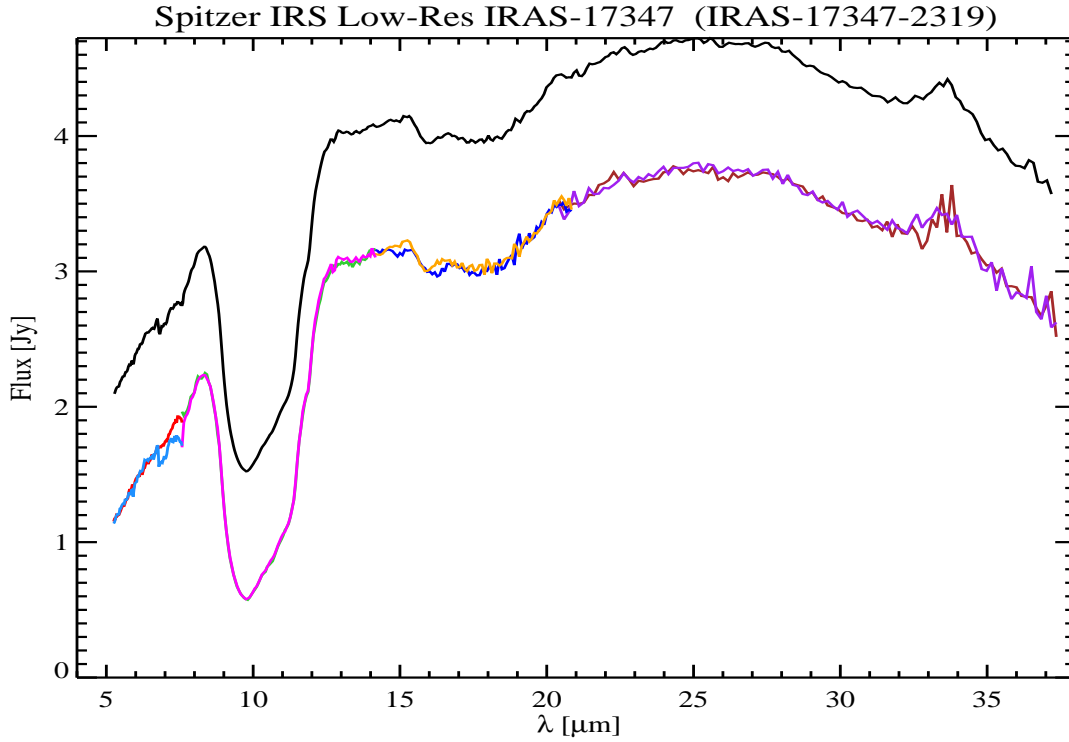


Figure G.101: **(IRAS-17347-2319)** This is the final spectrum of IRAS-17347-2319. Figure G.102 indicates the number of sources that have been extracted in each nod and module. After extraction, no significant residual was left to mask. The background was corrected through modeling except that, after modeling, there was still residuals left from the background. Therefore we have corrected the residuals with further subtracting a constant offset (polynomial order zero). Finally, we scaled long low modules with respect to the short low modules using the following scale factors, in order to eliminate the mismatch between them and obtain the continuum shown here.

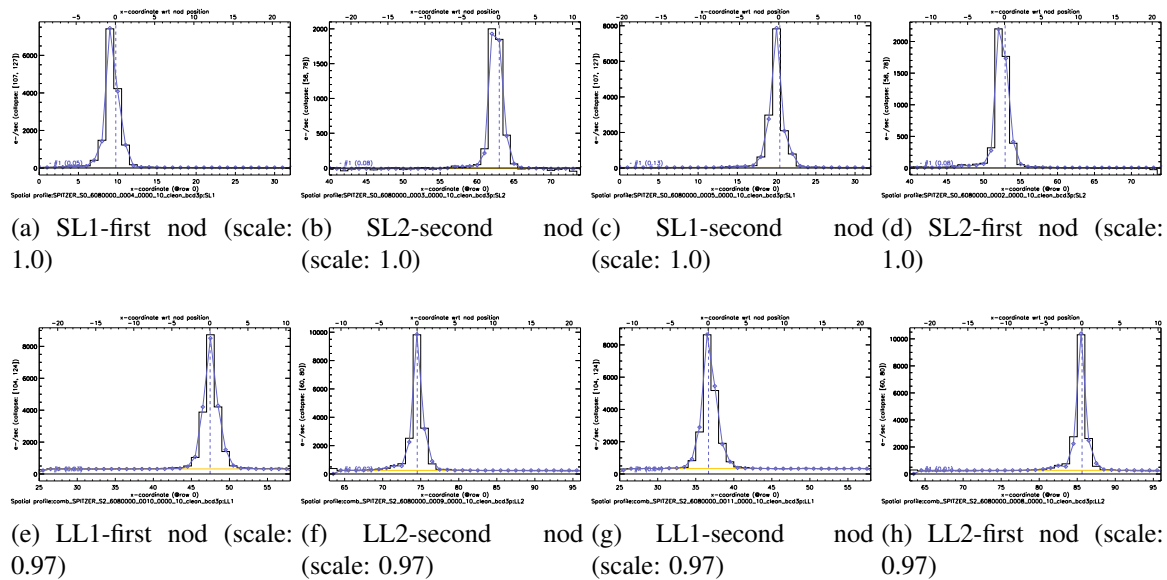


Figure G.102: SL and LL modules spatial profiles after subtraction of the background

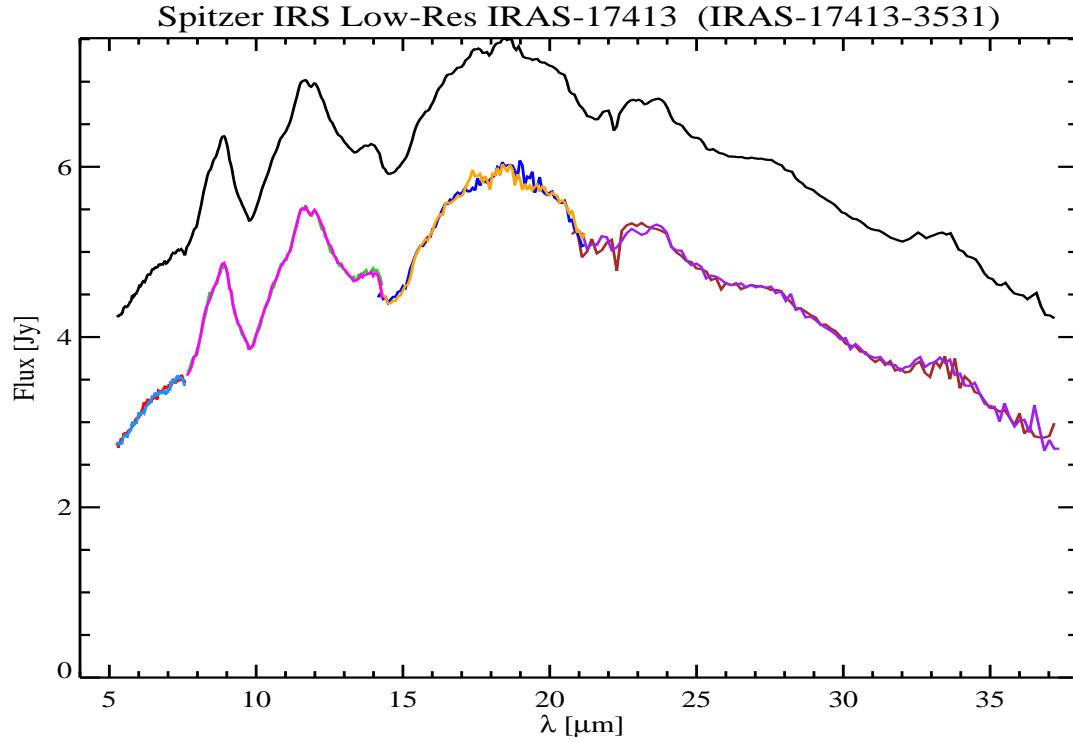


Figure G.103: (**IRAS-17413-3531**) This is the final spectrum of IRAS-17413-3531. Figure G.104 indicates the number of sources that have been extracted in each nod and module. After extraction, no significant residual was left to mask. The background was corrected through modeling except that, in the long low modules, there were residuals left from the background. We removed those residuals by further subtracting a constant offset (polynomial order zero). Finally, we scaled all modules with respect to the SL1 modules using the following scale factors, in order to eliminate the mismatch between them and obtain the continuum shown here.

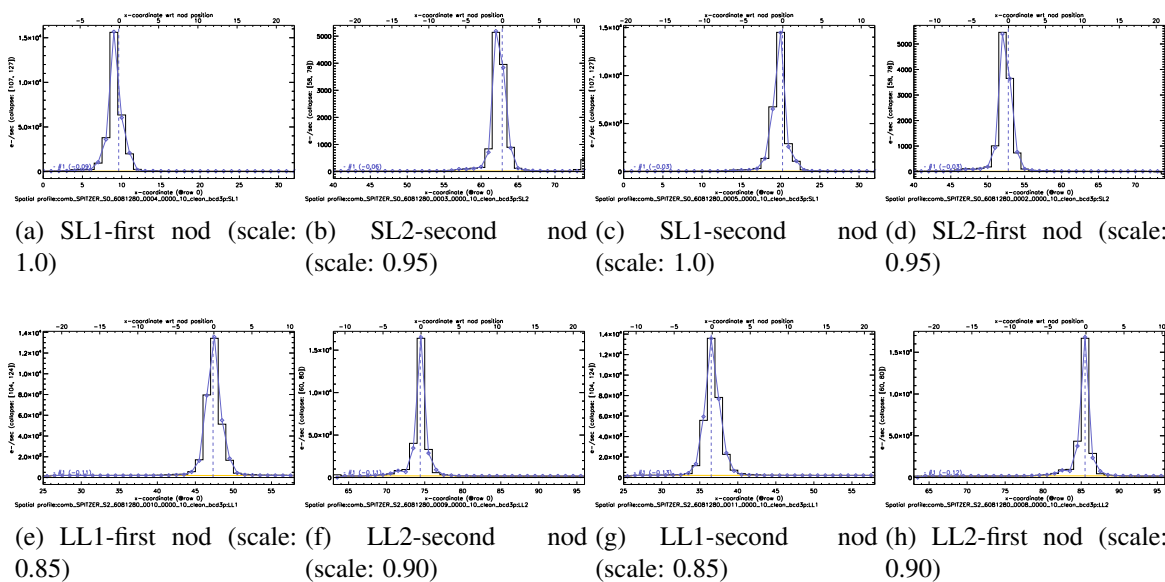


Figure G.104: SL and LL modules spatial profiles after subtraction of the background

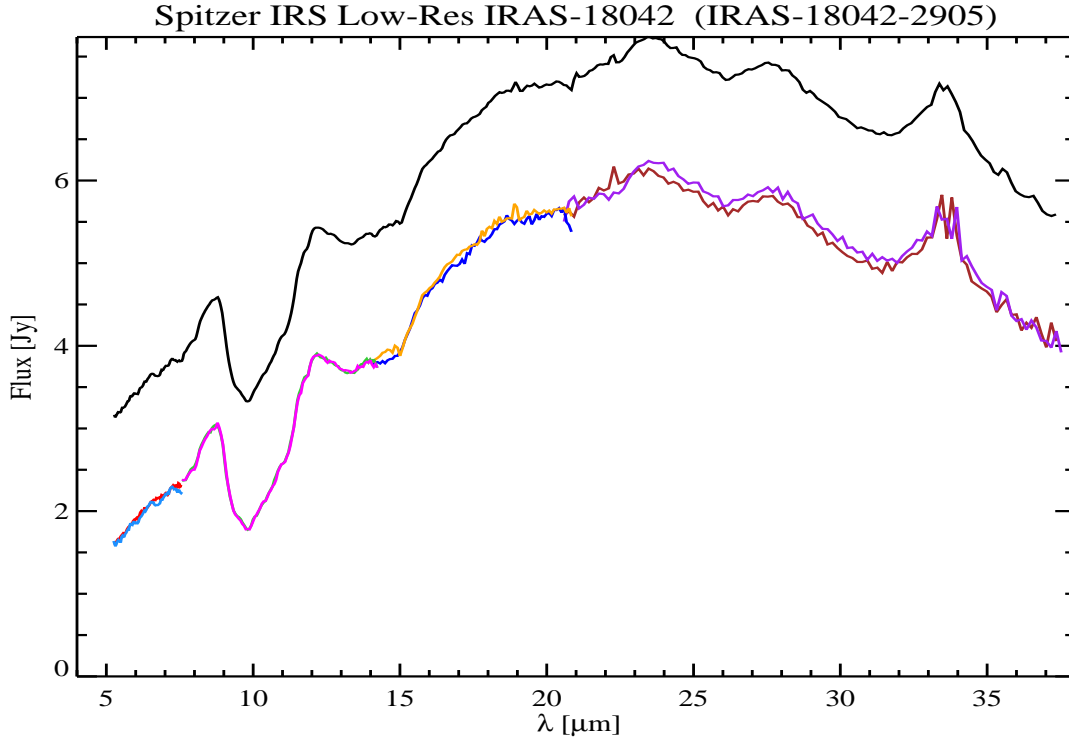


Figure G.105: **(IRAS-18042-2905)** This is the final spectrum of IRAS-18042-2905. Figure G.106 indicates the number of sources that have been extracted in each nod and module. After extraction, no significant residual was left to mask. The background was corrected through modeling. Finally, we scaled all modules with respect to the SL1 modules using the following scale factors, in order to eliminate the mismatch between them and obtain the continuum shown here.

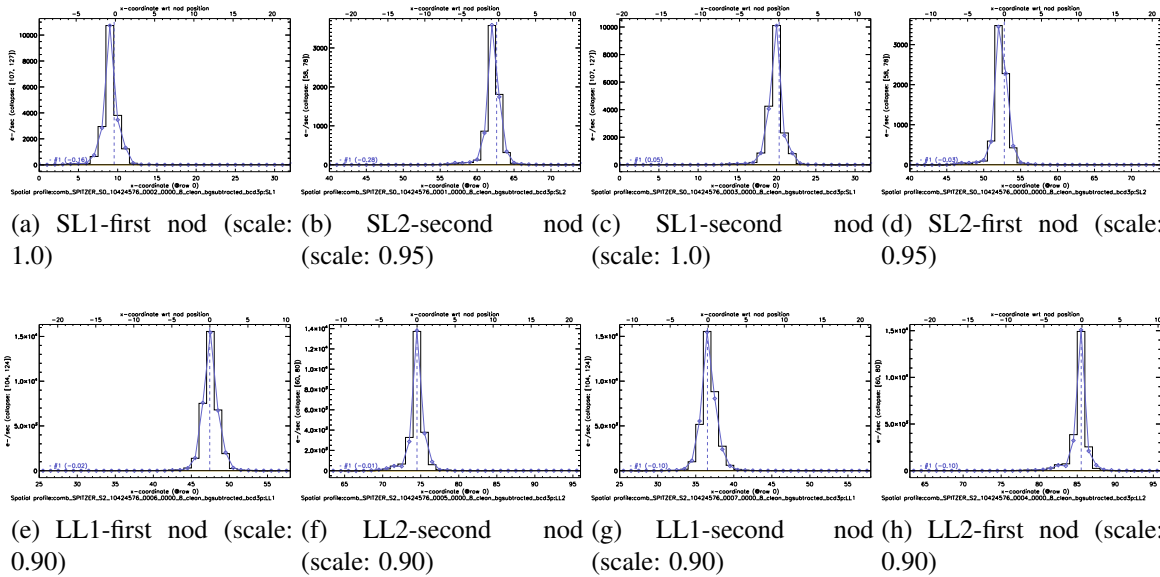


Figure G.106: SL and LL modules spatial profiles after subtraction of the background

Curriculum Vitae

Publications:

- *Title: Infrared Spectroscopy of Asymptotic Giant Branch Stars in the Galactic Bulge, I. Sample selection, observation & data reduction.*
Authors: S.S. Golriz, J. Cami, et al., Status : Published in Monthly Notices of the Royal Astronomical Society (MNRAS), Manuscript ID: MN-14-0103-MJ - (June-10-2014)
- *Title: Ultra-violet Spectrum Synthesis of Iota Herculis*
Authors: S.S. Golriz, J.D. Landstreet, Status: Submitted to Monthly Notices of the Royal Astronomical Society (MNRAS, Manuscript ID: MN-15-0393-MJ)
- *Title: Ultra-violet Spectrum Synthesis of HD72660*
Authors: S.S. Golriz, J.D. Landstreet, Status: Submitted to Monthly Notices of the Royal Astronomical Society (MNRAS, Manuscript ID: MN-15-0604-MJ)

Name:	Sanaz Golriz
Post-Secondary Education and Degrees:	<p>Sharif University Of Technology Tehran, IRAN 2003–2008 BSc., Physics</p> <p>University of Western Ontario London, ON 2009 - 2011 MSc., Astrophysics</p> <p>University of Western Ontario London, ON 2011 - 2015 PhD, Astrophysics</p>
Honors and Awards:	<p>First Place Prize, Mathematical Olympiad Tehran, Iran, August-2001</p> <p>Third Place Prize, Provincial Competition in Mathematical Concepts Tehran, Iran, October-2003</p> <p>Nominated, Ontario Graduate Scholarship (OGS) London, Ontario, Canada, July-2011</p>
Related Work Experience:	<p>Teaching & Research Assistant The University of Western Ontario, London, Ontario, 2008 - 2012</p> <p>Private Tutor for Physics & Calculus (Grades 10-12 & University, Part Time) London, Ontario, Canada, 2009 - 2015</p> <p>Vector Marketing Corporation, Sales Representative (Part Time) Sear Outlet, Customer Service Representative (Part Time) London, Ontario, Canada, Summer & Fall 2014</p> <p>High School Tutor for Mathematics, Differential Equations, Electricity and Magnetism, General Physics Mullah-Sadra Institute, Tehran,Iran, 2003-2008</p> <p>Imen Tarh Engineering Inc., Administrative Assistant (Full Time) Tehran, Iran, 2008-2009</p>